

How cucumbers lost
their bitterness p. 1084

Shooting bullets through
graphene sheets p. 1092

A potential peptide treatment
for tetanus p. 1118

Science

\$10
28 NOVEMBER 2014
sciencemag.org

AAAS

Object of desire

A castaway from
ancient Mars p. 1044



CONTENTS

28 NOVEMBER 2014 • VOLUME 346 • ISSUE 6213



1058 & 1106

How collective memory forgets



1052 & 1078

RESEARCH

IN BRIEF

1074 From *Science* and other journals

REVIEW

1077 GENOME EDITING

The new frontier of genome engineering with CRISPR-Cas9 *J. A. Doudna and E. Charpentier*

REVIEW SUMMARY; FOR FULL TEXT:
dx.doi.org/10.1126/science.1258096

RESEARCH ARTICLES

1078 FUNGAL BIOGEOGRAPHY

Global diversity and geography of soil fungi *L. Tedersoo et al.*

RESEARCH ARTICLE SUMMARY; FOR FULL TEXT:
dx.doi.org/10.1126/science.1256688

► PERSPECTIVE P. 1052

1079 SYSTEMS BIOLOGY

Conditional density-based analysis of T cell signaling in single-cell data *S. Krishnaswamy et al.*

RESEARCH ARTICLE SUMMARY; FOR FULL TEXT:
dx.doi.org/10.1126/science.1250689

1080 BLACK HOLE PHYSICS

Black hole lightning due to particle acceleration at subhorizon scales *J. Aleksić et al.*

1084 PLANT SCIENCE

Biosynthesis, regulation, and domestication of bitterness in cucumber *Y. Shang et al.*

REPORTS

1089 PALEOMAGNETISM

Solar nebula magnetic fields recorded in the Semarkona meteorite *R. R. Fu et al.*

1092 MATERIALS SCIENCE

Dynamic mechanical behavior of multilayer graphene via supersonic projectile penetration *J.-H. Lee et al.*

1096 REPELLENT SURFACES

Turning a surface superrepellent even to completely wetting liquids *T. Liu and C.-J. Kim*

1100 MINERALOGY

Discovery of bridgmanite, the most abundant mineral in Earth, in a shocked meteorite *O. Tschauner et al.*

► PERSPECTIVE P. 1057

1102 CHEMICAL OCEANOGRAPHY

Increasing anthropogenic nitrogen in the North Pacific Ocean *I.-N. Kim et al.*

1106 COGNITIVE PSYCHOLOGY

Forgetting the presidents *H. L. Roediger III and K. A. DeSoto*

► PERSPECTIVE P. 1058

1109 MITOCHONDRIA

Cell cycle-dependent regulation of mitochondrial preprotein translocase *A. B. Harbauer et al.*

► PERSPECTIVE P. 1059

1113 PALEOGENOMICS

Genomic structure in Europeans dating back at least 36,200 years *A. Seguin-Orlando et al.*

1118 TETANUS TOXIN ENTRY

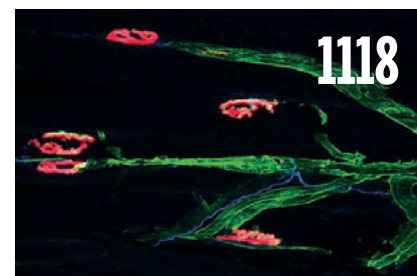
Nidogens are therapeutic targets for the prevention of tetanus *K. Bercsenyi et al.*

1123 T CELL SIGNALING

Antigen affinity, costimulation, and cytokine inputs sum linearly to amplify T cell expansion *J. M. Marchingo et al.*

1127 DNA REPAIR

Mechanism of DNA interstrand cross-link processing by repair nuclease FANCD1 *R. Wang et al.*



1118

ON THE COVER



A 239-gram piece of NWA 7034, or "Black Beauty," a 4.4-billion-year-old meteorite from Mars. The rock, valued at more than \$10,000 per gram, is both the oldest martian meteorite and the first one made

of pieces that were once eroded by wind or water. One of more than a dozen pieces that fell into the Sahara desert, this sample was the first to be recognized as martian. See page 1044. Photo: © Joe McNally

SCIENCE (ISSN 0036-8075) is published weekly on Friday, except the last week in December, by the American Association for the Advancement of Science, 1200 New York Avenue, NW, Washington, DC 20005. Periodicals mail postage (publication No. 484460) paid at Washington, DC, and additional mailing offices. Copyright © 2014 by the American Association for the Advancement of Science. The title SCIENCE is a registered trademark of the AAAS. Domestic individual membership and subscription (51 issues): \$153 (\$74 allocated to subscription). Domestic institutional subscription (51 issues): \$1282. Foreign postage extra: Mexico, Caribbean (surface mail) \$55; other countries (air assist delivery) \$85. First class, airmail, student, and new address rates on request. Canadian rates with GST available upon request. GST #R1254 88122. Publications Mail Agreement Number 1069624. Printed in the U.S.A. Change of address: Allow 4 weeks, giving old and new addresses and 8-digit account number. Postmaster: Send change of address to AAAS, P.O. Box 96178, Washington, DC 20090-6178. Single-copy sales: \$10.00 current issue, \$15.00 back issue prepaid includes surface postage; bulk rates on request. Authorization to photocopy material for internal or personal use under circumstances not falling within the fair use provisions of the Copyright Act is granted by AAAS to libraries and other users registered with the Copyright Clearance Center (CCC) Transactional Reporting Service, provided that \$30.00 per article is paid directly to CCC, 222 Rosewood Drive, Danvers, MA 01923. The identification code for Science is 0036-8075. Science is indexed in the Reader's Guide to Periodical Literature and in several specialized indexes.

Editor-in-Chief Marcia McNutt

Executive Editor Monica M. Bradford **News Editor** Tim Appenzeller

Managing Editor, Research Journals Katrina L. Kelner

Deputy Editors Barbara R. Jasny, Andrew M. Sugden(UK), Valda J. Vinson, Jake S. Yeston

Research and Insights

SR. EDITORS Caroline Ash(UK), Gilbert J. Chin, Lisa D. Chong, Maria Cruz(UK), Julia Fahrenkamp-Uppenbrink(UK), Pamela J. Hines, Stella M. Hurtley(UK), Paula A. Kiberstis, Marc S. Lavine(Canada), Kristen L. Mueller, Ian S. Osborne(UK), Beverly A. Purnell, L. Bryan Ray, Guy Riddiough, H. Jesse Smith, Jelena Stajic, Peter Stern(UK), Phillip D. Szurmi, Brad Wible, Nicholas S. Wigginton, Laura M. Zahn **ASSOCIATE EDITORS** Brent Grocholski, Melissa R. McCartney, Margaret M. Moerchen, Sacha Vignieri **ASSOCIATE BOOK REVIEW EDITOR** Valerie B. Thompson **ASSOCIATE LETTERS EDITOR** Jennifer Sills **CHIEF CONTENT PRODUCTION EDITOR** Cara Tate **SR. CONTENT PRODUCTION EDITORS** Harry Jach, Trista Wagoner **CONTENT PRODUCTION EDITORS** Jeffrey E. Cook, Chris Filiatreau, Cynthia Howe, Lauren Kmec, Barbara P. Ordway **SR. EDITORIAL COORDINATORS** Carolyn Kyle, Beverly Shields **EDITORIAL COORDINATORS** Ramatoulaye Diop, Joi S. Granger, Lisa Johnson, Anita Wynn **PUBLICATIONS ASSISTANTS** Aneera Dobbins, Jeffrey Hearn, Dona Mathieu, Le-Toya Mayne Flood, Shannon McMahon, Scott Miller, Jerry Richardson, Rachel Roberts(UK), Alice Whaley(UK), Brian White **EXECUTIVE ASSISTANT** Anna Bashkirova **ADMINISTRATIVE SUPPORT** Janet Clements(UK), Michael Crabtree(UK, Intern), Lizanne Newton(UK), Maryrose Madrid, John Wood(UK)

News

NEWS MANAGING EDITOR John Travis **INTERNATIONAL EDITOR** Richard Stone **DEPUTY NEWS EDITORS** Daniel Clery(UK), Robert Coontz, Elizabeth Culotta, David Grimm, David Malakoff, Leslie Roberts **CONTRIBUTING EDITORS** Martin Enserink(Europe), Mara Hvistendahl (Asia) **SR. CORRESPONDENTS** Jeffrey Mervis, Elizabeth Pennisi **NEWS WRITERS** Adrian Cho, John Cohen, Jennifer Couzin-Frankel, Carolyn Gramling, Eric Hand, Jocelyn Kaiser, Kelly Servick, Robert F. Service, Erik Stokstad, Emily Underwood **INTERNS** David Shultz, Jia You **CONTRIBUTING CORRESPONDENTS** Pallava Bagla(South Asia), Michael Balter(Paris), John Bohannon, Ann Gibbons, Sam Kean, Richard A. Kerr, Eli Kintisch, Kai Kupferschmidt(Berlin), Andrew Lawler, Christina Larson(Beijing), Mitch Leslie, Charles C. Mann, Eliot Marshall, Virginia Morell, Dennis Normile(Tokyo), Heather Pringle, Tania Rabesandratana(Brussels), Gretchen Vogel(Berlin), Lizzie Wade(Mexico City) **CAREERS** Jim Austin(Editor), Donisha Adams **COPY EDITORS** Kara Estelle, Nora Kelly, Jennifer Levin **ADMINISTRATIVE SUPPORT** Scherraine Mack

Executive Publisher Alan I. Leshner

Publisher Kent R. Anderson **Chief Digital Media Officer** Rob Covey

BUSINESS OPERATIONS AND ADMINISTRATION DIRECTOR Deborah Rivera-Wienhold **BUSINESS SYSTEMS AND FINANCIAL ANALYSIS DIRECTOR** Randy Yi **MANAGER OF FULFILLMENT SYSTEMS** Marc Hawkins **SYSTEMS ANALYST** Nicole Mehmedovich **ASSISTANT DIRECTOR, BUSINESS OPERATIONS** Eric Knott **MANAGER, BUSINESS OPERATIONS** Jessica Tierney **BUSINESS ANALYSTS** Cory Lipman, Cooper Tilton, Celeste Troxler **FINANCIAL ANALYST** Jeremy Clay **RIGHTS AND PERMISSIONS ASSISTANT DIRECTOR** Emilie David **PERMISSIONS ASSOCIATE** Elizabeth Sandler **RIGHTS, CONTRACTS, AND LICENSING ASSOCIATE** Lili Kiser

MARKETING DIRECTOR Ian King **MARKETING MANAGER** Julianne Wielga **MARKETING ASSOCIATE** Elizabeth Sattler **SR. MARKETING EXECUTIVE** Jennifer Reeves **SR. ART ASSOCIATE, PROJECT MANAGER** Tzeitel Sorrosa **ART ASSOCIATE** Seil Lee **ASSISTANT COMMERCIAL EDITOR** Selby Frame **MARKETING PROJECT MANAGER** Angelissa McArthur **SR. WRITER** Bill Zimmer **PROGRAM DIRECTOR, AAAS MEMBER CENTER** Peggy Mihelich **FULFILLMENT SYSTEMS AND OPERATIONS** membership@aaas.org **MANAGER, MEMBER SERVICES** Pat Butler **SPECIALISTS** LaToya Casteel, Javia Flemmings, Latasha Russell **MANAGER, DATA ENTRY** Mickie Napoleoni **DATA ENTRY SPECIALISTS** JJ Regan, Jaimee Wise, Fiona Giblin

DIRECTOR, SITE LICENSING Tom Ryan **DIRECTOR, CORPORATE RELATIONS** Eileen Bernadette Moran **SR. PUBLISHER RELATIONS SPECIALIST** Kiki Forsythe **PUBLISHER RELATIONS MANAGER** Catherine Holland **PUBLISHER RELATIONS, EASTERN REGION** Keith Layson **PUBLISHER RELATIONS, WESTERN REGION** Ryan Rexroth **MANAGER, SITE LICENSE OPERATIONS** Iquo Edim **FULFILLMENT ANALYST** Lana Guz **ASSOCIATE DIRECTOR, MARKETING** Christina Schlecht **MARKETING ASSOCIATES** Thomas Landreth, Minah Kim

DIRECTOR OF WEB TECHNOLOGIES Ahmed Khadr **SR. DEVELOPER** Chris Coleman **DEVELOPERS** Dan Berger, Jimmy Marks **SR. PROJECT MANAGER** Trista Smith **SYSTEMS ENGINEER** Luke Johnson **PRODUCT MANAGER** Walter Jones

CREATIVE DIRECTOR, MULTIMEDIA Martyn Green **DIRECTOR OF ANALYTICS** Enrique Gonzales **SR. WEB PRODUCER** Sarah Crespi **WEB PRODUCER** Alison Crawford **VIDEO PRODUCER** Nguyen Nguyen **SOCIAL MEDIA PRODUCER** Meghna Sachdev

DIRECTOR OF OPERATIONS PRINT AND ONLINE Lizabeth Harman **PRINT PRODUCTION DIRECTOR** Wendy K. Shank **PREFLIGHT MANAGER** Marcus Spiegler **ASSISTANT MANAGER ONLINE** Lisa Stanford **ASSISTANT MANAGER PRINT** Rebecca Doshi **SR. SPECIALISTS** Steve Forrester, Jason Hillman, Antoinette Hodal, Tara Kelly, Anthony Rosen **SPECIALISTS** Jacob Hedrick, Nichole Johnston, Lori Murphy, Kimberley Oster

DESIGN DIRECTOR Beth Rakouskas **ASSOCIATE ART DIRECTOR** Laura Creveling **SR. ILLUSTRATORS** Chris Bickel, Katharine Sutliff **ILLUSTRATOR** Valerie Altounian **SR. ART ASSOCIATES** Holly Bishop, Preston Huey **ART ASSOCIATES** Kay Engman, Garvin Grullón, Chrystal Smith **SR. PHOTO EDITOR** William Douthitt **PHOTO EDITOR** Leslie Blizard

DIRECTOR, GLOBAL COLLABORATION, CUSTOM PUBLICATIONS, ADVERTISING Bill Moran **EDITOR, CUSTOM PUBLISHING** Sean Sanders: 202-326-6430 **ASSISTANT EDITOR, CUSTOM PUBLISHING** Tianna Hicklin: 202-326-6463 **ADVERTISING MARKETING MANAGER** Justin Sawyers: 202-326-7061 **science_advertising@aaas.org** **ADVERTISING MARKETING ASSOCIATE** Javia Flemmings **ADVERTISING SUPPORT MANAGER** Karen Foote: 202-326-6740 **ADVERTISING PRODUCTION OPERATIONS MANAGER** Deborah Tompkins **SR. PRODUCTION SPECIALIST/GRAPHIC DESIGNER** Amy Hardcastle **PRODUCTION SPECIALIST** Yuse Lajminmuhip **SR. TRAFFIC ASSOCIATE** Christine Hall **SALES COORDINATOR** Shirley Young **ASSOCIATE DIRECTOR, COLLABORATION, CUSTOM PUBLICATIONS/CHINA/TAIWAN/KOREA/SINGAPORE** Ruolei Wu: +86-186 0822 9345, rwu@aaas.org **COLLABORATION/CUSTOM PUBLICATIONS/JAPAN** Adarsh Sandhu + 81532-81-5142 asandhu@aaas.org **EAST COAST/CANADA** Laurie Faraday: 508-747-9395, FAX 617-507-8189 **WEST COAST/W. CANADA** Lynne Stickrod: 415-931-9782, FAX 415-520-6940 **MIDWEST** Jeffrey Dembski: 847-498-4520 x3005, Steven Loerch: 847-498-4520 x3006 **UK EUROPE/ASIA** Roger Goncalves: TEL/FAX +41 43 243 1358 **JAPAN** Katsuyoshi Fukumizu(Tokyo): +81-3-3219-5777 kfukumizu@aaas.org **CHINA/TAIWAN** Ruolei Wu: +86-0082-9345

WORLDWIDE ASSOCIATE DIRECTOR OF SCIENCE CAREERS Tracy Holmes: +44 (0) 1223 326525, FAX +44 (0) 1223 326532 tholmes@science-int.co.uk **CLASSIFIED** advertise@sciencecareers.org **U.S. SALES** Tina Burks: 202-326-6577, Nancy Toema: 202-326-6578 **SALES ADMINISTRATOR** Marci Gallun **EUROPE/ROW SALES** Axel Gesatzki, Sarah Lelarge **SALES ASSISTANT** Kelly Grace **JAPAN** Hiroyuki Mashiki(Kyoto): +81-75-823-1109 hmashiki@aaas.org **CHINA/TAIWAN** Ruolei Wu: +86-186 0822 9345 rwu@aaas.org **MARKETING MANAGER** Allison Pritchard **MARKETING ASSOCIATE** Aimee Aponte

AAAS BOARD OF DIRECTORS **RETIRING PRESIDENT, CHAIR** Phillip A. Sharp **PRESIDENT** Gerald R. Fink **PRESIDENT-ELECT** Geraldine (Geri) Richmond **TREASURER** David Evans **SHAW CHIEF EXECUTIVE OFFICER** Alan I. Leshner **BOARD** Bonnie L. Bassler, May R. Berenbaum, Carlos J. Bustamante, Claire M. Fraser, Laura H. Greene, Elizabeth Loftus, Raymond Orbach, Inder M. Verma

SUBSCRIPTION SERVICES For change of address, missing issues, new orders and renewals, and payment questions: 866-434-AAAS (2227) or 202-326-6417, FAX 202-842-1065. Mailing addresses: AAAS, P.O. Box 96178, Washington, DC 20090-6178 or AAAS Member Services, 1200 New York Avenue, NW, Washington, DC 20005

INSTITUTIONAL SITE LICENSES 202-326-6755 **REPRINTS:** Author Inquiries 800-635-7181 **COMMERCIAL INQUIRIES** 803-359-4578 **PERMISSIONS** 202-326-6765, permissions@aaas.org **AAAS Member Services** 202-326-6417 or http://membercentral.aaas.org/discouints

Science serves as a forum for discussion of important issues related to the advancement of science by publishing material on which a consensus has been reached as well as including the presentation of minority of conflicting points of view. Accordingly, all articles published in Science—including editorials, news and comment, and books reviews—are signed and reflect the individual views of the authors and not official points of view adopted by AAAS or the institutions with which the authors are affiliated.

INFORMATION FOR AUTHORS See pages 680 and 681 of the 7 February 2014 issue or access www.sciencemag.org/about/authors

SENIOR EDITORIAL BOARD

A. Paul Alivisatos, Lawrence Berkeley Nat'l Laboratory, Ernst Fehr, U. of Zürich
Susan M. Rosenberg, Baylor College of Medicine, Michael S. Turner, U. of Chicago

BOARD OF REVIEWING EDITORS

(Statistics board members indicated with \$)
Adriano Aguzzi, U. Hospital Zürich
Takuzo Aida, U. of Tokyo
Leslie Aiello, Wenner-Gren Foundation
Judith Allen, U. of Edinburgh
Sonia Altizer, U. of Georgia
Virginia Armbrust, U. of Washington
Sebastian Amigorena, Institut Curie
Kathryn Anderson, Memorial Sloan-Kettering Cancer Center
Peter Andolfatto, Princeton U.
Meinrat O. Andreae, Max-Planck Inst. Mainz
Paola Ariotta, Harvard U.
Johan Auwerx, EPFL
David Awschalom, U. of Chicago
Jordi Bascompte, Estación Biológica de Doñana CSIC
Facundo Batista, London Research Inst.
Ray H. Baughman, U. of Texas, Dallas
David Baum, U. of Wisconsin
Kamran Behnia, ESPCI-ParisTech
Yasmine Belkaid, NIAID, NIH
Philip Benfey, Duke U.
Stephen J. Benkovic, Penn State U.
Carlo Beenakker, Leiden U.
Gabriele Bergers, U. of California, San Francisco
Christophe Bernard, Aix-Marseille U.
Bradley Bernstein, Massachusetts General Hospital
Peer Bork, EMBL
Bernard Bourdon, Ecole Normale Supérieure de Lyon
Chris Bowler, Ecole Normale Supérieure
Ian Boyd, U. of St. Andrews
Emily Brodsky, U. of California, Santa Cruz
Ron Brookmeyer, U. of California Los Angeles (\$) **Christian Büchel**, U. Hamburg-Eppendorf
Joseph A. Burns, Cornell U.
Gyorgy Buzsaki, New York U. School of Medicine
Blanche Capel, Duke U.
Mats Carlsson, U. of Oslo
David Clapham, Children's Hospital Boston
David Clary, U. of Oxford
Joel Cohen, Rockefeller U., Columbia U.
Jonathan D. Cohen, Princeton U.
James Collins, Boston U.
Robert Cook-Deegan, Duke U.
Alan Cowman, Walter & Eliza Hall Inst.
Robert H. Crabtree, Yale U.
Roberta Croce, Vrije Universiteit
Janet Currie, Princeton U.
Jeff L. Dangl, U. of North Carolina
Tom Daniel, U. of Washington
Frans de Waal, Emory U.
Stanislas Dehaene, Collège de France
Robert Desimone, MIT
Claude Desplan, New York U.
Ap Dijksterhuis, Radboud U. of Nijmegen
Dennis Discher, U. of Pennsylvania
Gerald W. Dorn II, Washington U. School of Medicine
Jennifer A. Doudna, U. of California, Berkeley
Bruce Dunn, U. of California, Los Angeles
Christopher Dye, WHO
Todd Ehlers, U. of Tuebingen
David Ehrhardt, Carnegie Inst. of Washington
Tim Elston, U. of North Carolina at Chapel Hill
Gerhard Ertl, Fritz-Haber-Institut, Berlin
Barry Everitt, U. of Cambridge
Ernst Fehr, U. of Zurich
Anne C. Ferguson-Smith, U. of Cambridge
Michael Feuer, The George Washington U.
Kate Fitzgerald, U. of Massachusetts
Peter Fratzl, Max-Planck Inst.
Elaine Fuchs, Rockefeller U.
Daniel Geschwind, UCLA
Andrew Gewirth, U. of Illinois
Karl-Heinz Glassmeier, TU Braunschweig
Ramon Gonzalez, Rice U.
Julia R. Greer, Caltech
Elizabeth Grove, U. of Chicago
Kip Guy, St. Jude's Children's Research Hospital
TaeKjip Ha, U. of Illinois at Urbana-Champaign
Christian Haass, Ludwig Maximilians U.
Steven Hahn, Fred Hutchinson Cancer Research Center
Michael Hasselmo, Boston U.
Martin Heimann, Max-Planck Inst. Jena
Yia X. Heiarutzu, U. of Cambridge
James A. Hendler, Rensselaer Polytechnic Inst.
Janet C. Hering, Swiss Fed. Inst. of Aquatic Science & Technology
Michael E. Himmel, National Renewable Energy Lab.
Kai-Uwe Hinrichs, U. of Bremen
Kei Hirose, Tokyo Inst. of Technology
David Holdell, U. of Cambridge
David Holden, Imperial College
Lora Hooper, UT Southwestern Medical Ctr. at Dallas
Raymond Huey, U. of Washington
Steven Jacobson, U. of California, Los Angeles
Kai Johnson, EPFL Lausanne
Peter Jonas, Inst. of Science & Technology (IST) Austria
Matt Kaebberlein, U. of Washington
William Kaelin Jr., Dana-Farber Cancer Inst.
Daniel Kahne, Harvard U.
Daniel Kammen, U. of California, Berkeley
Masashi Kawasaki, U. of Tokyo
Joel Kingsolver, U. of North Carolina at Chapel Hill
Robert Kingston, Harvard Medical School
Eitonne Koechlin, Ecole Normale Supérieure
Alexander Koldobin, Johns Hopkins U.
Roberto Kolter, Harvard Medical School
Alberto R. Kornblihtt, U. of Buenos Aires
Leonid Kruglyak, UCLA
Thomas Langer, U. of Cologne
Mitchell A. Lazar, U. of Pennsylvania
David Lazer, Harvard U.
Thomas Lecuit, IBDM
Virginia Lee, U. of Pennsylvania
Stanley Lemon, U. of North Carolina at Chapel Hill
Ottoline Leyser, Cambridge U.
Marcia C. Linn, U. of California, Berkeley
Jianguo Liu, Michigan State U.
Luis Liz-Marzan, CIC biomaGUNE
Jonathan Losos, Harvard U.
Ke Lu, Chinese Acad. of Sciences
Christian Lüscher, U. of Geneva
Laura Machesky, CRUK Beatson Inst. for Cancer Research
Anne Magurran, U. of St. Andrews
Oscar Marin, CSIC & U. Miguel Hernández
Charles Marshall, U. of California, Berkeley
C. Robertson McClung, Dartmouth College
Graham Medley, U. of Warwick
Yasushi Miyashita, U. of Tokyo
Richard Morris, U. of Edinburgh
Alison Moutsier-Reif, NC State U. (\$) **Sean Munro**, MRC Lab. of Molecular Biology
Thomas Murray, The Hastings Center
James Nelson, Stanford U. School of Med.
Karen Nelson, J. Craig Venter Institute
Daniel Neumark, U. of California, Berkeley
Timothy W. Nilsen, Case Western Reserve U.
Par Nordlund, Karolinska Inst.
Helga Nowotny, European Research Advisory Board
Ben Olken, MIT
Joe Orenstein, U. of California
Berkeley & Lawrence Berkeley National Lab
Harry Orr, U. of Minnesota
Andrew Oswald, U. of Warwick
Steve Palumbi, Stanford U.
Jane Parker, Max-Planck Inst. of Plant Breeding Research
Giovanni Parmigiani, Dana-Farber Cancer Inst. (\$) **Donald R. Paul**, U. of Texas, Austin
John H. A. Petri, Memorial Sloan-Kettering Cancer Center
Joshua Plotkin, U. of Pennsylvania
Albert Polman, FOM Institute AMOLF
Philippe Poulin, CNRS
David Randall, Colorado State U.
Colin Renfrew, U. of Cambridge
Felix Rey, Institut Pasteur
Trevor Robbins, U. of Cambridge
Jim Roberts, Fred Hutchinson Cancer Research Ctr.
Barbara A. Romanowicz, U. of California, Berkeley
Jens Rostrup-Nielsen, Haldor Topsøe
Mike Ryan, U. of Texas, Austin
Shin-ichi Sakata, Kyoto U.
Shimon Saitoku, Kyoto U.
Miquel Salmeron, Lawrence Berkeley National Lab
Jürgen Sandkühler, Medical U. of Vienna
Alexander Schlier, Harvard U.
Randy Seeley, U. of Cincinnati
Vladimir Shalae, Purdue U.
Anne C. Siliciano, Johns Hopkins School of Medicine
Joseph Silk, Institut d'Astrophysique de Paris
Denis Simon, Arizona State U.
Alison Smith, John Innes Centre
Richard Smith, U. of North Carolina (\$) **John Speakman**, U. of Aberdeen
Allan C. Spradling, Carnegie Institution of Washington
Jonathan Sprent, Garvan Inst. of Medical Research
Erie Steig, U. of Washington
Paula Stephan, Georgia State U. and National Bureau of Economic Research
Molly Stevens, Imperial College London
V. S. Subrahmanian, U. of Maryland
Ira Tabas, Columbia U.
Sarah Teichmann, Cambridge U.
John Thomas, North Carolina State U.
Shubha Tole, Tata Institute of Fundamental Research
Christopher Tyler-Smith, The Wellcome Trust Sanger Inst.
Herbert Virgin, Washington U.
Bert Vogelstein, Johns Hopkins U.
Cynthia Volkert, U. of Göttingen
Douglas Wallace, Dalhousie U.
David Wallace, Weizmann Inst. of Science
Ian Walmesley, U. of Oxford
David A. Warshaw, Swedish U. of Agric. Sciences
David Waxman, Fudan U.
Jonathan Weissman, U. of California, San Francisco
Chris Wikle, U. of Missouri (\$) **Ian A. Wilson**, The Scripps Res. Inst. (\$) **Timothy D. Wilson**, U. of Virginia
Rosemary Wyse, Johns Hopkins U.
Jean Zaanen, Leiden U.
Kenneth Zaret, U. of Pennsylvania School of Medicine
Jonathan Zehr, U. of California, Santa Cruz
Len Zon, Children's Hospital Boston
Maria Zuber, MIT

BOOK REVIEW BOARD

David Bloom, Harvard U. Samuel Bowring, MIT, Angela Creager, Princeton U., Richard Swedner, U. of Chicago, Ed Wasserman, DuPont

Innovating research in China

As the most populated country in the world, China carries an immense disease burden. Thanks to the rising life expectancy of its citizens, urbanization, and lifestyle changes that have accompanied rapid economic growth, the disease spectrum in China has expanded. Noncommunicable chronic conditions such as cardiovascular diseases, diabetes, and cancer are now major contributors to ill health. Fortunately, an overhaul of the national health care system has been under way, with universal health care coverage now available for more than 95% of the population. Such a sea change is also needed in China's biomedical research environment. This requires transforming a system that has existed for decades. The good news is that China is not shying away from this challenge.

Two national megaprojects were recently launched to address major bottlenecks: the development of innovative drugs and the control of major infectious diseases. The Major New Drug Innovation Program was funded with an ambitious goal of discovering 100 new drugs by 2020. Although China has seen a reduction in the incidence of infectious diseases over the past 10 years, hepatitis B and drug-resistant tuberculosis remain serious public health threats. The 2003 outbreak of SARS in China spurred the government to bolster early detection, disease research, and response systems. These improvements enabled the nation's rapid response and management of the avian influenza virus H7N9 in 2013. The current Ebola crisis is a reminder that newly emerging diseases are a major global threat. Indeed, China's Control and Prevention of Major Infectious Diseases Program was launched with the goal of establishing a support system for potential emerging diseases, in addition to controlling the incidence of major infectious diseases such as hepatitis B, tuberculosis, and HIV.

Whereas these initiatives will affect China's public health management, ensuring the implementation and success of other future initiatives will demand an innovative system of medical research as a new driving force.



“...a sea change is also needed in China's biomedical research environment.”

For many years, the Chinese Academy of Medical Sciences (CAMS) has played a pivotal role in spearheading biomedical research in China. As the country's most comprehensive and only national biomedical research organization, CAMS is prepared to lead the national effort by introducing a new medical research system. With strong support from the National Health and Family Planning Commission of China (formerly the Ministry of Health), CAMS has established the National Cancer Center, the National Center for Cardiovascular Diseases (NCCD), and integrated innovation research centers focusing on System Medicine, Neuroscience, Regenerative Medicine, and

Pharmaceutical Sciences. The goal of these new institutions is to integrate basic and clinical research and to provide new funding mechanisms to support China's best scientists and physicians. For example, the NCCD has a state-of-the-art infrastructure with the largest tissue banking system in the world. It has recruited top talent from different countries as well as in China and has forged collaborations with the world's leading universities and institutions. And there is more on the way: Research centers focusing on metabolic disorders, aging, inflammation, and infectious diseases are in the planning stages. In addition to strengthening an emphasis on frontier medical sciences, these centers will be encouraged to coordinate national efforts for large-scale, long-term transla-

tional and clinical research that focus on major diseases, something that cannot be accomplished by individual scientists or research groups.

CAMS is also planning to explore new ways to evaluate, support, and lead the next generation of medical researchers in China. Based on the experiences of successful biomedical research organizations in Europe and the United States, CAMS will emphasize an investigator's scientific merits and the strategic priority, novelty, and long-term objectives of research projects.

Building this innovative research system will bring China into a new era of research and development. The hope is that this will fuel health science advances to benefit China and the world.

— Xuetao Cao



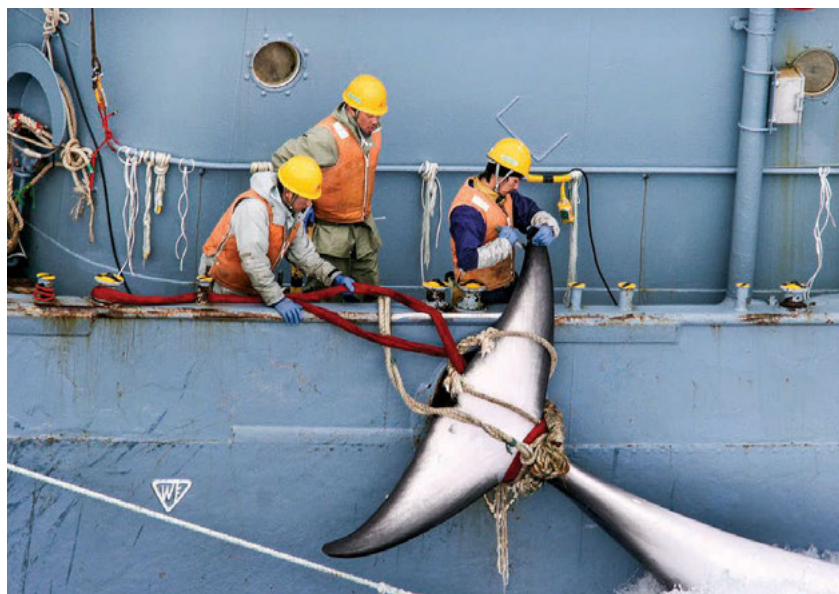
Xuetao Cao is president of the Chinese Academy of Medical Sciences (CAMS), president of Global Alliance for Chronic Disease (GACD), and president of the Federation of Immunological Societies of Asia-Oceania (FIMSA). E-mail: caoxt@immunol.org

“At times, I thought he was me.”

Stephen Hawking, on Facebook, praising actor Eddie Redmayne, who played him in the new movie *The Theory of Everything*.

IN BRIEF

New research whaling plan still divisive



A catcher ship of the Japanese whaling fleet hunts minke whales in the Southern Ocean in 2006.

Japan's widely anticipated new whaling research program for the Antarctic, unveiled on 18 November, sets a target of capturing 333 minke whales annually as part of a 12-year-long research effort with the stated aim to “achieve conservation” of Antarctic marine ecosystem resources while also pursuing “sustainable utilization.” The New Scientific Whale Research Program in the Antarctic Ocean replaces JARPA II, a similar program halted by the International Court of Justice (ICJ) in The Hague last March. JARPA II called for taking 850 minke whales, 50 humpbacks, and 50 fin whales annually, which the ICJ found was not scientifically justified. The new draft plan addresses the ICJ's findings one by one and explains why collecting accurate data on the ages of minke whales requires killing them; it also includes an appendix detailing why 333 whales are needed. Conservation organizations immediately denounced the new plan, suggesting that the research program remains a fig leaf to sidestep the International Whaling Commission's (IWC's) 1982 moratorium on commercial whaling. The draft plan, which is open to revision, will now be presented to IWC's Scientific Committee. <http://scim.ag/Japanwhaling>

AROUND THE WORLD

Big payoff for disease nonprofit

BETHESDA, MARYLAND | The Cystic Fibrosis Foundation announced last week that it made \$3.3 billion by selling the royalty rights to treatments that its funding helped develop. The charitable organization invested \$150 million in Boston-based Vertex Pharmaceuticals to create therapies for the fatal lung disease. The new deal with Royalty Pharma will “supercharge” the foundation's efforts, president and CEO Robert Beall said in a 19 November press release, by funding more drug discovery research and helping care for cystic fibrosis (CF) patients at centers accredited by the foundation. This increasingly popular profit model for foundations has received some criticism, however, for netting large royalties while patients pay for costly treatments. Vertex's first CF drug to win U.S. approval costs \$300,000 a year.

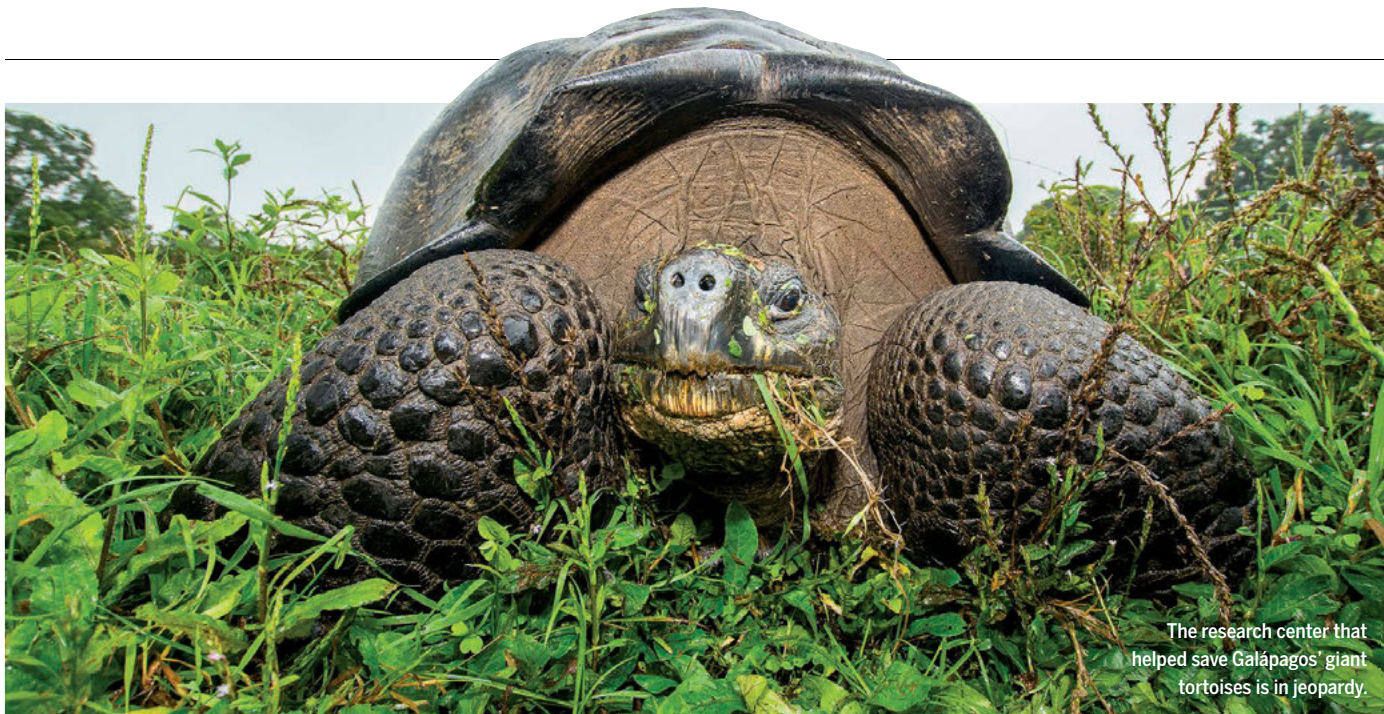
UNAIDS's push to end epidemic

GENEVA, SWITZERLAND | No HIV vaccine exists, but advances in prevention and treatment have led to a growing conviction that the HIV/AIDS epidemic can be halted with existing tools. A report released 18 November by the Joint United Nations Programme on HIV/AIDS (UNAIDS) emphasizes this point, yet cautions that the epidemic will continue to grow if treatment and prevention efforts remain at 2013 levels. The report, *Fast-Track: ending the AIDS epidemic by 2030*, notes that although antiretroviral treatments in lower income countries have helped slow new infections and AIDS-related deaths from 2012 to 2013, more ambitious goals need to be set. *Fast Track* says the key is to increase three things to 90%: people who know their HIV status, receive treatment, and adhere to medication so that the virus in their blood drops below detectable levels. <http://scim.ag/FastTrackAIDS>

Science agency under threat

BRUSSELS | Belgian researchers have launched a petition to save the country's federal science policy office (BELSPO).

PHOTO: © JEREMY SUTTON-HIBBERT/ALAMY



The research center that helped save Galápagos' giant tortoises is in jeopardy.

Galápagos guardian may shut its doors

A 50-year-old conservation organization in Ecuador's Galápagos Islands is about to fall off a financial cliff. The Charles Darwin Foundation has helped control invasive species such as goats and blackberries and helped restore endangered species such as giant tortoises and mangrove finches. Yet it's been on shaky financial ground after growing too fast a decade ago. A plan to sell off land and build a gift shop seemed to help—but a few months ago, a key sale fell through and local authorities shut down the

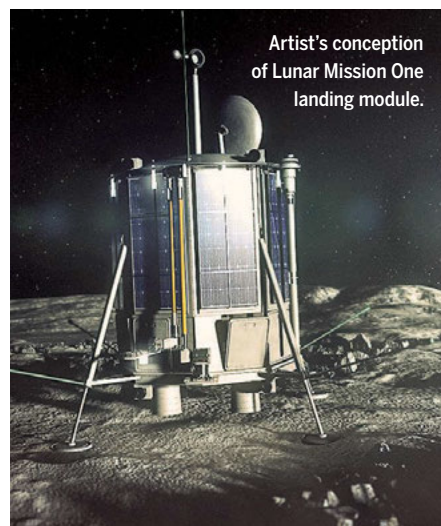
store. The foundation has launched an online fundraising campaign (#savedarwin) and membership drive; last week, it approached its largest supporters for a bailout. But as *Science* went to press, no one had stepped forward to help. If the foundation should close before the year's end, as predicted, that would be "a disaster for both fundamental research and conservation," says board member William Sutherland, a conservation biologist at the University of Cambridge in the United Kingdom. <http://scim.ag/Darwinshutdown>

The new center-right government plans to ax the funding and management agency, arguing the move will make Belgian science more efficient. Although a large part of the nation's science funds are managed at the regional level, BELSPO is in charge of 10 federal science institutes, funds basic research projects that bring together scientists from the country's different language communities, and manages Belgium's contribution to the European Space Agency, among other tasks. In a petition launched on 13 November, scientists urged the government to reverse the decision, saying it would push the country "below the threshold of scientific ... poverty." The plea had some 8500 signatures as *Science* went to press. <http://scim.ag/BELSPO>

Kick-starting a moon mission

LONDON | A British team is asking the public to donate £600,000 to send an unmanned lander to the moon in 10 years—and so far, the public is coming through. The crowdfunding campaign for Lunar Mission One kicked off on 19 November; as *Science* went to press,

it had earned £293,354. Founded by David Iron, a former Royal Navy engineering officer and financial consultant specializing in space projects, the project has earned the support of space scientists and politicians alike. The probe, which will land at the moon's south pole, will drill 20 to 100 meters into the lunar surface and bury



Artist's conception of Lunar Mission One landing module.

BY THE NUMBERS

\$2.6
billion

How much it takes to create a new drug and bring it to market, according to the Tufts Center for the Study of Drug Development.

\$186
million

A high estimate of new drug development costs, according to Doctors Without Borders, which notes that the Tufts center receives some funding from pharmaceutical companies.

a time capsule in it. To sweeten the deal, the team is offering funders a perk: the chance to leave some remnant—from a digital message to a strand of hair—in the capsule.

Immigration plan nods to science

WASHINGTON, D.C. | President Barack Obama announced changes to U.S. immigration policy on 20 November, including two moves that affect the research community. One would expand the Optional Practical Training (OPT) program, which enables foreign students studying science, technology, engineering, and mathematics (STEM) at U.S. universities to work in the United States for up to 29 months. Obama also wants to make it easier for foreign entrepreneurs to enter the country. Both steps will “make it easier and faster for high-skilled immigrants, graduates, and entrepreneurs to stay and contribute to our economy,” Obama said. <http://scim.ag/immplan>

Chinese undergrads flock to U.S.

WASHINGTON, D.C. | Almost as many Chinese students earn undergraduate

degrees in the United States as do graduate work, the result of surging interest in undergraduate studies and a flattening of demand for graduate training. Those new numbers—110,550 versus 115,727—come from the Institute of International Education (IIE), whose annual Open Doors report tracks the flow of international students into and from the United States. A report out last week from the Council of Graduate Schools highlighted another trend: U.S. graduate schools continue to be a huge draw for Indian students. First-year enrollment is up 27% this fall, on top of a 40% rise last year. But Indians remain largely indifferent to U.S. undergraduate degrees, IIE reports, composing only 3% of the foreign-born undergraduate pool compared with China's 30% share. <http://scim.ag/forstudinUS>

Pledges of new protected areas

SYDNEY, AUSTRALIA | The International Union for Conservation of Nature (IUCN) concluded its once-a-decade World Parks Congress last week, trumpeting a list of more than 70 conservation commitments announced by countries around the world,

including a promise from Bangladesh to create the country's first marine protected area and pledges from Madagascar and Gabon to expand marine protected areas in their territorial waters. “There has been a willingness to move beyond words to action,” said IUCN Director General Julia Marton-Lefèvre during the closing ceremony. The commitments were seen as a step toward achieving new conservation goals set out by the congress in a document dubbed The Promise of Sydney, which calls for protecting at least 17% of the world's land and 10% of its oceans by 2020. The 8-day congress attracted 6000 participants from more than 170 countries. <http://scim.ag/WorldParks>

NEWSMAKERS

French chemist to head ITER

ITER, the €13 billion international fusion reactor under construction in France, has chosen **Bernard Bigot**, chair of France's Alternative Energies and Atomic Energy Commission (CEA), as its next director general. Bigot will replace Osamu Motojima and will begin his 5-year term next year. Bigot, 64, studied physics and chemistry; he has held senior positions in government, academia, and industry and was appointed as head of CEA in 2009. ITER involves seven international partners—China, the European Union, India, Japan, South Korea, Russia, and the United States—and is years behind schedule and hugely over budget. Motojima, the second ITER director general, was heavily criticized in an external management review completed earlier this year. <http://scim.ag/BigotITER>

Obama nominates fatigue expert

Mark Rosekind, a psychologist who has demonstrated the benefits of brief naps and in-flight sleeping berths for pilots, has been tapped to head the National Highway Traffic Safety Administration. Rosekind led research into fatigue among airline pilots in the early 1990s at NASA's Ames Research Center in Mountain View, California. The beds he studied are now standard on such flights. In 2010, he was named to the federal National Transportation Safety Board, where he has advocated lowering the drunk driving threshold from 0.08 blood alcohol content to 0.05, something no state has done. The Senate must confirm his nomination to the highway safety agency, which has been criticized for not doing more to correct faulty car ignition switches and flawed air bags. <http://scim.ag/Rosekind>



Donald Rickelman received a left hand transplant in July 2011.

Restoring touch to reattached hands

Roughly 85 people worldwide have undergone hand replant or transplant surgery, in which surgeons reattach a patient's hand or one from a donor by stitching together nerves and blood vessels. It takes about 2 years for nerves in the hand to regenerate after surgery—and studies suggest that even after the nerves have regrown, the surgically attached hand is less sensitive to touch than the original hand was. Last week, however, at the Society for Neuroscience's annual conference in Washington, D.C., scientists presented evidence that touch can return to near normal. Brain imaging data suggest that the brain's sensory map reorganizes after surgery, gradually adapting to new sensations from the reattached hand. Damage directly to the brain is trickier to repair, but people who have experienced spinal cord injury and stroke “may have more potential to recover than we ever thought,” says Scott Frey, a computational neuroscientist at the University of Missouri, Columbia, who led the work. <http://scim.ag/transhandtouch>



INFECTIOUS DISEASES

A new phase in the Ebola war

As new cases drop in Liberia, experts call for a fresh strategy that would target flare-ups

By Kai Kupferschmidt, in Monrovia

When Kevin De Cock flew home from this city of 1 million in August, he was leaving behind an apocalyptic scene. More than 100 people were coming down with Ebola daily. Patients were dying outside of treatment units filled to capacity, and bodies lay rotting in the streets. Some mathematical models projected that Liberia would face thousands of new cases weekly by December. “There was really no way of knowing how much worse this might get,” says De Cock, an epidemiologist at the U.S. Centers for Disease Control and Prevention (CDC) in Atlanta.

But when he returned to Monrovia on 9 November, the situation was very different. The grim projections had been wrong. Although the Ebola epidemic is still growing in Sierra Leone, and Guinea’s numbers are swinging up and down, Liberia is now reporting only about 20 new patients a day. Treatment units have hundreds of empty beds, and Liberian President Ellen Johnson Sirleaf has lifted the state of emergency put in place in August. Now the country faces new challenges: rebuilding a shattered health care system, tamping down local outbreaks, and looking for ways to drive the number of new cases to zero.

No one here is quite sure what has caused the epidemic to wane. Safe burials may be a big factor, says Katri Jalava, a Finnish veterinarian and an epidemiological consultant to the World Health Organization.

It’s a local custom to wash the corpse and then use the same water to wash the hands of the bereaved, she says. “In terms of a disease like Ebola that is absolutely mad.” Most agree that people’s everyday behavior has changed as well. Ubiquitous street signs warn that “Ebola is real” and tell Monroviens “Don’t be the next case.” Outside many homes are small hand-washing stations with bleach, and Liberians have stopped hugging and shaking hands.

Yet “this is still a catastrophe,” De Cock says. Even 20 daily Ebola cases would have been unimaginable a year ago. And Guinea has shown that success in fighting Ebola

A gravedigger at the cemetery of the Ebola treatment unit in Suakoko District in Bong County.

can be short-lived: Twice, that country was on the cusp of ending the outbreak, and twice the virus came roaring back.

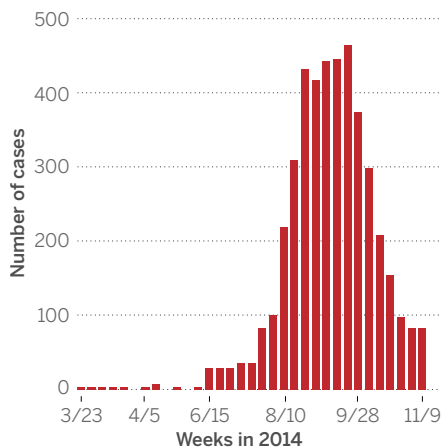
Some have even questioned whether Liberia’s recent drop in cases is real. At a meeting at the Liberian ministry of health last week, a U.S. Agency for International Development representative said he had been sent specifically to find out if the numbers can be trusted. “Yes,” answered Swedish statistician Hans Rosling, who has spent the past month in Monrovia helping the Liberian government interpret epidemiological data. CDC researchers, for instance, have used mouth swabs to test dead bodies in Monrovia for Ebola; about 20% to 30% are now positive, down from close to 90% during the height of the epidemic. The real number of cases may be twice the reported number, but not much more, Rosling says. “We’re in a new phase now.”

The international response has been slow to adapt. Although the Pentagon has said it will build fewer new Ebola treatment centers, their construction is ongoing. “That doesn’t make sense at all,” says Thierry Goffeau, emergency coordinator for Doctors Without Borders (MSF) in Liberia. “It’s clearly a waste of human and financial resources.” Rosling, too, says tactics have to change. In September, the main job was building clinics, removing the dead, and keeping as many patients as possible isolated. Now, it’s about setting up a flexible system to respond to new outbreaks, identifying patients quickly, and tracing their contacts to prevent more infections. “What we needed to do in the first phase was rugby,” Rosling says. “Now it is chess.”

Liberia’s medical system, which collapsed under the weight of Ebola, is gearing up again. Doctors are returning to work, and clinics are reopening. Goffeau says

Past its peak?

Confirmed and probable Ebola cases in Liberia, by week



that is sorely needed: “People are dying at home of many other diseases than Ebola, because they have no access to health care.” But medical staff still face an important risk. One in every hundred or thousand patients may carry the Ebola virus—which could start new cycles of infection. There are reports that doctors at some clinics are now doing surgery and delivering babies in Ebola protection suits.

At Redemption Hospital in Monrovia, whose inpatient department was closed this summer after several doctors died from Ebola, MSF is trying to protect staff with a new triage unit, which opened on 19 November. Patients with Ebola-like symptoms are interviewed; if they meet the criteria for a suspect case, they stay in one of 10 small rooms while their blood is tested. Those who test negative can enter the inpatient ward, while an ambulance takes Ebola patients to a treatment unit. MSF has also started distributing malaria drugs to hundreds of thousands of people, not just to lower the burden of that disease, which was neglected for months, but also to reduce the number of people visiting hospitals with a fever.

Reopening Monrovia’s schools poses similar quandaries. One idea is to screen pupils’ temperature as they enter the school. “But what do you do if a 10-year-old kid has a high temperature and the other kids start pointing at him and shouting ‘Ebola?’” Rosling says. In a meeting with President Sirleaf, he has argued for a cautious approach: Opening some schools and carefully studying what happens.

The capital region still serves as a reservoir from which patients travel to rural areas and spark fresh outbreaks, De Cock says—and now that the rainy season has ended, travel may pick up. In Bong County, for instance, a few hours northwest of Monrovia, two big outbreaks are spreading, at least one seeded from the capital. The treatment unit in the district of Suakoko, run by the International Medical Corps, is full, and new patients are brought in daily. Sambhavi Cheemalapati, the unit’s program coordinator, says she is seeing far more patients than are accounted for in the official numbers. Aid should focus on spreading prevention messages in these remote locales, Goffeau says. “If the people really understand what Ebola is and how to avoid infection, we might stop this epidemic,” he says.

Such regional flare-ups make it unlikely that the Liberian epidemic will be over anytime soon, Rosling says. Still, he believes it’s possible that the country may see its first day without a single case as early as December. Given the cataclysmic projections of just 2 months ago, that would be a remarkable turnaround. ■



Hayabusa 2 releases its impactor (artist's conception).

PLANETARY SCIENCE

Japan to assault asteroid

Hayabusa 2 will blast open carbon-rich celestial body

By Dennis Normile

Eighteen days after the European Space Agency’s Philae lander touched down on a comet, another spacecraft will set out to attempt an even more intimate encounter with a small solar system body. On 30 November, Hayabusa 2 will lift off from Japan’s Tanegashima Space Center on a 6-year round trip to asteroid 1999 JU3. If all goes as planned, it should bring home samples not just from the asteroid’s surface but also from beneath it, by blasting a crater and collecting ejecta.

“By comparing samples from the surface and from underground, we’ll get a better idea of what kind of material makes up asteroids and how it has changed over time,” says Sei-ichiro Watanabe, project scientist and a planetary scientist at Nagoya University. Observations of the impact will also provide clues about the kilometer-wide body’s structural properties, says Erik Asphaug, a planetary scientist at Arizona State University, Tempe, who is not involved with the mission. That could help scientists foretell the destruction in store should an asteroid ever hit Earth.

A decade ago, the original Hayabusa was the first probe to sample an asteroid. It snagged a few grains from asteroid Itokawa, an S-type, or stony, asteroid thought to have formed in the inner regions of the asteroid belt, where water and organic material have burned off. Overcoming fuel leaks and numerous equipment failures, Hayabusa delivered the samples to Earth in June 2010.

Its successor’s target is a carbonaceous, or C-type, asteroid from the outer regions of the asteroid belt, potentially bearing water and

organic elements. Watanabe says that combining findings from the two asteroids and the comet will help scientists sharpen their picture of the early solar system and which of its varied bodies might have brought water and organic material—the seeds of life—to Earth.

The roughly \$245 million Hayabusa 2 uses thrusters and stabilizers similar to but more robust than those of its predecessor, says Hitoshi Kuninaka, project manager at the Japan Aerospace Exploration Agency’s Institute of Space and Astronautical Science in Sagamihara. Hayabusa 2’s instruments are also largely updated versions of its predecessor’s, but “they are tuned for a C-type asteroid,” which has a very dark surface, Kuninaka says. The first Hayabusa carried a single small lander, which missed Itokawa and drifted off into space. Hayabusa 2 will release four landers carrying a variety of cameras and instruments. One, the Mobile Asteroid Surface Scout, or MASCOT, contributed by the German Aerospace Center and the French government space agency, will explore the surface by hopping across it.

Hayabusa 2’s most audacious gambit will be blasting that crater. The spacecraft will touch down to capture surface samples. Then it will release an explosive-laden impactor and duck behind the asteroid for safety. Detonating the explosives will drive a projectile into the asteroid at 2000 meters per second, digging a crater anywhere from 2 to 7 meters in diameter. “We really don’t know what the asteroid is made up of,” Watanabe says.

A floating camera will record the show. Once the dust settles, Hayabusa 2 will touch down near the crater, retrieve ejecta, and then head home. ■

China supersizes its underground physics lab

Planned expansion could pave way for “ultimate dark matter experiment”

By Dennis Normile

The world's deepest physics laboratory is about to become one of its largest. Early next year, workers will start carving four cavernous experiment halls along a tunnel through Jinping Mountain in China's Sichuan province. Once the science at the China Jinping Underground Laboratory (CJPL) is scaled up as well, “it will be a milestone for Chinese physics,” says Nigel Smith, director of the underground SNOLAB in Sudbury, Canada.

Opened in December 2010, CJPL is the deepest facility of its kind, with 2400 meters of rock shielding it from background radiation (see chart). The lab so far has focused on the hunt for dark matter, the universe's postulated missing mass. More space will allow larger and more sensitive dark matter detectors and an expanded research agenda that will include a nuclear astrophysics accelerator to replicate the inner workings of stars. CJPL also hopes to branch out into observing neutrinos and studying exotic particle phenomena.

Deep underground labs elsewhere have a head start in all of these areas. This means the Chinese will have to choose research targets carefully based on “if and where they can do better” than existing experiments, says Alessandro Bettini, director of the Canfranc Underground Laboratory in Spain. Others have confidence in the Chinese quickly coming up to speed. “It's a highly competitive site [with] lots of potential,” says John Ellis, a theorist at King's College London who chairs a new international advisory committee that visited the lab last month.

China's ascent in underground physics began serendipitously in August 2008, when Qian Yue, a physicist at Tsinghua University in Beijing, saw a TV report about access tunnels being bored through Jinping Mountain for a massive hydroelectric project. Tsinghua approached the Yalong River Hydropower Development Co. Ltd., which agreed to excavate two experiment halls totaling 4000 cubic meters along one of the tunnels (*Science*, 5 June 2009, p. 1246).

CJPL, run by Tsinghua, now hosts two dark matter experiments. The Particle and Astrophysical Xenon (PandaX) experiment uses a 37-kilogram liquid xenon target to watch for dark matter in the form of postulated weakly interacting massive particles (WIMPs). If

WIMPs exist, they should occasionally travel unmolested through the mountain and collide with a xenon nucleus, producing a flash of light. In the other experimental hall, the China Dark Matter Experiment (CDEX) aims to catch the electrical signal produced if a WIMP bumps into a nucleus within a germanium crystal. “There is complementarity” between the two approaches, says Henry Wong, a physicist at Academia Sinica's Institute of Physics in Taipei and member of the CDEX collaboration. Xenon detectors should be better at distinguishing a WIMP signal from flashes sparked by some kinds of background radiation, whereas the more sensitive germanium detectors ought to be able to spot interactions involving lighter WIMPs. Although neither experiment has yet detected a WIMP, they both have helped confirm results from

other labs indicating that WIMPs are likely to have very little mass.

For an initial effort, the results are “pretty decent,” says Wick Haxton, a theorist at the University of California, Berkeley. To boost its chances of sighting WIMPs and determining their mass, CJPL needs a larger volume of xenon, more germanium crystals, and better shielding. All of that requires more space. “If they significantly enlarge those experiments over the next couple years,” Haxton says, “they could end up being very competitive.”

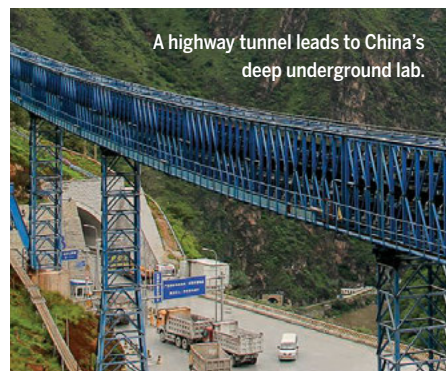
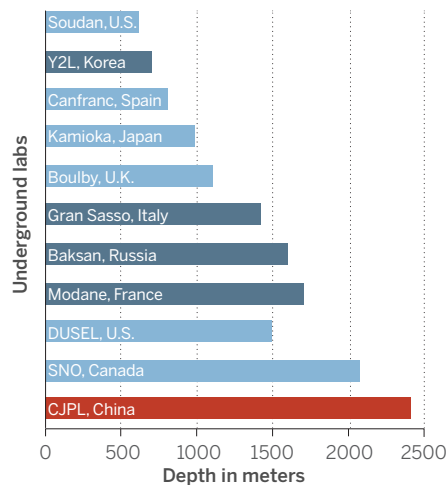
CJPL is about to get the elbow room it needs. Before the hydropower construction work wraps up next year, crews will bore another four 130-meter-long experiment halls. When lined with concrete, each will be 13.2 meters wide with an arched ceiling 13.2 meters high. All told, the enlarged facility will have 120,000 cubic meters of research space, second only to Italy's Gran Sasso National Laboratory, which has 180,000 cubic meters. By piggybacking on the hydropower project, Tsinghua limited the expansion's cost to \$50 million. Yue hopes to start experiments in the new halls by the end of 2016.

CDEX aims to boost its sensitivity by increasing its germanium target from 1 to 10 kilograms and by adding more elaborate shielding. The PandaX team is thinking much bigger. “We are interested in building the ultimate dark matter experiment: a 20-ton scale liquid xenon experiment,” says Xiangdong Ji, a physicist at Shanghai Jiao Tong University and the University of Maryland, College Park. That would be several times larger than existing liquid xenon experiments. Realizing such a mammoth project, says Ji, who leads PandaX, could require teams worldwide to pool resources.

A new experiment planned for the expanded space is the Jinping Underground laboratory for Nuclear Astrophysics (JUNA). Its pièce de résistance would be a particle accelerator used to replicate the nuclear processes generating energy within stars and the synthesis of heavier elements from hydrogen and helium in the primordial universe. The rock shielding would reduce background noise, making it easier for researchers to detect rare and subtle signals. With a more powerful accelerator and a deeper location than other efforts, says project head Weiping Liu, a physicist at the China Institute of Atomic Energy in Beijing, “JUNA has the potential to take a favorable position among underground nuclear astrophysics labs.” ■

Deep, dark labs

In the hunt for dark matter, deeper is better. Labs are built in mines (light blue) and tunnels (dark blue and red).



CLIMATE SCIENCE

Chasing South America's monsoon

Future of key rain pattern in doubt as climate negotiators gather in Peru

By Lizzie Wade

When delegates from nearly 200 nations gather in Lima next week to begin laying the groundwork for a new international accord to curb global warming, few may realize that they've stepped into the middle of a climate mystery. In the past few decades, researchers have recognized that tropical South America's summer rainy season, which fills parched rivers and brings new snow to rapidly shrinking mountain glaciers, is part of a larger monsoon system. They are now starting to unravel the complex dynamics of the system, which helps supply water to some 350 million people—and struggling to forecast how climate change may transform it.

"There [are] millions of people who rely on that water, and we take it for granted," says climate scientist Mathias Vuille of the University at Albany, State University of New York. "But it's a very, very sensitive system, and we have to be aware of that." He and other researchers have found hints that the monsoon pattern may already be changing. Now, they are turning to ancient lake sediments to reconstruct the monsoon's past behavior, and using simulations to see how the wet and dry seasons might shift in the future if nations can't agree on ways to reduce greenhouse gas emissions.

The South American monsoon is "not your typical monsoon," says Broxton Bird, a paleoclimatologist at the Indiana University-Purdue University Indianapolis School of Science. Traditionally, scholars defined a monsoon as a seasonal reversal in wind patterns that creates wet and dry seasons. That's exactly what happens over India, where the English word first came into common usage. There, it is "the Monsoon" with "a capital M," says Paul Baker, a geologist at Duke University in Durham, North Carolina.

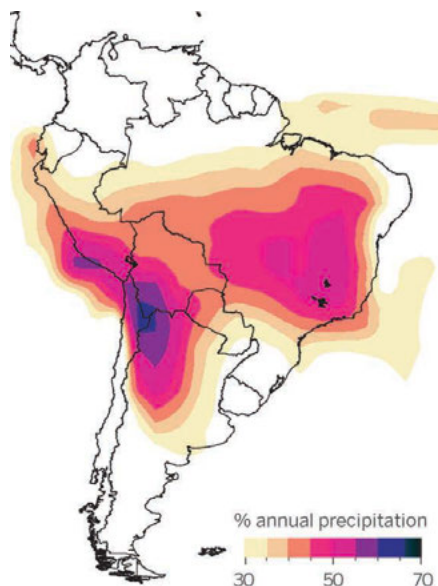
Over time, however, researchers "started talking more about monsoon with a little m," Baker says, using the term to refer to strong

seasonal changes in precipitation, not necessarily wind. In the late 1990s, researchers realized that a monsoon in this sense affects a large swath of South America, stretching from western Peru and northern Argentina across Amazonia to Brazil's east coast (see map). Each region's rainy season is not an independent, local phenomenon, but rather part of a climate web that reaches far beyond the continent's borders.

Understanding what drives the monsoon and why it varies from year to year is proving tricky. One obstacle is a lack of historical data. Researchers studying India's monsoon have benefited from "rain gauges ... that go back more than 100 years," says Charles Jones, a climate modeler at the University of California, Santa Barbara.

Rainmaker

Between 1979 and 2004, the South American monsoon provided more than half of the annual precipitation in some areas.



"We don't have [that] over the Amazon."

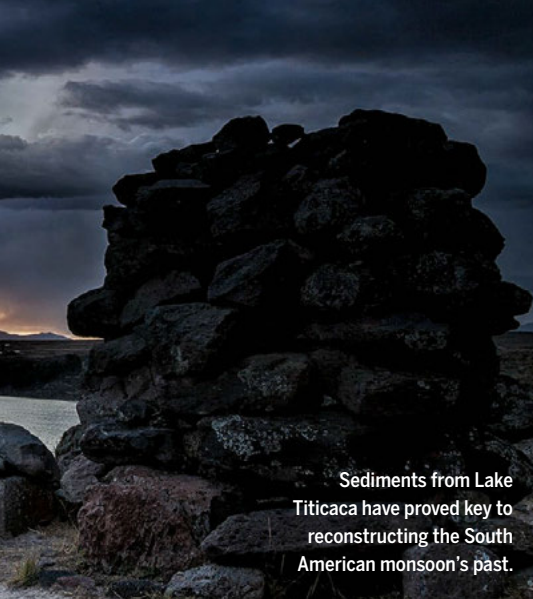
To fill the gap, some researchers are picking through sediment cores taken from lake bottoms, which hold clues to past climates. Baker, for instance, has reconstructed 25,000 years of South America's climate history by studying the remains of tiny aquatic plants, called phytoplankton, trapped in sediments from Lake Titicaca on the border of Peru and Bolivia. Because rainfall feeds the lake, it becomes shallower during weak monsoon years, causing plankton species that thrive under those conditions to boom. More shallow-water plankton in a sediment layer means a weaker monsoon at that time.

The sediments reveal a pattern: Over thousands of years, the South American monsoon was particularly strong when sea surface temperatures in the North Atlantic were relatively cool. But when the North Atlantic warmed, the monsoon rains weakened, the researchers reported in a 2001 paper in *Science*.

More recent studies have confirmed the link, and scientists believe they understand the mechanism. When the North Atlantic cools, Bird explains, the atmosphere's Intertropical Convergence Zone (ITCZ), an equatorial band typified by heavy clouds and precipitation, moves south. That leads to stronger summer monsoon rains. When the North Atlantic warms, however, the ITCZ and its moisture drift north, drying out the monsoon belt. Two recent record-breaking droughts in Amazonia, in 2005 and 2010, were associated with particularly warm periods in the North Atlantic, Bird notes.

Paleoclimate studies have also helped reveal that the monsoon has weakened in the past century. "The monsoon as we know it today is not necessarily representative of the conditions over the last 1000 years," Vuille says. "It's rather on the weak end of the spectrum."

What future global warming may do to the South American monsoon is unclear.



Sediments from Lake Titicaca have proved key to reconstructing the South American monsoon's past.

When researchers use computer models to create a world with twice as much atmospheric carbon dioxide as today and temperatures several degrees higher, they get mixed results. “Half of the models say ... it’s going to get wetter in the monsoon area, and the other half say it’s going to be drier,” Baker says. “Half the models are right, but we don’t know which half.”

The models do, however, tend to suggest the winter dry season could get longer. That may already be happening: The dry season is now “about 3 weeks to 1 month longer” than in recent decades, with the rains beginning in November instead of October, notes José Marengo, a senior scientist at the Brazilian National Institute for Space Research in São Paulo. Such extended dry spells could spell trouble for farmers and hydropower dams. (Brazil gets 80% of its electricity from dams, Marengo notes.) If the trend continues, the historic 2005 drought could become “the new norm” in southern Amazonia by the late 21st century, a team of climate researchers concluded in a 2013 paper in the *Proceedings of the National Academy of Sciences*.

Some models also hint that wet seasons could become shorter but more intense, says Hervé Douville, a climate modeler at the National Centre for Meteorological Research in Toulouse, France. That’s worrying because extreme rainfall can lead to flash floods and landslides, a particular concern because the monsoon belt includes hilly, densely populated cities.

Delegates heading to the Lima climate negotiations hope they can reduce such climate threats. The goal is to advance a follow-on pact to the 2005 Kyoto Protocol, which would be finalized in December 2015 at a meeting in Paris and then enter into force in 2020. Although South America’s monsoon isn’t likely to be a major topic in Lima, the meeting’s outcome could loom large in its future. ■

MEDICAL RESEARCH

U.S. to expand public access to clinical study results

Proposals would require sponsors to report data on thousands of additional trials each year

By Jocelyn Kaiser

The amount of clinical data that drug companies must share with the public would vastly expand under new rules proposed last week. A proposal from the U.S. Department of Health and Human Services (HHS) would require trial sponsors to report summary results for drugs and devices that are never approved, not just for those that reach the market. And a draft policy from the National Institutes of Health (NIH) would expand the requirement—which now applies only to trials regulated by the U.S. Food and Drug Administration (FDA)—to all trials funded by the health agency.

Sharing these results should not only be useful for researchers, but also “helps fulfill society’s ethical responsibility” to people who volunteer for trials, said NIH Director Francis Collins during a press teleconference. “We owe to our patients, to our participants in these trials, the explanation of what happened.”

The results would be posted on ClinicalTrials.gov, a public database launched in 2000 that now contains registration data for more than 178,000 trials regulated by FDA. Under existing rules, drug companies must also submit summary results that include information such as the number of participants, their age and gender, outcomes, and adverse events. These results have been posted for more than 15,000 trials.

But the summary results requirement applies only to drugs and devices approved by FDA. Under the HHS proposal, companies will also need to report results for unapproved products—although only for late-stage trials, not early safety trials, known as phase I. The new requirement together with the NIH proposal, which would require reports from roughly 650 trials a year, should add another 100 to 150 reports

to the 100 that the database now receives each week, said Deborah Zarin, director of ClinicalTrials.gov.

NIH officials cite a 2014 analysis of 400 clinical trials that found that 4 years after completion, 30% of the studies had not shared results in a journal or ClinicalTrials.gov. Under both the NIH and HHS draft rules, which won’t take effect until after the final policies are published, results must be reported within a year after the trial ends. Noncompliance could be punished by withholding funding for NIH grantees or imposing fines on companies regulated by FDA,

said Kathy Hudson, NIH’s deputy director for science, outreach, and policy.

Peter Doshi of the University of Maryland School of Pharmacy in Baltimore, an advocate of clinical data sharing, welcomes the new requirements. Hidden trial results are “not good from an evidence perspective and it’s embarrassing from a policy perspective,” he says. Requiring that trial results for unapproved drugs be shared is also a positive step, Doshi says. “You’re

reducing the chance that somebody will redo experiments that were already done and put people in harm’s way because the research wasn’t shared.” But Doshi says the U.S. plans compare unfavorably with Europe’s, where the European Medicines Agency plans to make detailed clinical data reports publicly available for approved drugs and to provide data on individual patients to researchers.

Doshi is an associate editor of *The BMJ*, which is part of a group called AllTrials that is pushing for release of detailed clinical trial data. “The white elephant in the room is that FDA sits on more data, across more drugs, across more therapeutic indications than anybody else on the planet,” he says. “And their attitude is, ‘Great idea [to make the data public], let somebody else take care of this.’” ■

Sharing clinical trial results “helps fulfill society’s ethical responsibility. ... We owe to our patients, to our participants in these trials, the explanation of what happened.”

Francis Collins, National Institutes of Health

FEATURES

By Eric Hand

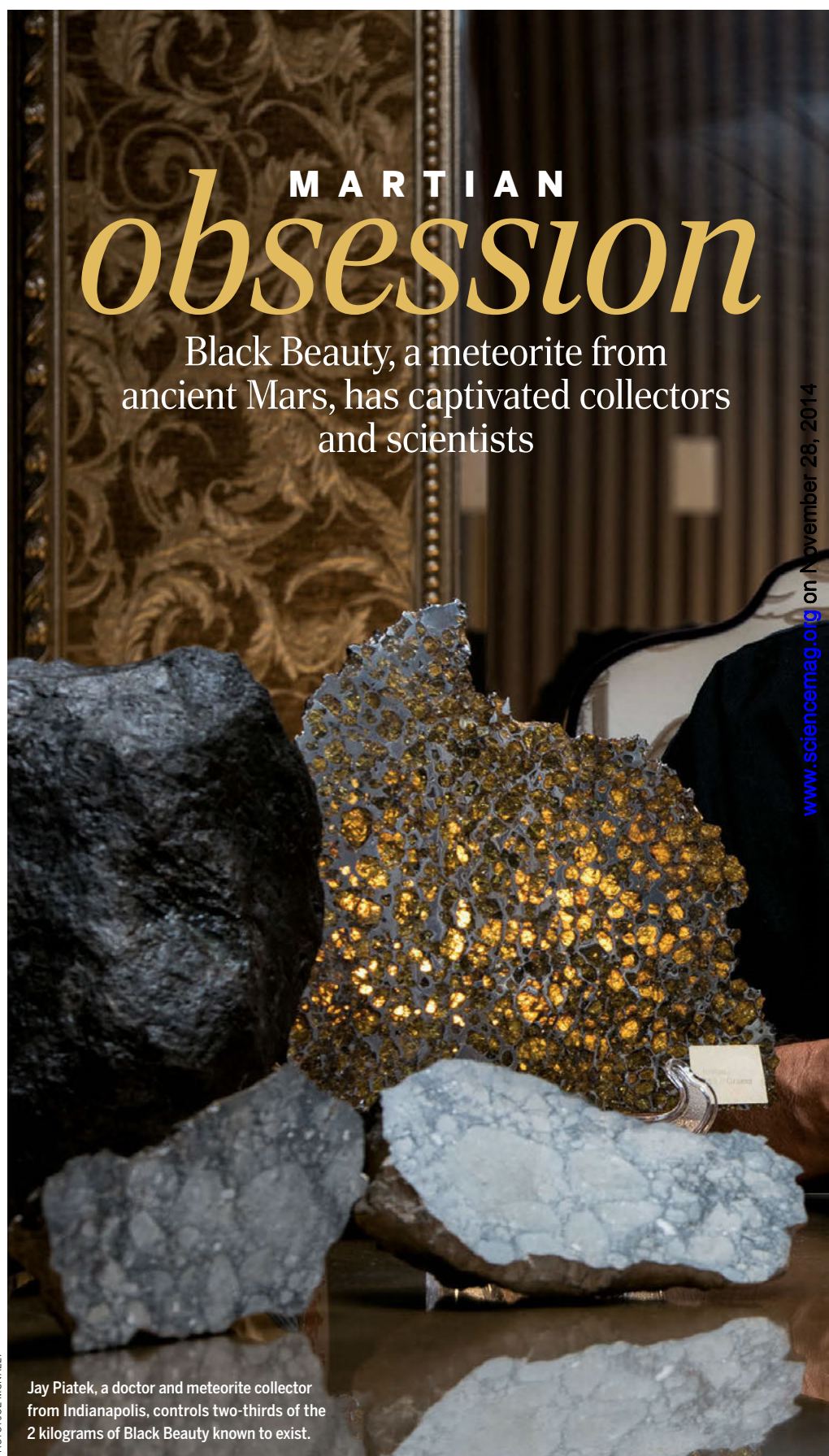
Jay Piatek pulls his Jaguar convertible onto the highway frontage road and turns past the billboard that bears his name and a slogan: *Weight loss. Health. Motivation.* It is here, at the Piatek Institute, on the bland, exurban edge of Indianapolis, that the doctor made his fortune, ministering to thousands of patients who struggle with eating compulsions.

Piatek has his own compulsions. Locked away at the clinic is a climate-controlled vault for his abiding passion: meteorites. With a near-photographic memory, he is able to rattle off the names and provenance of some of his more exotic specimens—Itzawisis, a pallasite found in Namibia; Gubba, a bencubbinite found in Nigeria. “They’re like little movie stars,” he says dreamily.

There is one diva in particular that I’m here to pay homage to: Black Beauty, a shiny, scaly-skinned, 4.4-billion-year-old rock from Mars. It began its journey to Earth more than 5 million years ago, about the time humans and chimpanzees were splitting from a common ancestor. That is when an asteroid struck Mars, catapulting the rock into space. Sometime in the last thousand years or so, orbital mechanics and gravity delivered the wandering rock to Earth. Surviving an incendiary plunge through the atmosphere, it landed in more than a dozen pieces in the western Sahara. There the fragments sat, untouched except by wind and sand. Finally, a nomad plucked a piece from the dunes. After passing through the hands of several Moroccan middlemen, the first piece wound up in Piatek’s hands in 2011. He would acquire nine more.

Black Beauty has since set the collecting world on fire, reaching values of more than \$10,000 per gram. (Gold trades for \$40 per gram.) The price is in no small part due to the parade of scientific discoveries emerging from the rock’s jumbled-up guts. It is the oldest rock from Mars and chock-full of the planet’s primordial water. Most intriguing of all, it appears to be the first martian meteorite made of sediment, deposited by wind or water. That makes Black Beauty not only a cosmic blessing—sedimentary rocks are fragile and thought unlikely to survive interplanetary launches—but also a boon for astrobiologists. “If you’re going to look for life, you want a sedimentary rock,” says Munir Humayun, a meteoriticist at Florida State University in Tallahassee who led a

PHOTO: JOE MCNALLY



Jay Piatek, a doctor and meteorite collector from Indianapolis, controls two-thirds of the 2 kilograms of Black Beauty known to exist.

MARTIAN *obsession*

Black Beauty, a meteorite from ancient Mars, has captivated collectors and scientists

www.sciencemag.org on November 28, 2014





In 2012 and 2013, hundreds of meteorite hunters combed the sands of the western Sahara for Black Beauty—and found pieces like this 241-gram specimen.

study that last year pinpointed the rock's age.

Even if it holds no trace of life, Black Beauty has plenty to captivate scientists. It is a breccia—a rock made of rocks, welded together in a fine-grained matrix. Each embedded pebble has a history to be unraveled. Black Beauty holds not just a geological story but an immense anthology. “We’re looking at the equivalent of a martian geological field area,” says Carl Agee, a meteoriticist at the University of New Mexico, Albuquerque.

Agee led the team that, in a 2013 publication in *Science*, was the first to recognize that Black Beauty was from Mars—and yet was unlike any of the other 74 known martian meteorites. As expensive as Black Beauty has become, it is still a bargain compared with proposals for a robotic Mars sample return mission. “I sort of half-jokingly say ‘Morocco sample return,’” Agee says. “Some of these meteorites, like Black Beauty, are the next best thing.”

About a dozen institutions have paid dearly—or traded choice holdings—for the privilege of working with tiny slices. Many more scientists are in the queue for pieces. And Piatek, through a combination of luck, money, and quick action, has cornered the market. He controls about two-thirds of the 2 kilograms of Black Beauty known to exist. The pieces are waiting for us at the clinic.

THE SUN HAS STARTED TO FALL on this steamy July day, but Piatek is just revving up as he parks. Entering the clinic, he shows me a room-sized tank stocked with tropical triggerfish, a tank so big that Piatek puts on a wetsuit and goes diving to clean it. There are empty patient waiting rooms, decked out in a style you might call Greco-Vegas: plastic fruit, purple drapes, faux-Doric col-

umns. A few hours before, they would have been filled with people waiting for 5-minute visits with Piatek and his prescriptions of hormones, vitamins, and stimulants. His fellow doctors may look askance, but Piatek doesn't really care. “They think we’re just giving out speed,” he says. “I’d rather have my patients love me. Screw my colleagues.”

Normally, Piatek keeps Black Beauty and his other most valuable specimens at a bank

“It was the most expensive stone of my life. ... I have never been so stressed.”

Aziz Habibi, meteorite dealer

vault. But he has just recently returned from the Smithsonian Institution National Museum of Natural History in Washington, D.C., where he attempted to make a trade, and so he hasn't yet returned the stones to the bank. They lie in a carry-on roller bag inside the clinic's vault. Piatek punches in numbers and tugs on the door. “Unbelievable,” he says. “Look at that.” The door handle is jammed.

He fetches some tools and pops out the hinges, but the door is still wedged. Piatek calls his niece to summon more muscle: her husband, Brock. “Tell him to bring a couple screwdrivers, and a few pliers, but not little ones.” Then he calls another number. “It’s me, Piatek. I’m coming in with a friend.” He hangs up and faces me. “Do you like steak?” he asks.

RUTH’S CHRIS STEAK HOUSE is Piatek’s customary retreat after watching Indiana Pacers basketball games from his courtside

seats. There, over steaks and California cabernet, Piatek begins the saga of a 4.4-billion-year-old rock and the 53-year-old man who owns it.

Piatek was born in Gary, Indiana, to a mother who worked in the steel mills. His adoptive father was a driver for the fire department. He spent college summers at the mill, working in the coke ovens. “It was, like, brutal,” he recalls. “You’re blowing your nose for 2 weeks afterwards and coke is coming out, and it’s not the coke that’s good.” Medical school at Indiana University opened the way to a different life.

After marriage, four children, and nearly a decade as an emergency room doctor, Piatek started his weight loss practice in 1995. Business was brisk. At one point, he was seeing 150 patients a day. But in 2003 his son was working on a fourth-grade school project on meteorites. “What’s a meteorite?” Piatek asked him—and an obsession was born. “I loved that you could get a piece of outer space that’s billions of years old, and you can hold it in your hand,” he says.

There are more than 50,000 named and classified meteorites. The vast majority are chondrites, pieces of asteroids filled with little glassy beads called chondrules. Much rarer—and more expensive—are meteorites from the moon, Mars, and other special bodies in the solar system, such as the asteroid Vesta. At first, Piatek was disappointed to learn that he couldn't own a piece of everything: Some were locked up in institutional collections, others destroyed or lost. He made a list of priorities and started hunting on eBay, quickly graduating to gem and mineralogy shows. At his peak, he had 1300 specimens. By comparison, Arizona State University, Tempe, which has the largest

university-owned collection in the world, has about 2000, says Meenakshi Wadhwa, the director of Arizona State's Center for Meteorite Studies, who recently traded with Piatek for a 20-gram cut of Black Beauty.

A few years ago, spurred by chest pains and intimations of his mortality, Piatek decided to cut back on both his working hours and his meteorite addiction. He brought on another doctor to do most of the work at the clinic. And he sold 400 of his specimens—including a couple of Black Beauty fragments—for more than a million dollars to Naveen Jain, a tech billionaire. Although the transaction delighted his wife, who never quite understood the value of collecting these rocks, Piatek winces at the memory. "I had stuff that no one had," he says. "I had the one that hit the lady, I had the one that hit the dog."

Piatek has whittled his collection down to a prized 400 or so. But his passion still burns. One paramount goal: completing his collection of pallasites, pretty meteorites that often contain green olivine crystals suspended in a gray matrix like luminous polka dots. Of the 59 pallasites that are possible to get (a few others reside in untouchable collections), Piatek has 57.

One, the El Rancho Grande pallasite, came in a trade from Agee, a genteel scholar who was once chief scientist for NASA's Johnson Space Center in Houston, Texas, and now curates the University of New Mexico's meteorite collection. "Our relationship was sealed at that point," Piatek says. He has donated more of Black Beauty to the University of New Mexico than anywhere else, elevating its collection from obscurity.

The relationship would prove crucial when it came to figuring out the rock's origin. In 2011, Piatek bought the first piece, a 320-gram mass, from Aziz Habibi, a dealer from Erfoud, Morocco, who had been regularly sending Piatek pictures of meteorites for sale—including one he called Black Beauty. Almost on a whim, Piatek paid \$6000 for the stone—cheap in the meteorite world—thinking it was nothing more than a regular chondrite. (Piatek says he later paid a bonus to Habibi when its true nature was revealed.)

Piatek sent the stone to Agee, who wasn't convinced that it was a meteorite at all. It didn't have the heft of a chondrite, which are typically rich in dense metals. And the scaly skin—the "fusion crust" that forms on the superheated surface of a falling meteorite—seemed so shiny that it might be fake. "I thought someone had taken a desert stone and spray-painted it," Agee says. Nonplussed, he stuck the rock on a shelf for a few months. Eventually, in the fall of 2011, he took a diamond-tipped rock saw, sliced

off one end of the stone—and marveled at what he saw inside. Dark, angular crystals of pyroxene floated alongside white, chunky feldspars. Large, faint pebbles sat next to tiny, dark beads. It was evocative of the lunar breccias Agee recalled from the Apollo days—except that Black Beauty's spherules were much more diverse.

Agee now knew he had a meteorite, but what was it? He chipped off a gram piece and put it under an electron microprobe, which uses an electron beam to excite atoms in the rock's minerals. The atoms then emit x-rays that reveal the sample's chemical makeup. It turned out that the rock had an elevated manganese-to-iron ratio—higher than that in Earth rocks and consistent with other martian meteorites. Next, Agee and his colleagues used a laser to extract water molecules trapped within minerals in the meteorite and fed them into a mass spectrometer to calculate the ratio of deuterium, a heavy isotope of hydrogen, to ordinary hydrogen. Every place in solar system has a distinctive ratio. Lo and behold, the copious water in Black Beauty was Mars-like.

Agee was convinced that Black Beauty was from Mars—and also that it was unlike all the other martian meteorites. In a talk at the Lunar and Planetary Science Conference in Texas in March 2012, he and his team described the rock as a volcanic breccia—a mélange of mineral crystals that formed

underground in different slow-cooling magma chambers and were blasted together and fused by an explosive eruption.

After Agee's team published their findings in *Science* in February 2013, Piatek's life instantly became more complicated. "You guys killed me," he says. Almost overnight, Moroccan dealers raised their asking prices for chunks of Black Beauty from tens to hundreds to thousands of dollars per gram. And while Piatek had previously had the market to himself, he now had rivals. Chief among them was another doctor-cum-collector: a Frenchman named Luc Labenne. "I knew he was going to be my competition," Piatek says. "Then, it was on."

LABENNE HAS A SMALL PIECE OF MARS

in the pocket of his bright red pants. He came to Casablanca, Morocco, this past September for the annual meeting of the Meteoritical Society. Like many collectors and dealers, Labenne cares deeply about the science and spends much of his time at the conference diligently attending the scientific sessions—especially the dozen talks that focus on Black Beauty. But he is also here to do business. He has just paid a local dealer nearly €10,000 for a 25-gram martian meteorite called a shergottite. The most common type of martian meteorite, shergottites are relatively cheap and not nearly as scientifically interesting as Black Beauty, but this particular rock's delicate fusion crust should boost its value. "It's just magnificent," he says. "It's black and fresh. So great."

Like Piatek, Labenne is a semiretired physician. But unlike the frenetic Piatek, Labenne is contemplative and keeps his own counsel. He often takes several trips a year to Libya, Morocco, Chile, and Oman to hunt for meteorites with his brother. Driving slowly and systematically across the desert from sunup until sundown, he takes a quiet pleasure in scanning the landscape for dark objects that don't belong. At night, he uses LED lights to search for meteorites near the campsite—and has found two lunar meteorites this way. Labenne owns seven pieces of Black Beauty, the second most after Piatek, and has been a primary source of material for scientists in Europe.

During a coffee break at the conference, Labenne lurks quietly behind Habibi, the flashy, chain-smoking impresario of Morocco's meteorite dealers. Habibi has a suitcase open and is showing off samples to scientists, unwrapping them from foil or old socks. He was hooked on fossils and meteorites as a teenager, when he explored the quarries in his hometown, Erfoud, for ammonites, the nautilus-shaped mollusks that lived hundreds of millions of years ago. Habibi now operates a 140-room hotel in Erfoud, but his

A winding journey

The martian meteorite called Black Beauty is the oldest in existence.

4.4 billion years ago

The earliest pieces of Black Beauty form in a subterranean magma chamber.

5 million years ago

An asteroid impact strikes Mars, launching Black Beauty from the surface and toward Earth.

<1000 years ago

Black Beauty falls in the dunes of the Sahara desert in more than a dozen pieces.

2011

Jay Piatek, a doctor from Indiana, acquires a first 320-gram piece.

2012

Researchers identify Black Beauty as a 2.1-billion-year-old volcanic rock from Mars.

2013

Martian origin confirmed and published; samples reinterpreted as sedimentary, 4.4 billion years old.

main love is meteorites—and the wheeling and dealing in them.

In 2011, Habibi was in the town of Agadir, recovering from gallstone surgery, when he met another dealer who offered him a shiny black stone. No one could agree what it was, or was worth, and Habibi passed on it. But as he was driving away, he had second thoughts. He turned around and made a deal for the first, 320-gram piece of Black Beauty.

With meteorites, where there is one, there are usually more. In 2012, as reports of Black Beauty's significance began circulating, Habibi went searching. He worked upstream from the Agadir dealer and discovered that the original finder was a nomad who worked the desolate terrain between Mauritania and southwestern Morocco. The nomad, whose name is Bahba, had picked up the stone from a void, featureless place called Rabt Sbayta ("sand dunes of Sbayta"), a few hundred kilometers from the coast within the disputed territories of Western Sahara.

Habibi wasn't the only dealer making inquiries. Rabt Sbayta soon became a village, with dozens of encampments and hundreds of people combing the shifting dunes. The rules were simple: finders keepers. A "strewn field" emerged: a stretch of desert roughly 10 kilometers long and a few kilometers wide strewn with pieces that fell as Black Beauty broke up in the final moments of its descent. Newfound stones were sold up through the food chain of dealers like Habibi and usually wound up in the hands of Piatek or Labenne. "It was a big race," Habibi says. "It was the most expensive stone of my life. We were paying \$1000 per gram here in Morocco. I have never been so stressed."

Meteorite collectors, dealers, and scientists are intertwined in wary but symbiotic relationships. Science gains from a long-standing "20/20" rule: To get a meteorite name and an official classification—which makes a stone more valuable—a dealer or collector must hand over to a scientific institution 20 grams or 20% of the weight of the stone, whichever is less. Scientists have now studied and classified seven of the fallen Black Beauty stones. But the rest—including most of Piatek and Labenne's stones—are unclassified, as the owners have little incentive to give up the material gratis.

Hasnaa Chennaoui, a meteoriticist at Hassan II University in Casablanca who organized the conference, complains that the 20/20 rule rewards scientists in Europe and North America, where collectors have the most money and scientists the best equipment. Her university lacks an electron microprobe—the primary tool used for classification—and so she understands why collectors and dealers tend to go to Western scientists. But she feels that she and her



Rock of ages

Black Beauty is a breccia, or a rock made of smaller rocks—as this slice of the original 320-gram mass reveals.

- 1. Fusion crust:** The shiny, scaly skin comes from a fiery fall and years of desert sandblasting.
- 2. Large pebbles:** The rounded outline of pebbles suggests erosion in wind or water.
- 3. Blueberries:** These iron-oxide concretions may have precipitated out of water.
- 4. Igneous rocks:** There are many igneous rock pieces, or clasts, that originally formed in cooling magma chambers.
- 5. Impact melts:** Glassy teardrops and beads are impact melts, a sign that asteroid impacts were important in fusing the rock together.

Moroccan colleagues ought to have a chance to study their own country's meteorites. So far, she has had no research access to Black Beauty. "Yes, it goes to science," she says, "but to science outside of Morocco."

ALL THE PLAYERS in the world of meteorites have their incentives. Hunters want to make money. Collectors want to make a complete set. And scientists want to make their name. That holds for Florida State's Humayun, who knew that Black Beauty was going to be special from the moment Agee spoke at the 2012 Lunar and Planetary Science Conference. In his talk, Agee presented the results of the isotope analysis for oxygen as well as hydrogen. The hydrogen for isotopes were consistent with Mars-like water. But the

oxygen isotope ratios were puzzlingly different from those in all other martian meteorites. Humayun thought he had the solution. After the talk, he jumped up and asked for a sample. "Carl said he'd give me one, but he wasn't in a hurry," he says. "I just wanted to get my hands on it, to tell the truth."

Tidy in dress and excitable in manner, Humayun is a perfect foil to the laid-back Agee, who says he wasn't trying to sideline Humayun from access to Black Beauty; he just didn't get around to sending him any in time. So Humayun arranged to work on a sample held by the National Museum of Natural History in Paris. He realized that the skewed oxygen isotope ratios could be explained if the rock had been exposed to martian air or water for a long period. That

couldn't have happened in Agee's explosive-eruption origin scenario, because the rock's interior would have been quickly sealed off from the elements.

"It struck me," Humayun says, "that this was not a volcanic breccia." Instead, Humayun argues, Black Beauty is a sedimentary rock. The mineral and rock ingredients had formed igneously, from cooling magma, but they then eroded into sediments that were altered by water and air. Sometime later, asteroid impacts fused the breccia into a solid rock, before a final impact launched it into space. Humayun published his conclusions in *Nature* in November 2013.

The *Nature* paper also reassessed Black Beauty's age. Agee's team had pegged it at 2.1 billion years, based on a radiometric dating of rubidium and strontium, averaged across the sample in bulk. That age would have made Black Beauty much older than the shergottites, which are on average a few hundred million years old, but not nearly as old as the 4.1-billion-year-old Allan Hills 84001, a softball-sized Mars meteorite that sparked lasting controversy in 1996, when some scientists claimed it contained fossilized bacteria. In Humayun's scenario, however, different components of the rock could have formed at different times.

Humayun's team analyzed rock pieces rich in pyroxene and feldspar—minerals that would have been among the first to settle out of a cooling magma chamber. In these regions they found zircons, hardy little crystals that are valued because they suck up enough radioactive uranium to be used for dating. The age Humayun's team obtained from these minerals—4.4 billion years—would make Black Beauty, or at least these regions within it, the very oldest martian meteorite. It would also mean that, just a hundred million years after Mars itself coalesced as a molten ball of rock, its crust had cooled enough to support magma chambers in which zircons could form.

Now scientists are pressing further into the rock. Every cut and slice seems to yield a surprise. In September, at the Meteoritical Society meeting in Casablanca, Humayun reported finding veins of pyrite, fool's gold. The veins crosscut other parts of the meteorite—meaning they must have been among the last features to form while the rock was sitting on Mars—and the mineral is intrinsically interesting because it forms in the presence of water.

Also at the meeting, Francis McCubbins, a colleague of Agee's at the University of New Mexico, presented evidence that the rounded appearance of the large faint pebbles suggests erosion by water or wind. CT scans have also revealed smaller iron-rich spherules resembling "blueberries," the iron-oxide

concretions discovered on Mars a decade ago by the Opportunity rover and thought to have precipitated out of water. The edges of these veins and spherules would all be good places to look for organic signals, says Andrew Steele, a biogeochemist at the Carnegie Institution for Science in Washington, D.C., who is probing the rock for organics.

So far, Steele has found no hint of martian biology—just trace amounts of organic molecules associated with volcanic processes. But he has found plenty of Earth bugs in the cracks—something that he takes as a good sign. "It's a very habitable rock," he says. "All it needs is a little warmth."

While the scientists continue to poke and prod, Piatek totes his martian meteorites to events and institutions around the world. He is a loving but not always careful guardian. In 2013, after the Tucson, Arizona, Gem and Mineral Show—a mecca for meteorite collectors—Piatek visited the house of Robert Ward, a meteorite hunter, dealer, and collector in Prescott, Arizona. The two started drinking and playing around with Ward's new night vision goggles. They figured that Black Beauty's fragments, full of heat-retaining minerals, would stand out in the darkness like living things. So Piatek hid the stones outside in a freshly fallen snow. "We got done with the tequila and then remembered the Black Beauties hanging out in the snow," Ward recalls. "It was like an Easter egg hunt," Piatek says, chuckling. "It was crazy!"

River of rocks

In a nowhere place called Rabt Sbayta, meteorite hunters found pieces of Black Beauty across a strewn field more than 10 kilometers long.



TOWARD THE END OF DINNER at the Indianapolis steakhouse, Piatek receives a text from his niece-slash-personal assistant. "We're in!" he says. He asks the waitress to bag up our scraps of beef for the 13 dogs he and his wife keep at home.

Brock's sanctioned break-in has done the job. Piatek unzips the roller carry-on bag and begins to take out his pieces of Black Beauty, one by one. Accidentally, he drops one and picks it up a bit sheepishly. "Oh, yeah, Smithsonian would have died on that one," he says.

Piatek is handling the oldest rocks on

Earth—hundreds of millions of years older than any rock native to our planet, where the constant churn of plate tectonics renews the crust. Black Beauty waited billions of years to get to Earth.

Then, all in the last few years, pieces of it traveled to Rome; Washington, D.C.; Tucson; Tempe; Albuquerque; Toronto—a meteoritical Grand Tour. As Piatek continues to make donations and trades, and as researchers slice and dice the stones into ever smaller chips, Black Beauty is spreading itself, entropically, across the world. Mars to Earth, rock to dust.

Piatek shows me his favorite Black Beauty party trick. He takes the 525-gram main mass and the 241-gram piece and a little 7.7-gram shard, and twists the three around until, like a jigsaw puzzle, they lock perfectly into place—the way they must have been before the parent body broke up in the atmosphere. "Look at that," he says, marveling at the fit. "Isn't that crazy?" In this moment, the arrow of time spins backward, and you can imagine all the pieces coalescing in reverse motion, gathering heft and speed and youth as they return from whence they came. Earth to Mars, dust to rock.

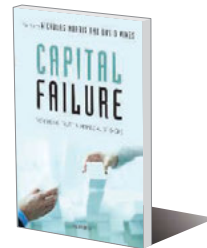
A few months later, I call Piatek and catch him creaky-voiced, lying in the bed of a hotel room in Bally's casino in Las Vegas, Nevada. Things have not gone well lately, and not just at the craps table. He and his wife are divorcing. His kids have left the nest. He's not going to renew his Indiana Pacers season tickets. He is resolving to lead a simpler life, spending more time with family and friends. It also means shedding more of his meteorite collection. But not Black Beauty. That's his touchstone, his bedrock—monetarily and metaphysically. It has both the pedigree of 4.4 billion years and the promise of a future.

"Some Black Beauty I'm going to have to keep forever," he says. "For the kids, or for when I die. Because they might find something in it."

"What if they find life? It's the 'what if' is what I'm into. It's like wow. That's the cool thing about it: the potential of Black Beauty." ■

PODCAST

To hear a podcast with author Eric Hand, see http://scim.ag/pod_6213.



PERSPECTIVES

ECOLOGY

Disentangling global soil fungal diversity

A worldwide sampling effort reveals the global drivers of soil fungal biodiversity

By David A. Wardle¹ and Björn D. Lindahl²

Ecologists have long sought to understand global patterns of biological diversity (1, 2). Most work on this topic has focused on visible aboveground organisms that can easily be counted, such as birds, butterflies, reptiles, and plants. In contrast, knowledge of the global ecology of most belowground organism groups is limited because of their microscopic size and hidden existence. Rapid advances in molecular techniques for analyzing soil communities are now offering unprecedented opportunities for understanding soil biodiversity (3, 4). On page 1078 of this issue, Tedersoo *et al.* (5) use pyrosequencing of soil samples to provide a comprehensive global study of a major group of soil organisms: soil fungi.

Soil ecologists have long been aware of the need to test whether global diversity patterns established for aboveground biota also apply

Fungal diversity. Tedersoo *et al.* (5) show that the ratio of fungal to plant diversity rises with increasing distance from the equator. Consistent with this finding, high-latitude boreal forests support few tree and understory plant species, yet fungal diversity is high, as shown in the diverse range of fruiting bodies (including those of ectomycorrhizal, saprotrophic, and pathogenic fungi) found within a ~150-m radius in Lunsen forest near Uppsala, central Sweden.



PHOTOS: K. E. CLEMMENSEN/SWEDISH UNIVERSITY OF AGRICULTURAL SCIENCE

to soil biota (6, 7). However, attempts to understand the global ecology of soil biota have typically either synthesized data from different and often disparate studies, or included too few independent sites to usefully separate the effects of large-scale drivers such as geography, latitude, and macroclimate from local variation in soil properties. Tedersoo *et al.* overcome this problem by characterizing fungal communities in soil samples from 365 separate locations worldwide (including all continents except Antarctica), all of which were sampled, processed, and analyzed in exactly the same way.



Hidden diversity. The highly diverse fungal fruiting bodies shown in the previous figure were photographed during a brief walk through this Swedish forest, which supports low plant diversity.

The results indicate that at the global scale, mean annual precipitation is the strongest driver of the richness of fungal operational taxonomic units (“richness”). However, soil properties, notably soil pH and calcium concentration, also had important positive effects. Soil fungi are generally viewed as acidophiles (relative to bacteria), but the current results suggest that they have a wider range of tolerance, rather than a preference, for acidic conditions (8).

Tedersoo *et al.* found that the relative richness of the main functional groups—ectomycorrhizal fungi, saprotrophs, and pathogens—varies widely among Earth’s major biomes, consistent with these groups each being driven by a separate set of factors. Ectomycorrhizal fungal richness is most strongly related to the richness of host plant species and high soil pH; saprotroph richness is positively related to mean annual precipitation; and pathogen richness is negatively related to latitude but positively related to nitrogen availability.

The decline of species richness with increasing latitude is one of the most pro-

nounced patterns in the natural world, at least above ground (9). In line with this, total fungal richness increases toward the equator, but major groups of fungi defy this pattern. For example, ectomycorrhizal fungal richness is greatest at mid- to high northern latitudes (coinciding with temperate and boreal forest), and richness within several ascomycete groups (notably the Leotiomycetes, which include fungi that form mycorrhizal associations with ericoid dwarf shrubs) increases toward the poles. Globally, fungal richness does not decline as sharply as plant species diversity with increasing latitude; the result

is that the ratio of fungal to plant richness rises exponentially toward the poles. Fungi are thus a key component of total terrestrial biodiversity at high latitudes, with important implications for conservation (see the figures). Reliable estimates of this ratio are important for deriving global fungal diversity from measures of plant diversity (10).

Tedersoo *et al.*’s analysis also highlights the roles of biogeography and evolutionary history in driving fungal communities within regions. First, fungal taxa at higher latitudes on average had larger geographic ranges than did those nearer the equator, pointing to higher fungal endemism in tropical regions. This is supportive of Rapoport’s rule, which predicts more restricted geographic ranges for higher-latitude taxa and has often been demonstrated for aboveground biota. Second, through analyses aimed at assessing shared fungal diversity among different biomes or regions, the authors could identify similarities in communities between Southern Hemisphere land masses, between Northern and Southern Hemisphere temperate regions, and between paleo- and neotropical regions. These biogeographic patterns can be explained in part through comigration with hosts over Pleistocene land bridges and in part through long-distance dispersal by spores.

The main functional groups of fungi drive many ecological processes, and questions therefore remain as to how the global variation in fungal communities characterized by Tedersoo *et al.* interacts with other ecosystem components. For example, saprotrophs and mycorrhizal fungi play opposite roles in soil organic matter formation (11, 12). Shifts in their relative dominance may therefore have major implications for net ecosystem carbon exchange and sequestration. Furthermore, vegetation and soil fungi are tightly linked via mycorrhizal symbiosis, pathogenic interactions, and nutrient release during decomposition. Shifts in the relative diversity of major fungal groups could thus potentially affect plant productivity and diversity (13). Moreover, soil fungi serve as food for many soil invertebrates. It remains to be shown whether the variation in fungal communities characterized by Tedersoo *et al.* is reflected in corresponding global patterns in soil nematodes, mites, and springtails.

Global studies of the type performed by Tedersoo *et al.* are also helpful for better understanding how the belowground subsystem may respond to global environmental change. Improved knowledge about links between macroclimate and fungal communities will help to predict how global climate change is likely to affect the relative abundances of key fungal groups and thereby alter fungal-driven ecological processes. Further, because most of the soil fungal community remains undescribed, we are currently unable to assess with any reliability the extent to which subsets of this community are likely to be threatened or to be spread (and potentially become invasive) through human activity. Studies such as that by Tedersoo *et al.* that enable better characterization of the soil mycobiome may serve as benchmarks against which we can assess rearrangement of species assemblages caused by human activity. ■

REFERENCES

1. M. Huston, *Biological Diversity: The Coexistence of Species on Changing Landscapes* (Cambridge Univ. Press, Cambridge, 1994).
2. K. J. Gaston, T. M. Blackburn, *Pattern and Process in Macroecology* (Blackwell Science, Oxford, 2000).
3. N. Fierer *et al.*, *Science* **342**, 621 (2013).
4. J. M. Talbot *et al.*, *Proc. Natl. Acad. Sci. U.S.A.* **111**, 6341 (2014).
5. L. Tedersoo *et al.*, *Science* **346**, 1256688 (2014).
6. D. A. Wardle, *Communities and Ecosystems: Linking the Aboveground and Belowground Components* (Princeton Univ. Press, Princeton, NJ, 2002).
7. T. Decaëns, *Glob. Ecol. Biogeogr.* **19**, 287 (2010).
8. J. Rousk *et al.*, *Soil Biol. Biochem.* **42**, 926 (2010).
9. P. H. Taylor, S. D. Gaines, *Ecology* **80**, 2474 (1999).
10. D. L. Taylor *et al.*, *Ecol. Monogr.* **84**, 3 (2014).
11. K. E. Clemmensen *et al.*, *Science* **339**, 1615 (2013).
12. C. Averill, B. L. Turner, A. C. Finzi, *Nature* **505**, 543 (2014).
13. W. H. Van der Putten *et al.*, *J. Ecol.* **101**, 265 (2013).

¹Department of Forest Ecology and Management, Swedish University of Agricultural Sciences, SE-901 83 Umeå, Sweden.

²Department of Soil and Environment, Swedish University of Agricultural Sciences, SE-750 07 Uppsala, Sweden. E-mail: david.wardle@slu.se

MEDICINE

Big data meets public health

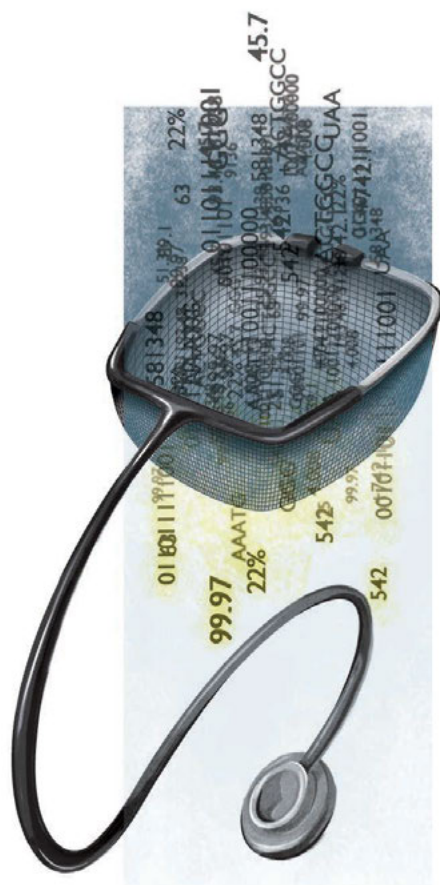
Human well-being could benefit from large-scale data if large-scale noise is minimized

By Muin J. Khoury^{1,2} and
John P. A. Ioannidis³

In 1854, as cholera swept through London, John Snow, the father of modern epidemiology, painstakingly recorded the locations of affected homes. After long, laborious work, he implicated the Broad Street water pump as the source of the outbreak, even without knowing that a *Vibrio* organism caused cholera. “Today, Snow might have crunched Global Positioning System information and disease prevalence data, solving the problem within hours” (1). That is the potential impact of “Big Data” on the public’s health. But the promise of Big Data is also accompanied by claims that “the scientific method itself is becoming obsolete” (2), as next-generation computers, such as IBM’s Watson (3), sift through the digital world to provide predictive models based on massive information. Separating the true signal from the gigantic amount of noise is neither easy nor straightforward, but it is a challenge that must be tackled if information is ever to be translated into societal well-being.

The term “Big Data” refers to volumes of large, complex, linkable information (4). Beyond genomics and other “omic” fields, Big Data includes medical, environmental, financial, geographic, and social media information. Most of this digital information was unavailable a decade ago. This swell of data will continue to grow, stoked by sources that are currently unimaginable. Big Data stands to improve health by providing insights into the causes and outcomes of disease, better drug targets for precision medicine, and enhanced disease prediction and prevention. Moreover, citizen-scientists will increasingly use this information to promote their own health and wellness. Big Data can improve our understanding of health behaviors (smoking, drinking, etc.) and accelerate the knowledge-to-diffusion cycle (5).

But “Big Error” can plague Big Data. In 2013, when influenza hit the United States hard and early, analysis of flu-related Internet searches drastically overestimated peak



From validity to utility. Big Data can improve tracking and response to infectious disease outbreaks, discovery of early warning signals of disease, and development of diagnostic tests and therapeutics.

flu levels (6) relative to those determined by traditional public health surveillance. Even more problematic is the potential for many false alarms triggered by large-scale examination of putative associations with disease outcomes. Paradoxically, the proportion of false alarms among all proposed “findings” may increase when one can measure more things (7). Spurious correlations and ecological fallacies may multiply. There are numerous such examples (8), such as “honey-producing bee colonies inversely correlate with juvenile arrests for marijuana.”

The field of genomics has addressed this problem of signal and noise by requiring replication of study findings and by asking for much stronger signals in terms of statistical significance. This requires the use of collaborative large-scale epidemiologic studies.

For nongenomic associations, false alarms due to confounding variables or other biases are possible even with very large-scale studies, extensive replication, and very strong signals (9). Big Data’s strength is in finding associations, not in showing whether these associations have meaning. Finding a signal is only the first step.

Even John Snow needed to start with a plausible hypothesis to know where to look, i.e., choose what data to examine. If all he had was massive amounts of data, he might well have ended up with a correlation as spurious as the honey bee-marijuana connection. Crucially, Snow “did the experiment.” He removed the handle from the water pump and dramatically reduced the spread of cholera, thus moving from correlation to causation and effective intervention.

How can we improve the potential for Big Data to improve health and prevent disease? One priority is that a stronger epidemiological foundation is needed. Big Data analysis is currently largely based on convenient samples of people or information available on the Internet. When associations are probed between perfectly measured data (e.g., a genome sequence) and poorly measured data (e.g., administrative claims health data), research accuracy is dictated by the weakest link. Big Data are observational in nature and are fraught with many biases such as selection, confounding variables, and lack of generalizability. Big Data analysis may be embedded in epidemiologically well-characterized and representative populations. This epidemiologic approach has served the genomics community well (10) and can be extended to other types of Big Data.

There also must be a means to integrate knowledge that is based on a highly iterative process of interpreting what we know and don’t know from within and across scientific disciplines. This requires knowledge management, knowledge synthesis, and knowledge translation (11). Curation can be aided by machine learning algorithms. An example is the ClinGen project (12) that will create centralized resources of clinically annotated genes to improve interpretation of genomic variation and optimize the use of genomics in practice. And new funding, such as the Biomedical Data to Knowledge awards of the U.S. National Institutes of Health, will develop new tools and training in this arena.

¹Office of Public Health Genomics, Centers for Disease Control and Prevention, Atlanta, GA 30333, USA. ²Epidemiology and Genomics Research Program, National Cancer Institute, Bethesda, MD 20850, USA. ³Stanford Prevention Research Center and Meta-Research Innovation Center at Stanford, Stanford University, Palo Alto, CA 94305, USA. E-mail: muk1@cdc.gov; jioannid@stanford.edu

Another important issue to address is that Big Data is a hypothesis-generating machine, but even after robust associations are established, evidence of health-related utility (i.e., assessing balance of health benefits versus harms) is still needed. Documenting the utility of genomics and Big Data information will necessitate the use of randomized clinical trials and other experimental designs (13). Emerging treatments based on Big Data signals need to be tested in intervention studies. Predictive tools also should be tested. In other words, we should embrace (and not run away from) principles of evidence-based medicine. We need to move from clinical validity (confirming robust relationships between Big Data and disease) to clinical utility (answering the “who cares?” health impact questions).

As with genomics, an expanded translational research agenda (14) for Big Data is needed that goes beyond an initial research discovery. In genomics, most published research consists of either basic scientific discoveries or preclinical research designed to develop health-related tests and interventions. What happens after that in the bench-to-bedside journey is a “road less traveled” with <1% of published research (15) dealing with validation, evaluation, implementation, policy, communication, and outcome research in the real world. Reaping the benefits of Big Data requires a “Big Picture” view.

Bringing Big Data to bear on public health is where the rubber meets the road. The combination of a strong epidemiologic foundation, robust knowledge integration, principles of evidence-based medicine, and an expanded translation research agenda can put Big Data on the right course. ■

REFERENCES

1. Harvard School of Public Health (2014); www.hsph.harvard.edu/news/magazine/big-datas-big-visionary.
2. A. Standen, KQED Science (2014); blogs.kqed.org/science/audio/how-big-data-is-changing-medicine.
3. G. Eysenbach, *Am. J. Prev. Med.* **40** (suppl. 2), S154 (2011).
4. National Institutes of Health, BD2K (2014); bd2k.nih.gov/index.html#sthash.OuOeCsq3.dpbs.
5. R. High, J. Low, *Scientific American* blogs (2014); blogs.scientificamerican.com/mind-guest-blog/2014/10/20/expert-cancer-care-may-soon-be-everywhere-thanks-to-watson.
6. D. Butler, *Nature News* (2013); www.nature.com/news/when-google-got-flu-wrong-1.12413.
7. J. P. A. Ioannidis *et al.*, *PLOS Med.* **2**, e24 (2005).
8. Spurious Correlations (2014); tylervigen.com.
9. J. P. A. Ioannidis, E. Y. Loy, R. Poulton, K. S. Chia, *Sci. Transl. Med.* **1**, 7ps8 (2009).
10. M. J. Khoury, M. Gwinn, M. Clyne, W. Yu, *Genet. Epidemiol.* **35**, 845 (2011).
11. M. J. Khoury *et al.*, *Genet. Med.* **14**, 643 (2012).
12. National Human Genome Research Institute (2013); www.nih.gov/news/health/sep2013/nhgri-25.htm.
13. J. P. A. Ioannidis, M. J. Khoury, *Genome Med.* **5**, 32 (2013).
14. S. D. Schully, M. J. Khoury, *Appl. Transl. Genomics* www.sciencedirect.com/science/article/pii/S2212066114000313 (2014).
15. M. Clyne *et al.*, *Genet. Med.* **16**, 535 (2014).

10.1126/science.aaa2709

MATERIALS DESIGN

Simulation as a tool for biopolymers design

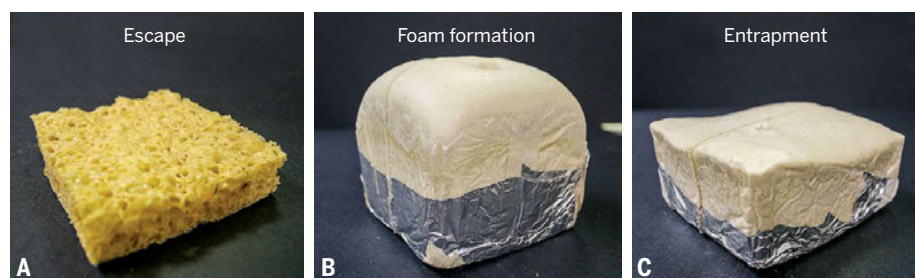
New materials made from biobased raw materials can be formulated faster with computer simulation of their reaction chemistry

By Galen J. Suppes

Many polymers are made from simple small molecules (monomers) derived through many processing steps from petroleum. Biologically sourced materials are more sustainable, but to be cost competitive, new products will likely need to be based on different structures composed of natural oils or alcohols that have undergone minimal processing. For example, plant-derived oils can be made into polymers, but these oils can bear many more functional groups in variable positions, which poses considerable challenges to controlling their reaction chemistry. The use of computer simulation

heated and then molded, thermosets adopt a final fixed shape.

The degrees of freedom of a typical urethane foam formulation include selecting types and amounts of monomers (4 to 7 degrees of freedom), catalysts (2 to 4), surfactants (2), and blowing agents (2 to 4). Biobased materials (1–5), fillers, and fire retardants can add additional degrees of freedom. Historically, the handling of these 10 to 23 degrees of freedom in specifying a urethane has been much like an “art” in the hands of a Ph.D. chemist with decades of experience. Predicting the reaction progress is not simple because of the many simultaneous physical and chemical processes. Hundreds of customer-specific urethane formulations



Just right. Curing a polyurethane foam is like baking bread—it must trap gas bubbles in order to rise (B). If the “dough” is too runny (too low in viscosity), bubbles escape (A); too stiff (too high in viscosity), the gas is trapped and no bubbles form (C).

based on experimental inputs offers a way to control this complexity and transform materials design, just as process simulators have transformed engineering design. This perspective presents a case that simulation is ready to change the way we research, develop, and design thermoset polymer recipes (formulations).

THERMOSET POLYMERS. The spray foam insulation dispensed from pressurized cans for filling cracks and crevices is an example of a thermoset polymer. The two components, isocyanate and polyol monomers, combine during the spray and react to form a polyurethane; the degree of foaming is controlled by in situ gas generation from reactions (e.g., water and isocyanate) or evaporation. Unlike thermoplastics, which can be

depend on the proper combinations of these parameters and must meet constraints on product performance, raw material costs, and throughput (i.e., cure time).

USE OF SIMULATION. Chemical process simulators have transformed the design of many reaction and separation processes when applications have a large numbers of degrees of freedom, simultaneous solution of multiple governing equations, and large markets that provide good returns on investment in simulation process. Simulation is used for both designing new processes and controlling existing processes. With cumulative markets exceeding \$20 billion

Department of Chemical Engineering, University of Missouri, Columbia, MO, USA. E-mail: suppesg@missouri.edu

per year, urethane foam formulations share these characteristics.

During simulation, an ordinary differential equation solver is used to simultaneously solve dozens of component reaction rates, mass and energy balances, and mass-transfer rates. The output starts with concentration, temperature, degree of polymerization, foam density and height, and viscosity profiles. From these profiles, the success or failure of a foam formulation can be projected. The first figure shows how the viscosity increase of the polymer must be coordinated with temperature increase (evaporation of blowing agent). If viscosity increases too fast, the blowing agent is entrapped in the resin; too slow, and percolating bubbles escape to the atmosphere.

Ultimately, even greater detail on such properties, such as thermal conductivity, compressive strength, and stress-strain relations, are desired. Simulation can guide the modification of formulations to accommodate alternative monomers, catalysts, or blowing agents that might improve performance or lower costs. Basic kinetic and physical property data are needed to simulate the effect of new formulation components. Kinetic information can be obtained by evaluating the temperature profiles of components in gel tests, which are simplified formulations without blowing agents) (6).

A computer simulation that can predict the performance of numerous mixtures based on the performance of a limited number of pure components allows for rapid and relatively inexpensive analysis of how new components affect performances of existing formulations. If the simulator accurately predicts the performance profiles of an existing formulation, it will likely also predict the effect of a formulation change. For the urethane industry, formulations are tested with a series of cup or box mold foam samples followed by testing and final adjustment with pilot scale or production line equipment. Simulation can substantially reduce or eliminate laboratory work.

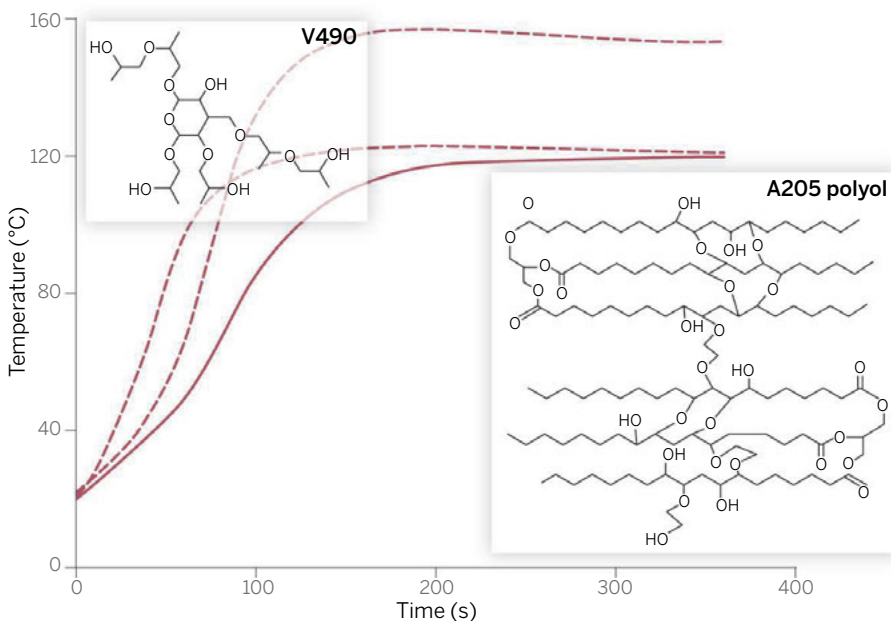
Reducing the time and expense of adopting new biobased polymers can be critical for their adoption, and simulation can create evolutionary paths in polymer development that would otherwise not occur. Unlike petroleum polyols such as V490 that are built typically from ethylene oxide and propylene oxide with a small number of hydroxyl groups (2 to 6), soybean oil has 6 to 7 carbon-carbon π bonds through which chemistry is used to add reactive moieties and control oligomerization. A practical application of the effect of gel temperature profiles is illustrated with the soy-based polyol (A205) (see the second figure). Compared with the petroleum-based monomer V490, A205 has a lower heat release associated with its lower hydroxyl

number and is more reactive. This higher reactivity was unexpected and provided the opportunity to reduce the catalyst loading from 0.3 to 0.12 weight percent, which cannot be done for the less reactive V490.

FUNDAMENTAL INSIGHT. Temperature profiles can confirm that the anticipated urethane-forming reactions are occurring. Ghoreshi *et al.* (7) identified that polyol reactivity can be specified by identifying the fractions of primary, secondary, and hindered secondary alcohols. The kinetic and thermodynamic parameters of the polyol are then specified by its functionality (number of alcohol moieties per molecule), the concentration of alcohol moieties (hydroxyl number), and these fractions. This approach reduces the number of parameters needed to characterize a polyol, and such analysis verifies that the polyol performs as anticipated.

Typical polyols may have reactive moieties other than alcohols, may have nitrogen heteroatoms that provide catalytic ability, or may be marketed as mixtures including catalysts. Concentration profiles generated by the simulation provide insight into the process that is not available from experimental study alone. Simulation of the blowing agent allows the height (density) of the foam to be estimated and fine-tuned. Density is a primary indicator of performance and a key characteristic matched with application.

Comparing synthetic and natural sources



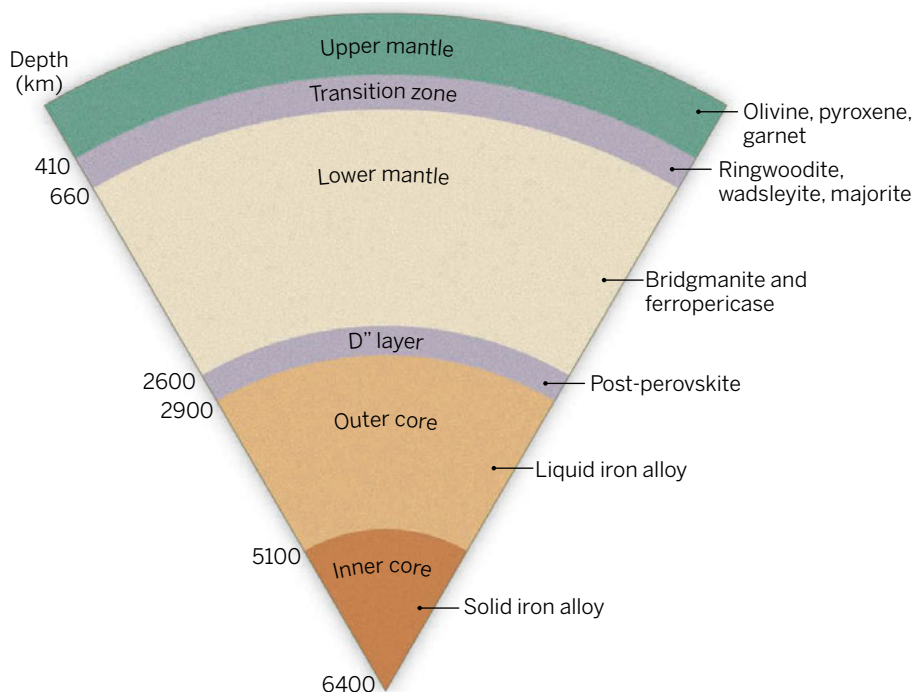
Simulations can help lower costs. Comparison of petroleum-based polyol (V490) to soy-based polyol (A205). Dashed lines are for catalyst loading of 0.3%, and solid line is for catalyst loading of 0.12%. The more reactive soy polyol will provide similar performance (based on the temperature-time profiles) but will use less of the relatively expensive catalyst.

AN ENABLING TECHNOLOGY. An exciting aspect of simulation of thermoset polymerization is the ability to enable fundamental sciences to more directly impact commercial product development. Niche successes in this application can expand and even transform how new materials are created. The databases and standards of performances established by simulators can form a foundation for advancing science and engineering that exceed alternatives like archival refereed publications. Simulators represent a key step in the evolution of science and technology when fields reach a certain point of sophistication. ■

REFERENCES

1. X.X. Du, J. Miller, *2nd Generation Honey Bee High Molecular Weight and High Functionality Natural Oil Polyols for Foam and CASE Applications* (American Chemistry Council, Washington, DC, 2012).
2. T.W. Abraham, *ACS Symp. Ser.* **1105**, 165 (2012).
3. W.C. Gower, *A New Versatile High Renewable Content Based Polyol for the Production of Multiple Flexible Slabstock Foam Technologies* (American Chemistry Council, Washington, DC, 2011).
4. N. Nodelman *et al.*, *Polyurethane Rigid Foams from Agrol Polyols* (American Chemistry Council, Washington, DC, 2012).
5. B.R. Vaughan *et al.*, *J. Appl. Polym. Sci.* **119**, 2683 (2011).
6. Y. Zhao *et al.*, *J. Appl. Polym. Sci.* **130**, 1131 (2013).
7. R.Y. Ghoreshi, Y. Zhao, G.J. Suppes, *J. Appl. Polym. Sci.*, **131**, 40388/1 (2014).

10.1126/science.1259181



Peeking into Earth's interior. This schematic cross section shows the layered structure and mineralogical model of Earth. The mantle transition zone is defined by a rapid increase in seismic velocities bracketed by the 410- and 660-km seismic discontinuities. The lower mantle, which makes up the largest volume portion of Earth, consists of predominantly bridgmanite and ferropericase. The key to understanding the structure and dynamics of the deep earth is to understand the physical and chemical properties of bridgmanite.

EARTH SCIENCE

Bridgmanite—named at last

The most abundant mineral in Earth's interior gets a name

By Thomas Sharp

The most abundant solid phase in Earth's interior, making up 38% of Earth's volume, is magnesium iron silicate (Mg,Fe)SiO₃. This material is known to form a perovskite structure. However, no samples of the mineral can be obtained from Earth's lower mantle; without a well-characterized natural sample, it has not been possible to formally name the mineral. On page 1100 of this issue, Tschauner *et al.* (1) use synchrotron micro-x-ray diffraction and electron probe microanalysis to determine the crystal structure and composition of natural (Mg,Fe)SiO₃-perovskite in a shocked L chondrite (a stony, low-iron meteorite). They name it bridgmanite, after the father of high-pressure experiments, Percy W. Bridgman (1882 to 1961).

A mineral is a naturally occurring crystalline solid with distinct, but not fixed,

chemical composition. According to the commission on new mineral names, one must characterize the structure and composition of a natural sample to give it a mineral name. Previous reports of natural MgSiO₃-perovskite have shown that it can occur in shocked meteorites (2, 3), but in both cases, the material was damaged by irradiation during transmission electron microscope analysis, and the structure had not been well characterized. Tschauner *et al.*'s careful characterization finally allows this important mineral to be named.

Earth scientists know the physical structure of the deep Earth mainly from seismic studies, which have shown that seismic velocities change suddenly at particular depths. These seismic discontinuities show that Earth has a layered structure consisting of a solid inner core, a liquid outer core, a lower mantle, and an upper mantle (see the first figure). To determine which solid materials make up these layers of the inner Earth, we need to know how Earth's materials react to extreme pressures and what structures are stable under the extreme

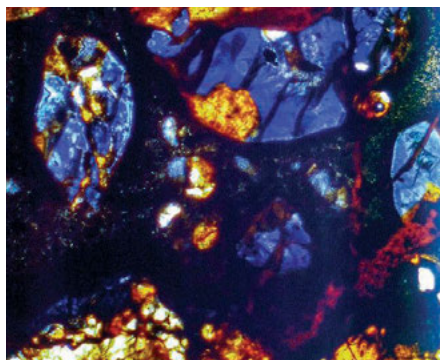
conditions of pressure and temperature within Earth (4). This information is gained from a combination of high-pressure experiments, thermodynamics, and modeling studies, with important confirmation from natural samples, usually (although not always) from meteorites.

High-pressure experiments use devices such as the diamond-anvil cell (DAC) and the multi-anvil apparatus to generate the extreme pressures of planetary interiors. The groundwork for these experiments was laid by Bridgman. More than 100 years ago, he invented a high-pressure apparatus and pressure seal that solved the problem of sample containment (5). With this press, Bridgman was able to compress materials to 7000 atmospheres (atm). By incorporating first a hydraulic press and then carbide anvils, he could eventually reach pressures of 50,000 to 100,000 atm (5 to 10 GPa) (6). Bridgman's opposing-anvil design with a cylindrical gasket led to the development of the DAC, which has allowed mineral physicists to reproduce the conditions found in the deep Earth and other planetary interiors (4).

The combination of experimental mineral physics, thermodynamics, and first-principles theory has provided a detailed model of the inner Earth that is consistent with geophysical observations and a bulk-earth chemistry resembling that of chondrites (see the first figure). High-pressure experiments provide a direct means of determining the stabilities of various structures as a function of pressure, temperature, and composition, as well as physical properties such as elasticity. From mineral physics, we know that the upper mantle consists of familiar minerals such as olivine, pyroxenes, and garnet. However, in the mantle transition zone, higher-density spinel and garnet structures predominate. In the lower mantle, the even denser perovskite and rock-salt structures are stable. Bridgmanite (perovskite structure) differs from upper mantle and crustal minerals in that silicon fills octahedral rather than tetrahedral sites. The high-density structure of bridgmanite is unstable at ambient pressures, where it readily transforms to a low-density glass if heated.

Some materials from the deep Earth, such as diamonds, are delivered to Earth's surface, but most deep-mantle silicates do not survive the journey to the surface. An exception is a sample of ringwoodite, which reached the surface as an inclusion in diamond and provided evidence for substantial amounts of water in the mantle transition zone (7). Nearly all other natural examples of deep-mantle minerals come from the asteroid belt (8). Hypervelocity impacts on meteorite parent bodies cause short pulses

School of Earth and Space Exploration, Arizona State University, Tempe, AZ, USA. E-mail: tom.sharp@asu.edu



Deep-mantle minerals in a meteorite. This shock-melt vein in the L chondrite, Roosevelt County 106, consists of quenched chondritic melt (nearly black matrix) with entrained meteorite fragments. The olivine in the fragments has transformed into deep-blue ringwoodite. The image is about 1 mm wide.

of very high pressures and locally high temperatures that melt and transform meteoritic materials into the same high-pressure phases that make up the deep Earth. During shock, the impacted rocks are compressed to pressures of more than 25 GPa. In highly deformed regions, such as shear bands or collapsed pores, sample temperatures exceed the melting temperatures of the materials (~2500 K at 25 GPa), resulting in shock-melt veins and pockets (9). It is in and adjacent to these melt zones that olivine, pyroxene, and plagioclase get hot enough to transform into their high-density polymorphs.

Shocked meteorites have provided natural examples of deep-mantle minerals (see the second figure) since Binns *et al.* (10) discovered ringwoodite, the spinel-structured polymorph of olivine, in a shocked chondrite and named it after A. E. Ringwood. Many high-pressure minerals have been named after important high-pressure experimentalists. Bridgmanite is thus a very fitting name for the most abundant mineral in the Earth. Continued investigation of shock effects in meteorites and terrestrial rocks will likely provide many more natural examples of minerals from deep within Earth or other planetary bodies. ■

REFERENCES

1. O. Tschauer *et al.*, *Science* **346**, 1100 (2014).
2. N. Tomioka, K. Fujino, *Science* **277**, 1084 (1997).
3. M. Miyahara *et al.*, *Proc. Natl. Acad. Sci. U.S.A.* **108**, 5999 (2011).
4. J. D. Bass, B. Parise, *Elements* **4**, 157 (2008).
5. P. F. McMillan, *Nat. Mater.* **4**, 715 (2005).
6. R. M. Hazen, *The Diamond Makers* (Cambridge Univ. Press, 1999).
7. D. G. Pearson *et al.*, *Nature* **507**, 221 (2014).
8. D. Stöffler, *Science* **278**, 1576 (1997).
9. T. G. Sharp, P. S. De Carli, in *Meteorites and the Early Solar System II*, D. S. Lauretta, H. Y. McSweeney Jr., Eds. (Lunar and Planetary Institute, Houston, 2006), pp. 653–677.
10. R. A. Binns, R. J. Davis, S. J. B. Reed, *Nature* **221**, 943 (1969).

10.1126/science.1261887

PSYCHOLOGY

How quickly we forget

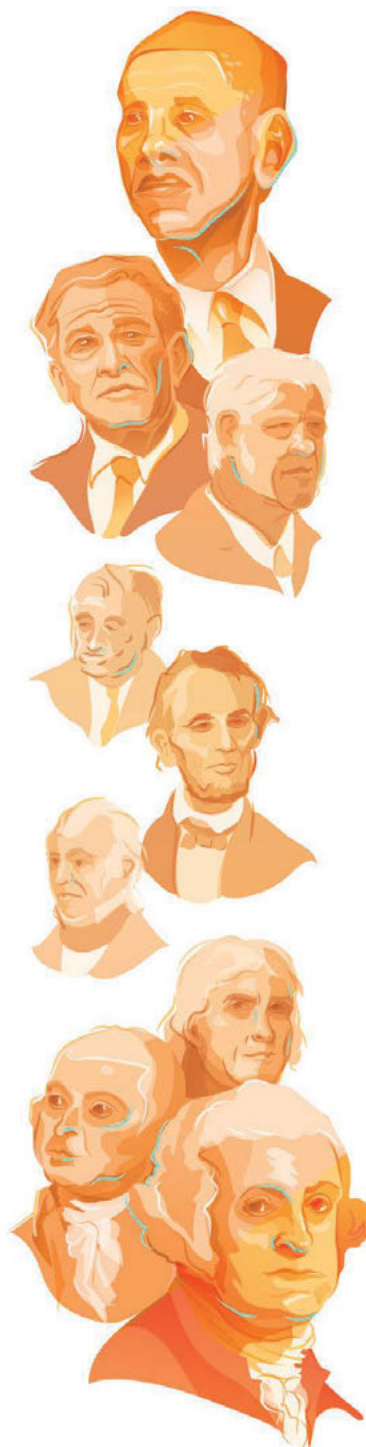
Why do we recall some things better than others?

By David C. Rubin

Since the beginning of the scientific study of human memory, there has been a tension between those who stress experimental control, even at the risk of oversimplifying and thus losing aspects of the behavior of interest (1), and those who stress studying behavior as close as possible to the way it exists naturally, with only enough control to produce replicable results (2, 3). The first approach optimistically assumes that the theory tested in the laboratory will generalize to more varied situations; the second counters that a careful, preferably quantitative, description of the phenomenon is needed—close to its full complexity—before a reasonable theory can be formulated, otherwise important aspects may be removed before a theory is considered. When it is possible, as in the study by Roediger and DeSoto (4) on page 1106 of this issue, combining both approaches is the most productive strategy.

Roediger and DeSoto examined the pattern and rate at which individuals (in the United States) forget U.S. presidents over time. The authors examined two groups—three generations of students (totaling 415 individuals in 1974, 1991, and 2009) from different U.S. universities, and 497 adults in 2014. Among their observations is a similar pattern of enhanced recall of the first U.S. presidents (Washington, Adams, and Jefferson), of Lincoln, of the current president (at the time of testing), and of presidents close in time to the time of the test (attributed to the “recency effect”). On the basis of their results, Roediger and DeSoto extrapolate when the fame of recent presidents, as measured by the ability of people to recall them, will reach the level of Presidents Fillmore, Buchanan, and McKinley (who were not well remembered).

The findings of the study overall suggest an integration of personal memory and the memory of major historical events. This is because of an observed continuity in memory for historical events (U.S. presidents) that occurred before and after one’s birth. The recall data of Roediger and DeSoto decrease smoothly with time from the pres-

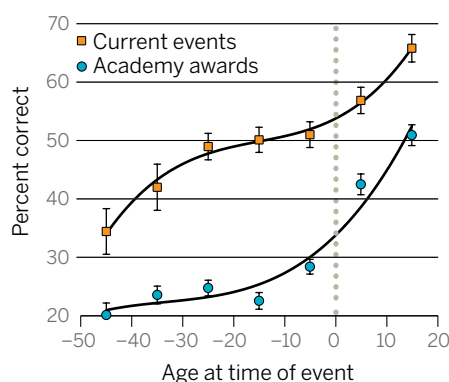


Remember the president? Across generations (since the 1970s), people in the United States forget U.S. presidents in the same way, with strongest recall only for the earliest and most recent presidents (but also for Lincoln) (4).

Department of Psychology and Neuroscience, Duke University, Durham, NC 27708, USA, and Center on Autobiographical Memory Research, Aarhus University, 8000 Aarhus C, Denmark. E-mail: david.rubin@duke.edu

PHOTO: THOMAS SHARP; ILLUSTRATION: V. ALTOUNIAN/SCIENCE

Knowledge of events



Awards and events. Correct answers to multiple-choice questions are shown as a function of participants' age at the time of the event. The vertical dotted line denotes the birth of the participants. The y axis begins at the chance guessing level of 20%. [Adapted from (5).]

ent that does not change dramatically at birth or during early development, a time period from which adults can recall few memories. For a variety of topics, including current events, entertainment, and sports, the difference between one's life and historical time is not a major factor (5). Two examples are winners of Academy Awards and important news events (see the graph). Acquisition of such historical knowledge is from exposure that need not come at the time of the event and in which the number and spacing of repeated exposures and the mechanisms of human cognition can make some events memorable beyond their historical importance (5–8).

There are two explanations for the smooth decrease in recall from the present observed by Roediger and DeSoto that are based on when and how often a person is reminded of an event, not on other factors. At a systems level, the probability that particular knowledge will be needed can be estimated from its recent past usage, with remote usage having a smaller effect. This past usage can be used to adjust its availability for recall—much as a library might arrange books for ease of access by recent popularity—but also considering, to a lesser degree, remote usage (9). In addition, based on past usage, the number and recency of past exposures could be all that affects ease of recall. Thus, if one has repeatedly heard about something in the past few months, it is more likely to be recalled.

However, beyond the impact of the environment, there is considerable knowledge of memory mechanisms from studies of information learned and retained over the life span and over generations, which can be used to understand why some things are recalled better than others. A key factor is

the nature of the longer-term spacing of “rehearsal.” For instance, Bahrick and Hall (8) found minimal loss in knowledge of high school algebra over 50 years among people who took at least one college course at or above calculus level, whereas those who did equally well in high school algebra but took no college mathematics declined to near-chance levels of remembering algebra. Similarly, Bahrick (7) found that individuals who took Spanish courses in high school or during college (spaced over multiple semesters) but were not exposed to Spanish thereafter lost much of that knowledge within the first 6 years after their final Spanish class. This observed recall as a function of time is similar to that observed by Roediger and DeSoto. Similarly, annual holidays (such as Veterans Day in the United States) and more widely spaced commemorations (such as might occur at 10-, 25-, or 100-year intervals after the end of a war) provide this spaced rehearsal for historical events.

With respect to cognitive mechanisms, memories of historical events, people, and even monuments meant to serve as reminders are all affected more by visual and spatial imagery than by other factors such as narrative (6). The combination of cues from various sensory modalities, emotion, language, narrative, and especially visual and spatial imagery of scenes helps keep memory available and stable for centuries, well above what would be expected from the mnemonic effects of individual cognitive systems used in isolation (10–12).

By combining careful measurement techniques with the study of events that span centuries, Roediger and DeSoto demonstrate the potential for the scientific study of the transmission and retention of cultural knowledge based both on exposure and the mechanisms that shape human memory. ■

REFERENCES AND NOTES

1. H. Ebbinghaus, *Memory: A Contribution to Experimental Psychology*, H. A. Ruger, C. E. Bussenius, transl. (Dover, New York, 1964). (Original work published 1885).
2. F. Galton, *Inquiries into the Human Faculty and Its Development* (Macmillan, London, 1883).
3. F. C. Bartlett, *Remembering: A Study in Experimental and Social Psychology* (Cambridge Univ. Press, London, 1932).
4. H. L. Roediger III, K. A. DeSoto, *Science* **346**, 1106 (2014).
5. D. C. Rubin, *Psychon. Bull. Rev.* **5**, 397 (1998).
6. W. Hirst, D. Manier, *Memory* **16**, 183 (2008).
7. H. P. Bahrick, *J. Exp. Psychol. Gen.* **113**, 1 (1984).
8. H. P. Bahrick, L. K. Hall, *J. Exp. Psychol. Gen.* **120**, 20 (1991).
9. J. R. Anderson, L. J. Schooler, *Psychol. Sci.* **2**, 396 (1991).
10. D. C. Rubin, *Memory in Oral Traditions: The Cognitive Psychology of Epic, Ballads, and Counting-out Rhymes* (Oxford Univ. Press, New York, 1995).
11. D. C. Rubin, *Perspect. Psychol. Sci.* **1**, 277 (2006).
12. D. C. Rubin, S. Umanath, *Psychol. Rev.* **10.1037/a0037907** (2014).

ACKNOWLEDGMENTS

I thank D. Berntsen for critical comments.

CELL BIOLOGY

Powering the cell cycle

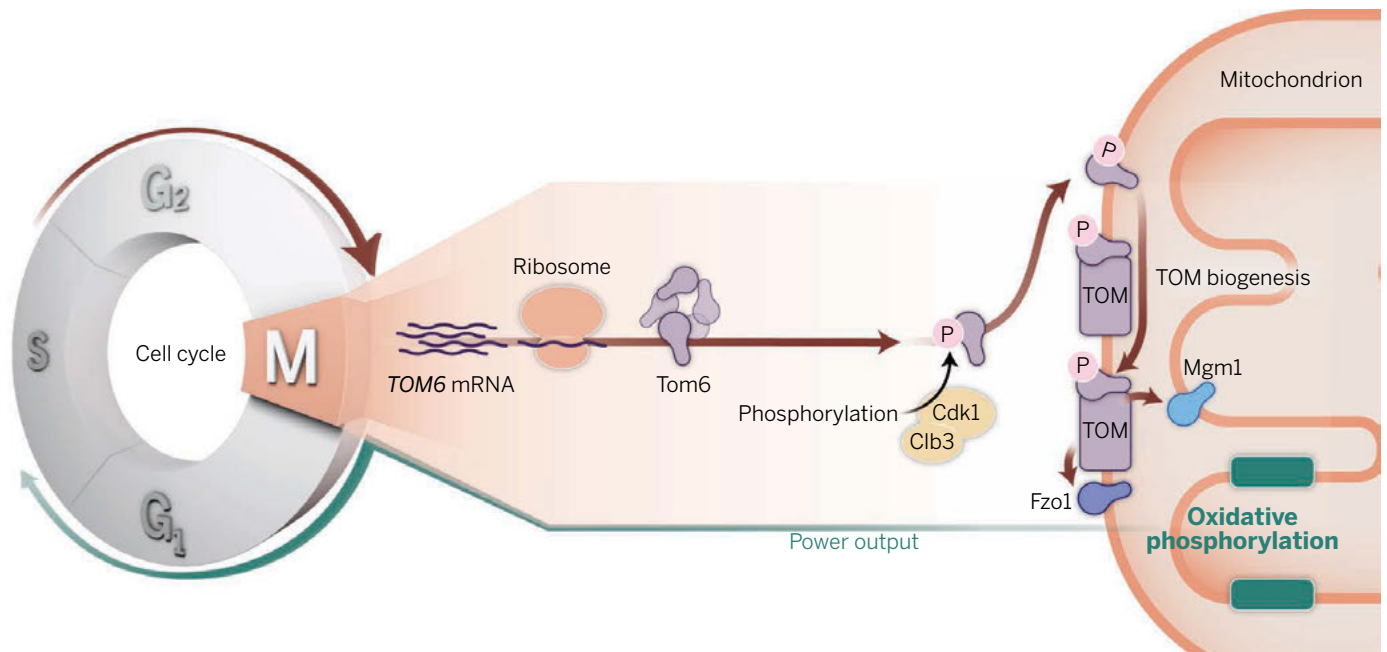
Cell division is linked to mitochondrial protein transport

By Christian Schulz¹ and Peter Rehling^{1,2}

To live means to grow, respond, reproduce, and adapt. All these processes require energy, which in most eukaryotic cells is provided by mitochondrial oxidative phosphorylation. Moreover, mitochondria have been implicated in other vital cellular processes, including programmed cell death (apoptosis) and calcium signaling. Hence, mitochondrial functions have to be tightly integrated into the cellular context, and the mechanisms that participate in this coordination are only just beginning to be understood. On page 1109 of this issue, Harbauer *et al.* (1) identify a link between the cell division cycle and mitochondrial protein transport as a driver of this process.

To maintain mitochondrial functionality and thus ensure cellular survival, newly synthesized mitochondrial proteins must be imported into the organelle from the cytoplasm. Numerous pathways supply the various mitochondrial subcompartments with their resident proteins. How these transport processes are integrated into the cellular context and adapted to the cellular requirements is only recently becoming apparent (2, 3). An unexpected observation is that mitochondrial protein translocation is regulated by cytosolic and mitochondrial enzymes (protein kinases). A major phosphorylation target of these kinases is the translocase of the outer membrane (TOM), which represents the entry gate for almost all protein precursors destined for the mitochondria.

Tom6 is a constituent of the TOM complex, and its expression (at the transcription level) undergoes a cell cycle-dependent regulation (see the figure) (4). Thus, Harbauer *et al.* investigated the fate of the Tom6 protein during the cell cycle in budding yeast. A marked increase of Tom6 during the G₂ phase–M phase transition in the cell cycle led to the identification of a cyclin-dependent kinase 1 (Cdk1)- and cyclin Clb3-mediated phosphorylation event on serine-16 of cytosolic Tom6 protein. This modification increased the rate of import of Tom6



Mitochondria and mitosis. During M phase of the cell division cycle, *TOM6* mRNA and protein abundance increase. Cdk1-Clb3 phosphorylates Tom6, thereby improving its targeting to mitochondria. This increases TOM biogenesis, which imports Mgm1 and Fzo1, proteins that stimulate energy production to support efficient progression through M phase.

into the mitochondrial outer membrane.

Tom6 displays characteristic features of a tail-anchored protein. The mitochondrial import protein 1 (Mim1) promotes insertion of Tom6 into the outer mitochondrial membrane. Tom6 is then assembled into the TOM complex, a process mediated by the sorting and assembly machinery (2). Mim1 itself is regulated by a casein kinase 2-dependent phosphorylation event that stimulates its ability to import other constituents of the TOM complex (Tom20 and Tom70) (2). This interconversion of Mim1 function allows coupling of mitochondrial import capacity to the metabolic activity of the cell.

The increase in steady-state amounts of membrane-integrated, phosphorylated Tom6 promotes the biogenesis of the TOM complex. Surprisingly, an increase in the amount of TOM complex does not lead to a notable acceleration in precursor translocation per se; instead, only import of a small subset of substrates, namely mitochondrial genome maintenance 1 (Mgm1) and fuzzy onions 1 (Fzo1), is stimulated. How is this substrate selectivity explained? The phosphorylated cytosolic domain of Tom6 recognizes the targeting signal of Mgm1, thereby facilitating its targeting and subsequent import. In the case of the outer membrane protein Fzo1, a different mechanism applies; its transmembrane segment and the intermembrane space loop are recognized by Tom6. As previously

observed, the increased presence of these proteins in the mitochondria stimulates respiration and consequently, energy output (5). Harbauer *et al.* suggest that this mitochondrial supply of energy powers progression through mitosis (6), particularly the energy-demanding steps of cytokinesis. Intriguingly, Mgm1 and Fzo1 are components of the fusion machinery of the inner and outer mitochondrial membrane, respectively (7, 8). It may be that these proteins ensure equilibrium of mitochondrial fusion and fission, which is critical for controlled distribution of the organelle during mammalian cell division (9).

Whereas Harbauer *et al.* describe how mitochondrial functions are adapted to cellular demands through signaling pathways, direct physical contact between mitochondria and other organelles also coordinates this responsive interaction. Such contacts have been observed for decades, although their functions and molecular make-up have only recently been explored (10). Direct connection between the endoplasmic reticulum and mitochondria is thought to benefit calcium signaling, lipid metabolism, mitochondrial division and distribution during cell division, and autophagosome formation (11, 12). Contacts between mitochondria and the plasma membrane, peroxisomes, and the vacuole have been found, but their roles remain mysterious (10, 13, 14). These direct contacts allow for integration of mitochondria with cellular processes in other parts of the cell.

The findings of Harbauer *et al.* now extend our views on how mitochondrial function can be regulated. At the same time, the study raises questions about further

communication mechanisms between mitochondria and the signaling pathways that drive, and control, cell division. Signaling processes apparently help to adapt mitochondrial activity to the requirements of mitosis through a modulation of TOM complex function. It is unclear if newly assembled TOM complexes are also controlled to specifically increase import of other substrates despite Mgm1 and Fzo1. It is also unknown how mRNA abundance, especially of *TOM6*, is controlled. In addition to the integration of mitochondria into cellular signaling networks during metabolic shift and the cell cycle, it can be expected that the same will hold true during cell differentiation (15). Revealing the signaling pathways regulating this integration will be a major area of future research. ■

REFERENCES

1. A. B. Harbauer *et al.*, *Science* **346**, 1109 (2014).
2. O. Schmidt *et al.*, *Cell* **144**, 227 (2011).
3. A. M. Nargund, M. W. Pellegrino, C. J. Fiorese, B. M. Baker, C. M. Haynes, *Science* **337**, 587 (2012).
4. P. T. Spellman *et al.*, *Mol. Biol. Cell* **9**, 3273 (1998).
5. H. Chen, A. Chomyn, D. C. Chan, *J. Biol. Chem.* **280**, 26185 (2005).
6. Z. Wang *et al.*, *Dev. Cell* **29**, 217 (2014).
7. S. Meeusen, J. M. McCaffery, J. Nunnari, *Science* **305**, 1747 (2004).
8. S. Meeusen *et al.*, *Cell* **127**, 383 (2006).
9. J. L. Rohm *et al.*, *Curr. Biol.* **24**, 2598 (2014).
10. T. Klecker, S. Böckler, B. Westermann, *Trends Cell Biol.* **24**, 537 (2014).
11. B. Kornmann *et al.*, *Science* **325**, 477 (2009).
12. M. Hamasaki *et al.*, *Nature* **495**, 389 (2013).
13. Y. Elbaz-Alon *et al.*, *Dev. Cell* **30**, 95 (2014).
14. C. Hönscher *et al.*, *Dev. Cell* **30**, 86 (2014).
15. A. Sing *et al.*, *Cell* **158**, 1293 (2014).

¹Department of Cellular Biochemistry, University Medical Center Göttingen, D-37073 Göttingen, Germany. ²Max Planck Institute for Biophysical Chemistry, D-37077 Göttingen, Germany. E-mail: peter.rehling@medizin.uni-goettingen.de

Universal education is key to enhanced climate adaptation

Fund more educators rather than just engineers

By Wolfgang Lutz, Raya Muttarak,
Erich Striessnig*

Over the coming years, enormous amounts of money will likely be spent on adaptation to climate change. The international community recently made pledges of up to \$100 billion per year by 2020 for the Green Climate Fund. Judging from such climate finance to date, funding for large projects overwhelmingly goes to engineers to build seawalls, dams, or irrigation systems (1). But with specific projections of future changes in climate in specific locations still highly uncertain, such heavy concrete (in

POLICY both meanings) and immobile investments that can lock countries into certain paths may not be the best way to go (2). Our new study suggests that it may be efficient and effective to give part of this fund to educators rather than engineers. Public investment in universal education in poor countries in the near future should be seen as a top priority for enhancing societies' adaptive capacity vis-à-vis future climate change.

Recent research suggests that general empowerment of populations through universal primary and secondary education is not only essential to poverty alleviation and economic growth but also to reducing vulnerability to natural disasters (3, 4). It is not unreasonable to assume that factors that helped reduce vulnerability to floods, tropical storms, and droughts over the past decades will help reduce future vulnerability to climate change. We present findings from the most comprehensive global-level assessment of the effects of education on disaster fatalities (measured as the logged number of deaths per million of population) from hydro-meteorological hazards that are likely to be intensified by climate change, e.g., floods, droughts, storms, and extreme temperatures. The data cover 167 countries for the period 1970 to 2010. Data on disasters come from the Emergency Events Database (EM-DAT), which provides

the best available information on the number of disasters and reported fatalities from around the world (5).

EDUCATE FEMALES, REDUCE FATALITIES. Because the literature on disaster vulnerability has conventionally emphasized economic growth while disregarding education, our statistical analysis focuses on the relative assessment of these two factors as measured by Gross Domestic Product (GDP) per capita and the proportion of women aged 20 to 39 with at least junior secondary education. The latter was shown to be a good indicator for recent improvements in human capital in other contexts (3).

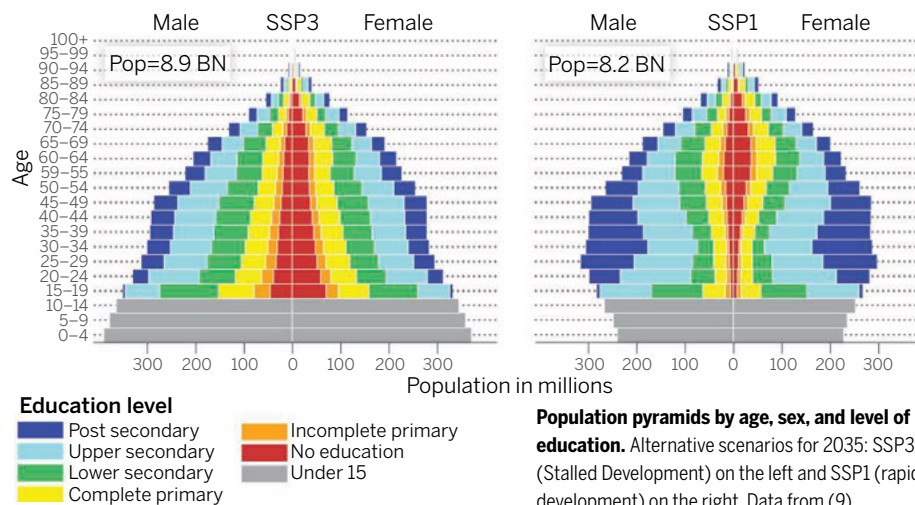
To account for differences in the frequency of natural hazards experienced and size of the countries affected, we include as controls the number of registered disasters per population, total arable land area, a dummy variable for being landlocked, the recent rate of population growth to capture stress on infrastructure, and 43 regional fixed effects for countries with comparable settings and climate zones. As documented in the supplementary materials (SM) (table S1 and sensitivity analysis in table S2 and fig. S1), several alternative model specifications combined with different estimation techniques resulted in very consistent findings: When estimating the relative effects of

income and education in the same models, GDP per capita turns out to be insignificant, whereas female education is highly significant across all models with the expected negative sign. Hence, this empirical analysis of national-level time series clearly indicates that female education is indeed strongly associated with a reduction in disaster fatalities.

Assuming that this robust association between education and lower mortality risk from natural disasters will continue in the future, we present alternative scenarios for future disaster-related fatalities as a function of alternative future education and population trends. When studying the effects of improvements in school enrollment on the human capital stock of the adult population, it is essential to account for significant inertia in the process of human capital formation. Because primary and junior secondary education tend to happen almost exclusively during childhood, it will take several decades until an expansion of education among children translates into higher human capital for men and women around age 50. This process of human capital formation along cohort lines can be appropriately modeled using the tools of multidimensional demography (6).

This approach has recently been applied to produce a new set of SSP (Shared Socioeconomic Pathways) scenarios for the international integrated assessment and vulnerability, risk, and adaptation research communities replacing the older Special Report on Emissions Scenarios which contained only total population size and GDP as socioeconomic variables (7). The SSPs were defined to address simultaneously the socioeconomic challenges to climate change mitigation and adaptation (8). Besides many

Projecting the population by level of education



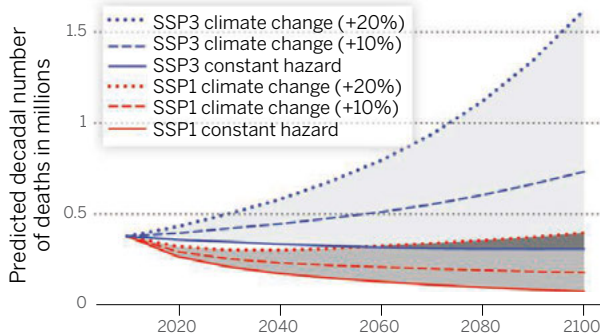
Wittgenstein Centre for Demography and Global Human Capital (IIASA, VID/ÖAW, WU), Austria. All authors contributed equally and are listed in alphabetic order. *E-mail: striessnig@iiasa.ac.at

other economic and technological variables, alternative population scenarios by age, sex, and seven levels of educational attainment for all countries form the “human core” of the full SSPs (9). SSP1 illustrates the case of rapid social development in all parts of the world associated with rapidly expanding education (see the first chart). SSP2 is the middle-of-the-road scenario where current development trends continue while SSP3 anticipates a fragmented world with stalled socioeconomic development. The figure also illustrates the great inertia of progress in improving educational attainment where, by 2035, the differences between the scenarios are only evident for the younger cohorts.

The results of combining the estimated coefficients (table S1) with two contrasting SSP scenarios (SSP1 and SSP3) for the rest of the century are shown in the second chart. We did this by taking the time-varying population and education variables from the respective SSPs. Different assumptions were made for the frequency of disasters representing possible greater future hazards. The solid lines in the second chart show the hypothetical case of constant hazard (i.e., no climate change). Under SSP1, this results in a significant decline of disaster deaths because of underlying progress in educational expansion. If we assume stalled development, which also implies higher fertility and thus higher population size, we observe almost no change under SSP3. The dashed lines assume an increase in the number of hydro-meteorological extreme events of on average 10% per decade (Climate Change +10%). Although there is still a slight reduction in future disaster deaths for SSP1, we observe a strong increase according to SSP3. The more extreme assumption of the hazard increasing on average by 20% per decade (Climate Change +20%; dotted line) leads to an increase in future disaster deaths in the longer run for all SSPs, although to different degrees.

COGNITIVE CAPACITY, SOCIAL SPILLOVER. Our macrolevel finding that education reduces disaster-related mortality is consistent with evidence from recent empirical studies for different parts of the world and at different levels of analysis (from individual-, household-, and community-level to global-level data). These studies demonstrate that education contributes to vulnerability reduction and adaptive capacity enhancement in the predisaster phase and during disaster events and the disaster aftermath [for review, see (2)].

Expanded education limits deaths



Predicted decadal number of disaster deaths (in millions). Difference in deaths resulting from estimated education and population effects according to the contrasting scenarios SSP1 and SSP3 to 2100. See SM for details.

Before a disaster, disaster mitigation efforts like living in low-risk areas or undertaking disaster preparedness measures, such as stockpiling emergency supplies, are found to be greater among more highly educated individuals and households (10). Similarly, loss of life, injury, morbidity, and physical damage from natural disasters were reported to be lower in communities and countries with a higher proportion of populations with at least a junior secondary education (11). The better educated were also found to cope better with both income loss and the psychological impacts of natural disasters (12). Most of these studies explicitly compare the effects of education to those of household income with education consistently emerging as more important. Given such systematically strong associations and a sound causal narrative described below, there is firm ground to assume functional causality of the effects of education on reducing vulnerability. This implies that a continuation of this association in the future can be reasonably assumed.

One important mechanism through which education influences human well-being is neurocognitive development. Learning basic literacy, numeracy, and abstraction skills enhances cognitive capacities through raising the efficiency of individuals' cognitive processes and logical reasoning (13). Accordingly, because preventive action is initiated by stressors, such as perception of risk, followed by assessments of one's ability to respond to the threat, the more educated tend to have greater risk awareness because of better understanding of the consequences of their actions, e.g., as found in the case of smoking and cancer prevention (14). In addition to these individual-level effects, there are also spillover effects of education at the community level as is evident for the effect of female education on

lowering infant mortality (15). Opportunities of social interaction with more-educated members may speed up the diffusion of information and knowledge, or access to institutions that favor disaster risk reduction.

Of course, in our study the association between educational level and disaster vulnerability has only been estimated on the basis of the past 40 years and can change in the longer-term future because of all kinds of uncertainties. Instead of assuming different percentage changes in the hazard as we did, more differentiated global climate models could be applied. But our calculations show a clear picture of the strong effects of empowerment through education on reducing disaster vulnerability

and enhancing adaptive capacity to climate change, which is unlikely to change when using more sophisticated models. Accordingly, given uncertainty about the precise manifestations of climate change in specific areas, it seems beneficial to increase general flexibility and enhance human and social capital in order to empower populations to better and more flexibly cope with climate change in a way best for their long-term benefit. ■

REFERENCES AND NOTES

1. S. Nakhooda et al., *Mobilising International Climate Finance: Lessons from the Fast-Start Finance Period* (World Resources Institute, Washington, DC, 2013); www.wri.org/publication/mobilising-international-climate-finance.
2. B. Walker, D. Salt, W. Reid, *Resilience Thinking: Sustaining Ecosystems and People in a Changing World* (Island Press, Washington, DC, ed. 2, 2006).
3. W. Lutz, J. C. Cuarema, W. Sanderson, *Science* **319**, 1047 (2008).
4. R. Muttarak, W. Lutz, *Ecol. Soc.* **19**, art42 (2014).
5. Center for Research on the Epidemiology of Disasters (CRED), EM-DAT (Université Catholique de Louvain, Brussels, 2010); www.em-dat.net.
6. N. Keyfitz, *Applied Mathematical Demography* (Springer, New York, ed. 2, 1985).
7. N. Nakicenovic, R. J. Lempert, A. C. Janetos, *Clim. Change* **122**, 351 (2014).
8. B. C. O'Neill et al., *Clim. Change* **122**, 387 (2014).
9. S. KC, W. Lutz, *Global Environ. Chang.* (2014).10.1016/j.gloenvcha.2014.06.004
10. R. Muttarak, W. Pothisiri, *Ecol. Soc.* **18**, art51 (2013).
11. E. Frankenberg et al., *Ecol. Soc.* **18**, art16 (2013).
12. J. F. Helgeson et al., *Ecol. Soc.* **18**, art2 (2013).
13. D. P. Baker, D. Salinas, P. J. Eslinger, *Dev. Cogn. Neurosci.* **2** (suppl. 1), S6 (2012).
14. J. Niederdeppe, A. G. Levy, *Cancer Epidemiol. Biomarkers Prev.* **16**, 998 (2007).
15. E. R. Pamuk, R. Fuchs, W. Lutz, *Popul. Dev. Rev.* **37**, 637 (2011).

SUPPLEMENTARY MATERIALS

www.sciencemag.org/content/346/6213/1061/suppl/DC1

ACKNOWLEDGMENTS

The work leading to this paper was in part funded by the European Research Council Advanced Investigator Grant on “Forecasting societies’ adaptive capacities to climate change” (ERC-2008-AdG 230195-FutureSoc).

Social media for large studies of behavior

Large-scale studies of human behavior in social media need to be held to higher methodological standards

By Derek Ruths^{1*} and Jürgen Pfeffer²

On 3 November 1948, the day after Harry Truman won the United States presidential elections, the *Chicago Tribune* published one of the most famous erroneous headlines in newspaper history: “Dewey Defeats Truman” (1, 2). The headline was informed by telephone surveys, which had inadvertently undersampled Truman supporters (1). Rather than permanently discrediting the practice of polling, this event led to the development of more sophisticated techniques and higher standards that produce the more accurate and statistically rigorous polls conducted today (3).

Now, we are poised at a similar technological inflection point with the rise of online personal and social data for the study of human behavior. Powerful computational resources combined with the availability of massive social media data sets has given rise to a growing body of work that uses a combination of machine learning, natural language processing, network analysis, and statistics for the measurement of population structure and human behavior at unprecedented scale. However, mounting evidence suggests that many of the forecasts and analyses being produced misrepresent the real world (4–6). Here, we highlight issues that are endemic to the study of human behavior through large-scale social media data sets and discuss strategies that can be used to address them (see the table). Although some of the issues raised are very basic (and long-studied) in the social sciences, the new kinds of data and the entry of a variety of communities of researchers into the field make these issues worth revisiting and updating.

REPRESENTATION OF HUMAN POPULATIONS. *Population bias.* A common assumption underlying many large-scale social media-based studies of human behavior is that a large-enough sample of users will drown out noise introduced by peculiarities of the platform’s population (7). However, substantial population biases vary across

different social media platforms (8). For instance, Instagram is “especially appealing to adults aged 18 to 29, African-American, Latinos, women, urban residents” (9) whereas Pinterest is dominated by females, aged 25 to 34, with an average annual household income of \$100,000 (10). These sampling biases are rarely corrected for (if even acknowledged).

Proprietary algorithms for public data. Platform-specific sampling problems, for example, the highest-volume source of public Twitter data, which are used by thousands of researchers worldwide, is not an accurate representation of the overall platform’s data (11). Furthermore, researchers are left in the dark about when and how social media providers change the sampling and/or filtering of their data streams. So long as the algorithms and processes that govern these public data releases are largely dynamic, proprietary, and secret or undocumented, designing reliable and reproducible studies of human behavior that correctly account for the resulting biases will be difficult, if not impossible. Academic efforts to characterize aspects of the behavior of such proprietary systems can provide details needed to begin reporting biases.

The rise of “embedded researchers” (researchers who have special relationships with providers that give them elevated access to platform-specific data, algorithms, and resources) is creating a divided social media research community. Such researchers, for example, can see a platform’s inner workings and make accommodations, but may not be able to reveal their corrections or the data used to generate their findings.

REPRESENTATION OF HUMAN BEHAVIOR. *Human behavior and online platform design.* Many social forces that drive the formation and dynamics of human behavior and relations have been intensively studied and are well-known (12–14). For instance, homophily (“birds of a feather flock together”), transitivity (“the friend of a friend is a friend”), and propinquity (“those close by form a tie”) are all known by designers of social media platforms and, to increase platform use and adoption, have been incorporated in their link suggestion algorithms. Thus, it may be necessary to untangle psychosocial from platform-driven behavior. Unfortunately, few studies attempt this.

Social platforms also implicitly target

Reducing biases and flaws in social media data

DATA COLLECTION

- 1. Quantifies platform-specific biases (platform design, user base, platform-specific behavior, platform storage policies)
- 2. Quantifies biases of available data (access constraints, platform-side filtering)
- 3. Quantifies proxy population biases/mismatches

METHODS

- 4. Applies filters/corrects for nonhuman accounts in data
- 5. Accounts for platform and proxy population biases
 - a. Corrects for platform-specific and proxy population biases
 - OR
 - b. Tests robustness of findings
- 6. Accounts for platform-specific algorithms
 - a. Shows results for more than one platform
 - OR
 - b. Shows results for time-separated data sets from the same platform
- 7. For new methods: compares results to existing methods on the same data
- 8. For new social phenomena or methods or classifiers: reports performance on two or more distinct data sets (one of which was not used during classifier development or design)

Issues in evaluating data from social media. Large-scale social media studies of human behavior should address issues listed and discussed herein (further discussion in supplementary materials).

¹Department of Computer Science, McGill University, Montreal, Quebec H3A 0G4, Canada. ²Institute for Software Research, Carnegie Mellon University, Pittsburgh, PA 15213, USA. *E-mail: derek.ruths@mcgill.ca

and capture human behavior according to behavioral norms that develop around and as a result of the specific platforms. For instance, the ways in which users view Twitter as a space for political discourse affects how representative political content will be. The challenge of accounting for platform-specific behavioral norms is compounded by their temporal nature: They change with shifts in population composition, the rise and fall of other platforms, and current events (e.g., revelations concerning interest and tracking of social media platforms by intelligence services). In the absence of new methodologies, we must rely on assessments of where such entanglements likely occur.

Distortion of human behavior. Developers of online social platforms are building tools to serve a specific, practical purpose—not necessarily to represent social behavior or provide good data for research. So, the way data are stored and served can destroy aspects of the human behavior of interest. For instance, Google stores and reports final searches submitted, after auto-completion is done, as opposed to the text actually typed by the user (5); Twitter dismantles retweet chains by connecting every retweet back to the original source (rather than the post that triggered that retweet). There are valid, practical reasons for platforms to make such design decisions, but in many cases these either obscure or lose important aspects of the underlying human behavior. Quantifying and, if possible, correcting for these storage and access policies should be part of the data set reporting and curation process.

Nonhumans in large-scale studies. Despite attempts by platform designers to police accounts, there are large populations of spammers and bots masquerading as “normal” humans on all major online social platforms. Moreover, many prominent individuals maintain social media accounts that are professionally managed to create a constructed image or even behave so as to strategically influence other users. It is hard to remove or correct for such distortions.

ISSUES WITH METHODS. *Proxy population mismatch.* Every social media research question defines a population of interest: e.g., voting preference among California university students. However, because human populations rarely self-label, proxy populations of users are commonly studied instead, for example, the set of all Facebook users who report attending a UC school. However, the quantitative relation between the proxy and original populations studied, typically, is unknown—a source of potentially serious bias. A recent study revealed that this proxy effect has caused substantially incorrect estimates of political orientation on Twitter (6).

Incomparability of methods and data. With few exceptions, the terms of usage for social media platforms forbid the retention or sharing of data sets collected from their sites. As a result, canonical data sets for the evaluation and comparison of computational and statistical methods—common in many other fields—largely do not exist. Furthermore, few researchers publish code implementing their methods. The result is a culture in which new methods are introduced (and often touted as being “better”) without having been directly compared to existing methods on a single data set. Given

There is “...the need for increased awareness of what is actually being analyzed...”

platforms’ understandable sensitivity to user privacy and the competitive value of their data, the research community will likely improve method and result comparison issues more quickly by focusing on enforcing the sharing of methods at publication time.

Multiple comparison problems. The body of social media analysis that concerns the development of user/content classification and prediction has unaddressed issues with overfitting. Specifically, when building a computational machine that recognizes two or more classes (of users, for example), it is customary to introduce tens to hundreds of features as the basis for the classifier. At the very least, the performance of the classifier should take into account the number of features being used. Of greater concern, however, is the extent to which the classifier performance is a result of “feature hunting”—testing feature after feature until one is found that delivers significant performance on the specific data set. Standard practices of reporting the *P* value for classifiers based on the number of features involved, as well as keeping a data set independent of the training set for final classifier evaluation, would work toward addressing these issues (15).

Multiple hypothesis testing. In an academic culture that celebrates only positive findings, a meta-issue emerges as multiple groups report successes in modeling or predicting a specific social phenomenon. Without seeing the failed studies, we cannot assess the extent to which successful findings are the result of random chance. This issue has been observed when predicting political election outcomes with Twitter (16). We are not the only field struggling with this issue (17). Solutions to this problem could involve enabling the publication of negative results or requiring the use of more data sets in a single study

(so as to permit the calculation of a significance score within the study itself).

CONCLUSIONS. The biases and issues highlighted above will not affect all research in the same way. Well-reasoned judgment on the part of authors, reviewers, and editors is warranted here. Many of the issues discussed have well-known solutions contributed by other fields such as epidemiology, statistics, and machine learning. In some cases, the solutions are difficult to fit with practical realities (e.g., as in the case of proper significance testing) whereas in other cases the community simply has not broadly adopted best practices (e.g., independent data sets for testing machine learning techniques) or the existing solutions may be subject to biases of their own. Regardless, a crucial step is to resolve the disconnect that exists between this research community and other (often related) fields with methods and practices for managing analytical bias.

Moreover, although the issues highlighted above all have different origins and specific solutions, they share in common the need for increased awareness of what is actually being analyzed when working with social media data. ■

REFERENCES AND NOTES

1. This was not the first or last such erroneous prediction, e.g., the *Literary Digest* on the 1936 U.S. Presidential election.
2. F. Mosteller, H. Hyman, P. J. McCarthy, E. S. Marks, D. B. Truman, *The Pre-Election Polls of 1948* (Bulletin 60, Social Science Research Council, New York, 1949).
3. I. Crespi, *Public Opinion, Polls, and Democracy* (Westview Press, Boulder, CO, 1989).
4. Z. Tufekci, in *ICWSM '14: Proceedings of the Eighth International Association for the Advancement of Artificial Intelligence (AAAI) Conference on Weblogs and Social Media (AAAI, Palo Alto, CA, 2014)*.
5. D. Lazer, R. Kennedy, G. King, A. Vespignani, *Science* **343**, 1203 (2014).
6. R. Cohen, D. Ruths, *ICWSM '13: Proceedings of the Seventh International AAAI Conference on Weblogs and Social Media (AAAI, Palo Alto, CA, 2013)*, pp. 91–99.
7. V. Mayer-Schoenberger, K. Cukier, *Big Data: A Revolution That Will Transform How We Live, Work, and Think* (Houghton Mifflin Harcourt, New York, 2013).
8. A. Mislove, S. Lehmann, Y.-Y. Ahn, J.-P. Onnella, J. N. Rosenquist, *ICWSM '11: Proceedings of the Fifth International AAAI Conference on Weblogs and Social Media (AAAI, Palo Alto, CA, 2011)*, pp. 554–557.
9. M. Duggan, J. Brenner, The demographics of social media users; www.pewinternet.org/2013/02/14/the-demographics-of-social-media-users-2012/.
10. 13 ‘pinteresting’ facts about Pinterest users; www.pinterest.com/pin/23425761808745827/.
11. F. Morstatter, J. Pfeffer, H. Liu, *Proceedings of Web Science Track, at the 23rd Conference on the WWW (Association for Computing Machinery, New York, 2014)*, pp. 555–556.
12. M. McPherson et al., *Annu. Rev. Sociol.* **27**, 415 (2001).
13. F. Heider, *J. Psychol.* **21**, 107 (1946).
14. L. Festinger, S. Schachter, K. Back, in *Social Pressure in Informal Groups*, L. Festinger, S. Schachter, and K. Back, Eds. (MIT Press, Cambridge, MA, 1950), chap. 4.
15. S. J. Russell, P. Norvig, *Artificial Intelligence: A Modern Approach* (Pearson Education, Upper Saddle River, NJ, 2003).
16. H. Schoen et al., *Internet Res.* **23**, 528 (2013).
17. J. P. A. Ioannidis, *PLOS Med.* **2**, e124 (2005).

SUPPLEMENTARY MATERIALS

www.sciencemag.org/content/346/6213/1063/suppl/DC1

10.1126/science.1257756

ECONOMICS

First, do no harm

By Robert M. May

This book is based on a year-long series of meetings and seminars, organized by Nicholas Morris and David Vines at Oxford University, that brought together economists, lawyers, and philosophers to discuss ideas for ensuring greater accountability in the financial services sector. In particular, it addresses the question of why, in the banking and finance community, there is no formal “duty of care” as there is in the legal and medical professions. In those professions, the kind of behavior manifested by some in the financial community in recent years might well have resulted in disbarment.

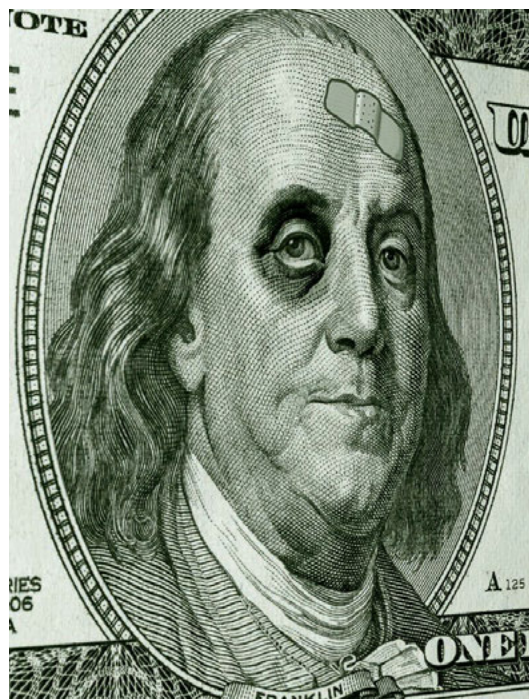
The book emphasizes that there have, of course, been previous banking crises in the United Kingdom and elsewhere, notably in 1792, 1825, 1857, 1907, and 1929. In earlier years, specifically before 1825, banks in England and Wales were owner-managed, with the consequence that a bank’s failure not only wiped out depositors but wiped out owners also.

As in recent events, these earlier incidents put the financial system in jeopardy, and each prompted major reforms. It is, however, argued by *The Economist*’s Richard Davies in Chapter 4 that over these past two centuries such repeated cycles of crisis and reform served gradually to “drive a wedge between the economic interests of banks’ managers and their owners and creditors.” In Chapter 3, corporate governance expert Thomas Noe and economist H. Peyton Young describe how reforms have come to limit the risk to bank owners and managers. The unintended and perverse consequence of these reforms is that it has become less rational for banks to take full account of such risks, which can now be imposed on clients.

A substantial part of the problem arguably lies in the textbook assumption that selfish motives will produce sensible outcomes, a belief that dates back to Adam Smith’s *Wealth of Nations*. Data, such as there are, supply little support for this warmly em-

braced belief. Like much else in economic theory, this particular belief is in accord with Robert Skidelsky’s unkind suggestion that economics “is a form of post-Christian theology, with economists as priests of warring sects” (1).

In retrospect, it is perhaps not surprising that increasing patterns of misallocation of risk and reward arose and initially seemed acceptable. The high charges levied by hedge funds—2% of the fund under management, plus 20% of any excess of returns above a benchmark—seemed acceptable in good times, when both the investor and intermediary are receiving high returns. But in bad times, although the intermediary gets no 20%, he also suffers no loss. Losses are concentrated on the investor. Capital markets’ bonus pools work in a similar way.



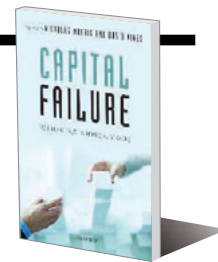
Of course, the creators of hedge funds and the like did not set out to create grossly risky products. A large part of the problem was that the underpinning theory upon which calculations of such risks were based was grievously flawed, a concept that is elaborated upon in Chapter 2. Quoting Alan Greenspan, the former chairman of the U.S. Federal Reserve, the authors refer to the “virtually indecipherable complexity of ... products and markets that developed with the advent of sophisticated mathematical techniques to evaluate risks” (2). The essential problem is that these techniques, although undoubtedly complex, were certainly not sophisticated.

But to what extent did banks, hedge funds, and other intermediaries really un-

Capital Failure Rebuilding Trust in Financial Services

Nicholas Morris and
David Vines, Eds.

Oxford University Press,
2014. 422 pp.



derstand the risks? It is surprising that so little note was taken of Warren Buffett’s statement, clearly expressed in 2002, that “derivatives are financial weapons of mass destruction” (3). Nor was he alone in this perception. In his book *The Big Short: Inside the Doomsday Machine*, Michael Lewis describes young investors who, after the recent financial crisis, ask, “Were these guys crooks or stupid?” An older and darker character answers, “Most of them were stupid, but some of them were crooks, and they tended to be higher up” (4).

As noted in *Capital Failure*, and elsewhere by the Banking Commission, one important question is whether the competence and behavior of individuals working within the system would benefit from a professional oversight organization. In Chapter 9, legal scholar Joshua Getzler observes that, even with the benefit of retrospect, Goldman Sachs’s executives had difficulty acknowledging that it was inherently wrong to have the bank aggressively marketing investments to clients while taking a short position on the same investments, thus taking handsome remuneration from both sides. Although it was at one time thought possible that some of the more egregious instances of such unprofessional behavior might result in jail sentences, this has not happened. The popular explanation for this is that mechanisms for such legal action are nonexistent; however, this argument has recently and decisively been demolished (5).

REFERENCES

1. R. Skidelsky, *John Maynard Keynes: 1883–1946: Economist, Philosopher, Statesman* (Penguin, London, 2005).
2. A. Greenspan, *Brookings Pap. Econ. Act.* **41**, 201–246 (2010).
3. W. E. Buffett, Letter to the Shareholders of Berkshire Hathaway Inc. (2003); www.berkshirehathaway.com/letters/2002pdf.pdf.
4. M. Lewis, *The Big Short: Inside the Doomsday Machine* (Norton, New York, 2010).
5. J. S. Rakoff, The financial crisis: Why have no high-level executives been prosecuted? *New York Rev. Books* (9 January 2014).

The reviewer is at the Department of Zoology, University of Oxford, South Parks Road, Oxford OX1 3PS, UK. E-mail: robert.may@zoo.ox.ac.uk



PUBLIC HEALTH

The tangled web of dengue fever

By Kristin Harper

According to the U.S. Centers for Disease Control and Prevention, one-third of the world's population is at risk for contracting dengue fever (1), a mosquito-borne viral infection so painful it is sometimes referred to as “breakbone fever.” Although only nine countries experienced severe dengue epidemics before 1970, today the disease is endemic in more than 100 countries (2). These dire statistics are familiar to many in public health, but the story of dengue's rise in the 21st century is less well known. Alex M. Nading's *Mosquito Trails: Ecology, Health, and the Politics of Entanglement* is a timely exploration of dengue prevention efforts in Ciudad Sandino, a slum outside Nicaragua's capital city, Managua.

To tell this story, Nading, an anthropologist by training, embedded himself in the lives of those on the front lines of the dengue epidemic. His interviewees range from the community health workers known as brigadistas, who go from house to house stamping out mosquito breeding grounds, to the garbage collectors who have become scapegoats for the epidemic, implicated for their role in providing mosquito breeding places. He also spent time with the epidemiologists charged with implementing control efforts and families affected by dengue.

Nading offers a much-needed discussion of the broader context in which the dengue epidemic is taking place. An environment tailor-made for the virus and its vector has been produced by the global trade in garbage, the growth of peri-urban slums, changes in insecticide use, and an approach to public health that increasingly shifts the

responsibility for mosquito control from the government to individual households. This book provides a fascinating, if meandering, tour of dengue and the changing face of public health in Nicaragua from the 1979 Sandinista revolution up to the current era of structural readjustment.

Nading devotes a substantial part of the book to discussing “entanglement,” defined as “the unfolding, often incidental attachments and affinities, antagonisms and animosities that bring people, nonhuman animals, and things into each other's worlds.” Certainly, his descriptions of life in Ciudad Sandino illustrate the dense web of interactions between people, places, politics, mosquitos, and the dengue virus, providing insight into why control is so challenging. Unfortunately, the lengthy sections of the book devoted to entanglement are often convoluted and disappointing when it comes to potential solutions. For example, Nading calls for a solution in which “basic and complex infrastructures, national and transnational belonging, and, above all, a recognition that environments and bodies are entangled, lead to a more relational ethic of health” but fails to elaborate on what such an approach might look like. Similarly, he argues that factors such as climate change and uneven urban development necessitate a “holistic, even radical” solution to mosquito control, but again, we are left to wonder what such a solution might look like. Ultimately, it is not clear how entanglement, as an analytical framework, represents a conceptual advance over simply describing dengue control as complicated.

Nading concludes the book with three practical considerations for those who would confront dengue. The first is the idea that politics and poverty are critical components of the disease process. The second is that community health workers are underpaid

Mosquito Trails
Ecology, Health, and the
Politics of Entanglement
Alex M. Nading
University of California
Press, 2014. 287 pp.



and underappreciated. His final recommendation for tackling vector-borne diseases is to consider the relationships between people and other creatures. All of these conclusions are well supported by the book's vignettes. However, while Nading considers disruption of current approaches to be a goal of his framework of entanglement, his conclusions are consistent with ideas long espoused by global health institutions, including the World Health Organization and the Rockefeller Foundation (3, 4).

Although this book is light on solutions to the dengue epidemic, researchers and clinicians involved in dengue research and care, medical anthropologists, and anyone interested in the intersection of politics and global health will likely find this a worthwhile read. *Mosquito Trails* documents the many challenges inherent in Nicaragua's struggle with dengue and gives a voice to the residents of Ciudad Sandino who have found themselves entangled with virus, vector, and one other.

REFERENCES AND NOTES

- Centers for Disease Control and Prevention, Dengue (2014); www.cdc.gov/dengue.
- World Health Organization, Dengue and Severe Dengue (2014); www.who.int/mediacentre/factsheets/fs117/en.
- World Health Organization, World Health Report Executive Summary (1995); www.who.int/whr/1995/media_centre/executive_summary1/en.
- The Rockefeller Foundation, Annual Report for 1918; www.rockefellerfoundation.org/uploads/files/1a897fb6-dd34-4ce6-9f17-13c9e1478fdc-1918.pdf.

The reviewer is at MetaMed Research, New York, NY 10016, USA. E-mail: kristin.nicole.harper@gmail.com

10.1126/science.aaa0330

LETTERS

Edited by Jennifer Sills

Salamander protection starts with the newt

IN THEIR REPORT “Recent introduction of a chytrid fungus endangers Western Palearctic salamanders” (31 October, p. 630), A. Martel *et al.* warned that a newly discovered pathogenic chytrid fungus *Batrachochytrium salamandrivorans* (Bs) likely originated in Asia and poses a threat to naïve European and North American salamander populations. However, they did not address the conservation crisis facing the apparent vector of Bs, Asian salamanders in the family Salamandridae (“newts”).

Eight years ago, one of us expressed concern for the fate of the Lao Newt (now *Laotriton laoensis*), a newly discovered species in Laos that was targeted by commercial collectors from Germany and Japan after it was inadvertently “advertised” by its formal description in a scientific journal (1). The species is now endangered in the wild (2), primarily due to continued overharvesting for the international pet trade (3). *Laotriton* is a member of the same phylogenetic clade that contains the three Asian

species [genera *Paramesotriton* and *Cynops* (4)] that were identified by Martel *et al.* as being reservoirs for Bs. Our efforts to curb the commercial trade of *Laotriton* in Laos have had limited success.

In 2008, the Lao government commendably listed it as the first amphibian species in the country to be protected from commercial trade (3). Unfortunately, *Laotriton* are small and easily smuggled across Laos’s porous international borders, and wildlife law enforcement in this relatively poor country is hindered by lack of resources (5). More than one-third of all Southeast and East Asian newt species are at risk of extinction (2). Many of these are threatened by overharvesting for the international pet trade (6), as interest in keeping Asian newts, particularly in the West, continues to grow (7). Last year, *Laotriton* was promoted as a pet on the cover of a U.S.-based amphibian and reptile hobbyist magazine that has wide international readership (8).

Martel *et al.*’s findings are foreboding for wild populations of European and North American salamanders. At the same time, wild *Laotriton* and other Asian newt populations are in dire need of better protection from international trade. Perhaps Martel *et al.*’s findings provide a glimmer of hope that exporting and importing countries can simultaneously address these threats,



albeit for different reasons. By stemming the trade of Asian newts to Europe and North America, risk of catastrophic extirpations of global salamander populations decreases: Asian newts remain in the wild, and naïve European and North American salamanders are not exposed (at least further) to a pathogenic fungus that Martel

et al. inferred has been restricted to Asia since the Paleogene. Source countries in Asia and destination countries in the West should work hand in hand to control the international trade of Asian newts. No Asian newt species are currently protected by the Convention on International Trade in Endangered Species of Wild Fauna and Flora (CITES), an international agreement that is intended to safeguard certain species from over-exploitation (9), but many probably should be. And importation of live Asian newts should be controlled in the same manner as livestock and poultry that pose disease threats to domestic populations. Persistence of wild salamanders on both sides of the planet may depend on it.

Bryan L. Stuart,^{1*} Jodi J. L. Rowley,²
Somphouthone Phimmachak,³ Anchalee
Aowphol,³ Niane Sivongxay⁴

¹North Carolina Museum of Natural Sciences, Raleigh, NC 27601, USA. ²Australian Museum Research Institute, Sydney, NSW 2010, Australia.

ONLINE BUZZ: HUMAN EVOLUTION

Roots of self-domestication

IN HER IN DEPTH NEWS story “How we tamed ourselves—and became modern” (24 October, p. 405), A. Gibbons reported on a symposium about human self-domestication, a process that allowed increased cooperation and the development of cognitive skills such as complex language. Readers expressed interest in the topic in the online comments section. Excerpts from their responses are below. Read the full comments, and add your own, at <http://comments.sciencemag.org/content/10.1126/science.346.6208.405>.

A selection of your thoughts:

...the idea that the process of killing sexually aggressive men was a driver [of self-domestication] seems flawed, in that many societies need to tolerate aggression as a protective factor, and dominance of one male over others has been a selection process for community leadership....

Philip Benjamin

...One of the story’s main conclusions is that “selection favored males who could work together.”...In my opinion, advantage (in strength or in intelligence) over others..., not

cooperation, is the feature favored by selection. Cooperation is one possible tool to achieve private aims (...for instance, politicians in democratic countries have to participate in elections [rather than making war as a way of attaining office]...). Maybe we are less aggressive (in a physical sense) in population centers but...our “self-domestication”...involves controlling the behaviors of other humans.

Konrad Szocik

...Research in this area should be heavily funded in order to help us to understand and mitigate the catastrophic deleterious effects of some...human communities [today]....

Silvio Pitlik

I think it may be important to consider the possibility that “selection for...facial feminization” can be rephrased as “selection for retention of facial (and other) traits of the young of the species in general, whether female or male.” My reasoning is that retention of such general “childlike” traits (neotony), which engender stronger feelings and behaviors of tenderness, care, and bonding in adults of the species toward their children, would itself go a long way toward reducing intraspecies aggression and increasing the possibilities of cooperation, even far outside the usual family unit....

Gene Partlow

³Department of Zoology, Faculty of Science, Kasetsart University, Bangkok, 10900, Thailand.

⁴Department of Biology, Faculty of Sciences, National University of Laos, Vientiane, Lao PDR.

*Corresponding author. E-mail: bryan.stuart@naturalsciences.org

REFERENCES

1. B. L. Stuart *et al.*, *Science* **312**, 1139 (2006).
2. IUCN, *The IUCN Red List of Threatened Species, Version 2014.2* (www.iucnredlist.org).
3. S. Phimmachak, B. L. Stuart, N. Sivongxay, *J. Herpetol.* **46**, 120 (2012).
4. P. Zhang *et al.*, *Mol. Phylogenet. Evol.* **49**, 586 (2008).
5. H. Nooren, G. Claridge, *Wildlife Trade in Laos: The End of the Game* (Netherlands Committee for IUCN, Amsterdam, 2001).
6. J. Rowley *et al.*, *Biol. Lett.* **6**, 336 (2010).
7. F. Pasmans *et al.*, *Salamanders: Keeping and Breeding* (Natur und Tier-Verlag, Münster, Germany, 2014).
8. F. Reves, *Reptiles* **21**, 30 (2013).
9. The CITES Secretariat, *Convention on International Trade in Endangered Species of Wild Fauna and Flora* (www.cites.org).

China's ecological steps forward

IN THEIR REPORT "A mid-term analysis of progress toward international biodiversity targets" (10 October, p. 241; published online 2 October), D. P. Tittensor and

colleagues concluded that despite accelerating policy and management responses to the biodiversity crisis on a global scale, these efforts are unlikely to improve the state of biodiversity by 2020. They did not acknowledge that sustained national policies in China have already produced positive effects on biodiversity.

The Chinese government initiated in 1999 the Natural Forest Resources Conservation Program and the Restoring Farmland into Forest Program. Logging has been prohibited in most natural forests, and cultivated land on areas with slopes of more than 25 degrees must be restored to forests or grasslands (1). The central government subsidized forest management and conservation, as well as seedling cultivation and reforestation (2, 3). Households that have returned their cultivated land to forests received subsidies from the central government (2, 3). Recently, the State Council updated the policies and increased subsidies to further promote ecosystem restoration (2).

A number of other key ecological programs continue to be implemented, such as forest belt construction in the Yangtze River basin. More than US\$80 billion

has been invested in these programs (1). Ecological conditions have improved (2). Forest area, growing stock (the total stock volume of trees growing in land), and coverage rate (the percentage of area of afforested land compared with total land) all increased between 2009 and 2013 (4–6). These programs have contributed to progress toward Aichi Targets 5, 14, and 15 (2), although these policies need to be fine-tuned to best fit the local environment.

Haigen Xu

Nanjing Institute of Environmental Sciences,
Ministry of Environmental Protection of China,
Nanjing, 210042, China. E-mail: xhg@nies.org

REFERENCES

1. Secretariat of the Convention on Biological Diversity, *Global Biodiversity Outlook 4* (Montreal, 2014).
2. Ministry of Environmental Protection, "China's 5th national report to the CBD" (www.cbd.int/doc/world/cn/cn-nr-05-en.pdf).
3. P. W. Leadley *et al.*, "Progress towards the aichi biodiversity targets: An assessment of biodiversity trends, policy scenarios, and key actions" (Secretariat of the Convention on Biological Diversity, Montreal, 2014).
4. State Forestry Administration, "China Forestry Statistics" (China Forestry Press, Beijing, 2013).
5. State Forestry Administration, "The promulgation of the eighth national forest resource inventory" (www.forestry.gov.cn/).
6. H. Xu *et al.*, *BioScience* **59**, 843 (2009).

As science grows in China, ethics education aims to keep up

By Brian Lin and Becky Ham

A massive national effort in China to improve scientific integrity has brought the issue to the attention of a staggering number of researchers in that country: In less than 4 years, more than 8 million undergraduate and graduate students have listened to 20,000 lectures on the topic.

But experts at a recent meeting held at AAAS said that ethics education should start even earlier for Chinese and American researchers and that such education faces stiff challenges from a research environment that, in some instances, serves as a breeding ground for authorship disputes and misuse of data, among other problems.

With international scientific collaborations on the rise, the issue of integrity is increasingly important, the meeting's participants agreed. "The only way the scientific enterprise can contribute to worldwide problems is for...scientists to be willing, able, and enthusiastic about collaborating on a worldwide scale," said AAAS CEO Alan I. Leshner. "Central to any collaboration are issues like trust, shared values, norms, and standards that drive the practice."

The China-U.S. Scientific Morality/Integrity Development Seminar was the fourth such meeting convened since the Scientists' Social and Ethical Responsibilities conference organized by the China Association for Science & Technology (CAST) and AAAS in 2007. Since then, CAST and AAAS have collaborated on several workshops on scientific integrity, and in 2010 established a joint steering committee to coordinate ethics work.

Total research funding for Chinese universities ballooned from US\$7.6 billion in 2009 to US\$12.7 billion in 2012, said Guangxian Li, the executive vice president of Sichuan University, who spoke at the 8 to 9 October seminar on behalf of Shen Yan, vice chairman of CAST and deputy director of the National Natural Science Foundation of China. Research papers published by Chinese universities saw a 10% increase—to more than 1.1 million—during the same period.



Graduate students attend a public lecture on research ethics at the Great Hall of the People, in Beijing.

The desire to achieve higher international standings has put enormous pressures on Chinese researchers to publish, said Li. The QS World University Rankings and Times Higher Education World University Rankings, for example, base 60 to 70% of their scores on research and citations.

But a national Chinese survey of more than 30,000 Chinese researchers found 51% of respondents admitted to frequently or occasionally improperly attributing sources, while 42% submitted manuscripts to multiple journals. Another survey of nearly 5500 graduate students from 24 universities, conducted a year later, revealed a similar trend.

An ambitious national campaign launched in 2011 by the Chinese Ministry of Education, Li said, is raising awareness of these issues. Six thousand graduate students from 60 universities have attended annual lectures on research ethics, held at the iconic Great Hall of the People, in Beijing. But education should start even earlier in a student's career, said Diange Yang, a professor in Tsinghua University's department of automotive engineering and deputy dean responsible for research work and international cooperation.

"Strengthening academic integrity education of graduate students...should be the responsibility of the whole society, and it should be done from childhood," said Yang.

The United States is unlikely to hold national ethics lectures as has happened in China, but AAAS has joined the National Science Foundation and the Office of Research Integrity in conducting ethics education for scientists, said Mark S. Frankel, director of the AAAS Scientific Responsibility, Human

Rights and Law Program. By the end of the year, AAAS will post on its website seven case studies from a 2012 workshop that address issues of authorship, conflict of interest, collaboration, and plagiarism. And Frankel, Leshner, and Yang Wei, director of China's National Natural Science Foundation, are co-authors of a chapter on Chinese and American research integrity and ethics education that will be published in the "Handbook of Academic Integrity" in 2015.

Though essential, education in responsible research conduct is not enough, said Philip Langlais, professor of psychology and former vice provost of graduate studies and research at Old Dominion University. A 2006 survey he conducted with 222 faculty and 534 graduate students in the United States found that while up to 90% of faculty reported providing training in responsible research conduct, up to 35% of students claimed they received no training. Only 8% of students and faculty reported having discussed and reached consensus on topics such as authorship, ownership, and use of data.

"We've been targeting individuals, but not other layers of influence," Langlais said. "Scientists who have received proper training in responsible conduct of research have violated best practices and principles of scientific integrity as a result of a 'toxic' research environment" of higher workloads, shifting university priorities, and increasing competition for funding.

In both China and the United States, "you can't change climate and culture overnight," he said. "But, you can make small, incremental changes." ■

AAAS
NEWS &
NOTES

EDITED BY KATHY WREN

AAAS members elected as Fellows

In October 2014, the AAAS Council elected 401 members as Fellows of AAAS. These individuals will be recognized for their contributions to science and technology at the Fellows Forum to be held on 14 February 2015 during the AAAS Annual Meeting in San Jose, California. Presented by section affiliation, they are:

Section on Agriculture, Food, and Renewable Resources

Andrew F. Bent, Univ. of Wisconsin-Madison
Douglas R. Call, Washington State Univ.
Andrew D. Hanson, Univ. of Florida
Daniel A. Herms, Ohio State Univ.
Ann M. Hirsch, Univ. of California, Los Angeles
Harold Corby Kistler, USDA Agricultural Research Service
Ian H. Mather, Univ. of Maryland
Bruce A. McPherson, Ohio State Univ.
Charles Michael Smith, Kansas State Univ.
Christopher K. Tuggle, Iowa State Univ.
Diane E. Ullman, Univ. of California, Davis
Esther van der Knaap, Ohio State Univ.

Section on Anthropology

David G. Anderson, Univ. of Tennessee, Knoxville
Robert L. Anemone, Univ. of North Carolina at Greensboro
Robert G. Franciscus, Univ. of Iowa
Dale L. Hutchinson, Univ. of North Carolina at Chapel Hill
Bertis Britt Little, Tarleton State Univ.
Dwight W. Read, Univ. of California, Los Angeles
Daniel H. Sandweiss, Univ. of Maine
Pauline W. Wiessner, Univ. of Utah

Section on Astronomy

Tom Abel, Stanford Univ./Kavli Institute for Particle Astrophysics & Cosmology/SLAC National Accelerator Laboratory
Andreas J. Albrecht, Univ. of California, Davis
Stanislav George Djorgovski, California Institute of Technology
Martin S. Elvis, Harvard-Smithsonian Center for Astrophysics
Paul G. Kalas, Univ. of California, Berkeley/SETI Institute
Margaret Meixner, Space Telescope Science Institute/Johns Hopkins Univ.

Section on Atmospheric and Hydrospheric Sciences

William D. Collins, Lawrence Berkeley National Laboratory/Univ. of California, Berkeley
Kelvin K. Droegemeier, Univ. of Oklahoma
Willard S. Moore, Univ. of South Carolina
Drew T. Shindell, Duke Univ.
Frank J. Wentz, Remote Sensing Systems
Diane E. Wickland, NASA

Section on Biological Sciences

Alan A. Aderem, Seattle Biomedical Research Institute

Russ B. Altman, Stanford Univ.
Scott Allen Armstrong, Memorial Sloan Kettering Cancer Center
Bernard P. Arulanandam, Univ. of Texas at San Antonio
Alan D. Attie, Univ. of Wisconsin-Madison
David Mansfield Bader, Vanderbilt Univ. School of Medicine
Gregory F. Ball, Univ. of Maryland, College Park
Marisa Susan Bartolomei, Univ. of Pennsylvania Perelman School of Medicine
Steven A. Benner, Foundation for Applied Molecular Evolution
Christoph Benning, Michigan State Univ.
Aviv Bergman, Albert Einstein College of Medicine
Jeffrey D. Blaustein, Univ. of Massachusetts Amherst
Richard Merrill Breyer, Vanderbilt Univ.
Craig Eugene Cameron, Pennsylvania State Univ.
Lon R. Cardon, GlaxoSmithKline
Douglas R. Cavener, Pennsylvania State Univ.
Aravinda Chakravarti, Johns Hopkins Univ. School of Medicine
Cheng-Ming Chuong, Univ. of Southern California
Gino A. Cortopassi, Univ. of California, Davis
Robert J. Cousins, Univ. of Florida
Richard D. Cummings, Emory Univ. School of Medicine
Stephen P. Daiger, Univ. of Texas Health Science Center at Houston
Ann Dean, National Institute of Diabetes and Digestive and Kidney Diseases/NIH
Lynn Eleanor DeLisi, VA Boston Healthcare System/Harvard Medical School
Ronald A. DePinho, Univ. of Texas MD Anderson Cancer Center
Burton F. Dickey, Univ. of Texas MD Anderson Cancer Center
Valerian V. Dolja, Oregon State Univ.
David C. Dorman, North Carolina State Univ.
Gregory Roland Dressler, Univ. of Michigan
Daniela Drummond-Barbosa, Johns Hopkins Univ.
Josée Dupuis, Boston Univ. School of Public Health
Geoffrey M. Duyk, Texas Pacific Group (TPG)
Irene Anne Eckstrand, National Institute of General Medical Sciences/NIH
Sean R. Eddy, HHMI Janelia Research Campus
Alan N. Engelman, Dana-Farber Cancer Institute
Peter J. Espenshade, Johns Hopkins Univ. School of Medicine

Rosann A. Farber, Univ. of North Carolina at Chapel Hill
Joanna Floros, Pennsylvania State Univ. College of Medicine
Jeffrey M. Friedman, Rockefeller Univ.
Haian Fu, Emory Univ. School of Medicine
David J. Garfinkel, Univ. of Georgia
Deborah E. Goldberg, Univ. of Michigan
Margaret A. Goodell, Baylor College of Medicine
Dan Graur, Univ. of Houston
Marilyn R. Gunner, City College of New York
Marnie E. Halpern, Carnegie Institution for Science
T. Kendall Harden, Univ. of North Carolina at Chapel Hill
A. Wallace Hayes, Harvard Univ.
Chuan He, Univ. of Chicago
John R. Hepler, Emory Univ. School of Medicine
Oliver Hobert, Columbia Univ. Medical Center
Stefan Hohmann, Univ. of Gothenburg (Sweden)
Richard L. Hoover, Vanderbilt Univ. Medical Center
Ya-Ming Hou, Thomas Jefferson Univ.
Elizabeth Ehrhardt Howell, Univ. of Tennessee, Knoxville
Trey Ideker, Univ. of California, San Diego
W. Gray Jerome, Vanderbilt Univ. School of Medicine
Teh-hui Kao, Pennsylvania State Univ.
Jack H. Kaplan, Univ. of Illinois at Chicago
Paul Andrew Karplus, Oregon State Univ.
Tom Klaus William Kerppola, Univ. of Michigan
Shohei Koide, Univ. of Chicago
Stephen F. Konieczny, Purdue Univ.
Bruce R. Korf, Univ. of Alabama at Birmingham
Robert G. Kranz, Washington Univ. in St. Louis
Lee Kroos, Michigan State Univ.
David Landsman, National Center for Biotechnology Information/NIH
David H. Ledbetter, Geisinger Health System
Brendan Lee, Baylor College of Medicine
Michael J. Leibowitz, Univ. of California, Davis
Norman G. Lewis, Washington State Univ.
Erwin London, Stony Brook Univ.
Manyuan Long, Univ. of Chicago
William L. Lowe Jr., Northwestern Univ. Feinberg School of Medicine
Bruce J. MacFadden, Florida Museum of Natural History, Univ. of Florida
Nicholas Gordon Martin, Queensland Institute of Medical Research (Australia)
Andrea M. Mastro, Pennsylvania State Univ.
U. Thomas Meier, Albert Einstein College of Medicine
Karen L. Mohlke, Univ. of North Carolina at Chapel Hill
Andrew W. Murray, Harvard Univ.

Jeffrey C. Murray, Univ. of Iowa/Bill and Melinda Gates Foundation
 David L. Nelson, Baylor College of Medicine
 Phillip Allan Newmark, Howard Hughes Medical Institute/Univ. of Illinois at Urbana-Champaign
 Ian C.T. Nisbet, I.C.T. Nisbet and Company (retired)
 Michael J. Oglesbee, Ohio State Univ.
 Mark D. Ohman, Scripps Institution of Oceanography/Univ. of California, San Diego
 Ian Michael Orme, Colorado State Univ.
 Mary Ann Ottinger, Univ. of Houston
 Tao Pan, Univ. of Chicago
 Patricia Ann Peyser, Univ. of Michigan School of Public Health
 Sara C. Pryor, Cornell Univ.
 B. Franklin Pugh, Pennsylvania State Univ.
 Richard Anthony Rachubinski, Univ. of Alberta (Canada)
 Danny F. Reinberg, New York Univ.
 Daniel Martin Roberts, Univ. of Tennessee, Knoxville
 Roy Martin (Marty) Roop II, East Carolina Univ. School of Medicine
 Jocelyn Kenneth Campbell Rose, Cornell Univ.
 Barry Philip Rosen, Florida International Univ. Herbert Wertheim College of Medicine
 Stanley J. Roux, Univ. of Texas at Austin
 Peter A. Rubenstein, Univ. of Iowa
 Paolo Sassone-Corsi, Univ. of California, Irvine
 Todd A. Schlenke, Reed College
 Jon Seger, Univ. of Utah
 K. Krishna Sharma, Univ. of Missouri-Columbia
 Sanjay S. Shete, Univ. of Texas MD Anderson Cancer Center
 Robert H. Singer, Albert Einstein College of Medicine/HHMI Janelia Research Campus
 Michael Snyder, Stanford Univ.
 Benjamin C. Stark, Illinois Institute of Technology
 Rainer Storb, Fred Hutchinson Cancer Research Center
 William S. Talbot, Stanford Univ.
 Stephen E. Ullrich, Univ. of Texas MD Anderson Cancer Center
 Karen M. Vasquez, Univ. of Texas at Austin
 Leslie B. Voss, Rockefeller Univ.
 Pamela J. Weathers, Worcester Polytechnic Institute
 Theodore G. Wensel, Baylor College of Medicine
 Mark Winey, Univ. of Colorado Boulder
 Edward W. Yu, Iowa State Univ.

Section on Chemistry

Nancy L. Allbritton, Univ. of North Carolina at Chapel Hill
 Jerry L. Atwood, Univ. of Missouri-Columbia
 Bill J. Baker, Univ. of South Florida

Thomas Edwin Bitterwolf, Univ. of Idaho
 Bruce S. Brunschwig, California Institute of Technology
 Michelle V. Buchanan, Oak Ridge National Laboratory
 Jef Karel De Brabander, Univ. of Texas Southwestern Medical Center at Dallas
 Henry C. Foley, Univ. of Missouri-Columbia
 Heinz M. Frei, Lawrence Berkeley National Laboratory
 Michael T. Green, Pennsylvania State Univ.
 Brian A. Gregg, National Renewable Energy Laboratory
 Patrick L. Holland, Yale Univ.
 Timothy F. Jamison, Massachusetts Institute of Technology
 David M. Jonas, Univ. of Colorado Boulder
 Christopher W. Jones, Georgia Institute of Technology
 Silvia Sabine Jurisson, Univ. of Missouri-Columbia
 Christine Dolan Keating, Pennsylvania State Univ.
 John Z. Larese, Univ. of Tennessee, Knoxville
 Richard Alan LeSar, Iowa State Univ.
 Arumugam Manthiram, Univ. of Texas at Austin
 Thomas J. Meade, Northwestern Univ.
 Deane Fremont Mosher Jr., Univ. of Wisconsin-Madison
 Vincent T. Remcho, Oregon State Univ.
 David Duncan Roberts, National Cancer Institute/NIH
 Laurel L. Schafer, Univ. of British Columbia (Canada)
 Charles Albert Schmuttenmaer, Yale Univ.
 Richard R. Schrock, Massachusetts Institute of Technology
 Yang Shao-Horn, Massachusetts Institute of Technology
 C. David Sherrill, Georgia Institute of Technology
 Mikiko Sodeoka, RIKEN (Japan)
 Mark T. Spitler, U.S. Department of Energy
 George G. Stanley, Louisiana State Univ.
 Judith Stein, GE Global Research (Retired)
 JoAnne Stubbe, Massachusetts Institute of Technology
 Lai-Xi Wang, Univ. of Maryland
 Shi-Qing Wang, Univ. of Akron
 Bert Weckhuysen, Utrecht Univ. (Netherlands)
 David W. Wright, Vanderbilt Univ.
 Jin Zhang, Johns Hopkins Univ. School of Medicine

Section on Dentistry and Oral Health Sciences

Matthew J. Doyle, The Procter & Gamble Company
 Ophir David Klein, Univ. of California, San Francisco
 Ann Progulske-Fox, Univ. of Florida

Section on Education

Cynthia Margaret Bauerle, Howard Hughes Medical Institute

Bianca L. Bernstein, Arizona State Univ.
 Elizabeth S. Boylan, Alfred P. Sloan Foundation
 Elaine A. Johnson, Bio-Link/City College of San Francisco
 David E. Lopatto, Grinnell College
 Patricia A. Marsteller, Emory Univ.
 David Hillyer Voorhees, Waubesa Community College
 Daniel A. Wubah, Washington and Lee Univ.

Section on Engineering

John S. Baras, Univ. of Maryland
 Edward J. Berbari, Indiana Univ. Purdue Univ. Indianapolis
 Roger T. Bonnecaze, Univ. of Texas at Austin
 Lance R. Collins, Cornell Univ.
 Placid M. Ferreira, Univ. of Illinois at Urbana-Champaign
 Shekhar Garde, Rensselaer Polytechnic Institute
 Brendan A. Harley, Univ. of Illinois at Urbana-Champaign
 Gilbert V. Herrera, Sandia National Laboratories
 Mark C. Hersam, Northwestern Univ.
 Yun Hang Hu, Michigan Technological Univ.
 David A. Kofke, Univ. at Buffalo, SUNY
 K. Lu, Chinese Academy of Sciences
 Joseph William Lyding, Univ. of Illinois at Urbana-Champaign
 Manos Mavrikakis, Univ. of Wisconsin-Madison
 Karen Anne Moxon, Drexel Univ.
 Debbie A. Niemeier, Univ. of California, Davis
 Christopher Kemper Ober, Cornell Univ.
 Viluppanur A. Ravi, Cal Poly Pomona
 Clinton T. Rubin, Stony Brook Univ.
 Ka-Yiu San, Rice Univ.
 Wolfgang M. Sigmund, Univ. of Florida
 Igal Szleifer, Northwestern Univ.
 George Alexander Truskey, Duke Univ.
 Marjolein Christine H. van der Meulen, Cornell Univ.
 Gordana Vunjak-Novakovic, Columbia Univ.
 Norman J. Wagner, Univ. of Delaware
 Ge Wang, Rensselaer Polytechnic Institute
 Robert K. Whitman, Univ. of Denver
 Jessica O. Winter, Ohio State Univ.
 Mohammed A. Zikry, North Carolina State Univ.

Section on General Interest in Science and Engineering

John Katzenberger, Aspen Global Change Institute
 Mary K. Miller, Exploratorium, San Francisco
 Peter N. Spotts, The Christian Science Monitor

Section on Geology and Geography

Rodey Batiza, National Science Foundation
 Hilary H. Birks, Univ. of Bergen (Norway)
 Steven C. Cande, Univ. of California, San Diego
 Kenneth H. Coale, Moss Landing Marine Laboratories

Thomas Cronin, U.S. Geological Survey
 Rane L. Curl, Univ. of Michigan
 Samantha B. Joye, Univ. of Georgia
 Michael Keller, USDA Forest Service
 Kenneth P. Kodama, Lehigh Univ.
 Daniel A. Lashof, Natural Resources Defense Council
 David López-Carr, Univ. of California, Santa Barbara
 Derek R. Lovley, Univ. of Massachusetts Amherst
 Melanie A. Mayes, Oak Ridge National Laboratory
 Nora Noffke, Old Dominion Univ.
 Harry H. Roberts, Louisiana State Univ.
 George D. Stanley Jr., Univ. of Montana
 Brian William Stump, Southern Methodist Univ.
 Thomas William Swetnam, Univ. of Arizona
 James W. C. White, Univ. of Colorado Boulder
 Carol M. Wicks, Louisiana State Univ.

Section on History and Philosophy of Science

Cathryn Carson, Univ. of California, Berkeley
 Robert J. Malone, History of Science Society/Univ. of Notre Dame
 Joseph C. Pitt, Virginia Tech
 C. Kenneth Waters, Univ. of Minnesota

Section on Industrial Science and Technology

Cammy R. Abernathy, Univ. of Florida
 Liyuan Liang, Oak Ridge National Laboratory
 J. Stephen Rottler, Sandia National Laboratories
 Justin Schwartz, North Carolina State Univ.

Section on Information, Computing, and Communication

Francine Berman, Rensselaer Polytechnic Institute
 Ahmed K. Elmagarmid, Qatar Computing Research Institute, Qatar Foundation
 Thomas D. Garvey, SRI International
 Peter D. Karp, SRI International
 Madhav V. Marathe, Virginia Tech
 Eric Mjolsness, Univ. of California, Irvine
 Dan Roth, Univ. of Illinois at Urbana-Champaign
 William H. Sanders, Univ. of Illinois at Urbana-Champaign
 Thomas L. Sterling, Indiana Univ.

Section on Linguistics and Language Sciences

Ralph W. Fasold, Georgetown Univ.
 Lise Menn, Univ. of Colorado Boulder
 Pamela Munro, Univ. of California, Los Angeles

Section on Mathematics

James M. Crowley, Society for Industrial and Applied Mathematics
 Charles L. Epstein, Univ. of Pennsylvania
 Nataša Jonoska, Univ. of South Florida
 Kirk E. Jordan, IBM Research Division

Yuri Tschinkel, New York Univ.
 Howard (Howie) Weiss, Georgia Institute of Technology

Section on Medical Sciences

Lynne V. Abruzzo, Ohio State Univ.
 Naji N. Abumrad, Vanderbilt Univ. School of Medicine
 Rexford S. Ahima, Univ. of Pennsylvania Perelman School of Medicine
 Andrew Arnold, Univ. of Connecticut School of Medicine
 Linda Gwen Baum, Univ. of California, Los Angeles Geffen School of Medicine
 Jeremy M. Boss, Emory Univ. School of Medicine
 Myles A. Brown, Dana-Farber Cancer Institute
 David Michael Center, Boston Univ. Medical Center
 Jeffrey S. Chamberlain, Univ. of Washington School of Medicine
 Bandana Chatterjee, Univ. of Texas Health Science Center at San Antonio
 Xinbin Chen, Univ. of California, Davis
 Jeffrey I. Cohen, National Institute of Allergy and Infectious Diseases/NIH
 Ronald B. Corley, Boston Univ. School of Medicine
 Christopher M. Counter, Duke Univ. Medical Center
 Jules L. Dienstag, Harvard Medical School
 Mary C. Dinauer, Washington Univ. School of Medicine in St. Louis
 Jeffrey M. Drazen, *New England Journal of Medicine*
 Garth D. Ehrlich, Drexel Univ. College of Medicine
 Agnes B. Fogo, Vanderbilt Univ. Medical Center
 Scott Laurence Friedman, Icahn School of Medicine at Mount Sinai
 Sanjiv Sam Gambhir, Stanford Univ.
 Katherine Amberson Hajjar, Weill Cornell Medical College
 Barbara C. Hansen, Univ. of South Florida
 Christopher Charles William Hughes, Univ. of California, Irvine
 Rakesh K. Jain, Massachusetts General Hospital/Harvard Medical School
 Robert Gordon Kalb, Children's Hospital of Philadelphia/Univ. of Pennsylvania Perelman School of Medicine
 Fadlo Raja Khuri, Winship Cancer Institute, Emory Univ.
 Margaret Kielian, Albert Einstein College of Medicine
 Richard N. Kitsis, Albert Einstein College of Medicine
 Carol Ann Kumamoto, Tufts Univ.
 Stephen B. Liggett, Univ. of South Florida College of Medicine
 Jay S. Loeffler, Massachusetts General Hospital
 Joseph Loscalzo, Brigham and Women's Hospital/Harvard Medical School

Simon Alexander Mallal, Vanderbilt Univ. School of Medicine
 John Mendelsohn, Univ. of Texas MD Anderson Cancer Center
 Dennis W. Metzger, Albany Medical College
 Jeffrey J. Molldrem, Univ. of Texas MD Anderson Cancer Center
 David R. Piwnica-Worms, Univ. of Texas MD Anderson Cancer Center
 Fernando P. Polack, Vanderbilt Univ. School of Medicine
 Katya Ravid, Boston Univ. School of Medicine
 Barrett Jon Rollins, Dana-Farber Cancer Institute
 Nancy Hartman Ruddle, Yale Univ. School of Public Health
 David J. Salant, Boston Univ. Medical Center
 Erica Ollmann Saphire, Scripps Research Institute
 P. Sarita Soni, Indiana Univ.
 David Samuel Stephens, Emory Univ. Woodruff Health Sciences Center School of Medicine
 Patrick J. Stover, Cornell Univ.
 Bruce Alan Sullenger, Duke Univ. Medical Center
 James Ward Thomas II, Vanderbilt Univ. School of Medicine
 Kevin J. Tracey, Feinstein Institute for Medical Research
 Jan Vijg, Albert Einstein College of Medicine
 Paul A. Welling, Univ. of Maryland School of Medicine

Section on Neuroscience

Richard Warren Aldrich, Univ. of Texas at Austin
 Silvia Arber, Univ. of Basel/Friedrich Miescher Institute for Biomedical Research (Switzerland)
 Rita Balice-Gordon, Pfizer, Inc.
 Francisco Bezanilla, Univ. of Chicago
 Samuel A. Deadwyler, Wake Forest Univ. School of Medicine
 Daniel J. Goldman, Univ. of Michigan
 David M. Holtzman, Washington Univ. in St. Louis
 Christof Koch, Allen Institute for Brain Science
 Alex Leo Kolodkin, Johns Hopkins Univ. School of Medicine
 Michael Stephen Levine, Univ. of California, Los Angeles
 David G. Morgan, Univ. of South Florida
 Ronald William Oppenheim, Wake Forest Univ. School of Medicine
 Marina R. Picciotto, Yale Univ. School of Medicine
 Jeffrey D. Schall, Vanderbilt Univ.
 Masatoshi Takeichi, RIKEN (Japan)
 Stephen Francis Traynelis, Emory Univ. School of Medicine
 Fan Wang, Duke Univ. Medical Center
 George D. Yancopoulos, Regeneron Pharmaceuticals, Inc.
 Charles Zuker, Columbia Univ.

Section on Pharmaceutical Sciences

Suresh V. Ambudkar, National Cancer Institute/NIH
Douglas A. Bayliss, Univ. of Virginia
Peter Buchwald, Univ. of Miami School of Medicine
Alice M. Clark, Univ. of Mississippi
Varsha Gandhi, Univ. of Texas MD Anderson Cancer Center
Randy A. Hall, Emory Univ. School of Medicine
Stephen S. Hecht, Univ. of Minnesota Medical School
Sung Wan Kim, Univ. of Utah College of Pharmacy
Gary R. Matzke, Virginia Commonwealth Univ. School of Pharmacy

Section on Physics

Andrew J. Baker, Rutgers, The State Univ. of New Jersey
Robert Allen Bartynski, Rutgers, The State Univ. of New Jersey
Philip G. Collins, Univ. of California, Irvine
Priscilla B. Cushman, Univ. of Minnesota
Carlos Henrique de Brito Cruz, São Paulo Research Foundation (FAPESP) (Brazil)
Alan T. Dorsey, Univ. of Georgia
John Harte, Univ. of California, Berkeley
Mary Y.P. Hockaday, Los Alamos National Laboratory
David Larbalestier, National High Magnetic Field Laboratory, Florida State Univ.

Marvin L. Marshak, Univ. of Minnesota
Roberto Daniel Merlin, Univ. of Michigan
Mark Newman, Univ. of Michigan
Harrison B. Prosper, Florida State Univ.
Bruce Arne Sherwood, North Carolina State Univ.
Milton Dean Slaughter, Florida International Univ.
Christopher Michael Sorensen, Kansas State Univ.
Nancy L. Thompson, Univ. of North Carolina at Chapel Hill
Amir Yacoby, Harvard Univ.

Section on Psychology

John T. Bruer, James S. McDonnell Foundation
Robert S. Feldman, Univ. of Massachusetts, Amherst
Wilma Koutstaal, Univ. of Minnesota
Stanley Abraham Kuczaj II, Univ. of Southern Mississippi
Nan Bernstein Ratner, Univ. of Maryland, College Park
Eric Wanner, Russell Sage Foundation

Section on Social, Economic, and Political Sciences

Julia Ingrid Lane, American Institutes for Research/Univ. of Strasbourg (France)/Univ. of Melbourne (Australia)
Dudley L. Poston Jr., Texas A&M Univ.

Barbara Schneider, Michigan State Univ.
Mitchel B. Wallerstein, Baruch College
Michael Joseph White, Brown Univ.

Section on Societal Impacts of Science and Engineering

Elizabeth A. Chornesky, Independent Analyst
T. Taylor Eighmy, Univ. of Tennessee, Knoxville
Anthony Fainberg, Institute for Defense Analyses
Micah Daniel Lowenthal, National Academy of Sciences

Section on Statistics

Susmita Datta, Univ. of Louisville
Mark Andrew Espeland, Wake Forest Univ. School of Medicine
Robert Jackson Hardy, Univ. of Texas School of Public Health
William Q. Meeker Jr., Iowa State Univ.
Paula Karen Roberson, Univ. of Arkansas for Medical Sciences
John P. Sall, SAS Institute
James J. Schlesselman, Univ. of Pittsburgh
Stephanie Shipp, Virginia Tech
Clifford Spiegelman, Texas A&M Univ.

AAAS Kavli Science Journalism Award winners named

By Earl Lane

Stories exploring human biology, including our interactions with the trillions of microbes we all harbor, the influences of our fishy evolutionary forebears on how we look, and the enduring challenge of understanding cancer, are among the winners of the 2014 AAAS Kavli Science Journalism Awards.

Large Newspaper—Circulation of 100,000 or more: George Johnson, *The New York Times*, for “Why Everyone Seems to Have Cancer,” 5 January 2014; “A Tumor, the Embryo’s Evil Twin,” 18 March 2014; and “An Apple a Day, and Other Myths,” 22 April 2014.

Small Newspaper—Circulation less than 100,000: Matthew LaPlante and Paul Christiansen, *Salt Lake City Weekly*, for “Devastated: The World’s Largest Organism is in Utah—and It’s Dying,” 21 November 2013.

Magazine: David Dobbs, *Pacific Standard*, for “The Social Life of Genes,” September/October 2013.

Television—Spot News/Feature Reporting (20 minutes or less): Michael Werner, KCTS 9/QUEST, for “The Ecology of Fear,” 6 March 2014.

Television—In Depth Reporting (more than 20 minutes): Michael Rosenfeld, David Dugan, and Neil Shubin, Tangled Bank Studios/Windfall Films for PBS, for “Your Inner Fish,” 9 April, 16 April, & 23 April 2014.

Radio: Rob Stein, NPR, for “Staying Healthy May Mean Learning To Love Our Microbiomes,” 22 July 2013; “From Birth, Our Microbes Become As Personal As A Fingerprint,” 9 September 2013; and “Getting Your Microbes Analyzed Raises Big Privacy Issues,” 4 November 2013.

Online: Amy Dockser Marcus, *The Wall Street Journal*, for “Trials: A Desperate Fight to Save Kids and Change Science,” 14 November 2013.



Children’s Science News: Mara Grunbaum, *Scholastic Science World*, for “Biting Back,” 16 September 2013; “Underwater Adventurer,” 7 October 2013; and “Swallowed Up,” 3 February 2014.

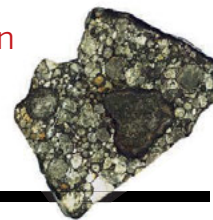
The awards, administered by AAAS since their inception in 1945, go to professional journalists for distinguished reporting for a general audience. The Kavli Foundation provided a generous endowment in 2009 that ensures the future of the program.

Independent panels of science journalists pick the winners, who will receive \$3000 and a plaque at the 2015 AAAS Annual Meeting in San Jose, California, in February. Learn more at www.aaas.org/sja2014. ■

RESEARCH

Remnant magnetization in a primitive meteorite

Fu et al., p. 1089



IN SCIENCE JOURNALS

Edited by Stella Hurlley



Wild cucumber

PLANT SCIENCE

Biosynthetic pathway holds roots of domestication

The wild cucumber is a spiky, bitter relative of what we now grow in our gardens. The bitterness comes from cucurbitacin, which helps the plant to ward off herbivores. Cucurbitacin is also useful to people for its anti-tumor properties. Shang *et al.* have now worked out the biosynthetic pathway of cucurbitacin. Along the way, they discovered genetic traces of the domestication process and unraveled the mystery of why some cucumbers, if grown in chilly conditions, become bitter. — PJH

Science, this issue p. 1084

BLACK HOLE PHYSICS

Timing tells the structure of the unseen

Nothing can move faster than the speed of light, but some gamma rays seem to break that rule. Powerful jets that balance the angular momentum of accreting black holes are difficult to discern in images, so astronomers often resort to timing their emission to reveal the physics at work. Aleksić *et al.* found that gamma rays from the active galaxy IC 310 varied faster than the time required for light to cross the event horizon of the supermassive black hole at its nucleus. Particle acceleration at the base of the jet may enable this apparent speed, adding a piece to the puzzle of how jets form at supermassive black holes. — MMM

Science, this issue p. 1080

MATERIALS SCIENCE

Graphene: A miniature bulletproof vest?

To stop a speeding projectile, you need a combination of strength and toughness so that the impact doesn't just pierce the stopping material. The material also needs to dissipate the absorbed kinetic energy. Lee *et al.* measured the response of multilayer graphene to the projection of microbullets using miniaturized ballistic tests. The findings confirm graphene's exceptional strength and stiffness. — MSL

Science, this issue p. 1092

CHEMICAL OCEANOGRAPHY

Polluting the way to more productivity

Most biologically available nitrogen comes from the recycling of organic matter and nitrogen

fixation. However, airborne anthropogenic nitrogen—air pollution—can also provide a source of such nitrogen. Kim *et al.* reconstructed changes in the N content of surface water across the North Pacific Ocean for the past four decades. N concentrations have increased markedly. This trend could enhance microbial growth in the ocean and eventually increase production of the greenhouse gas N_2O . — HJS

Science, this issue p. 1102

COGNITIVE PSYCHOLOGY

Forgetting history one president at a time

Memory for past events and famous people, some of which may have happened or lived before we were born, fades with time. Roediger and DeSoto measured the extent and rate

at which former U.S. presidents have been forgotten (see the Perspective by Rubin). Three cohorts of college students, spanning four decades, forgot in the same way: Each group remembered Washington and Lincoln and also the most recent office holders (Ford, Reagan, and Obama). — GJC

Science, this issue p. 1106; see also p. 1058

SKIN DISEASE

Personalized cell therapy for skin disorder

Mutations in the *COL7A1* gene cause severely fragile skin and painful blistering in a rare disease, recessive dystrophic epidermolysis bullosa (RDEB). There is no cure, but Sebastiano *et al.* now show that cell therapy could be a viable option. The authors took skin biopsies from

three patients with RDEB and generated induced pluripotent stem cells, or iPSCs, from the tissue. They genetically corrected the *COL7A1* mutation and made keratinocytes (skin cells) that expressed normal collagen VII. In mice, these “repaired” keratinocytes formed layers of human skin expressing collagen VII. The skin grafts only lasted for a few weeks, but the ability to genetically correct and bank a patient’s own cells is an important step toward treating RDEB. — MLF

Sci. Transl. Med. **6**, 264ra163 (2014).

PALEOGENOMICS

Secrets of human ancestor evolution revealed

Studies of ancient humans help us understand the movement and evolution of modern populations of humans. Seguin-Orlando *et al.* present the genome of an ancient individual, K14, from northern Russia who lived over 36,000 years ago. K14 is more similar to west Eurasians and Europeans than to east Asians, indicating that these populations had already diverged. — LMZ

Science, this issue p. 1113

REPELLENT SURFACES

Undercutting the surface keeps liquids at bay

The shape of an umbrella is designed both to protect the holder from falling droplets and to have the collected rainwater flow away from the



person underneath. Liu and Kim exploited the idea of an umbrella to make materials with a surface that repels almost any liquid.

— MSL

Science, this issue p. 1096

MITOCHONDRIA

Cross talk between mitochondria and mitosis

Mitochondria, the power houses of the cell, contain their own genome. Nevertheless, the majority of their constituent proteins are encoded by nuclear genes and are translated in the cytosol. During the cell cycle, a cell needs to duplicate each of its constituent parts and organelles. Surprisingly, it has never been clear how or whether mitochondrial protein import is linked with the cell cycle. Harbauer *et al.* (see the Perspective by Schulz and Rehling) now show that one of the main conduits for mitochondrial protein import is directly regulated by phosphorylation during mitosis, and that this in turn promotes respiratory activity. — SMH

Science, this issue p. 1109

CANCER IMMUNOLOGY

Retaining a barrier to cancer metastasis

One way cancers can spread, or metastasize, is by invading blood vessels, which are lined with endothelial cells. Pignatelli *et al.* found that cells from biopsies of invasive breast cancers crossed a layer of endothelial cells more readily than those from less aggressive breast cancers, particularly when cultured with macrophages (see the Perspective by Kiersse *et al.*). Macrophages promoted breast cancer cell invasion by secreting the growth factor EGF, which induced breast cancer cells to secrete the cytokine CSF-1. The cytokine acted on macrophages and on some types of cancer cell. Blocking the binding of CSF-1 to its receptor prevented cancer cells from crossing endothelial cultures. — LKF

Sci. Signal. **7**, ra112 and pe28 (2014).

IN OTHER JOURNALS

Edited by **Kristen Mueller**
and **Jesse Smith**

Common ravens (*Corvus corax*) engaged in a mating behavior.



ANIMAL BEHAVIOR

Up and down the raven social ladder

Social hierarchies are complex, and threats abound for people and, as it turns out, for ravens, too. Massen *et al.* followed a group of approximately 200 individually marked ravens in the Austrian Alps. They found that strongly bonded breeding pairs at the top of the raven social hierarchy disrupted interactions between loosely bonded pairs lower in the hierarchy. They also tended to ignore nonbonded individuals located at the bottom of the hierarchy. In doing so, the higher-ranking birds may prevent the lower-status breeding pairs from rising up the hierarchy and becoming a social threat. — GR

Curr. Biol. **24**, 2733 (2014).

The physiology of turtle breathing differs from that of other vertebrates



VERTEBRATE EVOLUTION

Turtles' breathing evolved at a turtle's pace

In most vertebrates, muscles associated with the lungs (intercostal muscles) work with the abdominal muscles to control breathing. In turtles, however, the rigid shell immobilizes the intercostal muscles, so only the abdominal muscles control lung expansion. How did such a major shift in an essential physiological function evolve? To find out, Lyson *et al.* compared extinct and extant vertebrates. The authors found that this transition proceeded slowly and began with a broadening of the ribs in a species that existed 50 million years before the first fully shelled turtle. — SNV

Nat. Commun. 10.1038/ncomms6211 (2014).

NEUROSCIENCE

Virtual reality changes neuronal firing

Place cells are a type of neuron in the brain that gives you a sense of place and allows for spatial navigation. Visual cues are important for determining place cell function, but do other sensory or motor cues also play a role? To find out, Aghajani *et al.* compared rats navigating mazes in the real world and rats doing the same thing in virtual reality, where the only input they received was from distal visual cues. By monitoring the firing of place cells, the

authors found that these cells did not perform optimally in the rats experiencing the virtual reality mazes. These results suggest that place cells need more than just visual signals. — PRS

Nat. Neurosci. 10.1038/nn.3884 (2014).

ORGANIC GEOCHEMISTRY

Looking at lipids with lasers

The remnants of microbial lipids preserved in sediments provide reliable records of past aquatic environments.

Extracting trace amounts of these molecules from sediment cores is often tricky and requires a large amount of material, which causes the time resolution of these records to be rather coarse. Wörmer *et al.* used a high-resolution mass spectrometer coupled to a laser ionization source to track variations of nanogram levels of archaeal tetraethers at a resolution of ~4 years. Tiny variations in lipid structure and abundance in sediments from the Mediterranean Sea with ages of over 10,000 years show that planktonic archaea there were

strongly influenced by ~200-year-long solar cycles. — NW

Proc. Natl. Acad. Sci. U.S.A. 10.1073/pnas.1405237111 (2014).

GENE REGULATION

Insulin secretion organized in the nucleus

Cells can modify gene expression by changing the spatial and physical landscape of DNA in the nucleus. This allows a gene to influence the expression of another gene that may be located several megabases down the chromosome. With this in mind and to find new genes that may influence how insulin functions, Xu *et al.* looked for genes that physically contacted the insulin gene in human pancreatic beta cells, cells that make and store insulin. They found that the insulin promoter contacted and regulated the *ANO1* gene, located more than half a chromosome away, which encodes a calcium-activated chloride channel. Glucose increased *ANO1* expression, and loss of *ANO1* inhibited insulin secretion. — LBR

Proc. Natl. Acad. Sci. U.S.A. 10.1073/pnas.1419240111 (2014).

MICROFLUIDICS

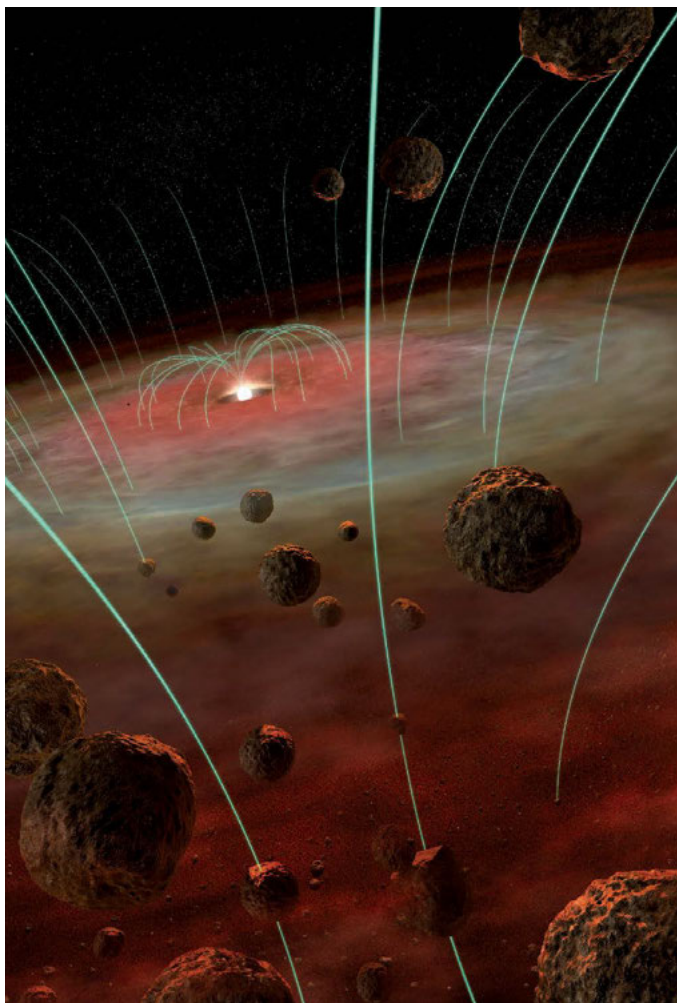
Sorting cells by subpopulations

The loss of cells from a tumor into the bloodstream creates circulating tumor cells (CTCs) that may allow a cancer to metastasize. Within this population of CTCs, a heterogeneous range of cells may exist. Mohamadi *et al.* have built a microfluidic device that can collect CTCs and differentiate them into distinct groups. Separation is based on the quantity of the epithelial marker EpCAM found on the surface, which may be related to the metastatic potential of the CTC. Magnetic nanoparticles that target EpCAM may cling to the cell surface, allowing the particles to be separated in controlled flow zones based on their ability to resist to the fluid flow due to magnetic attraction. — MSL

Angew. Chem. 10.1002/ange.201409376 (2014).

ALSO IN SCIENCE JOURNALS

Edited by Stella Hurtley



MINERALOGY

A mineral name for mantle perovskite

A rock from outer space finally puts a name to Earth's most abundant mineral, frequently referred to as perovskite. Mineral names are only bestowed on specimens that are found in nature and characterized. Tschauner *et al.* isolate a magnesium silicate in the perovskite structure, now called bridgmanite, in the Tenham L6 chondrite meteorite (see the Perspective by Sharp). Bridgmanite formed in this meteorite during a high-pressure and -temperature shock event. Other minerals associated with bridgmanite allow the pressure-temperature conditions to be narrowly bound,

giving insight into the shock process. The long-sought-after specimen finally puts to rest a confusing nomenclature of this dense deep mantle silicate. — BG

Science, this issue p. 1100; see also p. 1057

PALEOMAGNETISM

Magnetic moments in planetary history

To know the magnetic history of the solar nebula in the age of planet formation, researchers turn to the most primitive meteorites. Samples such as the Semarkona chondrite are composed partly of chondrules, which reflect the strength of the ambient magnetic field when

this material was last molten. Fu *et al.* used a SQUID microscope to measure the remnant magnetization in a section of Semarkona. The findings reveal secrets about what goes on inside protoplanetary disks. — MMM

Science, this issue p. 1089

GENOME ENGINEERING

CRISPR-cas: A revolution in genome engineering

The ability to engineer genomic DNA in cells and organisms easily and precisely will have major implications for basic biology research, medicine, and biotechnology. Doudna and Charpentier review the history of genome editing technologies, including oligonucleotide coupled to genome cleaving agents that rely on endogenous repair and recombination systems to complete the targeted changes, self-splicing introns, and zinc-finger nucleases and TAL effector nucleases. They then describe how clustered regularly interspaced palindromic repeats (CRISPRs), and their associated (Cas) nucleases, were discovered to constitute an adaptive immune system in bacteria. They document development of the CRISPR-Cas system into a facile genome engineering tool that is revolutionizing all areas of molecular biology. — GR

Science, this issue p. 1077

TETANUS TOXIN ENTRY

A potential peptide to prevent tetanus?

Tetanus (TeNT) and botulinum (BoNT) neurotoxins represent a family of powerful bacterial protein toxins that cause tetanus and botulism in humans and animals. The molecular mechanisms responsible for the entry and axonal retrograde transport of these toxins have been the subject of intense research. However, tetanus and botulism remain incurable, at least in part because

of their high-affinity binding to synapses. Although the receptors for BoNT have recently been characterized at the molecular level, no protein receptor for TeNT at the neuromuscular junction has been identified. Bercsenyi *et al.* now suggest that TeNT exploits nidogen-1 and -2 for its binding to motor neurons. This binding is required for TeNT's internalization and axonal retrograde transport. Nidogens are extracellular matrix proteins that engage in multiple protein-protein interactions essential for the integrity of several tissues, including the nervous system. Interfering with the interaction between nidogens and TeNT by administering short nidogen-derived peptides blocked toxin binding to the neuromuscular junction and protected mice from tetanus. — SMH

Science, this issue p. 1118

T CELL SIGNALING

Stimulatory signals add up for T cells

T cell activation is a dynamic process. T cells encounter multiple input signals such as antigens, costimulatory molecules, and cytokines at different times and anatomical locations during an infection. But how do T cells integrate this information to determine the extent to which they divide? To find out, Marchingo *et al.* stimulated mouse T cells in culture with different combinations of inputs and also tracked antigen-specific T cell responses in mice infected with influenza virus. They found that T cells linearly sum the various stimulatory inputs they receive to determine their "division destiny." — KLM

Science, this issue p. 1123

FUNGAL BIOGEOGRAPHY

Assessing fungal diversity worldwide

Fungi are hyperdiverse but poorly known, despite their ecological

PHOTO: FU ET AL.

and economic impacts. Tedersoo *et al.* collected nearly 15,000 topsoil samples from 365 sites worldwide and sequenced their genomes (see the Perspective by Wardle and Lindahl). Overall, they found a striking decline in fungal species richness with distance from the equator. For some specialist groups though, diversity depended more on the abundance of host plants than host diversity or geography. The findings reveal a huge gap between known and described species and the actual numbers of distinct fungi in the world's soils. — CA

Science, this issue p. 1078;
see also p. 1052

DNA REPAIR

Staggered incisions unhook DNA crosslinks

Mutations that covalently link the two stands of DNA together, known as interstrand cross-links (ICLs), can wreak havoc with the many processes that need to separate the DNA strands to read the genome. For example, ICLs are commonly generated in the skin by exposure to UV. Wang *et al.* determined the crystal structure of the ICL repair exonuclease FAN1 bound to a branched segment of DNA that mimics an intermediate on the ICL repair pathway. The enzyme anchors itself at a cut

end of DNA and then cleaves successively at three nucleotide intervals, a pattern ideal for unhooking the ICL. FAN1 seems to have evolved to act, at least in part, at sites coupled to DNA synthesis or homologous recombination. — GR

Science, this issue p. 1127

SYSTEMS BIOLOGY

Deciphering information flow in T cells

We can now measure the activation state of multiple components of biochemical signaling pathways in single cells. This ability reveals how

information flows through such cellular regulatory pathways and how it is altered in disease. Krishnaswamy *et al.* applied statistical techniques to overcome the complexity and variation (or noise) in such single-cell measurements. They used these techniques to quantify information transfer between proteins that participate in antigen recognition in cells of the immune system. The methods should prove useful in analysis of other signaling circuits to enhance basic understanding and reveal potential therapeutic targets to fight disease. — LBR

Science, this issue p. 1079

REVIEW SUMMARY

GENOME EDITING

The new frontier of genome engineering with CRISPR-Cas9

Jennifer A. Doudna* and Emmanuelle Charpentier*

BACKGROUND: Technologies for making and manipulating DNA have enabled advances in biology ever since the discovery of the DNA double helix. But introducing site-specific modifications in the genomes of cells and organisms remained elusive. Early approaches relied on the principle of site-specific recognition of DNA sequences by oligonucleotides, small molecules, or self-splicing introns. More recently, the site-directed zinc finger nucleases (ZFNs) and TAL effector nucleases (TALENs) using the principles of DNA-protein recognition were developed. However, difficulties of protein design, synthesis, and validation remained a barrier to

widespread adoption of these engineered nucleases for routine use.

ADVANCES: The field of biology is now experiencing a transformative phase with the advent of facile genome engineering in animals and plants using RNA-programmable CRISPR-Cas9. The CRISPR-Cas9 technology originates from type II CRISPR-Cas systems, which provide bacteria with adaptive immunity to viruses and plasmids. The CRISPR-associated protein Cas9 is an endonuclease that uses a guide sequence within an RNA duplex, tracrRNA:crRNA, to form base pairs with DNA target sequences, enabling Cas9 to introduce a site-specific double-strand break

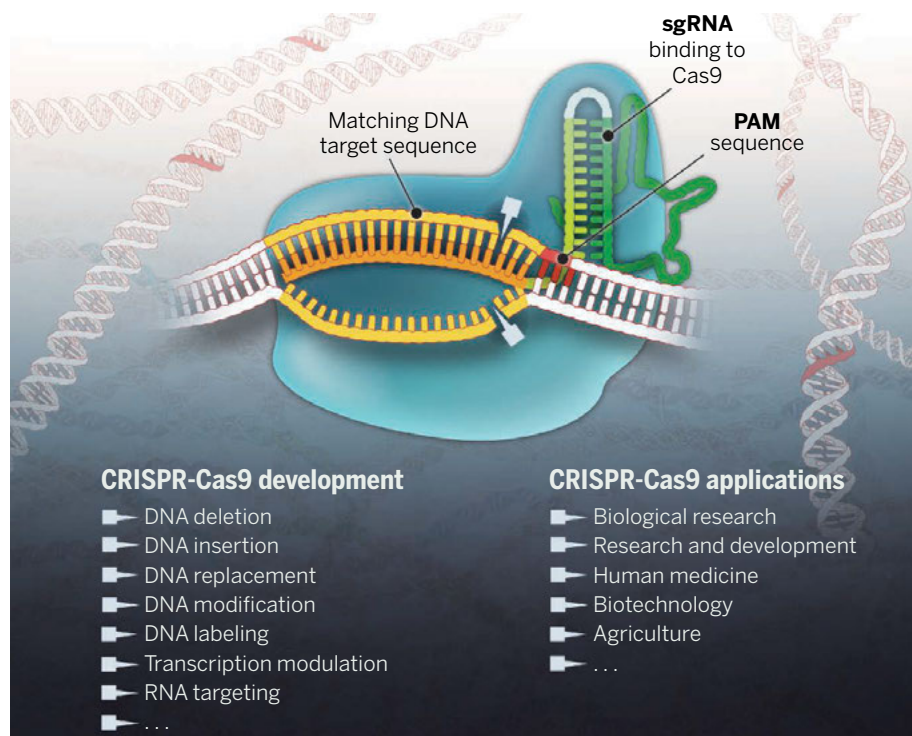
in the DNA. The dual tracrRNA:crRNA was engineered as a single guide RNA (sgRNA) that retains two critical features: a sequence at the 5' side that determines the DNA target site by Watson-Crick base-pairing and a duplex RNA structure at the 3' side that binds to Cas9. This finding created a simple two-component system in which changes in the guide sequence of the sgRNA program Cas9 to target any DNA sequence of interest. The simplicity of CRISPR-Cas9 programming, together with a unique DNA cleaving mechanism, the capacity for multiplexed target recognition, and the existence of many natural type II CRISPR-Cas system variants, has enabled remarkable developments using this cost-effective and easy-to-use technology to precisely and efficiently target, edit, modify, regulate, and mark genomic loci of a wide array of cells and organisms.

OUTLOOK: CRISPR-Cas9 has triggered a revolution in which laboratories around the world are using the technology for innovative applications in biology. This Review illustrates the power of the technology to systematically analyze gene functions in mammalian cells, study genomic rearrangements and the progression of cancers or other diseases, and potentially correct genetic mutations responsible for inherited disorders. CRISPR-Cas9 is having a major

impact on functional genomics conducted in experimental systems. Its application in genome-wide studies will enable large-scale screening for drug targets and other phenotypes and will facilitate the generation of engineered animal models that will benefit pharmacological studies and the understanding of human diseases. CRISPR-Cas9 applications in plants and fungi also promise to change the pace and course of agricultural research. Future research directions to improve the technology will include engineering or identifying smaller Cas9 variants with distinct specificity that may be more amenable to delivery in human cells. Understanding the homology-directed repair mechanisms that follow Cas9-mediated DNA cleavage will enhance insertion of new or corrected sequences into genomes. The development of specific methods for efficient and safe delivery of Cas9 and its guide RNAs to cells and tissues will also be critical for applications of the technology in human gene therapy. ■

ON OUR WEB SITE

Read the full article at <http://dx.doi.org/10.1126/science.1258096>



The Cas9 enzyme (blue) generates breaks in double-stranded DNA by using its two catalytic centers (blades) to cleave each strand of a DNA target site (gold) next to a PAM sequence (red) and matching the 20-nucleotide sequence (orange) of the single guide RNA (sgRNA). The sgRNA includes a dual-RNA sequence derived from CRISPR RNA (light green) and a separate transcript (tracrRNA, dark green) that binds and stabilizes the Cas9 protein. Cas9-sgRNA-mediated DNA cleavage produces a blunt double-stranded break that triggers repair enzymes to disrupt or replace DNA sequences at or near the cleavage site. Catalytically inactive forms of Cas9 can also be used for programmable regulation of transcription and visualization of genomic loci.

The list of author affiliations is available in the full article online.

*Corresponding author. E-mail: doudna@berkeley.edu (J.A.D.); emmanuelle.charpentier@helmholtz-hzi.de (E.C.)
Cite this article as J. A. Doudna, E. Charpentier, *Science* **346**, 1258096 (2014). DOI: 10.1126/science.1258096

REVIEW

GENOME EDITING

The new frontier of genome engineering with CRISPR-Cas9

Jennifer A. Doudna^{1,2,3*} and Emmanuelle Charpentier^{4,5,6*}

The advent of facile genome engineering using the bacterial RNA-guided CRISPR-Cas9 system in animals and plants is transforming biology. We review the history of CRISPR (clustered regularly interspaced palindromic repeat) biology from its initial discovery through the elucidation of the CRISPR-Cas9 enzyme mechanism, which has set the stage for remarkable developments using this technology to modify, regulate, or mark genomic loci in a wide variety of cells and organisms from all three domains of life. These results highlight a new era in which genomic manipulation is no longer a bottleneck to experiments, paving the way toward fundamental discoveries in biology, with applications in all branches of biotechnology, as well as strategies for human therapeutics.

Technologies for making and manipulating DNA have enabled many of the advances in biology over the past 60 years. This era began with the discovery of the DNA double helix and continued with the development of chemical methods for solid-phase DNA synthesis, enabling detection and exploration of genome organization. Enzymes (including polymerases, ligases, and restriction endonucleases) and the polymerase chain reaction (PCR) provided ways to isolate genes and gene fragments, as well as to introduce mutations into genes in vitro, in cells, and in model organisms. The advent of genomic sequencing technologies and the rapid generation of whole-genome sequencing data for large numbers and types of organisms, including humans, has been one of the singular advances of the past two decades. Now, the RNA-guided enzyme Cas9, which originates from the CRISPR-Cas adaptive bacterial immune system, is transforming biology by providing a genome engineering tool based on the principles of Watson-Crick base pairing. Ease of use and efficiency have led to rapid adoption by laboratories around the world. Below we discuss the history and biology of CRISPR systems, describe the molecular mechanisms underlying genome editing by Cas9, and review the rapid advances in applications of this technology since its initial publication in 2012.

Genome engineering—A decades-long goal

Ever since the discovery of the DNA double helix, researchers and clinicians have been contemplating the possibility of making site-specific changes to the genomes of cells and organisms. Many of the earliest approaches to what has been referred to as genome editing relied on the principle of site-specific recognition of DNA sequences (Fig. 1). The study of natural DNA repair pathways in bacteria and yeast, as well as the mechanisms of DNA recombination (1–5), revealed that cells have endogenous machinery to repair double-strand DNA breaks (DSBs) that would otherwise be lethal (6–9). Thus, methods for introducing precise breaks in the DNA at sites where changes are to be introduced was recognized as a valuable strategy for targeted genomic engineering.

Early approaches to such targeted DNA cleavage took advantage of DNA base pair recognition by oligonucleotides or small molecules. Building on the original description of triple helix formation by Rich and colleagues in the late 1950s (10, 11), oligonucleotides coupled to chemical cleavage or cross-linking reagents such as bleomycin and psoralen were shown to be useful for site-specific chromosome modification in yeast and mammalian cells (12–17). Other methods for chemical recognition of DNA sequences, such as peptide nucleic acids (PNAs) and polyamides, were shown to enable targeted binding of chromosomal loci that could be modified if the chemical recognition agent was coupled to a cleavage reagent such as bleomycin (18–20). Another strategy that relied on nucleic acid base pairing was the use of self-splicing introns to change sequences at the DNA (21, 22) or RNA (23) level. Although these approaches did not lead to robust methods, they demonstrated the utility of base pairing for site-specific genome modification.

The use of self-splicing introns for genome editing also suggested the possibility of using intron-encoded nucleases—homing endonucleases—that are capable of site-specific DNA cleavage and integration of the intron sequence. By inserting desired sequences into the intron first, researchers could incorporate selected genetic information into a genome at sites recognized by the homing endonuclease (24, 25). At around the same time, the initial reports of zinc finger-mediated DNA binding (26, 27) led to the creation of modular DNA recognition proteins that, when coupled to the sequence-independent nuclease domain of the restriction enzyme FokI, could function as site-specific nucleases (28). When designed to recognize a chromosomal sequence, such zinc finger nucleases (ZFNs) were found to be effective at inducing genomic sequence changes in *Drosophila* and mammalian cells (29, 30). Although ZFNs are effective genome editing reagents for some experiments, they were not widely adopted because of the difficulty inherent in designing and validating such proteins for a specific DNA locus of interest. Thus, the field was primed for the first reports of transcription activator-like (TAL) effectors, which occur naturally in bacteria that infect plants, enabling rapid creation of FokI-coupled versions that could be used similarly to ZFNs for site-directed genome editing (31–33). Such TAL effector nucleases (TALENs) were easier than ZFNs to produce and validate, generating widespread excitement about the possibility of facile genome editing that would be fast and inexpensive. But difficulties of protein design, synthesis, and validation remained a barrier to widespread adoption of these engineered nucleases for routine use.

History and biology of CRISPR-Cas systems

In a parallel but completely separate area of research, a few microbiology and bioinformatics laboratories in the mid-2000s began investigating CRISPRs (clustered regularly interspaced palindromic repeats), which had been described in 1987 by Japanese researchers as a series of short direct repeats interspaced with short sequences in the genome of *Escherichia coli* (34) (Fig. 1). CRISPRs were later detected in numerous bacteria and archaea (35), and predictions were made about their possible roles in DNA repair or gene regulation (36, 37). A key insight came in 2005 with the observation that many spacer sequences within CRISPRs derive from plasmid and viral origins (38–40). Together with the finding that CRISPR loci are transcribed (41) and the observation that *cas* (CRISPR-associated) genes encode proteins with putative nuclease and helicase domains (38, 40, 42, 43), it was proposed that CRISPR-Cas is an adaptive defense system that might use antisense RNAs as memory signatures of past invasions (44). In 2007, infection experiments of the lactic acid bacterium *Streptococcus thermophilus* with lytic phages provided the first experimental evidence of CRISPR-Cas-mediated adaptive immunity (45). This finding led to the idea that natural CRISPR-Cas systems

¹Howard Hughes Medical Institute, Department of Molecular and Cell Biology, University of California, Berkeley, CA 94720, USA. ²Department of Chemistry, University of California, Berkeley, CA 94720, USA. ³Physical Biosciences Division, Lawrence Berkeley National Laboratory, Berkeley, CA 94720, USA. ⁴Department of Regulation in Infection Biology, Helmholtz Centre for Infection Research, D-38124 Braunschweig, Germany. ⁵Laboratory for Molecular Infection Medicine Sweden, Umeå Centre for Microbial Research, Department of Molecular Biology, Umeå University, S-90187 Umeå, Sweden. ⁶Hannover Medical School, D-30625 Hannover, Germany.

*Corresponding author. E-mail: doudna@berkeley.edu (J.A.D.); emmanuelle.charpentier@helmholtz-hzi.de (E.C.)

existing in cultured bacteria used in the dairy industry could be harnessed for immunization against phages—a first successful application of CRISPR-Cas for biotechnological purposes (46). In 2008, mature CRISPR RNAs (crRNAs) were shown to serve as guides in a complex with Cas proteins to interfere with virus proliferation in *E. coli* (47). The same year, the DNA targeting activity of the CRISPR-Cas system was reported in the pathogen *Staphylococcus epidermidis* (48).

Functional CRISPR-Cas loci comprise a CRISPR array of identical repeats intercalated with invader DNA-targeting spacers that encode the crRNA components and an operon of *cas* genes encoding the Cas protein components. In natural environments, viruses can be matched to their bacterial or archaeal hosts by examining CRISPR spacers (49, 50). These studies showed that viruses are constantly evolving to evade CRISPR-mediated attenuation.

Adaptive immunity occurs in three stages [for recent reviews, see (51–53)]: (i) insertion of a short sequence of the invading DNA as a spacer sequence into the CRISPR array; (ii) transcription of precursor crRNA (pre-crRNA) that undergoes maturation to generate individual crRNAs, each

composed of a repeat portion and an invader-targeting spacer portion; and (iii) crRNA-directed cleavage of foreign nucleic acid by Cas proteins at sites complementary to the crRNA spacer sequence. Within this overall theme, three CRISPR-Cas system types (I, II, and III) use distinct molecular mechanisms to achieve nucleic acid recognition and cleavage (54, 55). The protospacer adjacent motif (PAM), a short sequence motif adjacent to the crRNA-targeted sequence on the invading DNA, plays an essential role in the stages of adaptation and interference in type I and type II systems (39, 56–58). The type I and type III systems use a large complex of Cas proteins for crRNA-guided targeting (47, 59–63). However, the type II system requires only a single protein for RNA-guided DNA recognition and cleavage (64, 65)—a property that proved to be extremely useful for genome engineering applications (see below).

Functionality of CRISPR-Cas9

Bioinformatic analyses first identified Cas9 (formerly COG3513, Csx12, Cas5, or Csn1) as a large multifunctional protein (36) with two putative nuclease domains, HNH (38, 43, 44) and RuvC-like (44). Genetic studies showed that *S. thermophilus*

Cas9 is essential for defense against viral invasion (45, 66), might be responsible for introducing DSBs into invading plasmids and phages (67), enables in vivo targeting of temperate phages and plasmids in bacteria (66, 68), and requires the HNH and RuvC domains to interfere with plasmid transformation efficiency (68).

In 2011 (66), trans-activating crRNA (tracrRNA)—a small RNA that is trans-encoded upstream of the type II CRISPR-Cas locus in *Streptococcus pyogenes*—was reported to be essential for crRNA maturation by ribonuclease III and Cas9, and tracrRNA-mediated activation of crRNA maturation was found to confer sequence-specific immunity against parasite genomes. In 2012 (64), the *S. pyogenes* CRISPR-Cas9 protein was shown to be a dual-RNA-guided DNA endonuclease that uses the tracrRNA:crRNA duplex (66) to direct DNA cleavage (64) (Fig. 2). Cas9 uses its HNH domain to cleave the DNA strand that is complementary to the 20-nucleotide sequence of the crRNA; the RuvC-like domain of Cas9 cleaves the DNA strand opposite the complementary strand (64, 65) (Fig. 2). Mutating either the HNH or the RuvC-like domain in Cas9 generates a variant protein with single-stranded DNA cleavage (nickase)

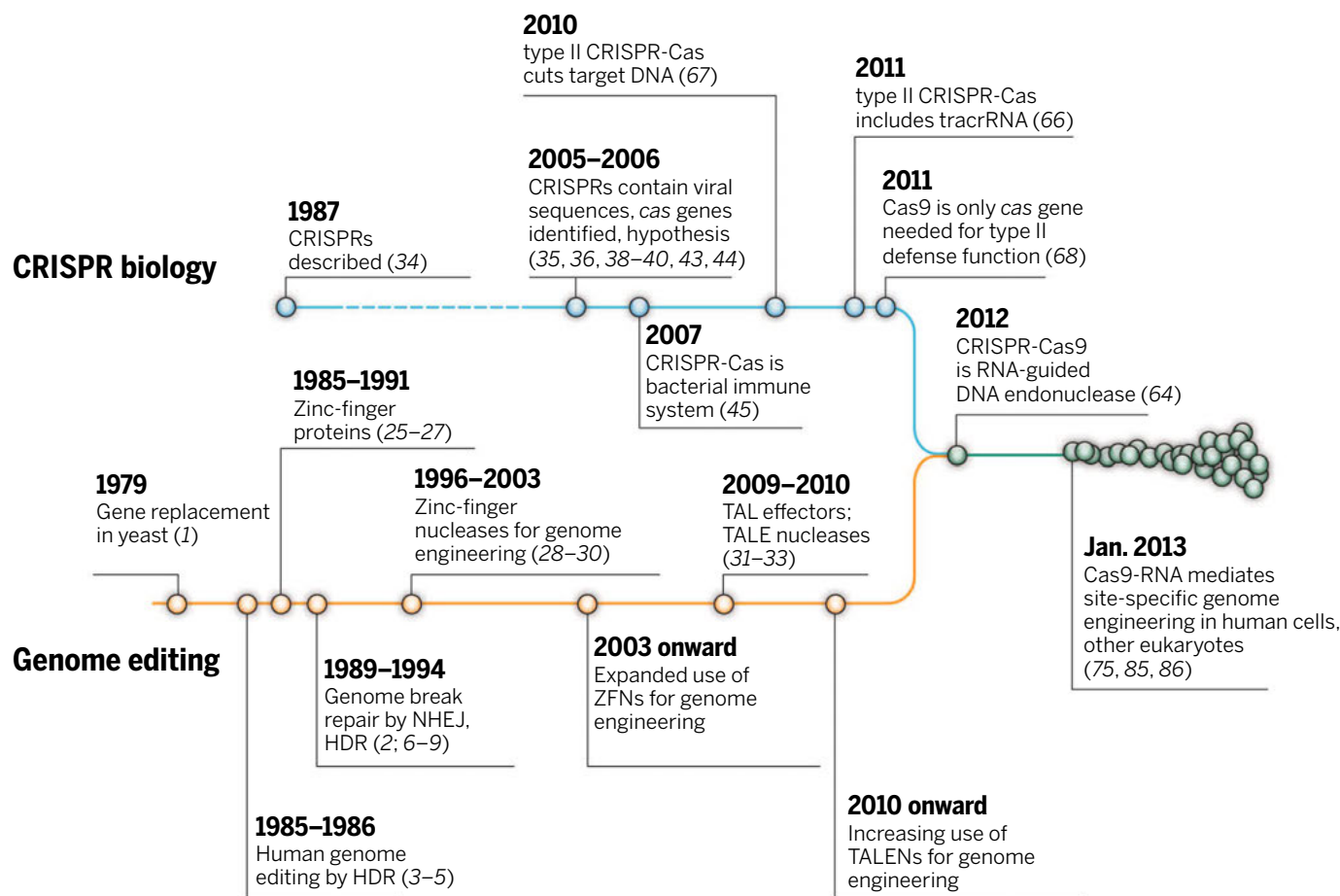


Fig. 1. Timeline of CRISPR-Cas and genome engineering research fields. Key developments in both fields are shown. These two fields merged in 2012 with the discovery that Cas9 is an RNA-programmable DNA endonuclease, leading to the explosion of papers beginning in 2013 in which Cas9 has been used to modify genes in human cells as well as many other cell types and organisms.

activity, whereas mutating both domains (dCas9; Asp¹⁰ → Ala, His⁸⁴⁰ → Ala) results in an RNA-guided DNA binding protein (64, 65). DNA target recognition requires both base pairing to the crRNA sequence and the presence of a short sequence (PAM) adjacent to the targeted sequence in the DNA (64, 65) (Fig. 2).

The dual tracrRNA:crRNA was then engineered as a single guide RNA (sgRNA) that retains two critical features: the 20-nucleotide sequence at the 5' end of the sgRNA that determines the DNA target site by Watson-Crick base pairing, and the double-stranded structure at the 3' side of the guide sequence that binds to Cas9 (64) (Fig. 2). This created a simple two-component system in which changes to the guide sequence (20 nucleotides in the native RNA) of the sgRNA can be used to program CRISPR-Cas9 to target any DNA sequence of interest as long as it is adjacent to a PAM (64). In contrast to ZFNs and TALENs, which require substantial protein engineering for each DNA target site to be modified, the CRISPR-Cas9 system requires only a change in the guide RNA sequence. For this reason, the CRISPR-Cas9

technology using the *S. pyogenes* system has been rapidly and widely adopted by the scientific community to target, edit, or modify the genomes of a vast array of cells and organisms. Phylogenetic studies (69–71) as well as in vitro and in vivo experiments (64, 71, 72) show that naturally occurring Cas9 orthologs use distinct tracrRNA: crRNA transcripts as guides, defined by the specificity to the dual-RNA structures (69–71) (Fig. 3). The reported collection of Cas9 orthologs constitutes a large source of CRISPR-Cas9 systems for multiplex gene targeting, and several orthologous CRISPR-Cas9 systems have already been applied successfully for genome editing in human cells [*Neisseria meningitidis* (73, 74), *S. thermophilus* (73, 75), and *Treponema denticola* (73)].

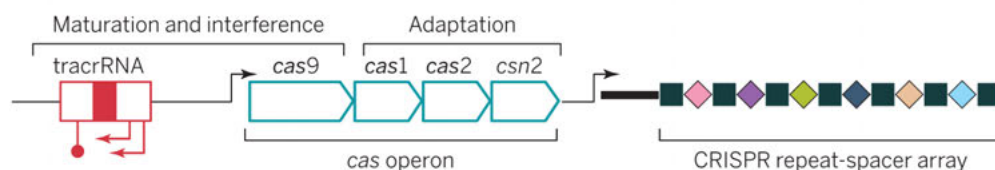
Although the CRISPR acronym has attracted media attention and is widely used in the scientific and popular literature, nearly all genome editing applications are based on the use of the protein Cas9 together with suitable sgRNAs. As discussed above, CRISPR refers to the repetitive nature of the repeats in the CRISPR arrays that encode crRNAs, and the term does not relate

directly to genome engineering. Nonetheless we prefer to use “CRISPR-Cas9” in a way that is less restrictive than other nomenclatures that have been used in the field (76).

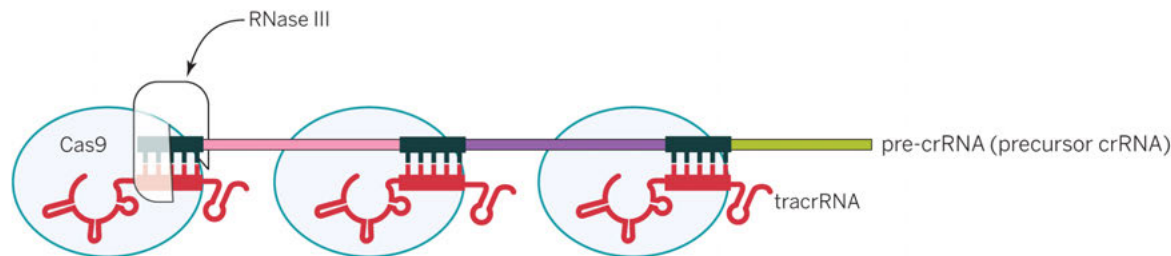
Mechanism of CRISPR-Cas9-mediated genome targeting

Structural analysis of *S. pyogenes* Cas9 has revealed additional insights into the mechanism of CRISPR-Cas9 (Fig. 3). Molecular structures of Cas9 determined by electron microscopy and x-ray crystallography show that the protein undergoes large conformational rearrangement upon binding to the guide RNA, with a further change upon association with a target double-stranded DNA (dsDNA). This change creates a channel, running between the two structural lobes of the protein, that binds to the RNA-DNA hybrid as well as to the coaxially stacked dual-RNA structure of the guide corresponding to the crRNA repeat-tracrRNA antirepeat interaction (77, 78). An arginine-rich α helix (77–79) bridges the two structural lobes of Cas9 and appears to be the hinge between them, in addition

A Genomic CRISPR locus



B tracrRNA:crRNA co-maturation and Cas9 co-complex formation



C RNA-guided cleavage of target DNA

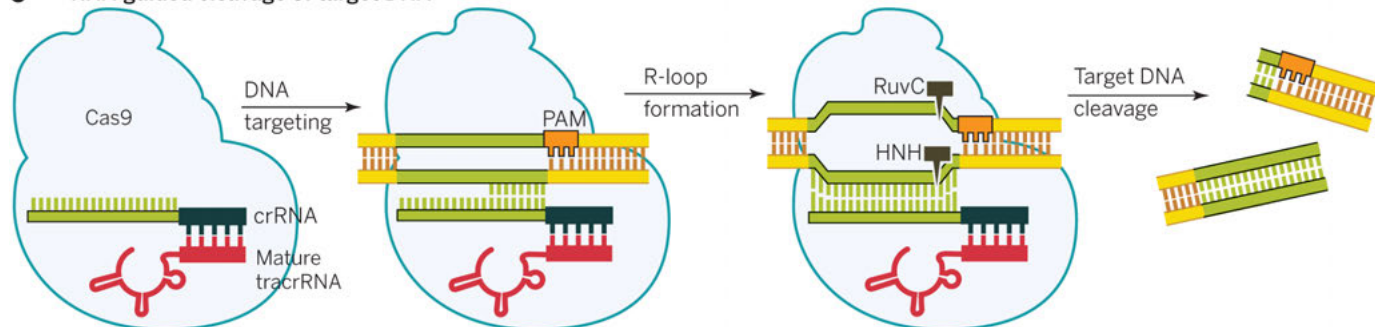


Fig. 2. Biology of the type II-A CRISPR-Cas system. The type II-A system from *S. pyogenes* is shown as an example. **(A)** The *cas* gene operon with tracrRNA and the CRISPR array. **(B)** The natural pathway of antiviral defense involves association of Cas9 with the antirepeat-repeat RNA (tracrRNA: crRNA) duplexes, RNA co-processing by ribonuclease III, further trimming, R-loop formation, and target DNA cleavage. **(C)** Details of the natural DNA cleavage with the duplex tracrRNA:crRNA.

to playing a central role in binding the guide RNA–target DNA hybrid as shown by mutagenesis (77, 78). The conformational change in Cas9 may be part of the mechanism of target dsDNA unwinding and guide RNA strand invasion, although this idea remains to be tested. Mechanistic studies also show that the PAM is critical for initial DNA binding; in the absence of the PAM, even target sequences fully complementary to the guide RNA sequence are not recognized by Cas9 (80). A crystal structure of Cas9 in complex with a guide RNA and a partially dsDNA target demonstrates that the PAM lies within a base-paired DNA structure (81). Arginine motifs in the C-terminal domain of Cas9 interact with the PAM on the noncomplementary strand within the major groove. The phosphodiester group at position +1 in the target DNA strand interacts with the minor groove of the duplexed PAM, possibly resulting in local strand separation, the so-called R-loop, immediately upstream of the PAM (81). Single-molecule experiments also suggest that R-loop association rates are affected primarily by the PAM, whereas R-loop stability is influenced mainly by protospacer elements distal to the PAM (82). Together with single-molecule and bulk biochemical experiments using mutated target DNAs, a mechanism can be proposed whereby target DNA melting starts at the level of PAM recognition, resulting in directional R-loop formation expanding toward the distal protospacer end and concomitant RNA strand invasion and RNA–DNA hybrid formation (80–82).

To assess the target-binding behavior of Cas9 in cells, researchers used chromatin immunoprecipitation and high-throughput sequencing (ChIP-seq) to determine the numbers and types of Cas9 binding sites on the chromosome. Results showed that in both human embryonic kidney (HEK293) cells (83) and mouse embryonic stem cells (mESCs) (84), a catalytically inactive version of Cas9 bound to many more sites than those matching the sequence of the sgRNA used in each case. Such off-target interactions with DNA, typically at sites bearing a PAM and partially complementary to the guide RNA sequence, are consistent with established modes

of DNA interrogation by Cas9 (80). Active Cas9 rarely cleaves the DNA at off-target binding sites, implying decoupled binding and cleavage events in which nearly perfect complementarity between the guide RNA and the target site are necessary for efficient DNA cleavage. These observations are consistent with results obtained for Cas9–guide RNA complexes in single-molecule experiments (80). Furthermore, Cas9 binding events occur more densely in areas of open chromatin as compared to regions of compact, transcriptionally inactive chromatin. However, because the method involves cross-linking cells for ~10 min before quenching the reaction, transient and long-lived binding interactions cannot be distinguished. It is possible that many of the apparent off-target DNA interactions in fact reflect brief encounters that would not normally trigger strand invasion by the guide RNA.

Engineering cells and model organisms

Following the 2012 publication of Jinek *et al.* (64), three studies in January 2013 demonstrated that CRISPR–Cas9 represents an efficient tool to edit the genomes of human cells (75, 85, 86). The “humanized” versions of *S. pyogenes* Cas9 (75, 85, 86) and *S. thermophilus* Cas9 (75) were coexpressed with custom-designed sgRNAs (75, 85, 86) or with tracrRNA coexpressed with custom-designed crRNAs (75) in human embryonic kidney, chronic myelogenous leukemia, or induced pluripotent stem cells (75, 85, 86) as well as in mouse cells (75). The expected alterations in the target DNA were observed, indicating that site-specific DSBs by RNA-guided Cas9 had stimulated gene editing by nonhomologous end joining repair or gene replacement by homology-directed repair (Fig. 4). Targeting with multiple sgRNAs—referred to as multiplexing—was also successfully achieved (75, 86). RNA-programmable *S. pyogenes* Cas9-mediated editing has now been applied to various human cells and embryonic stem cells [(87–90); for reviews, see (91–93)]. Although direct comparisons can be difficult to assess because of differences in target sites and protein expression levels, some analyses show that CRISPR–Cas9-mediated editing efficiencies can reach 80% or more depending on the target,

which is as high as or higher than levels observed using ZFNs or TALENs (89, 94).

These initial studies were only the beginning of what has become an incredibly fast-paced field in which laboratories around the world have used CRISPR–Cas9 to edit genomes of a wide range of cell types and organisms (summarized in Fig. 5). As of this writing, more than 1000 papers have been published that include the CRISPR acronym in the title or abstract, with the majority of these published since the beginning of 2013. Many of these applications have been discussed in recent reviews (91–93). Here we highlight a few examples that illustrate the power of the technology (Fig. 6). The first example is the precise reproduction of tumor-associated chromosomal translocations, which come about during carcinogenesis through illegitimate nonhomologous joining of two chromosomes. The ability of CRISPR–Cas9 to introduce DSBs at defined positions has made it possible to generate human cell lines and primary cells bearing chromosomal translations resembling those described in cancers such as lung cancer (95), acute myeloid leukemia, and Ewing’s sarcoma (96, 97). An improved method to generate liver cancer or myeloid malignancy models in mice facilitated by CRISPR–Cas9 was recently reported (98, 99). CRISPR–Cas9 thus provides a robust technology for studying genomic rearrangements and the development and progression of cancers or other diseases.

A second example is the systematic analysis of gene functions in mammalian cells. A genome-scale lentiviral sgRNA library was developed to generate a pooled loss-of-function genetic screening approach suitable for both positive and negative selection (100, 101). This approach was also used to identify genes essential for cell viability in cancer and pluripotent stem cells (102). Although such studies have been attempted using RNA interference (RNAi) to reduce the expression of genes, this strategy does not allow the generation of gene knockouts and can suffer from substantial off-target effects. The use of CRISPR–Cas9 for genome-wide studies will enable large-scale screening for drug targets and other phenotypes and thus will expand the nature and utility of genetic screens in human and other nonmodel cell types and organisms.

Other pertinent examples of CRISPR–Cas9 applications with relevance to human health include the ability to correct genetic mutations responsible for inherited disorders. A dominant mutation in the *Crygc* gene responsible for cataracts was successfully corrected in mice (103). Using cultured primary adult intestinal stem cells derived from cystic fibrosis patients, the CFTR locus responsible for cystic fibrosis was corrected by homologous recombination, resulting in the clonal expansion of miniature organlike cell cultures (organoids) harboring the desired, exact genetic change (104). These

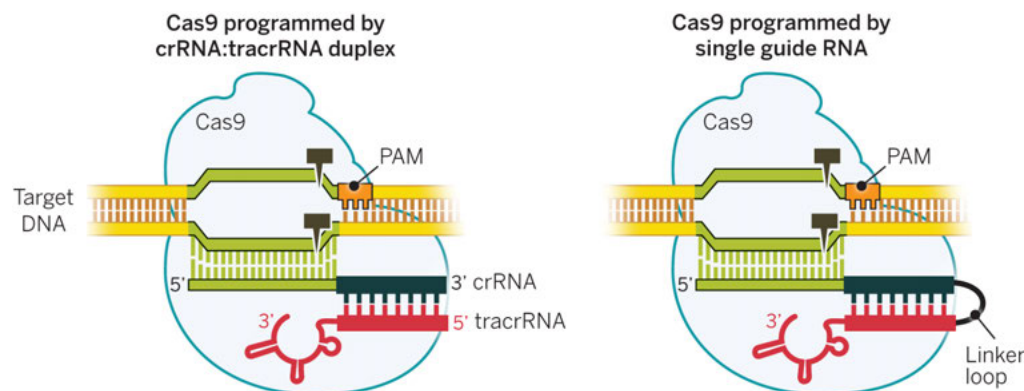


Fig. 3. Evolution and structure of Cas9. The structure of *S. pyogenes* Cas9 in the unliganded and RNA–DNA-bound forms [from (77, 81)].

studies underscore the potential for this technology to be used for human gene therapy to treat genetic disorders.

A last example of CRISPR-Cas9 as a genome engineering technology is its application to plants and fungi. Since its demonstration as a genome editing tool in *Arabidopsis thaliana* and *Nicotiana benthamiana* (105, 106), editing has been demonstrated in crop plants including rice, wheat, and sorghum as well as sweet orange and liverwort

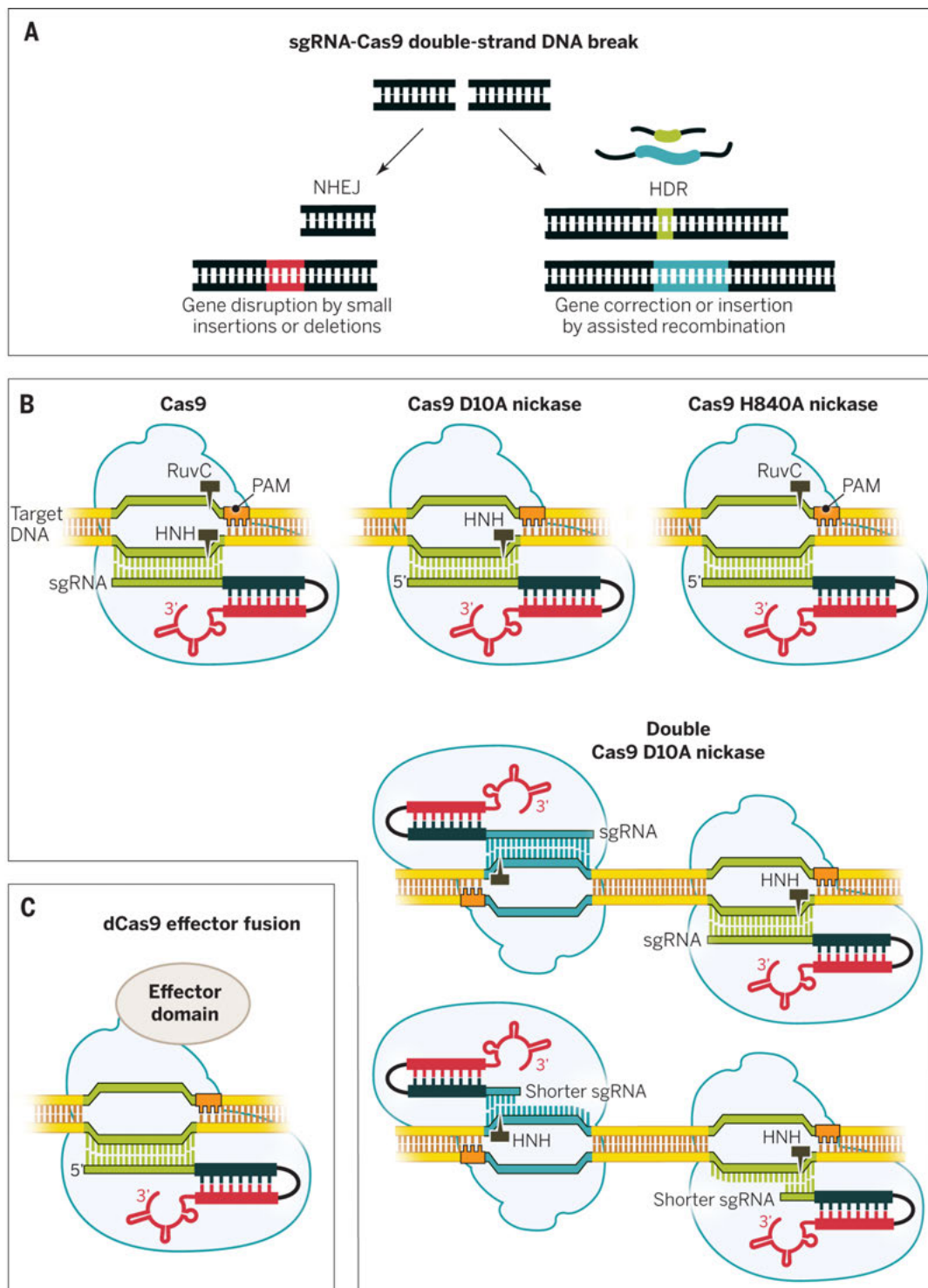
(107–111). This technology promises to change the pace and course of agricultural research. For example, a recent study in rice found that target genes were edited in nearly 50% of the embryogenic cells that received the Cas9–guide RNA constructs, and editing occurred before the first cell division (112). Furthermore, these genetic changes were passed to the next generation of plants without new mutation or reversion, and whole-genome sequencing did not reveal substantial off-target

editing. Such findings suggest that modification of plant genomes to provide protection from disease and resistance to pests may be much easier than has been the case with other technologies. The regulatory implications of CRISPR-Cas9 technology for use in plants are not yet clear and will certainly depend on the type of mutation(s) to be introduced.

In general, the lack of efficient, inexpensive, fast-to-design, and easy-to-use precision genetic

Fig. 4. CRISPR-Cas9 as a genome engineering tool. (A)

Different strategies for introducing blunt double-stranded DNA breaks into genomic loci, which become substrates for endogenous cellular DNA repair machinery that catalyze non-homologous end joining (NHEJ) or homology-directed repair (HDR). **(B)** Cas9 can function as a nickase (nCas9) when engineered to contain an inactivating mutation in either the HNH domain or RuvC domain active sites. When nCas9 is used with two sgRNAs that recognize offset target sites in DNA, a staggered double-strand break is created. **(C)** Cas9 functions as an RNA-guided DNA binding protein when engineered to contain inactivating mutations in both of its active sites. This catalytically inactive or dead Cas9 (dCas9) can mediate transcriptional down-regulation or activation, particularly when fused to activator or repressor domains. In addition, dCas9 can be fused to fluorescent domains, such as green fluorescent protein (GFP), for live-cell imaging of chromosomal loci. Other dCas9 fusions, such as those including chromatin or DNA modification domains, may enable targeted epigenetic changes to genomic DNA.



tools has also been a limiting factor for the analysis of gene functions in model organisms of developmental and regenerative biology. Efficient genome engineering to allow targeted genome modifications in the germ lines of animal models such as fruit flies (113, 114), zebrafish (94, 115), nematodes (116), salamanders (117), and frogs (118, 119) is now possible with the development of the CRISPR-Cas9 technology. The technology can also facilitate the generation of mouse (120–122) and rat (123, 124) models better suited to pharmacological studies and the understanding of human diseases, as well as pigs (125) and monkeys (126). Overall, CRISPR-Cas9 is already having a major impact on functional genomic experiments that can be conducted in these model systems, which will advance the field of experimental biology in ways not imagined even a few years ago.

Further development of the technology

A key property of Cas9 is its ability to bind to DNA at sites defined by the guide RNA sequence and the PAM, allowing applications beyond permanent modification of DNA. In particular, a catalytically deactivated version of Cas9 (dCas9) has been repurposed for targeted gene regulation on a genome-wide scale. Referred to as CRISPR interference (CRISPRi), this strategy was shown to block transcriptional elongation, RNA polymerase binding, or transcription factor binding, depending on the site(s) recognized by the dCas9–guide RNA complex. Demonstrated first in *E. coli*, whole-genome sequencing showed that there were no detectable off-target effects (127). CRISPRi has been used to repress multiple target genes simultaneously, and its effects are reversible (127–130).

By generating chimeric versions of dCas9 that are fused to regulatory domains, it has been possible to use CRISPRi for efficient gene regulation in mammalian cells. Specifically, fusion of dCas9 to effector domains including VP64 or KRAB allowed stable and efficient transcriptional activation or repression, respectively, in human and yeast cells (129). As observed in bacteria, site(s) of regulation were defined solely by the coexpressed guide RNA(s) for dCas9. RNA-seq analysis showed that CRISPRi-directed transcriptional repression is highly specific. More broadly, these results demonstrated that dCas9 can be used as a modular and flexible DNA-binding platform for

the recruitment of proteins to a target DNA sequence in a genome, laying the foundation for future experiments involving genome-wide screening similar to those performed using RNAi. The lack of CRISPR-Cas systems in eukaryotes is an important advantage of CRISPRi over RNAi for various applications in which competition with the endogenous pathways is problematic. For example, using RNAi to silence genes that are part of the RNAi pathway itself (i.e., Dicer, Argonaute) can lead to results that are difficult to interpret due to multiple direct and indirect effects. In addition, any RNAs used to silence specific genes may compete with endogenous RNA-mediated gene regulation in cells. With its ability to permanently change the genetic code and to up- or down-regulate gene expression at the transcriptional or posttranscriptional level, CRISPR-Cas9 offers a large versatility in harnessing alternatives, whereas RNAi is mostly restricted to knocking down gene expression. Although RNAi has been improving over the years, incomplete knockdowns or unpredictable off-targeting are still reported bottlenecks of this technology, and future comparative analyses should address the superiority of CRISPRi over RNAi in these aspects.

The programmable binding capability of dCas9 can also be used for imaging of specific loci in live cells. An enhanced green fluorescent protein-tagged dCas9 protein and a structurally optimized sgRNA were shown to produce robust imaging of repetitive and nonrepetitive elements in telomeres and coding genes in living cells (131). This CRISPR imaging tool has the potential to improve the current technologies for studying conformational dynamics of native chromosomes in living cells, particularly if multicolor imaging can be developed using multiple distinct Cas9 proteins. It may also be possible to couple fluorescent proteins or small molecules to the guide RNA, providing an orthogonal strategy for multicolor imaging using Cas9.

Novel technologies aiming to disrupt proviruses may be an attractive approach to eliminating viral genomes from infected individuals and thus curing viral infections. An appeal of this strategy is that it takes advantage of the primary native functions of CRISPR-Cas systems as antiviral adaptive immune systems in bacteria. The targeted CRISPR-Cas9 technique was shown to efficiently cleave and mutate the long terminal repeat sites of HIV-1 and also to remove internal

viral genes from the chromosome of infected cells (132, 133).

CRISPR-Cas9 is also a promising technology in the field of engineering and synthetic biology. A multiplex CRISPR approach referred to as CRISPRm was developed to facilitate directed evolution of biomolecules (134). CRISPRm consists of the optimization of CRISPR-Cas9 to generate quantitative gene assembly and DNA library insertion into the fungal genomes, providing a strategy to improve the activity of biomolecules. In addition, it has been possible to induce Cas9 to bind single-stranded RNA in a programmable fashion by using short DNA oligonucleotides containing PAM sequences (PAMmers) to activate the enzyme, suggesting new ways to target transcripts without prior affinity tagging (135).

A series of studies have reported the efficiency with which the RNA-programmable *S. pyogenes* Cas9 targets and cleaves DNA and have also addressed the level of its specificity by monitoring the ratio of off-site targeting (136–140). Off-site targeting is defined by the tolerance of Cas9 to mismatches in the RNA guide sequence and is dependent on the number, position, and distribution of mismatches throughout the entire guide sequence (136–140) beyond the initial seed sequence originally defined as the first 8 to 12 nucleotides of the guide sequence proximal to the PAM (64) (Fig. 2). The amount of Cas9 enzyme expressed in the cell is an important factor in tolerance to mismatches (138). High concentrations of the enzyme were reported to increase off-site targeting, whereas lowering the concentration of Cas9 increases specificity while diminishing on-target cleavage activity (137). Several groups have developed algorithmic tools that predict the sequence of an optimal sgRNA with minimized off-target effects (for example, <http://tools.genome-engineering.org>, <http://zifit.partners.org>, and www.e-crisp.org) (141–145). The development of alternative genome-wide approaches that would also consider other features of the reaction, such as the thermodynamic properties of the sgRNA, may also increase the specificity of the design.

Several studies of the CRISPR-Cas9 technology relate to the specificity of DNA targeting (Fig. 4): a double-nicking approach consisting of using the nickase variant of Cas9 with a pair of offset sgRNAs properly positioned on the target DNA (146–148); an sgRNA-guided dCas9 fused to the FokI nuclease where two fused dCas9-FokI monomers can simultaneously bind target sites at a defined distance apart (149, 150); and shorter sgRNAs truncated by two or three nucleotides at the distal end relative to the PAM that can be used with the double nicking strategy to further reduce off-target activity (151). The first two methods rely on Cas9 dimerization similar to the engineered dimeric ZFNs and TALENs, with the principle that two adjacent off-target binding events and subsequent cleavage

Biology

Cell lines

HEK293
U2OS
K562

Model organisms

Mice
Rats
Fruit flies
Nematodes
Arabidopsis
Salamanders
Frogs
Monkeys

Biotechnology

Crop plants

Rice
Wheat
Sorghum
Tobacco

Fungi

Kluyveromyces
Chlamydomonas

Biomedicine

Organoids

hESCs
iPSCs

Fig. 5. Examples of cell types and organisms that have been engineered using Cas9.

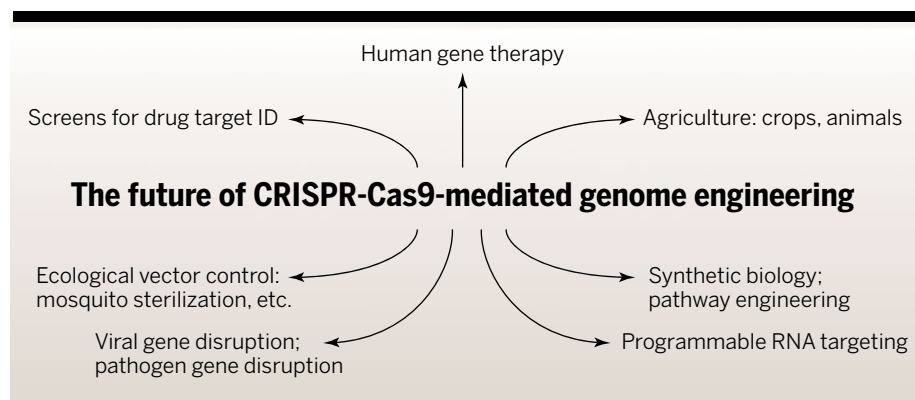


Fig. 6. Future applications in biomedicine and biotechnology. Potential developments include establishment of screens for target identification, human gene therapy by gene repair and gene disruption, gene disruption of viral sequences, and programmable RNA targeting.

are less likely to occur than a single off-target cleavage (146–150). The latter method follows the reasoning according to which the 5'-end nucleotides of the sgRNAs are not necessary for their full activity; however, they may compensate for mismatches at other positions along the guide RNA–target DNA interface, and thus shorter sgRNAs may be more specific (151). Future efforts will focus on further developing the precision of the technology, as well as increasing the frequency of homology-directed repair relative to nonhomologous end joining in order to favor site-specific insertion of new genetic information.

Conclusions and perspectives

Our understanding of how genomes direct development, normal physiology, and disease in higher organisms has been hindered by a lack of suitable tools for precise and efficient gene engineering. The simple two-component CRISPR-Cas9 system, using Watson-Crick base pairing by a guide RNA to identify target DNA sequences, is a versatile technology that has already stimulated innovative applications in biology. Understanding the CRISPR-Cas9 system at the biochemical and structural level allows the engineering of tailored Cas9 variants with smaller size and increased specificity. A crystal structure of the smaller Cas9 protein from *Actinomyces*, for example, showed how natural variation created a streamlined enzyme, setting the stage for future engineered Cas9 variants (77). A deeper analysis of the large panel of naturally evolving bacterial Cas9 enzymes may also reveal orthologs with distinct DNA binding specificity, will broaden the choice of PAMs, and will certainly reveal shorter variants more amenable for delivery in human cells.

Furthermore, specific methods for delivering Cas9 and its guide RNA to cells and tissues should benefit the field of human gene therapy. For example, recent experiments confirmed that the Cas9 protein-RNA complex can be introduced directly into cells using nucleofection or cell-penetrating peptides to enable rapid and timed editing (89, 152), and transgenic organisms

that express Cas9 from inducible promoters are being tested. An exciting harbinger of future research in this area is the recent demonstration that Cas9–guide RNA complexes, when injected into adult mice, provided sufficient editing in the liver to alleviate a genetic disorder (153). Understanding the rates of homology-directed repair after Cas9-mediated DNA cutting will advance the field by enabling efficient insertion of new or corrected sequences into cells and organisms. In addition, the rapid advance of the field has raised excitement about commercial applications of CRISPR-Cas9.

The era of straightforward genome editing raises ethical questions that will need to be addressed by scientists and society at large. How can we use this powerful tool in such a way as to ensure maximum benefit while minimizing risks? It will be imperative that nonscientists understand the basics of this technology sufficiently well to facilitate rational public discourse. Regulatory agencies will also need to consider how best to foster responsible use of CRISPR-Cas9 technology without inhibiting appropriate research and development.

The identification of the CRISPR-Cas9 technology underscores the way in which many inventions that have advanced molecular biology and medicine emanated, through basic research on natural mechanisms of DNA replication, repair, and defense against viruses. In many cases, key methodologies emerged from the study of bacteria. The CRISPR-Cas9 technology originated through a similar process: Once the mechanism underlying how the CRISPR-Cas9 system works was understood, it could be harnessed for applications in molecular biology and genetics that were not previously envisioned.

REFERENCES AND NOTES

- S. Scherer, R. W. Davis, Replacement of chromosome segments with altered DNA sequences constructed in vitro. *Proc. Natl. Acad. Sci. U.S.A.* **76**, 4951–4955 (1979). doi: [10.1073/pnas.76.10.4951](#); pmid: [388424](#)
- Y. S. Rong, K. G. Golc, Gene targeting by homologous recombination in *Drosophila*. *Science* **288**, 2013–2018 (2000). doi: [10.1126/science.288.5473.2013](#); pmid: [10856208](#)
- O. Smithies, R. G. Gregg, S. S. Boggs, M. A. Koralewski, R. S. Kucherlapati, Insertion of DNA sequences into the

- human chromosomal beta-globin locus by homologous recombination. *Nature* **317**, 230–234 (1985). doi: [10.1038/317230a0](#); pmid: [2995814](#)
- K. R. Thomas, K. R. Folger, M. R. Capecchi, High frequency targeting of genes to specific sites in the mammalian genome. *Cell* **44**, 419–428 (1986). doi: [10.1016/0092-8674\(86\)90463-0](#); pmid: [3002636](#)
- S. L. Mansour, K. R. Thomas, M. R. Capecchi, Disruption of the proto-oncogene int-2 in mouse embryo-derived stem cells: A general strategy for targeting mutations to non-selectable genes. *Nature* **336**, 348–352 (1988). doi: [10.1038/336348a0](#); pmid: [3194019](#)
- N. Rudin, E. Sugarman, J. E. Haber, Genetic and physical analysis of double-strand break repair and recombination in *Saccharomyces cerevisiae*. *Genetics* **122**, 519–534 (1989). pmid: [2668114](#)
- A. Plessis, A. Perrin, J. E. Haber, B. Dujon, Site-specific recombination determined by I-SceI, a mitochondrial group I intron-encoded endonuclease expressed in the yeast nucleus. *Genetics* **130**, 451–460 (1992). pmid: [1551570](#)
- P. Rouet, F. Smih, M. Jasin, Introduction of double-strand breaks into the genome of mouse cells by expression of a rare-cutting endonuclease. *Mol. Cell. Biol.* **14**, 8096–8106 (1994). pmid: [7969147](#)
- A. Chouliska, A. Perrin, B. Dujon, J. F. Nicolas, Induction of homologous recombination in mammalian chromosomes by using the I-SceI system of *Saccharomyces cerevisiae*. *Mol. Cell. Biol.* **15**, 1968–1973 (1995). pmid: [7891691](#)
- G. Felsenfeld, D. R. Davies, A. Rich, Formation of a three-stranded polynucleotide molecule. *J. Am. Chem. Soc.* **79**, 2023–2024 (1957). doi: [10.1021/ja01565a074](#)
- A. Varshavsky, Discovering the RNA double helix and hybridization. *Cell* **127**, 1295–1297 (2006). doi: [10.1016/j.cell.2006.12.008](#); pmid: [17190591](#)
- S. A. Strobel, L. A. Doucette-Stamm, L. Riba, D. E. Housman, P. B. Dervan, Site-specific cleavage of human chromosome 4 mediated by triple-helix formation. *Science* **254**, 1639–1642 (1991). doi: [10.1126/science.1836279](#); pmid: [1836279](#)
- S. A. Strobel, P. B. Dervan, Single-site enzymatic cleavage of yeast genomic DNA mediated by triple helix formation. *Nature* **350**, 172–174 (1991). doi: [10.1038/350172a0](#); pmid: [1848684](#)
- S. A. Strobel, P. B. Dervan, Site-specific cleavage of a yeast chromosome by oligonucleotide-directed triple-helix formation. *Science* **249**, 73–75 (1990). doi: [10.1126/science.2195655](#); pmid: [2195655](#)
- A. F. Faruqi, M. M. Seidman, D. J. Segal, D. Carroll, P. M. Glazer, Recombination induced by triple-helix-targeted DNA damage in mammalian cells. *Mol. Cell. Biol.* **16**, 6820–6828 (1996). pmid: [8943337](#)
- G. Wang, D. D. Levy, M. M. Seidman, P. M. Glazer, Targeted mutagenesis in mammalian cells mediated by intracellular triple helix formation. *Mol. Cell. Biol.* **15**, 1759–1768 (1995). pmid: [7862165](#)
- Z. Sandor, A. Bredberg, Deficient DNA repair of triple helix-directed double psoralen damage in human cells. *FEBS Lett.* **374**, 287–291 (1995). doi: [10.1016/0014-5793\(95\)01133-Y](#); pmid: [7589555](#)
- J. Cho, M. E. Parks, P. B. Dervan, Cyclic polyamides for recognition in the minor groove of DNA. *Proc. Natl. Acad. Sci. U.S.A.* **92**, 10389–10392 (1995). doi: [10.1073/pnas.92.22.10389](#); pmid: [7479790](#)
- A. F. Faruqi, M. Egholm, P. M. Glazer, Peptide nucleic acid-targeted mutagenesis of a chromosomal gene in mouse cells. *Proc. Natl. Acad. Sci. U.S.A.* **95**, 1398–1403 (1998). doi: [10.1073/pnas.95.4.1398](#); pmid: [9465026](#)
- J. M. Gottesfeld, L. Neely, J. W. Trauger, E. E. Baird, P. B. Dervan, Regulation of gene expression by small molecules. *Nature* **387**, 202–205 (1997). doi: [10.1038/387202a0](#); pmid: [9144294](#)
- J. Yang, S. Zimmerly, P. S. Perlman, A. M. Lambowitz, Efficient integration of an intron RNA into double-stranded DNA by reverse splicing. *Nature* **381**, 332–335 (1996). doi: [10.1038/381332a0](#); pmid: [8692273](#)
- S. Zimmerly et al., A group II intron RNA is a catalytic component of a DNA endonuclease involved in intron mobility. *Cell* **83**, 529–538 (1995). doi: [10.1016/0092-8674\(95\)90092-6](#); pmid: [7589555](#)
- B. A. Sullenger, T. R. Cech, Ribozyme-mediated repair of defective mRNA by targeted, trans-splicing. *Nature* **371**, 619–622 (1994). doi: [10.1038/371619a0](#); pmid: [7935797](#)
- A. Jacquier, B. Dujon, An intron-encoded protein is active in a gene conversion process that spreads an intron into a mitochondrial gene. *Cell* **41**, 383–394 (1985). doi: [10.1016/S0092-8674\(85\)80011-8](#); pmid: [3886163](#)

25. B. S. Chevalier *et al.*, Design, activity, and structure of a highly specific artificial endonuclease. *Mol. Cell* **10**, 895–905 (2002). doi: [10.1016/S1097-2765\(02\)00690-1](#); pmid: [12419232](#)
26. J. Miller, A. D. McLachlan, A. Klug, Repetitive zinc-binding domains in the protein transcription factor IIIA from *Xenopus oocytes*. *EMBO J.* **4**, 1609–1614 (1985). pmid: [4040853](#)
27. N. P. Pavletich, C. O. Pabo, Zinc finger-DNA recognition: Crystal structure of a Zif268-DNA complex at 2.1 Å. *Science* **252**, 809–817 (1991). doi: [10.1126/science.2028256](#); pmid: [2028256](#)
28. Y. G. Kim, J. Cha, S. Chandrasegaran, Hybrid restriction enzymes: Zinc finger fusions to Fok I cleavage domain. *Proc. Natl. Acad. Sci. U.S.A.* **93**, 1156–1160 (1996). doi: [10.1073/pnas.93.3.1156](#); pmid: [8577732](#)
29. M. Bibikova, K. Beumer, J. K. Trautman, D. Carroll, Enhancing gene targeting with designed zinc finger nucleases. *Science* **300**, 764 (2003). doi: [10.1126/science.1079512](#); pmid: [12730594](#)
30. M. Bibikova, M. Golic, K. G. Golic, D. Carroll, Targeted chromosomal cleavage and mutagenesis in *Drosophila* using zinc-finger nucleases. *Genetics* **161**, 1169–1175 (2002). pmid: [12136019](#)
31. J. Boch *et al.*, Breaking the code of DNA binding specificity of TAL-type III effectors. *Science* **326**, 1509–1512 (2009). doi: [10.1126/science.1178811](#); pmid: [19933107](#)
32. M. J. Moscou, A. J. Bogdanove, A simple cipher governs DNA recognition by TAL effectors. *Science* **326**, 1501 (2009). doi: [10.1126/science.1178817](#); pmid: [19933106](#)
33. M. Christian *et al.*, Targeting DNA double-strand breaks with TAL effector nucleases. *Genetics* **186**, 757–761 (2010). doi: [10.1534/genetics.110.120717](#); pmid: [20660643](#)
34. Y. Ishino, H. Shinagawa, K. Makino, M. Amemura, A. Nakata, Nucleotide sequence of the *iap* gene, responsible for alkaline phosphatase isozyme conversion in *Escherichia coli*, and identification of the gene product. *J. Bacteriol.* **169**, 5429–5433 (1987). pmid: [3316184](#)
35. F. J. Mojica, C. Díez-Villaseñor, E. Soria, G. Juez, Biological significance of a family of regularly spaced repeats in the genomes of Archaea, Bacteria and mitochondria. *Mol. Microbiol.* **36**, 244–246 (2000). doi: [10.1046/j.1365-2958.2000.01838.x](#); pmid: [10760181](#)
36. K. S. Makarova, L. Aravind, N. V. Grishin, I. B. Rogozin, E. V. Koonin, A DNA repair system specific for thermophilic Archaea and bacteria predicted by genomic context analysis. *Nucleic Acids Res.* **30**, 482–496 (2002). doi: [10.1093/nar/30.2.482](#); pmid: [11788711](#)
37. C. P. Guy, A. I. Majernik, J. P. J. Chong, E. L. Bolt, A novel nuclease-ATPase (Nar71) from archaea is part of a proposed thermophilic DNA repair system. *Nucleic Acids Res.* **32**, 6176–6186 (2004). doi: [10.1093/nar/gkh960](#); pmid: [15570068](#)
38. A. Bolotin, B. Quinquis, A. Sorokin, S. D. Ehrlich, Clustered regularly interspaced short palindromic repeats (CRISPRs) have spacers of extrachromosomal origin. *Microbiology* **151**, 2551–2561 (2005). doi: [10.1099/mic.0.28048-0](#); pmid: [16079334](#)
39. F. J. Mojica, C. Díez-Villaseñor, J. García-Martínez, E. Soria, Intervening sequences of regularly spaced prokaryotic repeats derive from foreign genetic elements. *J. Mol. Evol.* **60**, 174–182 (2005). doi: [10.1007/s00239-004-0046-3](#); pmid: [15791728](#)
40. C. Pourcel, G. Salvignol, G. Vergnaud, CRISPR elements in *Yersinia pestis* acquire new repeats by preferential uptake of bacteriophage DNA, and provide additional tools for evolutionary studies. *Microbiology* **151**, 653–663 (2005). doi: [10.1099/mic.0.27437-0](#); pmid: [15758212](#)
41. T.-H. Tang *et al.*, Identification of 86 candidates for small non-messenger RNAs from the archaeon *Archaeoglobus fulgidus*. *Proc. Natl. Acad. Sci. U.S.A.* **99**, 7536–7541 (2002). doi: [10.1073/pnas.112047299](#); pmid: [12032318](#)
42. R. Jansen, J. D. Embden, W. Gaastra, L. M. Schouls, Identification of genes that are associated with DNA repeats in prokaryotes. *Mol. Microbiol.* **43**, 1565–1575 (2002). doi: [10.1046/j.1365-2958.2002.02839.x](#); pmid: [11952905](#)
43. D. H. Haft, J. Selengut, E. F. Mongodin, K. E. Nelson, A guild of 45 CRISPR-associated (Cas) protein families and multiple CRISPR/Cas subtypes exist in prokaryotic genomes. *PLoS Comput. Biol.* **1**, e60 (2005). doi: [10.1371/journal.pcbi.0010060](#); pmid: [16292354](#)
44. K. S. Makarova, N. V. Grishin, S. A. Shabalina, Y. I. Wolf, E. V. Koonin, A putative RNA-interference-based immune system in prokaryotes: Computational analysis of the predicted enzymatic machinery, functional analogies with eukaryotic RNAi, and hypothetical mechanisms of action. *Biol. Direct* **1**, 7 (2006). doi: [10.1186/1745-6150-1-7](#); pmid: [16545108](#)
45. R. Barrangou *et al.*, CRISPR provides acquired resistance against viruses in prokaryotes. *Science* **315**, 1709–1712 (2007). doi: [10.1126/science.1138140](#); pmid: [17379808](#)
46. R. Barrangou, P. Horvath, CRISPR: New horizons in phage resistance and strain identification. *Annu. Rev. Food Sci. Technol.* **3**, 143–162 (2012). doi: [10.1146/annurev-food-022811-101134](#); pmid: [22224556](#)
47. S. J. J. Brouns *et al.*, Small CRISPR RNAs guide antiviral defense in prokaryotes. *Science* **321**, 960–964 (2008). doi: [10.1126/science.1159689](#); pmid: [18703739](#)
48. L. A. Marraffini, E. J. Sontheimer, CRISPR interference limits horizontal gene transfer in staphylococci by targeting DNA. *Science* **322**, 1843–1845 (2008). doi: [10.1126/science.1165771](#); pmid: [19095942](#)
49. A. F. Andersson, J. F. Banfield, Virus population dynamics and acquired virus resistance in natural microbial communities. *Science* **320**, 1047–1050 (2008). doi: [10.1126/science.1157358](#); pmid: [18497291](#)
50. C. L. Sun *et al.*, Phage mutations in response to CRISPR diversification in a bacterial population. *Environ. Microbiol.* **15**, 463–470 (2013). doi: [10.1111/j.1462-2920.2012.02879.x](#); pmid: [23057534](#)
51. R. Barrangou, L. A. Marraffini, CRISPR-Cas systems: Prokaryotes upgrade to adaptive immunity. *Mol. Cell* **54**, 234–244 (2014). doi: [10.1016/j.molcel.2014.03.011](#); pmid: [24766887](#)
52. J. van der Oost, E. R. Westra, R. N. Jackson, B. Wiedenheft, Unravelling the structural and mechanistic basis of CRISPR-Cas systems. *Nat. Rev. Microbiol.* **12**, 479–492 (2014). doi: [10.1038/nrmicro3279](#); pmid: [24909109](#)
53. J. Bondy-Denomy, A. R. Davidson, To acquire or resist: The complex biological effects of CRISPR-Cas systems. *Trends Microbiol.* **22**, 218–225 (2014). doi: [10.1016/j.tim.2014.01.007](#); pmid: [24582529](#)
54. K. S. Makarova, L. Aravind, Y. I. Wolf, E. V. Koonin, Unification of Cas protein families and a simple scenario for the origin and evolution of CRISPR-Cas systems. *Biol. Direct* **6**, 38 (2011). doi: [10.1186/1745-6150-6-38](#); pmid: [21756346](#)
55. K. S. Makarova *et al.*, Evolution and classification of the CRISPR-Cas systems. *Nat. Rev. Microbiol.* **9**, 467–477 (2011). doi: [10.1038/nrmicro2577](#); pmid: [21552286](#)
56. H. Deveau *et al.*, Phage response to CRISPR-encoded resistance in *Streptococcus thermophilus*. *J. Bacteriol.* **190**, 1390–1400 (2008). doi: [10.1128/JB.01412-07](#); pmid: [18065545](#)
57. P. Horvath *et al.*, Diversity, activity, and evolution of CRISPR loci in *Streptococcus thermophilus*. *J. Bacteriol.* **190**, 1401–1412 (2008). doi: [10.1128/JB.01415-07](#); pmid: [18065539](#)
58. S. A. Shah, S. Erdmann, F. J. M. Mojica, R. A. Garrett, Protospacer recognition motifs: Mixed identities and functional diversity. *RNA Biol.* **10**, 891–899 (2013). doi: [10.4161/rna.23764](#); pmid: [23403393](#)
59. K. H. Nam *et al.*, Cas5d protein processes pre-crRNA and assembles into a cascade-like interference complex in subtype I-C/Dvulg CRISPR-Cas system. *Structure* **20**, 1574–1584 (2012). doi: [10.1016/j.str.2012.06.016](#); pmid: [22841292](#)
60. R. E. Haurwitz, M. Jinek, B. Wiedenheft, K. Zhou, J. A. Doudna, Sequence- and structure-specific RNA processing by a CRISPR endonuclease. *Science* **329**, 1355–1358 (2010). doi: [10.1126/science.1192272](#); pmid: [20829488](#)
61. A. Hatoum-Aslan, I. Maniv, L. A. Marraffini, Mature clustered, regularly interspaced, short palindromic repeats RNA (crRNA) length is measured by a ruler mechanism anchored at the precursor processing site. *Proc. Natl. Acad. Sci. U.S.A.* **108**, 21218–21222 (2011). doi: [10.1073/pnas.1112832108](#); pmid: [21260698](#)
62. C. Rouillon *et al.*, Structure of the CRISPR interference complex CSM reveals key similarities with cascade. *Mol. Cell* **52**, 124–134 (2013). doi: [10.1016/j.molcel.2013.08.020](#); pmid: [24119402](#)
63. C. R. Hale *et al.*, RNA-guided RNA cleavage by a CRISPR RNA-Cas protein complex. *Cell* **139**, 945–956 (2009). doi: [10.1016/j.cell.2009.07.040](#); pmid: [19945378](#)
64. M. Jinek *et al.*, A programmable dual-RNA-guided DNA endonuclease in adaptive bacterial immunity. *Science* **337**, 816–821 (2012). doi: [10.1126/science.1225829](#); pmid: [22745249](#)
65. G. Gasiunas, R. Barrangou, P. Horvath, V. Siksnys, Cas9-crRNA ribonucleoprotein complex mediates specific DNA cleavage for adaptive immunity in bacteria. *Proc. Natl. Acad. Sci. U.S.A.* **109**, E2579–E2586 (2012). doi: [10.1073/pnas.1208507109](#); pmid: [22949671](#)
66. E. Deltcheva *et al.*, CRISPR RNA maturation by trans-encoded small RNA and host factor RNase III. *Nature* **471**, 602–607 (2011). doi: [10.1038/nature09886](#); pmid: [21455174](#)
67. J. E. Garneau *et al.*, The CRISPR/Cas bacterial immune system cleaves bacteriophage and plasmid DNA. *Nature* **468**, 67–71 (2010). doi: [10.1038/nature09523](#); pmid: [21048762](#)
68. R. Sapranaukas *et al.*, The *Streptococcus thermophilus* CRISPR/Cas system provides immunity in *Escherichia coli*. *Nucleic Acids Res.* **39**, 9275–9282 (2011). doi: [10.1093/nar/gkr606](#); pmid: [21813460](#)
69. K. Chylinski, K. S. Makarova, E. Charpentier, E. V. Koonin, Classification and evolution of type II CRISPR-Cas systems. *Nucleic Acids Res.* **42**, 6091–6105 (2014). doi: [10.1093/nar/gku241](#); pmid: [24728998](#)
70. K. Chylinski, A. Le Rhun, E. Charpentier, The tracrRNA and Cas9 families of type II CRISPR-Cas immunity systems. *RNA Biol.* **10**, 726–737 (2013). doi: [10.4161/rna.24321](#); pmid: [23663642](#)
71. I. Fontana *et al.*, Phylogeny of Cas9 determines functional exchangeability of dual-RNA and Cas9 among orthologous type II CRISPR-Cas systems. *Nucleic Acids Res.* **42**, 2577–2590 (2014). doi: [10.1093/nar/gkt1074](#); pmid: [24270795](#)
72. T. Karvelis *et al.*, crRNA and tracrRNA guide Cas9-mediated DNA interference in *Streptococcus thermophilus*. *RNA Biol.* **10**, 841–851 (2013). doi: [10.4161/rna.24203](#); pmid: [23535272](#)
73. K. M. Esvelt *et al.*, Orthogonal Cas9 proteins for RNA-guided gene regulation and editing. *Nat. Methods* **10**, 1116–1121 (2013). doi: [10.1038/nmeth.2681](#); pmid: [24076762](#)
74. Z. Hou *et al.*, Efficient genome engineering in human pluripotent stem cells using Cas9 from *Neisseria meningitidis*. *Proc. Natl. Acad. Sci. U.S.A.* **110**, 15644–15649 (2013). doi: [10.1073/pnas.1313587110](#); pmid: [23940360](#)
75. L. Cong *et al.*, Multiplex genome engineering using CRISPR/Cas systems. *Science* **339**, 819–823 (2013). doi: [10.1126/science.1231143](#); pmid: [23287718](#)
76. L. Nissim, S. D. Peril, A. Fridkin, P. Perez-Pinera, T. K. Lu, Multiplexed and programmable regulation of gene networks with an integrated RNA and CRISPR/Cas toolkit in human cells. *Mol. Cell* **54**, 698–710 (2014). doi: [10.1016/j.molcel.2014.04.022](#); pmid: [24837679](#)
77. M. Jinek *et al.*, Structures of Cas9 endonucleases reveal RNA-mediated conformational activation. *Science* **343**, 1247997 (2014). doi: [10.1126/science.1247997](#); pmid: [24505130](#)
78. H. Nishimasu *et al.*, Crystal structure of Cas9 in complex with guide RNA and target DNA. *Cell* **156**, 935–949 (2014). doi: [10.1016/j.cell.2014.02.001](#); pmid: [24529477](#)
79. T. S. Sampson, S. D. Saroj, A. C. Llewellyn, Y.-L. Tzeng, D. R. Weiss, A CRISPR/Cas system mediates bacterial innate immune evasion and virulence. *Nature* **497**, 254–257 (2013). doi: [10.1038/nature12048](#); pmid: [23584588](#)
80. S. H. Sternberg, S. Redding, M. Jinek, E. C. Greene, J. A. Doudna, DNA interrogation by the CRISPR RNA-guided endonuclease Cas9. *Nature* **507**, 62–67 (2014). doi: [10.1038/nature13011](#); pmid: [24476820](#)
81. C. Anders, O. Niewoehner, A. Duerst, M. Jinek, Structural basis of PAM-dependent target DNA recognition by the Cas9 endonuclease. *Nature* **513**, 569–573 (2014). doi: [10.1038/nature13579](#); pmid: [25079318](#)
82. M. D. Szczelkun *et al.*, Direct observation of R-loop formation by single RNA-guided Cas9 and Cascade effector complexes. *Proc. Natl. Acad. Sci. U.S.A.* **111**, 9798–9803 (2014). doi: [10.1073/pnas.1402597111](#); pmid: [24912165](#)
83. C. Kuscu, S. Arslan, R. Maniv, J. Thorpe, M. Adli, Genome-wide analysis reveals characteristics of off-target sites bound by the Cas9 endonuclease. *Nat. Biotechnol.* **32**, 677–683 (2014). doi: [10.1038/nbt.2916](#); pmid: [24837660](#)
84. X. Wu *et al.*, Genome-wide binding of the CRISPR endonuclease Cas9 in mammalian cells. *Nat. Biotechnol.* **32**, 670–676 (2014). doi: [10.1038/nbt.2889](#); pmid: [24752079](#)
85. M. Jinek *et al.*, RNA-programmed genome editing in human cells. *eLife* **2**, e00471 (2013). doi: [10.7554/eLife.00471](#); pmid: [23386978](#)
86. P. Mali *et al.*, RNA-guided human genome engineering via Cas9. *Science* **339**, 823–826 (2013). doi: [10.1126/science.1232033](#); pmid: [23287722](#)
87. N. A. Kearns *et al.*, Cas9 effector-mediated regulation of transcription and differentiation in human pluripotent stem cells. *Development* **141**, 219–223 (2014). doi: [10.1242/dev.103341](#); pmid: [24346702](#)
88. J. M. Kim, D. Kim, S. Kim, J.-S. Kim, Genotyping with CRISPR-Cas-derived RNA-guided endonucleases. *Nat. Commun.* **5**, 3157 (2014). doi: [10.1038/ncomms4157](#); pmid: [24445736](#)
89. S. Kim, D. Kim, S. W. Cho, J. Kim, J.-S. Kim, Highly efficient RNA-guided genome editing in human cells via delivery of purified Cas9 ribonucleoproteins. *Genome Res.* **24**, 1012–1019 (2014). doi: [10.1101/gr.171322.113](#); pmid: [24696461](#)

90. Z. Rong, S. Zhu, Y. Xu, X. Fu, Homologous recombination in human embryonic stem cells using CRISPR/Cas9 nickase and a long DNA donor template. *Protein Cell* **5**, 258–260 (2014). doi: [10.1007/s12328-014-0032-5](#); pmid: [24622843](#)
91. P. D. Hsu, E. S. Lander, F. Zhang, Development and applications of CRISPR-Cas9 for genome engineering. *Cell* **157**, 1262–1278 (2014). doi: [10.1016/j.cell.2014.05.010](#); pmid: [24906146](#)
92. P. Mali, K. M. Esvelt, G. M. Church, Cas9 as a versatile tool for engineering biology. *Nat. Methods* **10**, 957–963 (2013). doi: [10.1038/nmeth.2649](#); pmid: [24076990](#)
93. J. D. Sander, J. K. Joung, CRISPR-Cas systems for editing, regulating and targeting genomes. *Nat. Biotechnol.* **32**, 347–355 (2014). doi: [10.1038/nbt.2842](#); pmid: [24584096](#)
94. W. Y. Hwang *et al.*, Efficient genome editing in zebrafish using a CRISPR-Cas system. *Nat. Biotechnol.* **31**, 227–229 (2013). doi: [10.1038/nbt.2501](#); pmid: [23360964](#)
95. P. S. Choi, M. Meyerson, Targeted genomic rearrangements using CRISPR/Cas technology. *Nat. Commun.* **5**, 3728 (2014). doi: [10.1038/ncomms4728](#); pmid: [24759083](#)
96. C. Chen *et al.*, MLL3 is a haploinsufficient 7q tumor suppressor in acute myeloid leukemia. *Cancer Cell* **25**, 652–665 (2014). doi: [10.1016/j.ccr.2014.03.016](#); pmid: [24794707](#)
97. R. Torres *et al.*, Engineering human tumour-associated chromosomal translocations with the RNA-guided CRISPR-Cas9 system. *Nat. Commun.* **5**, 3964 (2014). doi: [10.1038/ncomms4964](#); pmid: [24888982](#)
98. W. Xue *et al.*, CRISPR-mediated direct mutation of cancer genes in the mouse liver. *Nature* **514**, 380–384 (2014). doi: [10.1038/nature13589](#); pmid: [25119044](#)
99. D. Heckl *et al.*, Generation of mouse models of myeloid malignancy with combinatorial genetic lesions using CRISPR-Cas9 genome editing. *Nat. Biotechnol.* **32**, 941–946 (2014). doi: [10.1038/nbt.2951](#)
100. T. Wang, J. J. Wei, D. M. Sabatini, E. S. Lander, Genetic screens in human cells using the CRISPR-Cas9 system. *Science* **343**, 80–84 (2014). doi: [10.1126/science.1246981](#); pmid: [24336569](#)
101. Y. Zhou *et al.*, High-throughput screening of a CRISPR/Cas9 library for functional genomics in human cells. *Nature* **509**, 487–491 (2014). doi: [10.1038/nature13166](#); pmid: [24717434](#)
102. O. Shalem *et al.*, Genome-scale CRISPR-Cas9 knockout screening in human cells. *Science* **343**, 84–87 (2014). doi: [10.1126/science.1247005](#); pmid: [24336571](#)
103. Y. Wu *et al.*, Correction of a genetic disease in mouse via use of CRISPR-Cas9. *Cell Stem Cell* **13**, 659–662 (2013). doi: [10.1016/j.stem.2013.10.016](#); pmid: [24315440](#)
104. G. Schwank *et al.*, Functional repair of CFTR by CRISPR/Cas9 in intestinal stem cell organoids of cystic fibrosis patients. *Cell Stem Cell* **13**, 653–658 (2013). doi: [10.1016/j.stem.2013.11.002](#); pmid: [24315439](#)
105. J.-F. Li *et al.*, Multiplex and homologous recombination-mediated genome editing in *Arabidopsis* and *Nicotiana benthamiana* using guide RNA and Cas9. *Nat. Biotechnol.* **31**, 688–691 (2013). doi: [10.1038/nbt.2654](#); pmid: [23929339](#)
106. V. Nekrasov, B. Staskiewicz, D. Weigel, J. D. G. Jones, S. Kamoun, Targeted mutagenesis in the model plant *Nicotiana benthamiana* using Cas9 RNA-guided endonuclease. *Nat. Biotechnol.* **31**, 691–693 (2013). doi: [10.1038/nbt.2655](#); pmid: [23929340](#)
107. K. Xie, Y. Yang, RNA-guided genome editing in plants using a CRISPR-Cas system. *Mol. Plant* **6**, 1975–1983 (2013). doi: [10.1093/mp/sss119](#); pmid: [23956122](#)
108. W. Jiang *et al.*, Demonstration of CRISPR/Cas9/sgRNA-mediated targeted gene modification in *Arabidopsis*, tobacco, sorghum and rice. *Nucleic Acids Res.* **41**, e188 (2013). doi: [10.1093/nar/gkt780](#); pmid: [23999092](#)
109. S. K. Upadhyay, J. Kumar, A. Alok, R. Tuli, RNA-guided genome editing for target gene mutations in wheat. *G3* **3**, 2233–2238 (2013). doi: [10.1534/g3.113.008847](#)
110. S. S. Sugano *et al.*, CRISPR/Cas9-mediated targeted mutagenesis in the liverwort *Marchantia polymorpha* L. *Plant Cell Physiol.* **55**, 475–481 (2014). doi: [10.1093/pcp/pcu014](#); pmid: [24443494](#)
111. H. Jia, N. Wang, Targeted genome editing of sweet orange using Cas9/sgRNA. *PLOS ONE* **9**, e93806 (2014). doi: [10.1371/journal.pone.0093806](#); pmid: [24710347](#)
112. H. Zhang *et al.*, The CRISPR/Cas9 system produces specific and homozygous targeted gene editing in rice in one generation. *Plant Biotechnol. J.* **12**, 797–807 (2014). doi: [10.1111/pbi.12200](#); pmid: [24854982](#)
113. S. J. Gratz *et al.*, Genome engineering of *Drosophila* with the CRISPR RNA-guided Cas9 nuclease. *Genetics* **194**, 1029–1035 (2013). doi: [10.1534/genetics.113.152710](#); pmid: [23709638](#)
114. A. R. Bassett, C. Tibbit, C. P. Ponting, J.-L. Liu, Highly efficient targeted mutagenesis of *Drosophila* with the CRISPR/Cas9 system. *Cell Rep.* **4**, 220–228 (2013). doi: [10.1016/j.celrep.2013.06.020](#); pmid: [23827738](#)
115. N. Chang *et al.*, Genome editing with RNA-guided Cas9 nuclease in zebrafish embryos. *Cell Res.* **23**, 465–472 (2013). doi: [10.1038/cr.2013.45](#); pmid: [23528705](#)
116. A. E. Friedland *et al.*, Heritable genome editing in *C. elegans* via a CRISPR-Cas9 system. *Nat. Methods* **10**, 741–743 (2013). doi: [10.1038/nmeth.2532](#); pmid: [23817069](#)
117. G. P. Flowers, A. T. Timberlake, K. C. McLean, J. R. Monaghan, C. M. Crews, Highly efficient targeted mutagenesis in axolotl using Cas9 RNA-guided nuclease. *Development* **141**, 2165–2171 (2014). doi: [10.1242/dev.105072](#); pmid: [24764077](#)
118. I. L. Blitz, J. Biesinger, X. Xie, K. W. Y. Cho, Biallelic genome modification in *F0 Xenopus tropicalis* embryos using the CRISPR/Cas system. *Genesis* **51**, 827–834 (2013). doi: [10.1002/dvg.22719](#); pmid: [24123579](#)
119. T. Nakayama *et al.*, Simple and efficient CRISPR/Cas9-mediated targeted mutagenesis in *Xenopus tropicalis*. *Genesis* **51**, 835–843 (2013). doi: [10.1002/dvg.22720](#); pmid: [24123613](#)
120. H. Wang *et al.*, One-step generation of mice carrying mutations in multiple genes by CRISPR/Cas-mediated genome engineering. *Cell* **153**, 910–918 (2013). doi: [10.1016/j.cell.2013.04.025](#); pmid: [23643243](#)
121. H. Yang *et al.*, One-step generation of mice carrying reporter and conditional alleles by CRISPR/Cas-mediated genome engineering. *Cell* **154**, 1370–1379 (2013). doi: [10.1016/j.cell.2013.08.022](#); pmid: [23992847](#)
122. A. W. Cheng *et al.*, Multiplexed activation of endogenous genes by CRISPR-on, an RNA-guided transcriptional activator system. *Cell Res.* **23**, 1163–1171 (2013). doi: [10.1038/cr.2013.122](#); pmid: [23979020](#)
123. Y. Ma *et al.*, Heritable multiplex genetic engineering in rats using CRISPR/Cas9. *PLOS ONE* **9**, e89413 (2014). doi: [10.1371/journal.pone.0089413](#); pmid: [24589843](#)
124. X. Hu *et al.*, Heritable gene-targeting with gRNA/Cas9 in rats. *Cell Res.* **23**, 1322–1325 (2013). doi: [10.1038/cr.2013.141](#); pmid: [24145754](#)
125. K. M. Whitworth, K. Lee, J. A. Benne, B. P. Beaton, L. D. Spate, S. L. Murphy, M. S. Samuel, J. Mao, C. O'Gorman, E. M. Walters, C. N. Murphy, J. Driver, A. Mileham, D. McLaren, K. D. Wells, R. S. Prather, Use of the CRISPR/Cas9 system to produce genetically engineered pigs from in vitro-derived oocytes and embryos. *Biol. Reprod.* **114**, 121723 (2014). doi: [10.1095/biolreprod.114.121723](#)
126. Y. Niu *et al.*, Generation of gene-modified cynomolgus monkey via Cas9/RNA-mediated gene targeting in one-cell embryos. *Cell* **156**, 836–843 (2014). doi: [10.1016/j.cell.2014.01.027](#); pmid: [24486104](#)
127. L. S. Qi *et al.*, Repurposing CRISPR as an RNA-guided platform for sequence-specific control of gene expression. *Cell* **152**, 1173–1183 (2013). doi: [10.1016/j.cell.2013.02.022](#); pmid: [23452860](#)
128. Y. Zhao *et al.*, Sequence-specific inhibition of microRNA via CRISPR/CRISPRi system. *Sci. Rep.* **4**, 3943 (2014). doi: [10.1038/srep03943](#); pmid: [24487629](#)
129. L. A. Gilbert *et al.*, CRISPR-mediated modular RNA-guided regulation of transcription in eukaryotes. *Cell* **154**, 442–451 (2013). doi: [10.1016/j.cell.2013.06.044](#); pmid: [23849981](#)
130. D. Bikard *et al.*, Programmable repression and activation of bacterial gene expression using an engineered CRISPR-Cas system. *Nucleic Acids Res.* **41**, 7429–7437 (2013). doi: [10.1093/nar/gkt520](#); pmid: [23761437](#)
131. B. Chen *et al.*, Dynamic imaging of genomic loci in living human cells by a optimized CRISPR/Cas system. *Cell* **155**, 1479–1491 (2013). doi: [10.1016/j.cell.2013.12.001](#); pmid: [24360272](#)
132. H. Ebina, N. Misawa, Y. Kanemura, Y. Koyanagi, Harnessing the CRISPR/Cas9 system to disrupt latent HIV-1 provirus. *Sci. Rep.* **3**, 2510 (2013). doi: [10.1038/srep02510](#); pmid: [23974631](#)
133. W. Hu *et al.*, RNA-directed gene editing specifically eradicates latent and prevents new HIV-1 infection. *Proc. Natl. Acad. Sci. U.S.A.* **111**, 11461–11466 (2014). doi: [10.1073/pnas.1405186111](#); pmid: [25049410](#)
134. O. W. Ryan *et al.*, Selection of chromosomal DNA libraries using a multiplex CRISPR system. *eLife* **3**, 03703 (2014). doi: [10.7554/eLife.03703](#); pmid: [25139909](#)
135. M. R. O'Connell *et al.*, Programmable RNA recognition and cleavage by CRISPR/Cas9. *Nature* **10.1038/nature13769** (2014). doi: [10.1038/nature13769](#)
136. Y. Fu *et al.*, High-frequency off-target mutagenesis induced by CRISPR-Cas nucleases in human cells. *Nat. Biotechnol.* **31**, 822–826 (2013). doi: [10.1038/nbt.2623](#); pmid: [23792628](#)
137. P. D. Hsu *et al.*, DNA targeting specificity of RNA-guided Cas9 nucleases. *Nat. Biotechnol.* **31**, 827–832 (2013). doi: [10.1038/nbt.2647](#); pmid: [23873081](#)
138. V. Pattanayak *et al.*, High-throughput profiling of off-target DNA cleavage reveals RNA-programmed Cas9 nuclease specificity. *Nat. Biotechnol.* **31**, 839–843 (2013). doi: [10.1038/nbt.2673](#); pmid: [23934178](#)
139. T. J. Cradick, E. J. Fine, C. J. Antico, G. Bao, CRISPR/Cas9 systems targeting β -globin and CCR5 genes have substantial off-target activity. *Nucleic Acids Res.* **41**, 9584–9592 (2013). doi: [10.1093/nar/gkt174](#); pmid: [23939622](#)
140. S. W. Cho *et al.*, Analysis of off-target effects of CRISPR/Cas-derived RNA-guided endonucleases and nickases. *Genome Res.* **24**, 132–141 (2014). doi: [10.1101/gr.162339.113](#); pmid: [24253446](#)
141. M. Güell, L. Yang, G. M. Church, Genome editing assessment using CRISPR Genome Analyzer (CRISPR-GA). *Bioinformatics* **30**, 2968–2970 (2014). doi: [10.1093/bioinformatics/btu427](#)
142. T. G. Montague, J. M. Cruz, J. A. Gagnon, G. M. Church, E. Valen, CHOPCHOP: A CRISPR/Cas9 and TALEN web tool for genome editing. *Nucleic Acids Res.* **42**, W401–W407 (2014). doi: [10.1093/nar/gku410](#); pmid: [24861617](#)
143. A. O'Brien, T. L. Bailey, GT-Scan: Identifying unique genomic targets. *Bioinformatics* **30**, 2673–2675 (2014). doi: [10.1093/bioinformatics/btu354](#)
144. A. Xiao *et al.*, CasOT: a genome-wide Cas9/gRNA off-target searching tool. *Bioinformatics* **30**, 1180–1182 (2014). doi: [10.1093/bioinformatics/btt764](#)
145. S. Xie, B. Shen, C. Zhang, X. Huang, Y. Zhang, sgRNACas9: A software package for designing CRISPR sgRNA and evaluating potential off-target cleavage sites. *PLOS ONE* **9**, e100448 (2014). doi: [10.1371/journal.pone.0100448](#); pmid: [24956386](#)
146. P. Mali *et al.*, Cas9 transcriptional activators for target specificity screening and paired nickases for cooperative genome engineering. *Nat. Biotechnol.* **31**, 833–838 (2013). doi: [10.1038/nbt.2675](#); pmid: [23907171](#)
147. F. A. Ran *et al.*, Double nicking by RNA-guided CRISPR Cas9 for enhanced genome editing specificity. *Cell* **154**, 1380–1389 (2013). doi: [10.1016/j.cell.2013.08.021](#); pmid: [23992846](#)
148. B. Shen *et al.*, Efficient genome modification by CRISPR-Cas9 nickase with minimal off-target effects. *Nat. Methods* **11**, 399–402 (2014). doi: [10.1038/nmeth.2857](#); pmid: [24584192](#)
149. J. P. Gulinger, D. B. Thompson, D. R. Liu, Fusion of catalytically inactive Cas9 to FokI nuclease improves the specificity of genome modification. *Nat. Biotechnol.* **32**, 577–582 (2014). doi: [10.1038/nbt.2909](#); pmid: [24770324](#)
150. S. Q. Tsai *et al.*, Dimeric CRISPR RNA-guided FokI nucleases for highly specific genome editing. *Nat. Biotechnol.* **32**, 569–576 (2014). doi: [10.1038/nbt.2908](#); pmid: [24770325](#)
151. Y. Fu, J. D. Sander, D. Reyon, V. M. Cascio, J. K. Joung, Improving CRISPR-Cas nuclease specificity using truncated guide RNAs. *Nat. Biotechnol.* **32**, 279–284 (2014). doi: [10.1038/nbt.2808](#); pmid: [24463574](#)
152. S. Ramakrishna *et al.*, Gene disruption by cell-penetrating peptide-mediated delivery of Cas9 protein and guide RNA. *Genome Res.* **24**, 1020–1027 (2014). doi: [10.1101/gr.171264.113](#); pmid: [24696462](#)
153. H. Yin *et al.*, Genome editing with Cas9 in adult mice corrects a disease mutation and phenotype. *Nat. Biotechnol.* **32**, 551–553 (2014). doi: [10.1038/nbt.2884](#); pmid: [24681508](#)

ACKNOWLEDGMENTS

J.A.D. is a co-founder of Caribou Biosciences Inc. and Editas Medicine and is on the scientific advisory board of Caribou Biosciences Inc. E.C. is a cofounder of CRISPR Therapeutics and is on the scientific advisory board of CRISPR Therapeutics and Horizon Discovery. E.C. is supported by the Alexander von Humboldt Foundation, the German Federal Ministry for Education and Research, the Helmholtz Association, the German Research Foundation, the Göran Gustafsson Foundation, the Swedish Research Council, the Kempe Foundation, and Umeå University. J.A.D. acknowledges financial support from the Howard Hughes Medical Institute, NSF, the Gates Foundation, the Li Ka Shing Foundation, and NIH; J.A.D. is a Howard Hughes Medical Institute Investigator and a member of the Center for RNA Systems Biology at UC Berkeley (J. Cate, P.I.).

10.1126/science.1258096

RESEARCH ARTICLE

FUNGAL BIOGEOGRAPHY

Global diversity and geography of soil fungi

Leho Tedersoo,^{1*}† Mohammad Bahram,^{2†} Sergei Põlme,¹ Urmas Kõljalg,² Nourou S. Yorou,³ Ravi Wijesundera,⁴ Luis Villarreal Ruiz,⁵ Aída M. Vasco-Palacios,⁶ Pham Quang Thu,⁷ Ave Suija,² Matthew E. Smith,⁸ Cathy Sharp,⁹ Erki Saluveer,² Alessandro Saitta,¹⁰ Miguel Rosas,¹¹ Taavi Riit,² David Ratkowsky,¹² Karin Pritsch,¹³ Kadri Põldmaa,² Meike Piepenbring,¹¹ Cherdchai Phosri,¹⁴ Marko Peterson,² Kaarin Parts,² Kadri Pärtel,² Eveli Otsing,² Eduardo Nouhra,¹⁵ André L. Njouonkou,¹⁶ R. Henrik Nilsson,¹⁷ Luis N. Morgado,¹⁸ Jordan Mayor,¹⁹ Tom W. May,²⁰ Luiza Majuakim,²¹ D. Jean Lodge,²² Su See Lee,²³ Karl-Henrik Larsson,²⁴ Petr Kohout,² Kentaro Hosaka,²⁵ Indrek Hiiesalu,² Terry W. Henkel,²⁶ Helery Harend,² Liang-dong Guo,²⁷ Alina Greslebin,²⁸ Gwen Grelet,²⁹ Jozsef Geml,¹⁸ Genevieve Gates,¹² William Dunstan,³⁰ Chris Dunk,¹⁹ Rein Drenkhan,³¹ John Dearnaley,³² André De Kesel,³³ Tan Dang,⁷ Xin Chen,³⁴ Franz Buegger,¹³ Francis Q. Brearley,³⁵ Gregory Bonito,²⁰ Sten Anslan,² Sandra Abell,³⁶ Kessy Abarenkov¹

Fungi play major roles in ecosystem processes, but the determinants of fungal diversity and biogeographic patterns remain poorly understood. Using DNA metabarcoding data from hundreds of globally distributed soil samples, we demonstrate that fungal richness is decoupled from plant diversity. The plant-to-fungus richness ratio declines exponentially toward the poles. Climatic factors, followed by edaphic and spatial variables, constitute the best predictors of fungal richness and community composition at the global scale. Fungi show similar latitudinal diversity gradients to other organisms, with several notable exceptions. These findings advance our understanding of global fungal diversity patterns and permit integration of fungi into a general macroecological framework.

Fungi are eukaryotic microorganisms that play fundamental ecological roles as decomposers, mutualists, or pathogens of plants and animals; they drive carbon cycling in forest soils, mediate mineral nutrition of plants, and alleviate carbon limitations of other soil organisms. Fungi comprise some 100,000 described species (accounting for synonyms), but the actual extent of global fungal diversity is estimated at 0.8 million to 5.1 million species (1).

Globally, the biomass and relative proportions of microbial groups, including fungi, co-vary with the concentration of growth-limiting nutrients in soils and plant tissues. Such patterns suggest that the distribution of microbes reflects latitudinal variation in ecosystem nutrient dynamics (2–4). Richness of nearly all terrestrial and marine macroorganisms is negatively related to increasing latitude (5)—a pattern attributed to the combined effects of climate, niche conservatism, and rates of evolutionary radiation and extinction (6). Although morphological species of unicellular microbes are usually cosmopolitan (7), there is growing evidence that the distribution of microorganisms is shaped by macroecological and community assembly processes (8). Only a few of these biogeographic processes have been demonstrated for fungi at the local scale (9). Despite their enormous diversity and importance in ecosystem function, little is known about general patterns of fungal diversity or functional roles over large

geographic scales. We used a global data set to disentangle the roles of climatic, edaphic, floristic, and spatial variables governing global-scale patterns of soil fungal diversity. We also address macroecological phenomena and show that fungi largely exhibit strong biogeographic patterns that appear to be driven by dispersal limitation and climate.

Materials and methods

We collected 40 soil cores from natural communities in each of 365 sites across the world using a uniform sampling protocol (Fig. 1A and data file S1). Most plots (2500 m²) were circular, but in steep mountain regions and densely forested areas, some plots were oblong. We randomly selected 20 trees located at least 8 m apart. In two opposite directions, 1 to 1.5 m from each tree trunk, loose debris was removed from the forest floor. Polyvinyl chloride (PVC) tubes (5 cm in diameter) were hammered into the soil down to 5 cm depth. These soil cores almost always included fine roots and comprised both the organic layer and top mineral soil. Although deep soil may contain some distinctive organisms adapted to anoxic conditions or low nutrient levels, our sampling was limited to topsoil for the following reasons. First, in the vast majority of soil types, >50% of microbial biomass and biological activity occur in the topmost organic soil layer. Second, deeper sampling was impossible in shallow, rocky

soils or those with high clay concentrations and hardpans. Third, differences among soil horizons may be masked by other variables across large geographic scales (10). The 40 soil cores taken in each site were pooled, coarse roots and stones were removed, and a subset of the soil was air-dried at <35°C. Dried soil was stored in zip-lock plastic bags with silica gel in order to minimize humidity during transit. In the laboratory, we ground dried soil into fine powder using bead beating.

We extracted DNA from 2.0 g of soil using the PowerMax Soil DNA Isolation kit (MoBio, Carlsbad, CA) following manufacturer's instructions. We performed polymerase chain reaction (PCR) using a mixture of six forward primers (in equimolar concentration) analogous to ITS3 and a degenerate reverse primer analogous to ITS4 (hereafter referred to as ITS4ngs). We shortened and modified forward and reverse primers to

¹Natural History Museum, University of Tartu, Tartu, Estonia. ²Institute of Ecology and Earth Sciences, University of Tartu, Tartu, Estonia. ³Faculté d'Agronomie, Université de Parakou, Parakou, Benin. ⁴Department of Plant Sciences, University of Colombo, Colombo 3, Sri Lanka. ⁵Postgrado en Recursos Genéticos y Productividad-Genética, LARGEMBIO, Colegio de Postgraduados-Líneas Prioritarias de Investigación 6, México City, Mexico. ⁶The Fungal Biodiversity Centre, Centraalbureau voor Schimmelcultures-Royal Netherlands Academy of Arts and Sciences, Utrecht, Netherlands. ⁷Vietnamese Academy of Forest Sciences, Hanoi, Vietnam. ⁸Department of Plant Pathology, University of Florida, Gainesville, FL, USA. ⁹Natural History Museum, Bulawayo, Zimbabwe. ¹⁰Department of Agricultural and Forest Sciences, Università di Palermo, Palermo, Italy. ¹¹Department of Mycology, Goethe University Frankfurt, Frankfurt am Main, Germany. ¹²Tasmanian Institute of Agriculture, Hobart, Tasmania, Australia. ¹³Institute of Soil Ecology, Helmholtz Zentrum München, Neuherberg, Germany. ¹⁴Department of Biology, Nakhon Phanom University, Nakhon Phanom, Thailand. ¹⁵Instituto Multidisciplinario de Biología Vegetal, Córdoba, Argentina. ¹⁶Department of Biological Sciences, University of Bamenda, Bamenda, Cameroon. ¹⁷Department of Biological and Environmental Sciences, University of Gothenburg, Göteborg, Sweden. ¹⁸Naturalis Biodiversity Center, Leiden, Netherlands. ¹⁹Department of Forest Ecology and Management, Swedish University of Agricultural Sciences, Umeå, Sweden. ²⁰Royal Botanic Gardens Melbourne, Melbourne, Victoria, Australia. ²¹Institute for Tropical Biology and Conservation, University Malaysia Sabah, Sabah, Malaysia. ²²Center for Forest Mycology Research, U.S. Department of Agriculture-Forest Service, Luquillo, Puerto Rico. ²³Forest Research Institute Malaysia, Kepong, Selangor, Malaysia. ²⁴Natural History Museum, University of Oslo, Oslo, Norway. ²⁵Department of Botany, National Museum of Nature and Science, Tsukuba, Japan. ²⁶Department of Biological Sciences, Humboldt State University, Arcata, CA, USA. ²⁷State Key Laboratory of Mycology, Institute of Microbiology, Chinese Academy of Sciences, Beijing, China. ²⁸Consejo Nacional de Investigaciones Científicas y Técnicas-Facultad de Cs. Naturales, Universidad Nacional de la Patagonia SJB, Esquel, Chubut, Argentina. ²⁹Ecosystems and Global Change team, Landcare Research, Lincoln, New Zealand. ³⁰School of Veterinary & Life Sciences, Murdoch University, Western Australia, Australia. ³¹Institute of Forestry and Rural Engineering, Estonian University of Life Sciences, Tartu, Estonia. ³²Faculty of Health, Engineering and Sciences, University of Southern Queensland, Toowoomba, Queensland, Australia. ³³Botanic Garden Meise, Meise, Belgium. ³⁴College of Life Sciences, Zhejiang University, Hangzhou 310058, China. ³⁵School of Science and the Environment, Manchester Metropolitan University, Manchester, UK. ³⁶School of Marine and Tropical Biology, James Cook University, Cairns, Queensland, Australia.

*Corresponding author. E-mail: leho.tedersoo@ut.ee †These authors contributed equally to this work.

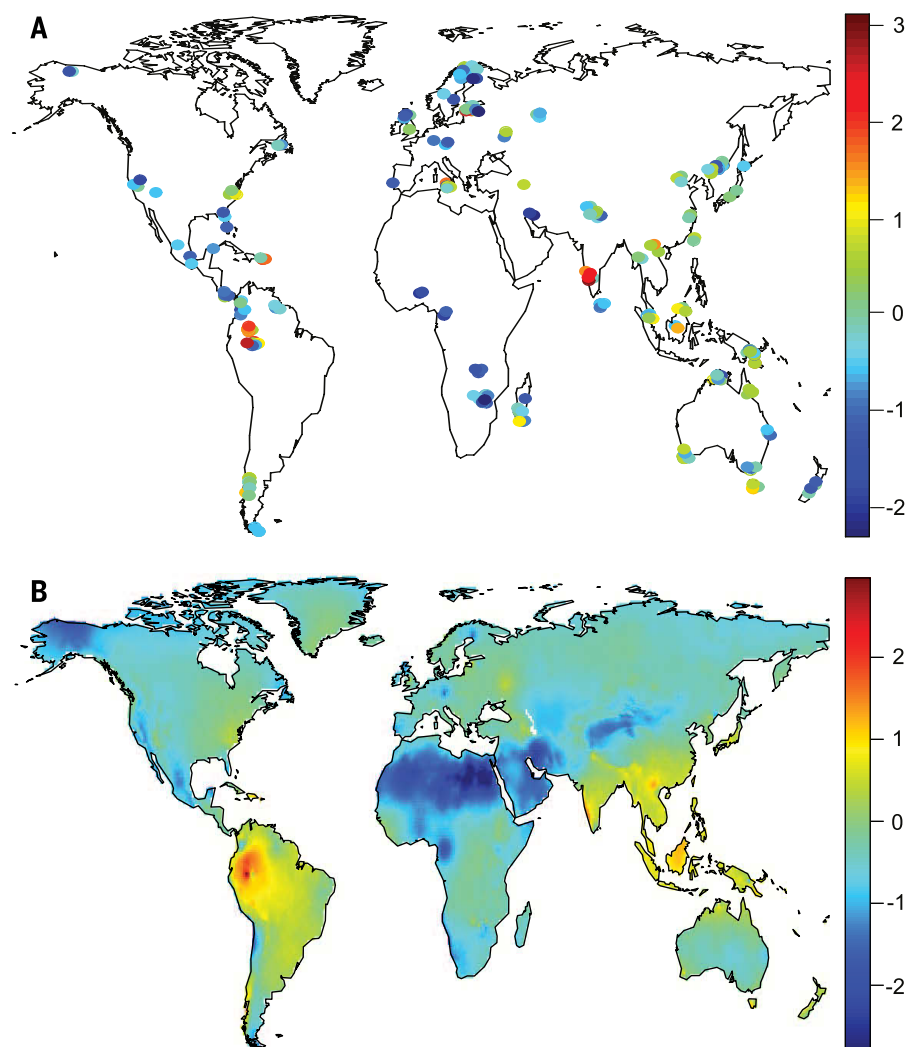


Fig. 1. Maps of global sampling and interpolated taxonomic richness of all fungi. (A) Map of global sampling. Circles indicate study sites. (B) Interpolated taxonomic richness of all fungi using IDW algorithm and accounting for the relationship with mean annual precipitation (based on the best multiple regression model). Different colors depict residual OTU richness of all fungi accounting for sequencing depth. Warm colors indicate OTU-rich sites, whereas cold colors indicate sites with fewer OTUs.

completely match >99.5% of all fungi [except ~60% of Tulasnellaceae that exhibit highly divergent 5.8S ribosomal DNA (rDNA) and Microsporidia that exhibit rearrangements in rDNA] (table S1). The ITS4ngs primer was tagged with one of 110 identifiers (multiplex identifiers, 10 to 12 bases) that were modified from those recommended by Roche (Basel, Switzerland) to differ by >3 bases, start only with adenosine, and consist of between 30 and 70% adenosine and thymidine in order to optimize the adaptor ligation step. The PCR cocktail consisted of 0.6 μ l DNA extract, 0.5 μ l each of the primers (20 pmol), 5 μ l 5xHOT FIREPol Blend Master Mix (Solis BioDYne, Tartu, Estonia), and 13.4 μ l double-distilled water. We carried out PCR in four replicates using the following thermocycling conditions: an initial 15 min at 95°C, followed by 30 cycles at 95°C for 30 s, 55°C for 30 s, 72°C for 1 min, and a final cycle of 10 min at 72°C. PCR products were pooled, and their relative quantity was estimated

by running 5 μ l amplicon DNA on 1% agarose gel for 15 min. DNA samples yielding no visible band were reamplified by using 35 cycles in an effort to obtain sufficient PCR product, whereas samples with a very strong band were reamplified with only 25 cycles. It is important to use as few cycles as possible to minimize chimera formation and to be able to interpret sequence abundance in a semiquantitative manner (17). We used negative (for DNA extraction and PCR) and positive controls throughout the experiment. Amplicons were purified with Exonuclease I and FastAP thermosensitive alkaline phosphatase enzymes (Thermo Scientific, Pittsburgh, PA). Purified amplicons were subjected to quantity normalization with a SequelPrep Normalization Plate Kit (Invitrogen, Carlsbad, CA) following manufacturer's instructions. We divided normalized amplicons into five pools that were subjected to 454 adaptor ligation, emulsion PCR, and 454 pyrosequencing by using the GS-FLX+ tech-

nology and Titanium chemistry as implemented by Beckman Coulter Genomics (Danvers, MA).

Bioinformatics

Pyrosequencing on five half-plates resulted in 2,512,068 reads with a median length of 409 bases. The sequences were reassigned to samples in mothur 1.32.2 (www.mothur.org) based on the barcodes and then trimmed (parameters: minlength = 300; maxambigs = 1; maxhomop = 12; qwindowaverage = 35; qwindowsize = 50; and bdiffs = 1) to exclude short and low-quality sequences, resulting in 2,231,188 high-quality sequences. We used ITSx 1.0.7 (<http://microbiology.se/software/itsx>) to remove the flanking 5.8S and 28S rRNA genes for optimal resolution of ITS2 clustering and removal of compromised and nontarget sequences. As a filter to remove most of the partial sequences, we retained only sequences >99 base pairs (bp) in length. Chimera control was exercised through UCHIME 4.2 (www.drive5.com/uchime). After these filtering steps, 1,397,679 sequences were retained and further clustered at 90.0% and 95.0 to 99.0% sequence similarity thresholds (12) as implemented in CD-Hit 4.6.1 (www.cd-hit.org). Clustering revealed 37,387, 59,556, 66,785, 77,448, 94,255, and 157,956 taxa based on 90.0, 95.0, 96.0, 97.0, 98.0, and 99.0% sequence similarity thresholds, respectively. The longest sequence of each Operational Taxonomic Unit (OTU), based on clustering at 98.0% sequence similarity, was selected as the representative for BLASTn searches (word size = 7; penalties: gap = -1; gap extension = -2; and match = 1) against the International Nucleotide Sequence Databases Collaboration (INSDC; www.insdc.org) and UNITE (unit.eut.ee) databases. In addition, we ran BLASTn searches against established reference sequences of all fungi in 99.0% similarity clusters that include third-party taxonomic and metadata updates (12) as implemented in the PlutoF workbench (13). For each query, we considered the 10 best-matching references to annotate our global sequences as accurately as possible. If no reliable taxon name was available, we ran manual BLASTn searches against INSDC with 500 best-matching sequences as output. We typically relied on 90, 85, 80, and 75% sequence identity as a criterion for assigning OTUs with names of a genus, family, order, or class, respectively. Sequence identity levels were raised in subsets of Sordariomycetes, Leotiomycetes, and Eurotiomycetes, because these taxa contain multiple genera and families that have unusually conserved internal transcribed spacer (ITS) sequences. As a rule, we considered e -values of BLASTn search results e^{-50} reliable to assign sequences to the fungal kingdom, whereas those $>e^{-20}$ were considered "unknown." E -values between e^{-20} and e^{-50} were manually checked against the 10 best matches for accurate assignment. We followed INSDC for higher-level taxonomy of eukaryotes (14) and the Index Fungorum (www.indexfungorum.org) for species through class-level taxonomy of fungi. Our group of taxonomic experts assigned each fungal genus, family, or order to functional categories (data file S2). If different functional categories

were present within a specific genus, we chose the dominant group (>75% of species assigned to a specific category) or considered its ecology unknown (<75% of species assignable to a single category). All Glomeromycota were considered to be arbuscular mycorrhizal (AM). Taxa were considered to be ectomycorrhizal (EcM) if they best matched any sequences of known EcM lineages (15) and exhibited sequence length/BLASTn scores above lineage-specific thresholds. For several taxonomic groups, we constructed phylogenetic trees to assess the performance of clustering, sequence quality of singletons, accuracy of OTU separation, and taxonomic assignments (fig. S1). In the course of this project, we provided 10,232 third-party taxonomic reannotations to INSDDC sequences to improve subsequent identification of fungal sequences and made these available through the UNITE database.

Statistical analyses

Estimates of the mean annual temperature (MAT), mean annual precipitation (MAP), soil moisture, and soil carbon at 30 arc second resolution were obtained from the WorldClim database (www.worldclim.org). Estimates of potential evapotranspiration (PET) and net primary productivity (NPP) at 30 arc minute resolution were obtained from the Atlas of the Biosphere (www.sage.wisc.edu/atlas/maps.php). Variation coefficients for MAT and MAP were computed based on the average monthly values to represent seasonality of temperature and precipitation. We also calculated the difference of MAP to PET in order to evaluate the effect of rainfall surplus or deficit. On the basis of vegetation type and geographical distribution, sites were categorized into biogeographic regions and biomes following the classification of the World Wildlife Foundation (<http://worldwildlife.org>) with a few exceptions: (i) temperate deciduous forests in the Northern and Southern hemispheres were treated separately; (ii) tropical montane forests (>1500 m elevation) were separated from the tropical lowland moist forests; and (iii) grasslands and shrublands of all geographic origins were pooled. At each site, we also determined the age of vegetation, time since the last fire, and EcM plant species along with their relative contribution to stand basal area. EcM plants are usually conspicuous trees or prominent shrubs that are relatively easy to identify, and their mycorrhizal status is verifiable in the field by using root excavation and microscopy. Complete lists of tree species were available for <10% of the sites, so we did not directly include plant community composition parameters in our analyses.

Concentrations of N, C, $^{13}\text{C}/^{12}\text{C}$, and $^{15}\text{N}/^{14}\text{N}$ were determined from 1 to 20 mg of soil by using GC-combustion coupled to isotope-ratio mass spectrometry (16). Concentrations of soil calcium, potassium, magnesium, and phosphorus were determined as in (16). Soil pH was measured in 1 N KCl solution.

For analyses of fungal richness, we calculated residuals of OTU richness in relation to the square root of the number of obtained sequences to

account for differences in sequencing depth. This method outperformed the commonly used rarefaction to the lowest number of sequences method, which removes most of the data (17). We also calculated the richness of major class-level taxonomic and functional groups (comprising >100 OTUs). We excluded outlying samples dominated by a few OTUs of molds, which are indicative of poor sample preservation (relative abundance of sequences belonging to Trichocomaceae >5%, Mortierellaceae >20%, or Mucoraceae >20% that exceeded three times the mean + SD). Although these samples were fairly homogeneously distributed across the world, they had conspicuously lower fungal richness. We also excluded samples that yielded less than 1200 sequences per sample.

To determine the relationship between plant and fungal richness, we relied on co-kriging values from the global vascular plant species richness data set (18), which covered 96.7% of our sites. These scale-free values of plant richness were then regressed with residuals from the best-fit models for fungal richness and fungal functional groups. We further calculated the ratio of relative plant richness to fungal richness and fitted this ratio with latitude using polynomial functions to test the assumed uniformity of plant-to-fungal richness ratios at the global scale (1, 19, 20). To account for potential latitudinal biases in plant-to-fungal diversity estimates, we took into account the nonuniform distribution of land surfaces by calculating an inverse distance weighting (IDW) spatial interpolation of standardized ratios of plant-to-residual fungal diversity using the “gstat” package in R (27). We then used IDW to interpolate total fungal diversity beyond sampling sites by accounting for MAP as based on the best-fitting multiple regression model.

Distance from the equator, altitude, age of vegetation, time since last fire, climatic variables, and concentrations of nutrients were log-transformed before analyses in order to improve the distribution of residuals and reduce nonlinearity. To account for potential autocorrelation effects, we calculated spatial eigenvectors using SAM version 4 (22). To determine the best predictors of global fungal diversity, we included edaphic, climatic, floristic, and spatial variables in multiple regression models. Because of the large number of predictors, we preselected 16 candidate predictors that were revealed through exploratory multiple linear and polynomial regression analyses based on coefficients of determination and forward selection criteria. The most parsimonious models were determined according to the corrected Akaike information criterion (AICc), which penalizes over-fitting. Last, components of the best models were forward-selected to determine their relative importance as implemented in the “packfor” package in R.

To test the direct effects of climatic variables on richness of fungi and their functional groups, and indirect climatic effects (via soil nutrients and vegetation), we used Structural Equation Modeling (SEM) in Amos version 22 (SPSS Software, Chicago, IL). Model fits were explored based on both χ^2 test and root-mean-square error of

approximation (RMSEA). First, we included all potentially important variables (inferred from both the multiple regression models and correlations for individual response variables) to construct separate SEM models. We tested all direct and indirect relations between exogenous and endogenous variables, including their error terms. Then, we used backward elimination to remove nonsignificant links to maximize whole-model fit. Last, we combined the obtained SEM models in a unified path model, following the same elimination procedure.

In addition to full models, we specifically tested the relationships between OTU richness and distance from the equator and soil pH because these or closely related variables were usually among the most important predictors. For these analyses, we calculated residuals of richness that accounted for other significant variables of the best models. To address nonlinear relationships, we fitted up to fifth-order polynomial functions and selected best-fit models on the basis of AICc values.

The relative effects of climatic, edaphic, spatial, and floristic variables on the total fungal community composition and on particular functional groups were determined by using Hellinger dissimilarity (calculated if >90% sites were represented by >1 shared OTUs), exclusion of all OTUs that occurred once, and a multistage model selection procedure as implemented in the DISTLM function of Permanova+ (www.primer-e.com/permanova.htm). Considering computational requirements, 15 candidate variables were preselected based on unifactorial (marginal test based on largest F_{pseudo} values) and multifactorial (forward selection) models. Spatial eigenvectors were not included in these analyses because they typically were of minor importance in variation partitioning analyses and to avoid making the models computationally prohibitive. Optimal models were selected based on the AICc. To obtain coefficients of determination (cumulative R^2_{adjusted}) and statistics (F_{pseudo} and P values) for each variable, components of the best models were forward selected. In parallel, we prepared Global Nonmetric Multidimensional Scaling (GNMDS) graphs using the same options. Significant variables were fitted into the GNMDS ordination space by using the “envfit” function in the “vegan” package of R. We also grouped all climatic, edaphic, spatial, and floristic variables into a variation partitioning analysis by integrating procedures in the “vegan” and “packfor” packages of R. Besides group effects, variation partitioning estimates the proportion of shared variation among these groups of predictors.

For global biogeographic analyses, we excluded OTUs from the order Hypocreales and family Trichocomaceae (both Ascomycota) because the ITS region provides insufficient taxonomic resolution, and known biological species are grouped together within the same OTU (23). We tested the differences among fungal taxonomic and functional groups for the occurrence frequency (number of sites detected) and latitudinal range of OTUs using a nonparametric Kruskal-Wallis

test and Bonferroni-adjusted multiple comparisons among mean ranks. To test the validity of Rapoport's rule in soil fungi, we calculated the average latitudinal range of OTUs for each site (24). The average latitudinal range was regressed with the latitude of study sites by means of polynomial model selection based on the AICc criterion. This analysis was run with and without OTUs only detected at a single site (range = 0). Because the results were qualitatively similar, we report results including all OTUs. To construct biogeographic relationships among major regions and biomes, we generated cross-region and cross-biome networks based on the number of shared OTUs. We excluded occurrences represented by a single sequence per site. Ward clustering of biogeographic regions and biomes was constructed

by using the Morisita-Horn index of similarity, which is insensitive to differences in samples size, by use of the "pvclust" package of R. In this procedure, *P* values are inferred for nonterminal branches based on multiscale bootstrap resampling with 1000 replicates.

Taxonomic and functional diversity

Pyrosequencing analysis of global soil samples revealed 1,019,514 quality-filtered sequences that were separated into 94,255 species-level OTUs (supplementary materials). Altogether, 963,458 (94.5%) sequences and 80,486 (85.4%) OTUs were classified as Fungi. Most other taxa belonged to animals (Metazoa, 3.3%), plants (Viridiplantae, 3.1%), alveolates (Alveolata, 2.8%), and amoebae (mostly Rhizaria, 1.3%). Kingdom-level assign-

ment of 3.8% OTUs remained elusive. The fungal subset included 35,923 (44.6%) OTUs that were represented by a single sequence; these were removed from further analyses in order to avoid overestimating richness based on these potentially erroneous sequences (25). The remaining 44,563 nonsingleton fungal OTUs in our data set numerically correspond to approximately half of the described fungal species on Earth (1). For comparison, there are currently 52,481 OTUs based on 98.0% similarity clustering of all fungal ITS sequences in publicly available databases (12). Global soil sampling revealed representatives of all major phyla and classes of Fungi. Of fungal taxa, Basidiomycota (55.7%), Ascomycota (31.3%), Mortierellomycotina (6.3%), and Mucoromycotina (4.4%) encompassed the

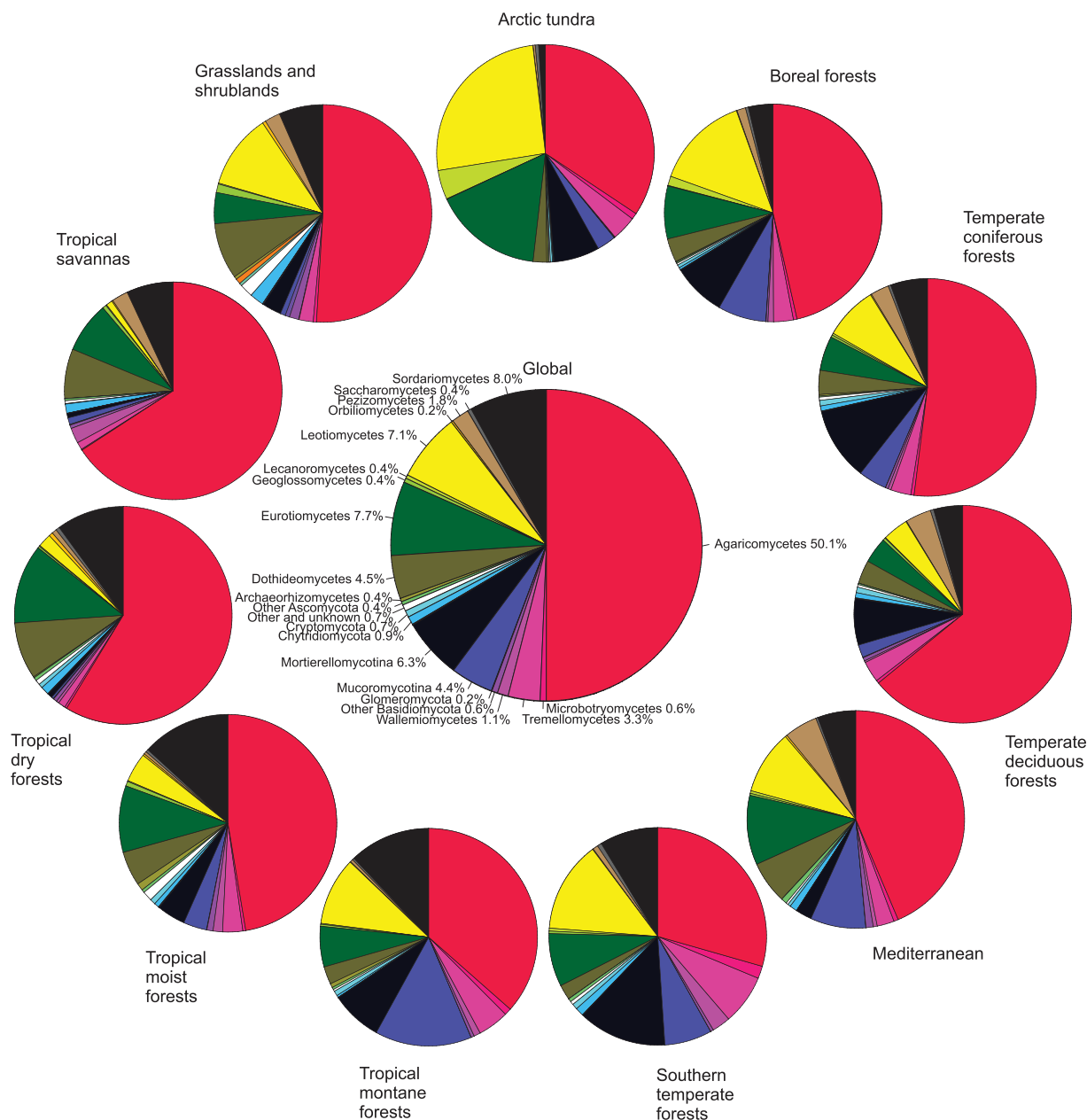


Fig. 2. Relative proportion of fungal sequences assigned to major taxonomic groups in different biomes.

largest proportion of sequences (Fig. 2), whereas the most OTU-rich phyla were the Ascomycota (48.7%), Basidiomycota (41.8%), Chytridiomycota (2.3%), and Cryptomycota (syn. Rozellida; 2.1%) (fig. S2 and data file S1). Except for the recently described phylum Cryptomycota (26), the relative proportions of major phyla correspond to the proportional distribution of taxa described and sequenced to date (www.indexfungorum.org) (12). Below the phylum level, ~6% of all fungal OTUs could not be assigned to any known class of fungi. Further clustering of unidentified fungal sequences at 70% sequence similarity revealed 14 distinct taxonomic groups comprising >7 OTUs, suggesting that there are several deeply divergent class-level fungal lineages that have not yet been described or previously sequenced.

Our classification revealed that 10,801 (24.2%) fungal OTUs exhibited >98% sequence similarity, and 33.8% exhibited >97% similarity, to pre-existing ITS sequences in public databases. This is consistent with (19), reporting 48% of OTUs amplified from Alaskan soils with >97% similarity to any database sequences. In our study, only 4353 fungal OTUs (9.8%) were matched to sequences from herbarium specimens or fully described culture collections at >98.0% sequence similarity. Although many type collections are yet to be sequenced, the paucity of matches to database entries indicates that a majority of soil-inhabiting fungal taxa remain undescribed (19, 20). These results highlight the current lack of data from understudied tropical and subtropical ecosystems. The phenomenon of high cryptic diversity and low success in naming OTUs at the genus or species level have been found in other groups of soil microbes and invertebrates, emphasizing our poor overall knowledge of global soil biodiversity (27, 28).

The main fungal phylogenetic and functional groups were present in all ecosystems, but their relative proportions varied severalfold across biomes (Fig. 2 and figs. S2 to S4). The ratio of Ascomycota to Basidiomycota OTUs was highest in grasslands and shrublands (1.86) and tropical dry forests (1.64) but lowest in the temperate deciduous forests (0.88). Chytridiomycota, Cryptomycota, and Glomeromycota were relatively more diverse in the grasslands and shrublands, accounting for 4.6, 3.6, and 1.4% of OTU richness, respectively. The relative OTU richness of Mortierellomycotina and Mucoromycotina (including most fast-growing molds but also some plant symbionts) peaked in the tundra biome (4.8 and 2.7%, respectively), but their abundance was lowest in tropical dry forests (1.0 and 0.6%, respectively). Archaeorhizomycetes, a recently described class of Ascomycetes from a boreal forest (29), was most diverse in tropical moist and montane forests, particularly in northern South America and New Guinea.

Among all fungal taxa, OTUs assigned to saprotrophs, EcM mutualists, and plant pathogens comprised 19,540 (43.8%), 10,334 (23.2%), and 1770 (4.0%), respectively (fig. S4). Other trophic categories contained <1% of remaining OTUs. EcM fungi contributed 34.1% of all taxa

in the northern temperate deciduous forests but accounted for a relatively low proportion (11.9%) in grasslands and shrublands, reflecting the paucity of host plants in these ecosystems. Similarly, the proportion of EcM fungal taxa was lowest in northern South America (8.0%), where AM trees often dominate. Plant pathogens were relatively more abundant and diverse in lowland tropical moist (6.2%) and dry (6.3%) forests.

Predictors of global richness

Structural equation models revealed that climate has both a strong direct effect on plant and fungal richness and functional groups, but it also indirectly affects these metrics by altering edaphic conditions (fig. S5). Both SEM and regression models suggest that the best predictors of diversity differed among phylogenetic and functional groups of fungi. Positive effects of mean annual precipitation (MAP) and soil calcium (Ca) concentration were the strongest predictors of total fungal diversity, explaining 7.2 and 8.9% of residual richness, respectively (table S2). Richness of EcM fungi responded positively to the relative proportion and species richness of EcM plants (explaining 18.3 and 8.5% of variance, respectively), as well as soil pH (13.0%). EcM host species richness (5.9%) and soil pH (20.4%) remained the strongest predictors in the best model for sites with EcM vegetation, accounting for >60% of basal area, a critical point above which the proportion of EcM plants had no further effect on EcM fungal richness. MAP had a strong positive effect (14.8%) on richness of saprotrophs. Diversity of plant pathogens declined with increasing distance from the equator (17.8%) and soil carbon/nitrogen (C/N) ratio (11.6%). Animal parasites responded positively to MAP (20.3%), whereas monthly variation of precipitation (MAP CV) had a negative impact on richness of mycoparasites (fungus-parasitic fungi; 8.2%). Richness of the AM Glomeromycota was negatively related to the age of vegetation (7.3%) but positively related to PET (3.5%) and soil pH (4.3%). Of the major taxonomic groups, the richness of Ascomycota in general (18.5%) and that of Archaeorhizomycetes (21.7%) were negatively related to distance from the equator in best-fit models. Climatic variables were the best predictors for richness of Mortierellomycotina (MAT, negative effect, 26.1%) and the ascomycete classes Dothideomycetes (MAT, positive effect, 20.9%), Lecanoromycetes (MAT, negative effect, 26.7%), Leotiomyces (MAT, negative effect, 30.1%), Orbiliomycetes (MAT, positive effect, 12.8%), and Sordariomycetes (MAP, positive effect, 33.4%). The richness of Chytridiomycota and the ascomycete class Pezizomycetes was best explained by a positive response to soil pH (8.6 and 40.5%, respectively). Concentration of soil nutrients or their ratio to other nutrients were the strongest predictors for OTU richness of Cryptomycota (N concentration, positive effect, 10.1%), Geoglossomycetes [N/phosphorus (P) ratio, positive effect, 3.7%], Mucoromycotina (C/N ratio, positive effect, 19.0%), and Wallemiomycetes (P concentration, negative effect, 14.9%). The richness of Basidiomycota and

its class Agaricomycetes were best explained by a positive response to soil Ca concentration (13.5 and 12.8%, respectively).

Although geographical distance per se had negligible effects on richness (Moran's $I = 0.267$), spatial predictors were included in the best richness models of nearly all functional and phylogenetic groups (except Glomeromycota), indicating regional- or continental-scale differences in OTU richness (Fig. 1B). Compared with other tropical regions, richness of fungi was conspicuously lower in Africa, independent of biome type. These results might reflect the relatively lower MAP in much of Africa as compared with other tropical continents. Alternatively, lower fungal richness could be related to the disproportionately strong shifts in biomes during the Pleistocene, which impoverished the African flora (18).

Among edaphic variables, soil pH and Ca concentration were typically the most important predictors of fungal OTU richness. These variables positively correlated with fungal richness at the global scale ($F_{1,335} = 290.7$; $R_{\text{Pearson}} = 0.682$; $P < 0.001$). The strong positive influence of soil Ca concentration on richness of fungi, in particular Basidiomycota, is congruent with a similar positive relationship found for Ca and EcM fungal richness associated with Northern Hemisphere *Alnus* spp. (30). Exchangeable Ca is important for many physiological processes in plants and microorganisms and influences the turnover rate of soil organic matter (31). In soil geochemical processes, pH and Ca concentration affect each other and thus may have both direct and indirect effects on soil biota. Fungal functional groups were differentially affected by pH. Richness of EcM fungi was greatest in slightly acidic to neutral soils (fig. S6), whereas saprotrophs, especially white rot decomposers, were more diverse in moderately to strongly acidic soils. Richness of Pezizomycetes peaked distinctly in neutral soils.

Macroecological patterns

In general agreement with biogeographic patterns of plants, animals, and foliar endophytic fungi (5, 32), the overall richness of soil fungi increased toward the equator (Fig. 3A). However, major functional and taxonomic groups showed dramatic departures from the general latitudinal richness patterns (Fig. 3 and fig. S7). Namely, diversity of saprotrophic fungi, parasites, and pathogens increased at low latitudes, whereas richness of EcM fungi peaked at mid-latitudes, especially in temperate forests and Mediterranean biomes of the Northern Hemisphere (40° to 60°N) (fig. S8). In contrast, saprotrophic fungi had a broad richness peak spanning from ~45°S to 25°N. Richness of Ascomycota—in particular, that of Archaeorhizomycetes, Dothideomycetes, Eurotiomycetes, Orbiliomycetes, and Sordariomycetes—peaked in tropical ecosystems (fig. S7). Conversely, the ascomycete classes Lecanoromycetes and Leotiomyces, as well as Microbotryomycetes (basidiomycete yeasts), Mortierellomycotina, and Mucoromycotina increased in diversity toward

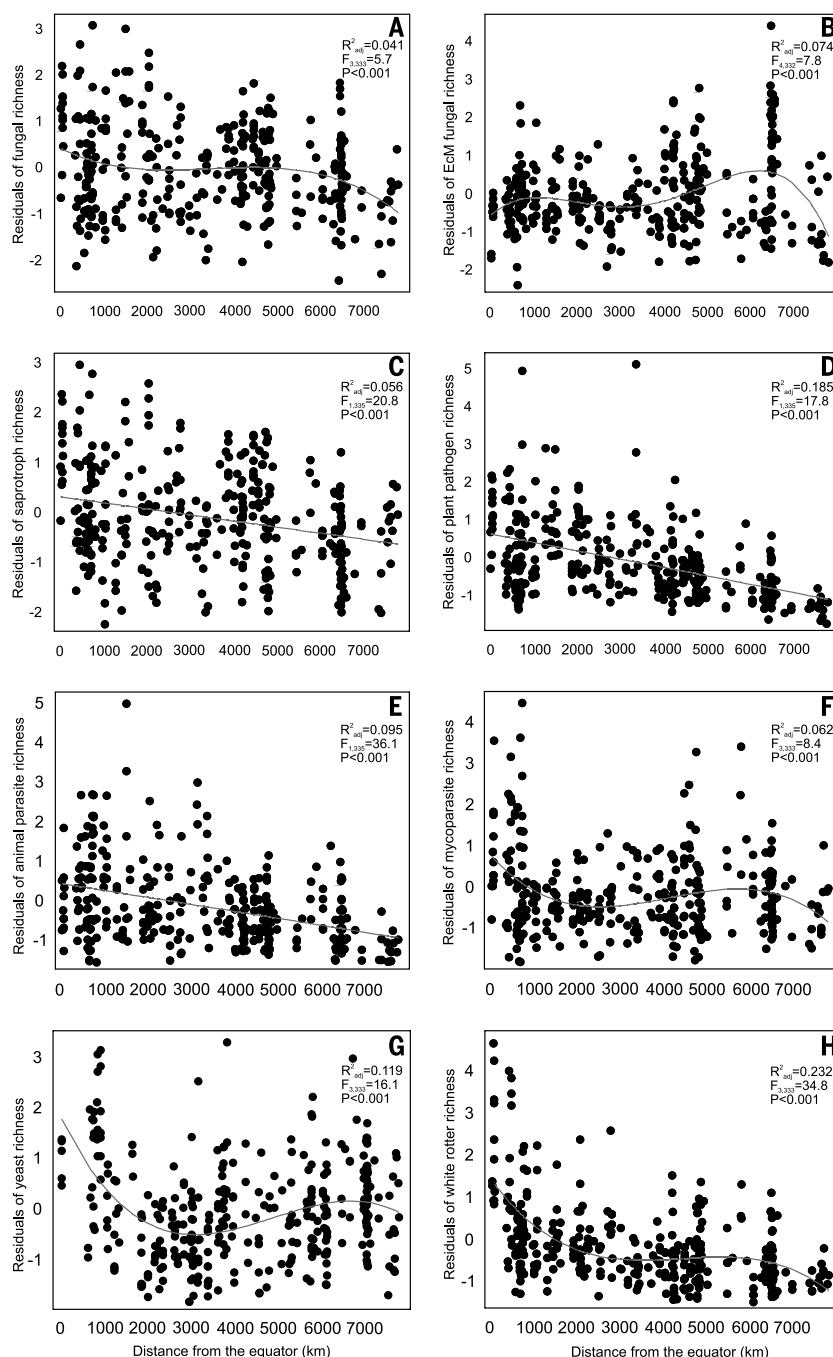


Fig. 3. Relationships between residual richness of fungal taxonomic or functional groups and distance from the equator. (A) All fungi. (B) EcM fungi. (C) Saprotrophic fungi. (D) Plant pathogens. (E) Animal parasites. (F) Mycoparasites. (G) White rot decomposers. (H) Yeasts. Lines indicate best-fitting linear or polynomial functions.

the poles, with no noticeable decline in boreal forests and tundra biomes. Agaricomycetes, Pezizomycetes, and Tremellomycetes exhibited distinct richness peaks at mid-latitudes. Richness of Agaricomycetes was greater in the Northern Hemisphere, whereas that of Microbotryomycetes, Tremellomycetes, and Wallemiomycetes peaked in the Southern Hemisphere temperate ecosystems (fig. S8).

All of these phylogenetic groups originated >150 million years ago on the supercontinent

Pangaea (33) and have had sufficient time for long-distance dispersal. However, our data suggest that particular regional biotic or abiotic conditions (such as soil pH and favorable climatic conditions) have likely stimulated evolutionary radiations in certain geographic areas and not in others. Adaptation to cold climate in younger fungal phyla has been suggested to explain differential latitudinal preferences among fungal groups (34). However, our global analysis provided no support for this hypothesis (fig. S9).

Instead, it revealed that ancient lineages are relatively more common in nonwooded ecosystems.

Relation of plant and fungal richness

Plant and fungal richness were positively correlated (fig. S10), but plant richness explained no residual richness of fungi according to the best regression model ($R^2_{adj} < 0.01$; $P > 0.05$). These results and SEM path diagrams suggest that correlations between plant and fungal richness are best explained by their similar response to climatic and edaphic variables (covariance) rather than by direct effects of plants on fungi. However, when separating functional categories, trophic groups of fungi exhibited differential response to plant diversity and relative proportion of potential hosts.

Plant pathogens usually attack a phylogenetically limited set of host plants (35), suggesting that plant pathogens have at least partly co-evolved with their hosts and may have radiated more intensively in the tropics, where high plant diversification and richness permit greater diversification. Strong phylogenetic signals in soil feedbacks, adaptive radiation, and negative density dependence (the Janzen-Connell hypothesis) have probably contributed to the pronounced richness of both plants and their pathogens at low latitudes (36, 37). However, our analyses revealed no significant effects of plant richness per se on residual richness of pathogens in soil. Similarly to pathogens, richness of AM fungi was unrelated to the proportion of AM host trees or interpolated host richness, which may result from non-specific associations with tree and understory species. Hence, both AM and soil pathogen richness were unaffected by plant richness. In contrast, host richness explained 6% of variation in EcM fungal richness, indicating either niche differentiation of fungi in forests of mixed hosts or sampling effects (forests with higher host diversity are more likely to include plant species that harbor high fungal diversity). With a few notable exceptions, most studies have found low levels of host preference or host specificity among EcM fungi (38). We found that relative EcM host density had a strong influence on EcM fungal richness, suggesting that greater availability of colonizable roots in soil provides more carbon for EcM fungi and thereby yields greater species density and local-scale richness regardless of latitude. The peak of EcM fungal taxonomic and phylogenetic richness in northern temperate biomes coincides with the geographical distribution and dominance of Pinaceae, which is the oldest extant EcM plant family (15, 39).

The ratio of plant-to-fungal richness decreased exponentially with increasing latitude because plant diversity dropped precipitously toward the poles relative to fungal diversity (Fig. 4). This finding calls into question present global fungal richness estimates. These estimates assume similar spatial turnover of plant and fungal species and a constant plant-to-fungus ratio and have been formulated mostly based on data from temperate and boreal ecosystems (1, 19, 20). Yet, local-scale beta diversity of both plants and fungi

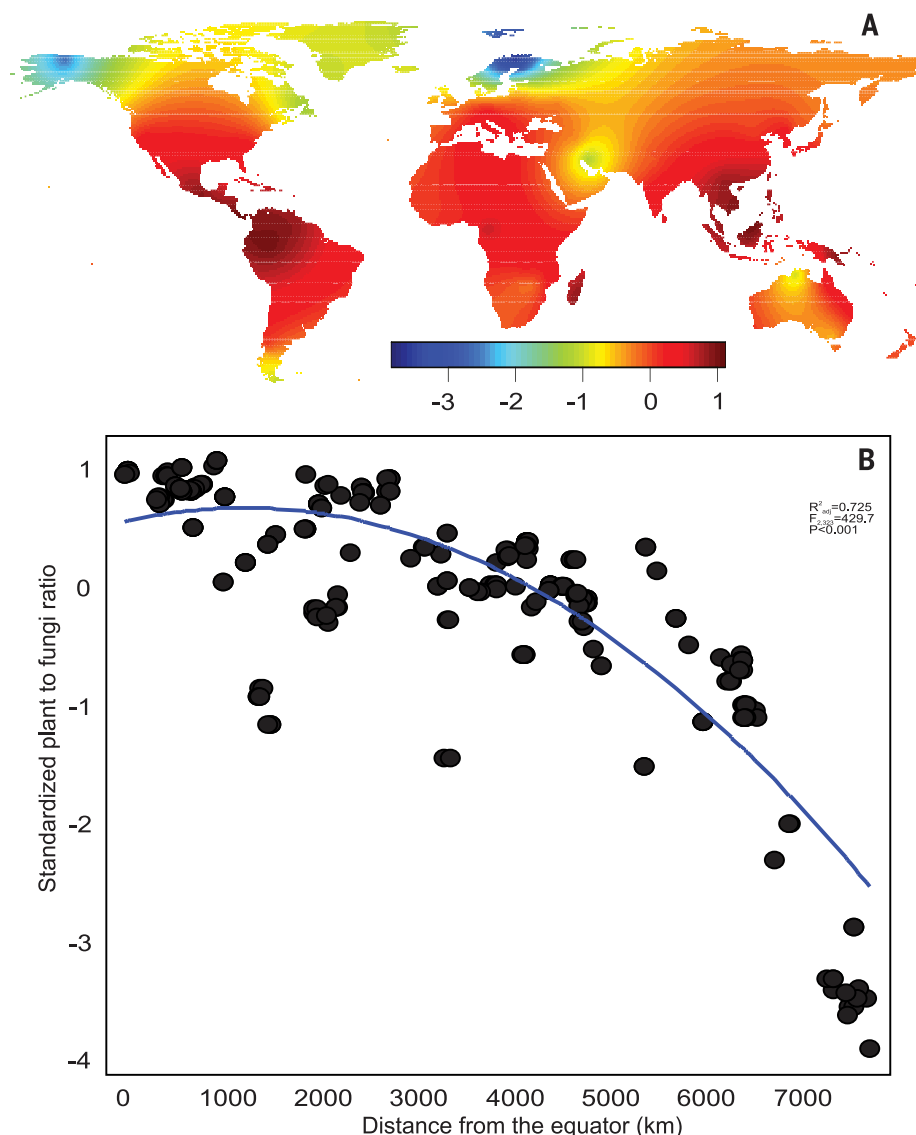


Fig. 4. Relationship between standardized plant richness to fungal richness ratio and distance from the equator. (A) Interpolated values. **(B)** Polynomial regression. Residuals of fungal richness are taken from the best linear regression model accounting for other significant predictors. Warm colors indicate high plant-to-fungal richness ratio, whereas cold colors indicate low plant-to-fungal richness.

differ among temperate and tropical sites (40, 41), and there are profound differences in plant species turnover depending on propagule size (42). Natural distribution of very few vascular plant species encompass several continents, but there are multiple fungal species with circumpolar or cosmopolitan distribution (43, 44). Although we cannot directly compare plant and fungal beta diversity, spatial turnover of plant species is arguably greater (42). Based on the function of fungi-to-plant richness ratio to latitude and latitudinal distribution of land, we calculated that fungal richness is overestimated by 1.5- and 2.5-fold on the basis of constant temperate (45° latitude) and boreal (65° latitude) richness ratios, respectively.

Because richness estimates are calculated based on the frequency of the rarest species, the reliability of singleton data call into question biologically meaningful extrapolations (17). In

metabarcoding studies such as ours, sequencing errors tend to give rise to singleton sequences, and the number of rare artificial taxa grows rapidly with increasing sequencing depth (25). Therefore, despite the size of our data set, it cannot readily be used to produce reliable taxonomic richness extrapolations.

Community ecology

Variation partitioning analysis revealed that climatic, edaphic, and floristic variables (and their shared effects) are the strongest predictors for community composition of all fungi and most of their functional groups (fig. S11). However, the saprotroph community composition was most strongly explained by purely spatial variables. More specifically, PET and soil pH explained 2.4 and 1.5%, respectively, of the variation in total fungal community composition

(table S3 and fig. S12). PET contributed 3.8, 2.8, and 11.7% to community structure of saprotrophs, plant pathogens, and yeasts, respectively. Distance from the equator (1.3%) and soil pH (0.7%) were the strongest predictors of EcM fungal community composition, whereas mean annual temperature (4.0%) was the strongest predictor for animal parasites, and distance from the equator (3.5%) was the best predictor for mycoparasites (table S3 and fig. S12).

These results indicate that both environmental and spatial predictors generally have a minor influence on species-level composition of fungi at the global scale. Nonetheless, the significant global-scale pH effect in several groups of fungi is consistent with the substantial influence of pH on the phylogenetic structure of soil fungal and bacterial communities in both local and continental scales (27, 45). The relatively stronger climatic and edaphic drivers of richness at the class and phylum level suggest that phylogenetic niche conservatism in fungal lineages is similar to cross-biome distribution patterns in vascular plants (46) and protists (47).

Global biogeography

Consistent with Rapoport's rule formulated for macro-organisms (24) and later applied to marine bacteria (48), the mean latitudinal range of fungi strongly increased toward the poles (fig. S13). These results also suggest that a greater proportion of fungi are endemic within tropical rather than extratropical ecosystems.

Major taxonomic and functional groups of fungi differed markedly in their distribution range (figs. S14 and S15). Animal parasites were more widely distributed as compared with all other groups, suggesting that there are many generalist OTUs with global distribution. Saprotrophs and plant pathogens had broader distribution ranges than EcM and AM root symbionts. Taxa belonging to Mortierellomycotina, Mucoromycotina, Tremellomycetes, and Wallemiomycetes—groups that include a large proportion of saprotrophs and parasites that produce exceptionally large quantities of aerially dispersed mitospores—were generally most widely distributed. Besides the AM Glomeromycota, OTUs belonging to the ascomycete classes Archaeorhizomycetes, Geoglossomycetes, and Orbiliomycetes were detected from the fewest sites.

The northernmost biogeographic regions (Europe, West Asia, East Asia, and North America) had the most similar fungal communities as revealed by shared fungal OTUs (Fig. 5). According to the Morisita-Horn similarity index, the northern and southern temperate regions clustered together with marginally nonsignificant support ($P = 0.064$) (Fig. 6A). In spite of the large geographical distance separating them, paleo- and neotropical biogeographic regions clustered together ($P = 0.059$). However, biogeographic clustering of regions deviated markedly in certain functional groups of fungi (Fig. 6). For instance, EcM fungi in the southern temperate and tropical regions had greater similarity as compared with northern temperate ecosystems

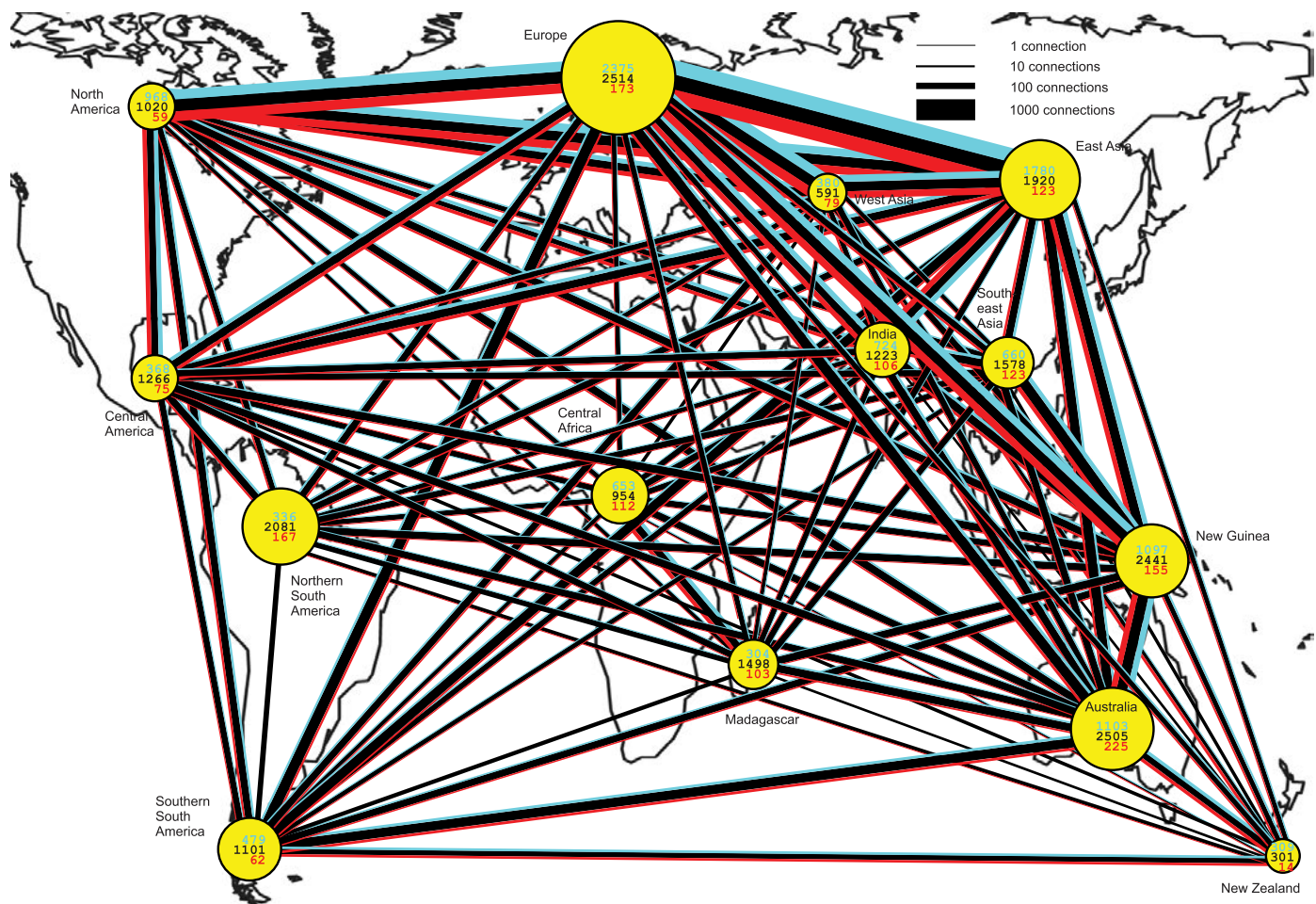


Fig. 5. Connectedness of biogeographic regions by shared OTUs of EcM fungi, saprotrophs, and plant pathogens. Blue, EcM fungi; Black, saprotrophs; and red, plant pathogens. The width of lines and diameter of circles are proportional to the square root of the number of connections and sample size (number of sites), respectively. Numbers in circles indicate the number of OTUs found in each region. OTUs with a single sequence per site and OTUs belonging to Hypocreales and Trichocomaceae (in which the ITS region is too conservative for species-level discrimination) were excluded.

($P = 0.001$). Among biomes, boreal forests, temperate coniferous forests, and temperate deciduous forests shared the largest numbers of fungal OTUs (fig. S16). Fungal OTUs in temperate deciduous forests were highly similar to Mediterranean and tropical montane forests, whereas fungal OTUs in tropical montane forests were linked to tropical moist forests, which in turn exhibited substantial connections with tropical dry forests and savannas. As a result, cluster analysis supported separation of tropical and nontropical biomes (Fig. 6B). Consistent with biogeographic region-level analysis, lowland tropical biomes, arctic tundra and boreal forests biomes, and temperate biomes formed three well-supported clusters. Tropical montane forests and grasslands and shrublands were clustered with temperate biomes according to distribution of all fungi and most functional groups. However, in EcM fungi, taxa from southern temperate forests, tropical montane forests, and grass/shrublands clustered with tropical lowland and Mediterranean biomes. A relatively large proportion of EcM fungal taxa were shared across various biomes in Australia and New Guinea, which explains these

deviating patterns. In contrast, plant pathogens from tropical montane forests clustered with tropical lowland biomes rather than with temperate biomes.

Our biogeographic analyses complement the community-level results, suggesting that both climate and biogeographic history shape macroecological patterns of fungi. Comigration with hosts over Pleistocene land bridges (such as Beringia, Wallacea, and Panamanian) and long-distance dispersal by spores appear to have played important roles in shaping current fungal distribution patterns (30, 43). The relative influence of climate and biotrophic associations with host plants of varying extant distributions probably contribute to differences in the range and biogeographic relationships among fungal functional groups (49). In addition, taxon-specific constraints for dispersal, such as shape and size of propagules and sensitivity to ultraviolet light, may differentially affect long-distance dispersal among taxa (7). For instance, Glomeromycota OTUs, which form relatively large non-wind-dispersed asexual spores, had the lowest average geographical range. In general, region-based dis-

tribution patterns of fungi are somewhat conflicting with clustering of plants and animals, where Holarctic lineages are deeply nested within larger tropical groups (50). Consistent with macroorganisms, fungi from the Southern Hemisphere temperate landmasses cluster together. Differences observed in macroecological patterns among fungi, plants, and animals may originate from the relative strength of dispersal limitation and phylogeographic history, but exaggeration from methodological differences among studies cannot be discounted. The use of homogenous sampling and analytical methods, as done in this study, are necessary to confidently compare macroecological patterns among distinct life forms and to reliably test degrees of consistency among all kingdoms of life.

Conclusions and perspectives

Climatic variables explained the greatest proportion of richness and community composition in fungal groups by exhibiting both direct and indirect effects through altered soil and floristic variables. The strong driving climatic forces identified here open up concerns regarding the

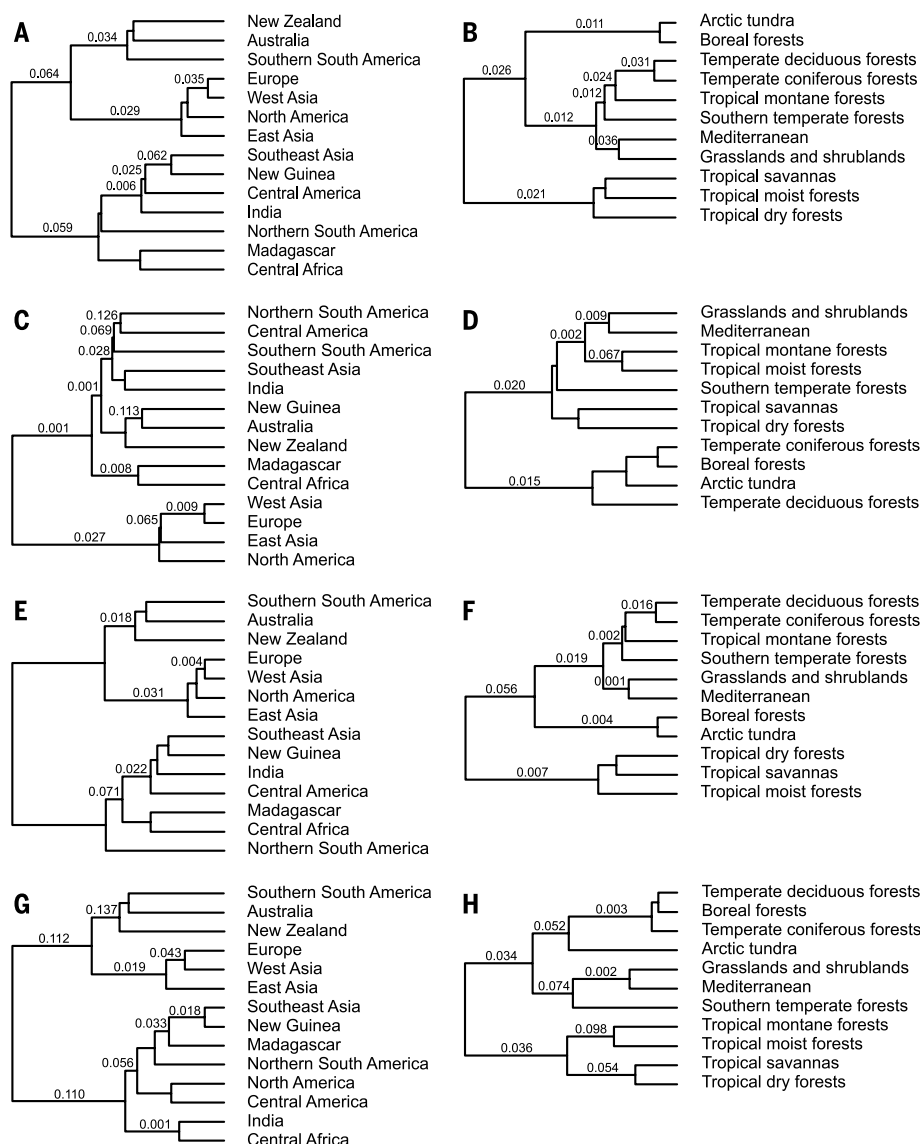


Fig. 6. Ward clustering of biogeographic regions and biomes based on the Morisita-Horn pairwise similarity index. Left, biogeographic regions; right, biomes. (A and B) All fungi. (C and D) ECM fungi. (E and F) Saprotrophs. (G and H) Plant pathogens. Numbers above branches indicate *P* values.

impact of climate change on the spread of disease (51) and the functional consequences of altered soil microorganism communities (52). The observed abrupt functional differences between fungal communities in forested and treeless ecosystems, despite spatial juxtaposition, suggests that plant life form and mycorrhizal associations determine soil biochemical processes more than plant species per se. Loss of tree cover and shrub encroachment resulting from drying and warming may thus have a marked impact on ecosystem functioning both above- and belowground.

In addition to natural mechanisms, such as long-distance dispersal and migration over past land bridges, global trade has enhanced the spread of some non-native soil organisms into other ecosystems, where they sometimes become hazardous to native biota, economy, and human health (53). Our results highlight how little insight we still

have into natural microbial distribution patterns, and this undermines our ability to appraise the actual role of humans in shaping these biogeographic processes. Even larger-scale sampling campaigns are needed to provide data for establishing natural distributions and building species distribution models (52), which will enable us to predict the spread and habitat suitability of non-native microorganisms.

REFERENCES AND NOTES

1. M. Blackwell, The fungi: 1, 2, 3 ... 5.1 million species? *Am. J. Bot.* **98**, 426–438 (2011). doi: [10.3732/ajb.1000298](https://doi.org/10.3732/ajb.1000298); pmid: [21613136](https://pubmed.ncbi.nlm.nih.gov/21613136/)
2. N. Fierer, M. S. Strickland, D. Liptzin, M. A. Bradford, C. C. Cleveland, Global patterns in belowground communities. *Ecol. Lett.* **12**, 1238 (2009). doi: [10.1111/j.1461-0248.2009.01360.x](https://doi.org/10.1111/j.1461-0248.2009.01360.x)
3. H. Serna-Chavez, N. Fierer, P. M. van Bodegom, Global drivers and patterns of microbial abundance in soil. *Glob. Ecol. Biogeogr.* **22**, 1162–1172 (2013). doi: [10.1111/geb.12070](https://doi.org/10.1111/geb.12070)

4. X. Xu, P. Thornton, W. M. Post, A global analysis of soil microbial biomass carbon, nitrogen and phosphorus in terrestrial ecosystems. *Glob. Ecol. Biogeogr.* **22**, 737–749 (2013). doi: [10.1111/geb.12029](https://doi.org/10.1111/geb.12029)
5. H. Hillebrand, On the generality of the latitudinal diversity gradient. *Am. Nat.* **163**, 192–211 (2004). doi: [10.1086/381004](https://doi.org/10.1086/381004); pmid: [14970922](https://pubmed.ncbi.nlm.nih.gov/14970922/)
6. G. G. Mittelbach *et al.*, Evolution and the latitudinal diversity gradient: Speciation, extinction and biogeography. *Ecol. Lett.* **10**, 315–331 (2007). doi: [10.1111/j.1461-0248.2007.01020.x](https://doi.org/10.1111/j.1461-0248.2007.01020.x); pmid: [17355570](https://pubmed.ncbi.nlm.nih.gov/17355570/)
7. B. J. Finlay, Global dispersal of free-living microbial eukaryote species. *Science* **296**, 1061–1063 (2002). doi: [10.1126/science.1070710](https://doi.org/10.1126/science.1070710); pmid: [12004115](https://pubmed.ncbi.nlm.nih.gov/12004115/)
8. D. R. Nemergut *et al.*, Patterns and processes of microbial community assembly. *Microbiol. Mol. Biol. Rev.* **77**, 342–356 (2013). doi: [10.1128/MMBR.00051-12](https://doi.org/10.1128/MMBR.00051-12); pmid: [24006468](https://pubmed.ncbi.nlm.nih.gov/24006468/)
9. K. G. Peay, M. I. Bidartondo, A. E. Arnold, Not every fungus is everywhere: Scaling to the biogeography of fungal-plant interactions across roots, shoots and ecosystems. *New Phytol.* **185**, 878–882 (2010). doi: [10.1111/j.1469-8137.2009.03158.x](https://doi.org/10.1111/j.1469-8137.2009.03158.x); pmid: [20356342](https://pubmed.ncbi.nlm.nih.gov/20356342/)
10. J. M. Talbot *et al.*, Endemism and functional convergence across the North American soil mycobiome. *Proc. Natl. Acad. Sci. U.S.A.* **111**, 6341–6346 (2014). doi: [10.1073/pnas.1402584111](https://doi.org/10.1073/pnas.1402584111); pmid: [24733885](https://pubmed.ncbi.nlm.nih.gov/24733885/)
11. B. D. Lindahl *et al.*, Fungal community analysis by high-throughput sequencing of amplified markers—A user's guide. *New Phytol.* **199**, 288–299 (2013). doi: [10.1111/nph.12243](https://doi.org/10.1111/nph.12243); pmid: [23534863](https://pubmed.ncbi.nlm.nih.gov/23534863/)
12. U. Kõljalg *et al.*, Towards a unified paradigm for sequence-based identification of fungi. *Mol. Ecol.* **22**, 5271–5277 (2013). doi: [10.1111/mec.12481](https://doi.org/10.1111/mec.12481); pmid: [24112409](https://pubmed.ncbi.nlm.nih.gov/24112409/)
13. K. Abarenkov *et al.*, *Evol. Bioinform.* **6**, 189 (2010).
14. S. M. Adl *et al.*, The revised classification of eukaryotes. *J. Eukaryot. Microbiol.* **59**, 429 (2012). doi: [10.1111/j.1550-7408.2012.00644.x](https://doi.org/10.1111/j.1550-7408.2012.00644.x); pmid: [22742560](https://pubmed.ncbi.nlm.nih.gov/22742560/)
15. L. Tedersoo, M. E. Smith, Lineages of ectomycorrhizal fungi revisited: Foraging strategies and novel lineages revealed by sequences from belowground. *Fungal Biol. Rev.* **27**, 83–99 (2013). doi: [10.1016/j.fbr.2013.09.001](https://doi.org/10.1016/j.fbr.2013.09.001)
16. L. Tedersoo *et al.*, Enzymatic activities and stable isotope patterns of ectomycorrhizal fungi in relation to phylogeny and exploration types in an afro-tropical rain forest. *New Phytol.* **195**, 832–843 (2012). doi: [10.1111/j.1469-8137.2012.04217.x](https://doi.org/10.1111/j.1469-8137.2012.04217.x); pmid: [22758212](https://pubmed.ncbi.nlm.nih.gov/22758212/)
17. I. Hiiesalu *et al.*, Species richness of arbuscular mycorrhizal fungi: Associations with grassland plant richness and biomass. *New Phytol.* **203**, 233–244 (2014). doi: [10.1111/nph.12765](https://doi.org/10.1111/nph.12765); pmid: [24641509](https://pubmed.ncbi.nlm.nih.gov/24641509/)
18. H. Kreft, W. Jetz, Global patterns and determinants of vascular plant diversity. *Proc. Natl. Acad. Sci. U.S.A.* **104**, 5925–5930 (2007). doi: [10.1073/pnas.0608361104](https://doi.org/10.1073/pnas.0608361104); pmid: [17379667](https://pubmed.ncbi.nlm.nih.gov/17379667/)
19. D. L. Taylor *et al.*, A first comprehensive census of fungi in soil reveals both hyperdiversity and fine-scale niche partitioning. *Ecol. Monogr.* **84**, 3–20 (2014). doi: [10.1890/12-1693.1](https://doi.org/10.1890/12-1693.1)
20. H. E. O'Brien, J. L. Parrent, J. A. Jackson, J. M. Moncalvo, R. Vilgalys, Fungal community analysis by large-scale sequencing of environmental samples. *Appl. Environ. Microbiol.* **71**, 5544–5550 (2005). doi: [10.1128/AEM.71.9.5544-5550.2005](https://doi.org/10.1128/AEM.71.9.5544-5550.2005); pmid: [16151147](https://pubmed.ncbi.nlm.nih.gov/16151147/)
21. R. Core Team, *R: A Language and Environment for Statistical Computing* (R Foundation for Statistical Computing, Vienna 2014).
22. T. F. Rangel, J. A. F. Diniz-Filho, L. M. Bini, SAM: A comprehensive application for Spatial Analysis in Macroecology. *Ecography* **33**, 46–50 (2010). doi: [10.1111/j.1600-0587.2009.06299.x](https://doi.org/10.1111/j.1600-0587.2009.06299.x)
23. C. L. Schoch *et al.*, Fungal Barcoding Consortium Fungal Barcoding Consortium Author List, Nuclear ribosomal internal transcribed spacer (ITS) region as a universal DNA barcode marker for Fungi. *Proc. Natl. Acad. Sci. U.S.A.* **109**, 6241–6246 (2012). doi: [10.1073/pnas.1117018109](https://doi.org/10.1073/pnas.1117018109); pmid: [22454494](https://pubmed.ncbi.nlm.nih.gov/22454494/)
24. G. C. Stevens, The latitudinal gradient in geographical range: How so many species coexist in the tropics. *Am. Nat.* **133**, 240 (1989). doi: [10.1086/284913](https://doi.org/10.1086/284913)
25. I. A. Dickie, Insidious effects of sequencing errors on perceived diversity in molecular surveys. *New Phytol.* **188**, 916–918 (2010). doi: [10.1111/j.1469-8137.2010.03473.x](https://doi.org/10.1111/j.1469-8137.2010.03473.x); pmid: [20854395](https://pubmed.ncbi.nlm.nih.gov/20854395/)
26. M. D. M. Jones *et al.*, Discovery of novel intermediate forms redefines the fungal tree of life. *Nature* **474**, 200–203 (2011). doi: [10.1038/nature09984](https://doi.org/10.1038/nature09984); pmid: [21562490](https://pubmed.ncbi.nlm.nih.gov/21562490/)

27. C. L. Lauber, M. Hamady, R. Knight, N. Fierer, Pyrosequencing-based assessment of soil pH as a predictor of soil bacterial community structure at the continental scale. *Appl. Environ. Microbiol.* **75**, 5111–5120 (2009). doi: [10.1128/AEM.00335-09](https://doi.org/10.1128/AEM.00335-09); pmid: [19502440](https://pubmed.ncbi.nlm.nih.gov/19502440/)
28. M. S. Robeson *et al.*, Soil rotifer communities are extremely diverse globally but spatially autocorrelated locally. *Proc. Natl. Acad. Sci. U.S.A.* **108**, 4406–4410 (2011). doi: [10.1073/pnas.1012678108](https://doi.org/10.1073/pnas.1012678108); pmid: [21368117](https://pubmed.ncbi.nlm.nih.gov/21368117/)
29. A. Rosling *et al.*, Archaeorhizomycetes: Unearthing an ancient class of ubiquitous soil fungi. *Science* **333**, 876–879 (2011). doi: [10.1126/science.1206958](https://doi.org/10.1126/science.1206958); pmid: [21836015](https://pubmed.ncbi.nlm.nih.gov/21836015/)
30. S. Pålme *et al.*, Biogeography of ectomycorrhizal fungi associated with alders (*Alnus* spp.) in relation to biotic and abiotic variables at the global scale. *New Phytol.* **198**, 1239–1249 (2013). doi: [10.1111/nph.12170](https://doi.org/10.1111/nph.12170); pmid: [23421531](https://pubmed.ncbi.nlm.nih.gov/23421531/)
31. P. B. Reich *et al.*, Linking litter calcium, earthworms and soil properties: A common garden test with 14 tree species. *Ecol. Lett.* **8**, 811–818 (2005). doi: [10.1111/j.1461-0248.2005.00779.x](https://doi.org/10.1111/j.1461-0248.2005.00779.x)
32. A. E. Arnold, Understanding the diversity of foliar endophytic fungi: Progress, challenges, and frontiers. *Fungal Biol. Rev.* **21**, 51–66 (2007). doi: [10.1016/j.fbr.2007.05.003](https://doi.org/10.1016/j.fbr.2007.05.003)
33. M. L. Berbee, J. W. Taylor, Dating the molecular clock in fungi—How close are we? *Fungal Biol. Rev.* **24**, 1–16 (2010). doi: [10.1016/j.fbr.2010.03.001](https://doi.org/10.1016/j.fbr.2010.03.001)
34. K. K. Treseder *et al.*, Evolutionary histories of soil fungi are reflected in their large-scale biogeography. *Ecol. Lett.* **17**, 1086–1093 (2014). pmid: [24912000](https://pubmed.ncbi.nlm.nih.gov/24912000/)
35. G. S. Gilbert, C. O. Webb, Phylogenetic signal in plant pathogen-host range. *Proc. Natl. Acad. Sci. U.S.A.* **104**, 4979–4983 (2007). doi: [10.1073/pnas.0607968104](https://doi.org/10.1073/pnas.0607968104); pmid: [17360396](https://pubmed.ncbi.nlm.nih.gov/17360396/)
36. X. Liu *et al.*, Experimental evidence for a phylogenetic Janzen-Connell effect in a subtropical forest. *Ecol. Lett.* **15**, 111–118 (2012). doi: [10.1111/j.1461-0248.2011.01715.x](https://doi.org/10.1111/j.1461-0248.2011.01715.x); pmid: [22082078](https://pubmed.ncbi.nlm.nih.gov/22082078/)
37. R. Bagchi *et al.*, Pathogens and insect herbivores drive rainforest plant diversity and composition. *Nature* **506**, 85–88 (2014). doi: [10.1038/nature12911](https://doi.org/10.1038/nature12911); pmid: [24463522](https://pubmed.ncbi.nlm.nih.gov/24463522/)
38. M. Bahram, H. Harend, L. Tedersoo, Network perspectives of ectomycorrhizal associations. *Fungal Ecol.* **7**, 70–77 (2013). doi: [10.1016/j.funeco.2013.10.003](https://doi.org/10.1016/j.funeco.2013.10.003)
39. L. Tedersoo *et al.*, Towards global patterns in the diversity and community structure of ectomycorrhizal fungi. *Mol. Ecol.* **21**, 4160–4170 (2012). doi: [10.1111/j.1365-294X.2012.05602.x](https://doi.org/10.1111/j.1365-294X.2012.05602.x); pmid: [22568722](https://pubmed.ncbi.nlm.nih.gov/22568722/)
40. M. Bahram *et al.*, The distance decay of similarity in communities of ectomycorrhizal fungi in different ecosystems and scales. *J. Ecol.* **101**, 1335–1344 (2013). doi: [10.1111/1365-2745.12120](https://doi.org/10.1111/1365-2745.12120)
41. H. Qian, S. Chen, L. Mao, Z. Ouyang, Drivers of β -diversity along latitudinal gradients revisited. *Glob. Ecol. Biogeogr.* **22**, 659–670 (2013). doi: [10.1111/geb.12020](https://doi.org/10.1111/geb.12020)
42. H. Qian, Beta diversity in relation to dispersal ability for vascular plants in North America. *Glob. Ecol. Biogeogr.* **18**, 327–332 (2009). doi: [10.1111/j.1466-8238.2009.00450.x](https://doi.org/10.1111/j.1466-8238.2009.00450.x)
43. J. Geml *et al.*, An arctic community of symbiotic fungi assembled by long-distance dispersers: Phylogenetic diversity of ectomycorrhizal basidiomycetes in Svalbard based on soil and sporocarp DNA. *J. Biogeogr.* **39**, 74–88 (2012). doi: [10.1111/j.1365-2699.2011.02588.x](https://doi.org/10.1111/j.1365-2699.2011.02588.x)
44. I. Timling, D. A. Walker, C. Nusbaum, N. J. Lennon, D. L. Taylor, Rich and cold: Diversity, distribution and drivers of fungal communities in patterned-ground ecosystems of the North American Arctic. *Mol. Ecol.* **23**, 3258–3272 (2014). doi: [10.1111/mec.12743](https://doi.org/10.1111/mec.12743); pmid: [24689939](https://pubmed.ncbi.nlm.nih.gov/24689939/)
45. J. Rousk *et al.*, Soil bacterial and fungal communities across a pH gradient in an arable soil. *ISME J.* **4**, 1340–1351 (2010). doi: [10.1038/ismej.2010.58](https://doi.org/10.1038/ismej.2010.58); pmid: [20445636](https://pubmed.ncbi.nlm.nih.gov/20445636/)
46. M. D. Crisp *et al.*, Phylogenetic biome conservatism on a global scale. *Nature* **458**, 754–756 (2009). doi: [10.1038/nature07764](https://doi.org/10.1038/nature07764); pmid: [19219025](https://pubmed.ncbi.nlm.nih.gov/19219025/)
47. S. T. Bates *et al.*, Global biogeography of highly diverse protistan communities in soil. *ISME J.* **7**, 652–659 (2013). doi: [10.1038/ismej.2012.147](https://doi.org/10.1038/ismej.2012.147); pmid: [23235291](https://pubmed.ncbi.nlm.nih.gov/23235291/)
48. W. J. Sul, T. A. Oliver, H. W. Ducklow, L. A. Amaral-Zettler, M. L. Sogin, Marine bacteria exhibit a bipolar distribution. *Proc. Natl. Acad. Sci. U.S.A.* **110**, 2342–2347 (2013). doi: [10.1073/pnas.1212424110](https://doi.org/10.1073/pnas.1212424110); pmid: [23324742](https://pubmed.ncbi.nlm.nih.gov/23324742/)
49. H. Sato, R. Tsujino, K. Kurita, K. Yokoyama, K. Agata, Modelling the global distribution of fungal species: New insights into microbial cosmopolitanism. *Mol. Ecol.* **21**, 5599–5612 (2012). doi: [10.1111/mec.12053](https://doi.org/10.1111/mec.12053); pmid: [23062148](https://pubmed.ncbi.nlm.nih.gov/23062148/)
50. I. Sanmartín, F. Ronquist, Southern Hemisphere biogeography inferred by event-based models: Plant versus animal patterns. *Syst. Biol.* **53**, 216–243 (2004). doi: [10.1080/10635150490423430](https://doi.org/10.1080/10635150490423430); pmid: [15205050](https://pubmed.ncbi.nlm.nih.gov/15205050/)
51. S. Altizer, R. S. Ostfeld, P. T. Johnson, S. Kutz, C. D. Harvell, Climate change and infectious diseases: From evidence to a predictive framework. *Science* **341**, 514–519 (2013). doi: [10.1126/science.1239401](https://doi.org/10.1126/science.1239401); pmid: [23908230](https://pubmed.ncbi.nlm.nih.gov/23908230/)
52. W. H. Van der Putten, M. Macel, M. E. Visser, Predicting species distribution and abundance responses to climate change: Why it is essential to include biotic interactions across trophic levels. *Philos. Trans. R. Soc. B* **365**, 2025–2034 (2010). doi: [10.1098/rstb.2010.0037](https://doi.org/10.1098/rstb.2010.0037)
53. M.-L. Desprez-Loustau *et al.*, The fungal dimension of biological invasions. *Trends Ecol. Evol.* **22**, 472–480 (2007). doi: [10.1016/j.tree.2007.04.005](https://doi.org/10.1016/j.tree.2007.04.005); pmid: [17509727](https://pubmed.ncbi.nlm.nih.gov/17509727/)

ACKNOWLEDGMENTS

The sequence data and metadata are deposited in the Short Read Archive (accession SRP043706) and UNITE databases. Data used for analyses are available as supplementary materials, data files S1 and S2. We thank A. Corrales, H. Mann, D. Sveshnikov, F. O. P. Stefani, A. Voik, and Y. Wu for supplying single soil samples; R. Puusepp, M. Haugas, and M. Nõukas for sample preparation; H. Kreft for providing interpolated plant diversity data; S. Jüris for designing the printed figure; M. I. Bidartondo, K. G. Peay, and three anonymous reviewers for constructive comments on the manuscript; and relevant institutions of multiple countries for issuing permissions for sampling and delivery. The bulk of this project was funded from Estonian Science Foundation grants 9286, 171PUT, and IUT20-30; EMP265; Frontiers in Biodiversity Research; European Research Council; and in part by numerous funding sources that facilitated co-author efforts in collecting and preprocessing samples.

SUPPLEMENTARY MATERIALS

www.sciencemag.org/content/346/6213/1256688/suppl/DC1
Figs. S1 to S17
Tables S1 to S3
Data Files S1 and S2

29 May 2014; accepted 16 October 2014
10.1126/science.1256688

Conditional density-based analysis of T cell signaling in single-cell data

Smita Krishnaswamy, Matthew H. Spitzer, Michael Mingueneau, Sean C. Bendall, Oren Litvin, Erica Stone, Dana Pe'er,†* Garry P. Nolan†

INTRODUCTION: Cellular circuits sense the environment, process signals, and compute decisions using networks of interacting proteins. Emerging high-dimensional single-cell technologies such as mass cytometry can measure dozens of protein epitopes simultaneously in millions of individual cells. With thousands of individual cells, each providing a point of data on co-occurring protein states, it is possible to infer and quantify the functional forms of the relationships between proteins. However, in practice these underlying relationships are typically obscured by statistical limitations of the data, hence rendering the analysis and interpretation of single-cell data challenging. We developed computational methods, tailored to single-cell data,

to more completely define the function and strength of signaling relationships.

RATIONALE: We demonstrate the utility of our methods using single-cell data collected from T cells. Although T cell subpopulations are phenotypically delineated into several cell subsets—such as regulatory, effector, and memory—and are thought to have similarly wired signaling networks, their responses to activation differ in ways that are not understood.

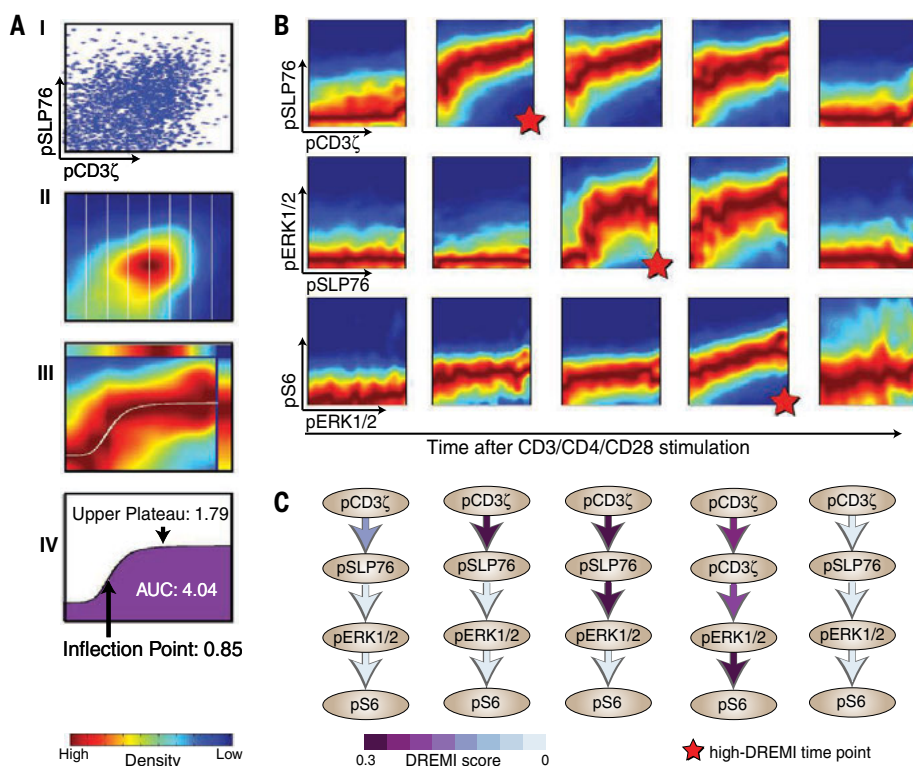
RESULTS: We used mass cytometry to measure the abundance of 20 internal and surface protein epitopes, at 13 time points, after two different types of T cell receptor (TCR) activation in T cells of B6 mice—resulting

in more than 2 million data points. To study TCR signaling, we developed conditional-Density Resampled Estimate of Mutual Information (DREMI) to quantify the strengths of the influence that a protein X has on protein Y, and conditional-Density Rescaled Visualization (DREVI) to visualize and characterize the edge-response function underlying their molecular interaction. A key conceptual shift in DREMI and DREVI is our use of the conditional probability of $Y|X$ rather than the joint probability of X and Y . We show that the consensus Y -response for each value of X is much easier to identify in the conditional density estimate, especially when the joint density is concentrated in a narrow range, which is typical of such data (Fig. 1A).

We used DREMI to characterize the rapid dynamics of signaling interactions upon TCR activation (Fig. 1B) and show that the strength of signal transfer peaks in canonical pathway order (Fig. 1C). We compared edges in naive and antigen-exposed $CD4^+$ T cells and identified differential signal transmission along a key signaling cascade that starts at $pCD3\zeta$ and continues through $pSLP76$, $pERK$, and $pS6$. At each stage in this cascade, more information (higher DREMI) is transferred downstream from one protein to another, over a longer time period, in naive cells than in antigen-exposed cells. We validated our characterization in mice lacking the extracellular-regulated mitogen-activated protein kinase (ERK2), demonstrating stronger influence of $pERK$ on $pS6$ in naive cells, as predicted.

CONCLUSION: DREMI solves a challenging problem: quantifying the strength of the underlying complex relationships between proteins from noisy data. Our approach reveals how signaling is fine-tuned between T cell subpopulations: The differences we identified between naïve and antigen-exposed T cells suggest that naïve cells more sensitively transmit upstream signaling inputs along a key signaling cascade. In contrast, trained effector or memory cells seem poised for fast responses upon repeated exposure.

DREVI and DREMI are broadly applicable across biological systems and single-cell technologies. As single-cell data become more abundant, our methods will enable the construction of quantitative models of cellular signaling and comparison between healthy and diseased cells. ■



Quantitative characterization of T cell signaling. (A) The $pCD3\zeta$ - $pSLP76$ signaling interaction shown as (I) a scatterplot, (II) a kernel density estimate, and (III) by using a conditional DREVI method. (IV) Shape features are extracted and quantified. (B) DREVI plots of a signaling cascade downstream of TCR show the time-varying nature of edge shapes and strengths. (C) Edge strengths are quantified by using conditional DREMI.

RESEARCH ARTICLE

SYSTEMS BIOLOGY

Conditional density-based analysis of T cell signaling in single-cell data

Smita Krishnaswamy,¹ Matthew H. Spitzer,² Michael Mingueneau,³ Sean C. Bendall,² Oren Litvin,¹ Erica Stone,⁴ Dana Pe'er,^{1*}† Garry P. Nolan^{2†}

Cellular circuits sense the environment, process signals, and compute decisions using networks of interacting proteins. To model such a system, the abundance of each activated protein species can be described as a stochastic function of the abundance of other proteins. High-dimensional single-cell technologies, such as mass cytometry, offer an opportunity to characterize signaling circuit-wide. However, the challenge of developing and applying computational approaches to interpret such complex data remains. Here, we developed computational methods, based on established statistical concepts, to characterize signaling network relationships by quantifying the strengths of network edges and deriving signaling response functions. In comparing signaling between naïve and antigen-exposed CD4⁺ T lymphocytes, we find that although these two cell subtypes had similarly wired networks, naïve cells transmitted more information along a key signaling cascade than did antigen-exposed cells. We validated our characterization on mice lacking the extracellular-regulated mitogen-activated protein kinase (MAPK) ERK2, which showed stronger influence of pERK on pS6 (phosphorylated-ribosomal protein S6), in naïve cells as compared with antigen-exposed cells, as predicted. We demonstrate that by using cell-to-cell variation inherent in single-cell data, we can derive response functions underlying molecular circuits and drive the understanding of how cells process signals.

Cells process external cues through the biological circuitry of signaling networks in which each protein species processes information pertaining to other proteins, whose activities themselves are determined by biochemical modifications (such as phosphorylation) or other allosteric interactions. Signaling networks can be remarkably attuned to distinguishing subtle features of stimuli to enable key decisions regarding cellular response or fate. For example, naïve CD4⁺ T cells take into account both dose and duration of T cell receptor (TCR) engagement, the strength of peptide binding in the major histocompatibility complex (MHC) cleft, and coreceptor cues in making a decision to differentiate into either regulatory or T helper cells (1–4). With this example as one among many, it follows then that to properly understand normal cellular responses and how these are dysregulated in disease, robust quantitative characterizations of signaling relationships will be required to enable more accurate models of signaling.

Despite progress in the quest to understand and represent the complexities of signaling biology, graph diagrams typically used as depictions of signaling relationships only offer qualitative abstractions. In such graphs, the vertices correspond to proteins, and a directional edge indicates the influence of one protein or molecular species on another, and as such, these graphs fail to capture many of the more complex ways through which signaling networks process information. Further, such representations are not designed to readily enable predictions of response to stimuli or therapeutic intervention. Although quantitative models have been proposed to describe signaling networks (3, 5, 6), these are specific to each system and require measurements of biochemical rates and many additional parameters. To scale to a large number of signaling networks and cell types, a robust data-driven approach that can quantify signaling interactions in molecular circuits is required. A data-driven approach would take advantage of statistically relevant differences in complex cell populations so as to better inform the function that is encoded by an inferred circuit diagram.

To this end, single-cell measurement technologies can offer quantitatively precise, even absolute (given appropriate probes and experimental design), measures of dozens of cellular components representing important biochemical functions. Variation in a complex cell population can be discerned in a functionally relevant context and enable insights into the underlying relation-

ships between signaling molecules. Mass cytometry, for example, can assay the abundance of dozens of internal and surface protein epitopes simultaneously in millions of individual cells (7, 8), offering an opportunity to quantitatively characterize signaling at circuit-wide scales. Modeling a signaling network as a computational system, in which each signaling protein computes a stochastic function of other proteins, and treating each single cell as an example of possible input-output enables the recovery of how a signaling network functions. With many thousands of individual cells, each providing a point of data about relationships between proteins, we can infer the network function.

However, a major challenge in deciphering single-cell signaling data are developing computational methods that can handle the complexity, noise (which can be either natural stochasticity or actual instrument noise), and bias in the measurements. First, because cell populations are rarely homogeneous, different cell subpopulations can manifest distinct behaviors—and therefore, the relationships between signaling proteins may be obscured beneath a mixture of multiple network states. For example, naïve primary B cells can have weak and stochastic responses to stimuli so that only a small fraction of the population responds (via activation of signaling pathways), whereas memory B cells are considered primed and even evolved toward a more avid binding of antigen. Similarly, naïve T cells manifest different kinetics of response to T cell receptor engagement than do effector T cells. Second, technical noise in the measurements can further confound the quantification of molecular interactions. Third, marker abundance (which often correlates with cell size) can lead to biased correlations and hence be misinterpreted as an influence between the assayed signaling proteins.

We addressed these challenges by developing an algorithm, based on the statistical concepts of conditional probability (9) and density estimation (10), termed “conditional-Density Resampled Estimate of Mutual Information” (DREMI) to quantify the strength of molecular interactions. Given a relationship between two proteins, where X influences Y , DREMI considers the abundance or activity of protein Y as a stochastic function of the abundance or activity of protein X . DREMI uses the variation in a population of individually measured single cells to quantify the amount of information transmitted from protein X to protein Y in the signaling network.

A key conceptual shift compared with previous approaches to single-cell analysis is that DREMI computes mutual information on the estimated “conditional probability” of $Y | X$ rather than the “joint probability” of X and Y (the latter being the preferred approach in most other mutual information-based metrics). Joint probability describes the density of cell states (such as in a traditional scatter or density plot), whereas conditional probability describes how the state of Y varies with different states of X . To explore such relationships, we couple DREMI to an algorithm we term “conditional-Density Rescaled

¹Department of Biological Sciences, Department of Systems Biology, Columbia University, New York, NY, USA. ²Baxter Laboratory in Stem Cell Biology, Department of Microbiology and Immunology, Stanford University, Stanford, CA, USA.

³Division of Immunology, Department of Microbiology and Immunobiology, Harvard Medical School, Boston, MA, USA.

⁴Molecular Biology Section, Division of Biological Sciences, Department of Cellular and Molecular Medicine, University of California San Diego, La Jolla, CA, USA.

*Corresponding author. E-mail: dpeer@biology.columbia.edu

†These authors contributed equally to this work.

LAT [the adaptor protein SH2 domain containing leukocyte protein and Linker of activated T cells, respectively (19)].

When the relation between pCD3 ζ and pSLP76 prestimulation and 30 s after stimulation (Fig. 1A) is visualized as a scatterplot (a traditional means used to analyze flow cytometry data), it is difficult to identify any clear characteristics of the data other than the range of expression values. Visualizing the data by using a density plot (Fig. 1B) (10), one observes that the abundance of pCD3 ζ and pSLP76 is concentrated at a particular value, but there is no clear statistical dependency between the two molecules, nor does this visualization method illuminate the nature of the well-researched influence that pCD3 ζ has on pSLP76 (20).

Why do traditional methods of visualizing data, such as scatterplots or density estimations, fail to reveal clear relationships between molecules? In Fig. 1, the majority of cells can be found in a narrow range of values for each marker. Therefore, the joint density of pCD3 ζ and pSLP76 is dominated by a narrow set of values and does not reveal the overall “functional response”—how

protein Y changes as a function of the activity of protein X . To understand Y as a function of X , we have to explore X 's full dynamic range and how values of Y are dependent on values of X .

To visualize and characterize signal transfer between proteins X and Y , we developed DREVI (Fig. 1, Box 1, and materials and methods), which represents in a visual form the stochastic function of how X influences Y . By using the natural variation in the amount of X and Y from cell to cell, we empirically learn the probability density $P(X,Y)$ from the data. To characterize the influence that X extends on Y , we shift from the joint density and empirically estimate the conditional density $P(Y|X)$ (materials and methods) by means of a kernel density estimation method based on heat diffusion (10, 21). The conditional density enables us to ascertain how Y 's values are changing with respect to the values of X , regardless of where the majority of cells are concentrated in the joint distribution. Although statisticians have previously developed sophisticated methods to directly compute the conditional density (22), these perform poorly on our data (fig. S3).

Box 1. Conditional density-rescaled visualization.

DREVI reveals the influence of protein X on protein Y . Most methods for visualizing pairwise data (such as scatterplots and density contours) depict the joint probability of X and Y . In contrast, we reveal signaling behavior along its full dynamic range by visualizing conditional probability. The main steps of DREVI are as follows:

- (i) Compute the joint kernel density estimate $\hat{f}(x,y)$ (10).
- (ii) Compute the marginal density of X , $\hat{f}(x)$, and the conditional density estimate of Y given X as $\hat{f}(y|x) = \frac{\hat{f}(y,x)}{\hat{f}(x)}$ on a fine grid of points $G = \{(x_i, y_j), 1 < i < n, 1 < j < m\}$ that span the range of X and Y (2, 12, 15).
- (iii) Rescale each value of the conditional density estimate by its column-maximum to obtain $\hat{f}^*(y_j|x_i) = \hat{f}(y_j|x_i) / \max_k [\hat{f}(y_k|x_i)]$
- (iv) Visualize $\hat{f}^*(G)$ as a heatmap, adding side-bars depicting the marginal densities of X and Y .

Box 2. Conditional density-resampled estimate of mutual information.

DREMI provides a score for the strength of the influence protein X has on protein Y . In many physiological conditions, only a small fraction of the cells have activated protein X in response to stimuli, and these active populations have little influence on the mutual information metric. DREMI explicitly factors these populations by computing a score based on the conditional distribution of $Y | X$ rather than joint distribution. DREMI estimates the computation I^c , given by $I^c(x,y) = \sum_x \sum_y p(y|x) \log \left[\frac{p(y|x)p(x)}{p(y)} \right]$

DREMI is computed as follows:

- (i) Begin with the rescaled conditional-density estimate $\hat{f}^*(G)$ as in DREVI (Box 1), computed on the grid of points $G = \{(x_i, y_j), 1 < i < n, 1 < j < m\}$.
- (ii) Round values $\hat{f}^*(x_i, y_j) < \epsilon$ to 0, for user-defined threshold ϵ , to eliminate technical noise from the measurements.
- (iii) Resample from G according to the conditional density estimate $\hat{f}(G)$.
- (iv) Equipartition the full range of the data and calculate mutual information, using this partition as the discretization.

DREVI plots are shown in Fig. 1C that depict pSLP76 abundance (Y) when conditioned on pCD3 ζ (X) abundance. This view of the data reveals a distinct difference in the relation between pCD3 ζ and pSLP76 before and after TCR activation that was not apparent in the scatterplots or joint distribution. Given an equal amount of pCD3 ζ , we observe that pSLP76 has a stronger response to increasing pCD3 ζ levels after TCR activation (in Fig. 1C, the increased values of the median response are represented by the white line). This suggests that after TCR activation, additional factors (perhaps ZAP70 or LAT) modulate the relationship between pCD3 ζ and pSLP76. Similarly, DREVI can help clarify the relationship between additional protein pairs (fig. S4) and visualize how the relationships change through time (fig. S5).

Conditional density-resampled estimate of mutual information

To systematically compare between conditions, time points, and cell types, a measure that quantifies the relationship between two proteins is needed. Often, mutual information (MI)-based metrics are used to evaluate relationships between gene or protein pairs. However, MI is difficult to compute on continuous data. To resolve this, a first step is to discretize the data. Currently, adaptive partitioning (23) is one of the most widely used approaches for such discretization (24, 25). However, adaptive partitioning assumes that denser regions of the data are more important than sparser regions, and therefore, the dense regions are partitioned more finely than are sparse regions and dominate the resultant mutual-information metric. In contrast, we developed a measure that allows for sparser populations to be accounted for, thus preventing bias against small cell populations that could have distinct and interesting biology that might inform understanding of the signaling relations in question.

To quantify the strength of the influence protein X has on protein Y , we developed DREMI (Box 2, Fig. 2, and materials and methods). Like MI (26), DREMI is a shape-agnostic measure that scores how predictive X is of Y , but—unlike MI—it is not symmetric (and therefore might inform directionality) and also captures the strength of this relationship over all populated regions of the dynamic range, regardless of the (often peaked) distribution of X in the data. This is achieved by computing mutual information on the conditional density estimate of the data rather than the raw data itself. DREMI begins with the conditional density estimate, computed for DREVI (Box 1). The data are then resampled evenly through the range of the conditional probability density, and MI is computed on the resampled data spanning the entire range.

To understand the differences between MI and DREMI, we use the data from Fig. 1. MI works well for data that is well distributed across the range of X and Y (Fig. 2A, for example); by equipartitioning slices of X , the range of Y drastically drops within each slice, and therefore, knowing the value of X provides substantial

information on the likely value of Y . However, in distributions typical of single-cell data (Fig. 2B), MI is dominated by a peak in density (a narrow range of X) in which only minor changes in Y are observed; thus, the relationship between X and Y is obscured. In contrast, DREMI (Fig. 2C) resamples from the conditional density estimate and equally weighs all regions along the entire range of X , as long as there are enough cells to form a robust conditional density estimate. Thus, DREMI takes into account sparse populations along the x axis and factors for the full range.

DREMI takes advantage of mass cytometry's ability to collect large sample sizes (data for millions of cells), facilitating the estimation of the conditional distribution in relatively sparse regions. For example, with 50,000 cells, an X range with only 1% of the data (typically treated as an outlier) still contains 500 cells, a sufficient number to robustly estimate $P(Y | X = x)$. To further ensure a robust estimation of $P(Y | X = x)$, DREMI incorporates an automated noise-filtering step in which points are eliminated if they have a low rescaled conditional density.

We evaluated the robustness of DREMI to noise (fig. S6) and subsampling (fig. S7). As shown in fig. S6, DREMI values generally decrease linearly as the SD of the noise increases, and the noise-elimination step can be used to adjust signal detection in noisy experimental conditions. A key strength of DREMI is that it is similarly resilient to noise, whether the underlying function is linear or sigmoid, making it well suited to capture the range of behaviors observed in biology. Further, DREMI is a robust measure that remains consistent under multiple subsamples of the data (fig. S7).

Characterization of signaling relations by curve-fitting

In the case of a strong relationship (high DREMI score), we can derive a “response function” from the conditional density using curve-fitting. Conditional density is particularly suited for the derivation of an edge response function because it allows for identification of the consensus Y response (densest region in DREVI; the deep red in the heat maps) for each value of X . We compare curve-fitting of the conditional density with directly fitting the raw data in order to demonstrate the superiority of the former—both in terms of fit [root mean squared error (RMSE)] and in terms of the interpretability of the parameters (fig. S8). For a well-fit curve, we expect most of the data points to fall in close proximity to this curve, as measured with RMSE. A fit to the conditional mean results in a sigmoidal curve that closely follows the data points (indicated by low RMSE), whereas the raw data best fits a line—but the fit is of lower quality (indicated by high RMSE). An optimal sigmoidal fit on the raw data results in degenerate curves, in which most data points reside at a large distance.

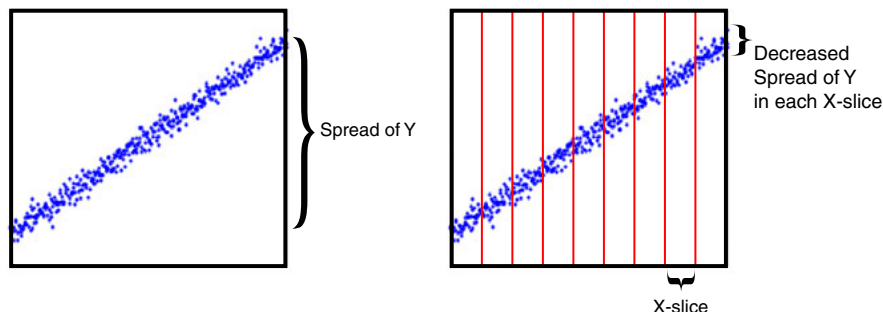
Fitting a curve in this manner allows for a parametric description of the relationship between the two proteins X and Y . Such a functional description of the relationship between X

and Y enables us to potentially predict the value of Y , if the value of X is altered by an intervention or drug. To derive the edge-response function, we fit points sampled from the conditional density to one of three models using regularized regression: linear, sigmoidal, or double sigmoidal (27). If none of the models result in a good fit, the model is then fit to a free-form curve.

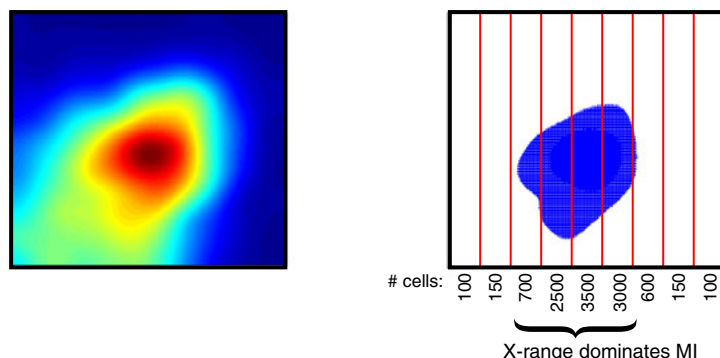
In Fig. 1, we fit DREVI plots of the pCD3 ζ -pSLP76 edge before and after TCR activation to a sigmoid curve (Fig. 1D, I and II). Among other characteristics, the parameters of the fitted sig-

moid specify the lower and upper asymptote that correspond to a digital “low” and “high” mode of activation for the protein Y , and the inflection point (the activation threshold of X at which the protein Y transitions from low to high state). Comparing the edge before TCR activation with after, there is a similar inflection point activation threshold in the pCD3 ζ axis but a considerably higher response on the SLP76 axis, and a corresponding increase in total activation of SLP76 (Fig. 1D). The postactivation state results in higher “area under the curve” (AUC),

A Mutual information measures the decrease in uncertainty of Y given X



B The high local joint density biases mutual information assessment



C DREMI resamples Y from conditional density in each X -slice to reveal relationship between X and Y

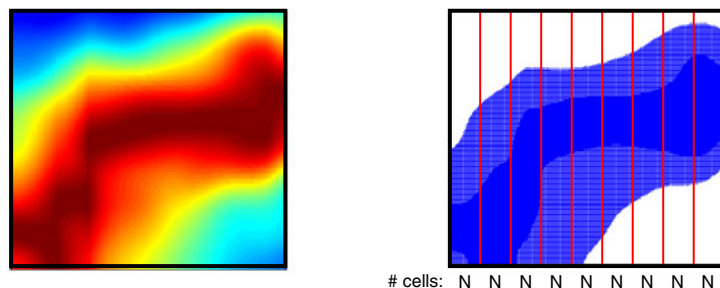


Fig. 2. Outline of the DREMI method. (A) Simulated data depicting a relationship with high MI. Across the entire range of X , Y has a wide range of values (left). After conditioning on X (red lines), the range of Y within each X -slice is substantially smaller (right). Thus, knowledge of X 's value provides information on Y 's likely value. (B) The data represent the relationship between pCD3 ζ and pSLP76 30 s after stimulation of the TCR, as in Fig. 1B, II. Most of the cells are concentrated around a single peak, as shown in the 2D density estimate (left). If we resample from this density estimate, samples will fall within a narrow range in which there is little change in Y 's range. This narrow range dominates the MI metric. (C) Instead, DREMI samples from the renormalized conditional density estimate, which covers entire X -range. So there is the same number of cells in each X -slice, as long as there are sufficient cells in the original data. MI information is calculated over this resampled data.

which is proportional to the average amount of pSLP76 generated per quantity of pCD3 ζ . A larger AUC implies more signal transfer activity so that after stimulation, less pCD3 ζ is required to induce a response in pSLP76. Thus, when the TCR is activated, not only do pCD3 ζ amounts increase, but this change is also more impactful than a similar increase would have been before stimulation. This increase in edge strength indicates that the pairwise relation between the two proteins is boosted by changes in the recruitment and localization of additional and potentially unknown proteins (the effects of which are successfully captured with DREVI and DREMI).

Not only do the DREMI and AUC scores increase after T cell stimulation, but they also enable distinguishing between different strengths and forms of stimulus (Fig. 3). Mouse T cells were stimulated with either CD3/CD28 or CD3/CD28/CD4, and mass cytometry analysis was undertaken as per above. CD4-costimulus, in addition to CD3/CD28, is known to boost signaling responses in CD4 $^{+}$ T cells by engaging additional pathways that reinforce the signal transmission

(28). When comparing these two forms of stimuli, we derive a higher DREMI score under the stronger stimulus in all three of the edges shown in Fig. 3. The CD3/CD28/CD4 stimulus clearly leads to a higher activation (magnitude) and/or a lower activation threshold in the edge-response functions. This translates to a higher AUC in both the sigmoidal (pCD3 ζ -pSLP76) (Fig. 3A, IV) and linear (pERK-pS6) (Fig. 3C, IV) cases. The pSLP76-pERK edge (Fig. 3B) can be interpreted as a stochastic “digital” response, with a larger percentage of cells responding upon CD3/CD28/CD4 stimulus (Fig. 3B, IV) (5). Together, DREMI, DREVI, and the edge-response function form a powerful toolbox for the analysis of signaling interactions.

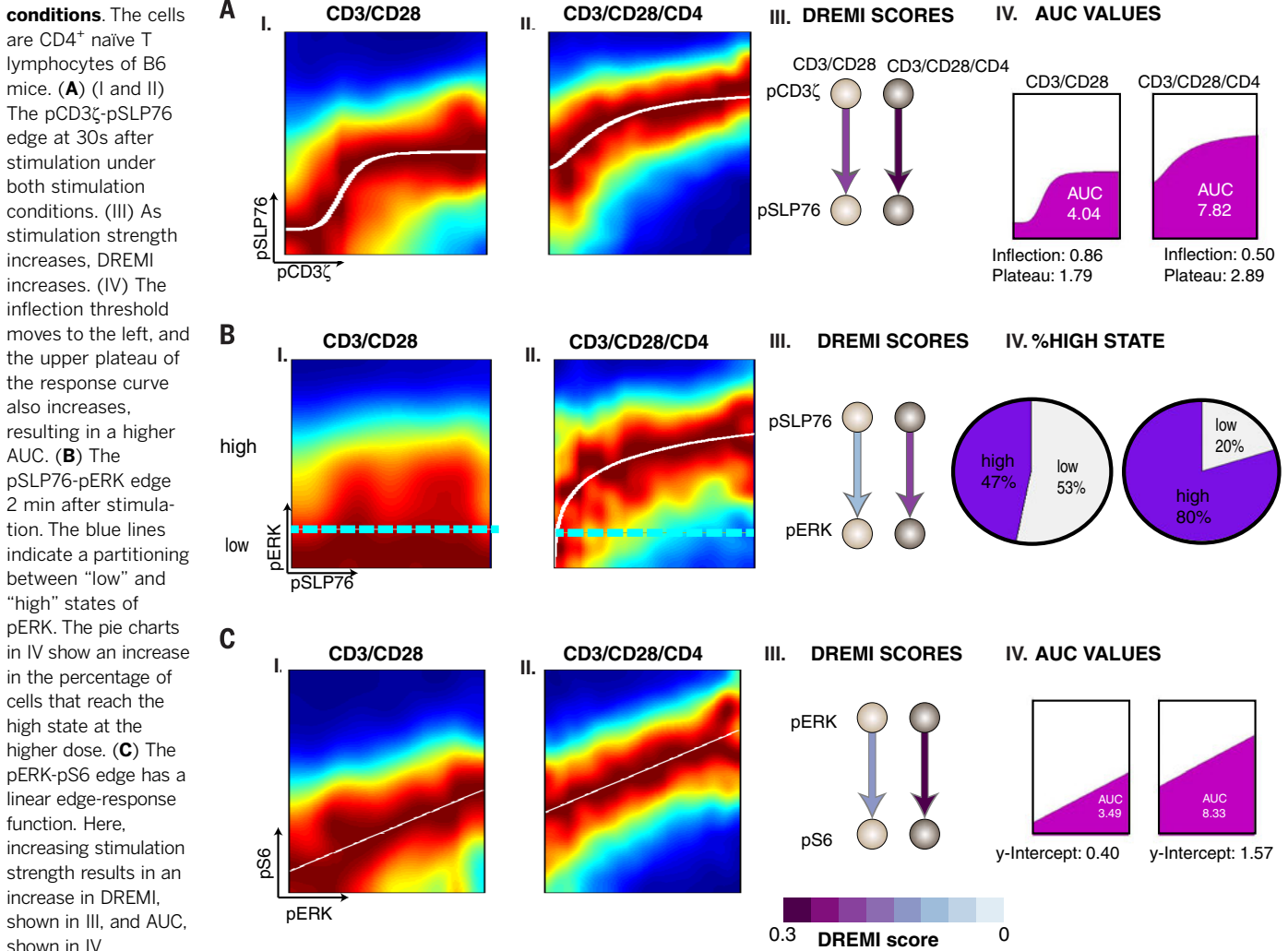
Canonically ordered signaling transfer in the TCR pathway

We used DREMI to analyze the dynamics of the pCD3 ζ -pSLP76-pERK-pS6 signaling cascade downstream of the TCR (Fig. 4). The edge strengths and shapes were highly dynamic within just a few minutes after TCR activation. The DREMI scores

pinpoint the “peak timing” of signal transduction, meaning the timing when protein activation of *Y* is most sensitive to changes in the activity of protein *X*. The peak timings of all edges in this signaling cascade followed the expected canonical order (Fig. 4). For example, a pCD3 ζ and pSLP76 relationship, or edge, was detectable in a small population of cells when pCD3 ζ is at its highest value even before stimulation (Fig. 4, top left). However, after TCR activation, pCD3 ζ reached maximum signal transfer within 30 s and decreased soon after. The pSLP76-pERK edge scored highest at 1 min after activation, and the pERK-pS6 edge peaked at 2 min after TCR activation. Thus, the peak response follows the canonical ordering of the pathway in a manner analogous to the “just-in-time” transcriptional networks of metabolic pathways in Zaslaver *et al.* (29).

The observed dynamics highlight the importance of time series data and the impact of signaling dynamics on the relationships that can be derived from each individual time point. For instance, the pSLP76-pERK edge (Fig. 4A) is only active in the 1- to 2-min time frame with a strong

Fig. 3. Comparison between stimulation conditions.



sigmoidal shape. The pSLP76-pERK edge is flat at other times. Such signaling dynamics are suggestive of the observed negative feedback loop, resulting in dephosphorylation of ERK perhaps by PTPN22 or SHP-1 (30, 31) because the influence of pSLP76 on pERK drastically decreased at 4 min, although pSLP76 remained activated at the 4-min time point (Fig. 4A, top row, fifth from left). The DREMI scores quantify the intuitive visual interpretation of the DREVI plots (Fig. 4B).

This canonical pathway ordering of peak timing is demonstrated again under the CD3/CD28 stimulation (fig. S9). However, we see that under the CD3/CD28/CD4 stimulation, signals are transferred downstream faster, and the signal transfer is sustained for longer periods. For example, the pCD3 ζ -pSLP76 edge is only activated up until 2 min under CD3/CD28 stimulation, whereas it remains active until 4 min under a CD3/CD28/CD4 stimulatory environment. Additionally, the pSLP76-pERK edge activates only after 2 min under the CD3/CD28 stimulation but is activated within 1 min under CD3/CD28/CD4 stimulation. This is in accordance with upstream influences that change the nature and speed of the signaling behavior downstream as reflected in the edges more distal to the TCR. This increased activation possibly is due to additional signaling pathways that converge through other signaling network components downstream of the TCR.

DREMI quantified the strength of each known edge in a given network, and the dynamics of how the molecular interactions underlying this edge changed over time. Together, they enabled an elucidation of a classically understood pathway in a single experiment while providing subtle insights into the timing of signaling relationships within the network.

Performance evaluation of DREMI

To compare the performance of DREMI with other approaches that quantify relations typically used for this data type, we used the canonical timing of signaling edges described in the previous section as a basis for comparison. We compared these metrics on six edges to evaluate the ability of each method to rank edge strengths at various time points after TCR stimulation. DREMI outperformed Pearson correlation and recently developed dependency measures such as maximal information coefficient (MIC) (32) and adaptively partitioned MI (Fig. 5I and fig. S10) (23). DREMI identified the peak timing of signal transfer in all six test cases. Adaptive partitioning missed the peak timing in four of the six cases, including two cases in which adaptive partitioning picked the prestimulation time as the peak, and typically does not perform well when the joint density is concentrated in a narrow range. In such cases, adaptive partitioning places many partitions in the dense region (so that the partitions are often finer than the sensitivity of the experimental technology) and only a few in the sparse regions. MIC tends to pick peaks similarly to adaptive partitioning, identifying the correct peak in only one case. MIC has a further limitation in that there is very

little range in the scores, possibly because it aims for equitability (33), which is a condition that does not hold in these data. Pearson correlation missed the peak timing in two cases and typically did not perform well for noisy and nonlinear relationships. We also compared the performance of DREMI in an additional biological system using published mass-cytometry data focused on human B cells after B cell receptor stimulation, as described in (8). Similar to T cell signaling, DREMI was able to quantify and rank relationships better than metrics typically used for such data (fig. S11).

Last, we compared DREMI with other approaches on synthetic data that was designed to exemplify features of realistic data (Fig. 5II). We

compared two weak, low-noise linear relationships against two strong, nonlinear noisy relationships. Specifically, we included a sigmoidal relationship and a nonmonotonic quadratic function typical of systems that simultaneously induce both protagonist and antagonistic pathways (34). The weak relationships were characterized by only slight changes in the distribution of Y compared with its dynamic range, as X increases (small slope), whereas the stronger nonlinear relationships have more pronounced change in the distribution of Y with changes in X . In both examples, the other methods scored the weaker linear relationship higher (Fig. 5II).

A key advantage of single-cell technologies such as mass cytometry and flow cytometry are

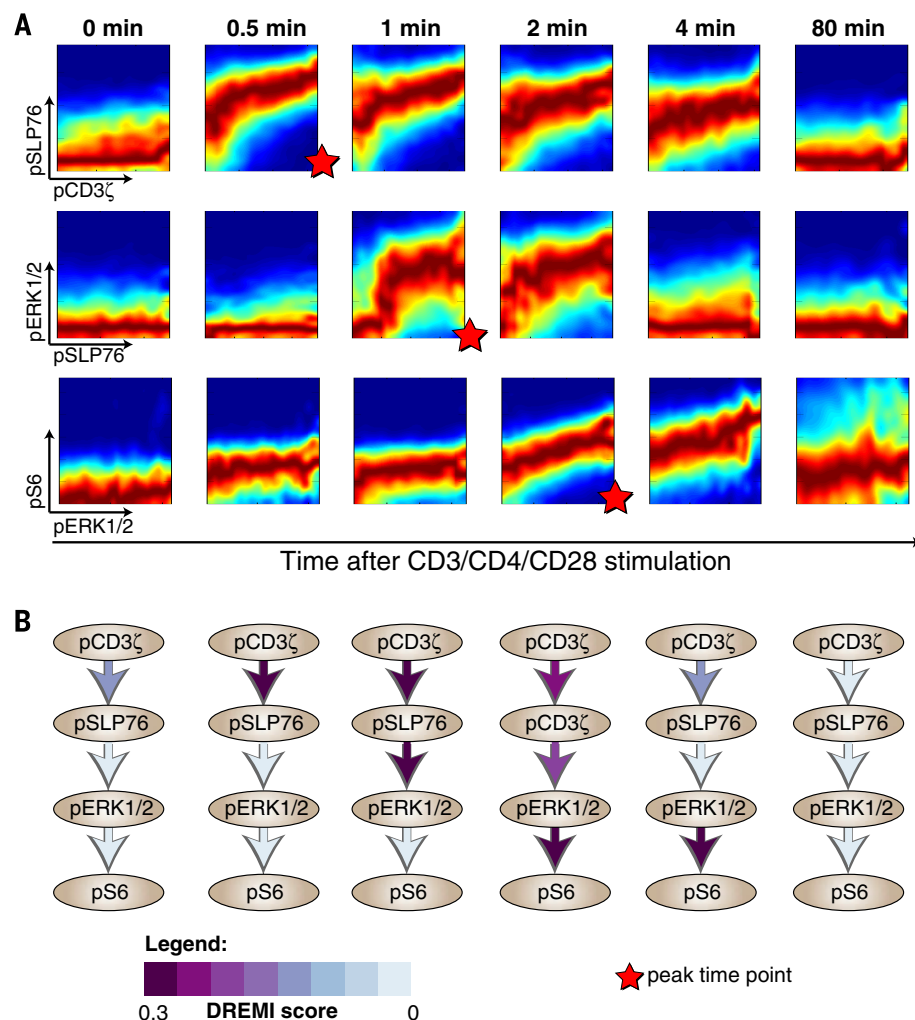
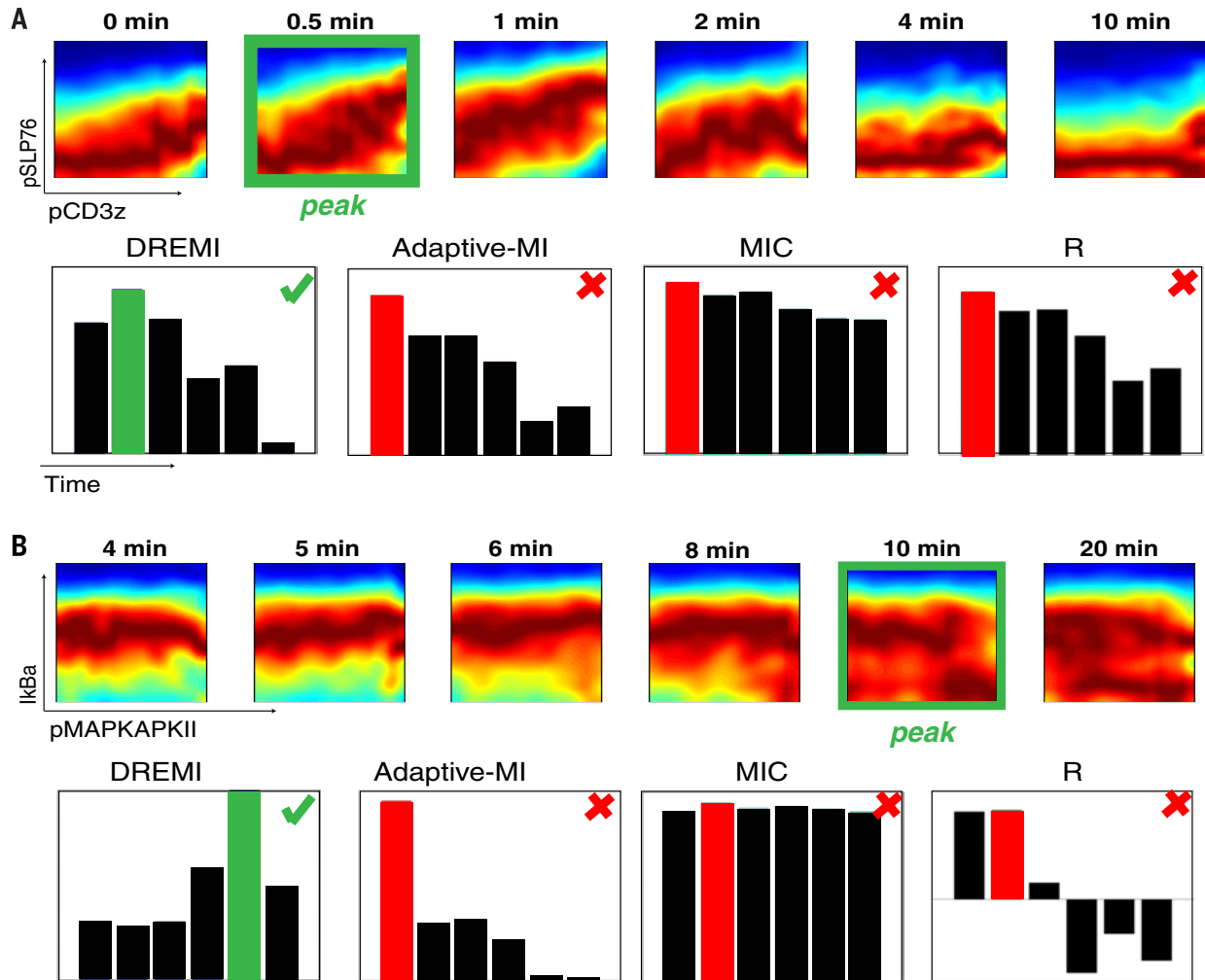


Fig. 4. DREVI and DREMI reveal the dynamics of TCR signaling. The pCD3 ζ -pSLP76-pERK-pS6 cascade at various time points after TCR activation. All panels represent data from CD4⁺ naive T lymphocytes from B6 mice with CD3, CD28, and CD4 cross-linking. **(A)** Each row represents an edge in the cascade, and each column represents a time point after TCR activation. DREVI plots show the dynamics of TCR signaling; edges change their strength and shape as signaling proceeds. The scale used is the same as in Fig. 1, with dark red representing the behavior of the majority of cells, whereas the other colors depict the heterogeneity and spread of the response. **(B)** Network diagrams with DREMI values indicated on each edge, columns matching the same time points as in (A). For each edge, the color indicates the computed DREMI values, with darker purple indicating a higher DREMI score. DREMI captures peak signal transfer timings in each of the three edges.

I. Comparison on mass cytometry Tcell data



II. Comparison on synthetic data

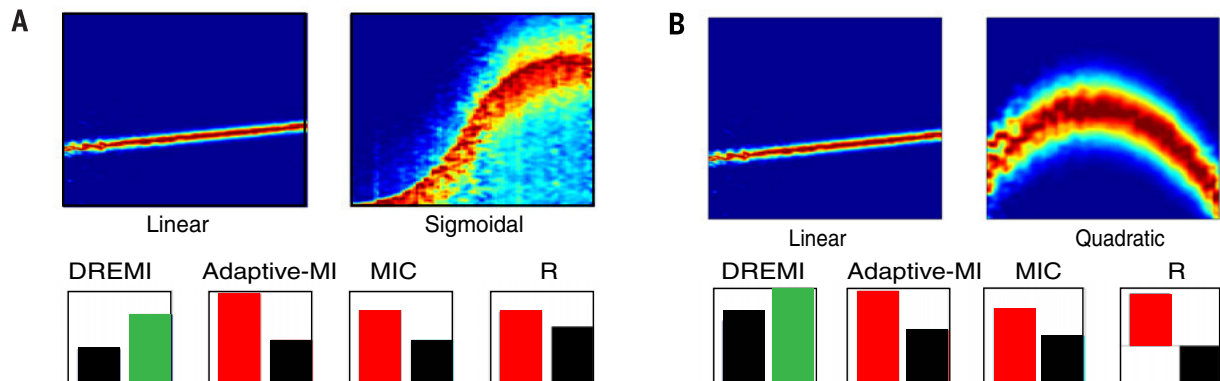


Fig. 5. Comparison of DREMI with three other metrics. The metrics compared are mutual information using adaptive partitioning (23), MIC (32), and Pearson correlation. (I) Comparisons are performed on edges in naïve CD4⁺ T cells under CD3 and CD28 stimulation. In each case, the green outline indicates the point with the strongest relationship upon visual inspection of the DREMI plot. (A) The pCD3z-pSLP76 edge. Only DREMI identifies the poststimulation 0.5 min time point as having a stronger signaling relationship than the prestimulation data. (B) The pMAPKAPKII-IkBa relationship as an example of a negative relationship.

relationship. DREMI successfully identifies this negative relationship, whereas other methods are unable to detect it. Four additional edges are compared in fig S10. (II) Comparison of dependency metrics on synthetic data. Both parts (A) and (B) show comparisons between a noiseless but weak dependence of Y on X, compared with a noisy but strong dependence of Y on X. (A) sigmoidal and (B) quadratic relationships. The other three metrics score the linear, weaker dependence higher than the noisier but stronger dependence. Because single-cell signaling data are often noisy and nonlinear, DREMI is better suited.

the provision of millions of data points in each experiment. Therefore, the scalability of the analysis is imperative to effectively analyze such data. DREMI is faster and more scalable than either MIC or adaptive partitioning (fig. S12). On a data set with 500,000 cells, DREMI analysis can be computed within 10 s. MI with adaptive partitioning takes over 90 min to perform the same computation, and MIC is limited to data

sets of less than 10,000 cells. Thus, DREMI is a versatile metric that can handle a variety of characteristics, including large sample size, non-linearity, and different degrees of stochasticity.

Unlike the other metrics, DREMI is a directional metric; $\text{DREMI}(X, Y)$ is not necessarily equal to $\text{DREMI}(Y, X)$ (fig. S13). We based our analysis on the known network diagram and scored DREMI in the causal direction of influ-

ence. Evaluating DREMI in the reverse direction shows a slight degradation of performance compared with DREMI in the correct direction (figs. S10, S11, and S14). However, reverse DREMI outperforms the three symmetric measures used in our comparison and has the advantage that it can handle nonlinearity and noise (fig. S14). The correct causal direction scores approximately equal or higher in three of the four edges explored at

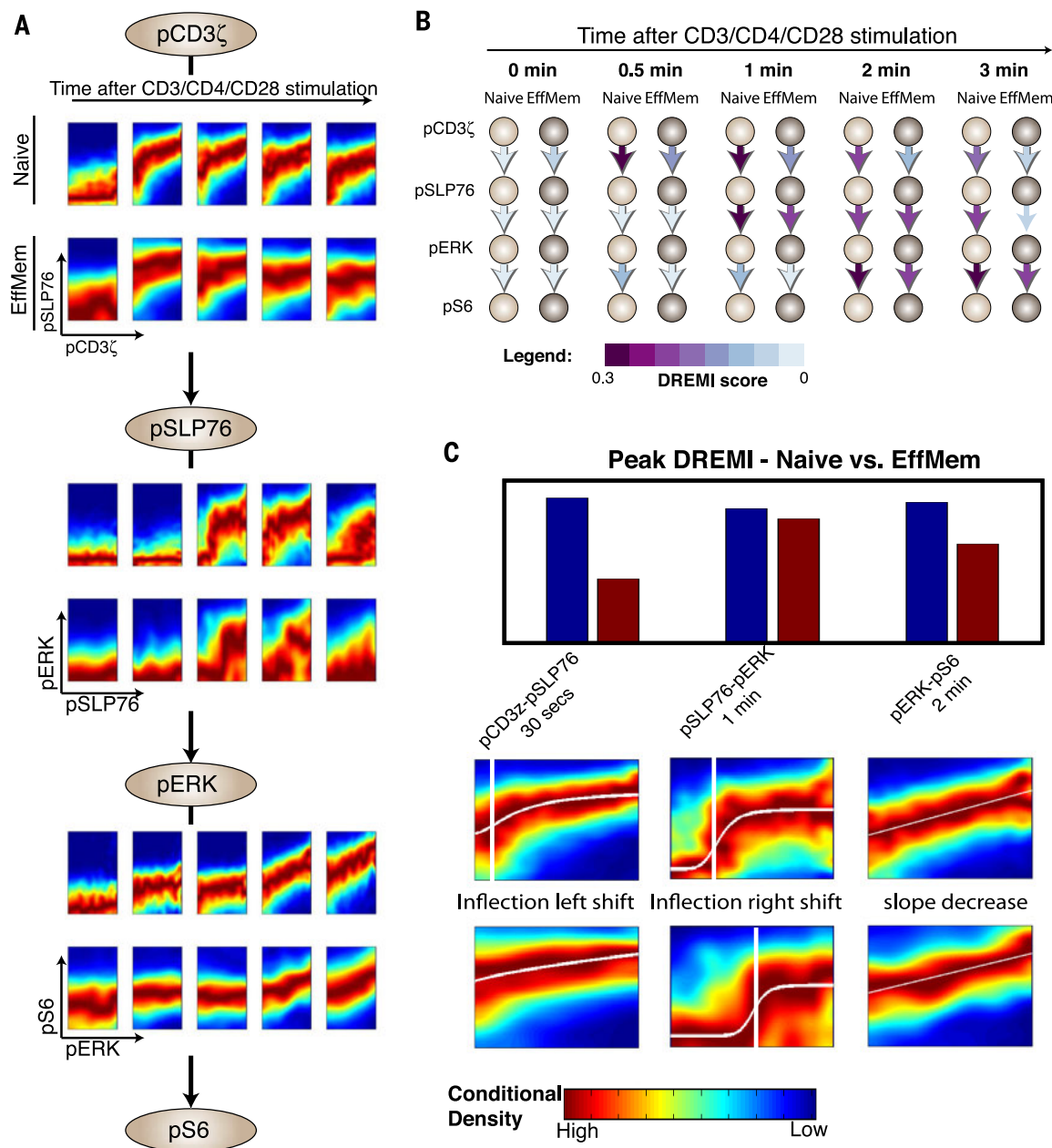


Fig. 6. Comparison of naïve with antigen-exposed T cells. Data from CD4⁺ naïve (CD44^{low}) and effector or memory (antigen-exposed, CD44^{high}) T lymphocytes from B6 mice with CD3, CD28, and CD4 cross-linking. **(A and B)** We compare the pCD3 ζ -pSLP76-pERK-pS6 cascade between the naïve and effector or memory CD4⁺ T cells using (A) DREVI and (B) DREMI. The time points in (A) match the indicated time points in (B). Both depictions show that signal transmission is sharper and more sustained in naïve cells. **(C)** Bar graph depicts the higher peak-DREMI detected in naïve cells; DREVI plots with edge

response functions show alterations in edge behavior during peak signaling. The pCD3 ζ -pSLP76 edge response function shows an earlier inflection point in effector or memory cells and is relatively flat after induction. This suggests only a small amount of pCD3 ζ is needed to initiate a complete response. In contrast, pSLP76 needs more pCD3 ζ for a similar response in naïve cells. The pSLP76-pERK edge indicates that the pERK response is weaker and requires more pSLP76 in these cells. Last, the pERK-pS6 edge shows a steeper slope in naïve cells, indicating that pS6 responds more strongly to pERK levels in naïve cells.

peak signaling times (fig. S13). The exception was pERK-pS6, where pS6 is known to have many additional factors influencing its activity, a recurring situation in cases in which DREMI in the reverse-causal direction scores higher. We show that increasing the number of parents decreases the DREMI in the causal direction more than in the reverse direction both in linear and non-linear functions (fig. S15).

Comparison of signaling interactions between T cell subtypes

The high dimensionality of mass cytometry enabled us to simultaneously treat and measure multiple T cell subsets, including both naïve and antigen-exposed CD4⁺ T cells. It is well documented that naïve T cells behave differently than cells that have previously seen and “remember” antigen. In naïve CD4⁺ T cells, the activation of the TCR and appropriate coreceptors under the right cytokine environment leads to differentiation toward different effector cell fates (17). In response to the same TCR activation, antigen-experienced effector or memory T cells proliferate and respond to the infection (12–14). Moreover, the activation response time is known to be faster and of greater magnitude in effector T cells than in naïve T cells. However, the signaling mechanisms that create these differ-

ences are not yet clear. The data set collected here enabled direct comparison of signaling responses in T cells before and after exposure to antigen because the cell subsets are in the same experimental tube and are resolved after measurement by means of gating techniques (such as the differential expression of the surface marker CD44).

We used DREMI and DREVI to analyze differences along the signaling cascade that starts at pCD3 ζ and continues down through pSLP76, pERK, and pS6. Naïve and antigen-exposed T cells had three main differences in their responses to TCR cross-linking. First, we found that along each edge in this pathway, naïve cells had higher peak-DREMI, indicating that signals were transferred more faithfully from the upstream molecule to the downstream molecule (Fig. 6, A to C). Second, we found that naïve cells had more sustained periods of high-DREMI (Fig. 6B), which indicated that signal transduction events transpired longer. Third, despite the fact that there was a more faithful signal transfer in naïve T cells, the levels of most of the measured phosphoproteins along this cascade, except pCD3 ζ , were observed to be higher (constitutively starting at time 0) in antigen-exposed cells (Fig. 6D).

The peak DREMI score (Fig. 6C) in either the naïve or the effector cascades occurs at 30 s for

the pCD3 ζ -pSLP76 edge, at 1 min for the pSLP76-pERK edge, and at 2 min for the pERK-pS6 edge. All three of these were substantially higher in naïve cells than in effector-memory cells. Further, the pCD3 ζ -pSLP76 relationship sustained signal transmission (high DREMI) for 2 min in naïve cells, compared with only 30 s in antigen-exposed cells. Similarly, the pSLP76-pERK edge had high DREMI between 1 and 3 min in naïve cells, whereas DREMI was only high between 1 and 2 min for antigen-exposed cells. Thus, at each stage in this cascade, *Y* transmitted more information about *X*, over a longer time period, in naïve cells than in antigen-exposed cells, suggesting tighter control in naïve cells. This difference between naïve and antigen-exposed cells was consistently observed across multiple replicates (fig. S16).

Although edge strength was higher in naïve cells, pSLP76 levels were higher in antigen-exposed cells independent of pCD3 ζ levels (Fig. 7A). The near-saturation of the pSLP76 levels can also be seen in the high and flat slope of pCD3 ζ -pSLP76 edge at 30 s (Fig. 6C). Similarly, pERK amounts were more faithfully transmitted to pS6 in naïve cells, whereas pS6 amounts were basally higher—independent of pERK—in antigen-exposed cells (Fig. 7A). In the case of TCR activation with CD4 costimulation, the analysis suggests that the

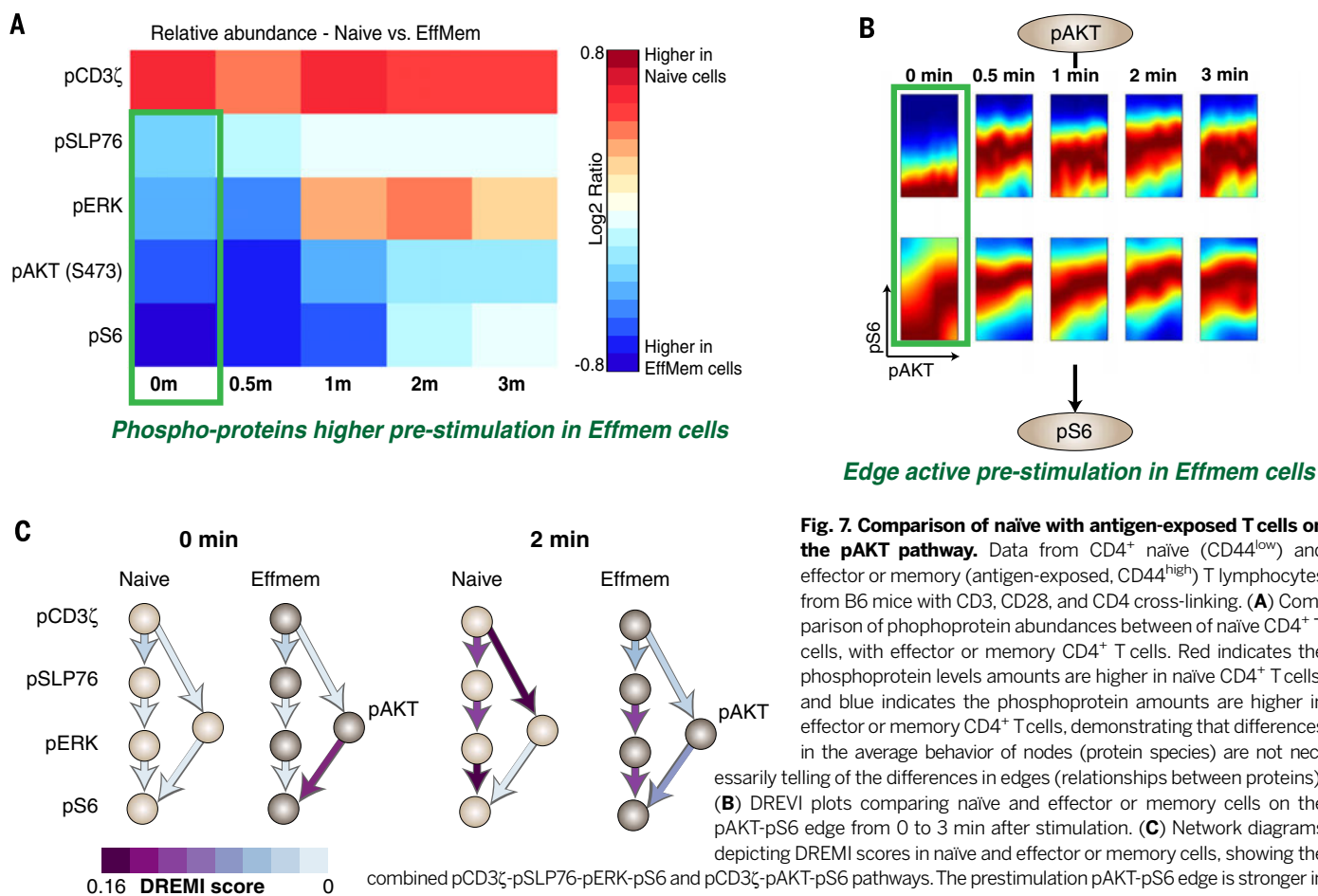


Fig. 7. Comparison of naïve with antigen-exposed T cells on the pAKT pathway. Data from CD4⁺ naïve (CD44^{low}) and effector or memory (antigen-exposed, CD44^{high}) T lymphocytes from B6 mice with CD3, CD28, and CD4 cross-linking. **(A)** Comparison of phosphoprotein abundances between of naïve CD4⁺ T cells, with effector or memory CD4⁺ T cells. Red indicates the phosphoprotein levels amounts are higher in naïve CD4⁺ T cells, and blue indicates the phosphoprotein amounts are higher in effector or memory CD4⁺ T cells, demonstrating that differences in the average behavior of nodes (protein species) are not necessarily telling of the differences in edges (relationships between proteins). **(B)** DREVI plots comparing naïve and effector or memory cells on the pAKT-pS6 edge from 0 to 3 min after stimulation. **(C)** Network diagrams depicting DREMI scores in naïve and effector or memory cells, showing the combined pCD3 ζ -pSLP76-pERK-pS6 and pCD3 ζ -pAKT-pS6 pathways. The prestimulation pAKT-pS6 edge is stronger in effector-memory cells at 0 and 2 min, whereas responses downstream of pCD3 ζ are stronger in naïve cells at 2 min.

AKT pathway might explain the higher level of pS6 in antigen-exposed cells. The AKT-pS6 edge had higher DREMI in antigen-exposed cells than in naïve cells (Fig. 7, B and C, and fig. S17) in early time points. Moreover, the AKT-pS6 relation was active before stimulation in antigen-exposed cells, providing a constitutive boost in signaling, perhaps through positive feedback between pS6 and pAKT (35).

Together, these differences suggest that antigen-exposed cells are poised toward a more easily

triggered response (12–14, 36). Because the basal levels of the phospho-proteins are higher, a shorter period of signal integration (as indicated by less sustained periods of high-DREMI) would be needed to elicit a cellular response. On the other hand, naïve cells, which are experiencing antigen for the first time, may need to mount a more cautious response, with the signaling cascade transmitting information carefully for longer periods of time to avoid spurious activation (12–14, 36).

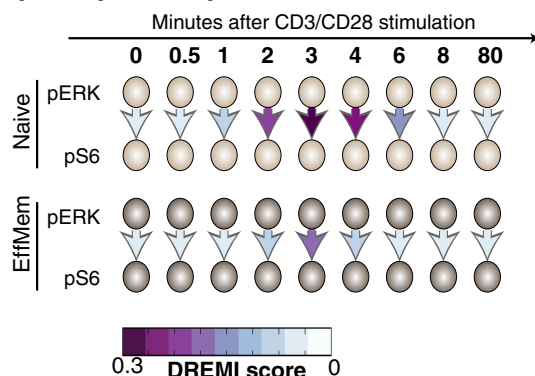
ERK-knockout validation

Because DREMI analysis determined that the influence of pERK on pS6 is stronger in naïve cells, this predicts that knockout of ERK2 should have a larger impact on pS6 levels in naïve cells (Fig. 8A), and this difference should be detected at the time the DREMI of this edge increases, 2 min after stimulation. We used the edge-response function and the measured difference in pERK abundance to approximate the expected change in pS6 levels at 2 min after knockout with

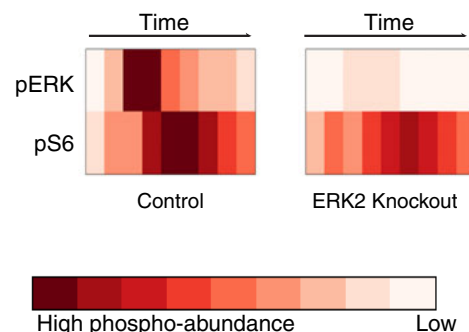
Fig. 8. Validation of differences in edge-strength using an inducible Erk2-knockout mouse. Data are from CD4⁺ naïve T lymphocytes from both B6 and Erk2-knockout mice with CD3 and CD28 cross-linking. (A) DREMI is used to compare the strength of the pERK-pS6 relationship between naïve and effector or memory T cells in B6 mice. Higher DREMI in naïve T cells predicts a bigger impact of Erk2

knockout on pS6 in naïve cells. (B) Heatmaps show the amounts of pERK and pS6 in the control and knockout mice cells. (C) Edge-response functions for B6 mice at the 2-min time point predict the outcome of a knockout experiment in (I) naïve cells and (II) effector or memory cells. The x axes of both figures are annotated with the measured change in mean pERK levels upon knockout, and the y axis shows the predicted decrease in pS6 levels based on the edge-response function. (D) I and II show two replicates demonstrating the change in pS6 amounts after ERK2 knockout. The blue bars represent the average difference between pS6 in normal and ERK2-knockout mice cells in naïve T cells. The maroon bars show the same difference in effector or memory cells. The blue bars are significantly higher than the maroon bars, especially after the 2-min time point (as predicted); therefore, our edge strength assessment is validated.

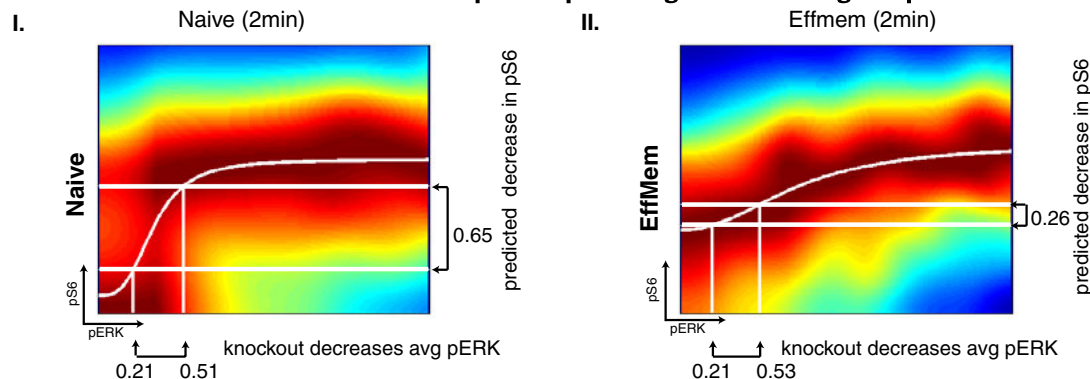
A pS6 depends on pERK more in naïve cells



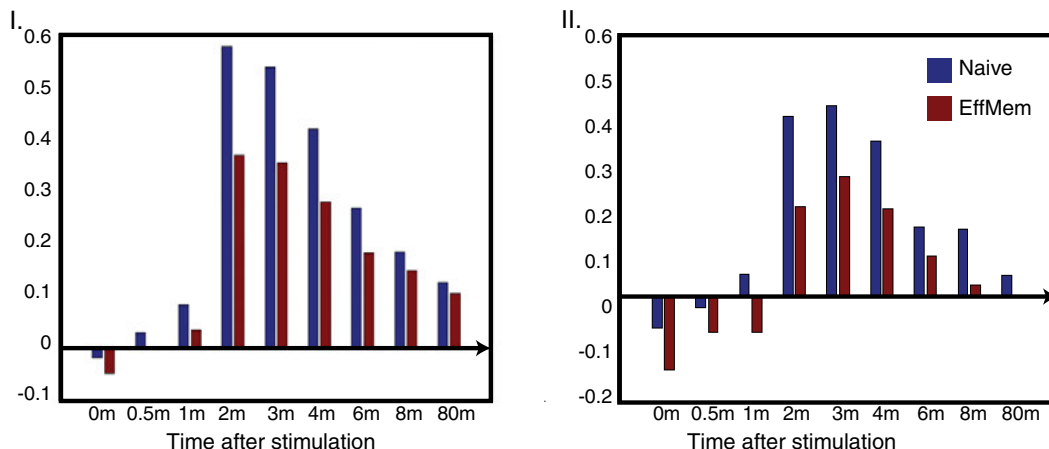
B Genetic deletion effects ERK abundance



C Prediction of differential knockdown impact on pS6 using DREMI and edge response functions



D Change in pS6 levels under ERK knockdown



an expectation to observe a change that is ~50 to 60% larger in naïve cells relative to effector/memory cells at 2 min (Fig. 8, B and C). To validate these predictions, we collected data from a mouse model (37), which enables tamoxifen-induced knockout of ERK2 within a normally differentiated T cell population. To allow for direct comparison, immune cells from both the B6 and ERK knockout mice were stimulated and measured in the same tube and subsequently identified through congenic markers CD45.1 and CD45.2.

To test the hypothesis that naïve T cells showed a stronger relationship between pERK and pS6, based on the relatively higher DREMI in naïve cells, we assessed the impact of the Erk2 depletion on pS6 levels in both naïve and antigen-exposed cells. As predicted, changes in pS6 abundance are larger in naïve cells than in antigen-exposed cells. Approximately 50% greater response in naïve cells began at 2 min, as predicted (Fig. 8D). DREMI also predicts that the influence of pERK on pS6 is stronger in CD4⁺ T cells than CD8⁺ T cells (fig. S18), which was also confirmed experimentally (fig. S19), demonstrating that DREMI can correctly predict differences in signaling edge strengths between related T cell subsets.

Discussion

DREVI and DREMI combined with single-cell data provide solutions to a challenging problem that has obstructed the analysis of single-cell biology: that of quantifying the strength of the underlying complex relationships between proteins from data. Other approaches such as correlation, mutual information, and MIC—which are typically used to quantify the strengths of interactions—are not always reliable in the face of technical noise, natural stochasticity, bimodality, spurious correlations, and nonlinearity inherent in single-cell data. DREMI, on the other hand, consistently quantifies the relative strengths of relationships and how they change after stimulation through time and between different cell types.

We used DREVI and DREMI to functionally and quantitatively analyze edges within intracellular protein networks. DREVI and DREMI directly regard the single-cell population as instantiations of an underlying signal processing circuit and infer the form and strength of each edge in the circuit. Many DREVI plots have a sigmoid (or partial sigmoid) response curve, suggestive of the signaling kinetics. With absolute quantification of cytometry data, it would be possible to derive biochemical rate constants for multiple enzymatic pairs and multiple subsets in a single experiment. This would provide an enormous advantage over laborious experiments currently needed to compute such rate constants. Therefore, a versatile, data-driven approach such as that represented here enables the systematic and quantitative comparison of signaling relationships between different stimuli, time points, and cell types.

The analysis in this manuscript focused on mass cytometry data collected from mouse T cells measuring 11 phosphoproteins and nine surface markers. The analysis determined that the TCR

signaling network is dynamic, with edges activating and deactivating quickly as the signals are transduced downstream. We used DREMI and DREVI to gain insights into how signaling is fine-tuned between related T cell populations. The differences we identified in TCR signaling between naïve and antigen-exposed T cells suggest that naïve cells more sensitively transmit upstream signaling inputs along a central signaling cascade. This more fine-tuned signaling response might help regulate the cell's decision to differentiate into either regulatory or helper T cells. In contrast, entrained effector or memory cells seem poised for fast responses upon secondary exposures. To explain this observation, we noted that several alternative pathways had higher activity in antigen-exposed cells, including AKT under CD4 costimulation, which likely bolsters phosphoprotein levels and shortens input integration time in antigen-exposed cells.

Cumulatively, these techniques can allow the tracking of subtle reconfigurations in signaling that occurs between related cell subtypes. These reconfigurations do not result in an essentially rewired network, but rather a network that is behaviorally reconfigured to produce changes in response. Although we have presented a specific application of our techniques, focused on TCR activation in T cell subsets, we believe that DREVI and DREMI are broadly applicable across biological systems and single-cell technologies (38, 39). Our ability to characterize signaling edges and their strengths is of particular value for disease studies because it has been shown that many disease alleles affect the edge strengths of the signaling network (40). In (16), we report the direct application of these methods to identify and characterize the impact of complex genetic variation associated with type-1 diabetes on TCR signaling networks. As single-cell data become more abundant, our methods will allow construction of more quantitative models of cellular signaling. Such models can then elucidate how these signaling circuits differ between cell types as well as characterize essential and therapy-targetable differences between health and disease.

Materials and methods

Mice

Mice were maintained in specific pathogen-free facilities at Harvard Medical School (Institutional Animal Care and Use Committee 99–20, 02954). Age-matched, 4- to 6-week-old male B6^{ERT} mice were used for all experiments. For TCR signaling responses in peripheral T cells from TCR transgenic mice, BDC2.5 and BDC2.5/B6^{ERT}.Rag^{-/-} mice were used. This mouse strain was previously described (41).

Cell stimulation

For analysis of phosphorylation events by means of mass cytometry, total lymph node cell suspensions from B6^{ERT} were used. Cells were stimulated in medium containing 2 or 6 µg/ml of biotinylated stimulatory antibodies to CD3e and CD28 and incubated for 2 min at 37°C before addition of 8 or 24 µg/ml streptavidin. At various times

after cross-linking, the stimulation was stopped by addition of paraformaldehyde (final concentration 2%) and incubation at room temperature for 20 min. In some experiments, biotinylated antibodies to CD4 were also included in the stimulation mix. The cells were measured before stimulation and at various time points after stimulation: 30 s, 1, 2, 3, 4, 6, 8, 10, 20, and 80 min.

Erk knockout experiment

To study the role of ERK in peripheral T cells, we used an inducible model that was developed in (37) with the Erk2 floxed-gene and ER-CRE, which is a tamoxifen-inducible adenosine 3',5'-monophosphate (cAMP) response element (CRE)-recombinase. Adult mice are injected with tamoxifen, every day (Sigma-Aldrich, St. Louis, MO) for 6 consecutive days, to induce the deletion of the floxed gene and create ERK2-deficient cells. The mice were analyzed 2 days later. There are normal numbers of peripheral T cells in these mice because they are analyzed only 2 days after the tamoxifen-induced deletion. Therefore, these peripheral cells are a result of normal differentiation and transportation from the thymus weeks before the tamoxifen treatment injections (37) but have ERK2 knocked-down for the TCR activation experiment.

Normal B6 and Erk knockout cells express different congenic CD45 surface antigens (Erk-knockout mice express CD45.1, and normal B6 express CD45.2), allowing for the stimulation of both cell types in the same tube. B6 and Erk knockout cells are therefore mixed before stimulation and identified after analysis with antibodies against CD45.1 and CD45.2. This strategy has the considerable advantage of eliminating any contribution of experimental variations during the stimulation, staining, and CyTOF processing of the samples (for each time point analyzed).

Measurement of phospho-signaling events with mass cytometry

In our experiments, we used mass cytometry to measure surface and internal proteins. Primary conjugates of the mass cytometry antibodies (complete list is provided in table S1) were prepared and titrated as described (8). Paraformaldehyde (PFA) fixed and frozen lymphocyte suspensions were thawed at room temperature and then transferred to ice.

Single samples of 1 million cells were stained in a 50 µl final volume. All samples from a given time series of a stimulation-condition were run in a single barcoded tube. Each barcoded tube contained 20 individual samples and was stained in 300 µl. Cells were stained with a cocktail of metal isotope conjugated antibodies (table S1) by using a two-step procedure (surface stains included CD4, CD8, TCRb, CD5, CD19, CD25, CD44, CD45.1, and CD45.2; intracellular stains included pCD3ζ, pSLP76, pERK1/2, pS6, pCREB, pMAPKAPKII, IkBa, pNFkB, pRb, pFAK, and pAKT). The signaling network consisting of all markers is shown in fig. S1. Cell fixation, permeation, and staining were performed as previously described (8). To make all samples maximally comparable, all data was acquired by using internal metal

isotope bead standards as previously described in (42). Approximately 100,000 events were acquired per sample on a CyTOF I (DVS Sciences, Sunnyvale, CA) by using instrument settings previously described in (42).

Barcoding of samples

To reduce sample-to-sample variability, cells corresponding to each stimulation condition and time point were barcoded by using all six stable palladium isotopes with a method similar to that described by (43). In the barcoding scheme, each isotope is used in binary fashion, high for “1” and low for “0.” Hence, the barcode itself is a binary string that can be decoded for each cell to determine the treatment condition for that cell. For this purpose, we developed an error-correcting 3-one barcoding scheme that both facilitates ease of debarcoding, and eliminates the majority of doublets. All legal barcodes in our scheme have exactly 3 ones and 3 zeroes, resulting in 20 possible barcodes. This barcoding scheme also enables the detection of most cell doublets because in a well-mixed tube, it is unlikely to have a doublet created by two cells from the same condition. Doublets with cells from two different conditions would have an illegal combined barcode (with more than 3 “1”s) that is represented by the logical OR of the individual barcodes. Therefore, this scheme eliminates almost all doublet events. Further, each pair of barcodes has a distance of at least 2, and therefore, this scheme is also robust to errors during the debarcoding.

Post-processing of mass cytometry data

Individual time series were normalized to the internal bead standards before analysis by using the method described in (42). In addition, as described in (8), for all analysis of the mass cytometry data, abundance values reported by the mass cytometer were transformed by using a scaled arcsinh, with scaling factor 5 to minimize the noise in measurements where the data are close to zero (the limit of detection on the mass cytometry scale). Events recorded by the mass cytometer were gated based on cell length and DNA content (to avoid debris and doublets), as described in (8).

Gating of cell subsets

Cells were then filtered through a series of gates, as depicted in fig. S2, for the purpose of isolating particular subpopulations of T cells such as CD4⁺ naïve T cells, CD8⁺ naïve T cells, and CD4⁺ effector/memory T cells. These gates include (gate 1) a gate that separates T cells (TCRb⁺ CD19⁻) from B cells (TCRb⁻ CD19⁺), (gate 2) a gate that further separates CD4⁺ T cells (CD4⁺) from CD8⁺ T cells (CD8⁺), (gate 3) a gate that further separates CD4⁺ T cells into conventional T cells (T_{conv} cells) (CD25⁻) and regulatory T cell (T_{reg} cell) (CD25⁺) populations, and (gate 4) a gate that further separates CD4⁺ T_{conv} cells and CD8⁺ T cells into naïve (CD44⁻) and antigen-exposed effector/memory populations (CD44⁺). Because there is no known CD8⁺ equivalent of the CD4⁺CD25⁺ T_{reg} population, CD8⁺ cells are not passed through gate 3. The final populations that we isolate and

use in our comparisons include (i) naïve CD4⁺ T cells (CD44⁻ CD25⁻ CD4⁺ CD8⁻ TCRb⁺ CD19⁻), (ii) naïve CD8⁺ T cells (CD44⁻ CD25⁻ CD8⁺ CD4⁻ TCRb⁺ CD19⁻), and (iii) Effector/memory CD4⁺ T cells (CD44⁺ CD25⁻ CD4⁺ CD8⁻ TCRb⁺ CD19⁻). The nodes, cell types, stimulation, and time points used in each figure are shown in table S2.

Data availability

All data are available for download at www.c2b2.columbia.edu/danapeerlab/html/dremi.html.

Description of computational methods

In the following sections, we provide a detailed explanation of how DREVI, DREMI, and the edge-response functions are computed,

Kernel density and conditional density estimation

A kernel density estimate $\hat{f}(x)$ is a nonparametric approximation of the probability density function $p(x)$. The standard method for computation of a kernel density estimate is to introduce a narrow Gaussian (or alternative) kernel at each point in the raw data and calculate the integral of the individual kernel values over a large set of points (21, 44). If $(x_1, x_2, x_3, \dots, x_n)$ are independent, identically distributed random samples from an unknown probability density function f , then the kernel density estimator is

$$\hat{f}(x) = \frac{1}{n} \sum_{i=1}^n K_h(x - x_i) \quad (1)$$

where K is the kernel function. The commonly used Gaussian kernel is given by

$$K(x) = \frac{1}{\sqrt{2\pi}} e^{-\left(\frac{x^2}{2}\right)} \quad (2)$$

K_h refers to the kernel density function scaled by $1/h$ (where h denotes the bandwidth). Intuitively, one can think of kernel density estimation as placing a small smooth kernel K_h at each sampled point and integrating over all such kernels to determine a smooth probability density function. The kernel density estimate in two dimensions is given by

$$\hat{f}_{h1h2}(x, y) = \sum_{i=1}^n K_{h1}(x - x_i) K_{h2}(y - y_i) \quad (3)$$

This standard method of kernel density estimation suffers from several deficiencies, including (i) sensitivity to selected bandwidth and the assumption of normalcy in many bandwidth estimation methods, (ii) boundary bias, and (iii) over- or under-smoothing.

Instead, we use the heat-diffusion method from (10) for two-dimensional (2D) kernel density estimation. This method views the kernel density estimate as a solution to the heat equation, which it evolves for a time period proportional to the bandwidth. This interpretation of a kernel density estimate derives from the notion of a “Weiner” process. A Weiner process W is a stochastic Markov process (the next state can be directly computed by the previous state) with

(i) Initial probability uniformly spread through the d -dimensional data points $(x_1, x_2, x_3, \dots, x_n)$.

(ii) The transition probability of going from point x_i to x_j is given by the Gaussian kernel $p_{\text{trans}}(x_i, x_j) = \frac{1}{\sqrt{2\pi t}} e^{-\frac{(x_j - x_i)^2}{2t}}$

The Gaussian kernel density estimation (KDE) can be interpreted as the probability distribution function (PDF) for this process at time t , which is the same as Eq. 2 with bandwidth h : $f_t(x) = \frac{1}{n} \sum_{i=1}^n \frac{1}{\sqrt{2\pi t}} e^{-\frac{(x - x_i)^2}{2t}}$

But because this is an iterative process, the transition satisfies the following differential equation, which is also known as the “heat equation”: $\frac{\partial}{\partial t} \hat{f}(x; t) = \frac{1}{2} \frac{\partial^2}{\partial x^2} \hat{f}(x; t)$, $t > 0$

The initial condition is given by $\hat{f}(x; 0) = \frac{1}{n} \sum_{i=1}^n \delta_{x_i}(x)$, where δ is the dirac delta function

(which gives point-masses to all data points). The advantage of writing this in PDF form is that if the PDF is known to be 0 outside the range, then boundary conditions enforcing this can be added, which results in a θ kernel rather than a Gaussian kernel:

$$\begin{aligned} \hat{f}(x; t) &= \frac{1}{n} \sum_{i=1}^n \theta(x, x_i; t) \\ &= \frac{1}{n} \sum_{i=1}^n \sum_{k=-\infty}^{\infty} e^{-k^2 \pi t / 2} \cos(k \pi x) \cos(k \pi x_i) \end{aligned} \quad (4)$$

The θ kernel is locally adaptive and has the property that it behaves like a Gaussian kernel for small bandwidths and like a uniform kernel for large bandwidths. The evolution of the heat equation decides the shape of the kernel rather than having a fixed Gaussian estimate. This often results in a smoother density function (fig S3). Additionally, (i) it can be solved quickly by using fast Fourier transform methods, (ii) it can be extended to a more general diffusion equation easily, and last (iii) the bandwidth t can be solved as a fixed point solution to a recursion without a normal assumption on the distribution. The superior performance and speed of computation of the heat-equation-based KDE is shown in fig. S3.

To obtain the standard conditional density estimate, the joint density estimate $\hat{f}(x, y)$ is divided by the marginal density estimate $\hat{f}(x)$ as follows (45):

$$\hat{f}(y|x) = \frac{\hat{f}(y, x)}{\hat{f}(x)} \quad (5)$$

We use the conditional density estimate as a starting point for DREVI and DREMI as explained in the following sections.

Conditional density-rescaled visualization

DREVI is aimed at visualizing the stochastic function representing how X influences Y by depicting the distribution of Y for each value of X . To visualize 2D relationships in single-cell data, we begin by computing a 2D kernel density estimate as described in Eq. 4 (10) on a square mesh grid. The mesh grid of points is denoted $G = \{(x_i, y_j), 1 < i < n, 1 < j < m\}$, and the 2-D kernel density estimate is a matrix $D = \hat{f}(G)$ where $D(i, j)$ corresponds to $\hat{f}(x_i, y_j)$. The mesh grid of points G is selected so that the X - Y ranges are restricted to regions that are well-populated by

cells. Most markers (such as phosphoproteins) are distributed among the measured cells as heavy-tailed multimodal distributions (fig. S7C). For any pair of markers X and Y , we remove 1% of both tails of these distributions as outliers, removing ~200 cells from a population of ~10,000 cells (per condition and time point). The remaining range is generally well populated by cells and is amenable for a robust density estimate, which results in robust visualization and scoring, as shown in fig. S7.

After the 2D kernel density estimate is computed, each column of D (corresponding to a fixed X -value, $X = x_i$) is renormalized by the marginal density estimate of $X = x_i$, as shown in Eq. 5, $\hat{f}(x)$ for that column to obtain the conditional density matrix

$$\Delta(x_i, y_j) = \hat{f}(y_j|x_i) \quad (6)$$

This is an estimate of $P(Y|X)$ on the same mesh grid. This matrix is rescaled for the purposes of visualization as follows:

$$\hat{f}^*(y_j|x_i) = \hat{f}(y_j|x_i) / \max_k [\hat{f}(y_k|x_i)] \quad (7)$$

We denote the matrix of rescaled kernel density estimates as

$$\Delta^*(x_i, y_j) = \hat{f}^*(x_i|y_j) \quad (8)$$

The matrix of Eq. 8 is visualized as a heatmap using the “jet” color scale, where densest regions, corresponding to the highest rescaled conditional density, are maroon/red and the sparsest regions are blue. This way, the X - Y relationship is revealed even in regions populated by fewer cells because each X -slice is renormalized individually. The computation of DREVI is demonstrated Fig. 1.

Conditional Density-Resampled Mutual Information (DREMI)

We developed a method for scoring relationships termed DREMI. Like MI, this will depend on how well the value of X can predict the value of Y . However, unlike MI, we are not interested in how the entropy of Y decreases with X in a given sample on average. Instead, we are interested in looking at the underlying stochastic function $F(X) = Y$, with the aim of learning the strength of this relationship over the entire dynamic range of X , regardless of the distribution in the specific sample.

The key mathematical insight in DREMI is that we provide a score for the conditional distribution of $P(Y|X)$ rather than joint distribution $P(X, Y)$. DREMI resamples from the conditional density estimate as described above, taking care to generate a uniform number of samples from each column of the matrix Δ^* , so that the relationship between X -and- Y is scored through the full dynamic range of X that is well sampled by the data.

DREMI begins with the rescaled conditional density matrix Δ^* described in Eq. 8. To filter out noise, we round values of $\Delta^*(x_i, y_j) < \epsilon$ to zero and eliminate the corresponding points from the grid G . We generate n new points $S_i = \{s_i^1, s_i^2, s_i^3, \dots, s_i^n\}$ from the density distribution in each column i of Δ^* , denoted Δ_i^* . We generate a total of

$n \times m$ samples $S = \{S_1, S_2, \dots, S_m\}$. Because points in each column of Δ_i^* have a similar value $X = x_i$, we are generating an equal number of samples from the entire range of X (up to the fine-mesh grid level of granularity).

Last, we define a discrete partition of the X and Y axes and compute mutual information $I(X:Y)$ as in Eq. 10 using the samples in S . We generally use eight equi-partitions of the X and Y axes to compute the mutual information on these samples, but our software can use any number of equi-partitions based on a user-defined parameter. Our partitions are formed by pooling all data from conditions being compared for a particular variable, taking the maximal range of the X and Y and partitioning that space into eight equal units along each axis. We normalize DREMI by the log base 2 of the number of partitions to provide a score that lies between 0 and 1.

To derive the mathematical expression for DREMI, we start with standard mutual information, computed as the differential entropy between Y and $Y|X$:

$$\begin{aligned} I(Y;X) &= H(Y) - H(Y|X) = \\ &= -\sum_j p(y_j) \log[p(y_j)] + \\ &\quad \sum_i \sum_j p(x_i, y_j) \log[p(y_j|x_i)] = \\ &\quad \sum_i \sum_j p(x_i, y_j) \log[p(y_j)] + \\ &\quad \sum_i \sum_j p(x_i, y_j) \log[p(y_j|x_i)] \end{aligned} \quad (9)$$

Alternatively, MI can be regarded as a measure of the distance between the joint distribution $P(X, Y)$ and the marginal distributions $P(X)$ and $P(Y)$. An equivalent formula for computing mutual information is given by (26)

$$I(x, y) = \sum_i \sum_j p(x_i, y_j) \log \left[\frac{p(x_i, y_j)}{p(x_i)p(y_j)} \right] \quad (10)$$

The first three steps of the DREMI algorithm involve estimating the conditional density by normalizing the joint kernel density estimate and filtering out noise. These steps result in a smoothed and de-noised conditional density estimate that will fill gaps in the raw data. The final step involves estimating MI from this computed conditional density. In fig. S20, we show intuitively how sampling from the conditional density estimate is equivalent to taking weighted samples from the joint distribution. Each point (x_i, y_j) from the joint distribution has sample weight proportional to $\frac{1}{p(x_i)}$.

Given this, DREMI can be written in terms of the differential entropy formulation of mutual information (Eq. 8) as follows:

$$I^c(Y|X) = H^c(Y) - H^c(Y|X) \quad (11)$$

where $H^c(Y)$ and $H^c(Y|X)$ are reweighted entropies so that each point (x_i, y_j) in the joint distribution is weighted by $\frac{1}{p(x_i)}$ given as follows:

$$H^c(Y) = -\sum_i \sum_j \frac{p(x_i, y_j)}{p(x_i)} \log[p(y_j)] \quad (12)$$

$$H^c(Y|X) = -\sum_i \sum_j \frac{p(x_i, y_j)}{p(x_i)} \log[p(y_j|x_i)] \quad (13)$$

Substituting Eq. 13 and Eq. 12 into Eq. 11 gives

$$\begin{aligned} I^c(Y|X) &= -\sum_i \sum_j \frac{p(x_i, y_j)}{p(x_i)} \log[p(y_j)] - \\ &\quad \left\{ -\sum_i \sum_j \frac{p(x_i, y_j)}{p(x_i)} \log[p(y_j|x_i)] \right\} \\ &= \sum_i \sum_j \frac{p(x_i, y_j)}{p(x_i)} \log[p(y_j|x_i)] - \log[p(y_j)] \\ &= \sum_i \sum_j \frac{p(x_i, y_j)}{p(x_i)} \log \left[\frac{p(y_j|x_i)}{p(y_j)} \right] \\ &= \sum_j \sum_i \frac{p(x_i, y_j)}{p(x_i)} \log \left[\frac{p(x_i, y_j)}{p(x_i)p(y_j)} \right] \\ &= \sum_j \sum_i p(y_j|x_i) \log \left[\frac{p(x_i, y_j)}{p(x_i)p(y_j)} \right] \end{aligned} \quad (14)$$

The final form in Eq. 14 is equivalent to Eq. 10, with each point reweighted by $\frac{1}{p(x_i)}$. Hence, I^c maintains many properties of mutual information, including the fact that $I^c(Y|X) = 0$ if $p(x, y) = p(x)p(y)$.

Robustness analysis

We demonstrate that DREVI and DREMI are robust methods. As shown in fig. S7, the down-sampling of the data by 20% results in virtually identical DREVI plots and very similar DREMI scores (SD of 0.02 or less) for several edges. The reason underlying this robustness is our use of density estimation with a locally adaptive smoothing that results from the evolution of a differential equation whose solution is equivalent to the kernel density estimate (10). The density estimation method interpolates and fills gaps within the data by integrating using a smooth kernel.

Fitting edge-response functions

For strong relationships, $P(Y|X)$ is highly peaked for any value of X . Moreover, the peak of $P(Y|X)$ for adjacent X -slices tend to follow along a smooth and continuous curve, the “edge-response function,” which we fit to the data. We derive the edge-response function by fitting points sampled from the noise-filtered conditional density Δ^* to one of three models using regularized regression: linear, sigmoidal, or double sigmoidal (27). If none of the models obtain significant fits (based on P values), we fit to a free-form curve (examples are provided in Figs. 1C, 3, and 5C).

We define the edge-response function as the function $f(X)$ that best fits the data. We derive the edge-response function by performing nonlinear, mixed-model regression (46) of the high-valued regions of the conditional-density estimate. The models we use are

- (i) linear: $f_i(x) = ax + b$
- (ii) sigmoidal: $f(x) = [(L - U)/1 + (x^n/K_0)] + U$
- (iii) double-sigmoidal: $f(x) = \{[(L_1 - U_1)/1 + (x^n/K_{d1})] + U_1\} + \{[(L_2 - U_2)/1 + (x^n/K_{d2})] + U_2\}$
- (iv) free-form curve

We minimize over both the models and parameters in (i) to (iii). If no model results in

sufficiently high significance of fit, we fit to a nonparametric curve.

Method availability

The methods described, along with an interactive graphic user interface (GUI) are available for download at www.c2b2.columbia.edu/danapeerlab/html/dremi.html.

Performance of DREMI on synthetic data

We used synthetic data to evaluate how DREMI behaves under increasingly noisy conditions (fig. S6). We generated the synthetic databases on characteristics of real pairwise relations observed in single-cell cytometry data:

(i) X is concentrated in a narrow band within the entire X -range.

(ii) The high-density region of the conditional distribution reveals a consensus of response that is smooth and can be fit to a curve.

(iii) The noise in Y is variable.

To fulfill these conditions, we generated data as follows:

For condition (i), the X is a random variable that follows the distribution normal distribution with SD 0.25: $N(2, 0.25)$.

For condition (ii), the mean Y is functionally related to X : $E(Y | X = x) = f(x)$. We use linear, sigmoidal, and quadratic functional relationships in the synthetic data.

For condition (iii), Y has varying degrees of Gaussian noise added on top of its mean value: $Y = f(X) + N(0, s)$, for parameter s .

Each synthetic data set contained ~20,000 points. We generated synthetic data following the above conditions for five different values of noise: $s = \{0.25, 0.5, 0.75, 1, 1.25\}$. As shown in fig. S6, the results of computing DREMI on this synthetic data show that DREMI scores decrease roughly linearly with the SD of the Gaussian noise, regardless of the underlying functional shape of the relationship.

In addition to the analysis described in the main text, we also evaluate how varying the noise-filtering threshold influences the results. Also shown in fig. S6 is how the noise-filtering threshold ϵ can be used to eliminate experimental noise. Depicted in fig. S6B is a horizontal line that equalizes the scores of all of the noise levels. Thus, the value of ϵ can be tuned to compensate for experimental or measurement noise.

There are certain settings that provide naturally noisier signals than others. For instance, certain antibodies can have weak binding affinities with their target proteins, others can non-specifically bind to a variety of proteins. In such cases, a higher level of the outlier-elimination threshold may be useful. In other situations, such as the pSP176-pERK edge, the response of the protein itself is stochastic, and therefore, the stochasticity itself has meaning. In such cases, the outlier-elimination threshold can be set higher to capture the natural stochasticity in the data. Other global contexts, such as measurements on primary cells as opposed to cell lines, lead to higher noise and weaker response. In these cases, it may be useful to set the noise-filtering threshold

to a particular global value. We use a globally fixed noise-filtering threshold of 0.85 for all figures and DREMI values computed for this manuscript. As shown in fig. S6, within any set noise-filtering threshold, the DREMI score decreases linearly with the SD of noise, and as such is able to relatively rank DREMI scores for comparison purposes.

Comparing DREMI to other methods

We compared the performance of DREMI against other commonly used dependency measures: (i) MIC (32), (ii) adaptively partitioned MI (47), and (iii) Pearson correlation (Fig. 5). Because no gold standard exists to compare strength of signal transfer along an edge, we created a framework to conduct the comparisons based on the dynamics of signaling. We used DREVI to visually determine the peak timing of the dynamic signaling response, and in cases in which peak timing is known, our visual inspection matched published literature (2). We then assess whether each of the four metrics can recover the peak timing and also order the time points correctly according to strength of signal transfer. We systematically computed all of the metrics along the time series in each of the six edges (Fig. 5I and fig S10). DREMI outperformed all other metrics.

To show that DREMI is able to quantify and rank relationships in settings other than TCR-stimulated mice cells, we also compared DREMI on three known signaling edges on previously published B cell data (8) from the bone marrow of healthy human donors after BCR (B cell receptor) stimulation (fig. S11). These data only have a single time point after BCR stimulation, therefore instead of ranking edge strength along time points, we rank edge strength across increasingly mature B cell populations. The five populations, in order of maturity, are (i) Pre-BI, (ii) Pre-BII, (iii) Immature B cells, (iv) Mature CD38+ B cells, and (v) Mature CD38- B cells. The cells are gated into these populations based on phenotypic B cell markers such as CD20, CD38, CD45RA, CD19, and CD123, as described in (8). We used prior biological knowledge to determine the cell population expected to have strongest signaling, determined before computing the metrics. DREMI outperformed all other metrics on this data.

An important goal of MIC is “equitability.” Intuitively, this means that different types of edge shapes are given similar scores if they are similarly “fuzzy” (33). Evaluating MICs’ performance, this does not seem to be a suitable assumption for molecular relations. Adaptive partitioning puts more weight into the densest part of the distribution. Although this might make sense, in essence, it makes a large number of microscopic partitions over the small range where most of the density lays. Thus, the partitions often represent random measurement noise rather than biological signal. Pearson correlation prefers linear dependencies to other types of dependencies, whereas nonlinear dependencies are frequently present in signaling relationships.

In Fig. 5, II, we compare DREMI on synthetic data, where the generating function is known. Here, we generate a weak linear relationship with low slope compared with the range of the data, $Y = \alpha X + N(0, 0.1)$, to compare against strong nonlinear relationships:

(i) A quadratic relationship with a high degree of noise, $Y = -\alpha X^2 + N(0, 0.75)$.

(ii) A sigmoidal relationship X - Y with both Gaussian noise and uniform noise in the range $[0, Y]$, for any value of Y : $Y = \text{sigmoid}(X) + N(0, 0.75) + U[0, \text{sigmoid}(X)]$, where U is a uniform random function.

In both cases, the noisy-yet-strong relationships scored lower than the weak linear relationship, with low noise for all metrics other than DREMI.

Evaluating edge-response functions on raw versus resampled conditional data

In fig. S8, we show that the data resampled from the conditional density is more suitable for curve-fitting than the raw data. In the first two columns, we use linear, sigmoidal, or double sigmoidal least-squares regression on the raw mass cytometry data. In the third column, we resample from the dense regions of the conditional density and perform the same types of regression on this resampled data. Last, in the fourth column we perform regression on the conditional mean (computed from the conditional density).

In each case, the best fit on the raw data has higher RMSE than the best-fit data that is resampled from the conditional density (measured on the raw data). In addition, the linear fit always results in a better fit on the raw data, whereas the conditional data result in a variety of shapes linear, sigmoidal, and double sigmoidal. The raw data tend to be concentrated in a small region of the X - Y plane, resulting in a weak penalty for deviations in most regions of the X - Y plane, and a heavy penalty for deviation only in the region of data concentration. Therefore, a line that passes through the concentrated region of the raw data generally results in the best fit.

REFERENCES AND NOTES

1. G. Iezzi, K. Karjalainen, A. Lanzavecchia, The duration of antigenic stimulation determines the fate of naive and effector T cells. *Immunity* **8**, 89–95 (1998). doi: [10.1016/S1074-7613\(00\)80461-6](https://doi.org/10.1016/S1074-7613(00)80461-6); pmid: [9462514](https://pubmed.ncbi.nlm.nih.gov/9462514/)
2. A. Lanzavecchia, G. Iezzi, A. Viola, From TCR engagement to T cell activation: A kinetic view of T cell behavior. *Cell* **96**, 1–4 (1999). doi: [10.1016/S0092-8674\(00\)80952-6](https://doi.org/10.1016/S0092-8674(00)80952-6); pmid: [9989490](https://pubmed.ncbi.nlm.nih.gov/9989490/)
3. N. Miskov-Zivanov, M. S. Turner, L. P. Kane, P. A. Morel, J. R. Faeder, The duration of T cell stimulation is a critical determinant of cell fate and plasticity. *Sci. Signal.* **6**, ra97 (2013). doi: [10.1126/scisignal.2004217](https://doi.org/10.1126/scisignal.2004217); pmid: [24194584](https://pubmed.ncbi.nlm.nih.gov/24194584/)
4. M. S. Turner, L. P. Kane, P. A. Morel, Dominant role of antigen dose in CD4⁺Foxp3⁺ regulatory T cell induction and expansion. *J. Immunol.* **183**, 4895–4903 (2009). doi: [10.4049/jimmunol.0901459](https://doi.org/10.4049/jimmunol.0901459); pmid: [19801514](https://pubmed.ncbi.nlm.nih.gov/19801514/)
5. G. Altan-Bonnet, R. N. Germain, Modeling T cell antigen discrimination based on feedback control of digital ERK responses. *PLoS Biol.* **3**, e356 (2005). doi: [10.1371/journal.pbio.0030356](https://doi.org/10.1371/journal.pbio.0030356); pmid: [16231973](https://pubmed.ncbi.nlm.nih.gov/16231973/)
6. Y. E. Antebi et al., Mapping differentiation under mixed culture conditions reveals a tunable continuum of T cell fates. *PLoS Biol.* **11**, e1001616 (2013). doi: [10.1371/journal.pbio.1001616](https://doi.org/10.1371/journal.pbio.1001616); pmid: [23935451](https://pubmed.ncbi.nlm.nih.gov/23935451/)
7. D. R. Bandura et al., Mass cytometry: Technique for real time single cell multitarget immunoassay based on inductively

- coupled plasma time-of-flight mass spectrometry. *Anal. Chem.* **81**, 6813–6822 (2009). doi: [10.1021/ac901049w](https://doi.org/10.1021/ac901049w); pmid: [19601617](https://pubmed.ncbi.nlm.nih.gov/19601617/)
8. S. C. Bendall *et al.*, Single-cell mass cytometry of differential immune and drug responses across a human hematopoietic continuum. *Science* **332**, 687–696 (2011). doi: [10.1126/science.1198704](https://doi.org/10.1126/science.1198704); pmid: [21551058](https://pubmed.ncbi.nlm.nih.gov/21551058/)
 9. M. H. DeGroot, M. J. Schervish, *Probability and Statistics* (Addison-Wesley, Boston, ed. 4, 2012).
 10. Z. I. Botev, J. F. Grotowski, D. P. Kroese, Kernel density estimation via diffusion. *Ann. Stat.* **38**, 2916–2957 (2010). doi: [10.1214/10-AOS799](https://doi.org/10.1214/10-AOS799)
 11. J. Zhu, H. Yamane, W. E. Paul, Differentiation of effector CD4 T cell populations. *Annu. Rev. Immunol.* **28**, 445–489 (2010). doi: [10.1146/annurev-immunol-030409-101212](https://doi.org/10.1146/annurev-immunol-030409-101212); pmid: [20192806](https://pubmed.ncbi.nlm.nih.gov/20192806/)
 12. M. Berard, D. F. Tough, Qualitative differences between naïve and memory T cells. *Immunology* **106**, 127–138 (2002). doi: [10.1046/j.1365-2567.2002.01447.x](https://doi.org/10.1046/j.1365-2567.2002.01447.x); pmid: [12047742](https://pubmed.ncbi.nlm.nih.gov/12047742/)
 13. M. R. Chandok, D. L. Farber, Signaling control of memory T cell generation and function. *Semin. Immunol.* **16**, 285–293 (2004). doi: [10.1016/j.smim.2004.08.009](https://doi.org/10.1016/j.smim.2004.08.009); pmid: [15528073](https://pubmed.ncbi.nlm.nih.gov/15528073/)
 14. M. K. MacLeod, J. W. Kappler, P. Marrack, Memory CD4 T cells: Generation, reactivation and re-assignment. *Immunology* **130**, 10–15 (2010). doi: [10.1111/j.1365-2567.2010.03260.x](https://doi.org/10.1111/j.1365-2567.2010.03260.x); pmid: [20331469](https://pubmed.ncbi.nlm.nih.gov/20331469/)
 15. K. Sachs, O. Perez, D. Pe'er, D. A. Lauffenburger, G. P. Nolan, Causal protein-signaling networks derived from multiparameter single-cell data. *Science* **308**, 523–529 (2005). doi: [10.1126/science.1105809](https://doi.org/10.1126/science.1105809); pmid: [15845847](https://pubmed.ncbi.nlm.nih.gov/15845847/)
 16. M. Mingueneau *et al.*, Single-cell mass cytometry of TCR signaling: Amplification of small initial differences results in low ERK activation in NOD mice. *Proc. Natl. Acad. Sci. U.S.A.* (2014). doi: [10.1073/pnas.1419337111](https://doi.org/10.1073/pnas.1419337111)
 17. B. J. Baaten, C. R. Li, L. M. Bradley, Multifaceted regulation of T cells by CD44. *Commun. Integr. Biol.* **3**, 508–512 (2010). doi: [10.4161/cib.3.6.13495](https://doi.org/10.4161/cib.3.6.13495); pmid: [21331226](https://pubmed.ncbi.nlm.nih.gov/21331226/)
 18. B. J. Baaten *et al.*, CD44 regulates survival and memory development in Th1 cells. *Immunity* **32**, 104–115 (2010). doi: [10.1016/j.immuni.2009.10.011](https://doi.org/10.1016/j.immuni.2009.10.011); pmid: [20079666](https://pubmed.ncbi.nlm.nih.gov/20079666/)
 19. J. E. Smith-Garvin, G. A. Koretzky, M. S. Jordan, T cell activation. *Annu. Rev. Immunol.* **27**, 591–619 (2009). doi: [10.1146/annurev-immunol.021908.132706](https://doi.org/10.1146/annurev-immunol.021908.132706); pmid: [19132916](https://pubmed.ncbi.nlm.nih.gov/19132916/)
 20. R. J. Brownlie, R. Zamojska, T cell receptor signalling networks: Branched, diversified and bounded. *Nat. Rev. Immunol.* **13**, 257–269 (2013). doi: [10.1038/nri3403](https://doi.org/10.1038/nri3403); pmid: [23524462](https://pubmed.ncbi.nlm.nih.gov/23524462/)
 21. M. Rosenblatt, Remarks on some nonparametric estimates of a density-function. *Ann. Math. Stat.* **27**, 832–837 (1956). doi: [10.1214/aoms/1177728190](https://doi.org/10.1214/aoms/1177728190)
 22. P. Hall, J. Racine, Q. Li, Cross-validation and the estimation of conditional probability densities. *J. Am. Stat. Assoc.* **99**, 1015–1026 (2004). doi: [10.1198/016214504000000548](https://doi.org/10.1198/016214504000000548)
 23. G. A. Darbellay, I. Vajda, Estimation of the information by an adaptive partitioning of the observation space. *IEEE Trans. Inf. Theory* **45**, 1315–1321 (1999). doi: [10.1109/18.761290](https://doi.org/10.1109/18.761290)
 24. A. A. Margolin *et al.*, Reverse engineering cellular networks. *Nat. Protoc.* **1**, 662–671 (2006). doi: [10.1038/nprot.2006.106](https://doi.org/10.1038/nprot.2006.106); pmid: [17406294](https://pubmed.ncbi.nlm.nih.gov/17406294/)
 25. I. S. Jang, A. Margolin, A. Califano, hARACNe: Improving the accuracy of regulatory model reverse engineering via higher-order data processing inequality tests. *Interface Focus* **3**, 20130011 (2013). doi: [10.1098/rsfs.2013.0011](https://doi.org/10.1098/rsfs.2013.0011); pmid: [24511376](https://pubmed.ncbi.nlm.nih.gov/24511376/)
 26. T. M. Cover, J. A. Thomas, *Elements of Information Theory* (Wiley-Interscience, Hoboken, NJ, ed. 2, 2006).
 27. T. Hastie, R. Tibshirani, J. H. Friedman, *The Elements of Statistical Learning: Data Mining, Inference, and Prediction: With 200 Full-Color Illustrations* (Springer, New York, 2001).
 28. M. N. Artyomov, M. Lis, S. Devadas, M. M. Davis, A. K. Chakraborty, CD4 and CD8 binding to MHC molecules primarily acts to enhance Lck delivery. *Proc. Natl. Acad. Sci. U.S.A.* **107**, 16916–16921 (2010). doi: [10.1073/pnas.1010568107](https://doi.org/10.1073/pnas.1010568107); pmid: [20837541](https://pubmed.ncbi.nlm.nih.gov/20837541/)
 29. A. Zaslaver *et al.*, Just-in-time transcription program in metabolic pathways. *Nat. Genet.* **36**, 486–491 (2004). doi: [10.1038/ng1348](https://doi.org/10.1038/ng1348); pmid: [15107854](https://pubmed.ncbi.nlm.nih.gov/15107854/)
 30. C. J. Caunt, S. M. Keyse, Dual-specificity MAP kinase phosphatases (MKPs): Shaping the outcome of MAP kinase signalling. *FEBS J.* **280**, 489–504 (2013). doi: [10.1111/j.1742-4658.2012.08716.x](https://doi.org/10.1111/j.1742-4658.2012.08716.x); pmid: [22812510](https://pubmed.ncbi.nlm.nih.gov/22812510/)
 31. G. Li *et al.*, Decline in miR-181a expression with age impairs T cell receptor sensitivity by increasing DUSP6 activity. *Nat. Med.* **18**, 1518–1524 (2012). doi: [10.1038/nm.2963](https://doi.org/10.1038/nm.2963); pmid: [23023500](https://pubmed.ncbi.nlm.nih.gov/23023500/)
 32. D. N. Reshef *et al.*, Detecting novel associations in large data sets. *Science* **334**, 1518–1524 (2011). doi: [10.1126/science.1205438](https://doi.org/10.1126/science.1205438); pmid: [22174245](https://pubmed.ncbi.nlm.nih.gov/22174245/)
 33. J. B. Kinney, G. S. Atwal, Equitability, mutual information, and the maximal information coefficient. *Proc. Natl. Acad. Sci. U.S.A.* **111**, 3354–3359 (2014). doi: [10.1073/pnas.1309933111](https://doi.org/10.1073/pnas.1309933111); pmid: [24550517](https://pubmed.ncbi.nlm.nih.gov/24550517/)
 34. K. A. Janes *et al.*, A systems model of signaling identifies a molecular basis set for cytokine-induced apoptosis. *Science* **310**, 1646–1653 (2005). doi: [10.1126/science.1116598](https://doi.org/10.1126/science.1116598); pmid: [16339439](https://pubmed.ncbi.nlm.nih.gov/16339439/)
 35. K. Okkenhaug, Signaling by the phosphoinositide 3-kinase family in immune cells. *Annu. Rev. Immunol.* **31**, 675–704 (2013). doi: [10.1146/annurev-immunol-032712-095946](https://doi.org/10.1146/annurev-immunol-032712-095946); pmid: [23330955](https://pubmed.ncbi.nlm.nih.gov/23330955/)
 36. K. Adachi, M. M. Davis, T-cell receptor ligation induces distinct signaling pathways in naïve vs. antigen-experienced T cells. *Proc. Natl. Acad. Sci. U.S.A.* **108**, 1549–1554 (2011). doi: [10.1073/pnas.1017340108](https://doi.org/10.1073/pnas.1017340108); pmid: [21205892](https://pubmed.ncbi.nlm.nih.gov/21205892/)
 37. C. F. Chang *et al.*, Polar opposites: Erk direction of CD4 T cell subsets. *J. Immunol.* **189**, 721–731 (2012). doi: [10.4049/jimmunol.1103015](https://doi.org/10.4049/jimmunol.1103015); pmid: [22675204](https://pubmed.ncbi.nlm.nih.gov/22675204/)
 38. C. Giesen *et al.*, Highly multiplexed imaging of tumor tissues with subcellular resolution by mass cytometry. *Nat. Methods* **11**, 417–422 (2014). doi: [10.1038/nmeth.2869](https://doi.org/10.1038/nmeth.2869); pmid: [24584193](https://pubmed.ncbi.nlm.nih.gov/24584193/)
 39. M. Angelo *et al.*, Quantitative imaging of ten markers in human breast tumors using multiplexed ion beam imaging (MIBI) and metal-tagged antibodies. *Lab. Invest.* **94**, 518A (2014).
 40. Q. Zhong *et al.*, Edgetic perturbation models of human inherited disorders. *Mol. Syst. Biol.* **5**, 321 (2009). doi: [10.1038/msb.2009.80](https://doi.org/10.1038/msb.2009.80); pmid: [19888216](https://pubmed.ncbi.nlm.nih.gov/19888216/)
 41. M. Mingueneau, W. Jiang, M. Feuerer, D. Mathis, C. Benoist, Thymic negative selection is functional in NOD mice. *J. Exp. Med.* **209**, 623–637 (2012). pmid: [22329992](https://pubmed.ncbi.nlm.nih.gov/22329992/)
 42. R. Finck *et al.*, Normalization of mass cytometry data with bead standards. *Cytometry A* **83**, 483–494 (2013). doi: [10.1002/cyto.a.22271](https://doi.org/10.1002/cyto.a.22271); pmid: [23512433](https://pubmed.ncbi.nlm.nih.gov/23512433/)
 43. B. Bodenmiller *et al.*, Multiplexed mass cytometry profiling of cellular states perturbed by small-molecule regulators. *Nat. Biotechnol.* **30**, 858–867 (2012). doi: [10.1038/nbt.2317](https://doi.org/10.1038/nbt.2317); pmid: [22902532](https://pubmed.ncbi.nlm.nih.gov/22902532/)
 44. E. Parzen, Estimation of a probability density-function and mode. *Ann. Math. Stat.* **33**, 1065–1076 (1962). doi: [10.1214/aoms/1177704472](https://doi.org/10.1214/aoms/1177704472)
 45. M. Rosenblatt, in *Multivariate Analysis II*, K. P.R., Ed. (Academic Press, New York, 1969), pp. 25–31.
 46. D. Koller, N. Friedman, *Probabilistic Graphical Models: Principles and Techniques*. (MIT Press, Cambridge, MA, 2009).
 47. R. Steuer, J. Kurths, C. O. Daub, J. Weise, J. Selbig, The mutual information: Detecting and evaluating dependencies between variables. *Bioinformatics* **18** (suppl. 2), S231–S240 (2002). doi: [10.1093/bioinformatics/18.suppl_2.S231](https://doi.org/10.1093/bioinformatics/18.suppl_2.S231); pmid: [12386007](https://pubmed.ncbi.nlm.nih.gov/12386007/)

ACKNOWLEDGMENTS

We thank B. Bodenmiller, N. Friedman, N. HaCohen, I. Pe'er, A. Regev, and S. Reiner for valuable comments. We respectfully appreciate the provision of mouse samples and key mechanistic discussions with C. Benoist and S. Hedrick. This research was supported by the National Science Foundation CAREER award through grant MCB-1149728 and National Centers for Biomedical Computing Grant 1U54CA121852-01A1 and the NIH S10 Shared instrumentation grant NIH S10 SIG S10RR027582-01. D.P. holds a Packard Fellowship for Science and Engineering. S.C.B. is supported by the Damon Runyon Cancer Research Foundation Fellowship (DRG-2017-09). E.S. is supported by NIH K01 award 1K01DK095008. G.P.N. is supported by the Rachford and Carlota A. Harris Endowed Professorship and grants from U19 AI057229, P01 CA034233, HHSN272200700038C, 1R01CA130826, CIRM DR1-01477, and RB2-01592, NCI RFA CA 09-011, NHLBIH-10-05 (2), European Commission HEALTH.2010.1.2-1, and the Bill and Melinda Gates Foundation (GF12141-137101). S.K., G.P.N., and D.P. conceived the study. S.K. and D.P. designed and developed DREVI, DREMI, and additional computational methods in this manuscript. S.K. wrote all computer programs used in this manuscript. M.H.S. and S.C.B. developed reagents. M.M. stimulated the mice and collected the biological samples. M.H.S., M.M., and S.C.B. designed mouse experiments and performed cognate data acquisition. E.S. developed the inducible ERK-knockdown mouse. S.K. and O.L. performed statistical analysis. S.K. and D.P. performed the biological analysis and interpretation. S.K., G.P.N., and D.P. wrote the manuscript.

SUPPLEMENTARY MATERIALS

www.sciencemag.org/content/346/6213/1250689/suppl/DC1
Figs. S1 to S20
Tables S1 and S2

10 January 2014; accepted 15 October 2014
[10.1126/science.1250689](https://doi.org/10.1126/science.1250689)

RESEARCH ARTICLES

BLACK HOLE PHYSICS

Black hole lightning due to particle acceleration at subhorizon scales

J. Aleksić,¹ S. Ansoldi,² L. A. Antonelli,³ P. Antoranz,⁴ A. Babic,⁵ P. Bangale,⁶ J. A. Barrio,⁷ J. Becerra González,^{8*} W. Bednarek,⁹ E. Bernardini,¹⁰ B. Biasuzzi,² A. Biland,¹¹ O. Blanch,¹ S. Bonney,⁷ G. Bonnoli,³ F. Borraici,⁶ T. Bretz,^{12†} E. Carmona,¹³ A. Carosi,³ P. Colin,⁶ E. Colombo,⁸ J. L. Contreras,⁷ J. Cortina,¹ S. Covino,³ P. Da Vela,⁴ F. Dazzi,⁶ A. De Angelis,² G. De Caneva,¹⁰ B. De Lotto,² E. de Oña Wilhelmi,¹⁴ C. Delgado Mendez,¹³ D. Dominis Prester,⁵ D. Dorner,¹² M. Doro,¹⁵ S. Einecke,¹⁶ D. Eisenacher,^{12**} D. Elsaesser,¹² M. V. Fonseca,⁷ L. Font,¹⁷ K. Frantzen,¹⁶ C. Fruck,⁶ D. Galindo,¹⁸ R. J. García López,⁸ M. Garczarek,¹⁰ D. Garrido Terrats,¹⁷ M. Gaug,¹⁷ N. Godinović,⁵ A. González Muñoz,¹ S. R. Gozzini,¹⁰ D. Hadasch,^{14,‡} Y. Hanabata,¹⁹ M. Hayashida,¹⁹ J. Herrera,⁸ D. Hildebrand,¹¹ J. Hose,⁶ D. Hrupec,⁵ W. Idec,⁹ V. Kadosius,²⁰ H. Kellermann,⁶ K. Kodani,¹⁹ Y. Konno,¹⁹ J. Krause,⁶ H. Kubo,¹⁹ J. Kushida,¹⁹ A. La Barbera,³ D. Lelas,⁵ N. Lewandowska,¹² E. Lindfors,^{20§} S. Lombardi,³ F. Longo,² M. López,⁷ R. López-Coto,¹ A. López-Oramas,¹ E. Lorenz,[‡] I. Lozano,⁷ M. Makariev,²¹ K. Mallot,¹⁰ G. Maneva,²¹ N. Mankuzhiyil,^{2||} K. Mannheim,^{12**} L. Maraschi,³ B. Marcote,¹⁸ M. Mariotti,¹⁵ M. Martínez,¹ D. Mazin,⁶ U. Menzel,⁶ J. M. Miranda,⁴ R. Mirzoyan,⁶ A. Moralejo,¹ P. Munar-Adrover,¹⁸ D. Nakajima,¹⁹ A. Niedzwiecki,⁹ K. Nilsson,^{20§} K. Nishijima,¹⁹ K. Noda,⁶ R. Orito,¹⁹ A. Overkemping,¹⁶ S. Paiano,¹⁵ M. Palatiello,² D. Paneque,⁶ R. Paoletti,⁴ J. M. Paredes,¹⁸ X. Paredes-Fortuny,¹⁸ M. Persic,² P. Poutanen,²⁰ P. G. Prada Moroni,²² E. Prandini,¹¹ I. Puljak,⁵ R. Reinthal,²⁰ W. Rhode,¹⁶ M. Ribó,¹⁸ J. Rico,¹ J. Rodríguez García,⁶ S. Rügemer,¹² T. Saito,¹⁹ K. Saito,¹⁹ K. Satalecka,⁷ V. Scalzotto,¹⁵ V. Scapin,⁷ C. Schultz,¹⁵ T. Schweizer,⁶ S. N. Shore,²² A. Sillanpää,²⁰ J. Sitarek,^{1,*} I. Snidarić,⁵ D. Sobczynska,⁹ F. Spanier,¹² V. Stamatescu,^{1¶} A. Stamerra,³ T. Steinbring,¹² J. Storz,¹² M. Strzys,⁶ L. Takalo,²⁰ H. Takami,¹⁹ F. Tavecchio,³ P. Temnikov,²¹ T. Terzić,⁵ D. Tescaro,⁸ M. Teshima,^{6,19} J. Thaele,¹⁶ O. Tibolla,¹² D. F. Torres,²³ T. Toyama,⁶ A. Treves,²⁴ M. Uellenbeck,¹⁶ P. Vogler,¹¹ R. Zanin,¹⁸ M. Kadler,¹² R. Schulz,^{12,25} E. Ros,^{26,27,28} U. Bach,²⁶ F. Krauß,^{12,25} J. Wilms²⁵

Supermassive black holes with masses of millions to billions of solar masses are commonly found in the centers of galaxies. Astronomers seek to image jet formation using radio interferometry but still suffer from insufficient angular resolution. An alternative method to resolve small structures is to measure the time variability of their emission. Here we report on gamma-ray observations of the radio galaxy IC 310 obtained with the MAGIC (Major Atmospheric Gamma-ray Imaging Cherenkov) telescopes, revealing variability with doubling time scales faster than 4.8 min. Causality constrains the size of the emission region to be smaller than 20% of the gravitational radius of its central black hole. We suggest that the emission is associated with pulsar-like particle acceleration by the electric field across a magnetospheric gap at the base of the radio jet.

More than three decades ago, it was proposed that the radio emission of extragalactic jets results from a relativistically moving plasma consisting of magnetic fields and accelerated particles following a power-law energy distribution (*1*). One of the major assets of the model is that it can explain the nonthermal emission of extragalactic jets across the entire electromagnetic spectrum, from radio waves up to gamma rays. The emission can be understood as synchrotron radiation and inverse Compton scattering (*2, 3*) due to particles accelerated at shock waves in the jets. The gamma rays can reach very high energies measured in giga-electron volts (1 GeV = 10^9 eV, correspond-

ing roughly to the rest mass energy equivalent of the proton) and tera-electron volts (1 TeV = 10^{12} eV). According to the Blandford-Znajek mechanism, the jets are powered by extracting rotational energy from the black holes, which have acquired angular momentum through the accretion of surrounding gas and black hole mergers (*4*), although so far astrophysical evidence for the role of black hole spin is still lacking (*5*). For a maximally rotating supermassive black hole of mass $M = 10^8 m_\odot$, where M_\odot denotes one solar mass, the size of the jet formation region should be of the order of its gravitational radius, $r_g = G_N M / c^2 \sim 1.5 \times 10^{11} m_\odot$ (G_N , gravitational constant; c^2 , speed of light) and twice this value for a non-

rotating Schwarzschild black hole. Astronomical telescopes do not yet provide the angular resolution needed to image structures on this scale. The highest-resolution images of jets obtained with very long baseline radio interferometry show radio-emitting knots traveling down the jets (*6*). Approaching the black hole, the spectra cut off at increasingly higher frequencies due to synchrotron self-absorption. Observations at very high frequencies where the core becomes transparent are needed to zoom into the region where the jets are emerging from. The record holder is a very long baseline radio interferometry observation of the jet of the nearby radio galaxy M87 at a frequency of 230 GHz, resolving a source with a size of 11.0 ± 0.8 gravitational radii (*7*).

The event horizon light-crossing time

Although direct imaging of the jet formation region has to await better angular resolution, indirect information about its size can be inferred

¹Institut de Física d'Altes Energies, Campus UAB, E-08193 Bellaterra, Spain. ²Università di Udine and Istituto Nazionale di Fisica Nucleare (INFN) Trieste, I-33100 Udine, Italy, and Istituto Nazionale di Astrofisica (INAF)-Trieste, I-34127 Trieste, Italy. ³INAF National Institute for Astrophysics, I-00136 Rome, Italy. ⁴Università di Siena and INFN Pisa, I-53100 Siena, Italy. ⁵Croatian MAGIC Consortium, Rudjer Boskovic Institute, University of Rijeka and University of Split, HR-10000 Zagreb, Croatia. ⁶Max-Planck-Institut für Physik, D-80805 München, Germany. ⁷Universidad Complutense, E-28040 Madrid, Spain. ⁸Instituto de Astrofísica de Canarias, E-38200 La Laguna, Tenerife, Spain. ⁹University of Łódź, PL-90236 Łódź, Poland. ¹⁰Deutsches Elektronen-Synchrotron, D-15738 Zeuthen, Germany. ¹¹ETH Zurich, CH-8093 Zurich, Switzerland. ¹²Universität Würzburg, D-97074 Würzburg, Germany. ¹³Centro de Investigaciones Energéticas, Medioambientales y Tecnológicas, E-28040 Madrid, Spain. ¹⁴Institute of Space Sciences, E-08193 Barcelona, Spain. ¹⁵Università di Padova and INFN, I-35131 Padova, Italy. ¹⁶Technische Universität Dortmund, D-44221 Dortmund, Germany. ¹⁷Unitat de Física de les Radiacions, Departament de Física, and Centro de Estudios e Investigación Espaciales-Institut d'Estudis Espacials de Catalunya, Universitat Autònoma de Barcelona, E-08193 Bellaterra, Spain. ¹⁸Universitat de Barcelona, Institut de Ciències del Cosmos, Institut d'Estudis Espacials de Catalunya-Universitat de Barcelona, E-08028 Barcelona, Spain. ¹⁹Japanese MAGIC Consortium, Division of Physics and Astronomy, Kyoto University, Japan. ²⁰Finnish MAGIC Consortium, Tuorla Observatory, University of Turku and Department of Physics, University of Oulu, Finland. ²¹Institute for Nuclear Research and Nuclear Energy, BG-1784 Sofia, Bulgaria. ²²Università di Pisa and INFN Pisa, I-56126 Pisa, Italy. ²³CREA and Institut de Space Sciences, E-08193 Barcelona, Spain. ²⁴Università dell'Insubria and INFN Milano Bicocca, Como, I-22100 Como, Italy. ²⁵Dr. Remeis-Sternwarte Bamberg, Astronomisches Institut der Universität Erlangen-Nürnberg, ECAP, D-96049 Bamberg, Germany. ²⁶Max-Planck-Institut für Radioastronomie, D-53121 Bonn, Germany. ²⁷Observatori Astronòmic, Universitat de València, E-46980 Paterna, València, Spain. ²⁸Departament d'Astronomia i Astrofísica, Universitat de València, E-46100 Burjassot, València, Spain. *Present address: NASA Goddard Space Flight Center, Greenbelt, MD 20771, USA, and Department of Physics and Department of Astronomy, University of Maryland, College Park, MD 20742, USA. †Present address: Ecole Polytechnique Fédérale de Lausanne (EPFL), Lausanne, Switzerland. ‡Present address: Institut für Astro- und Teilchenphysik, Leopold-Franzens-Universität Innsbruck, A-6020 Innsbruck, Austria. §Present address: Finnish Centre for Astronomy with ESO (FINCA), Turku, Finland. ||Present address: Astrophysics Science Division, Bhabha Atomic Research Centre, Mumbai 400085, India. ¶Present address: School of Chemistry and Physics, University of Adelaide, Adelaide 5005, Australia. #Deceased. **Corresponding author. E-mail: deisenacher@astro.uni-wuerzburg.de (D.E.); jsitarek@ifae.es (J.S.); mannheim@astro.uni-wuerzburg.de (K.M.)

from the temporal variability of the emission coming from that region. The observed gamma-ray variability time scales indeed reach down to the event horizon light-crossing time, $\Delta t_{\text{BH}} = r_g/c = G_N M/c^3 = 8.3 m_8$ minutes (8), vindicating the scenario that the jets originate from the magnetospheres of accreting black holes. An example is the radio galaxy M87 in the Virgo cluster of galaxies (9, 10). This galaxy harbors a central supermassive black hole with the enormous mass of $\sim 6.4 \times 10^9 M_\odot$ (11). M87 exhibits gamma-ray variability on a time scale of days (12), which is consistent with the light-crossing time of the event horizon $\Delta t_{\text{BH}}(\text{M87}) = 0.4$ days.

Smaller than a black hole?

Observations of Mrk 501 (13) and PKS 2155-304 (14) at very high energies have provided evidence for extreme variability events, with flux doubling time scales as short as ~ 2 min. The ultrafast variability corresponds to $\Delta t < \Delta t_{\text{BH}}$ and therefore casts a shadow of doubt on the current shock-in-jet paradigm. It has been suggested that relativistic bulk motion of the jets could explain the observed time scales (15). The argument relies on the observation that these flaring sources belong to the class of sources that astronomers call blazars. In blazars, the jets are pointing at a small angle toward the observer. Because the jet plas-

ma moves with a speed close to the speed of light $\beta = v_j/c \simeq 1$, leading to a bulk Lorentz factor $\Gamma_j > 1$, several effects arise due to the relativistic boosting of the emission (16). One of them affects the time scale of flux variations of the emission from a shock. The moving shock plasma almost catches up with its own radiation, and this leads to a shortening of the observed variability time scale Δt as compared with the variability time scale $\Delta t'$ in a frame co-moving with the shock given by $\Delta t = (1+z)\delta^{-1}\Delta t'$, where z denotes the cosmological redshift of the source. For a given value of Γ_j , the Doppler factor δ depends strongly on the orientation angle of the jet θ (Fig. 1). Note that $\theta = 0$ corresponds to perfect alignment. For Mrk 501 and PKS 2155-304, almost perfectly aligned jets with $\Gamma_j > 50$ would be needed to accommodate for $\Delta t < \Delta t_{\text{BH}}$ and to avoid self-absorption of the gamma rays because of pair production (15). In blazars, interferometric observations of the superluminal motion of radio knots suggest lower values of $\Gamma_j \sim 10$ and orientation angles of a few degrees (17). Larger values of Γ_j would lead to a problem with population statistics: The number of unbeamed counterparts of blazars viewed at larger angles would then exceed the number of radio galaxies, which are commonly believed to represent the misaligned blazars (18). Assuming lower black hole masses would bring down Δt_{BH} . However, lower masses conflict with the firmly established dynamical measurements of black hole masses and therefore do not seem to be a likely solution of the dilemma. Other possible solutions of this Doppler factor crisis (19) invoke models of structured jets (20, 21) or Poynting flux-dominated jets, in which only a few but very fast seed particles at the jet base reach high Lorentz factors (22–24) before the Poynting flux is converted into the kinetic energy of the bulk flow by mass entrainment.

All of these attempts to explain the subhorizon scale variability with relativistic projection effects alone ignore a fundamental problem. If the perturbations giving rise to the blazar variability are injected at the jet base, the time scale of the flux variations in the frame co-moving with the jet is affected by time dilation with Lorentz factor Γ_j . In blazars where $\delta \sim \Gamma_j$, the Lorentz factor cancels out and the observed variability time scale is ultimately bounded below by Δt_{BH} .

IC 310: A gamma-ray lightning inferno

IC 310 is a peculiar radio galaxy located in the outskirts of the Perseus cluster at a distance of 260 million light years from Earth. On 12/13 November 2012, MAGIC (Major Atmospheric Gamma-ray Imaging Cherenkov), a system of two Imaging Atmospheric Cherenkov telescopes located on the Canary island of La Palma (25), detected an extraordinary outburst of gamma rays from this object (Fig. 2 and fig. S1). The details of the analysis can be found in section S2. Before these observations, variable gamma-ray emission from IC 310 had already been detected by satellite and ground-based gamma-ray instruments at GeV and TeV energies; e.g., Fermi-LAT and MAGIC (26–28). On the night of the flare in

Fig. 1. The relation between Doppler factor and orientation angle evaluated for various values of the bulk Lorentz factor compared with the observational constraints of these parameters. The blue box shows the constraints on the Doppler factor arising from radio observations (32). For illustrative purposes, the red box shows the constraint from the gamma-ray optical depth to pair creation, assuming $L_{\text{syn}} \sim 1\% L_{\text{VHE}}$.

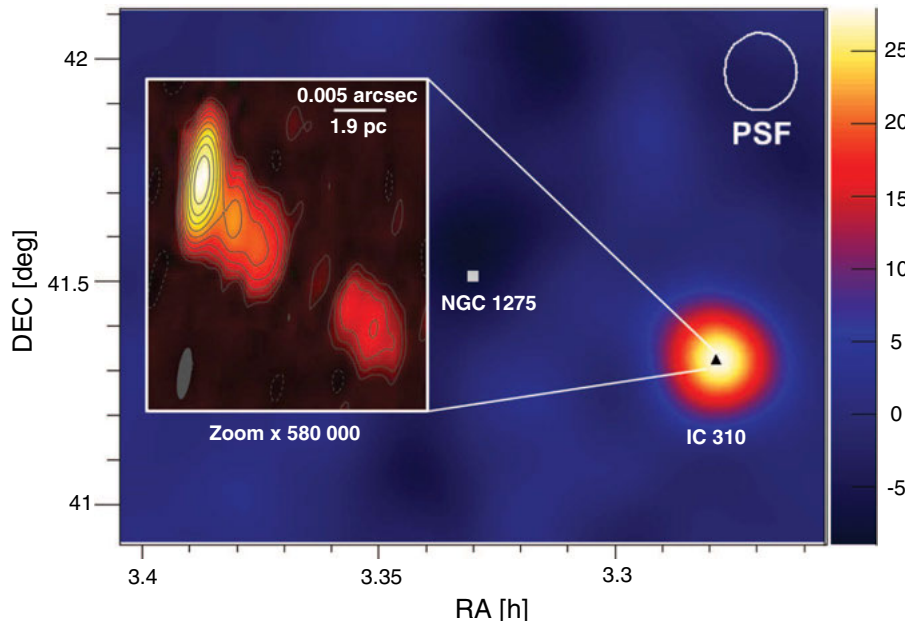
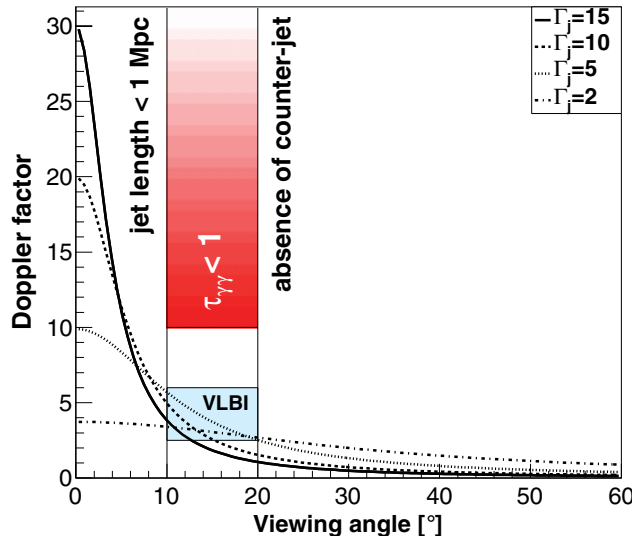


Fig. 2. Significance map (color scale) of the Perseus cluster in gamma rays observed on the night of 12/13 November 2012 with the MAGIC telescopes. The inset shows the radio jet image of IC 310 at 5.0 GHz obtained with the European Very Long Baseline Interferometry Network (EVN) on 29 October 2012. Contour lines (and the color scale associated with them) increase logarithmically by factors of 2, starting at three times the noise level (see the supplementary materials for image parameters). The ratio of the angular resolution between MAGIC and the EVN is 1:580 000.

November 2012, the mean flux above 300 GeV was $(6.08 \pm 0.29) \times 10^{-11} \text{ cm}^{-2} \text{ s}^{-1}$; that is, four times higher than the highest flux during previous observations in 2009/2010. The measured spectrum (Fig. 3) can be described by a simple power law with a differential photon spectral index of $\Gamma = 1.90 \pm 0.04_{\text{stat}} \pm 0.15_{\text{syst}}$ in the energy range of 70 GeV to 8.3 TeV (table S2). Owing to its proximity, the spectrum of IC 310 is only marginally affected by photon-photon absorption in collisions with the extragalactic background light (EBL).

IC 310 harbors a supermassive black hole with a mass of $M = (3^{+4}_{-2}) \times 10^8 M_{\text{sun}}$ (section S1.1), corresponding to an event horizon light-crossing time of $\Delta t_{\text{BH}} = (23^{+34}_{-15}) \text{ min}$. The mass has been inferred from the correlation of black hole masses with the central velocity dispersion of their surrounding galaxies (29, 30). The reported errors are dominated by the intrinsic scatter of the distribution. The same value of the mass is obtained from the fundamental plane of black hole activity (31). The scatter in the fundamental plane for a single measurement is larger and corresponds to a factor of ~ 7.5 .

During 3.7 hours of observations, extreme variability with multiple individual flares was detected (Fig. 4 and figs. S3 and S4). The flare has shown the most rapid flux variations ever observed in extragalactic objects, comparable only to those seen in Mrk 501 and PKS 2155-304. A conservative estimate of the shortest variability time scale in the frame of IC 310 yields $\Delta t/(1+z) = 4.8 \text{ min}$. It is the largest doubling time scale with which the rapidly rising part of the flare can be fitted with a probability $> 5\%$ (fig. S4). The light curve also shows pronounced large-amplitude flickering characterized by doubling time scales down to $\Delta t \sim 1 \text{ min}$. The conservative variability time scale corresponds to 20% of the light travel time across the event horizon, or 60% of it, allowing for the scatter in the dynamical black hole mass measurement.

From the absence of a counter radio jet and the requirement that the proper jet length does not exceed the maximum of the distribution of jet lengths in radio galaxies, the orientation angle was found to be in the range $\theta \sim 10^\circ$ to 20° (section S1.2), and the Doppler factor consistent with $\delta \approx 4$ (32). These values put IC 310 at the borderline between radio galaxies and blazars. The jet power estimated from observations of the large-scale radio jet is $L_j = 2 \times 10^{42} \text{ erg s}^{-1}$, assuming that it contains only electrons, positrons, and magnetic fields in equipartition of their energy densities (section S1.3). For a radiative efficiency of 10%, the Doppler-boosted average luminosity of the jet emission amounts to $0.1\delta^4 L_j \approx 5 \times 10^{43} \text{ erg s}^{-1}$, which is close to the one observed in very high-energy gamma rays. For $\delta \sim 4$, the variability time scale in the co-moving frame of the jet, where it should be larger than $\Gamma_j \Delta t_{\text{BH}}$, is actually close to Δt_{BH} (Fig. 1). A very high value of the Doppler factor is required to avoid the absorption of the gamma rays due to interactions with low-energy synchrotron photons, inevitably co-produced with the gamma rays in the shock-in-jet scenario. The optical depth to pair creation by

the gamma rays can be approximated by $\tau_{\gamma\gamma}(10 \text{ TeV}) \sim 300(\delta/4)^{-6}(\Delta t/1 \text{ min})^{-1}(L_{\text{syn}}/10^{42} \text{ erg s}^{-1})$. Adopting a nonthermal infrared luminosity of $\sim 1\%$ of the gamma-ray luminosity during the flare, the emission region would be transparent to the emission of 10-TeV gamma rays only if $\delta \gtrsim 10$.

For the range of orientation angles inferred from radio observations, the Doppler factor is constrained to a value of $\delta < 6$ (Fig. 1). One can speculate whether the inner jet, corresponding to the unresolved radio core, bends into a just-right orientation angle to produce the needed high

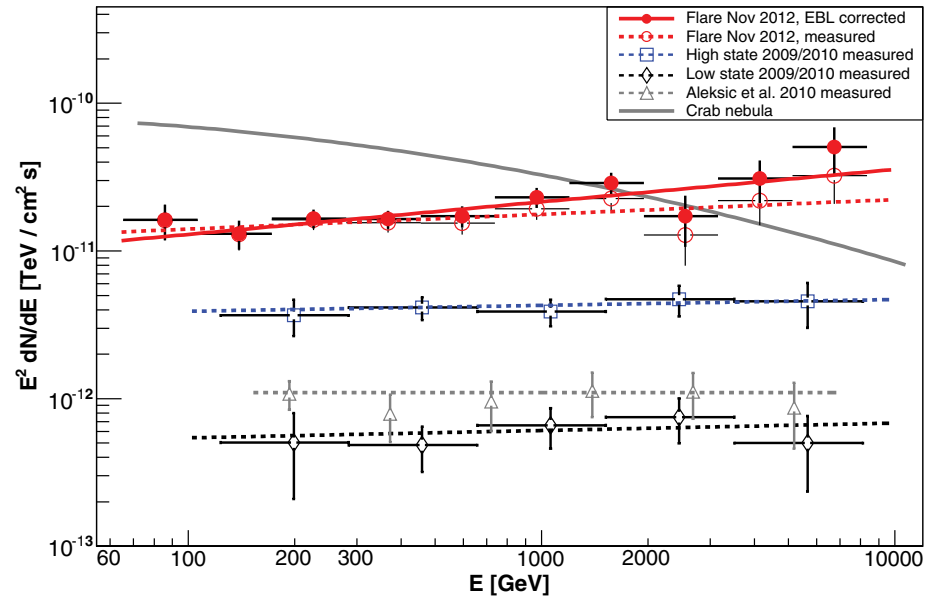


Fig. 3. Average spectral energy distributions during the flare (red) along with previous measurements of IC 310 as observed by MAGIC. We show the results from the high (blue, open squares) and low (black, open markers) states reported in (28) and the average results (gray triangles) from (27) for the whole period. The dashed lines show power-law fits to the measured spectra, and the solid line with solid circles depicts the spectrum corrected for absorption in the extragalactic background light. As a reference, the spectral power-law fit of the Crab Nebula observations from (25) is shown (gray, solid line). Vertical error bars show 1 SD statistical uncertainty. Because of the unfolding procedure, spectral points are correlated. Horizontal error bars show the energy binning.

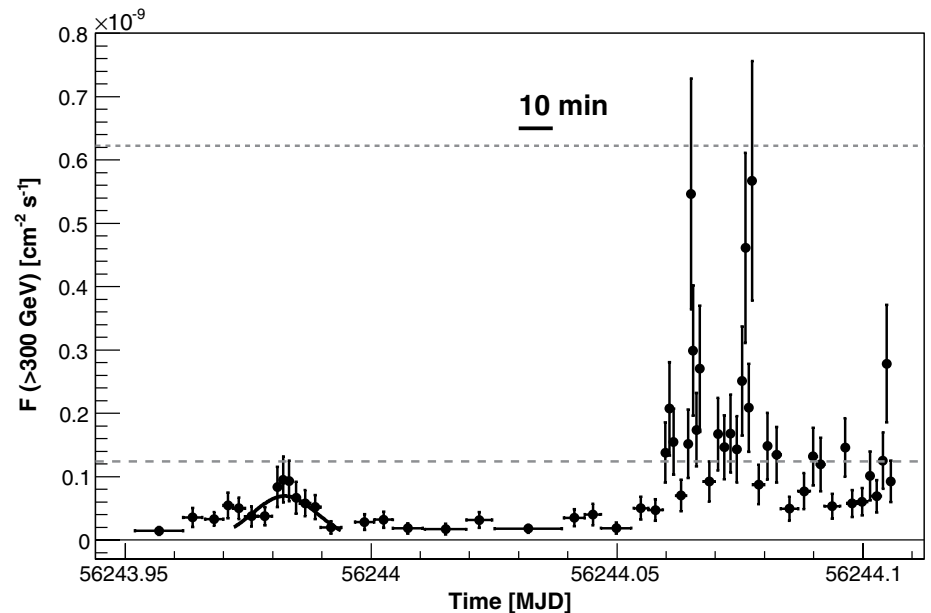


Fig. 4. Light curve of IC 310 observed with the MAGIC telescopes on the night of 12/13 November 2012, above 300 GeV. As a flux reference, the two gray lines indicate levels of 1 and 5 times the flux level of the Crab Nebula, respectively. The precursor flare (MJD 56243.972-56243.994) has been fitted with a Gaussian distribution. Vertical error bars show 1 SD statistical uncertainty. Horizontal error bars show the bin widths.

value of the Doppler factor (section S1.2). The probability of such an alignment seems to be rather low. Moreover, the observed radio jet does not show any signs of a perturbation of its flow direction on the parsec and kiloparsec scales. Because perturbations of the flow direction of the inner jet would later propagate to larger scales, major bends apparently never occurred in the past.

In summary, trying to interpret the data in the frame of the shock-in-jet model meets difficulties. Considering the role of time dilation renders a solution of this problem impossible for any value of Γ_j . Therefore, we conclude that the observations indicate a subhorizon-scale emission region of a different nature.

Possible origins of subhorizon-scale variability

Substructures smaller than the event horizon scale emitting highly anisotropic radiation (to avoid pair absorption) seem to be responsible for the minute-scale flux variations. The possible explanations fall into three categories: (i) mini-jet structures within the jets (33); (ii) jet-cloud interactions, where the clouds may originate from stellar winds (34–36); and (iii) magnetospheric models (37–41), similar to those known from pulsar theory.

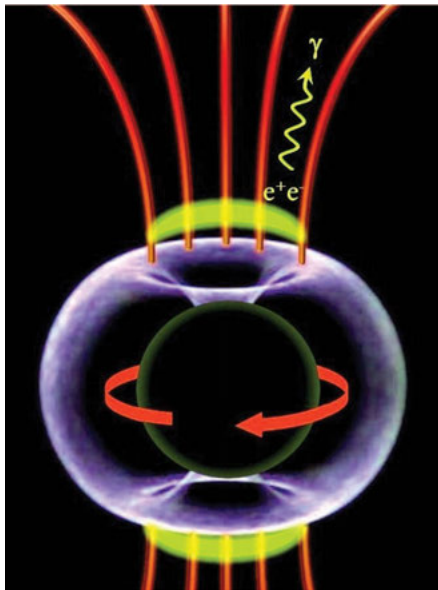


Fig. 5. Scenario for the magnetospheric origin of the gamma rays: A maximally rotating black hole with event horizon r_g (black sphere) accretes plasma from the center of galaxy IC 310. In the apple-shaped ergosphere (blue) extending to $2r_g$ in the equatorial plane, Poynting flux is generated by the frame-dragging effect. The rotation of the black hole induces a charge-separated magnetosphere (red) with polar vacuum gap regions (yellow). In the gaps, the electric field of the magnetosphere has a component parallel to the magnetic field that is accelerating particles to ultrarelativistic energies. Inverse Compton scattering and copious pair production due to interactions with low-energy thermal photons from the plasma accreted by the black hole lead to the observed gamma rays.

According to the mini-jet model (i), plasmoids resulting from magnetic reconnection traveling down the jet with a relativistic speed are responsible for the minute-scale flux variations observed in blazars. The model could help to mitigate the constraints on the bulk Lorentz factor by introducing a larger effective bulk Lorentz factor for the plasmoids. The mechanism also predicts reconnection events from regions outside of the beaming cone $\sim \Gamma_j^{-1}$ that could explain the day-scale flares from the radio galaxy M87 invoking external radiation fields as a target for inverse Compton scattering (33). However, the off-axis mini-jet luminosity depends on $(\Gamma_j \theta)^{-8}$, and the jet power required for IC 310 is two orders of magnitude higher than the one estimated from radio observations (section S3.2). Thus, this model is challenged by the observed high luminosity in IC 310 during the flares.

Substructures smaller than the jet radius may also be introduced by considering interactions between clouds and the jet (ii). The original shock-in-jet model (1) considered this to be the main source of mass entrainment and predicted variability from the process. Recently, more elaborate work on the model has had some success in explaining the variability of M87 by proton-proton collisions due to the bombardment of clouds boiled off of red giants with protons in the jet (36). However, the model is linked to the cloud crossing time of the jet and the proton-proton cooling time, both of which far exceed the event horizon scale. Faster variability could be observed if the cloud gets destroyed, but a strong beaming effect would then be needed to explain the observed luminosities. In another variant, drift acceleration of particles along the trailing shock behind the stellar wind of a star interacting with the jet is considered. This might lead to an extremely anisotropic emission pattern. As mass-losing stars sweep across the jet, passing magnetic field lines pointing to the observer, the postulated accelerated particle beams in their trails become visible for a short time. For IC 310, the emission would have to be confined to within an angle of $\alpha \sim 10^{-5}$ rad to explain the observed variability time scale, requiring a very stable direction of the accelerated particle beams, at a large angle to the jet main thrust. Because two-fluid particle beams are prone to numerous plasma instabilities, the scenario relies on unphysical assumptions.

In magnetospheric models (iii), particle acceleration is assumed to be due to electric fields parallel to the magnetic fields. This mechanism is known to operate in the particle-starved magnetospheres of pulsars, but it could also operate in the magnetospheres anchored to the ergospheres of accreting black holes (Fig. 5). Electric fields can exist in vacuum gaps when the density of charge carriers is too low to warrant their short-cut. The critical charge density for the vacuum gaps is the so-called Goldreich-Julian charge density. Electron-positron pairs in excess of the Goldreich-Julian charge density can be produced thermally by photon-photon collisions in a hot accretion torus or corona surrounding the black

hole. It has also been suggested that particles can be injected by the reconnection of twisted magnetic loops in the accretion flow (39). A depletion of charges from thermal pair production is expected to happen when the accretion rate becomes very low. In this late phase of their accretion history, supermassive black holes are expected to have spun up to maximal rotation. Black holes can sustain a Poynting flux jet by virtue of the Blandford-Znajek mechanism (4). Jet collimation takes place rather far away from the black hole at the scale of the light cylinder beyond $\sim 10r_g$. Gaps could be located at various angles, with the jet axis corresponding to the polar and outer gaps in pulsar magnetospheres leading to fan beams at rather large angles with the jet axis. The gap emission must be highly variable, because gap height and seed particle content depend sensitively on plasma turbulence and accretion rate. For an accretion rate of $\dot{m} \sim 10^{-4}$ (in units of the Eddington accretion rate) and maximal black hole rotation, the gap height in IC 310 is expected to be $h \sim 0.2 r_g$ (40), which is in line with the observations. Depending on the electron temperature and geometry of the radiatively inefficient accretion flow, its thermal cyclotron luminosity can be low enough to warrant the absence of pair creation attenuation in the spectrum of gamma rays. In this picture, the intermittent variability witnessed in IC 310 is due to a runaway effect. As particles accelerate to ultrahigh energies, electromagnetic cascades develop, multiplying the number of charge carriers until their current short-cuts the gap. The excess particles are then swept away with the jet flow, until the gap reappears.

Radio galaxies and blazars with very low accretion rates allow us to obtain a glimpse of the jet formation process near supermassive black holes. The subhorizon variability in combination with the results from direct imaging campaigns invite us to explore analogies with pulsars, where particle acceleration takes place in two stages. In the first stage, particle acceleration occurs in the gaps of a charge-separated magnetosphere anchored in the ergosphere of a rotating black hole, and in a second stage, particle acceleration occurs at shock waves in the force-free wind beyond the outer light cylinder.

REFERENCES AND NOTES

1. R. D. Blandford, A. Königl, *Astrophys. J.* **232**, 34 (1979).
2. L. Maraschi, G. Ghisellini, A. Celotti, *Astrophys. J.* **397**, L5 (1992).
3. C. D. Dermer, R. Schlickeiser, *Astrophys. J.* **416**, 458 (1993).
4. R. D. Blandford, R. L. Znajek, *Mon. Not. R. Astron. Soc.* **179**, 433–456 (1977).
5. S. van Velzen, H. Falcke, *Astron. Astrophys.* **557**, L7 (2013).
6. A. P. Marscher, W. K. Gear, *Astrophys. J.* **298**, 114 (1985).
7. S. S. Doeleman et al., *Science* **338**, 355–358 (2012).
8. I. Vovk, A. Neronov, *Astrophys. J.* **767**, 103 (2013).
9. J. Albert et al., *Astrophys. J.* **685**, L23–L26 (2008).
10. A. Abramowski et al., *Astrophys. J.* **746**, 151 (2012).
11. K. Gebhardt, J. Thomas, *Astrophys. J.* **700**, 1690–1701 (2009).
12. V. A. Acciari et al., *Science* **325**, 444–448 (2009).
13. J. Albert et al., *Astrophys. J.* **669**, 862–883 (2007).
14. F. Aharonian et al., *Astrophys. J.* **664**, L71–L74 (2007).
15. M. C. Begelman, A. C. Fabian, M. J. Rees, *Mon. Not. R. Astron. Soc.* **384**, L19–L23 (2008).
16. In special relativity, the Lorentz and Doppler factors are defined as $\Gamma_j = (1 - \beta^2)^{-1/2}$ and

$\delta = [\Gamma_1(1-\beta\cos\theta)]^{-1}$, respectively, where β denotes the dimensionless shock velocity and θ the angle between the line of sight and the direction of the jet, ignoring the cosmological $(1+z)$ factor. The apparent bolometric luminosity differs from its isotropic co-moving-frame value by the factor δ^4 .

17. M. L. Lister *et al.*, *Astron. J.* **138**, 1874–1892 (2009).
18. C. M. Urry, P. Padovani, M. Stickel, *Astrophys. J.* **382**, 501 (1991).
19. M. Lyutikov, M. Lister, *Astrophys. J.* **7**, 197–203 (2010).
20. G. Ghisellini, F. Tavecchio, *Mon. Not. R. Astron. Soc.* **386**, L28–L32 (2008).
21. D. Giannios, D. A. Uzdensky, M. C. Begelman, *Mon. Not. R. Astron. Soc.* **395**, L29–L33 (2009).
22. F. C. Michel, *Phys. Rev. Lett.* **23**, 247–249 (1969).
23. M. Lyutikov, *Mon. Not. R. Astron. Soc.* **396**, 1545–1552 (2009).
24. J. G. Kirk, I. Mocho, *Astrophys. J.* **729**, 104 (2011).
25. J. Aleksić *et al.*, *Astropart. Phys.* **35**, 435–448 (2012).
26. A. Neronov, D. Semikov, I. Vovk, *Astron. Astrophys.* **519**, L6 (2010).
27. J. Aleksić *et al.*, *Astrophys. J.* **723**, L207–L212 (2010).
28. J. Aleksić *et al.*, *Astron. Astrophys.* **563**, A91 (2014).
29. K. Gültekin *et al.*, *Astrophys. J.* **698**, 198–221 (2009).
30. D. B. McElroy, *Astrophys. J.* **S**, 100, 105 (1995).
31. A. Merloni, S. Heinz, T. di Matteo, *Mon. Not. R. Astron. Soc.* **345**, 1057–1076 (2003).
32. M. Kadler *et al.*, *Astron. Astrophys.* **538**, L1 (2012).
33. D. Giannios, D. A. Uzdensky, M. C. Begelman, *Mon. Not. R. Astron. Soc.* **402**, 1649–1656 (2010).
34. W. Bednarek, R. J. Protheroe, *Mon. Not. R. Astron. Soc.* **287**, L9–L13 (1997).
35. M. V. Barkov, F. A. Aharonian, V. Bosch-Ramon, *Astrophys. J.* **724**, 1517–1523 (2010).
36. M. V. Barkov, V. Bosch-Ramon, F. A. Aharonian, *Astrophys. J.* **755**, 170 (2012).
37. F. M. Rieger, K. Mannheim, *Astron. Astrophys.* **353**, 473 (2000).
38. A. Neronov, F. A. Aharonian, *Astrophys. J.* **671**, 85–96 (2007).
39. A. Y. Neronov, D. V. Semikoz, I. I. Tkachev, *New J. Phys.* **11**, 065015 (2009).
40. A. Levinson, F. Rieger, *Astrophys. J.* **730**, 123 (2011).
41. V. S. Beskin, Y. N. Istomin, V. I. Pavov, *SOVSAT* **36**, 642 (1992).

ACKNOWLEDGMENTS

We thank the Instituto de Astrofísica de Canarias for the excellent working conditions at the Observatorio del Roque de los Muchachos in La Palma. The support of the German BMBF and MPG, the Italian INFN, the Swiss National Fund SNF, and the Spanish MICINN is gratefully acknowledged. This work was also supported by the CPAN CSD2007-00042 and MultiDark CSD2009-00064 projects of the Spanish Consolider-Ingenio 2010 program, by grant 127740 of the Academy of Finland, by the DFG Cluster of Excellence “Origin and Structure of the Universe”, by the Croatian Science Foundation (HrZZ) Projects 09/176, by the University of Rijeka Project 13.12.1.3.02, by the DFG Collaborative Research Centers SFB823/C4 and SFB876/C3, and by the Polish MNiSzW grant 745/N-HESS-MAGIC/2010/0. We thank also the support by DFG WI 1860/10-1. J. S. was supported by ERDF and the Spanish MINECO through FPA2012-39502 and JCI-2011-10019 grants. E. R. was partially supported by the Spanish MINECO projects AYA2009-13036-C02-02 and AYA2012-38491-C02-01 and by the Generalitat Valenciana project PROMETEO/2009/104, as well as by the COST MP0905 action “Black Holes in a Violent Universe.” The European VLBI Network is a joint facility of European, Chinese, South African and other radio astronomy institutes funded by their national research councils. The leading to these results has received funding from the European Commission Seventh Framework Programme (FP/2007-2013) under grant agreement No. 2833393 (RadioNet3). The MAGIC data are archived in the data center at the Port d'Informació Científica (PIC) in Barcelona. The EVN data are available at the Data Archive at the Joint Institute for VLBI in Europe (JIVE).

SUPPLEMENTARY MATERIALS

www.sciencemag.org/content/346/6213/1080/suppl/DC1
Materials and Methods
Figs. S1 to S5
Tables S1 and S2
References (42–69)

16 May 2014; accepted 23 October 2014
10.1126/science.1256183

PLANT SCIENCE

Biosynthesis, regulation, and domestication of bitterness in cucumber

Yi Shang,^{1,2*} Yongshuo Ma,^{1,3*} Yuan Zhou,^{1,4*} Huimin Zhang,^{1,3*} Lixin Duan,⁵ Huiming Chen,⁶ Jianguo Zeng,⁴ Qian Zhou,¹ Shenhao Wang,¹ Wenjia Gu,^{1,7} Min Liu,^{1,3} Jinwei Ren,⁸ Xingfang Gu,¹ Shengping Zhang,¹ Ye Wang,¹ Ken Yasukawa,⁹ Harro J. Bouwmeester,¹⁰ Xiaoquan Qi,⁵ Zhonghua Zhang,¹ William J. Lucas,¹¹ Sanwen Huang^{1,2†}

Cucurbitacins are triterpenoids that confer a bitter taste in cucurbits such as cucumber, melon, watermelon, squash, and pumpkin. These compounds discourage most pests on the plant and have also been shown to have antitumor properties. With genomics and biochemistry, we identified nine cucumber genes in the pathway for biosynthesis of cucurbitacin C and elucidated four catalytic steps. We discovered transcription factors *Bi* (Bitter leaf) and *Bt* (Bitter fruit) that regulate this pathway in leaves and fruits, respectively. Traces in genomic signatures indicated that selection imposed on *Bt* during domestication led to derivation of nonbitter cucurbits from their bitter ancestors.

Plant specialized metabolites play essential roles in mediating interactions between the plant and its environment and constitute a valuable resource in discovery of economically important molecules. In the plant family *Cucurbitaceae*, a group of highly oxygenated tetracyclic and bitter triterpenes, the cucurbitacins, mediated the coevolution between cucurbits and herbivores. They serve either as protectants against generalists or feeding attractants to specialists (1–3). Widely consumed as vegetables and fruits, cucurbits were domesticated from their wild ancestors that had extremely bitter fruits. Drought and temperature stress can increase the bitterness in certain domesticated cultivars, which can affect fruit quality and marketability. Molecular insights into the occurrence and domestication of bitterness in cucurbits remain largely unknown.

Despite their presence in fruits as a negative agricultural taste, cucurbitacins have for centuries been exploited for anti-inflammatory and

hepatoprotective activities, in the form of traditional herbal medicines (4, 5). Bitter fruits and leaves of wild cucurbit plants have been used as a purgative and emetic in India (6). The bitter fruit stem of melon (in Chinese, “gua di”) is prescribed as a traditional hepatoprotective medicine whose effect and usage were well documented in *Ben Cao Gang Mu*, the Chinese Encyclopedia of Botany and Medicines composed by the Ming Dynasty physician Li Shi-Zhen in 1590 CE. Recent studies revealed that cucurbitacins can cause cell-cycle arrest, apoptosis, and growth suppression of cancer cells through the specific inhibition of the Janus kinase–signal transducers and activators of transcription (JAK-STAT) pathway (7, 8). At present, their low concentrations in plants and nonspecific cytotoxicity limit their pharmaceutical applications.

To date, plant metabolic diversification studies (9, 10), as well as recently reported gene clusters in plants [reviewed in (11)], indicate that clustering of functionally-related genes for the biosynthesis of secondary metabolites may well be a common feature of plant genomes. In cucumber, two interacting Mendelian loci were reported to control the bitterness, conferred predominantly by cucurbitacin C (CuC) (3, 12). The *Bi* gene (1) confers bitterness to the entire plant and is genetically associated with an operon-like gene cluster (13), similar to the gene cluster involved in thalianol biosynthesis in *Arabidopsis* (14). Fruit bitterness requires both *Bi* and the dominant *Bt* (Bitter fruit) gene. Nonbitterness of cultivated cucumber fruit is conferred by *bt*, an allele selected during domestication as indicated by population genomics (15). Exploiting these genetic clues, here we report the discovery of 11 genes involved in the biosynthesis, regulation, and domestication of cucumber bitterness.

First committed step in CuC biosynthesis

To identify genetic variants associated with *Bi*, a genome-wide association study was performed

¹Institute of Vegetables and Flowers, Chinese Academy of Agricultural Sciences, Key Laboratory of Biology and Genetic Improvement of Horticultural Crops of the Ministry of Agriculture, Sino-Dutch Joint Laboratory of Horticultural Genomics, Beijing 100081, China. ²Agricultural Genomic Institute at Shenzhen, Chinese Academy of Agricultural Sciences, Shenzhen 518124, China. ³College of Life Sciences, Nanjing Agricultural University, Nanjing 210095, China. ⁴Horticulture and Landscape College, Hunan Agricultural University, National Chinese Medicinal Herbs Technology Center, Changsha 410128, China. ⁵Institute of Botany, Chinese Academy of Sciences, Beijing 100093, China. ⁶Hunan Vegetable Research Institute, Hunan Academy of Agricultural Sciences, Changsha 410125, China. ⁷College of Life Sciences, Wuhan University, Wuhan 430072, China. ⁸Institute of Microbiology, Chinese Academy of Sciences, Beijing 100190, China. ⁹School of Pharmacy, Nihon University, Tokyo 101-8308, Japan. ¹⁰Laboratory of Plant Physiology, Wageningen University, Wageningen 6700, Netherlands. ¹¹Department of Plant Biology, College of Biological Sciences, University of California, Davis, CA 95616, USA.

*These authors contributed equally to this work. †Corresponding author. E-mail: huangsanwen@caas.cn

based on the variation map (15) of 115 diverse cucumber lines (Fig. 1A and table S1). The most significant single-nucleotide polymorphism (SNP) was located within the region where *Bi* had been mapped and resulted in a nonsynonymous

change from cysteine (C) to tyrosine (Y) at residue 393 (C393Y) of the cucumber gene *Csa6G088690* (Fig. 1B). In the 115 lines, this SNP explained the phenotype in all but one line, CG7744. In-depth analysis of the variation map identified a 1-base

pair (bp) deletion at *Csa6G088690* in CG7744 that resulted in a frameshift mutation at the 760th amino acid residue (FS760) (Fig. 1B). Genetic analysis pinpointed that *Csa6G088690* defines the Mendelian *Bi* gene (fig. S1A).

Bi is a member of the oxidosqualene cyclase (OSC) gene family. Phylogenetic analysis showed that *Bi* is the ortholog of cucurbitadienol synthase gene *CPQ* in squash (*Cucurbita pepo*) (16) (fig. S1B). We next used yeast to express *Bi*, as well as its two mutant alleles, C393Y and FS760, to test its biochemical function. As revealed by gas chromatography–mass spectrometry (GC-MS) analysis, formation of cucurbitadienol occurred only in the yeast strain expressing the wild-type gene (Fig. 1C and fig. S1, C and D). Thus, in cucumber, *Bi* encodes a cucurbitadienol synthase that catalyzes the cyclization of 2,3-oxidosqualene into the tetracyclic cucurbitane skeleton, the first committed step of CuC biosynthesis (fig. S1E).

A leaf-specific regulator of *Bi*

To investigate the molecular mechanism in regulating CuC biosynthesis, we searched for naturally occurring mutants and screened an ethylmethane sulfonate–induced cucumber mutant library and subsequently identified two non-bitter mutants (XY-3 and E3-231). The foliage expression level of *Bi* in the natural mutant XY-3

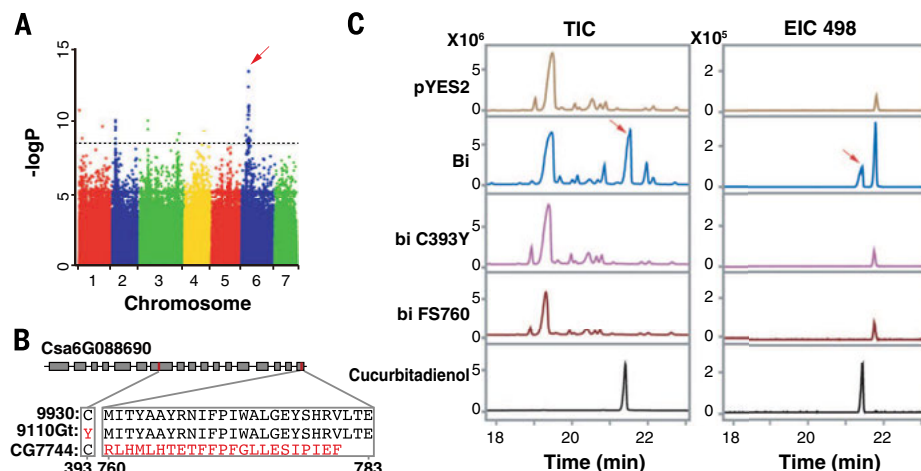
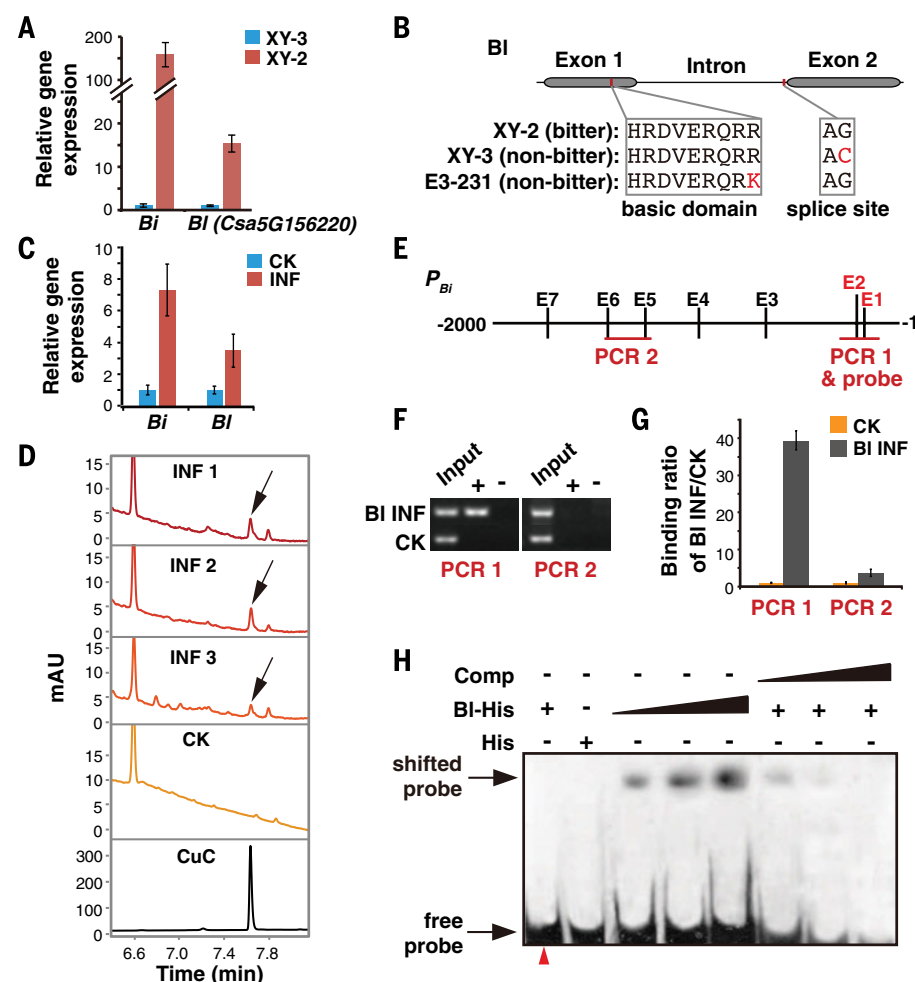


Fig. 1. The *Bi* gene. (A) Genome-wide association study for the bitter foliage trait. Red arrow, most significant association. Scale, $-\log_{10}$ of P value of SNPs. (B) Amino acid alignment between wild *Csa6G088690* and two mutant alleles. (C) GC-MS analysis of extracts prepared from yeast INVSc1 that harbored *Bi*, two mutant alleles (C393Y and FS760), empty vector, or an authentic standard. TIC, total ion chromatograms; EIC 498, extracted ion chromatograms at a mass/charge ratio (m/z) of 498 [M +TMS (trimethylsilyl)].

Fig. 2. The *Bi* gene. (A) Expression of *Bi* (*Csa5G156220*) and *Bi* in nonbitter mutant XY-3 and bitter XY-2 cucumber lines (means \pm SEM, $n = 3$). (B) Sequence alignment between wild *Bi* and two mutated alleles. (C and D) Transient expression of *Bi* in cotyledons complemented the non-bitter phenotype of XY-3. (C) Expression of *Bi* and *Bi* determined 7 days after agroinfiltration (means \pm SEM, $n = 6$). Value obtained from control (CK) was set to 1 and used to obtain relative values for the test sample. INF, sample infiltrated with *Bi*; CK, sample infiltrated with empty vector. (D) Presence or absence of CuC detected by high-performance liquid chromatography (HPLC) analysis of extracts prepared from *Bi* or control infiltrated cotyledons. mAU, milli-arbitrary units. (E) Schematic of the *Bi* promoter region (2000 bp upstream of the start codon). Black vertical lines indicate locations of E-box motifs, and red horizontal lines indicate regions amplified in ChIP assays or used in EMSA. Localization of mutated E-box used in EMSA is indicated in red. (F) ChIP analysis of *Bi* recruitment to the *Bi* promoter region by PCR. ChIP assays conducted with or without (+/–) Myc antibody. INF, sample infiltrated with *Bi*; CK, sample infiltrated with empty vector. (G) qPCR analysis of *Bi* recruitment to the indicated *Bi* promoter region (means \pm SEM, $n = 3$). (H) EMSA showing that *Bi*-His specifically binds, in vitro, to the E-box region within the *Bi* promoter. Lane identified by a red triangle indicates that the E-box element within the probe has been mutated from CANN TG to GANNTG. Comp, competitor (unlabeled probe); His, His-tag; +/–, presence or absence of protein or competitor; closed triangle, increasing amount of protein or competitor.



was reduced to less than 1% of that in the bitter isogenic line XY-2 (Fig. 2A), which indicated that cucurbitacin biosynthesis is disrupted in XY-3. Genomes of XY-2 and XY-3 were resequenced and compared to identify possible mutations. A SNP in the cucumber gene *Csa5G156220* caught our attention, as it encodes a putative basic helix-loop-helix (bHLH) transcription factor (TF) expressed specifically in leaves (table S2). The mutation resides at the splicing site of the predicted intron that likely disrupts proper gene transcription (Fig. 2, A and B).

Resequencing of E3-231 revealed another SNP located within *Csa5G156220* that caused a change from arginine (R) to lysine (K) at the 85th amino acid residue (R85K), which is located inside the basic domain (Fig. 2B). This mutation may affect regulatory ability, as the basic domain is essential for DNA binding ability for bHLH TFs (17). Genetic analyses showed that the mutations in XY-3 and E3-231 are actually two recessive alleles of the same gene (fig. S2A). Increased expression of both *Bi* and *Csa5G156220* was also observed in cucumber plants either exposed to drought stress or treated with the phytohormone ABA (fig. S2, B and C), which indicated that abiotic stress may stimulate the bitterness biosynthesis in cucumber by up-regulation of *Csa5G156220*.

A cucumber cotyledon transient agro-infiltration expression system was developed to further confirm the *in vivo* function of *Csa5G156220* (18). Increasing expression of *Csa5G156220* in XY-3 cotyledons up-regulated expression of *Bi*, which in turn functionally complemented the nonbitter phenotype (Fig. 2, C and D, and fig. S3, A and B). Thus *Csa5G156220* regulates the bitterness biosynthesis in cucumber leaves, and hence, this gene was named *Bl* (Bitter leaf).

Next, we investigated how *Bl* regulates *Bi*. Analysis of the *Bi* promoter region revealed the occurrence of seven E-box (CANNTG) sequences (Fig. 2E), a cis-element to which bHLH TFs could potentially bind (17). Yeast one-hybrid (Y1H) assay and a tobacco transient reporter (luciferase) activation system showed that *Bl* indeed could bind to this promoter (fig. S2, D and E). Chromatin immunoprecipitation (ChIP) assays were performed by using formaldehyde-fixed cotyledons of XY-3 that were transiently expressing a *Bl*-Myc fusion protein. As revealed by the polymerase chain reaction (PCR) products and quantitative real-time PCR (qPCR), *Bl* was selectively recruited to the *Bi* promoter region containing E-box elements (Fig. 2, F and G). Electrophoretic mobility-shift assays (EMSAs) also confirmed selective binding of *Bl* to the E-box elements within the *Bi* promoter (Fig. 2H). Thus, *Bl* regulates cucurbitacin biosynthesis by activating transcription of *Bi* in cucumber leaves.

A cucumber domestication gene

Bt was previously mapped to a 442-kilobase (kb) region on chromosome 5 that harbors 67 predicted genes (15). *Bl* and its two homologs (*Csa5G157220* and *Csa5G157230*) are among these candidates and clustered in an 8.5-kb region (Fig. 3A). As *Bl* positively regulates *Bi* in cucumber leaves, we

considered *Csa5G157230* to be a candidate for *Bt*, given that it is specifically expressed in the fruit of the wild line, PI 183967, consistent with the distribution of bitterness in these plants (Fig. 3A and table S2). In addition, positive correlations were observed between expression levels of *Csa5G157230* and *Bi*, and between fruit bitterness and gene expression in various cucumber lines, especially in those five extremely bitter wild lines (Fig. 3B). These studies established a correlation between *Csa5G157230* expression and accumulation of bitterness in the fruit.

Next, we performed a local association analysis within the 442-kb region to further identify genetic variants associated with the extremely bitter phenotype. This led to finding 11 signals at the regulatory region of *Csa5G157230*, including

10 SNPs and one structural variant, a 699-bp insertion 2195 bp upstream of the *Csa5G157230* start codon (SV-2195). Another variant was also identified at the regulatory region of *Csa5G157230*, a SNP at the 1601 bp upstream of the start codon (SNP-1601), which cosegregated with the *Bt* locus in a large F₂ population (*n* = 1822). In the 115 lines, 22 carrying a homozygous “A” at SNP-1601 all bear nonbitter fruits (table S3). These analyses indicated that selection at the regulatory region of *Csa5G157230* may down-regulate *Csa5G157230* expression in cultivated lines, which results in reduced fruit bitterness.

In some cucumber lines, fruits become bitter under stress conditions. For instance, the fruits of the cucumber line HAN become bitter when plants were grown at a low temperature (18°C

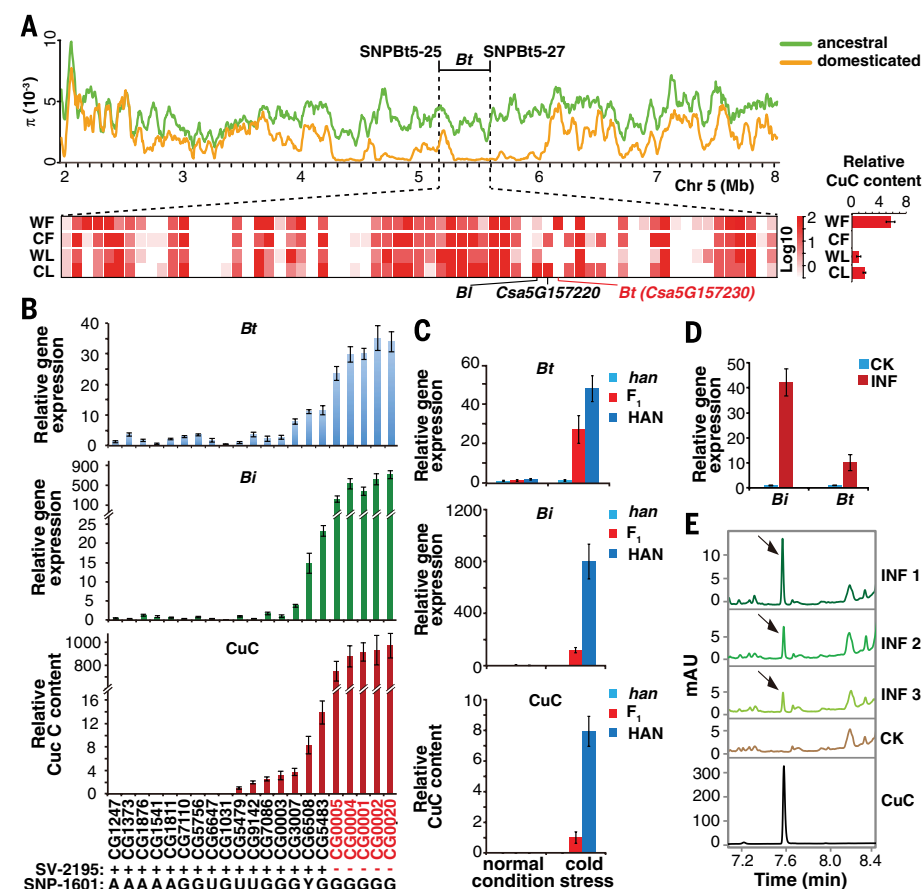


Fig. 3. The *Bt* gene. (A) The *Bt*-mapped region on chromosome 5 overlaps with a large domestication sweep region showing almost zero nucleotide diversity in the domesticated population (top). Differential expression profiles of genes predicted within the *Bt* region illustrated by a gradient in red (bottom). Numeric expression values of predicted genes are shown in table S2. Candidate *Bt* gene is indicated in red. CuC content of wild and cultivated cucumber was compared (means \pm SEM, *n* = 3). WF, wild fruit; CF, cultivated fruit; WL, wild leaf; CL, cultivated leaf. (B) High consistency observed between expression of *Bt*, *Bi*, and the CuC content in 21 cucumber lines, including five extremely bitter lines (means \pm SEM, *n* = 3, indicated in red). Presence or absence of SV-2195 indicated by +/-. Genotype of SNP-1601 (Y: A or G, U: unknown). (C) High consistency among cold-stress treatment: expression of *Bt*, *Bi*, and CuC content in fruit of HAN, *han*, and F₁ individual plants (means \pm SEM, *n* = 3). (D and E) Transient expression of *Bt* in fruit complemented the nonbitter phenotype of cucumber line *XinTaiMiCi-2*. (D) Expression of *Bt* and *Bi* determined 15 days after agroinfiltration (means \pm SEM, *n* = 3). Value obtained from control (CK) was set to 1 and used to obtain relative values for the test sample. INF, sample infiltrated with *Bt*; CK, sample infiltrated with empty vector. (E) Presence or absence of CuC detected by HPLC analysis of extracts prepared from *Bt* or control infiltrated fruits 15 days after agroinfiltration. mAU, milli-arbitrary units.

day, 12°C night), whereas, at a normal temperature (30°C day, 22°C night), the fruits are not bitter. We identified a natural HAN mutant (*han*), whose fruits were nonbitter even under such low temperature conditions. Resequencing both lines revealed a mutation corresponding to SNP-1601 (G in HAN and A in *han*). Genetic analysis showed that SNP-1601 cosegregates with the phenotype (fig. S4A). Our qPCR analysis indicated that SNP1601 is essential for regulating *Bi* expression in response to this environmental factor (Fig. 3C).

To confirm the *in vivo* function of *Csa5G157230*, a fruit transient gene expression system was developed (18). Expression of *Csa5G157230* activated transcription of *Bi* and promoted biosynthesis of CuC in the fruit (Fig. 3, D and E). In parallel experiments, we expressed *Csa5G157230* in XY-3 cotyledons, with the method described above. An increase in CuC content in the infiltrated XY-3 tissue was also observed (fig. S3C), which indicated that the TFs, *Bl*, and *Csa5G157230* have a similar biochemical function and that they control CuC biosynthesis in different organs. Next, we tested whether *Csa5G157230* could directly regulate the *Bi* gene. Here, we expressed the Myc-tagged protein in cotyledons of XY-3 to prepare sufficient material for ChIP assays. Similar to *Bl*, *Csa5G157230* could bind to the E-box elements within the *Bi* promoter (fig. S4, B to F). Taken together, these studies provide strong

support for the hypothesis that *Csa5G157230* is the *Bt* gene, which activates *Bi* and regulates CuC biosynthesis in the fruit.

Nine genes in CuC biosynthetic pathway

To catalyze the formation of CuC, cucurbitadienol has to be further modified with a series of oxidation reactions and acetylation, likely catalyzed by cytochrome P-450 enzymes (P450s) and an acyltransferase (ACT). On chromosome 6, *Bi* co-localizes with four P450 genes (*Csa6G088160*, *Csa6G088170*, *Csa6G088180*, and *Csa6G088710*) and one ACT gene (*Csa6G088700*) within a 35-kb genomic region. Except for *Csa6G088180*, all other genes shared nearly identical expression patterns, with high expression occurring in leaves of line 9930 as well as in fruits of wild line PI 183967 (Fig. 4, A and B). In addition, these co-expressed genes were down-regulated in leaves of XY-3 as compared with XY-2 and in fruits of *han* as compared to HAN, and they were up-regulated in cucumber leaves under ABA treatment or drought stress (Fig. 4, C to F, and table S4). Furthermore, our studies showed that *Bl* and *Bt* could specifically bind to the promoters of these coexpressed genes and could activate their transcription (Fig. 4G, and figs. S5 and S6). Mutation (R85K) within the basic domain of *Bl* appeared to affect its binding ability to the CuC biosynthetic genes (fig. S5, C and D),

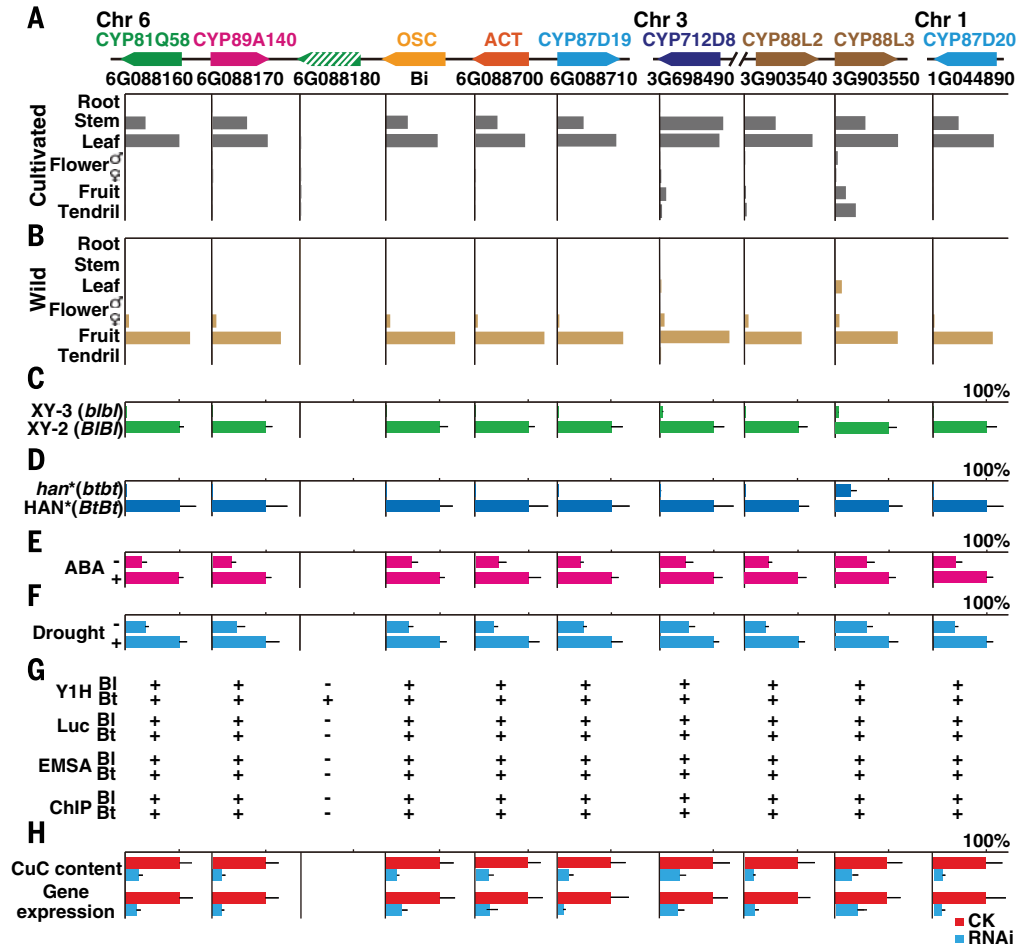
which in turn is likely to result in the nonbitter phenotype of cucumber (E3-231). Although the Y1H assay showed that *Bt* could also interact with the promoter of *Csa6G088180* (fig. S5A), *Bt* cannot activate *Csa6G088180*'s transcription (figs. S5B and S6C).

We failed in a search for the specific P450 within the cluster responsible for oxidizing cucurbitadienol, which suggests there should be other candidates located outside this 35-kb genomic region. We reasoned that other genes would be coexpressed with the *Bi* cluster and coregulated by *Bl* and *Bt*. Therefore, by applying the integrative bioinformatics and molecular biology approach described above, we identify four additional P450 genes (three on chromosome 3, *Csa3G698490*, *Csa3G903540*, and *Csa3G903550*, and one on chromosome 1, *Csa1G044890*) that are coexpressed with the *Bi* cluster and are activated by *Bl* and *Bt* in leaves and fruits, respectively (Fig. 4, A to F, and table S4).

The relation of CuC biosynthesis and these candidate tailoring enzymes was probed by using a transient RNA interference (RNAi) system acting on the bitter cotyledon of the cucumber line 9930 (18). RNAi-mediated target-specific down-regulation of transcripts for all these candidate genes resulted in a decrease in CuC content in the infiltrated cotyledons (Fig. 4H and fig. S7). Thus, *Bl* and *Bt* regulate bitterness formation in leaves and fruits,

Fig. 4. Nine pathway genes that are coordinately regulated. (A and B)

Identification of coexpressed candidate enzymes by analyzing transcriptomic data acquired from cultivar 9930 (A) and wild line PI 183967 (B). Candidate enzymes are indicated with different colors according to their annotations. Low-expressed gene *Csa6G088180* is indicated with hatched green and was used as a negative control in the following analyses. (C to F) Coregulation of candidate genes (means \pm SEM, $n = 3$). Down-regulation of the nine genes in XY-3 as compared with XY-2 (C) and *han* as compared with HAN (D) (asterisk indicates samples prepared from plants grown under low temperature), and up-regulation of the nine genes in the presence of ABA treatment (E) or drought stress (F). (G) Summary of interaction between candidate gene promoter and *Bl* or *Bt*. Luc, luciferase trans-activation assay. (H) Function of enzymes elucidated by transient RNAi assays (means \pm SEM, $n = 6$). RNAi sample in blue; CK in red. Value obtained from control (CK) was set to 1 and used to obtain relative values for the RNAi sample. CK, sample infiltrated with empty vector. More information is provided in figs. S5 to S7.



respectively, by direct transactivation of nine genes (one OSC, seven P450s, and one ACT) involved in the CuC biosynthetic pathway.

Three more steps in CuC biosynthesis

To characterize the biochemical function of these candidate P450s, we expressed each P450 in the engineered yeast (EY10) that accumulates 10 times as much cucurbitadienol as its original strain (18) (fig. S8). No expected product was detected from yeast extract at first (Fig. 5A). However, once an NADPH-cytochrome P450 oxidoreductase gene (*CPR*, *Csa1G423150*) was expressed with candidate P450 in the EY10, we detected a specific product catalyzed by *Csa3G903540* (a member of CYP88 family, located outside the *Bi* cluster) (Fig. 5A). The structure of this purified product (compound 1) was interrogated by nuclear magnetic resonance (NMR) spectroscopy (figs. S9 and S10), which indicated that it was a derivative of cucurbitadienol in which the 19-CH₃ was hydroxylated. The product of *Csa3G903540* was named 19-hydroxy cucurbitadienol.

We continued to search for downstream P450s using this same approach. As revealed by liquid chromatography–mass spectrometry (LC-MS) assays, we identified an expected peak in the yeast expressing *Bi*, *CPR*, *Csa3G903540*, and *Csa6G088160* (a member of CYP81 family, located within the *Bi* cluster) (Fig. 5B). Tandem mass spectrometry (MS/MS) and NMR analysis revealed that a hydroxyl group was transferred to the C-25 position of 19-hydroxy cucurbitadienol and that the double bond between C-24,25 was shifted to the position of C-23,24 (figs. S11 and S12). The product (compound 2) of *Csa6G088160* was named 19,25-dihydroxy cucurbitadienol.

From fresh bitter cucumber leaves, our NMR analysis identified a deacetyl CuC (figs. S13 and S14, compound 3). LC-MS analysis showed that the ACT enzyme (*Csa6G088700*) was able to acetylate this compound to yield CuC (Fig. 5C). These studies indicate that *Csa6G088700* is the enzyme involved in the final step in the CuC biosynthetic pathway.

In summary, we discovered that two TFs regulate nine genes in the CuC biosynthetic pathway and propose a model as to how extremely bitter wild cucumber was domesticated into nonbitter cultivars (fig. S15). As revealed in this study, such regulators must contribute to the highly coordinated and efficient transcription of plant specialized metabolic pathways. The new knowledge on cucurbitacin biosynthesis will open a door for biological manufacturing and engineering of these triterpenoids as anti-tumor drugs, for example, in a manner similar to the biosynthesis of artemisinic acid, the anti-malarial drug precursor (19, 20).

REFERENCES AND NOTES

1. C. P. Da Costa, C. M. Jones, *Science* **172**, 1145–1146 (1971).
2. R. L. Metcalf, R. A. Metcalf, A. M. Rhodes, *Proc. Natl. Acad. Sci. U.S.A.* **77**, 3769–3772 (1980).
3. A. G. Balkema-Boomsma et al., *J. Chem. Ecol.* **29**, 225–235 (2003).
4. X. Chen et al., *Anticancer Drugs* **23**, 777–787 (2012).
5. J. C. Chen, M. H. Chiu, R. L. Nie, G. A. Cordell, S. X. Qiu, *Nat. Prod. Rep.* **22**, 386–399 (2005).
6. N. K. Dwivedi, O. P. Dhariwal, S. Gopala Krishnan, D. C. Bhandari, *Genet. Resour. Crop Evol.* **57**, 443–452 (2010).
7. M. A. Blaskovich et al., *Cancer Res.* **63**, 1270–1279 (2003).
8. N. H. Thoenissen et al., *Cancer Res.* **69**, 5876–5884 (2009).
9. L. Chae, T. Kim, R. Nilo-Poyanco, S. Y. Rhee, *Science* **344**, 510–513 (2014).
10. V. De Luca, V. Salim, S. M. Atsumi, F. Yu, *Science* **336**, 1658–1661 (2012).
11. H. W. Nützmann, A. Osbourn, *Curr. Opin. Biotechnol.* **26**, 91–99 (2014).
12. H. Horie et al., *Jpn. Agric. Res. Q.* **41**, 65–68 (2007).
13. S. Huang et al., *Nat. Genet.* **41**, 1275–1281 (2009).
14. B. Field, A. E. Osbourn, *Science* **320**, 543–547 (2008).
15. J. Qi et al., *Nat. Genet.* **45**, 1510–1515 (2013).
16. M. Shibuya, S. Adachi, Y. Ebizuka, *Tetrahedron* **60**, 6995–7003 (2004).
17. G. Toledo-Ortiz, E. Huq, P. H. Quail, *Plant Cell* **15**, 1749–1770 (2003).
18. Materials and methods are available as supplementary material on Science Online.
19. D. K. Ro et al., *Nature* **440**, 940–943 (2006).
20. C. J. Paddon et al., *Nature* **496**, 528–532 (2013).

ACKNOWLEDGMENTS

We thank J. Bohlmann and D.-K. Ro for critical comments on the manuscript and J.-J. Qi, X.-Z. Lin, T. Lin, X.-F. Xue, and X.-Y. Liu for bioinformatic and experimental assistance. The P450s were named according to the alignment made by D. Nelson (<http://dmelson.uthsc.edu/cytochromeP450.html>). This work was funded by the National Program on Key Basic Research Projects in China (the 973 Program; 2012CB113900), National Science Fund for Distinguished Young Scholars (31225025), National Natural Science Foundation of China (31272161, 31322047, and 31101550), Agricultural Science and Technology Innovation Program, and National Key Technology R&D Program (the 863 Program; 2012BAI29B04). This work was also supported by the Shenzhen Municipal and Dapeng District Governments. The Institute of Flowers and Vegetables has three pending patent applications relating the genes reported in this study. Supplementary materials contain additional data. This whole-genome shotgun project has been deposited at DNA Data Bank of Japan/European Molecular Biology Laboratory/GenBank under the accession ACHRO0000000. The version described in this paper is version ACHRO2000000. Genes reported in the study are deposited in the National Center for Biotechnology Information (NCBI), NIH, with accession numbers (KM655851–KM655862, KM677686–KM677688). RNA-seq data may be obtained from NCBI with the accession number SRA046916.

SUPPLEMENTARY MATERIALS

www.sciencemag.org/content/346/6213/1084/suppl/DC1
Materials and Methods
Figs. S1 to S15
Tables S1 and S8
References (21–24)

25 July 2014; accepted 3 November 2014
10.1126/science.1259215

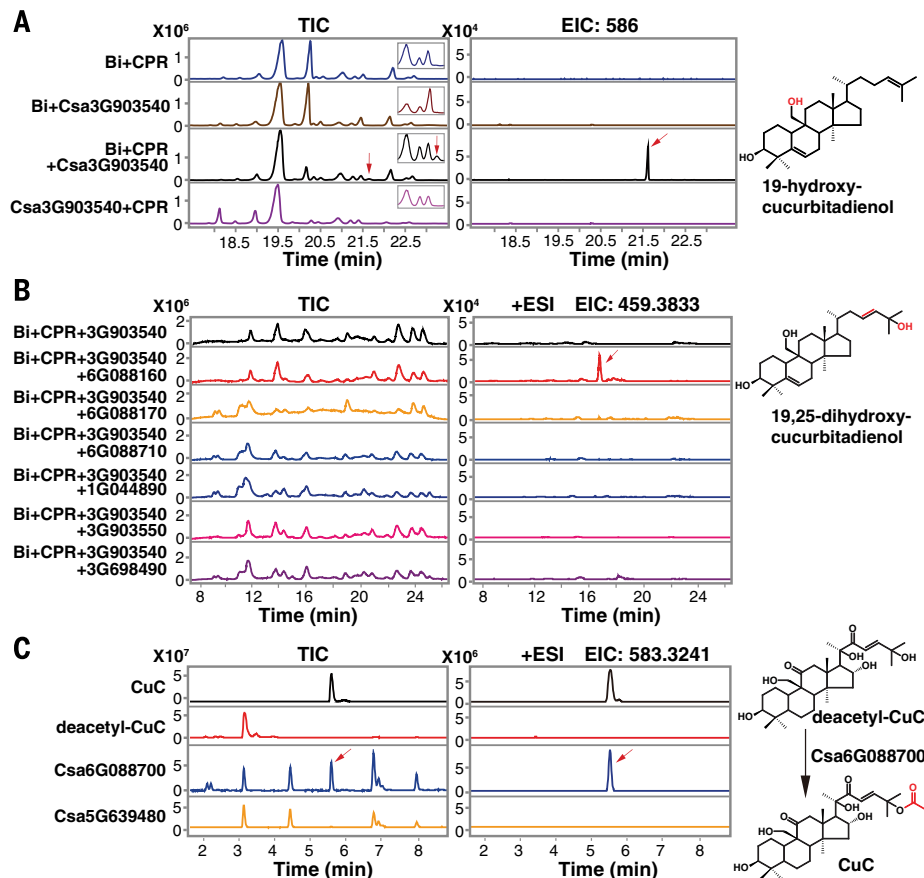


Fig. 5. Three more catalytic steps. (A) GC-MS analysis of putative product (red arrow) generated by *Csa3G903540* in the engineered yeast (EY10). Partial enlarged details are shown as insets. TIC, total ion chromatograms; EIC 586, extracted ion chromatograms at m/z of 586. The product structure (right) was elucidated by NMR (18). (B) Ultra-performance liquid chromatography coupled with quadrupole time-of-flight mass spectrometry (UPLC-qTOF-MS) analysis of yeast extracts with electrospray ionization (ESI) on positive mode. EIC 459.3833, extracted ion chromatograms of the accurate parent ion at m/z of 459.3833. The product (indicated by red arrow) structure was elucidated by MS/MS and NMR (18). (C) UPLC-qTOF-MS analysis of the acetyltransferase catalytic reaction product. Deacetyl-CuC is acetylated by *Csa6G088700*-His in vitro (indicated by red arrow). A leaf-specific ACT (*Csa5G639480*) served as a negative control. Schematic of this biosynthetic pathway from deacetyl-CuC to CuC is shown at right.

REPORTS

PALEOMAGNETISM

Solar nebula magnetic fields recorded in the Semarkona meteorite

Roger R. Fu,^{1*} Benjamin P. Weiss,¹ Eduardo A. Lima,¹ Richard J. Harrison,² Xue-Ning Bai,³ Steven J. Desch,⁴ Denton S. Ebel,⁵ Clément Suavet,¹ Huapei Wang,¹ David Glenn,⁶ David Le Sage,⁷ Takeshi Kasama,⁸ Ronald L. Walsworth,^{6,7} Aaron T. Kuan⁹

Magnetic fields are proposed to have played a critical role in some of the most enigmatic processes of planetary formation by mediating the rapid accretion of disk material onto the central star and the formation of the first solids. However, there have been no experimental constraints on the intensity of these fields. Here we show that dusty olivine-bearing chondrules from the Semarkona meteorite were magnetized in a nebular field of 54 ± 21 microteslas. This intensity supports chondrule formation by nebular shocks or planetesimal collisions rather than by electric currents, the x-wind, or other mechanisms near the Sun. This implies that background magnetic fields in the terrestrial planet-forming region were likely 5 to 54 microteslas, which is sufficient to account for measured rates of mass and angular momentum transport in protoplanetary disks.

Astronomical observations of young stellar objects indicate that early planetary systems evolve through a protoplanetary disk phase in <5 million years (My) following the collapse of their parent molecular clouds (1, 2). Disk evolution on such short time scales requires highly efficient inward transport of mass accompanied by outward angular momentum transfer, which allows disk material to accrete onto the central star while delivering angular momentum out of the protoplanetary system.

The mechanism of this rapid mass and angular momentum redistribution remains unknown. Several proposed processes invoke a central role for nebular magnetic fields. Among these, the magnetorotational instability (MRI) and magnetic braking predict magnetic fields with intensities of ~100 μ T at 1 astronomical unit (AU) in the active layers of the disk (3, 4). Alternatively, transport by magnetocentrifugal wind (MCW) requires large-scale, ordered magnetic fields stronger than ~10 μ T at 1 AU. Finally, nonmagnetic effects such as the baroclinic and Goldreich-Schubert-Fricke instabilities may be the dominant mechanism of angular momentum transport in the absence of sufficiently strong magnetic fields

(5). Direct measurement of magnetic fields in the planet-forming regions of the disk can potentially distinguish among and constrain these hypothesized mechanisms.

Although current astronomical observations cannot directly measure magnetic field strengths in planet-forming regions [(6, 7); supplementary text], paleomagnetic experiments on meteoritic materials can potentially constrain the strength of nebular magnetic fields. Chondrules

are millimeter-sized lithic constituents of primitive meteorites that formed in transient heating events in the solar nebula. If a stable field was present during cooling, they should have acquired a thermoremanent magnetization (TRM), which can be characterized via paleomagnetic experiments. Besides assessing the role of magnetic fields in disk evolution, such paleomagnetic measurements would constrain the currently unknown mechanism of chondrule formation.

Chondrules likely constituted a sizable fraction of the mass of asteroids and terrestrial planet precursors and may have facilitated the accretion of the first planetesimals (8, 9). The formation of chondrules therefore very likely represents a key stage in the evolution of the early solar system. The ambient magnetic field strength is a distinguishing characteristic among chondrule formation models. The x-wind model implies strong stellar fields of >80 to 400 μ T (10). In contrast, magnetic fields in the nebular shock and planetesimal collision models are likely considerably lower than 100 μ T (11, 12).

Previous paleomagnetic measurements of individual chondrules have focused mostly on the Allende CV chondrite (13). However, owing to extensive aqueous alteration on the CV parent body, magnetic phases in Allende chondrules are secondary and do not retain pre-accretionary magnetization [i.e., magnetization acquired during the last heating of chondrules in the nebula and before the accretion of the meteorite's parent body; (14)]. Reliable recovery of preaccretionary magnetization requires samples that have avoided appreciable postaccretionary remagnetization processes.

Among the most pristine known meteorites is the Semarkona LL3.00 ordinary chondrite. We conducted paleomagnetic studies on Semarkona,

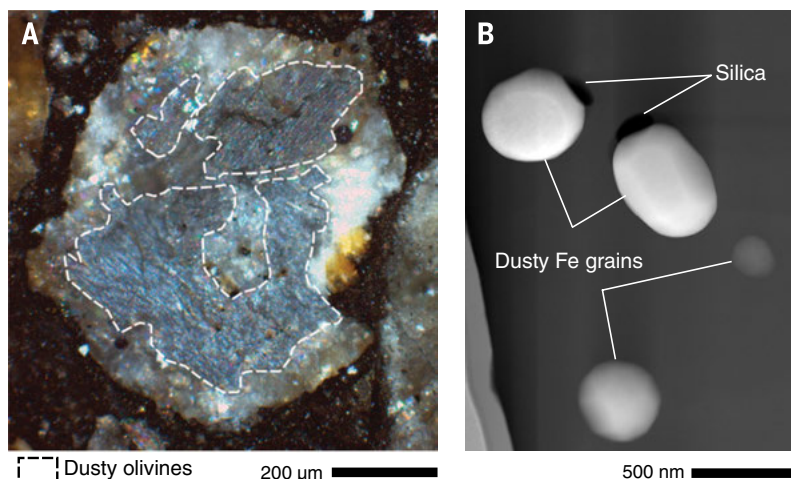


Fig. 1. Dusty olivine-bearing chondrules from the Semarkona meteorite. (A) Optical photomicrograph of chondrule DOC4 showing the location of dusty olivine grains. Image taken in reflected light with crossed polarizers. (B) Annular dark-field scanning transmission electron microscope (STEM) image of four dusty olivine Fe grains from chondrule DOC5. Brightness in image reflects column-averaged atomic number; darker grains are smaller in size, implying a higher relative abundance of olivine at their location and hence a lower mean atomic number. The euhedral morphology and chemical homogeneity of the Fe grains is apparent, which indicate the lack of secondary recrystallization and alteration. Such Fe grains are the primary carriers of preaccretionary magnetization in Semarkona chondrules.

¹Department of Earth, Atmospheric and Planetary Sciences, Massachusetts Institute of Technology (MIT), Cambridge, MA, USA. ²Department of Earth Sciences, University of Cambridge, Cambridge, UK. ³Hubble Fellow, Harvard-Smithsonian Center for Astrophysics, Cambridge, MA, USA. ⁴School of Earth and Space Exploration, Arizona State University, Tempe, AZ, USA. ⁵Department of Earth and Planetary Sciences, American Museum of Natural History (AMNH), New York, NY, USA. ⁶Harvard-Smithsonian Center for Astrophysics, Cambridge, MA, USA. ⁷Department of Physics, Harvard University, Cambridge, MA, USA. ⁸Center for Electron Nanoscopy, Technical University of Denmark, Kongens Lyngby, Denmark. ⁹School of Engineering and Applied Science, Harvard University, Cambridge, MA, USA. *Corresponding author. E-mail: rogerfu@mit.edu

focusing in particular on dusty olivine-bearing chondrules (Fig. 1). Dusty olivine crystals consist of submicrometer-sized grains of nearly pure body-centered cubic (bcc) Fe (kamacite) embedded in forsteritic olivine (15). Such olivine grains are found in approximately 1 in 10 chondrules in ordinary chondrites.

Because of their unique compositional and magnetic properties, dusty olivine grains are expected to retain preaccretional magnetization. The small grain size of dusty olivine metal implies that most are in the single domain (SD) or single vortex (SV) states, which can retain stable magnetization over the history of the solar system (16–19). Further, the Ni-poor composition (Ni <2 weight %) of dusty olivine metal precludes metamorphic recrystallization (15, 20). The domain states of dusty olivine metals imply very high coercivities ranging up to >200 mT, as confirmed by our demagnetization experiments (see below). The magnetization of grains with such high coercivities should not have been much altered by the low shock pressures likely experienced by Semarkona [4 to 10 GPa (21, 22)]. Finally, the low porosities of the surrounding olivine crystals have protected metal from aqueous alteration (Fig. 1B).

The distinctive, high coercivities of dusty olivine grains allow for the isolation of their remanent magnetization during alternating field

(AF) demagnetization as larger (10 to 100 μm) mesostasis metal grains are expected to demagnetize at AF levels <50 mT (23). Furthermore, because the postaccretional peak metamorphic temperature of Semarkona was likely only 200° to 260°C (24, 25), preaccretional remanence in dusty olivine metals should be isolated upon laboratory (1 hour duration) thermal demagnetization to <450°C assuming that metamorphism lasted ~5 My (16, 19). In summary, no known postaccretional process is likely to have compromised preaccretional remanent magnetization in Semarkona dusty olivines; strong-field AF demagnetization or thermal demagnetization above ~450°C is expected to isolate the preaccretional component of magnetization.

We isolated eight dusty olivine-bearing chondrules from two 15 mm by 10 mm by 150 μm -thick sections of Semarkona provided by the American Museum of Natural History (AMNH). Both sections contain fusion crust along one edge. We also extracted 5 non-dusty olivine-bearing chondrules and 29 bulk (i.e., mixed matrix and chondrule) samples to characterize any postaccretional overprints. All extracted samples are mutually oriented to within 5°. Owing to their weak moments [natural remanent magnetization (NRM) ranging between 10^{-10} and 3×10^{-12} A·m² before demagnetization], chondrules

were measured with the superconducting quantum interference device (SQUID) microscope (26, 27) at the MIT Paleomagnetism Laboratory (Fig. 2). Supporting magnetic imaging measurements with higher spatial resolution were performed with a nitrogen-vacancy (NV) quantum diamond microscope (supplementary text).

Bulk samples were subjected to AF demagnetization up to 85 to 145 mT or thermal demagnetization up to 580°C. We identified three unidirectional postaccretional overprints in our Semarkona samples: two low coercivity (LCa and LCb) and one medium coercivity (MCA) components. Twenty bulk samples carry the LCa overprint blocked up to between 4.5 and 13 mT (Fig. 3). This component is present in both fusion crust material and meteorite interior samples, indicating that it was acquired after arrival on Earth. Removal of the LCa magnetization during thermal demagnetization to only 70°C indicates that it is likely a viscous remanent magnetization (VRM) acquired during long-term exposure to the Earth's field.

In contrast, the MCA overprint is only present in samples within 4.7 mm of the fusion crust. The mean paleointensity of this component based on the isothermal remanent magnetization (IRM) and anhysteretic remanent magnetization (ARM) normalization methods (76 μT) is within uncertainty of the Earth's magnetic field. We conclude

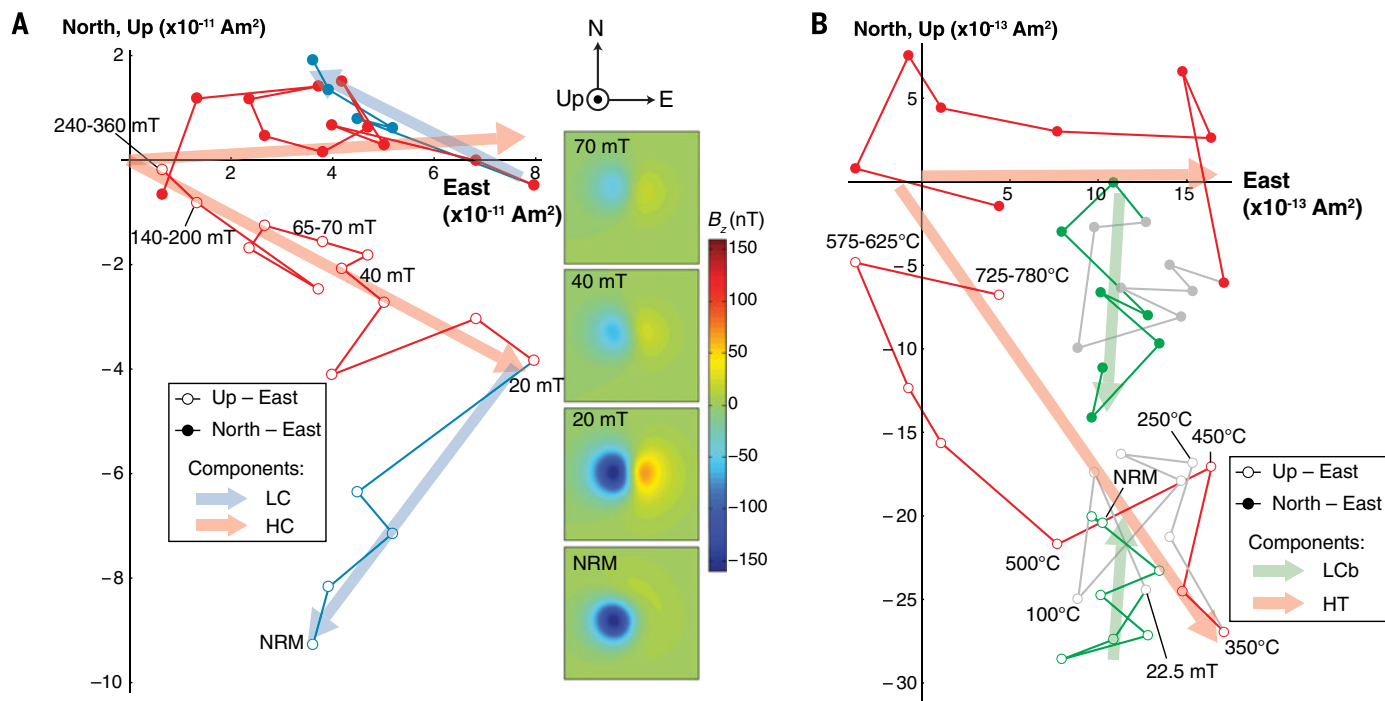


Fig. 2. AF and thermal demagnetization of single dusty olivine-bearing chondrules measured with SQUID microscopy. Orthogonal projection diagrams showing the evolution of the natural remanent magnetization (NRM) of two chondrules upon progressive demagnetization. Open and solid circles indicate the projection of the NRM vector onto the vertical (up-east) and horizontal (north-east) planes, respectively. **(A)** AF demagnetization of DOC1 reveals a low coercivity (LC) overprint removed by 20 mT and higher coercivity (HC) magnetization that persists to >290 mT while decaying in magnitude toward the origin. Insets show associated magnetic field maps

measured with the SQUID microscope at the indicated demagnetization levels where positive (red) field values are in the up direction. The stable directionality and steady decay of the magnetization can be seen during AF application above 20 mT. **(B)** Mixed AF and thermal demagnetization of DOC8 shows the removal of the postaccretional LCa overprint by 20.0 mT (green points), a stationary moment between room temperature and ~400°C (gray), and an origin-trending high temperature (HT) component removed by 780°C (red). Steps above 40 mT or 575°C have been averaged to suppress noise.

that the MCa component was acquired during heating from atmospheric passage. Finally, a small subset of seven samples from one edge of our Semarkona section carry the LCb overprint, which is completely removed by AF demagnetization up to between 10.5 and 30 mT. The high intensity of the LCb component (NRM to saturation IRM ratio of 0.23) suggests that it was acquired during exposure to artificial magnetic fields. Only two dusty olivine-bearing chondrules carried the LCb overprint, which was fully removed upon AF application to 20 mT. To summarize, all samples >1.0 mm from the fusion crust, which include all dusty olivine-bearing chondrules, do not carry any postaccretional remagnetization other than the LCa, MCa, and LCb components. These overprints, if present, are readily identified and removed via AF cleaning.

Eight dusty olivine-bearing chondrules were subjected to AF and thermal demagnetization up to 290 to 420 mT or 780°C. Six of these were found to carry a high coercivity (HC) or high temperature (HT) component of magnetization. We argue based on seven lines of evidence that these HC/HT components are preaccretional TRMs (supplementary text). (i) HC/HT components decay to the origin upon demagnetization, which is the expected behavior of primary magnetization (Fig. 2). (ii) The HC/HT magnetization directions in the six chondrules are collectively random, passing the conglomerate test at the 95% confidence level [Fig. 3; (28)]. No HC/HT component is oriented in the direction of any of the postaccretional overprints. (iii) The HC magnetizations in chondrules DOC3 and DOC4, which were each partitioned into two subsamples, are unidirectional within each chon-

drule and inconsistent with random magnetizations at the 99% confidence level. Such uniformity is expected of a TRM acquired by individual chondrules cooling in the solar nebula because the field should be uniform across the submillimeter scale of each sample (14). (iv) The blocking temperature range of the HT component (350° to 750°C) agrees closely with that expected of a preaccretional magnetization that was partially demagnetized for ~5 My at ~200°C [Fig. 2B; (16, 19)], which is the estimated metamorphic temperature for Semarkona on the LL parent body (16, 25). (v) Magnetic field maps of dusty olivine-bearing chondrules confirm that the HC magnetization is carried by dusty olivines, which formed in the nebula and are expected to retain preaccretional magnetization as outlined above. (vi) The magnetization direction acquired during cooling for a spinning chondrule is expected to be parallel to its rotation axis (29). The close alignment between the HC directions and the short axes of our chondrules, which are likely related to the rotation axis (supplementary text), are nonrandom at the 98% confidence level, suggesting that HC/HT magnetizations were indeed acquired parallel to the spin axis. (vii) The coercivity spectrum of the HC component of dusty olivine-bearing chondrules is very similar to that of an ARM and dissimilar to that of an IRM, which suggests that the HC component was acquired as a TRM (30). We therefore conclude with high confidence that the HC/HT magnetizations observed in dusty olivine-bearing chondrules are TRMs acquired in the solar nebula.

TRM acquisition experiments on analogs of dusty olivine chondrules have shown that the ARM normalization method potentially produces

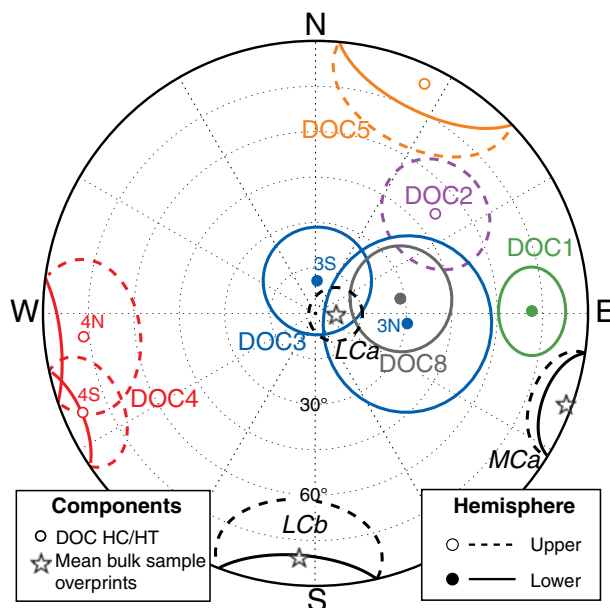
paleointensities accurate to ~40% [2σ; (30)]. Assuming that the five chondrules with recovered paleointensities formed in similar magnetic field conditions in the nebula, our nominal ARM paleointensities for six dusty olivines yielded a mean value of 27 μT. The morphology of chondrules (31) and the apparent correspondence between HC magnetization directions and the short axes of our chondrule samples (see above paragraph) strongly suggest that chondrules were rotating during remanence acquisition in the solar nebula. In the case of rotation around a single axis, which is the expected motion inherited from cooling of a viscous droplet, the true mean field intensity should have been greater than our experimental paleointensity by a factor of 2 (supplementary text). Meanwhile, precession of the chondrule's rotation axis would imply a multiplicative factor of up to 4. However, given the high inferred rotation rates of chondrules (>50 s⁻¹), the magnitudes of effects that may lead to precession are comparatively small. Therefore, we adopt nonprecessing rotation as the most likely state of cooling chondrules and recommend a value of 54 ± 21 μT (2σ) for the ambient nebular field strength. Although unlikely, if chondrules did not rotate or precessed strongly during remanence acquisition, the corresponding estimated ambient field strength would be 27 ± 8 μT or 108 ± 42 μT (2σ), respectively.

Our paleointensity constrains the magnetic field environment during the last time the chondrule cooled through the 765° to 350°C blocking temperature range of the HC/HT component, which likely was the chondrule-forming event. Our recommended paleointensity is significantly lower than the >80 to 400 μT expected for chondrules purportedly formed in the x-wind model (10). Furthermore, mechanisms that invoke intense electric currents such as magnetic reconnection flares and current sheets predict strong fields >500 μT during chondrule heating (32). The short-circuit instability may also imply similarly strong fields at high temperature (33), although the decay of field strength below 765°C has not been studied in detail. In contrast, assuming that magnetic fields inherited from the collapsing molecular cloud were on the order of 10 μT (12), nebular shocks, which may enhance the ambient magnetic field by a factor of <10, would result in paleointensities of <100 μT (17). Meanwhile, planetesimal collisions would likely not perturb the background field. Therefore, nebular shocks and planetesimal collisions are the chondrule formation models most consistent with our measured paleointensities.

Adopting nebular shocks and planetesimal collisions as the most likely origins of chondrules, background magnetic fields in the nebula may have been amplified by a factor between 1 and 10 during chondrule formation. We therefore infer that background magnetic fields in the solar nebula were between 5 and 54 μT (17). Assuming Semarkona chondrules formed near 2.5 AU, which is the present-day location of S-type asteroids (34), the vertical distribution of dust in the nebula strongly suggests that

Fig. 3. Magnetization directions in Semarkona chondrules and bulk samples.

Equal area stereonet projection diagram where colored points denote high coercivity or high temperature (HC/HT) magnetization in individual dusty olivine-bearing sample or subsamples. Circles indicate the associated maximum angular deviation (MAD) obtained from principle components analysis. Each color represents a single chondrule with chondrules DOC3 and DOC4 having two subsamples each. Black stars and associated ovals represent the mean directions of the three postaccretional overprints identified from bulk samples and their 95% confidence intervals. Open symbols represent the upper hemisphere; solid symbols represent the lower hemisphere. The wide scatter of the HC/HT magnetizations, the unidirectionality of subsamples from DOC3 and DOC4, and their noncorrespondence to the directions of postaccretional overprints provide strong evidence for a preaccretional origin of the HC/HT magnetizations in dusty olivine-bearing chondrules.



chondrule formation took place in the weakly ionized “dead zone,” which contains gas poorly coupled to local magnetic fields and occurs within ~ 3 gas scale heights of the midplane (35). Our measurements therefore indicate that a substantial magnetic field [yet still well below the $\sim 400 \mu\text{T}$ equipartition field strength (3)] existed in the dead zone, potentially as a result of fields inherited from the collapse of the solar system’s parent molecular cloud. Given our measured field strengths, mass accretion driven by the MRI or magnetic braking at 2.5 AU would have been $<0.04 \times 10^{-8}$ to $3.5 \times 10^{-8} M_{\text{sun}} \text{ year}^{-1}$, where M_{sun} is the Sun’s mass (supplementary text). Meanwhile, the MCW model would predict mass accretion rates of 0.3×10^{-7} to $30 \times 10^{-7} M_{\text{sun}} \text{ year}^{-1}$ or less. The inferred age of Semarkona chondrules is 2 to 3 My after the first calcium aluminum-rich inclusions (36). Given that protoplanetary disks are observed to have accretion rates of 10^{-9} – $10^{-7} M_{\text{sun}} \text{ year}^{-1}$ at 2 to 3 My after collapse of their parent molecular clouds (2), both magnetic mechanism could fully account for the expected accretion rates. This suggests that magnetic fields govern the observed rapid transformation of protoplanetary disks into planetary systems around Sun-like stars.

REFERENCES AND NOTES

- K. E. Haisch Jr., E. A. Lada, C. J. Lada, *Astrophys. J.* **553**, L153–L156 (2001).
- L. Hartmann, N. Calvet, E. Gullbring, P. D’Alessio, *Astrophys. J.* **495**, 385–400 (1998).
- M. Wardle, *Astrophys. Space Sci.* **311**, 35–45 (2007).
- X.-N. Bai, J. Goodman, *Astrophys. J.* **701**, 737–755 (2009).
- N. J. Turner, S. Fromang, C. Gammie, H. Klahr, G. Lesur, M. Wardle, X.-N. Bai, in *Protostars and Planets VI* (Univ. of Arizona Press, Tucson, AZ, 2014).
- R. M. Crutcher, *Annu. Rev. Astron. Astrophys.* **50**, 29–63 (2012).
- I. W. Stephens et al., *Nature* **514**, 597–599 (2014).
- J. N. Cuzzi, R. C. Hogan, K. Shariff, *Astrophys. J.* **687**, 1432–1447 (2008).
- T. Nakamura et al., *Science* **333**, 1113–1116 (2011).
- F. H. Shu, H. Shang, T. Lee, *Science* **271**, 1545–1552 (1996).
- S. J. Desch, H. C. Connolly Jr., *Meteorit. Planet. Sci.* **37**, 183–207 (2002).
- S. J. Desch, T. C. Mouschovias, *Astrophys. J.* **550**, 314–333 (2001).
- N. Sugiura, D. W. Strangway, *Proc. Lunar Planet. Sci. Conf. 15th*, C729 (1985).
- R. R. Fu, E. A. Lima, B. P. Weiss, *Earth Planet. Sci. Lett.* **404**, 54–66 (2014).
- H. Leroux, G. Libourel, L. Lemelle, F. Guyot, *Meteorit. Planet. Sci.* **38**, 81–94 (2003).
- M. Uehara, N. Nakamura, *Earth Planet. Sci. Lett.* **250**, 292–305 (2006).
- S.-C. L. L. Lappe et al., *Geochim. Geophys. Geosyst.* **12**, Q12235 (2011).
- M. Winkler, K. Fabian, F. Heider, *J. Geophys. Res.* **102**, 22695 (1997).
- I. Garrick-Bethell, B. P. Weiss, *Earth Planet. Sci. Lett.* **294**, 1–7 (2010).
- R. J. Reisener, J. I. Goldstein, in *Lunar Planet. Sci. Conf. XXX* (Lunar and Planetary Institute, Houston, TX, 1999), pp. 1868.
- D. Stöffler, K. Keil, E. R. D. Scott, *Geochim. Cosmochim. Acta* **55**, 3845 (1991).
- R. R. Fu et al., *Science* **338**, 238–241 (2012).
- J. Gattacceca et al., *Meteorit. Planet. Sci.* **49**, 652–676 (2014).
- C. M. O. D. Alexander, D. J. Barber, R. Hutchison, *Geochim. Cosmochim. Acta* **53**, 3045–3057 (1989).
- G. D. Cody et al., *Earth Planet. Sci. Lett.* **272**, 446–455 (2008).
- B. P. Weiss, E. A. Lima, L. E. Fong, F. J. Baudenbacher, *J. Geophys. Res.* **112**, B09105 (2007).
- E. A. Lima, B. P. Weiss, R. R. Fu, A. C. Bruno, in *AGU Fall Meeting* (San Francisco, 2013), vol. GP43B-07.
- G. S. Watson, *Mon. Not. R. Astron. Soc.* **7**, 160–161 (1956).
- C. Suavet, J. Gattacceca, P. Rochette, L. Folco, *Geology* **39**, 123–126 (2011).
- S.-C. L. L. Lappe, J. M. Feinberg, A. Muxworthy, R. J. Harrison, *Geochim. Geophys. Geosyst.* **14**, 2143–2158 (2013).
- H. Miura, T. Nakamoto, M. Doi, *Icarus* **197**, 269–281 (2008).
- E. H. Levy, S. Araki, *Icarus* **81**, 74–91 (1989).
- C. P. McNally, A. Hubbard, M.-M. Mac Low, D. S. Ebel, P. D’Alessio, *Astrophys. J.* **767**, L2 (2013).
- S. J. Bus, R. P. Binzel, *Icarus* **158**, 146–177 (2002).
- X.-N. Bai, *Astrophys. J.* **739**, 50 (2011).
- S. Mostefaoui et al., *Meteorit. Planet. Sci.* **37**, 421–438 (2002).

ACKNOWLEDGMENTS

We thank S. A. Balbus, A. J. Brearley, H. C. Connolly, A. M. Hughes, B. C. Johnson, J. L. Kirschvink, M. Mac Low, G. J. MacPherson, M. I. Petaev, D. D. Sasselov, H. E. Schlichting, J. B. Simon, N. Turner, and B. Zanda for discussions that improved the manuscript. We also thank J. Gross, S. Wallace, and Z. I. Balogh for help with SEM and STEM sample analyses and acknowledge S.-C. L. L. Lappe, N. S. Church, S. Russell, M. Uehara, and N. Nakamura for pioneering work on the magnetism of dusty olivines. We thank T. F. Peterson for supporting critical

instrumentation and analysis costs. R.R.F., B.P.W., E.A.L., S.J.D., and C.S. thank the NASA Origins Program, while R.R.F. and B.P.W. thank the U.S. Rosetta Project, Jet Propulsion Laboratory for support. R.R.F. thanks the NSF Graduate Research Fellowship Program, and C.S. thanks the NASA Lunar Science Institute and the NASA Solar System Exploration and Research Virtual Institute for support. R.J.H. and T.K. thank the European Research Council under the European Union’s Seventh Framework Programme and the Leverhulme Trust for support. X.N.B. acknowledges support from NASA through the Hubble Fellowship. D.G., D.L.S., and R.L.W. thank the Defense Advanced Research Projects Agency QuASAR program and the NSF for support.

SUPPLEMENTARY MATERIALS

www.sciencemag.org/content/346/6213/1089/suppl/DC1
Supplementary Text
Figs. S1 to S12
Tables S1 to S4
References (37–125)
Database S1

30 June 2014; accepted 31 October 2014
Published online 13 November 2014;
10.1126/science.1258022

MATERIALS SCIENCE

Dynamic mechanical behavior of multilayer graphene via supersonic projectile penetration

Jae-Hwang Lee,^{1,2*} Phillip E. Loya,¹ Jun Lou,¹ Edwin L. Thomas^{1*}

Multilayer graphene is an exceptional anisotropic material due to its layered structure composed of two-dimensional carbon lattices. Although the intrinsic mechanical properties of graphene have been investigated at quasi-static conditions, its behavior under extreme dynamic conditions has not yet been studied. We report the high-strain-rate behavior of multilayer graphene over a range of thicknesses from 10 to 100 nanometers by using miniaturized ballistic tests. Tensile stretching of the membrane into a cone shape is followed by initiation of radial cracks that approximately follow crystallographic directions and extend outward well beyond the impact area. The specific penetration energy for multilayer graphene is ~ 10 times more than literature values for macroscopic steel sheets at 600 meters per second.

Graphene, the atomic monolayer building block of graphite, is known for its exceptionally high intrinsic strength and stiffness arising from the two-dimensional (2D) hexagonal lattice of covalently bonded carbon atoms. Recently, graphene’s in-plane Young’s modulus (Y_0) was measured to be more than 1.0 TPa using atomic force microscope nanoindentation (1). Because tensile mechanical stresses in a material cannot be transmitted faster than the speed of sound [$c \sim (Y/\rho)^{1/2}$, where ρ is the density of the material], the nonequilibrium local stress arising from the inertial effect becomes important under dynamic conditions accompanying high-strain-rate, predominantly

tensile loading (2). In this regard, the relatively low density ($\sim 2200 \text{ kg m}^{-3}$) of graphene (3), along with its high modulus, leads to a superior in-plane speed of sound ($c_0 \sim 22.2 \text{ km s}^{-1}$), implying that concentrated stresses applied under extreme conditions can rapidly be delocalized.

Nanoindentation has served as an effective technique to study the tensile mechanical properties of monolayer graphene. It is inherently a low-speed test ($< 1 \text{ m s}^{-1}$), but strain rates can reach $\sim 10^5$ to 10^6 s^{-1} for very thin samples (4), whereas most high-speed, high-strain-rate mechanical characterization techniques, such as split-Hopkinson pressure bar (5) and ballistic tests (6), are inappropriate for testing very thin specimens. To address high-speed and high-strain-rate tensile-dominated penetration of thin films, we improved our laser-induced projectile impact test (LIPIT) (7). In this advanced LIPIT (or “ α -LIPIT”), a single micrometer-size solid silica sphere (or “ μ -bullet”) is fired at a high speed

¹Department of Materials Science and NanoEngineering, Rice University, Houston, TX 77005, USA. ²Department of Mechanical and Industrial Engineering, University of Massachusetts, Amherst, MA 01003, USA.

*Corresponding author. E-mail: leejh@umass.edu (J.-H.L.); elt@rice.edu (E.L.T.)

($<3 \text{ km s}^{-1}$) with a high aiming accuracy ($<1.1^\circ$ deflection) toward a thin film. The velocity of the μ -bullet is measured before and after penetration to determine the energy lost during the test. We employed multilayer graphene (MLG) membranes in a range of thicknesses (10 to 100 nm, equivalent to 30 to 300 graphene layers) to apply localized, very-high-strain-rate tensile deformation ($\sim 10^7 \text{ s}^{-1}$) at a specific area. As the thickness of the MLG membranes (h) is always considerably less than the diameter (D) of a μ -bullet ($D/h \geq 40$), the high-strain-rate in-plane tensile behavior of MLG can be assessed from the thickness-dependent characteristics of the energy required for projectile penetration through the membrane.

The MLG membranes are prepared by mechanical exfoliation of highly ordered pyrolytic graphite (grade SPI-1, SPI Supplies; fig. S1), as shown in Fig. 1A. A silica μ -bullet [$D = 3.7 \pm 0.02 \mu\text{m}$, based on imaging by scanning electron microscopy (SEM)] is propelled by expanding gases created by the laser ablation of a gold film ($\sim 50 \text{ nm}$

thick). A 20- μm -thick elastomeric layer of cross-linked polydimethylsiloxane is used to confine the ablation products, eliminates the temperature rise of the μ -bullet, and diminishes the strength of the shock waves propagating through air. The impact speed (v_i) is measured (with the reproducibility of v_i within $\pm 2\%$) using a triple-exposure photograph of the moving μ -bullet with $\pm 10 \text{ m s}^{-1}$ error, where the time gap between the three exposures is achieved by employing different travel distances for each laser pulse (fig. S2). The residual speed (v_r) of the μ -bullet is similarly measured after the μ -bullet has traveled a certain distance (d) beyond the membrane (Fig. 1B). An average thickness (h_{ave}) of the impact area was determined using a thickness-dependent optical transmittance measurement (fig. S3) given by an analytical formula (8) and the optical parameters of graphite (9). An additional postpenetration image allowed identification of the penetration area (Fig. 1C).

The schematic in Fig. 1D depicts the series of events during penetration accompanying the ki-

netic energy loss of a μ -bullet (ΔE_k). As the μ -bullet impacts a strike face area ($A_s = \pi D^2/4$), an elastic wave radially propagates at c_{\parallel} and a conic deformation of the MLG membrane follows with a radial speed of its base, v_c , which is generally slower than c_{\parallel} (step ii). The primary force is axisymmetric tension with a strong radial gradient and results in the cone shape. Typically, three to six cracks are initiated near the center of A_s and propagate outward in the radial direction (step iii), resulting in the creation of the same number of petals. The transferred momentum to the MLG membrane induces creasing and folding of each triangular-shaped petal at its base while the elastic extension of the membrane is rapidly relaxed along the radial direction via snap-back (step iv). The longest crack from the impact center is defined as the maximum crack distance, L_{max} , which we use as the estimation of the final radius of the conic deformation due to the reduction of the tangential stress. ΔE_k is composed of two terms, the net energy to penetrate a membrane (E_p) and the energy loss due to air drag (E_{air}). E_p depends on various energy dissipation mechanisms including elastic stretching of the membrane, fracture, and heating, as well as the kinetic energy transfer to the membrane petals and membrane debris.

$$\Delta E_k = \frac{1}{2} m (v_i^2 - v_r^2) = E_p + E_{\text{air}}(d) \quad (1)$$

As the mass of a μ -bullet, m is calculated to be $5.0 \pm 0.1 \times 10^{-14} \text{ kg}$, based on the measured diameter D and the density of silica (1900 kg m^{-3}) provided by its vendor (microParticles GmbH). The incident E_k is 9 nJ at 600 m s^{-1} and 21 nJ at 900 m s^{-1} while ΔE_k is in the range of 1 to 5 nJ. The measured deceleration by air drag (a_{air}) is $\sim 0.6 \times 10^8 \text{ m s}^{-2}$, assuming constant deceleration, which yields $E_{\text{air}} = m a_{\text{air}} d \sim 1.07 \text{ nJ}$ for $d \sim 350 \mu\text{m}$ (the travel distance of a μ -bullet after penetration when we take the triple exposure). Therefore, the primary contribution to the kinetic energy loss is the net energy to penetrate a MLG membrane (E_p) under our experimental conditions.

The MLG membranes had a typical lateral grain size of $\sim 10 \mu\text{m}$. Due to the stress concentration at the impact site, the grain boundary effects (10, 11) (if any; see the supplementary materials) would occur only if the grain boundaries exist within A_s . As the ratio, D/h is quite large (40 to 350), the mechanical response of the MLG film depends primarily on its in-plane tensile strength under a high strain rate. A typical penetration hole features a set of petals (Fig. 2). The area directly beneath the μ -bullet impact shows extensive damage through complex, fine-scale fractures, folding, delamination, and loss of parts of the membrane (indicated by the yellow arrowheads). As the initiation of the radial cracks may not be exactly at the impact center, asymmetric shaped petals are often observed (e.g., Fig. 2, A and D). The damage area is thus much wider than A_s , in strong contrast to the observed behavior of polycrystalline gold and amorphous, glassy poly(methyl methacrylate) (PMMA) membranes,

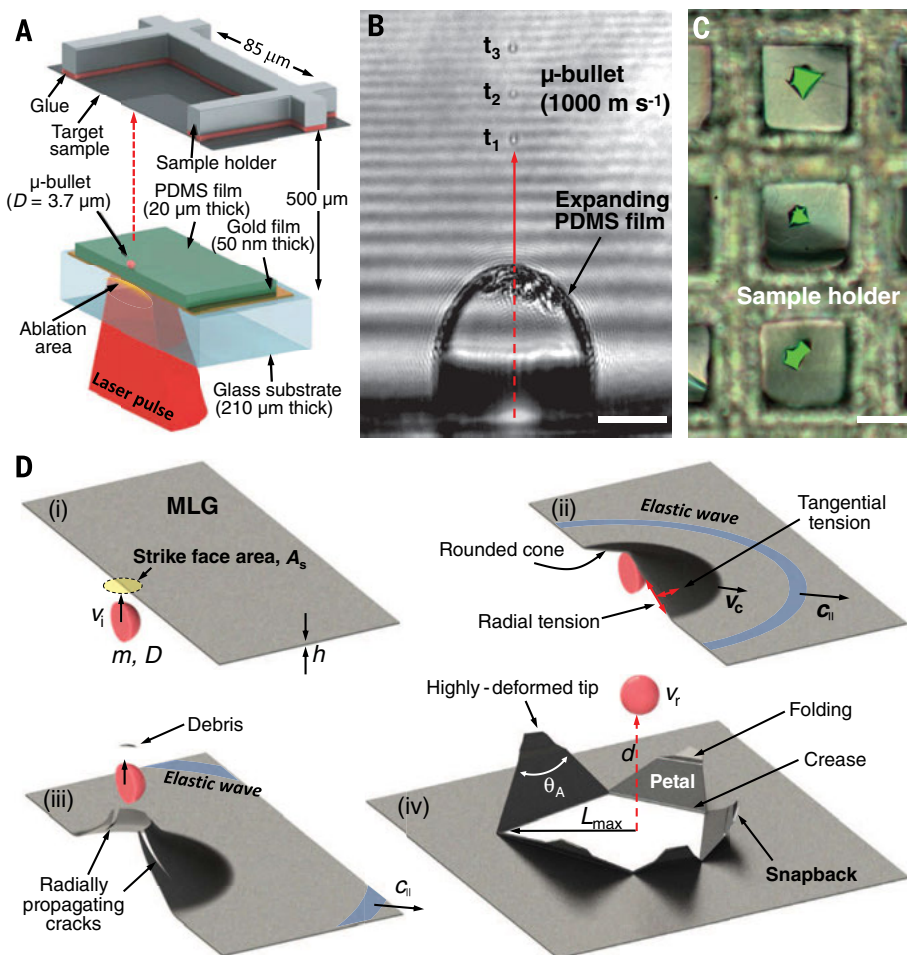


Fig. 1. The microballistic experiment. (A) Scheme of the experiment. PDMS, polydimethylsiloxane. (B) Side-view image of a moving μ -bullet taken by triple exposure at time steps t_1 to t_3 . (C) MLG membrane on a sample holder after α -LIPIT. Three separate impact test regions are highlighted by green backlight. (D) Schematic illustration of penetration steps: (i) prepenetration stage; (ii) conic deformation stage; (iii) fracture stage; and (iv) postpenetration stage, showing the film morphology after penetration and relaxation. Scale bars in (B) and (C), $50 \mu\text{m}$.

in which penetration results in a circular hole with an area of $\sim A_s$ (see figs. S6 and S7). Correspondingly, a much smaller penetration energy is measured.

Many independent penetration experiments (47 events for $v_i = 600 \text{ m s}^{-1}$ and 43 events for $v_i =$

900 m s^{-1}) were carried out for statistical analysis (figs. S4 and S5). The average apex angles (θ_A in Fig. 1D) of petals for the 600- and 900- m s^{-1} projectile velocities are $83 \pm 21^\circ$ (for 107 cracks) and $70 \pm 23^\circ$ (for 93 cracks), respectively, indicat-

ing that the higher tangential stresses induced at 900 m s^{-1} were relaxed through more radial cracks. Despite the in-plane isotropic elastic nature due to the approximate sixfold symmetry of graphene (12), the preferential crack propagation

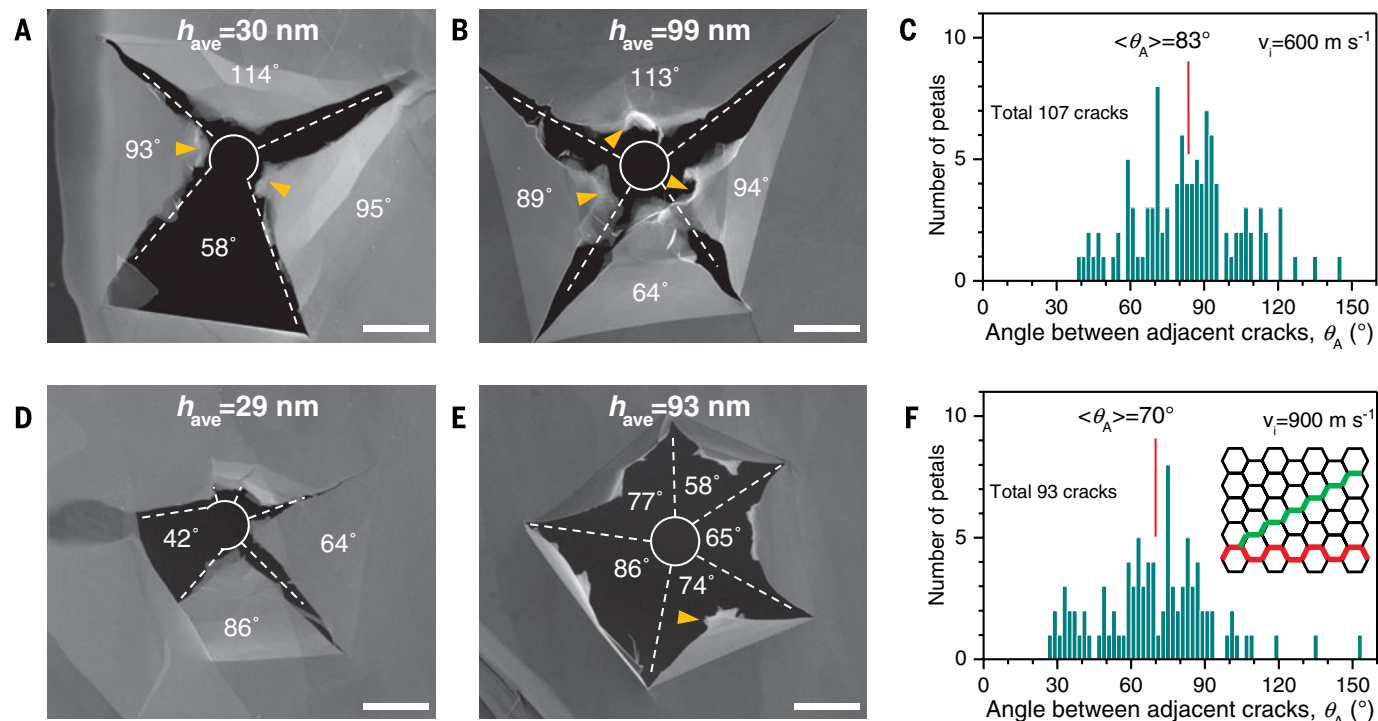
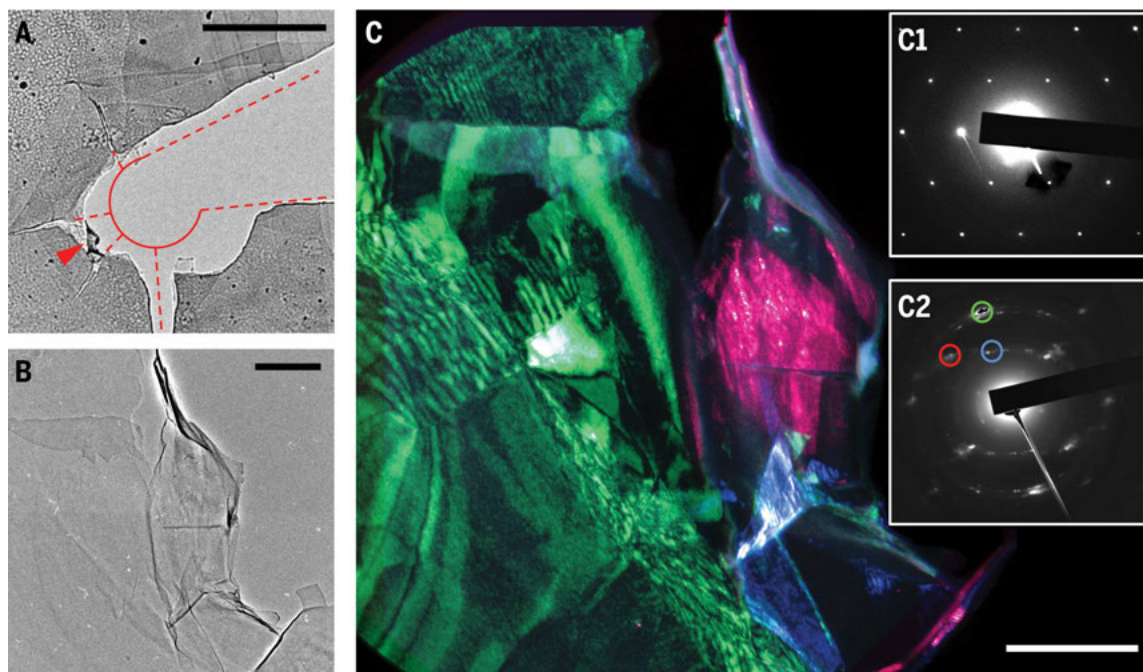


Fig. 2. Representative penetration features of MLG membranes. (A and B) SEM images of petals, radial cracks, folds, and snap-back damage to the petal tips and (C) the adjacent crack-pair angle distribution for $v_i = 600 \text{ m s}^{-1}$. (D and E) SEM images and (F) the adjacent crack-pair angle distribution for $v_i = 900 \text{ m s}^{-1}$. The inset in (F) shows the armchair (red) and zigzag (green) directions. The circles in the SEM images show A_s . Scale bars in (A), (B), (D), and (E), $5 \mu\text{m}$.

Fig. 3. Damage features of a thin MLG membrane. (A) Bright-field TEM micrograph of the impact region ($h_{\text{ave}} \sim 10 \text{ nm}$) for $v_i = 900 \text{ m s}^{-1}$. (B) Higher magnification of the petal apex area indicated by the red arrowhead in (A). (C) Three dark-field TEM micrographs are overlaid to show bend contours, rotation-tilt moiré fringes, and a fine-scale mosaic texture resulting from snap-back and membrane folding. The two diffraction patterns show (C1) a typical hexagonal spot pattern of the undeformed film and (C2) the altered, multireflection-satellite spot pattern from near the impact region. The red and blue regions correspond to imaging with $\bar{g} = (0\bar{1}10)$, and the green region corresponds to $\bar{g} = (\bar{2}110)$. Scale bars, (A) $5 \mu\text{m}$; (B) and (C), $0.5 \mu\text{m}$. The voidlike features at the upper left in (A) are a result of residual water-soluble polymer from film preparation.



directions $\langle 1\bar{1}00 \rangle$ (the armchair direction) and $\langle 2\bar{1}10 \rangle$ (the zigzag direction) cause preferred angles between adjacent cracks to be a multiple of 30° (13). Correlation to the underlying crystallographic orientation of the membrane is noted in the distribution of the angle between adjacent cracks displaying preferences for small multiples of 30° (Fig. 2, C and F).

Transmission electron microscopy (TEM) was carried out on snap-back portions of the petal regions of thin ($h_{\text{ave}} \sim 10$ nm) fractured membranes (Fig. 3). The bright-field TEM image shows complicated local folding of the membrane near the penetration (Fig. 3, A and B). The higher-magnification dark-field image shows bend contours and moiré fringes (upper left and left center regions in Fig. 3C, resulting from the interference of electrons scattered from superposed folded MLG regions; see diffraction pattern insets in Fig. 3C). In the extensively folded region nearest the impact origin, a fine-scale mosaic structure is evident in both the electron diffraction pattern and dark-field images due to the deformation resulting from the rapid elastic relaxation (i.e., petal snap-back).

Despite a relatively wide fluctuation in L_{max} , its lower limit is well fit by $0.1h_{\text{ave}} + D/2$ (Fig. 4A). The film thickness inhomogeneity is represented by the coefficient of variation (CV) of the local thicknesses measured over a circular area (radius $r = L_{\text{max}}$). MLG membranes that have $\text{CV} > 10\%$ in the impact area clearly lead to a greater fluctuation of L_{max} . The radial speed of the circumferential base of the expanding cone-shape deformation region of a membrane can be approximated by $v_c \approx 1.23c_{\parallel}[v_i/2^{1/2}c_{\parallel}]^{2/3}$ and thus scales with the cube root of the in-plane speed of sound in the material (14). Values for v_c correspond to 1950 and 2560 m s^{-1} for impacts of 600 and 900 m s^{-1} ,

respectively. An empirical estimation of deformation parameters is then possible by setting the lower limit of L_{max} to the maximum radius of the cone, because the tangential tensile stress (Fig. 1D) is the origin of the radial cracks. For example, assuming a simple 1D model for a 900-m s^{-1} impact to a 50-nm-thick MLG membrane, we estimate the penetration time $t_p \approx L_{\text{max}}/v_c \sim 3$ ns; the 1D-approximate average maximum tensile strain $\varepsilon_{\text{max}} \approx (v_i t_p / L_{\text{max}})^2 / 2 \approx \sim 6\%$, close to the lower boundary of the reported failure strain range, 5 to 25% (1, 15, 16); and the 1D-approximate average tensile strain rate as given by the maximum strain divided by the penetration time or $\dot{\varepsilon}_{\text{max}} = (v_i / L_{\text{max}})^2 t_p / 2 \sim 10^7 \text{ s}^{-1}$. A further discussion of the estimation of strain and strain rate is available in the supplementary materials.

From Eq. 1, $\Delta E_k(h_{\text{ave}})$ can be fit with a linear function (Fig. 4B), where the y -intercept value corresponds to E_{air} . Therefore, the intrinsic energy dissipation of a MLG membrane is given by $E_p(h_{\text{ave}}) = 0.026h_{\text{ave}}$ and $0.030h_{\text{ave}}$ for the two velocities we employed, and a similar trend is also found in macroscopic ballistic tests (17, 18). For $D/h_{\text{ave}} \gg 1$, E_p can be expressed by two terms, $E_p = (\rho A_s h_{\text{ave}}) v_i^2 / 2 + E_d$, where the first term represents the minimum inelastic energy transfer to target material within A_s and E_d represents all of the other energy dissipation mechanisms. The specific energy dissipation, $E_p^* = E_p / (\rho A_s h_{\text{ave}})$, which is insensitive to material density by taking account of the mass within $A_s h_{\text{ave}}$, is given by $E_p^* = v_i^2 / 2 + E_d^*$, where E_d^* is the specific delocalized penetration energy. E_d^* is thus a figure of merit to evaluate the impact energy delocalization ability of a material as more sample mass beyond A_s contributes to the energy dissipation, whereas the material-independent energy dissipation term, $v_i^2 / 2$, serves as a baseline.

Statistical values of $E_p h_{\text{ave}}^{-1}$ for MLG, PMMA, and polycrystalline gold were determined from the fitted slopes of E_p versus h_{ave} (Fig. 4B and figs. S6E and S7C). From this data (see square data points in Fig. 4C), MLG exhibits the highest E_p^* (or E_d^*), namely 1.26 MJ kg^{-1} (or 0.86 MJ kg^{-1}) at 900 m s^{-1} , compared with 0.58 MJ kg^{-1} (or 0.19 MJ kg^{-1}) for gold and 0.52 MJ kg^{-1} (or 0.08 MJ kg^{-1}) for PMMA. We also calculated E_p^* from previous macroscopic ballistic tests of several materials: PMMA (19), aluminum (20, 21), steel (22, 23), and Kevlar KM2-polyvinyl butyral (PVB) composite fabric (24). These macroscopic tests used a millimeter-scale spherical steel projectile to penetrate a thin sheet ($0.4 < h < 6$ and $1 < D/h < 20$) without appreciable deformation of the projectile (table S1). The overall trend of E_p^* is quite similar, despite the large differences in the microscopic α -LIPIT and traditional macroscopic tests and the huge range in tensile modulus, strength, and density among PMMA, aluminum, and steel. This implies that the principal energy dissipation mechanism for the three macroscopic materials is the kinetic energy transfer from the projectile to the target material within A_s (i.e., to the mass $\rho A_s h$), which results in a dishing process (25). This is why the E_p^* values of PMMA and gold from α -LIPIT also follow this trend and indicate a good correspondence between the micro- and macroscopic high-strain-rate evaluation methods for these materials, which also display localized penetration via a dishing process.

However, the two highly anisotropic layered materials—the Kevlar KM2-PVB composite fabric and the MLG membrane—deviate strongly from this trend. The Kevlar KM2-PVB composite is an armor-grade laminate made of strong, stiff polyaramid fibers (strength $\sim 4 \text{ GPa}$, $Y \sim 84 \text{ GPa}$, $c \sim 7.6 \text{ km s}^{-1}$) embedded in PVB resin (26). The

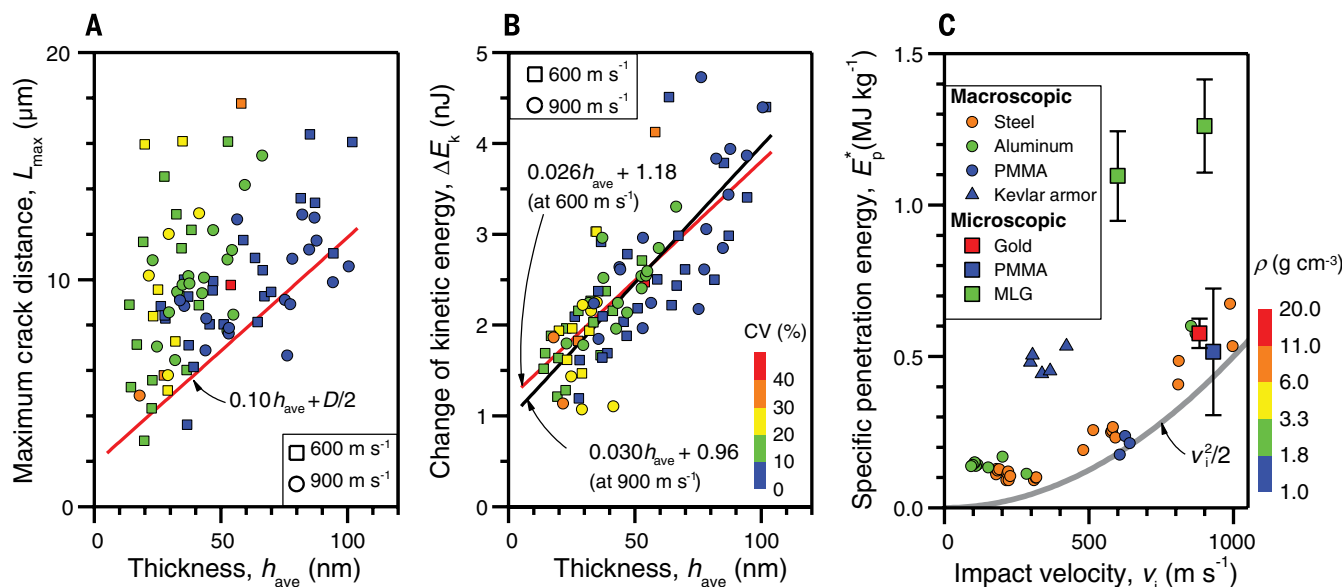


Fig. 4. Analyses of microballistic results. (A) Maximum crack distances in MLG membranes of various thicknesses for the two different penetrator velocities. (B) Kinetic energy changes of a μ -bullet versus thickness after penetration of MLG membranes. Colors in (A) and (B) represent the thickness inhomogeneity (via CV) of the film in the impact area. (C) Specific penetration energy of MLG, PMMA, and gold membranes compared with macroscopic materials at various impact velocities. The density of each material is represented by a logarithmic color scale. Error bars denote SD.

planar fourfold symmetric high-stiffness woven polyaramid multilayer fabric shows an extensive conelike deformation under ballistic impact, and the higher E_p^* (or E_d^*) values (see blue triangles in Fig. 4C) can be understood by the contribution of large sample mass well beyond the impact area to energy absorption (27). Similarly, the superior value of E_p^* for MLG (see green squares in Fig. 4C) can be explained by its ability to simultaneously be stiff, strong, and elastic, stretching into a cone shape due to the force imparted by the forward moving projectile. As a result, the E_d^* values of the MLG membrane (0.92 and 0.86 MJ kg⁻¹ for 600 and 900 m s⁻¹) substantially surpass those of steel (0.08 and 0.11 MJ kg⁻¹) at the same v_i . Therefore, the MLG demonstrates specific delocalized penetration energy 8 to 12 times higher than that of steel due to the strong delocalization behavior at these impact speeds. As the higher delocalization effect results in a wider penetration hole, this tendency could be disadvantageous in certain aspects such as multi-hit capability. However, this potential weakness of MLG will be substantially relieved when the crack propagation is deflected by forming a composite.

Our microscopic ballistic results reveal that the superior in-plane speed of sound, high strength, stiffness, and structural anisotropy make MLG an extraordinary armor material exhibiting excellent impact energy delocalization under a supersonic penetration event. Because material far beyond the strike face area can also consume kinetic energy from the μ -bullet while the MLG membrane sustains high dynamic tensile stress, the μ -bullet effectively experiences a higher areal density material. As large-scale production of graphene-based composite materials is becoming possible (28), other graphene-like materials are being studied (29), and the results suggest opportunities for the use of ordered anisotropic nanocomposites for surprising mechanical applications. The good correspondence between the micro- and macroscopic projectile penetration tests, especially in the measured specific energy absorption, suggests that the microballistic method with its high-energy resolution may offer an effective means for the exploration of high-strain-rate physics of various materials, as well as practical advantages in rapid, high-throughput testing.

REFERENCES AND NOTES

- C. Lee, X. Wei, J. W. Kysar, J. Hone, *Science* **321**, 385–388 (2008).
- J. E. Field, S. M. Walley, W. G. Proud, H. T. Goldrein, C. R. Siviour, *Int. J. Impact Eng.* **30**, 725–775 (2004).
- J. W. Anthony, R. Bideaux, K. Bladh, M. C. Nichols, *Handbook of Mineralogy* (Mineralogical Society of America, Chantilly, VA, 1990).
- B. Gotsmann, H. Rothuizen, U. Duerig, *Appl. Phys. Lett.* **93**, 093116 (2008).
- B. A. Gama, S. L. Lopatinikov, J. W. Gillespie, *Appl. Mech. Rev.* **57**, 223–250 (2004).
- J. A. Zukas, *High Velocity Impact Dynamics* (Wiley-Interscience, New York, 1990).
- J.-H. Lee et al., *Nat. Commun.* **3**, 1164 (2012).
- S. G. Tomlin, *J. Phys. D* **1**, 1667–1671 (1968).
- E. D. Palik, *Handbook of Optical Constants of Solids* (Academic Press, San Diego, 1998), vol. 2.
- H. I. Rasool, C. Ophus, W. S. Klug, A. Zettl, J. K. Gimzewski, *Nat. Commun.* **4**, 2811 (2013).
- G. H. Lee et al., *Science* **340**, 1073–1076 (2013).
- M. S. Dresselhaus, G. Dresselhaus, *J. Mater. Res.* **6**, 1114–1118 (1991).
- K. Kim et al., *Nano Lett.* **12**, 293–297 (2012).
- S. L. Phoenix, P. K. Porwal, *Int. J. Solids Struct.* **40**, 6723–6765 (2003).
- R. Grantab, V. B. Shenoy, R. S. Ruoff, *Science* **330**, 946–948 (2010).
- J. Zhang, J. Zhao, J. Lu, *ACS Nano* **6**, 2704–2711 (2012).
- M. A. Iqbal, N. K. Gupta, *Lat. Am. J. Solids Struct.* **5**, 259–287 (2008).
- S. K. Garcia-Castillo, S. Sanchez-Saez, E. Barbero, *J. Strain Anal. Eng. Des.* **47**, 444–452 (2012).
- L. H. Abbud, A. R. A. Talib, F. Mustapha, H. Tawfique, F. A. Najim, *Int. J. Mech. Mater. Eng.* **5**, 123–128 (2010).
- W. Goldsmith, S. A. Finnegan, *Int. J. Mech. Sci.* **13**, 843–866 (1971).
- N. K. Gupta, M. A. Iqbal, G. S. Sekhon, *Int. J. Impact Eng.* **32**, 1921–1944 (2006).
- J. Dean, C. S. Dunleavy, P. M. Brown, T. W. Clyne, *Int. J. Impact Eng.* **36**, 1250–1258 (2009).
- C. J. Yungwirth, J. O'Connor, A. Zakraysek, V. S. Deshpande, H. N. G. Wadley, *J. Am. Ceram. Soc.* **94**, S62–S75 (2011).
- B. L. Lee et al., *J. Compos. Mater.* **35**, 1605–1633 (2001).
- S. C. Wright, N. A. Fleck, W. J. Stronge, *Int. J. Impact Eng.* **13**, 1–20 (1993).
- M. Cheng, W. Chen, T. Weerasooriya, *J. Eng. Mater. Technol.* **127**, 197–203 (2005).
- R. J. Rabb, E. P. Fahrenthold, *Int. J. Numer. Methods Eng.* **83**, 537–557 (2010).
- D. Li, M. B. Müller, S. Gilje, R. B. Kaner, G. G. Wallace, *Nat. Nanotechnol.* **3**, 101–105 (2008).
- M. Xu, T. Liang, M. Shi, H. Chen, *Chem. Rev.* **113**, 3766–3798 (2013).

ACKNOWLEDGMENTS

This work was funded by the Defense Threat Reduction Agency under contract 1-12-10008 and the Welch Foundation grant C-1716.

SUPPLEMENTARY MATERIALS

www.sciencemag.org/content/346/6213/1092/suppl/DC1
Materials and Methods
Supplementary Text
Figs. S1 to S7
Table S1
Reference (30)

9 July 2014; accepted 23 October 2014
10.1126/science.1258544

REPELLENT SURFACES

Turning a surface superrepellent even to completely wetting liquids

Tingyi “Leo” Liu¹ and Chang-Jin “CJ” Kim^{1,2*}

Superhydrophobic and superoleophobic surfaces have so far been made by roughening a hydrophobic material. However, no surfaces were able to repel extremely-low-energy liquids such as fluorinated solvents, which completely wet even the most hydrophobic material. We show how roughness alone, if made of a specific doubly reentrant structure that enables very low liquid-solid contact fraction, can render the surface of any material superrepellent. Starting from a completely wettable material (silica), we micro- and nanostructure its surface to make it superomniphobic and bounce off all available liquids, including perfluorohexane. The same superomniphobicity is further confirmed with identical surfaces of a metal and a polymer. Free of any hydrophobic coating, the superomniphobic silica surface also withstands temperatures over 1000°C and resists biofouling.

The ability to understand the extraordinary liquid repellency of natural surfaces (1, 2) has affected a wide range of scientific and technological areas, from coatings (3), heat transfer (4), and drag reduction (5) to biomimetics (6). Whereas the wetting-resistant surfaces developed since the 1960s (7–10) used only surface roughness to trap gas with no interest in the apparent contact angles, superhydrophobic surfaces created since the late 1990s (11, 12) combined the roughness with a hydrophobic material to superrepel water—that is, to display a very large apparent contact angle ($\theta^* > 150^\circ$) and a very small roll-off angle ($\theta_{\text{roll-off}} < 10^\circ$). For low-energy liquids such as oils or organic solvents, a roughness with overhanging topology was necessary to make the hydrophobic material superoleophobic (13, 14), omniphobic (15), or superomniphobic (16, 17). Despite the use of the prefix “omni-” (6, 15–18), however, no natural

or man-made surface has been reported to repel liquids of extremely low surface tension or energy (i.e., $\gamma < 15$ mJ/m²), such as fluorinated solvents, which completely wet existing materials (10, 19–21). Departing from the prevailing approach of roughening a hydrophobic material, we first propose that the material’s inherent wettability, depicted by the intrinsic contact angle θ_Y , is irrelevant when dealing with a completely wetting liquid ($\theta_Y = 0^\circ$). Focusing instead solely on the roughness details, we develop a surface that superrepels all available liquids, including fluorinated solvents—for instance, perfluorohexane (C₆F₁₄; namely, 3M Fluorinert FC-72), whose surface energy ($\gamma = 10$ mJ/m²) is the lowest known and which has never been observed to bead up, let alone roll off, on any surface.

To avoid the confusion with the petal effect (22), in which a droplet with large contact angles sticks to the surface, it helps to first clarify that “repelling” means that droplets not only bead on but also roll off the surface. To repel (i.e., $\theta^* > 90^\circ$ with a small $\theta_{\text{roll-off}}$) or superrepel ($\theta^* > 150^\circ$ with $\theta_{\text{roll-off}} < 10^\circ$) a wetting liquid ($\theta_Y < 90^\circ$) on a structured surface, two conditions must be met:

¹Department of Mechanical and Aerospace Engineering, University of California, Los Angeles (UCLA), Los Angeles, CA 90095, USA. ²Department of Bioengineering, UCLA, Los Angeles, CA 90095, USA.

*Corresponding author. E-mail: cjkim@ucla.edu

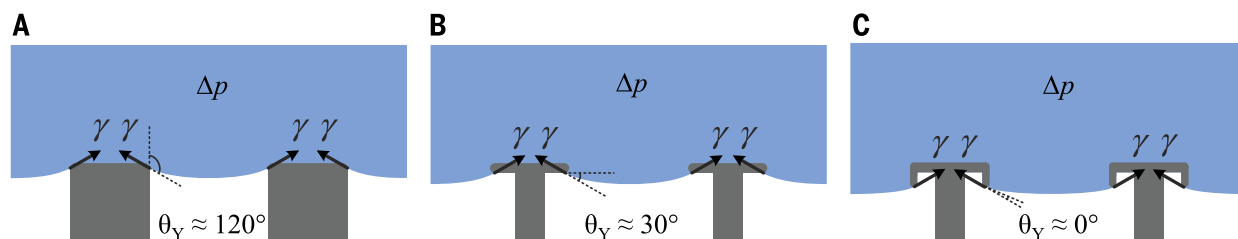
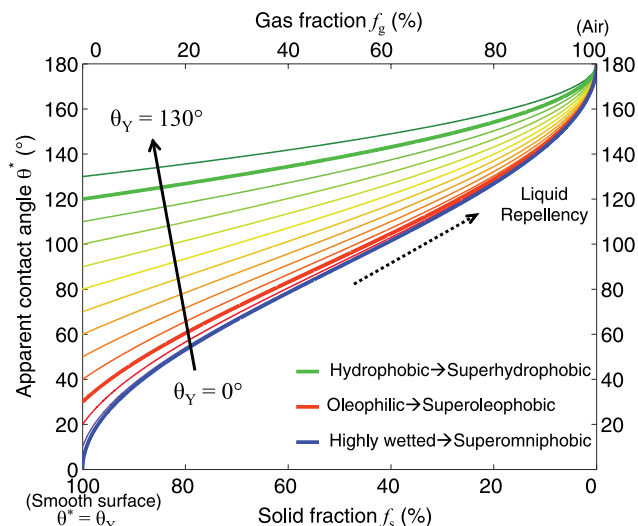


Fig. 1. Liquid suspension on surface structures of three different topologies. (A) Simple structures require $\theta_Y > 90^\circ$ to suspend water. Δp , is the pressure difference between the liquid and air. (B) Reentrant structures allow $\theta_Y < 90^\circ$ to suspend oils or solvents. They would fail if $\theta_Y \sim 0^\circ$, as surface tension acts parallel to the horizontal overhangs with little vertical component to suspend the liquid. (C) Doubly reentrant structures allow $\theta_Y \sim 0^\circ$ to suspend any liquid, as surface tension acts on the vertical overhangs with a substantial vertical component. If the liquid-solid contact fraction is small enough, the surfaces would also repel the liquids.

Fig. 2. Relation between apparent contact angle θ^* and solid fraction f_s for ideal Cassie-state droplets with intrinsic contact angle θ_Y as a parameter. As f_s decreases, the band of lines narrows, indicating that the influence of θ_Y on θ^* diminishes. If f_s is below 6%, θ^* is above 150° even if $\theta_Y \sim 0^\circ$. The green, red, and blue lines represent the inherent wettability: nonwetting (e.g., water on a hydrophobic surface), moderately wetting (e.g., solvent on a hydrophobic surface), and highly wetting (e.g., fluorinated solvents on any surface or most liquids on clean SiO_2), respectively. The three bold lines correspond to the three cases shown in Fig. 1.



(i) a successful liquid suspension on the roughness and (ii) a low liquid-solid contact. The microstructures should first be able to suspend the liquid, supporting a composite interface proposed by Cassie and Baxter (23). Once suspended, decreasing the liquid-solid contact would increase θ^* and reduce $\theta_{\text{roll-off}}$, hence increasing the repellency. In the rare cases of a highly wetting ($\theta_Y < 10^\circ$) liquid beading (i.e., successful suspension and $\theta^* > 90^\circ$) on a structured surface—for example, water on SiO_2 (13, 24) or hexane on nickel (16)—the liquid stuck on the surface rather than rolled off; these surfaces are not considered to repel the liquid, despite the beading.

Liquid suspension by surface structures (or resisting liquid wetting by surface topologies with characteristic length smaller than the liquid's capillary length) was proposed in the 1960s with θ_Y as a critical parameter (8, 10). For $\theta_Y > 90^\circ$, as in water or aqueous solutions on a hydrophobic material, a simple microstructure (Fig. 1A) would suspend the liquid to a Cassie state (1, 2, 8, 10–12) (figs. S1 and S2). For $\theta_Y < 90^\circ$, as in oils and organic solvents on a hydrophobic material or water on a slightly hydrophilic material, a reentrant microstructure (Fig. 1B) is required to suspend the liquid and resist it from wetting into the cavity (3, 8, 10, 13–18, 25). From simple force balance,

the reentrant topology of Fig. 1B would suspend a liquid even with $\theta_Y \sim 0^\circ$ in the absence of any positive liquid pressure. However, there is always a pressure in reality (e.g., hydrostatic, Laplace, or environmental perturbation), and once pushed into the cavity the liquid spreads spontaneously. So far, the most successful suspension was for liquids with surface energy as small as $\gamma \sim 15 \text{ mJ/m}^2$ [i.e., pentane (15, 16) and isopentane (16)], leaving many fluorinated solvents unresolved.

In addition to the reentrant microstructure, it has long been hypothesized that surface structures of a doubly reentrant topology (Fig. 1C) might provide a stronger resistance against wetting and retain suspension, even if $\theta_Y \sim 0^\circ$ (8–10, 15, 26). The mechanism of suspending such a completely wetting liquid on a doubly reentrant microstructure is reasoned as follows (see Fig. 1C): Upon contacting the surface, the liquid would wet the top surface and continue down along the sidewall of the vertical overhangs. The liquid would stop advancing at the bottom tip of the vertical overhangs, where the surface tension can start to point upward. Though this concept of suspending even highly wetting liquids on a doubly reentrant topology has been known (8–10, 15, 26) and confirmed with water (24), the liquid-solid contact fraction should be sufficiently low for the resulting surface to not only suspend

but also repel the liquid. A highly wetting ($\theta_Y < 10^\circ$) liquid suspended on the microstructures would still spread (i.e., $\theta^* < 90^\circ$) on the composite surface unless the liquid rests mostly on air. To understand how far we are from being able to repel the highly wetting liquids, let us assess the contribution of air to the repellency.

The apparent contact angle θ^* for a suspended droplet (i.e., in a Cassie state) is described by the Cassie-Baxter model (23) as

$$\cos \theta^* = f_s \cos \theta_Y - f_g \quad (1)$$

where f_s is the liquid-solid contact fraction [or “solid fraction” for short; i.e., the proportion of liquid-solid contact area (including the wetted regions inside the roughness) to the projected area of the entire composite interface], f_g is the gas fraction similarly defined for liquid-vapor interface, and $f_s + f_g \geq 1$ (27). If the liquid-solid and liquid-vapor interfaces are perfectly flat, neglecting any solid roughness and meniscus curvature—that is, the ideal Cassie state with $f_s + f_g = 1$ —Eq. 1 simplifies to

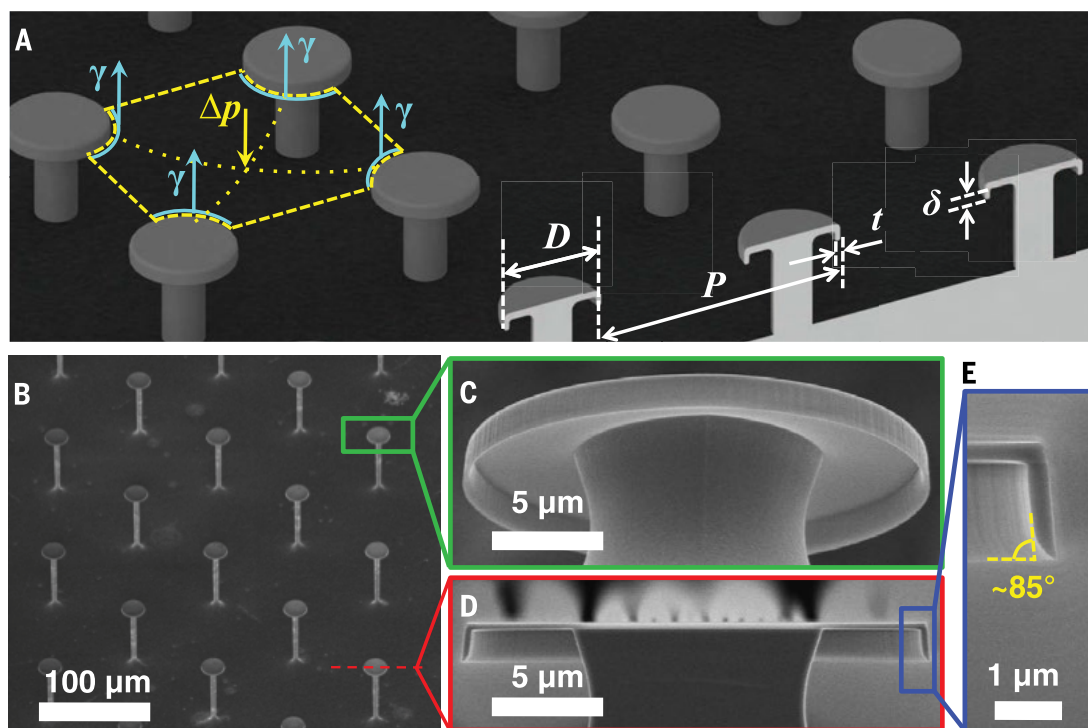
$$\cos \theta^* = f_s(1 + \cos \theta_Y) - 1 \quad (2)$$

Although valid only for the ideal Cassie state, Eq. 2 allows us to qualitatively explore the relation between θ^* , f_s , and θ_Y . In addition to the widely appreciated consequence that θ^* can be greatly increased as f_s decreases, we examine the role of the intrinsic contact angle θ_Y by plotting Eq. 2 with θ_Y as a parameter in Fig. 2. As is evident, the difference between the θ^* values of a large θ_Y and a small θ_Y decreases as f_s decreases. In other words, by minimizing f_s the contribution of the material's inherent nonwettability (described by the magnitude of θ_Y) on the liquid repellency (described by the magnitude of θ^*) diminishes. This diminishing trend suggests that a structured surface may repel extremely wetting liquids if f_s is very small. For example, even a completely wetting liquid ($\theta_Y = 0^\circ$) may be superrepelled ($\theta^* > 150^\circ$) if $f_s < 6\%$. However, it should not be forgotten that this argument is valid only for the Cassie state (i.e., the suspended state), which is exceedingly difficult to achieve if f_s becomes very small. Even for the reentrant topology of Fig. 1B, the suspension force becomes too small before f_s becomes small enough to repel liquids with very small θ_Y . This difficulty explains why superrepellency

Fig. 3. Design and fabricated results of the SiO₂ surface.

(A) Designed surface of microposts with doubly reentrant nano-overhangs. As key geometric parameters, D is the post top diameter, P is the center-to-center distance (i.e., pitch) between adjacent posts, and δ and t are the length and thickness, respectively, of the vertical overhang. To make f_s small enough ($f_s < 6\%$), δ and t should be shrunk to extreme values.

(B to E) Scanning electron micrographs of the fabricated surface. (B) Top-angled view of the square array of circular posts with $D \sim 20 \mu\text{m}$, $P = 100 \mu\text{m}$, $\delta \sim 1.5 \mu\text{m}$, and $t \sim 300 \text{ nm}$, resulting in $f_s \sim 5\%$. (C) Bottom-angled view of one post. (D) Cross-sectional view of one post. (E) Magnified cross-sectional view of the vertical overhang. Note the similarity with the ideal topology of Fig. 1C.



has been shown for liquids with surface tensions above $\sim 20 \text{ mN/m}$ (13) but not for those with surface tension values of 15 to 20 mN/m , such as pentane (15, 16) and isopentane (16), which have been suspended but not repelled.

From Figs. 1 and 2, one can now reason that a structured surface may repel any liquid if the microstructures are doubly reentrant and also of a low enough solid fraction. However, common doubly reentrant shapes in the literature (8, 10, 15, 18, 26) produce only a weak suspension and a moderate solid fraction insufficient to repel highly wetting liquids. To suspend completely wetting liquids on a surface with a minimal solid fraction, an entire surface should be uniformly covered with doubly reentrant structures having vertical overhangs as thin, vertical, and short as possible. As illustrated in Fig. 1C, such an ideal doubly reentrant structure minimizes the break-in force by the liquid pressure that wets the cavity and maximizes the surface tension force that suspends the liquid against wetting (eq. S1) (9). The thin and vertical geometry of the overhangs minimizes their projected area added to the solid fraction, and the shortness of the overhang keeps the increase of the solid fraction by the vertical surfaces at bay. Some superhydrophobic or superoleophobic surfaces described in the literature attempted to incorporate doubly reentrant structures but with little success. For example, only a few doubly reentrant structures were formed among predominantly simple or reentrant structures prone to wetting (3, 14, 25), and structures barely satisfying the doubly reentrant shape were replicated from springtail skin with only a moderate solid fraction (18).

To fulfill all the requirements reasoned above and quantified from Fig. 2, we designed a surface illustrated in Fig. 3A: an array of doubly reentrant structures consisting of microscale posts with nanoscale vertical overhangs. Posts were chosen over ridges or holes to minimize f_s more easily. Also, the post array allows the air underneath the droplet to remain connected to the atmosphere so that the liquid is suspended only by surface tension and is not assisted by the pressure of the trapped air. We chose to form the surface structures from SiO₂ for the following two reasons: First, clean SiO₂ is highly wetted (i.e., $\theta_Y < 10^\circ$) by most liquids (except liquid metals such as mercury), including water (1, 20). Because roughening of a SiO₂ surface is supposed to amplify the liquid affinity to complete wetting (1), structuring a SiO₂ surface to repel liquids should provide a stark contrast to the existing approach. Second, Si micro-machining provides sophisticated equipment and techniques to process SiO₂. With precisely controlled thermal oxidation of a shallow-etched silicon surface followed by three sequential etching steps on SiO₂ and Si (fig. S3E) (28), we successfully fabricated a SiO₂ surface (1.7 cm by 1.7 cm) with close-to-ideal doubly reentrant structures (Fig. 3, B to E). The inclined angle of the vertical overhang is measured to be $\sim 85 \pm 1^\circ$ (Fig. 3E), providing a maximum suspension force that is 99.6% of the perfectly vertical overhang shown in Fig. 1C. In spite of the overall resemblance between the microposts in Fig. 3B and those of superoleophobic surfaces (13, 15–17), it is the close-to-ideal nanoscale vertical overhangs in Fig. 3, C to E, that lead to an unprecedented liquid-repelleny.

To evaluate the liquid repelleny, we chose 14 different liquids (table S1) (29), including water,

ionic liquid, acid, oils, and numerous polar or non-polar organic or fluorinated solvents with surface tensions ranging from 72.8 mN/m (i.e., water) to the lowest known value of 10 mN/m (i.e., FC-72). As expected, a smooth SiO₂ surface was highly wetted ($\theta^* = \theta_Y < 10^\circ$) by all of the liquids (table S2). In contrast, our structured SiO₂ surface successfully suspended and repelled all of the tested liquids, beading them into Cassie-state droplets (water, methanol, and FC-72 shown in fig. S4A and movie S1) and letting them roll around (fig. S4B and movies S2 and S3); that is, behaving super-omniphobic in air.

To quantify the repelleny of our surface, we measured the advancing and receding contact angles (Fig. 4A) and roll-off angles (fig. S4C) of all 14 liquids. For comparison, Fig. 4A also includes the other two liquid-repellent surfaces analyzed in Fig. 1: a superhydrophobic surface consisting of cylindrical posts (Fig. 1A and fig. S3B) and a superoleophobic surface consisting of posts with reentrant overhangs (Fig. 1B and fig. S3D), both of which were coated with a hydrophobic layer of C₄F₈. As expected, although the superhydrophobic surface with vertical posts could not suspend liquids with surface tension below $\sim 40 \text{ mN/m}$, the superoleophobic surface with reentrant posts repelled liquids with lower surface tension (20 to 40 mN/m). However, liquids with even lower surface tension ($< 20 \text{ mN/m}$) could not be suspended, as they wicked between the reentrant posts. In contrast, on the surface with doubly reentrant posts, all 14 liquids formed large contact angles, even without any hydrophobic coating.

The extent to which wettability is modulated by surface roughness is shown in Fig. 4B, where the apparent wettability ($\cos\theta^*$) is plotted as a

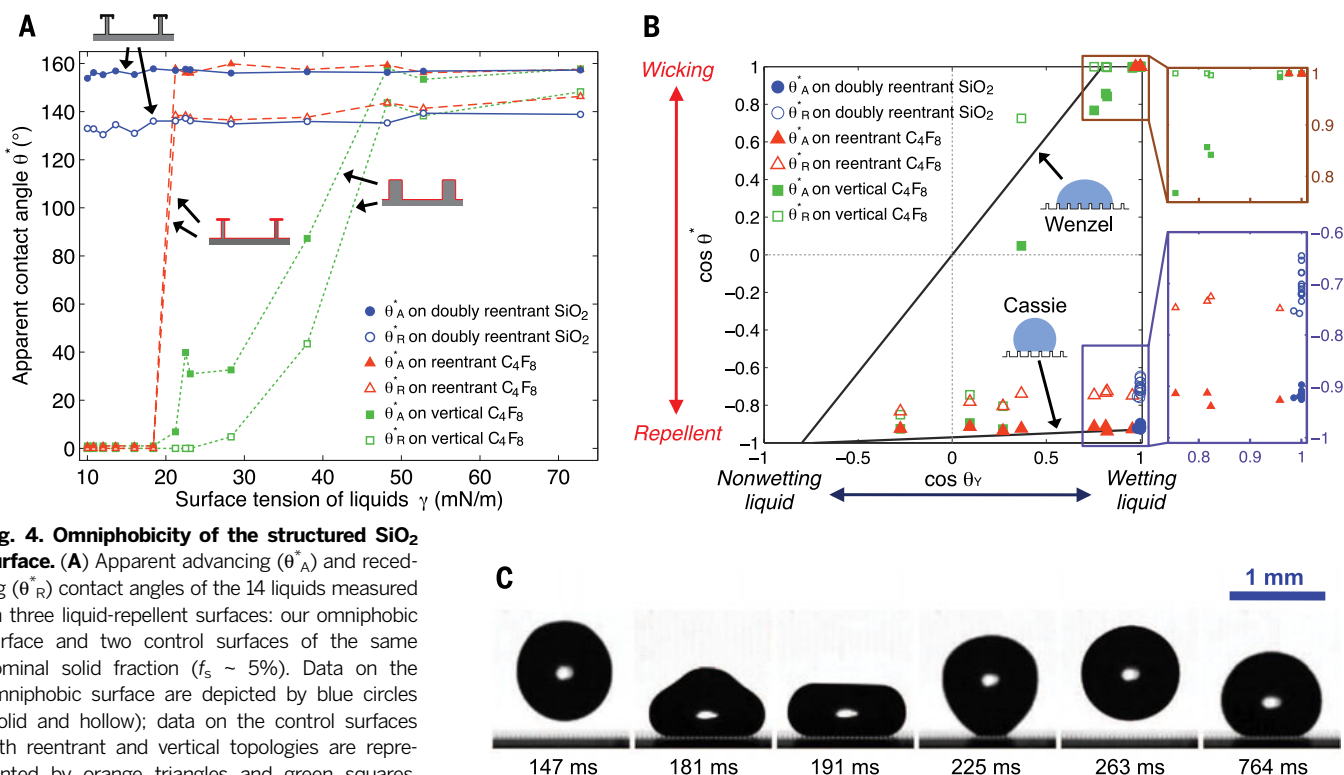


Fig. 4. Omniphobicity of the structured SiO_2 surface. (A) Apparent advancing (θ_A^*) and receding (θ_R^*) contact angles of the 14 liquids measured on three liquid-repellent surfaces: our omniphobic surface and two control surfaces of the same nominal solid fraction ($f_s \sim 5\%$). Data on the omniphobic surface are depicted by blue circles (solid and hollow); data on the control surfaces with reentrant and vertical topologies are represented by orange triangles and green squares, respectively. Each data point is an average of more than 100 measurements. Error bars are omitted here for clarity and are instead shown in fig. S6. (B) Relations of contact angles on a smooth surface ($\cos \theta_\gamma$) and on a structured surface ($\cos \theta^*$). The theoretical relations from the Wenzel and Cassie-Baxter models are plotted as solid black lines. Data near (1, -1) and (1, 1) are shown in the zoomed-in boxes, revealing the difference between our structured SiO_2 surface and the control surfaces, especially when liquids highly wet the material. (C) Robust repellency of the structured SiO_2 surface demonstrated by bouncing FC-72 off the super omniphobic SiO_2 surface with doubly reentrant posts of $D \sim 10 \mu\text{m}$, $P = 50 \mu\text{m}$, $\delta \sim 920 \text{ nm}$, $t \sim 270 \text{ nm}$, and $f_s \sim 5\%$ under Weber number ~ 0.42 .

function of the inherent wettability ($\cos \theta_\gamma$). Data from our surface with doubly reentrant posts (i.e., blue circles) were populated at the lower right corner in the fourth quadrant near point (1, -1), exhibiting the exceptional ability to render a highly wettable material superrepellent. In contrast, although the two control surfaces permit a Cassie state with nonwettable or partially wettable material, they got soaked when the material was highly wetted by the liquids of very low surface tension (i.e., hexane and six fluorinated solvents), displaying $\theta^* \sim 0^\circ$ with data populated near point (1, 1). These results are consistent with the theory schematically summarized in fig. S2.

In addition to repelling all 14 liquids (movie S2), our superomniphobic surfaces are also expected to sustain static (fig. S5 and movie S4) and dynamic (movie S5) pressures better than the existing superhydrophobic and superoleophobic surfaces (26). The doubly reentrant structures allow droplets to bounce on even extremely sparse posts (i.e., tens of micrometers of pitch and a solid fraction of only $\sim 5\%$). With high-speed imaging, water, methanol, and FC-72 droplets were confirmed to bounce off the truly superomniphobic SiO_2 surfaces (movie S5). Water ($\gamma = 72.8 \text{ mN/m}$) and methanol ($\gamma = 22.5 \text{ mN/m}$) droplets rebounded on a surface with microposts of $100\text{-}\mu\text{m}$ pitch; this pitch was much larger than those reported in the literature (3, 15). However, FC-72 ($\gamma = 10 \text{ mN/m}$) droplets penetrated and wetted the above surface at impact. A surface with uniformly halved

structures (i.e., f_s remaining at $\sim 5\%$) was further prepared to provide enough resistance against impalement and let FC-72 droplets rebound, as shown with snapshots in Fig. 4C. While resisting the physical intrusion of liquids, this surface has no defense against some other intrusion mechanisms such as condensation inside the cavity. The internal condensation would be a common issue to all existing superhydrophobic and superoleophobic surfaces (1), calling for a provision (5) for practical use.

Because the proposed superrepellency depends only on physical attributes, we further fabricated metal (i.e., tungsten) and polymer (i.e., parylene) counterparts based on the given SiO_2 surface and confirmed that they possess the same superrepellency as expected (fig. S4A). The ability to repel fluorinated solvents may allow the electronic circuits to be cooled by nucleate boiling (i.e., the most efficient mode of cooling (4)). Free of polymeric coating, the superomniphobic SiO_2 surface can serve at high temperatures. The surface was found unaltered after storage at $>1000^\circ\text{C}$ and was used to demonstrate rolling-off of another FC liquid at 150°C and a nonvolatile liquid at $>320^\circ\text{C}$ (fig. S8 and movie S6). The polymer-free parts are expected to last longer in outdoor environment, where polymeric materials tend to degrade faster. Unaffected by the surface chemistry, the superomniphobic SiO_2 surface also demonstrated prolonged repellency to biological fluids (such as the sheep serum we tested), whereas a

regular superhydrophobic surface lost the repellency (fig. S9 and movie S7).

REFERENCES AND NOTES

1. D. Quéré, *Rep. Prog. Phys.* **68**, 2495–2532 (2005).
2. W. Barthlott, C. Neinhuis, *Planta* **202**, 1–8 (1997).
3. X. Deng, L. Mammen, H.-J. Butt, D. Vollmer, *Science* **335**, 67–70 (2012).
4. A. R. Betz, J. Jenkins, C.-J. Kim, D. Attinger, *Int. J. Heat Mass Transfer* **57**, 733–741 (2013).
5. C. Lee, C.-J. Kim, *Phys. Rev. Lett.* **106**, 014502 (2011).
6. T.-S. Wong et al., *Nature* **477**, 443–447 (2011).
7. P. J. Marto, W. M. Rohsenow, *J. Heat Transfer* **88**, 196–203 (1966).
8. R. L. Webb, *Heat Transf. Eng.* **2**, 46–69 (1981).
9. C.-J. Kim, thesis, Iowa State University (1985).
10. V. P. Carey, *Liquid-Vapor Phase-Change Phenomena: An Introduction to the Thermophysics of Vaporization and Condensation Processes in Heat Transfer Equipment* (Hemisphere, Washington, DC, 1992).
11. T. Onda, S. Shibuichi, N. Satoh, K. Tsujii, *Langmuir* **12**, 2125–2127 (1996).
12. C.-H. Choi, C.-J. Kim, *Phys. Rev. Lett.* **96**, 066001 (2006).
13. A. Tuteja et al., *Science* **318**, 1618–1622 (2007).
14. A. K. Kota, Y. Li, J. M. Mabry, A. Tuteja, *Adv. Mater.* **24**, 5838–5843 (2012).
15. A. Tuteja, W. Choi, J. M. Mabry, G. H. McKinley, R. E. Cohen, *Proc. Natl. Acad. Sci. U.S.A.* **105**, 18200–18205 (2008).
16. A. Grigoryev, I. Tokarev, K. G. Kornev, I. Luzinov, S. Minko, *J. Am. Chem. Soc.* **134**, 12916–12919 (2012).
17. R. Dufour et al., *Langmuir* **26**, 17242–17247 (2010).
18. R. Hensel et al., *NPG Asia Mater.* **5**, e37 (2013).
19. D. Brutin et al., *Microgravity Sci. Technol.* **21** (suppl. 1), 67–76 (2009).
20. D. Janssen, R. De Palma, S. Verlaak, P. Heremans, W. Dehaen, *Thin Solid Films* **515**, 1433–1438 (2006).
21. C. Urata, B. Masheder, D. F. Cheng, A. Hozumi, *Langmuir* **29**, 12472–12482 (2013).
22. L. Feng et al., *Langmuir* **24**, 4114–4119 (2008).

23. A. Cassie, S. Baxter, *Trans. Faraday Soc.* **40**, 546–551 (1944).
24. T. Liu, C.-J. Kim, in *Proceedings of the International Conference on Solid State Sensors, Actuators and Microsystems (Transducers'13)*, Barcelona, Spain, 16 to 20 June 2013 (IEEE, Piscataway, NJ, 2013).
25. Y. Ma, X. Cao, X. Feng, Y. Ma, H. Zou, *Polymer (Guildf.)* **48**, 7455–7460 (2007).
26. R. Hensel *et al.*, *Langmuir* **29**, 1100–1112 (2013).
27. This general definitions of f_s and f_g follow Cassie and Baxter's original paper (23), which included all of the nonflat (e.g., rough, curved) effects on the liquid-solid and liquid-vapor interface. In addition to the most simplified version of flat liquid-solid and flat liquid-vapor interfaces, which results in $f_s + f_g = 1$, a less simplified version of nonflat liquid-solid and flat liquid-vapor interfaces is often adopted in the literature.
28. Materials and methods are available as supplementary materials on Science Online.
29. These liquids are commonly used for applications such as electrochemistry, fuel cells, integrated circuits fabrication, microfluidic systems, heat transfer, etc.

ACKNOWLEDGMENTS

C.-J.K. was encouraged by D. Attinger to start this research. T.L. acknowledges W. Choi and K. Ding for discussion of the fabrication, L.-X. Huang for assistance with high-speed imaging, and K. Shih for help with roll-off angle measurements. C.-J.K. and T.L. thank an anonymous referee for advice on the biofouling test; D. Di Carlo and O. Adeyiga for biofluid selection; and B. Dunn, R. Freeman, and S. Chen for manuscript preparation. The data reported in the paper are tabulated in the supplementary

materials. C.-J.K. and T.L. have filed a patent on this work ("Liquid-repellent surface made of any materials," International Application no. PCT/US2014/57797).

SUPPLEMENTARY MATERIALS

www.sciencemag.org/content/346/6213/1096/suppl/DC1
Materials and Methods
Supplementary Text
Figs. S1 to S9
Tables S1 and S2
References (30–36)
Movies S1 to S7

14 April 2014; accepted 24 October 2014
10.1126/science.1254787

MINERALOGY

Discovery of bridgmanite, the most abundant mineral in Earth, in a shocked meteorite

Oliver Tschauner,^{1*} Chi Ma,² John R. Beckett,² Clemens Prescher,³
Vitali B. Prakapenka,³ George R. Rossman²

Meteorites exposed to high pressures and temperatures during impact-induced shock often contain minerals whose occurrence and stability normally confine them to the deeper portions of Earth's mantle. One exception has been MgSiO_3 in the perovskite structure, which is the most abundant solid phase in Earth. Here we report the discovery of this important phase as a mineral in the Tenham L6 chondrite and approved by the International Mineralogical Association (specimen IMA 2014-017). MgSiO_3 -perovskite is now called bridgmanite. The associated phase assemblage constrains peak shock conditions to ~ 24 gigapascals and 2300 kelvin. The discovery concludes a half century of efforts to find, identify, and characterize a natural specimen of this important mineral.

In the geosciences, the complexity of compositions and histories of naturally occurring minerals and rocks provides an important ground truth against which experiment and theory are measured. One of the most glaring omissions in the study of Earth's mantle has been the

inability to find naturally occurring specimens of what we believe to be Earth's most abundant rock-forming phase, $(\text{Mg,Fe})\text{SiO}_3$ in an orthorhombic ABO_3 perovskite structure. Despite appearing for decades in numerous experimental and theoretical studies (1–5), characterizations of possible natural

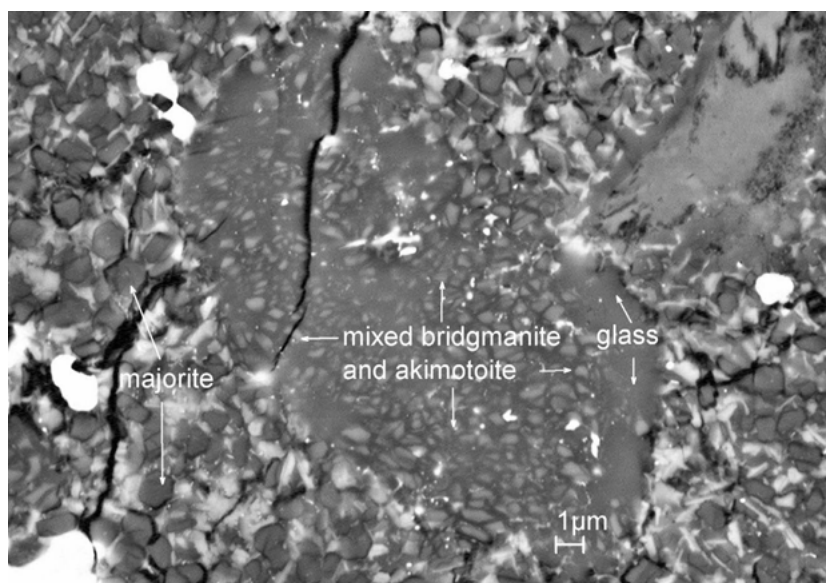
samples have not been sufficient to meet International Mineralogical Association criteria for naming a new mineral (6). Consequently, any detailed chemical, structural, and petrographic analysis of natural $(\text{Mg,Fe})\text{SiO}_3$ -perovskite has remained impossible. In addition, having a formal mineral name for a phase that is so important is important in itself. Various ambiguous or incorrect terms such as "silicate perovskite" and "perovskite" have been used for describing this phase, but they convey ambiguity to the description of research findings. We put this ambiguity to rest by describing the natural occurrence of bridgmanite: MgSiO_3 in the orthorhombic ABO_3 perovskite structure. The name bridgmanite honors Percy W. Bridgman (1882–1961), the 1946 Nobel laureate in Physics, for his fundamental contributions to high-pressure mineralogy in particular, and to high-pressure research in general.

The importance of bridgmanite in the lower mantle of Earth has long been recognized: Several lines of evidence show that it forms through a

¹Department of Geoscience and High Pressure Science and Engineering Center, University of Nevada, Las Vegas, NV 89134, USA. ²Division of Geology and Planetary Science, California Institute of Technology, Pasadena, CA 91125, USA. ³Center of Advanced Radiation Sources, University of Chicago, Chicago, IL 60632, USA.

*Corresponding author. E-mail: olivert@physics.unlv.edu

Fig. 1. Scanning electron microscope image of a bridgmanite-akimotoite aggregate. The backscatter electron image reveals an aggregate of submicrometer-sized crystals of bridgmanite and akimotoite enclosed in $(\text{Mg,Fe})\text{SiO}_3$ glass and within a Tenham shock-melt vein. Majorite is found in the vein matrix. The bridgmanite-akimotoite clast is a pseudomorph after pyroxene that was trapped in the melt. This observation is consistent with an earlier report about the possible occurrence of bridgmanite with akimotoite in Tenham (16).



breakdown of rock-forming $(\text{Mg,Fe})_2\text{SiO}_4$ into $(\text{Mg,Fe})\text{O}$ periclase and $(\text{Mg,Fe})\text{SiO}_3$ bridgmanite in the lower mantle of Earth below a depth of 660 km (1–5). Bridgmanite remains stable to the D'' layer, nearly down to the core-mantle boundary region at a depth of 2900 km (7). Thus, bridgmanite makes up about 38 volume % of the entire Earth (4). The chemical and physical properties of bridgmanite have a large influence on elemental distribution, mass flow, and heat flow within Earth's mantle. Numerous efforts have all failed to find a naturally occurring example of this elusive mineral for several reasons. Most im-

portantly, $(\text{Mg,Fe})\text{SiO}_3$ in the perovskite structure is stable only at very high pressures and temperatures (8). The mineral is metastable under ambient conditions but vitrifies above temperatures as low as 310 K (9). The exhumation of rocks originating in the lower mantle is far too slow to permit the preservation of terrestrial bridgmanite, although inclusions in some diamonds from such rocks have been interpreted as the breakdown products of bridgmanite (10, 11). Heavily shocked meteorites provide an alternative route for preserving bridgmanite. Pressures and temperatures during the shock event can be high

enough to stabilize bridgmanite, and the release to ambient conditions may be sufficiently fast to kinetically inhibit breakdown reactions. As a result, several high-pressure phases known to be stable only deep within Earth's mantle have been found as minerals in these meteorites (12–18). These observations instigated decades of efforts to find and characterize bridgmanite in shocked meteorites (15–19). Meticulous transmission electron microscopy examination yielded indications of the presence of bridgmanite in chondritic and martian meteorites (15–19). However, rapid vitrification in the electron beam, a lack of adequate sets of reflections for unique crystallographic indexing, and the absence of quantitative structure factor moduli rendered these observations insufficient to characterize a new mineral.

A different approach to the search for bridgmanite lies in using microfocused high-energy synchrotron x-ray beams instead of electron beams for diffraction. The intense high-energy x-ray beam does little to damage bridgmanite because of its low absorbance. Micro-focusing and novel fast readout area detector techniques permit efficient mapping of possible host regions in shocked meteorites (20). Our search focused on shock-melt veins and their inclusions, which were previously identified as the hosts of other high-pressure silicate phases (12–20). In particular, we examined the highly shocked Tenham L6 chondrite and identified bridgmanite in clasts within the shock-melt veins. We found bridgmanite always associated with akimotoite but never as isolated crystals in the melt vein. These two phases along with a vitreous matrix whose composition is identical within error to that of the bridgmanite (table S1) replace precursor orthopyroxene crystals trapped within a melt vein (Fig. 1 and fig. S1). We interpret this assemblage to reflect bridgmanite that partially vitrified upon release from the shock state on the parent body or during its residence on Earth after its fall in 1879. We hypothesize that the volume expansion upon transformation from bridgmanite or dense glass into normal glass by ~ 33% (21) and 1 to 2% (22), respectively, induces stresses in the surrounding rock that help preserve the remaining bridgmanite.

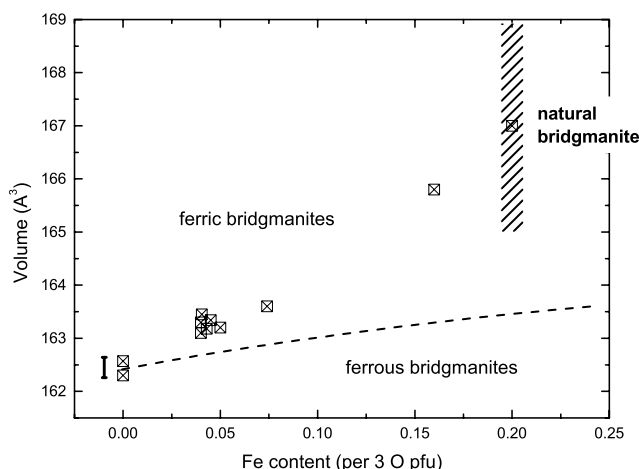
Bridgmanite assumes the Pnma perovskite structure with unit cell parameters $a = 5.02 \pm 0.03 \text{ \AA}$, $b = 6.90 \pm 0.03 \text{ \AA}$, and $c = 4.81 \pm 0.02 \text{ \AA}$, which yield a unit cell volume of $167 \pm 2 \text{ \AA}^3$ (Fig. 2) (23). The uncertainties (\pm SEM) are from (i) uncertainty in the Rietveld refinement (see Fig. 2) and (ii) variations in cell parameters due to varying chemical composition (fig. S2). Akimotoite and ringwoodite also contribute to the diffraction pattern. The average composition of the type material (table S1) has a formula unit of $(\text{Mg}_{0.75}\text{Fe}_{0.20}\text{Na}_{0.03}\text{Ca}_{0.02}\text{Mn}_{0.01}\text{Si}_{1.00}\text{O}_3)$ (23). The composition is well within the range of synthetic bridgmanites, despite being a quite sodic and Fe-rich composition in comparison (fig. S2).

The cell volume of natural bridgmanite lies on an extension of the trend of volume expansion along with increasing Fe^{3+} content (24), which is consistent with a large amount of ferric iron as

Fig. 2. Powder diffraction pattern and Rietveld refinement of bridgmanite. The figure shows the observed diffraction pattern (black line and symbols) of bridgmanite-bearing shock-melt vein material in thin section USNM 7703 (23), whole pattern refinement (red), refined pattern of bridgmanite (blue), residual of fit (green), and positions of observed reflections of bridgmanite, akimotoite, and ringwoodite (blue, red, and green tick marks, respectively). The x-ray wavelength was 0.3344 Å. The weighted-profile refinement factor was

0.08, and there were 799 observations. The examined portion of the Tenham meteorite revealed diffraction by bridgmanite, akimotoite, and ringwoodite in relative volume proportions of 11, 16, and 74%. Ringwoodite forms clasts within the shock-melt vein (fig. S1), some of which occur beneath the examined akimotoite-bridgmanite-glass clast (the x-ray beam covers a $3 \times 4 \mu\text{m}^2$ area but it passes through the entire ~30- μm -thick rock section). The bridgmanite-akimotoite aggregate has a volume proportion ~ 0.7:1, in accord with scanning electron microscope examination. rel., relative; a.u., arbitrary units.

Fig. 3. Correlation of unit cell volume with Fe content in synthetic and natural bridgmanite. Bridgmanites with dominantly ferrous iron exhibit a weak increase in volume with increasing iron content [dashed curve (24)]. Bridgmanites with large concentrations of ferric iron (24, 63) exhibit a more pronounced increase of volume with increasing Fe content (squares). Natural bridgmanite ranges in cell volumes due to chemical variations (fig. S2) as indicated by the hatched region. However, the average volume of natural bridgmanite from Tenham lies on an extension of the trend established by synthetic ferric bridgmanite. The black vertical bar indicates an approximate uncertainty for the volume measurements on synthetic bridgmanite based on the single-crystal diffraction studies of the Mg end member at ambient pressure (63–66). pfu, per formula unit.



compared to synthetic bridgmanites (Fig. 3). As noted above, the holotype specimen of bridgmanite also contains high concentrations of Na. This may extend the stability field of bridgmanite (25) and supports charge balance for ferric iron via Na-Fe³⁺-coupled substitution in holotype bridgmanites at redox conditions below the iron-wüstite buffer (26), but plausibly also in the terrestrial and martian (27) lower mantles.

The evaluation of the shock conditions in Tenham beyond the examination of plausible recovery paths for bridgmanite is outside the scope of this study. The strict association of akimotoite and bridgmanite and the likely absence of bridgmanite in the matrix of the shock-melt vein are pivotal to an assessment (fig. S3). They suggest that the peak pressure exceeded 23 GPa, with temperatures in the melt exceeding the solidus at ~2200 K. The absence of bridgmanite as isolated crystals within the shock-melt vein suggests that pressures were too low to permit crystallization from melt. Using these constraints, we estimate the conditions of formation of bridgmanite in Tenham to be 23 to 25 GPa and 2200 to 2400 K (fig. S3). This estimate is consistent with a more recent estimate by Xie *et al.* (20) based on observation of vitrified bridgmanite. The occurrence of bridgmanite along with conditions of formation of other high-pressure minerals imposes strong constraints on pressure and temperature conditions during high-level shock events in meteorites.

REFERENCES AND NOTES

- L. Liu, *Geophys. Res. Lett.* **1**, 277–280 (1974).
- A. E. Ringwood, *Geochim. Cosmochim. Acta* **55**, 2083–2110 (1991).
- R. J. Hemley, R. E. Cohen, *Annu. Rev. Earth Planet. Sci.* **20**, 553–600 (1992).
- L. Stixrude, C. Lithgow-Bertelloni, *Annu. Rev. Earth Planet. Sci.* **40**, 569–595 (2012).
- E. Ito, E. Takahashi, Y. Matsui, *Earth Planet. Sci. Lett.* **67**, 238–248 (1984).
- E. H. Nickel, J. D. Grice, *Can. Mineral.* **36**, 913–926 (1998).
- M. Murakami, K. Hirose, N. Sata, Y. Ohishi, *Geophys. Res. Lett.* **32**, L03304 (2005).
- L. Stixrude, C. Lithgow-Bertelloni, *Geophys. J. Int.* **184**, 1180–1213 (2011).
- D. J. Durben, G. H. Wolf, *Am. Mineral.* **77**, 890–893 (1992).
- S. E. Kesson, J. D. Fitz Gerald, *Earth Planet. Sci. Lett.* **111**, 229–240 (1992).
- F. E. Brenker, T. Stachel, J. W. Harris, *Earth Planet. Sci. Lett.* **198**, 1–9 (2002).
- R. A. Binns, R. J. Davis, S. J. B. Reed, *Nature* **221**, 943–944 (1969).
- J. V. Smith, B. Mason, *Science* **168**, 832–833 (1970).
- G. D. Price, A. Putnis, S. O. Agrell, D. G. W. Smith, *Can. Min.* **21**, 29–35 (1983).
- N. Tomioka, K. Fujino, *Am. Mineral.* **84**, 267–271 (1999).
- T. G. Sharp, C. M. Lengemann, C. Dupas, D. Stöffler, *Science* **277**, 352–355 (1997).
- H. Mori, *J. Mineral. Soc. Japan* **23**, 171–178 (1994).
- N. Miyajima *et al.*, *Am. Mineral.* **92**, 1545–1549 (2007).
- M. Miyahara *et al.*, *Proc. Natl. Acad. Sci. U.S.A.* **108**, 5999–6003 (2011).
- Z. D. Xie, T. G. Sharp, P. S. DeCarli, *Geochim. Cosmochim. Acta* **70**, 504–515 (2006).
- S.-N. Luo, J. A. Atkins, T. J. Ahrens, P. D. Asimow, *J. Geophys. Res.* **109** (B5), B05205 (2004).
- C. Sanchez-Valle, J. D. Bass, *Earth Planet. Sci. Lett.* **295**, 523–530 (2010).
- See the supplementary materials.
- D. R. Hummer, Y. W. Fei, *Am. Mineral.* **97**, 1915–1921 (2012).
- B. Grocholski, K. Katalli, S.-H. Shim, V. Prakapenka, *Proc. Natl. Acad. Sci. U.S.A.* **109**, 2275–2279 (2012).
- H. Y. McSweeney Jr., T. C. Labotka, *Geochim. Cosmochim. Acta* **57**, 1105–1114 (1993).
- C. M. Bertka, Y. Fei, *J. Geophys. Res.* **102**, 5251–5264 (1997).

ACKNOWLEDGMENTS

The crystallographic information about bridgmanite is available at the Inorganic Crystal Structure Database and American Mineralogist databases and in the supplementary materials. This work was supported by U.S. Department of Energy (DOE) award DESC0005278, NASA grant NNX12AH63G, and NSF grants EAR-1128799, DE-FG02-94ER14466, EAR-0318518, and DMR-0080065. Part of this work was performed at GeoSoilEnviroCARS (Sector 13), Advanced Photon Source, Argonne National Laboratory. GeoSoilEnviroCARS is supported by NSF-EAR-1128799 and DE-FG02-94ER14466. The Advanced

Photon Source, a DOE Office of Science User Facility, is operated by Argonne National Laboratory under contract no. DE-AC02-06CH11357. We thank reviewers N. Ross and T. Sharp for their helpful comments.

SUPPLEMENTARY MATERIALS

www.sciencemag.org/content/346/6213/1100/suppl/DC1
Materials and Methods
Figs. S1 to S5
Tables S1 and S2
References (28–66)
Data Tables S1 and S2

30 July 2014; accepted 22 October 2014
10.1126/science.1259369

CHEMICAL OCEANOGRAPHY

Increasing anthropogenic nitrogen in the North Pacific Ocean

Il-Nam Kim,¹ Kitack Lee,^{1*} Nicolas Gruber,² David M. Karl,³ John L. Bullister,⁴ Simon Yang,² Tae-Wook Kim⁵

The recent increase in anthropogenic emissions of reactive nitrogen from northeastern Asia and the subsequent enhanced deposition over the extensive regions of the North Pacific Ocean (NPO) have led to a detectable increase in the nitrate (N) concentration of the upper ocean. The rate of increase of excess N relative to phosphate (P) was found to be highest (~0.24 micromoles per kilogram per year) in the vicinity of the Asian source continent, with rates decreasing eastward across the NPO, consistent with the magnitude and distribution of atmospheric nitrogen deposition. This anthropogenically driven increase in the N content of the upper NPO may enhance primary production in this N-limited region, potentially leading to a long-term change of the NPO from being N-limited to P-limited.

The rate of deposition of reactive nitrogen (i.e., NO_y + NH_x and dissolved organic forms; see supplementary text S1) from the atmosphere to the open ocean has more than doubled globally over the past 100 years (1), reaching a magnitude that is comparable to about half of the global ocean N₂ fixation (2). The increase in atmospheric nitrogen deposition (AND) is particularly acute in the North Pacific Ocean (NPO) due to rapid population growth and burgeoning industrial activity in northeast Asian countries. These changes in northeast Asia have markedly increased reactive nitrogen fluxes in the adjacent marine environment (3, 4), largely through atmospheric transport by westerly winds and subsequent deposition. Though it has been recognized that such an increasing addition of

reactive nitrogen to the ocean could lead to major changes in the upper ocean nitrogen cycle and biological productivity (5), the majority of studies conducted to date have suggested that the impact is small and not detectable (1), except in near-shore environments and marginal seas (3). A recent study directly comparing nutrient measurements made over more than two decades showed that nitrate (N) concentration has increased in the northeast Asian marginal seas and that this increase was probably due to strongly growing AND (3). Here we extend this analysis to the entire NPO and show that the anthropogenic influence has already affected the open-ocean nitrogen cycle.

Owing to a lack of basin-wide, nutrient concentration data of sufficient duration (decades) at strategic locations, we reconstructed the temporal changes in N across the NPO using a method based on the relation between the excess of N in a water parcel relative to that expected based on the phosphate (P) concentration and the chlorofluorocarbon-12 (CFC-12)-derived ventilation age of that water parcel (6) (supplementary text S2). The excess in N relative to P—i.e., N* (7, 8)—at each sampling location was calculated as: N* = N - R_{N:P} × P, where N and P are the measured concentrations and R_{N:P} is the Redfield ratio of 16:1. Because of increasing

¹School of Environmental Sciences and Engineering, Pohang University of Science and Technology (POSTECH), Pohang, 790-784, Republic of Korea. ²Environmental Physics Group, Institute of Biogeochemistry and Pollutant Dynamics, ETH Zürich, Zürich, Switzerland. ³Daniel K. Inouye Center for Microbial Oceanography, University of Hawaii at Manoa, 1950 East West Road, Honolulu, HI 96822, USA. ⁴Pacific Marine Environmental Laboratory, National Oceanic and Atmospheric Administration (NOAA), Seattle, WA 98115, USA. ⁵Ocean Circulation and Climate Research Division, Korea Institute of Ocean Science and Technology, Ansan, 426-744, Republic of Korea.

*Corresponding author. E-mail: ktl@postech.ac.kr

biases and uncertainties in the CFC-12-derived ages for water masses >40 years old (9), we limited our analysis to water parcels <40 years old (i.e., waters ventilated between the mid-1960s and late-1990s). Although this single-ventilation-age approach has shortcomings compared with methods that estimate the full ventilation-age distribution of a water parcel (9), the data used in this study were collected during a period of quasi-linear growth of CFC-12 in the atmosphere (fig. S1 and table S1), and the differences between the two types of tracer-derived ages have little impact on trends examined in the present study (6).

Three distinct trends in N^* as a function of depth (or ventilation date) were found in the analysis. Trend 1 shows that if the magnitude of the N sources is similar to that of the N sinks (N sources \approx N sinks), the seawater N^* values remain approximately unchanged regardless of the age of the water parcels (see the black line in Fig. 1). Trend 1 is typically observed in deep waters (>3000 m) but is not confined to such waters. Trend 1 can also be seen in the upper waters of the Pacific Ocean sector of the Southern Ocean (solid and dotted lines in the upper inset in Fig. 1) and the Indian Ocean (dotted line in the lower inset in Fig. 1), which are regions far removed from major AND sources. Trend 2 shows that if the magnitude of the N sources is less than that of the N sinks (N sources < N sinks), the values of N^* fall below the black line representing trend 1 (see the purple curve and the lower inset in Fig. 1). Trend 2 is applicable to intermediate depths at locations where low O_2 concentrations promote denitrification processes

($NO_3^- \rightarrow N_2O/N_2$), which remove N. If the magnitude of the N sources in recent decades exceeded that of the N sinks (N sources > N sinks), as in trend 3, the values of N^* should increase as the age of a water parcel decreases (see the light blue line in Fig. 1). Trend 3 is usually applicable to the upper ocean, where AND and N_2 fixation overwhelmingly contribute to elevated N^* values (10). Thus, to infer the imprint of increasing AND in the NPO, we focus on data exhibiting trend 3.

As mixing of water masses with different initial values of N^* and ventilation age could bias trend 3, we used the extended optimum multi-parameter method (supplementary text S3) to separate the temporal N^* trend from any mixing contribution. This analysis was performed along density coordinates σ_θ for the core density layers of the main water masses in all six regions [i.e., region 1: $\sigma_\theta = 27.2$ to 27.3 for the East Sea Intermediate Water (ESIW), regions 2 to 6: $\sigma_\theta = 25.5$ to 26.5 for North Pacific Central Water (NPCW)] (insets in Fig. 2, C to H; see also supplementary text S3 and fig. S2). The rate of N^* increase from this isopycnal analysis is in good agreement with the depth-based rates estimated from linear regression of the relation between N^* and the partial pressure of CFC-12 ($pCFC-12$)-derived ventilation date for data found on trend 3 in all six regions (Fig. 2, B to H, and Table 1). This good consistency indicates that trend 3 is unlikely to be generated by mixing between low- N^* water from low- O_2 intermediate depths and high- N^* upper water. It remains possible that this temporal trend is an artifact arising from the

production and remineralization of organic matter occurring at a ratio that is substantially different from our assumed Redfield ratio of 16:1, especially in light of recent findings suggesting that organic matter formed in low latitudes tends to have an N:P ratio substantially above the Redfield ratio (11). However, the positive slope of the relation we observed [i.e., decreasing N^* with depth (Fig. 2, B to H)] indicated that this biological process is unimportant, as it would generate the opposite slope in the thermocline. Specifically, the formation of organic matter in the upper ocean with a high N:P ratio would lower N^* values in surface water (11) but increase N^* in thermocline waters where the N-rich organic matter is remineralized.

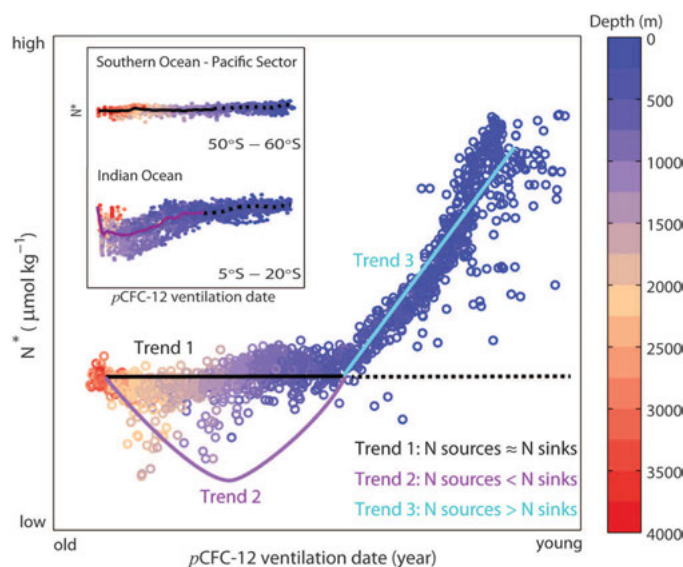
Our mixing-corrected reconstructions of the N^* trends between the late 1970s and mid-1990s show increases at all locations across the NPO (Fig. 2). The rate of N^* increase was highest ($\sim 0.24 \mu\text{mol kg}^{-1} \text{yr}^{-1}$) in the East Sea (region 1 in Fig. 2A) and steadily decreased in an eastward direction with increasing distance from the source continent (Fig. 3). In the East Sea, the N^* values for waters older than 30 years (<1970s) remained constant ($N^* = -6.6 \pm 0.5 \mu\text{mol kg}^{-1}$), whereas the values for waters younger than 30 years (>1970s) increased with time (Fig. 2C). In the mid-latitude NPO (20°N to 40°N), N^* values greater than deep water values began to appear in the upper waters (<600 m) ventilated in the late 1970s (Fig. 2, D to H).

To further confirm that the inferred trends of N^* in the NPO reflect temporal changes in AND and are not mixing artifacts, we analyzed the temporal evolution of N^* in the western and central NPO, where the temporal coverage of the data is sufficient to perform such an analysis. Using the PACIFICA database, we found that in the western and central NPO (upper left inset in Fig. 4A; areas of 20°N to 40°N and 130°E to 180°W), the subsurface N^* (300 to 400 m depth) substantially increased in the past decade (Fig. 4A); the estimated rates within this depth range were comparable to those obtained based on $pCFC-12$ age (upper right inset in Fig. 4A). This increase in N^* occurred without a concurrent change in dissolved O_2 (fig. S3A) or P (fig. S3B). Similar trends were also observed in the central NPO (i.e., the area between 20°N to 40°N along the 150°W line) (fig. S4). Furthermore, the overall rate of N^* increase ($0.04 \pm 0.02 \mu\text{mol kg}^{-1} \text{yr}^{-1}$ for the period 1988–2011 for the 100 to 200 m depth interval) observed at Station ALOHA (Hawaii Ocean Time-series) (Fig. 4B) was also comparable to the rate based on $pCFC-12$ age, although the time frame for the comparison is somewhat different.

To attribute the observed temporal trends in N^* to the recent increases in AND, we need to exclude alternative explanations, in particular the possibility of a recent increase in N_2 fixation. Although we cannot completely exclude this possibility, several lines of evidence indicate that N_2 fixation may not be a major contributor. First, an increase in N_2 fixation would also lead to a decrease in the upper ocean P concentration and a concomitant increase in its thermocline

Fig. 1. Three trends of N^* variation. This figure shows the relation between N^* and the $pCFC-12$ -derived ventilation date (which is the year that the CFC-12 concentration in the water sample would have last been in equilibrium with the atmosphere) for seawater samples obtained in the East Sea (Sea of Japan) as part of the Circulation Research of the East Asian Marginal Seas II program in 1999.

Trends in the N^* variations associated with three types of cases are presented: Trend line 1 (black solid and dotted lines) indicates a balance of N sources and N sinks, relative to P. Trend line 2 (purple line) would occur if N sinks > N sources (e.g., due to denitrification processes in low-oxygen waters). Trend line 3 (light blue line) indicates major sources of N in recently ventilated waters (and also indicates that N increased over time, regardless of changes in P). The color scale indicates depth. The inset shows the relation between N^* and the $pCFC-12$ -derived ventilation date in the Pacific Ocean sector of the Southern Ocean (50°S to 60°S) and in the tropical Indian Ocean (5°S to 20°S)—two regions far removed from major AND sources—using the PACIFICA and GLODAP databases, respectively.



concentration, which we do not observe (figs. S3 and S4). Second, an increase in N_2 fixation would be expected to shift the peak in the rate of increase of N^* from near the surface to greater depths, as N -rich organic matter of the N_2 fixers is remineralized in the thermocline. In contrast, we observed the highest rate of N^* increase in the surface ocean (Fig. 2). Taken together, these findings suggest that N_2 fixation does not add substantially to the long-term increase in N^* in the NPO. However, some contribution of N_2 fixation cannot be entirely excluded, especially given that the N^* -based rates of N increase exceed the modeled and observed rates of AND (Fig. 3). At region 5 near Hawaii, for example, the N^* -based rates are two to three times higher than the observed rates of AND (from dry and wet deposition). In this region, marine N_2 fixation is estimated to contribute to ~50% of the export production (12, 13).

Having excluded N_2 fixation as a major contributor for most of the NPO, AND remains the only major process that can explain the recent increases in N concentration in the NPO. Several lines of evidence strongly support the conclusion. First, the start of the increase in N^* in the mid-latitude NPO around the 1970s coincided with the onset of a rapid increase in anthropogenic nitrogen emissions from northeast Asian (14). Second, the spatial pattern and absolute magnitude of the rate of increase of N^* agreed well with the AND rates derived from an atmospheric transport model (15) and observations (16, 17) (Fig. 3). Furthermore, the meridional distribution of aerosol N concentrations was also consistent with the distribution of subsurface N^* in the central NPO (i.e., 200 to 300 m along the 160°E and 180°W lines; see fig. S5). In particular, atmospheric N concentrations measured at Midway (28.2°N and 177.4°W) in the spring (March to

Table 1. Comparison of rates of N^* increase based on isopycnal layer and depth for six regions. See Fig. 2A for region locations. For isopycnal analysis, $\sigma_\theta = 27.2$ to 27.3, representing the core density layer of ESIW, was chosen for region 1; and $\sigma_\theta = 25.5$ to 26.5, representing the core density layer of NPCW, was chosen for regions 2 to 6 (fig. S2). Depth rates were derived from Fig. 2.

Regions	Methods	
	Isopycnal	Depth
(μmol kg ⁻¹ yr ⁻¹)		
1	0.24 ± 0.03	0.25 ± 0.01
2	0.11 ± 0.03	0.12 ± 0.01
3	0.11 ± 0.04	0.10 ± 0.03
4	0.04 ± 0.02	0.13 ± 0.02
5	0.03 ± 0.04	0.08 ± 0.01
6	-0.03 ± 0.30	0.03 ± 0.01

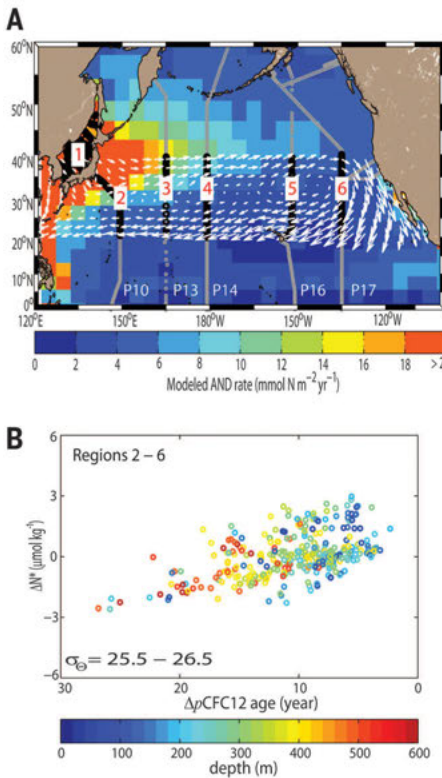
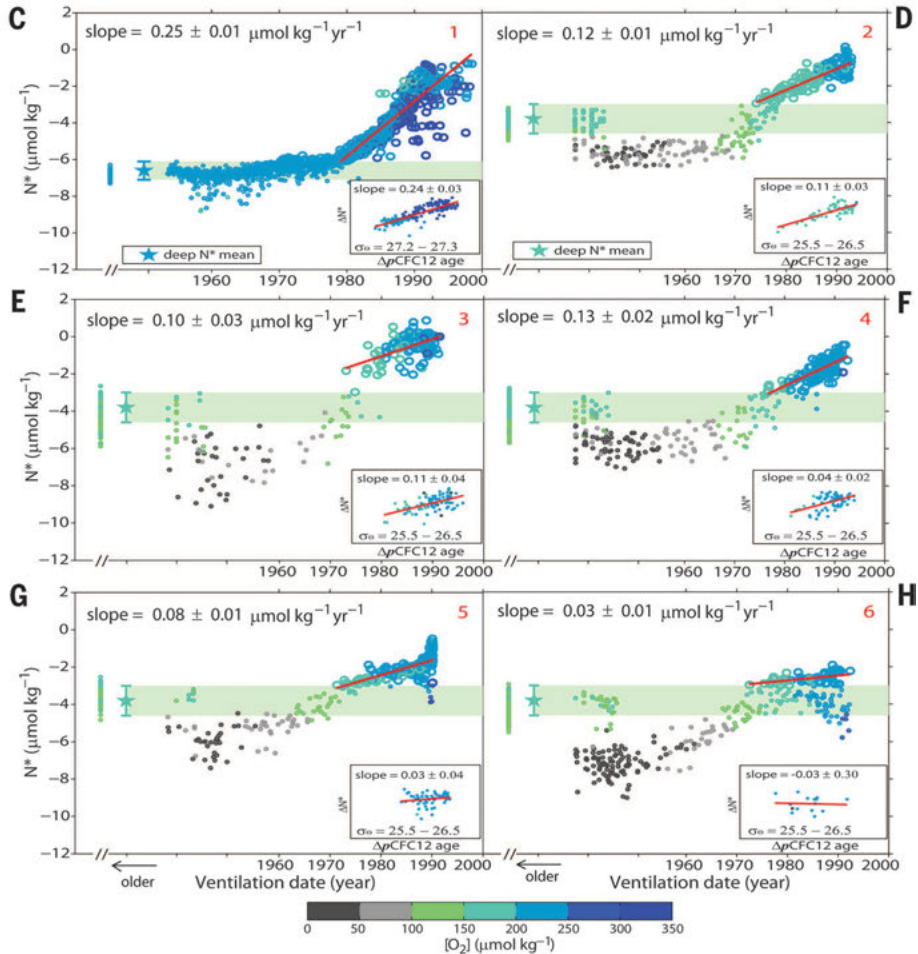


Fig. 2. Estimation of the rate of increase in excess N (N^*). (A) Map showing the NPO. The color scale indicates AND in 1993 (15) overlaid with the mean wind vectors over the period 1990–1999 (25). The numbers 1 to 6 in red indicate the East Sea and five sections in the NPO (P10, P13, P14, P16, and P17), respectively (table S1), and locations of data used in this analysis are shown as black circles. (B) Plot of ΔN^* ($\Delta N^* = N^*_{\text{OBS}} - \sum x_i N^*_i$) versus $\Delta p\text{CFC-12 age}$ ($\Delta p\text{CFC-12 age} = p\text{CFC-12 age}_{\text{OBS}} - \sum x_i p\text{CFC-12 age}_i$), corrected for the effect of physical mixing (x_i) among different water masses (i.e., Δ = observed value – estimated value from end-member mixing) (7), within the range of potential density $\sigma_\theta = 25.5$ to 26.5 in regions 2 to 6 from the mid-latitude NPO. The color scale indicates water depth. (C to H) Plots of seawater N^* values (micromoles per kilogram) versus ventilation date (derived from $p\text{CFC-12}$ ages) for regions 1 to 6. Numerical values for ventilation dates are



shown only for 1960–2000 due to large uncertainties in earlier dates (see text). The color scale indicates dissolved O_2 concentration. Green shading indicates the envelopes of the deep water N^* values. The star symbols and error bars indicate the mean of the deep water N^* values and the standard deviation (SD) from the mean, respectively. The rates of N^* increase ($N^*_{\text{OBS}} > N^*_{\text{DEEP}}$) were estimated from the linear regression analysis (shown as the red lines). The insets show plots of seawater ΔN^* versus $\Delta p\text{CFC-12 age}$ for the core density layers of the ESIW in region 1 ($\sigma_\theta = 27.2$ to 27.3) and the NPCW in regions 2 to 6 ($\sigma_\theta = 25.5$ to 26.5). See supplementary text S2 and S3 for the data and isopycnal analysis.

May) showed an increasing trend over the period 1981–2000 (18). Third, the magnitude of the AND-induced N^* increase is consistent with expect-

tations based on a simulation conducted with an updated version of the National Center for Atmospheric Research (NCAR) Community Earth

System Model (19) over the Anthropocene (supplementary text S4 and fig. S6), where AND increased from the pre-industrial era (1850) to modern times (2000). This model includes all of the key processes influencing the marine nitrogen cycle (water-column and benthic denitrification, N_2 fixation, AND, and river inputs) and thus is well suited to analyze the consequences of increasing AND on the ocean nitrogen cycle. Finally, such clear signals of seawater N^* increase are seen only in the NPO and not in comparable mid-latitude Southern Hemisphere sections (fig. S7), where AND has had little impact over the past decades. These observations are also compelling evidence that the observed N^* signals in the NPO are due to the effect of AND. Thus, the balance of evidence suggests that the observed increase in N^* in the upper NPO is a consequence of the recent increase in AND, resulting largely from the dramatic increase in anthropogenic nitrogen emissions in northeastern Asia.

The possible impacts of this anthropogenic perturbation on the open-ocean nitrogen cycle are numerous. The NPO is generally thought to be N-limited (2, 13); therefore, the input of nitrogen may increase primary and export production. In the mid-latitude NPO, the rate of N increase is equivalent to $10 \pm 2\%$ (20) of the export production ($\sim 1.5 \times 10^3 \text{ mmol C m}^{-2} \text{ yr}^{-1}$) (21), which is comparable to the rate derived from AND modeling (5). Given the likelihood that the magnitude of AND will continue to increase in the future (22), the mid-latitude NPO could rapidly switch to having surplus N. Thus, past and future increases in AND have the potential to alter the phytoplankton community composition and, in

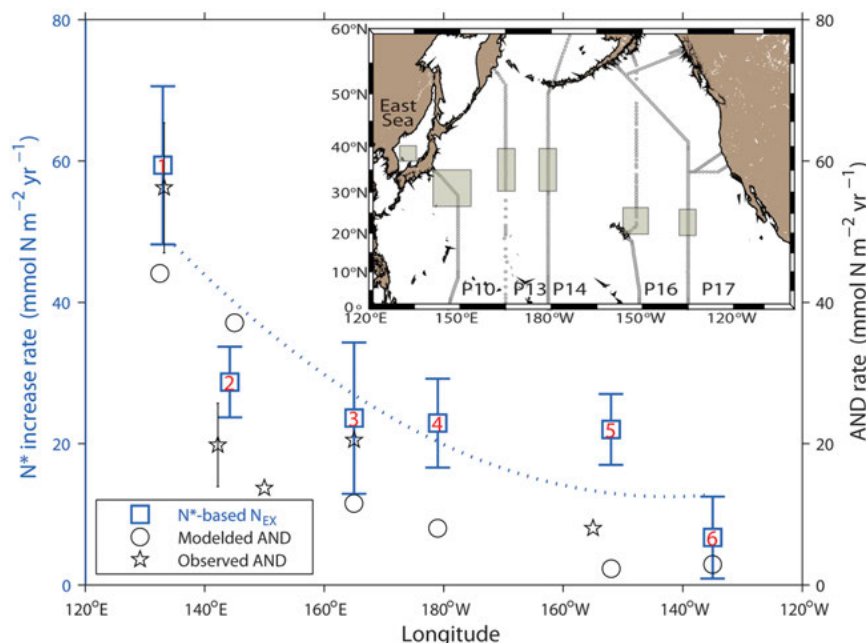
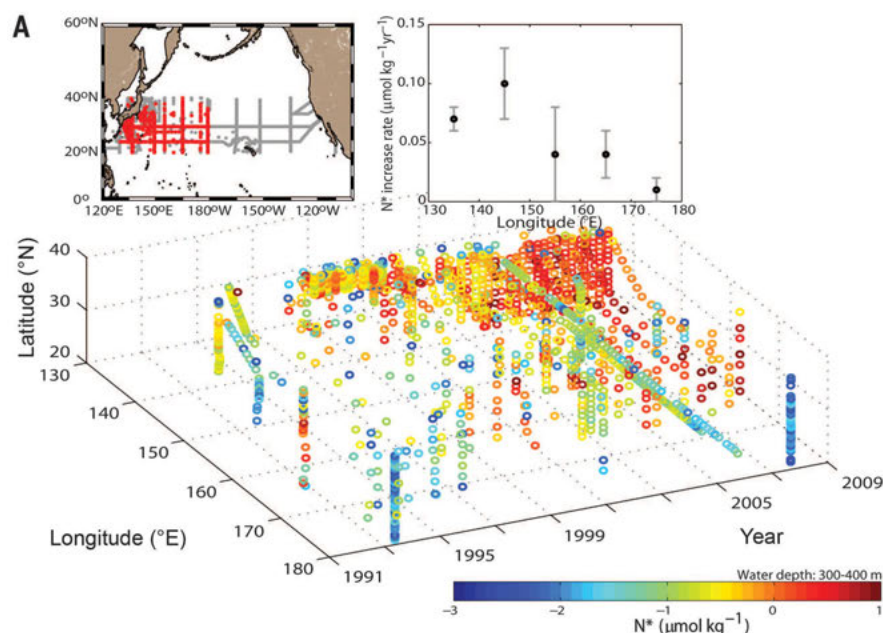


Fig. 3. Comparison of the N^* -based rates with AND rates. Comparison of the N^* values integrated over the water column [$\int_0^z N^* / pCFC-12 \text{ age } dz$, where z is the depth at which the N^* ($N^*_{\text{OBS}} > N^*_{\text{DEEP}}$) signal was observed, blue squares] with the modeled (circles) (15) and observed (stars) (16, 17) AND rates (see supplementary text S5 for the AND rates observed in the mid-latitude NPO). The blue dotted line indicates a least-squares curve fitting of the N^* -based rates. The inset shows the locations (shaded boxes) at which the experimental seawater N^* increase rates were compared with the modeled and observed AND rates. Error bars indicate the SD from the mean.



right) are plotted on the x axis. The error bars in the inset (upper right) indicate the SD from the mean. **(B)** Rate of N^* increase estimated from the annual mean N^* (averaged between 100 and 200 m) over the period 1988–2011 at Station ALOHA (see supplementary text S2 for the ALOHA nutrient data). Error bars indicate the SD from the mean. The rate of N^* increase is $0.04 \pm 0.02 \text{ } \mu\text{mol kg}^{-1} \text{ yr}^{-1}$, as was estimated from a least-squares linear regression of data obtained during the period 1988–2011.

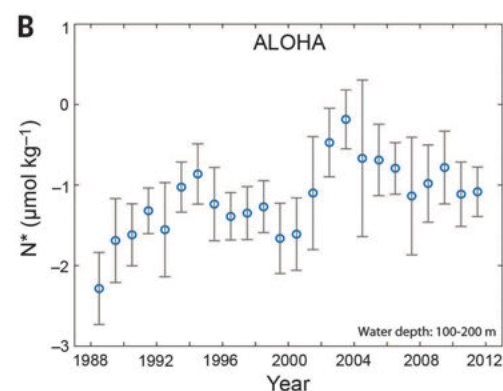


Fig. 4. Temporal variations of N^* . **(A)** Distribution of N^* in the western and central NPO (20°N to 40°N and 130°E to 180°W) determined from data in the PACIFIC database collected between 300 and 400 m in the period 1992–2008. The upper left inset shows the data points (red) used in this analysis. The upper right inset shows the rates of N^* increase averaged for each 10° longitude interval. Note that the midpoints in the inset (upper

the long term, the structure of the ecosystem. In addition, such anthropogenic nitrogen inputs into the NPO could also enhance N_2O production due to an increase in remineralization in association with enhanced export production levels and potentially stimulate denitrification (1, 23). If similar trends are confirmed across the other major ocean basins, it would constitute another example of a global-scale alteration of the Earth system.

REFERENCES AND NOTES

1. R. A. Duce *et al.*, *Science* **320**, 893–897 (2008).
2. N. Gruber, in *Nitrogen in the Marine Environment, The Marine Nitrogen Cycle: Overview and Challenges*, D. G. Capone, D. A. Bronk, M. R. Mulholland, E. J. Carpenter, Eds. (Elsevier, Amsterdam, 2008), pp. 1–50.
3. T.-W. Kim, K. Lee, R. G. Najjar, H.-D. Jeong, H. J. Jeong, *Science* **334**, 505–509 (2011).
4. J. N. Galloway, *Nutr. Cycl. Agroecosyst.* **57**, 1–12 (2000).
5. G. S. Okin *et al.*, *Global Biogeochem. Cycles* **25**, GB2022 (2011).
6. S. C. Doney, J. L. Bullister, *Deep-Sea Res. A* **39**, 1857–1883 (1992).
7. N. Gruber, J. L. Sarmiento, *Global Biogeochem. Cycles* **11**, 235–266 (1997).
8. A. F. Michaels *et al.*, *Biogeochemistry* **35**, 181–226 (1996).
9. R. A. Fine, *Annu. Rev. Mar. Sci.* **3**, 173–195 (2011).
10. A. Singh, M. W. Lomas, N. R. Bates, *Deep-Sea Res. II* **93**, 148–158 (2013).
11. A. C. Martiny *et al.*, *Nat. Geosci.* **6**, 279–283 (2013).
12. K. Lee, *Limnol. Oceanogr.* **46**, 1287–1297 (2001).
13. D. Karl *et al.*, *Nature* **388**, 533–538 (1997).
14. H. Akimoto, H. Narita, *Atmos. Environ.* **28**, 213–225 (1994).
15. F. J. Dentener, Global maps of atmospheric nitrogen deposition, 1860, 1993, and 2050. Data set (Oak Ridge National Laboratory Distributed Active Archive Center, Oak Ridge, TN, 2006); <http://daac.ornl.gov/>.
16. J. Jung, H. Furutani, M. Uematsu, *J. Atmos. Chem.* **68**, 157–181 (2011).
17. J. H. Carrillo, M. G. Hastings, D. M. Sigman, B. J. Huebert, *Global Biogeochem. Cycles* **16**, 1076 (2002).
18. J. M. Prospero, D. L. Savoie, R. Arimoto, *J. Geophys. Res.* **108**, 4019 (2003).
19. J. K. Moore, K. Lindsay, S. C. Doney, M. C. Long, K. Misumi, *J. Clim.* **26**, 9291–9312 (2013).
20. The 2% error is 1 SD from the mean export production estimated using the rate of seawater N^* increase found in regions 2 to 5 shown in Fig. 3.
21. K. Lee, D. M. Karl, R. Wanninkhof, J.-Z. Zhang, *Geophys. Res. Lett.* **29**, 1907 (2002).
22. Future projections suggest that AND in 2030 may be up to 30% higher than in 2000 in the mid-latitude NPO (1). In particular, NH_4 deposition in 2100 may be double that in 2000 (24), whereas NO_x deposition is likely to decrease substantially due to regulation of emissions. This perturbation, in conjunction with enhanced ocean stratification, could become a key factor determining future primary and export production in the NPO.
23. P. Suntharalingam *et al.*, *Geophys. Res. Lett.* **39**, L07605 (2012).
24. P. Ciais *et al.*, in *Climate Change 2013: The Physical Science Basis, Contribution of Working Group I to the Fifth Assessment Report of the Intergovernmental Panel on Climate Change*, T. F. Stocker *et al.*, Eds. (Cambridge Univ. Press, Cambridge, 2013), chap. 6.
25. Mean wind data during 1990–1999 are available at www.esrl.noaa.gov/psd/.

ACKNOWLEDGMENTS

We thank all scientists responsible for the CFC-12 and nutrient measurements in the GLODAP (<http://cdiac.ornl.gov/oceans/glodap/>) and PACIFICA (<http://cdiac.ornl.gov/oceans/PACIFICA/>) databases and the CREAMS II (<http://sam.ucsd.edu>) and HOT (<http://hahana.soest.hawaii.edu/hot/>) programs. This research was supported by the Mid-Career Researcher Program (no. 2012RIA2A1A01004631) and the Global Research Project funded by the National Research Foundation (NRF) of Ministry of Science, Information Communication Technology, and Future Planning,

Science and Technology (no. 2013K1A1A2A02078278). Partial support was provided by the “Management of marine organisms causing ecological disturbance and harmful effects” program funded by the Ministry of Oceans and Fisheries. T.-W.K. was supported by the Basic Science Research Program through NRF (no. 2012RIA6A3A0403883). D.M.K. was funded by the NSF (nos. OCE09-26766 and EF04-24599) and the Gordon and Betty Moore Foundation. J.L.B. was funded by NOAA’s Climate Program Office. N.G. and S.Y. acknowledge the financial support from ETH Zürich. Author contributions: I.-N.K. and K.L. designed the study and wrote the manuscript with support from N.G., D.M.K., and J.L.B. I.-N.K. analyzed the data. N.G., D.M.K., J.L.B., S.Y., and T.-W.K. contributed to the manuscript with discussions

and comments. S.Y. and N.G. performed NCAR Community Earth System Model simulations. The authors declare no competing financial interests.

SUPPLEMENTARY MATERIALS

www.sciencemag.org/content/346/6213/1102/suppl/DC1
Supplementary Text
Figs. S1 to S7
Tables S1 and S2
References (26–33)

7 July 2014; accepted 3 November 2014
10.1126/science.1258396

COGNITIVE PSYCHOLOGY

Forgetting the presidents

H. L. Roediger III* and K. A. DeSoto

Two studies examined how U.S. presidents are forgotten. A total of 415 undergraduates in 1974, 1991, and 2009 recalled as many presidents as possible and attempted to place them in their correct ordinal positions. All showed roughly linear forgetting of the eight or nine presidents prior to the president holding office at the time, and recall of presidents without respect to ordinal position also showed a regular pattern of forgetting. Similar outcomes occurred with 497 adults (ages 18 to 69) tested in 2014. We fit forgetting functions to the data to predict when six relatively recent presidents will recede in memory to the level of most middle presidents (e.g., we predict that Truman will be forgotten to the same extent as McKinley by about 2040). These studies show that forgetting from collective memory can be studied empirically, as with forgetting in other forms of memory.

The name of the president of the United States is known to virtually all adult Americans. When doctors wish to test the cognitive status of a concussion or stroke patient, they often ask the patient to identify the current president; a response of “Ronald Reagan” in 2014, for example, reveals a probable deficit. Once they leave office, however, presidents recede from the memory of U.S. citizens. For instance, today presidents such as Fillmore, Pierce, and Arthur are barely remembered at all, yet at one point in America’s past their names were known by all U.S. adults, just as the names Obama or Bush are known in 2014.

The purpose of this project was to study how presidents are forgotten from collective memory. Collective memory, sometimes called historical or popular memory, refers to the representation of the past shared by a group (1–4). Most studies in this tradition focus on how events of historical significance are remembered (e.g., the Holocaust, the 9/11 attacks), whereas our focus is on historical forgetting [see (5)].

We can assume that recall of a president is 100% while the president holds office and begins to drop when he leaves office. Our question is: What is the rate at which samples of U.S. citizens forget the presidents over time?

Across two studies, we determined the rate at which presidents recede from collective memory of (i) college students and (ii) a wider sample of

Americans (taken from Amazon Mechanical Turk; MTurk). We measured memory for each president using both ordinal position recall and free recall criteria. Ordinal position recall describes whether an individual can place a president in the ordinal position in which he served (e.g., Lincoln in position 16). Free recall assesses whether an individual can recall a president’s name at all, regardless of ordinal position. To measure forgetting, we applied two methods to the resulting sets of data. We examined the decline in recall within each group of subjects from the current president at the time of testing to the next most recent and so on (i.e., the recency effect in recall within groups of individuals). In the second method, we computed forgetting curves for six presidents across three generations of college students.

In our first study, we tested three generations of college undergraduates in three widely separated years: 159 subjects in 1974 (6), 106 in 1991 (7), and 150 in 2009. In each case the students were given a sheet of paper numbered according to the number of presidents (e.g., numbers 1 through 41 in 1991), with instructions to try to recall as many presidents as possible and to place them in their correct ordinal position. Students were told that if they recalled a president but not his ordinal position, they should guess or simply list that president off to the side of the page. They were given 5 min for recall, which prior research has shown is sufficient time to exhaust students’ knowledge (8). Figure 1A shows recall of presidents as a function of their chronological term in office, when students were given credit for

Department of Psychology, Washington University, St. Louis, MO 63130, USA.

*Corresponding author. E-mail: roediger@wustl.edu

recalling them only if placed in their correct ordinal position; Fig. 2A shows free recall of the presidents, giving credit for naming the person without regard to order.

In laboratory studies in which subjects are given a list of words or pictures to remember, a serial position function is obtained relating list position to probability of recall. This function is characterized by two components of interest: (i) the primacy effect (enhanced recall of items at the beginning of the list), and (ii) the recency effect (enhanced recall of items at the end of the list), both relative to lower recall of items in the middle of the list. The recency effect is of interest for our purposes because it shows how items are forgotten over time. Namely, the last item in a series is almost perfectly recalled, with preceding items showing systematically lower recall as a function of the amount of time or the number of intervening items (presidents in our case), counting backward from the most recent. See fig. S1 for an example of a serial position function for word lists.

Another characteristic of the serial position function is that a distinctive event (relative to other events that are similar in character) is well remembered even if it is in the middle of a list. For example, a picture appearing in the middle

of a list of words is recalled better than the surrounding words [the isolation effect (9–11)]. This feature occurs in our studies with a natural series rather than a list.

Figure 1A shows that memory for ordinal position of presidents follows a classic serial position function. All three groups showed a similar pattern of results: The first presidents were frequently recalled, with a steep drop until Lincoln, who showed elevated recall along with the two succeeding presidents (A. Johnson and Grant). This outcome is similar to the isolation effect in list recall, with Lincoln (or perhaps the U.S. Civil War) serving as the distinctive event. Recall then dropped back to a low baseline until the recency effect became noticeable. Even though the three groups of students were tested over a 35-year time period, the recency effect was remarkably consistent in that it occurred for the last 9 or 10 presidents in all groups. In addition, recall of presidents before the point of recency (located in what is called the pre-recency portion of the serial position curve) did not differ much among the groups; this point was confirmed in the second study (see below). The data also showed consistent forgetting of the order of recent presidents over time by different groups of college students. For example, in 1974 nearly all college

students recalled L. Johnson and his ordinal position (36), but by 1991 the proportion had dropped to 0.52 and by 2009 it had plummeted to 0.20.

Whether presidents have been forgotten altogether, not merely with respect to their ordinal position, is better answered by plotting the data using a free recall criterion. These data, shown in Fig. 2A for the three groups of undergraduates, appear noisier than the data in Fig. 1A. Nonetheless, recency effects are still apparent, and what appears to be noise may rather reflect regularities in the memorability of presidents. For example, the dips at Truman, L. Johnson, and Ford occur in at least two samples and were confirmed in the second study.

A second method of measuring forgetting, the classic one in experimental psychology, is to plot the forgetting curve over time (or intervening items). The shape of this function—whether a logarithmic function or a power function—has been debated, but the power function provides a somewhat better fit when the two are directly compared (12). Moreover, these forgetting functions appear to be the same across many different tasks (12, 13). Our data in Figs. 1A and 2A provide little evidence of forgetting for presidents prior to and including Coolidge. Memorability of these presidents seems to have reached an asymptote in U.S. students' collective memory. However, for presidents since Coolidge, we can fit a power function to the free recall data and estimate the rate at which they will be forgotten. We did this for the six most recent presidents for whom we had three data points (i.e., they had held office in 1974 or earlier): Truman, Eisenhower, Kennedy, L. Johnson, Nixon, and Ford. We assumed that these presidents had a 100% recall probability after leaving office and used the 1974, 1991, and 2009 data to estimate recall probability in those years. We fit power functions to the four points for each president. These forgetting functions are shown in Fig. 3, and it is apparent that Truman, L. Johnson, and Ford are fading fastest from historical memory in this group, whereas Kennedy has been better retained.

We can use these data to estimate the number of years that elapse before presidents fall to the baseline levels estimated by the line in Fig. 3 (the line represents a mean of 0.26, the average memorability of pre-recency presidents excluding Lincoln, his two successors, and the first seven presidents). Of course, with only four data points, the projections are tentative. They can be seen in Fig. 3, but to give one example, we estimate that Truman will be forgotten by three-quarters of college students (i.e., will reach 0.26 free recall probability) by 2040, 87 years after leaving office.

The data from the study described above were collected from students of the same age cohort (18 to 22) at three points in time across 35 years. In our second study, we used a complementary tactic: We tested adults across varying age ranges in May 2014 on the same task. We tested 116 adults aged 18 to 29 (millennials), 207 adults aged 30 to 49 (generation X), and 174 adults aged 50 to 69 (baby boomers) (14). These three

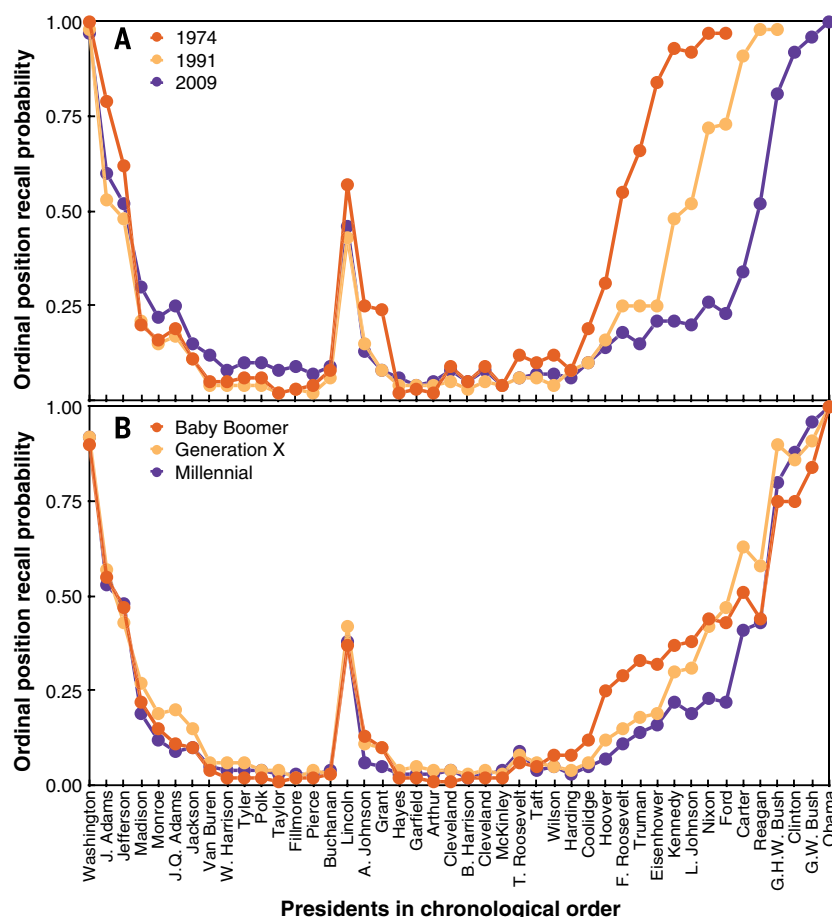


Fig. 1. Ordinal position recall probabilities. Ordinal position recall of presidents across (A) college students of three different generations (data collected in three different years) and (B) American adults of three different generations (data collected in 2014).

generations correspond approximately to the three generations of college students that participated in the first study (e.g., college students in 1974 are the same group that we call baby boomers in 2014). We sought to determine whether the serial position curves obtained in our earlier studies would replicate with this larger sample of adults.

The data in Fig. 1B show that the answer is generally yes with strict positional recall, except that the recency part of the curve shows more overlap. In fact, recall of presidents from Washington to Coolidge reveals hardly any differences among the three age bands, and the data are similar to those in Fig. 1A. This lends support to our supposition from the first study that recall of these presidents has reached the asymptote of the forgetting curve. The differences emerge in the recency part of the curve, with older adults recalling more presidents in order than younger adults, at least from Coolidge through L. Johnson. Free recall results (Fig. 2B) again replicated the results in Fig. 2A reasonably well. The correlations between the patterns of data of people of similar age in Fig. 1, A and B, were $r = 0.91, 0.95$, and 0.98 for the baby boomer, generation X, and millennial samples, respectively (i.e., the data collected in 1974 correlated 0.91 with the data collected for the baby boomer group assessed in 2014). The similar values for the free recall data in Fig. 2, A and B, were $r = 0.93, 0.94$, and 0.97 . All correlations were significant ($P < 0.001$); see tables S1 and S2 for the full correlation matrices. These strong correlations indicate that serial position curves in recall of U.S. presidents are remarkably similar and stable across age and across generations spanning 35 years.

The results from our two studies show forgetting of presidents in terms of their correct ordinal position in office (Fig. 1) and simply their name and the fact that they served (Fig. 2). The recency effect indicates that subjects can retrieve presidents relatively well if the presidents held office during or just before the subjects' lifetimes, but that recall of correct ordinal position drops as one attempts to retrieve presidents whose terms were more distant in time. By analogy to serial position curves in recall of lists, recent presidents appear to exist in a state of heightened accessibility, shown by the greater recency effect that is akin to a short-term component for other memory tasks involving recent events or people [according to one theory (15); see also (16)]. That is, collective memory has a window on the past that recedes, although doubtless through mechanisms different from those involved in short-term recall of lists.

Another interesting finding in our data is how consistently the pre-recency presidents are remembered across generations of students in the first study, as confirmed by the replication in our second study. All samples also recalled Lincoln and his immediate successors better than most presidents and also recalled their ordinal positions. Why are these data so consistent? A possible explanation is that presidents who are viewed as having been more historically influential are

better remembered across generations. According to one theory (17), forgetting is adaptive and corresponds to environmental demands for needs of information. By this view, recall of presidents may be due to their frequency of mention in popular media, and frequency of mention may be determined by importance. To investigate, we correlated the recall scores from our second

study with presidential rankings provided by history scholars and others (18). The correlation between recallability and ranking for presidents from Washington to Coolidge was high [$r(27) = 0.73, P < 0.001$]. This finding is in line with the theory and data in (17).

Another theory argues that position in a series accounts for some of the variance in presidential

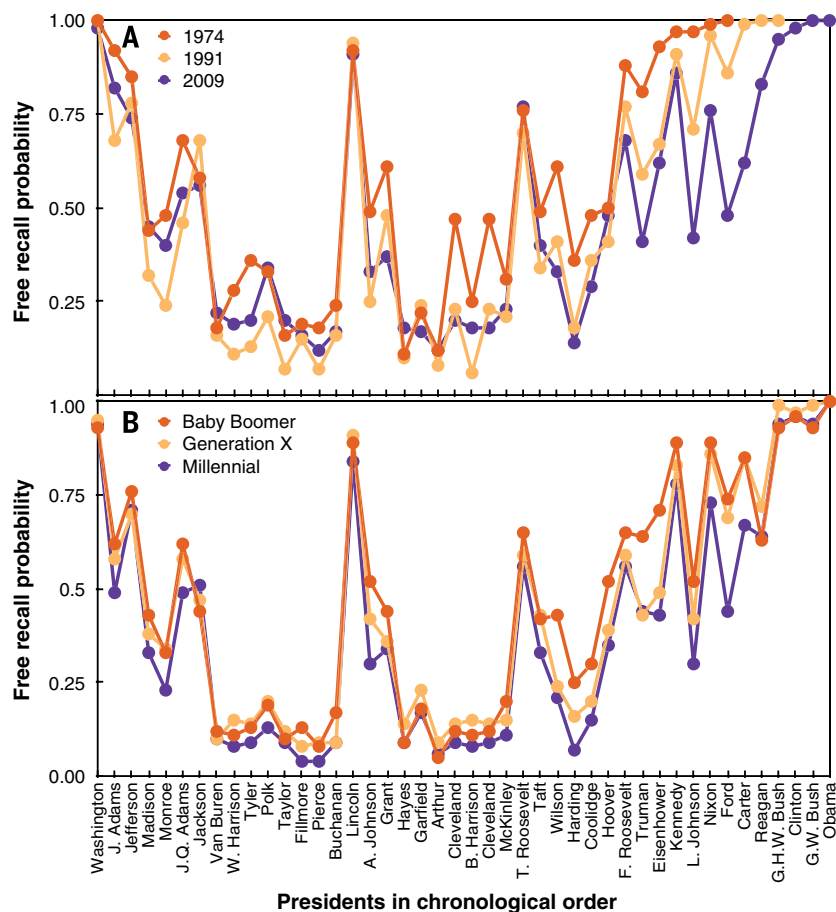
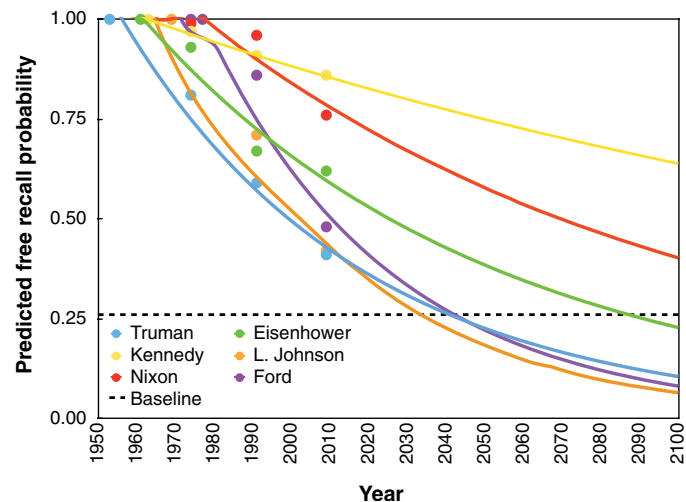


Fig. 2. Free recall probabilities. Free recall of presidents across (A) college students of three different generations (data collected in three different years) and (B) American adults of three different generations (data collected in 2014).

Fig. 3. Predicted forgetting curves.

Forgetting curves for six presidents were predicted using the power function and data from the three generations of college students. The points show the original data.



recall (especially ordinal position recall), perhaps explaining why the second president, John Adams, is recalled in position better than Thomas Jefferson, a figure of greater historical importance (6, 7). Other researchers have supported this claim (19, 20), but there are also dissenters (21–23). Clearly Lincoln and his successors are well remembered because of their association with the American Civil War and the ending of slavery, but it is notable that many students and adults also often know that Lincoln was the 16th president. This superior recall of a salient event in a series resembles the isolation effect in list recall (9–11).

Our results show that memories of famous historical people and events can be studied objectively [see also (4, 5, 24, 25)]. We find two different functions that characterize forgetting of the presidents. First, for individuals, memory for the order of presidents who served in office during the individual's lifetime (or a few years before) declines linearly. Second, forgetting of presidents across generations follows a power function until an asymptote is reached, in line with data from many other domains [(12, 13); see (5) for similar results]. The asymptote probably reflects both the importance and frequency of mention of the particular president (17). The other notable feature of our results is the highly consistent recall of presidents by college students from several universities across a spread of 35 years, as well as by other Americans recruited from MTurk in 2014. The high correlations point to a great stability in how the presidents are remembered across generations—a seemingly permanent form of collective memory [i.e., semantic memory (26)].

REFERENCES AND NOTES

1. J. V. Wertsch, *Voices of Collective Remembering* (Cambridge Univ. Press, New York, 2002).
2. J. V. Wertsch, H. L. Roediger, *Memory* **16**, 318–326 (2008).
3. H. L. Roediger, F. M. Zaromb, A. C. Butler, in *Memory in Mind and Culture*, P. Boyer, J. V. Wertsch, Eds. (Cambridge Univ. Press, Cambridge, 2009), chap. 6.
4. F. Zaromb, A. C. Butler, P. K. Agarwal, H. L. Roediger, *Mem. Cognit.* **42**, 383–399 (2014).
5. D. C. Rubin, *Psychon. Bull. Rev.* **5**, 397–400 (1998).
6. H. L. Roediger, R. G. Crowder, *Bull. Psychon. Soc.* **8**, 275–278 (1976).
7. R. G. Crowder, *Mem. Cognit.* **21**, 142–145 (1993).
8. H. L. Roediger, D. G. Payne, G. L. Gillespie, D. S. Lean, *J. Verb. Learn. Verb. Behav.* **21**, 635–655 (1982).
9. H. von Restorff, *Psychol. Forsch.* **18**, 299–342 (1933).
10. R. R. Hunt, *Psychon. Bull. Rev.* **2**, 105–112 (1995).
11. R. R. Hunt, C. A. Lamb, *J. Exp. Psychol. Learn. Mem. Cogn.* **27**, 1359–1366 (2001).
12. J. T. Wixted, E. B. Ebbesen, *Mem. Cognit.* **25**, 731–739 (1997).
13. D. C. Rubin, A. E. Wenzel, *Psychol. Rev.* **103**, 734–760 (1996).
14. G. Paolacci, J. Chandler, *Curr. Dir. Psychol. Sci.* **23**, 184–188 (2014).
15. R. C. Atkinson, R. M. Shiffrin, *Psychol. Learn. Motiv.* **2**, 89–195 (1968).
16. K. A. Ericsson, W. Kintsch, *Psychol. Rev.* **102**, 211–245 (1995).
17. J. R. Anderson, L. J. Schooler, *Psychol. Sci.* **2**, 396–408 (1991).
18. N. R. Silver, “Contemplating Obama's place in history, statistically.” *New York Times* (23 January 2013); <http://fivethirtyeight.blogs.nytimes.com/2013/01/23/contemplating-obamas-place-in-history-statistically>.
19. I. Neath, *Mem. Cognit.* **38**, 659–666 (2010).
20. I. Neath, J. Saint-Aubin, *Can. J. Exp. Psychol.* **65**, 77–83 (2011).
21. A. F. Healy, J. T. Parker, in *The Nature of Remembering: Essays in Honor of Robert G. Crowder*, H. L. Roediger, J. S. Nairne, I. Neath, A. M. Surprenant, Eds. (American Psychological Association, Washington, DC, 2001), chap. 9.
22. A. F. Healy, T. F. Cunningham, K. M. Shea, J. A. Kole, in *The Foundations of Remembering: Essays in Honor of Henry L. Roediger III*, J. S. Nairne, Ed. (Psychology Press, New York, 2007), chap. 12.
23. A. F. Healy, D. A. Havas, J. T. Parker, *J. Mem. Lang.* **42**, 147–167 (2000).
24. M. R. Kelley, I. Neath, A. M. Surprenant, *Mem. Cognit.* **41**, 600–610 (2013).
25. M. F. Overstreet, A. F. Healy, *Mem. Cognit.* **39**, 251–259 (2011).
26. E. Tulving, in *Organization of Memory*, E. Tulving, W. Donaldson, Eds. (Academic Press, New York, 1972), chap. 10.

ACKNOWLEDGMENTS

H.L.R. devised the concept and design of this research with the assistance of K.A.D.; H.L.R. and colleagues collected and analyzed

the 1974 and 1991 data; K.A.D. programmed, collected, and analyzed the 2009 and 2014 data; both authors analyzed and interpreted the aggregate data and contributed to writing and revising this manuscript. Data necessary to understand, assess, and extend the conclusions of the manuscript are available in the supplementary materials. A collaborative activity grant from the James S. McDonnell Foundation provided funding for the Internet research. We thank E. Tulving for his comments and A. M. Obenhaus, M. K. Bissell, C. D. Gordon, and M. E. McDonnell for their help with data collection and transcription. M. A. Wheeler collected the data reported in (7).

SUPPLEMENTARY MATERIALS

www.sciencemag.org/content/346/6213/1106/suppl/DC1

Materials and Methods

Figs. S1 to S3

Tables S1 and S2

References (27–31)

Data

5 August 2014; accepted 27 October 2014

10.1126/science.1259627

MITOCHONDRIA

Cell cycle-dependent regulation of mitochondrial preprotein translocase

Angelika B. Harbauer,^{1,2,3,4} Magdalena Opalińska,¹ Carolin Gerbeth,^{1,2,3} Josip S. Herman,¹ Sanjana Rao,^{1,3,5*} Birgit Schönfisch,¹ Bernard Guiard,⁶ Oliver Schmidt,^{1,4†} Nikolaus Pfanner,^{1,4‡} Chris Meisinger^{1,4‡}

Mitochondria play central roles in cellular energy conversion, metabolism, and apoptosis. Mitochondria import more than 1000 different proteins from the cytosol. It is unknown if the mitochondrial protein import machinery is connected to the cell division cycle. We found that the cyclin-dependent kinase Cdk1 stimulated assembly of the main mitochondrial entry gate, the translocase of the outer membrane (TOM), in mitosis. The molecular mechanism involved phosphorylation of the cytosolic precursor of Tom6 by cyclin Clb3-activated Cdk1, leading to enhanced import of Tom6 into mitochondria. Tom6 phosphorylation promoted assembly of the protein import channel Tom40 and import of fusion proteins, thus stimulating the respiratory activity of mitochondria in mitosis. Tom6 phosphorylation provides a direct means for regulating mitochondrial biogenesis and activity in a cell cycle-specific manner.

Mitochondria are crucial for numerous tasks, from adenosine 5'-triphosphate synthesis and metabolism of amino acids, lipids, iron, and heme to apoptosis (1–8). Mitochondria cannot be formed de novo, but can be formed only by growth and division of preexisting organelles. Growth of mitochondria depends on the import of a large number of cytosolically synthesized precursor proteins. Multiple pathways of protein import into mitochondria

have been identified (2, 3, 9). Nearly all pathways use the main mitochondrial entry gate, the translocase of the outer membrane (TOM). Mitochondria form a dynamic network that is continuously remodeled by fusion and fission events that, together with cytoskeleton-dependent transport and anchoring in daughter and mother cells, ensure a proper distribution of mitochondria during cell division (5, 7, 10–13). Cell cycle-dependent regulation of mitochondrial components has been observed in a few cases, including activation of the fission protein Drp1, of respiratory complex I, and of a mitochondrial DNA binding protein; the fusion protein Fzo1 is degraded upon arrest of yeast cells in G₁ phase (14–19). Whereas mitochondrial protein import is regulated by cytosolic kinases under different metabolic conditions (respiratory versus nonrespiratory) (20, 21), whether protein import and the cell cycle are connected is not clear.

We used budding yeast as model organism to study the mitochondrial protein import machinery in different phases of the cell cycle.

¹Institut für Biochemie und Molekularbiologie, ZBMZ, Universität Freiburg, 79104 Freiburg, Germany. ²Trinationales Graduiertenkolleg 1478, Universität Freiburg, 79104 Freiburg, Germany. ³Faculty of Biology, Universität Freiburg, 79104 Freiburg, Germany. ⁴BIOSS Centre for Biological Signalling Studies, Universität Freiburg, 79104 Freiburg, Germany. ⁵Spemann Graduate School of Biology and Medicine, Universität Freiburg, 79104 Freiburg, Germany. ⁶Centre de Génétique Moléculaire, CNRS, 91190 Gif-sur-Yvette, France. *Present address: Institute of Biochemistry, ETH Zürich, 8093 Zürich, Switzerland. †Present address: Division of Cell Biology, Biocentre, Medical University of Innsbruck, 6020 Innsbruck, Austria. ‡Corresponding author. E-mail: nikolaus.pfanner@biochemie.uni-freiburg.de (N.P.); chris.meisinger@biochemie.uni-freiburg.de (C.M.)

Spellman *et al.* (22) performed a genome-wide screen for mRNA levels during the yeast cell cycle. We analyzed the screen for components of the mitochondrial protein import machinery and noted a moderate increase of *TOM6* mRNA levels, but not of other translocase components in G₂/M phase (fig. S1A). Tom6 is a small integral membrane protein involved in the assembly of the TOM complex (23–25). To analyze if the change of mRNA levels resulted in altered Tom6 protein levels in different phases of the cell cycle, yeast cells were arrested in G₁ phase by the pheromone α -factor, in S phase by the DNA synthesis inhibitor hydroxyurea, and in M phase by the spindle poison nocodazole (26); *cdc14-1* yeast mutants were also arrested in M phase (late anaphase) (27, 28). The protein levels of Tom6 were increased in M phase (Fig. 1A; fig. S1, B to D; and table S1).

We asked if the large increase in mitochondrial Tom6 levels in M phase involved a direct regulatory mechanism in addition to the moder-

ate increase in mRNA levels. Ser16 of yeast Tom6 is a potential target site for cyclin-dependent kinases (CDKs) (20). Tom6 consists of an N-terminal hydrophilic domain and a C-terminal membrane anchor. A fusion protein containing the N-terminal domain was incubated with yeast cytosolic extract or purified Cdk1 (Cdc28), the CDK essential for cell cycle progression in yeast (29). Both cytosolic extract and purified Cdk1 (but not the CDK Pho85) phosphorylated Tom6; addition of the CDK inhibitor NU6102 or replacement of Ser¹⁶ by alanine blocked phosphorylation (Fig. 1B and fig. S2) (for the receptors Tom20, Tom22, and Tom70, CDK1- or cell cycle-dependent phosphorylation was not observed; fig. S3). The full-length precursor of Tom6 was phosphorylated with CDK1 and incubated with isolated mitochondria. Phosphorylated Tom6 was efficiently targeted to mitochondria and membrane integrated; in the absence of CDK1 or upon replacement of Ser¹⁶ by alanine, import of Tom6 into mitochondria was strongly inhibited (Fig. 1, C and D). The stability of imported Tom6 was not significantly altered by phosphorylation (fig. S4). Thus, Cdk1-mediated phosphorylation of the Tom6 precursor promotes its efficient import into mitochondria.

The mitochondrial levels of Tom40, the central channel-forming subunit of the TOM complex, were also increased in M phase (Fig. 1A, fig. S1D, and table S1). To determine if phosphorylation of Tom6 caused an alteration of the TOM complex, we generated yeast strains in which Ser¹⁶ of Tom6 was replaced either by alanine or phospho-mimetic glutamate. The levels of the TOM complex were decreased in Tom6^{S16A} mitochondria, yet increased in Tom6^{S16E} mitochondria (Fig. 2A). Tom6^{S16E} mitochondria contained increased levels of Tom40 (Fig. 2B). Tom6 is required for the stability of the TOM complex and thus in *tom6* Δ mitochondria, the amount of mature TOM complex is diminished (Fig. 2A) (23, 25). We asked if Tom6 was rate-limiting for Tom40 assembly and generated a

Fig. 1. Cdk1-mediated phosphorylation of Tom6 stimulates its import into mitochondria. (A) Immunoblots of yeast mitochondria isolated after cell cycle arrest with α -factor, hydroxyurea, or nocodazole. Tom6 was detected via an N-terminal FLAG tag. OM, outer membrane; IMS, intermembrane space; IM, inner membrane. Quantifications are shown in table S1. (B) Phosphorylation of purified Tom6^N-GST (glutathione S-transferase) with yeast cytosolic extract in the presence or absence of the CDK inhibitor NU6102, analyzed by a Tom6_{pS16}

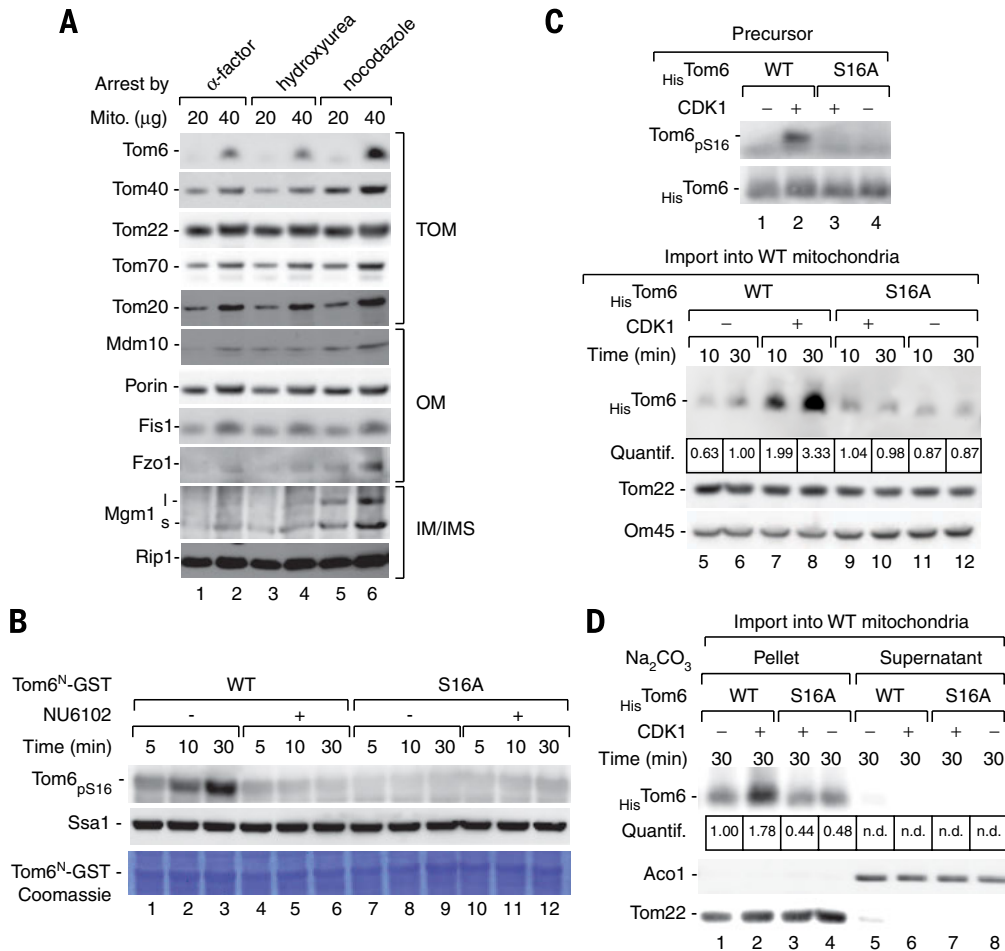


Fig. 1. Cdk1-mediated phosphorylation of Tom6 stimulates its import into mitochondria. (A) Immunoblots of yeast mitochondria isolated after cell cycle arrest with α -factor, hydroxyurea, or nocodazole. Tom6 was detected via an N-terminal FLAG tag. OM, outer membrane; IMS, intermembrane space; IM, inner membrane. Quantifications are shown in table S1. (B) Phosphorylation of purified Tom6^N-GST (glutathione S-transferase) with yeast cytosolic extract in the presence or absence of the CDK inhibitor NU6102, analyzed by a Tom6_{pS16}

phospho-specific antiserum. WT, wild type. (C) Mitochondrial import of full-length Tom6 precursor (containing an N-terminal His tag) with or without phosphorylation by CDK1. Lanes 1 to 4, input; lanes 5 to 12, reisolated mitochondrial pellets after incubation with Tom6 precursor (control import into WT mitochondria after 30 min set to 1). (D) Mitochondrial membrane integration of phosphorylated and nonphosphorylated Tom6 precursor assayed by carbonate extraction and quantified as in (C).

yeast strain overexpressing Tom6 (fig. S5A). Radiolabeled Tom40 precursor was incubated with isolated mitochondria, and the assembly stages were analyzed (24, 25). Overexpression of Tom6 stimulated the assembly of Tom40, but not of other β -barrel proteins like porin that are not assembled into TOM; the use of Tom6^{S16E} mitochondria also stimulated Tom40 assembly, whereas Tom6^{S16A} mitochondria were impaired in its assembly (Fig. 2, C to E, and fig. S5B). Thus, the Cdk1-triggered increase in mitochondrial Tom6 levels stimulates assembly of the mitochondrial protein import channel Tom40.

Yeast contains nine cyclins that activate Cdk1 in distinct cell cycle phases (G₁, S, or G₂/M) (29, 30). To synchronize growth of yeast cells, they were arrested in G₁ by α -factor, followed by removal of α -factor (26). We purified Cdk1 from different cell cycle phases under mild conditions (to maintain association with cyclins) and probed phosphorylation of the Tom6^N-fusion protein. Cdk1 purified from G₂/M phase was most efficient in phosphorylation of Tom6 (Fig. 3A). To identify the responsible cyclin, we expressed and purified individual cyclins and combined them with Cdk1. The G₂/M cyclin Clb3 activated Cdk1 for phosphorylation of

Tom6-Ser16 (Fig. 3B), whereas Cdk1 from *clb3*-deficient yeast was strongly inhibited in Tom6 phosphorylation (Fig. 3C) [as control, neither Pho85 nor Ssn3 (Cdk8) phosphorylated Tom6]. Thus, Clb3 activates Cdk1 to phosphorylate Tom6 in G₂/M phase. The assembly of Tom40 occurred with the highest efficiency in yeast cells arrested in M phase (Fig. 3D), in agreement with our model that Tom6 phosphorylation by Cdk1 in G₂/M phase promotes Tom40 biogenesis.

The levels of the two mitochondrial fusion guanosine triphosphatases (GTPases), outer-membrane Fzo1 and in particular inner-membrane Mgm1 (10–12), were increased in M phase (Fig. 1A, fig. S1D, and table S1). Overexpression of Tom6 stimulated Mgm1 import into mitochondria (Fig. 4A). The hydrophilic cytosol-exposed domain of Tom6 bound the precursor of Mgm1, but not the model preprotein b₂(167)-dihydrofolate reductase (DHFR); binding of Mgm1 depended on the phosphorylation of Tom6 by CDK1 and was blocked by removal of the N-terminal segment of the Mgm1 presequence (Fig. 4B). Thus, phosphorylated Tom6 specifically recognized the Mgm1 precursor. Mitochondrial import of Fzo1 was increased upon overexpression of Tom6 as well as after arrest

in M phase (Fig. 4C and fig. S6A). Because the Fzo1 precursor did not bind to the cytosol-exposed domain of Tom6 (Fig. 4B), the transmembrane segment of Tom6 may be involved in Fzo1 import. We imported the Fzo1 precursor and shortened constructs into mitochondria containing tagged full-length Tom6. Copurification of Fzo1 with Tom6 (Fig. 4D) depended on a region containing the first transmembrane segment of Fzo1 and was enhanced by the additional presence of its intermembrane space loop (fig. S6B). Whereas the import of control preproteins was not affected by Tom6 or by cell cycle phases (fig. S7), the increase in Fzo1 and Mgm1 levels in M phase was blocked in Tom6^{S16A} mutants (Fig. 4E). The stability of Fzo1 and Mgm1 was not altered in M phase (fig. S8) (Fzo1 levels are decreased upon G₁ arrest (14)). Neither the mitochondrial levels of Fis1 nor recruitment of the fission GTPase Dnm1 (10–12) to mitochondria were altered by Tom6 phosphorylation (Fig. 4E and fig. S9). Thus, phosphorylation of Tom6 stimulates TOM assembly and mitochondrial import of Fzo1 and Mgm1 in G₂/M phase.

To characterize the consequences on cell growth, wild-type and Tom6^{S16A} mutants were

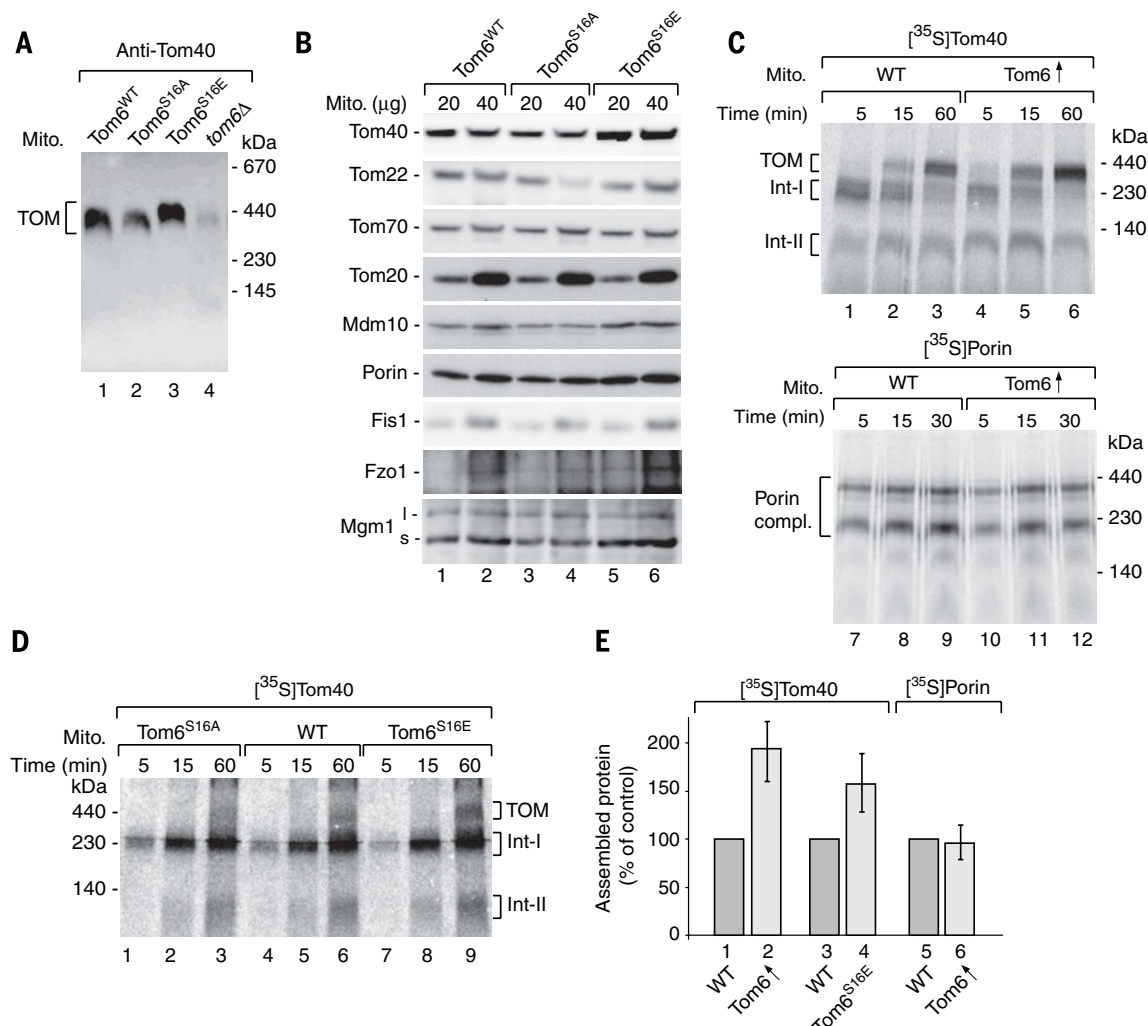
Fig. 2. Tom6-Ser16 phosphorylation enhances Tom40 biogenesis.

(A) TOM complex of Tom6 mutant mitochondria analyzed by blue native electrophoresis of digitonin-lysed mitochondria and immunoblotting.

(B) Steady-state levels of mitochondrial proteins in Tom6 mutant mitochondria.

(C) β -barrel assembly in mitochondria from WT and a Tom6-overexpressing strain using [³⁵S]Tom40 or [³⁵S]Porin precursor, analyzed by blue native electrophoresis. Tom40 assembly includes intermediate I (binding to sorting and assembly machinery SAM), intermediate II, and formation of mature TOM (35).

(D) Assembly of [³⁵S]Tom40 precursor in mitochondria of Tom6 phosphomutants. (E) Assembly of Tom40 and Porin as in (C) and (D) (mean \pm SEM, N \geq 3; WT controls set to 100%).



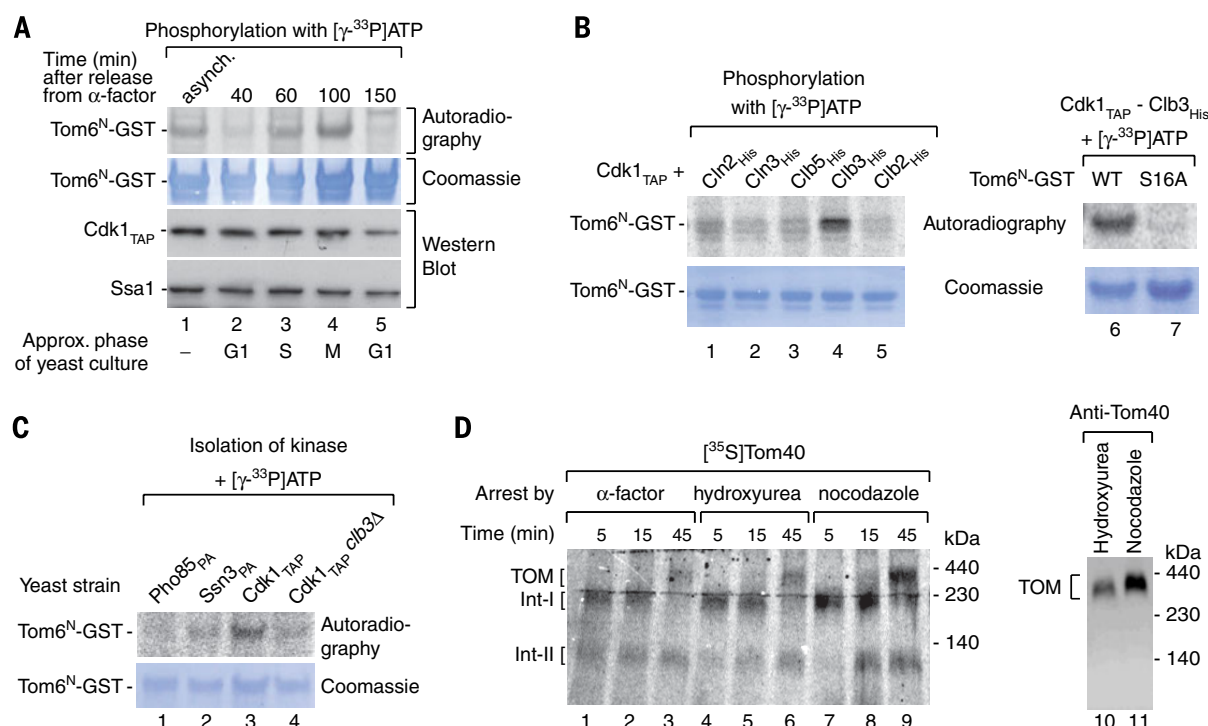


Fig. 3. Clb3 activates Cdk1 for phosphorylation of Tom6 in G₂/M phase. (A) Phosphorylation of Tom6^N-GST using Cdk1 purified from different phases of the cell cycle (36). (B) Phosphorylation of Tom6^N-GST by purified Cdk1-cyclin complexes. Lanes 1 to 6, WT Tom6; lane 7, Tom6^{S16A}. (C) Phosphorylation of Tom6^N-GST by kinases affinity purified from the indicated yeast strains. (D) Tom40 assembly is enhanced in mitochondria arrested in M phase. Lanes 1 to 9, import of [35 S]Tom40; lanes 10 and 11, immunoblot of endogenous TOM complex.

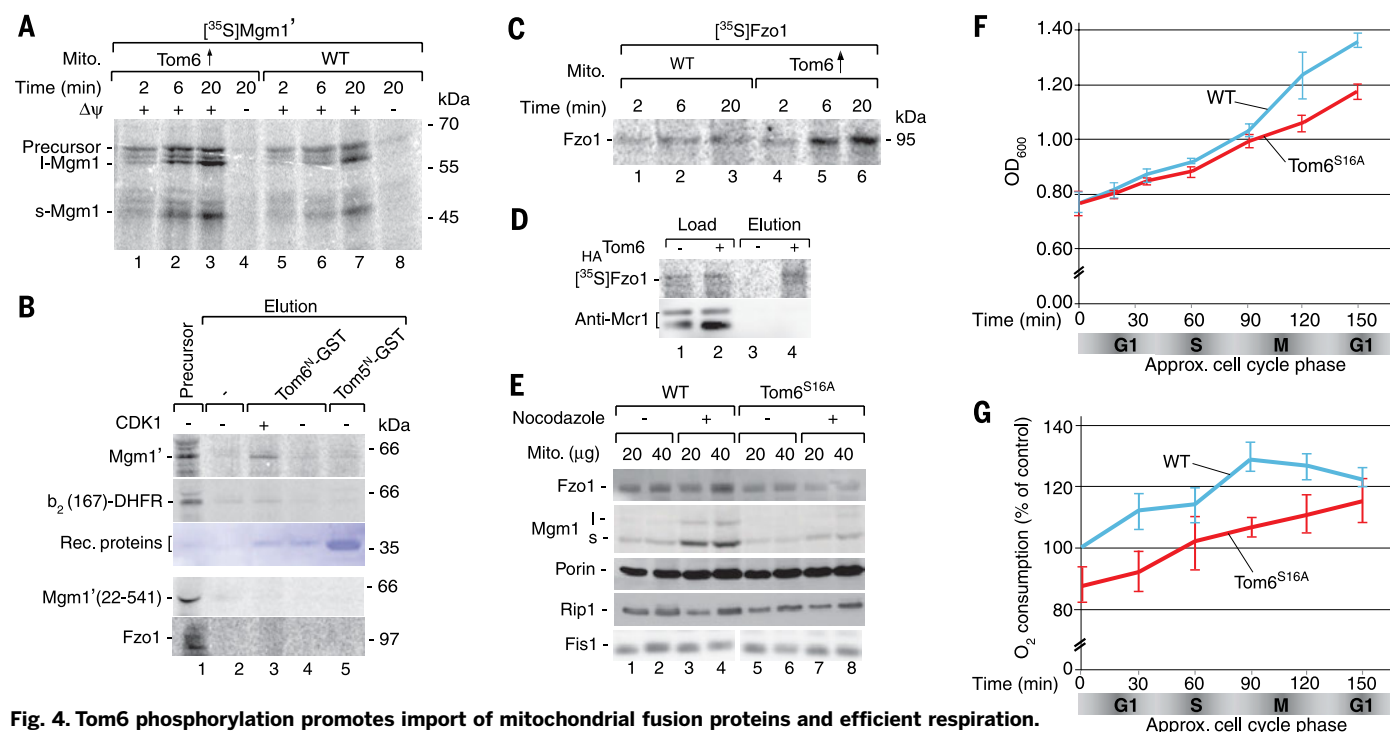


Fig. 4. Tom6 phosphorylation promotes import of mitochondrial fusion proteins and efficient respiration.

(A) Import of [35 S]Mgm1' precursor into mitochondria isolated from WT and Tom6-overexpressing strains, followed by treatment with proteinase K. $\Delta\psi$, membrane potential. (B) Pull-down of [35 S]precursor proteins with recombinant small Tom proteins with or without phosphorylation by CDK1. (C) Import of [35 S]Fzo1 precursor into mitochondria isolated from WT and Tom6-overexpressing strains, followed by carbonate extraction. (D) [35 S]Fzo1 was incubated with mitochondria containing WT or hemagglutinin A (HA)-tagged Tom6, followed by lysis and anti-HA pull-down. Load 6%, elution 100%. (E) Steady-state levels of proteins in mitochondria isolated from WT and Tom6^{S16A} yeast with or without M-phase arrest by nocodazole. (F) Growth curves of WT and Tom6^{S16A} yeast after synchronization by α -factor arrest and release (mean \pm SEM, $N = 3$). (G) O₂ consumption of WT and Tom6^{S16A} yeast after synchronization by α -factor arrest and release (mean \pm SEM, $N = 4$; WT control set to 100%).

synchronized by α -factor arrest and their growth compared. The initial growth curves of both strains were similar up to M phase. Then, the growth of Tom6^{S16A} mutants lagged considerably behind that of the wild type, and progression of the cell cycle was delayed (Fig. 4F and fig. S10). Oxygen consumption was increased in M phase, yet not in Tom6^{S16A} mutants (Fig. 4G and fig. S11). The mitochondrial morphology was comparable between wild-type and Tom6^{S16A} mutant yeast (fig. S12; unless the mitochondrial morphology was compromised by an additional mutation, fig. S13). Thus, phosphorylation of Tom6 and its effect on the levels of fusion GTPases primarily affected the bioenergetic activity of mitochondria. Mgm1/OPA1 is required for fusion and for the maintenance of cristae and thus can affect the energetic capacity of the oxidative phosphorylation machinery (7, 12, 31, 32). Overexpression of Mgm1 indeed enhanced oxygen consumption (fig. S11). Thus, phosphorylation of Tom6 in G₂/M stimulates the import of fusion GTPases, in particular of Mgm1, and enhances the bioenergetic activity of mitochondria.

The cell division cycle and import of proteins into mitochondria are essential for cell propagation and growth (1–3, 13, 29, 33). Here we have found a direct molecular connection between cell cycle control by Cdk1 and assembly of the main protein entry gate of mitochondria. Phosphorylation of the mitochondrial assembly factor Tom6 by Cdk1-Clb3 initiates a reaction cascade of enhanced Tom6 targeting and assembly of the protein import channel Tom40. Increased TOM6 mRNA levels in G₂/M underscore the importance of the assembly factor in this phase of the cell cycle (fig. S1A) (22). Screening of the PHOSIDA database revealed a conserved phosphorylated M-phase peptide of human Tom6 (34), indicating that phosphorylation of Tom6 has been conserved in yeast and humans (fig. S14). Notably, out of many mitochondrial proteins tested, the levels of assembled TOM complex and of membrane fusion GTPases are increased in G₂/M. Phosphorylation of Tom6 stimulates the mitochondrial import of Mgm1, leading to an increased respiratory activity of mitochondria. The increased supply of bioenergy can promote energy-dependent steps of cytokinesis (18). This direct link between cell cycle and mitochondrial protein import suggests a specific role for the import of fusion proteins for mitochondrial activity and efficient progression through the cell division cycle.

REFERENCES AND NOTES

- P. Dolezal, V. Likic, J. Tachezy, T. Lithgow, *Science* **313**, 314–318 (2006).
- W. Neupert, J. M. Herrmann, *Annu. Rev. Biochem.* **76**, 723–749 (2007).
- A. Chacinska, C. M. Koehler, D. Milenkovic, T. Lithgow, N. Pfanner, *Cell* **138**, 628–644 (2009).
- C. Osman, D. R. Voelker, T. Langer, *J. Cell Biol.* **192**, 7–16 (2011).
- T. E. Shutt, H. M. McBride, *Biochim. Biophys. Acta* **1833**, 417–424 (2013).
- R. Lill, *Nature* **460**, 831–838 (2009).
- L. Pellegrini, L. Scorrano, *Cell Death Differ.* **14**, 1275–1284 (2007).
- L. Galluzzi, O. Kepp, G. Kroemer, *Nat. Rev. Mol. Cell Biol.* **13**, 780–788 (2012).
- T. Endo, K. Yamano, S. Kawano, *Biochim. Biophys. Acta* **1808**, 955–970 (2011).
- B. Westermann, *Nat. Rev. Mol. Cell Biol.* **11**, 872–884 (2010).
- K. Okamoto, J. M. Shaw, *Annu. Rev. Genet.* **39**, 503–536 (2005).
- S. Hoppins, L. Lackner, J. Nunnari, *Annu. Rev. Biochem.* **76**, 751–780 (2007).
- J. D. Vevea, T. C. Swayne, I. R. Boldogh, L. A. Pon, *Trends Cell Biol.* **24**, 53–60 (2014).
- A. Neutznier, R. J. Youle, *J. Biol. Chem.* **280**, 18598–18603 (2005).
- M. Martínez-Díez, G. Santamaría, A. D. Ortega, J. M. Cuezva, *PLOS ONE* **1**, e107 (2006).
- N. Taguchi, N. Ishihara, A. Jofuku, T. Oka, K. Mihara, *J. Biol. Chem.* **282**, 11521–11529 (2007).
- M. Radulovic, E. Crane, M. Crawford, J. Godovac-Zimmermann, V. P. C. C. Yu, *Mol. Cell. Proteomics* **9**, 145–152 (2010).
- Z. Wang et al., *Dev. Cell* **29**, 217–232 (2014).
- L. Fajas, *Front. Oncol.* **3**, 4 (2013).
- O. Schmidt et al., *Cell* **144**, 227–239 (2011).
- C. Gerbeth et al., *Cell Metab.* **18**, 578–587 (2013).
- P. T. Spellman et al., *Mol. Biol. Cell* **9**, 3273–3297 (1998).
- P. J. T. Dekker et al., *Mol. Cell. Biol.* **18**, 6515–6524 (1998).
- K. Model et al., *Nat. Struct. Biol.* **8**, 361–370 (2001).
- J. Dukanovic, K. S. Dimmer, N. Bonnefoy, K. Krumpke, D. Rapaport, *Mol. Cell. Biol.* **29**, 5975–5988 (2009).
- A. Amon, *Methods Enzymol.* **351**, 457–467 (2002).
- G. S. Taylor, Y. Liu, C. Baskerville, H. Charbonneau, *J. Biol. Chem.* **272**, 24054–24063 (1997).
- F. Stegmeier, A. Amon, *Annu. Rev. Genet.* **38**, 203–232 (2004).
- J. Bloom, F. R. Cross, *Nat. Rev. Mol. Cell Biol.* **8**, 149–160 (2007).
- D. O. Morgan, *Annu. Rev. Cell Dev. Biol.* **13**, 261–291 (1997).
- S. Meeusen et al., *Cell* **127**, 383–395 (2006).
- H. Chen, A. Chomyn, D. C. Chan, *J. Biol. Chem.* **280**, 26185–26192 (2005).
- H. Hochegger, S. Takeda, T. Hunt, *Nat. Rev. Mol. Cell Biol.* **9**, 910–916 (2008).
- F. Gnäd, J. Gunawardena, M. Mann, *Nucleic Acids Res.* **39**, D253–D260 (2011).
- N. Wiedemann et al., *Nature* **424**, 565–571 (2003).
- Detailed experimental procedures are in the supplementary materials on Science Online.

ACKNOWLEDGMENTS

We thank M. Bohnert, N. Wiedemann, M. van der Laan, T. Becker, L. Ellenrieder, D. Mikropoulou, and W. Stroukov for discussion, materials, and basic characterization of yeast mutants. This work was supported by the Deutsche Forschungsgemeinschaft, Excellence Initiative of the German Federal and State Governments (EXC 294 BIOS; GSC-4 Spemann Graduate School), Bundesministerium für Bildung und Forschung (Dynamo), Sonderforschungsbereich 746, and Trinationales Graduiertenkolleg GRK 1478. Work included in this study has also been performed in partial fulfillment of the requirements for the doctoral theses of A.B.H. and O.S. at the University of Freiburg. The data presented in this paper are tabulated in the main paper and the supplementary materials.

SUPPLEMENTARY MATERIALS

www.sciencemag.org/content/346/6213/1109/suppl/DC1
Materials and Methods
Figs. S1 to S14
Tables S1 to S3
References (37–59)

15 September 2014; accepted 23 October 2014
Published online 6 November 2014;
10.1126/science.1261253

PALEOGENOMICS

Genomic structure in Europeans dating back at least 36,200 years

Andaine Seguin-Orlando,^{1,*} Thorfinn S. Korneliussen,^{1,*} Martin Sikora,^{1,*} Anna-Sapfo Malaspinas,¹ Andrea Manica,² Ida Moltke,^{3,4} Anders Albrechtsen,⁴ Amy Ko,⁵ Ashot Margaryan,¹ Vyacheslav Moiseyev,⁶ Ted Goebel,⁷ Michael Westaway,⁸ David Lambert,⁸ Valeri Khartanovich,⁶ Jeffrey D. Wall,⁹ Philip R. Nigst,^{10,11} Robert A. Foley,^{1,12} Marta Mirazon Lahr,^{1,12,†} Rasmus Nielsen,^{5,†} Ludovic Orlando,¹ Eske Willerslev^{1,†}

The origin of contemporary Europeans remains contentious. We obtained a genome sequence from Kostenki 14 in European Russia dating from 38,700 to 36,200 years ago, one of the oldest fossils of anatomically modern humans from Europe. We find that Kostenki 14 shares a close ancestry with the 24,000-year-old Mal'ta boy from central Siberia, European Mesolithic hunter-gatherers, some contemporary western Siberians, and many Europeans, but not eastern Asians. Additionally, the Kostenki 14 genome shows evidence of shared ancestry with a population basal to all Eurasians that also relates to later European Neolithic farmers. We find that Kostenki 14 contains more Neandertal DNA that is contained in longer tracts than present Europeans. Our findings reveal the timing of divergence of western Eurasians and East Asians to be more than 36,200 years ago and that European genomic structure today dates back to the Upper Paleolithic and derives from a metapopulation that at times stretched from Europe to central Asia.

The ancestors of contemporary Eurasians are believed to have left Africa some 60,000 to 50,000 years ago (60 to 50 ka) (1, 2), possibly 30,000 to 40,000 years later than Australo-Melanesian ancestors (3). Despite controversies about routes out of Africa, the first Upper Paleolithic (UP) industries of Eurasia are found

in the Levant from ~48 ka (4, 5). Expansion into Europe took place through multiple events that by ~40 ka had generated a spatially and culturally structured anatomically modern human (AMH) population—from Russia (6) to Georgia (7), Bulgaria (8), southern Europe (9, 10), and the United Kingdom (11). The few AMH fossils

associated with these initial UP industries are morphologically variable (9, 12–17). In western Eurasia, the distinctive Aurignacian toolkit, first observed at Willendorf (Austria) by 43.5 ka (18), became predominant across the earlier range by 39 ka. Although analyses of ancient human genomes have advanced our understanding of the European past, revealing contributions from Paleolithic Siberians, European Mesolithic, and Near Eastern Neolithic groups to the European gene pool (19–23), the possible contribution of the earliest Eurasians to these later cultures and to contemporary human populations remains unknown. To investigate this, we sequenced the genome of Kostenki 14 (K14, Markina Gora) (Fig. 1A).

The locality of Kostenki-Borshchevo on the Middle Don River, Russia, has one of the most extensive Paleolithic records in eastern Europe. The K14 human skeleton was excavated in 1954 (24) and was recently dated to $33,250 \pm 500$ radiocarbon years before the present (B.P.) (25), 38.7 to 36.2 thousand calendar years B.P. (ky cal B.P.), in agreement with the stratigraphic position of the burial that cuts into the Campanian Ignimbrite ash layer dated to ~ 39.3 ky cal B.P. (26). Below the skeleton, there is a distinctive early UP industry, with end scrapers, burins, prismatic cores, and bone artifacts (layer IV); the cultural layer above (layer III) has a regionally local character (27, 28) [supplementary materials (SM) S1 and S2].

We performed 13 DNA extractions from a total of 1.285 g of the left tibia (dorsal side of the shaft), using two extraction methods based on silica purification (29, 30). We first constructed seven Illumina libraries and validated the presence of typical signatures of postmortem DNA damage, using a fraction of DNA extracts (SM S3). The remaining extracts were built into 63 libraries after enzymatic uracil-specific excision reagent (USER) treatment to limit the effect of nucleotide

misincorporations in downstream analyses (31) (table S2). Additionally, a limited fraction of two DNA extracts was purified for methylated DNA fragments using methyl binding domain (MBD) enrichment (32) before USER treatment and library building, for a total of eight DNA libraries. Following stringent quality criteria for read alignment, we identified a total number of 175.2 million unique reads aligning against the human reference genome hg19, representing an average depth of coverage of 2.84X (SM S4). The eight USER-treated DNA libraries that exhibited limited error rates and contamination levels were selected for further analyses. This restricted the data set to 148.9 million unique reads, representing a final depth of coverage of 2.42X. We exploited the fact that K14 was a male and used the heterozygosity levels present in the X chromosome to estimate overall levels of contamination around 2.0% (SM S5 and S6 and table S5). The population genetics analyses results are robust to contamination of that level. In particular, we replicated the main analyses with selected libraries with varying contamination levels and observed no qualitative effect on the results (see SM S9 for details).

Mitochondrial analyses confirmed the sequence previously reported for K14 [haplogroup U2 (33)], which supports data authenticity. The Y chromosome belongs to haplogroup C M130, the same as in La Braña—a late Mesolithic hunter-gatherer (MHG) from northern Spain (22) (SM S7).

To identify patterns of shared ancestry and admixture among K14, other ancient genomes and contemporary Eurasians [based on a single-nucleotide polymorphism (SNP) array panel of 2091 individuals from 167 populations], we carried out a series of analyses—model-based clustering and principal component analysis (PCA)—to show the contribution of diverse genetic components within K14: D statistics to explore the affinity of K14 to pairs of populations (using Mbuti Pygmy as an outgroup); f_4 statistics to test whether a given modern population is equidistant to an ancient individual and a particular recent group (here, Sardinians), given an outgroup (here, Papuans); and f_3 statistics to explore both patterns of admixture (“admixture” f_3) and shared ancestry (“outgroup” f_3). Key results were also replicated using two whole-genome sequencing data sets of modern individuals from worldwide populations (23, 34).

Model-based clustering analyses (35) show that K14 has different genetic components of substantial size (Fig. 1B and SM S10), suggesting the sharing of sets of alleles with different Eurasian groups. The largest fraction of K14’s ancestry derives from a component that is maximized in European MHGs and also predominant in contemporary northern and eastern Europeans. The genetic affinity of K14 to contemporary Europeans is also observed using outgroup f_3 statistics (36). Using Mbuti Pygmy as an outgroup, we find that among a panel of 167 contemporary populations, Europeans have the greatest affinity (i.e., the largest f_3) to K14 (Fig. 1C). This conclusion is also formally supported by comparing

pairs of populations to K14 using the D statistics of the form $D(\text{Mbuti Pygmy}, \text{K14}; \text{Population 1}, \text{Population 2})$. This statistic is expected to be equal to zero if K14 is symmetrically related to Population 1 and Population 2, whereas its expectation is negative (positive) if K14 is more closely related to Population 1 (Population 2). For pairs of populations involving East Asians (Population 1) and Europeans (Population 2), K14 is always significantly more closely related to Europeans [e.g., $Z = 12.1$ (Han and Lithuanians)], in all data sets analyzed (SM S9 and table S7). We also confirmed that these results are robust to possible contamination from a modern DNA source by filtering for reads with a high likelihood of ancient DNA using a model-based approach (37), as well as calculating contamination-corrected D statistics (23) (SM S9 and fig. S18).

Within Europe, northern Europeans show the closest affinity to K14, based both on the f_3 (Fig. 1D) and D statistics [e.g., $Z = 6.7$ for Sardinians and Lithuanians; table S7 and fig. S16]. This pattern closely resembles that of European MHGs (La Braña, Ajv58, Loschbour, and Motala) and Mal’ta (MA1) (figs. S14 and S15), with the exception of the latter’s strong genetic affinity with Native Americans, which is unique to that individual. Furthermore, a direct comparison to ancient genomes in the outgroup f_3 statistics shows that K14 has a higher affinity with MHGs (Loschbour and La Braña) than any other ancient individual or contemporary population (fig. S14). Together with the rare Y chromosome lineage shared with La Braña, these results provide strong evidence of shared ancestry and extensive gene flow between UP West Eurasian people related to K14 and European MHGs and their contemporary European descendants.

An interpretation of the above results would be that K14 is an early member of a lineage leading to western Eurasian MHGs after their split from the proposed ancestral northern Eurasian lineage, including MA1. However, D statistics of the form $D(\text{Mbuti Pygmy}, \text{Modern}; \text{Ancient}, \text{K14})$ —which test whether K14 and an ancient individual form a clade with respect to a modern population—reject this simple tree-like relationship. We find that all contemporary non-Africans, except Australo-Melanesians, are closer to either MA1 or MHGs than to K14 [e.g., $Z = -5.3$ for D (Mbuti and Han; Loschbour and K14); SM S9, table S10, and fig. S19]. This would suggest a basal position of K14 with respect to MHGs and ancient north Eurasians, which is also shown in admixture graphs using TreeMix (SOM S12 and figs. S24 and S25). In addition, a sizeable component of K14’s ancestry observed in the model-based clustering analyses is predominant in contemporary Middle Eastern/Caucasus (ME/C) populations and Neolithic ancient genomes (NEOL) (Gok2, Iceman, and Stuttgart) but absent in MA1 or MHGs (Fig. 1B and fig. S20). This component has been associated with a suggested “basal Eurasian” lineage contributing to NEOL to explain an observed increase in allele sharing between MHGs/MA1 and East Asians compared with NEOL (27). Because K14 shows

¹Centre for GeoGenetics, Natural History Museum of Denmark, University of Copenhagen, Øster Voldgade 5–7, 1350 Copenhagen, Denmark. ²Department of Zoology, University of Cambridge, Downing Street, Cambridge, CB2 3EJ, UK. ³Department of Human Genetics, University of Chicago, 920 East 58th Street, Cummings Life Science Center, Chicago, IL 60637, USA. ⁴The Bioinformatics Center, University of Copenhagen, Ole Maaløes Vej 5, 2200 København N, Denmark. ⁵Department of Integrative Biology, University of California, Berkeley, CA 94720, USA. ⁶Department of Physical Anthropology, Kunstkamera, Peter the Great Museum of Anthropology and Ethnography, Russian Academy of Sciences, 24 Srednii Prospekt, Vassilievskii Island, St. Petersburg, Russia. ⁷Center for the Study of the First Americans and Department of Anthropology, Texas A&M University, TAMU-4352, College Station, Texas 77845-4352, USA. ⁸Environmental Futures Research Institute, Griffith University, 170 Kessels Road, Nathan, Brisbane, Queensland 4111, Australia. ⁹Department of Epidemiology and Biostatistics, University of California San Francisco, 185 Berry Street, Lobby 5, Suite 5700, San Francisco, CA 94107, USA. ¹⁰Division of Archaeology, University of Cambridge, Cambridge, Downing Street, CB2 3DZ, UK. ¹¹Department of Human Evolution, Max-Planck-Institute for Evolutionary Anthropology, Leipzig, Deutscher Platz 6, D-04103, Germany. ¹²Leverhulme Centre for Human Evolutionary Studies, Department of Archaeology and Anthropology, University of Cambridge, Cambridge, Fitzwilliam Street, CB2 1QH, UK.

*These authors contributed equally to the work. †Corresponding author. E-mail: ewillerslev@snm.ku.dk (E.W.), rasmus_nielsen@berkeley.edu (R.N.), mbml1@cam.ac.uk (M.M.L.)

the same pattern as NEOL, a parsimonious explanation would be that K14 also derives some ancestry from a related basal Eurasian lineage. Consistent with this hypothesis, we find that East Asians are equally distant to NEOL and K14, using D statistics as described above [e.g., $Z = 0.0$ for D (Mbuti, Han; Stuttgart, K14); tables S10 and S11]. This suggests that the main ancestral components proposed for contemporary Europeans, including the Middle Eastern component commonly attributed to the expansion of early farmers within Europe, were likely already genetically differentiated and related through complex gene flow by the time of K14, at least 36.2 ka (Fig. 2).

We further investigated the relationship of K14 and the other ancient genomes to East Asian and Siberian populations using f_4 statistics (f_4 (Sardinian, Ancient; Modern, Papuan), which measure whether a modern population shares more alleles with contemporary Europeans or an ancient genome.

We find that all Siberian and East Asians are equally distant from western MHGs (all $|Z| < 1.9$) (Fig. 3D and table S12), supporting the postulated early split between East Asians and western Eurasians. In contrast to MHGs and MAI, all Siberian populations are genetically closer to contemporary Europeans (Sardinians) than to K14 ($3.1 < |Z| < 9.9$) (table S12), particularly those from the Yenisei and Ob' basins (e.g., Shors, $Z = 8.0$) (Fig. 3A). Furthermore, these populations derive parts of their ancestry from a European hunter-gatherer (HG) component inferred in the clustering analysis (Fig. 1D and fig. S20), with populations showing a higher HG ancestry proportion also being closer to contemporary Europeans, using the f_4 statistic (Spearman $\rho = 0.96$; $P = 3.0 \times 10^{-18}$) (Fig. 3D and table S13). Notably, the opposite pattern is observed with Scandinavian MHGs (Afv58 and Motala), where the same populations tend to share more alleles

with MHGs than contemporary Europeans and the HG component is negatively correlated with f_4 (e.g., Motala $\rho = -0.85$; $P = 6.2 \times 10^{-10}$) (Fig. 3, C and D). Calculating admixture f_3 statistics, we find significant evidence for admixture in those populations, with a variety of Siberian and European source populations. The best pair of source populations (i.e., the most negative f_3 statistic) involves Swedish MHGs (Motala) and Evens (a northeast Siberian population) [e.g., f_3 (Shors; Evens, Motala) = -0.012 ; $Z = -9.1$] (table S14). Altogether, these results suggest that contemporary Siberian populations from the Yenisei basin derive part of their gene pool from a Eurasian HG population that shares ancestry with K14 but is more closely related to Scandinavian MHGs than to either MAI or western European MHGs, indicating gene flow between their ancestors and Scandinavian Europe after K14 but before the Mesolithic (between 36.3 and 7 ky B.P.).

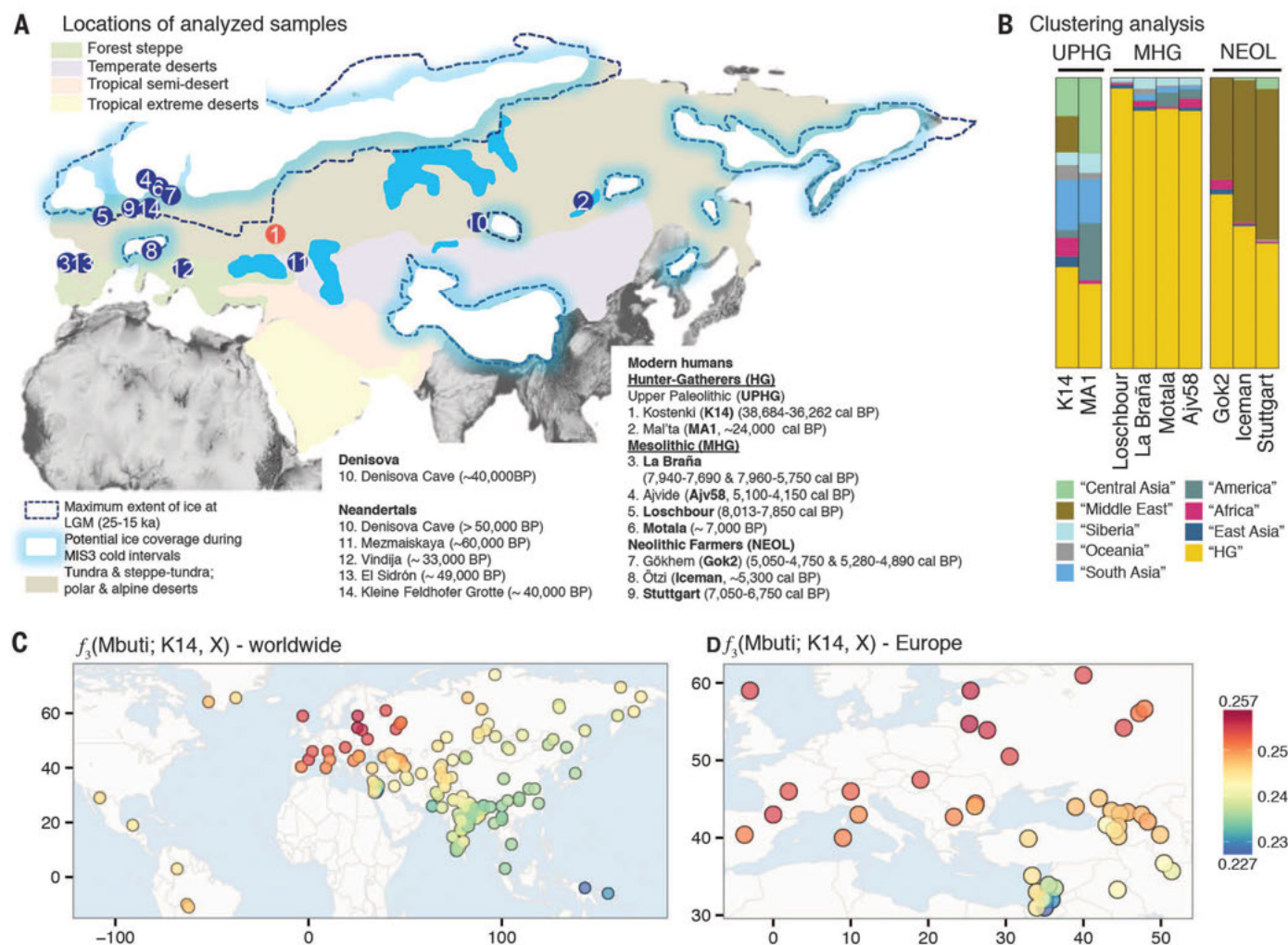


Fig. 1. Sampling locations and genomic affinities of K14 and other ancient genomes. (A) Location of Kostenki and the samples analyzed in this study. Kostenki (K14) is shown in red, while comparative ancient samples are shown in blue. (B) Admixture proportions for the ancient genomes, assuming nine ancestral components for a clustering analysis in a set of modern worldwide populations. We labeled the components according to the modern populations in which they are maximized for all but one case: The yellow component that we label HG is maximized in eastern Europeans. NEOL: Neolithic farmers. (C) Shared drift between K14 and a set of worldwide populations. For every modern population X on the map, we compute f_3 (Mbuti Pygmy; K14, X). The warmer colors indicate increased shared ancestry. (D) Shared drift between K14 and a set of European populations. This figure is a close-up of (C).

Fig. 2. Relationships of the K14 sample and MA1, MHG, NEOL, modern Europeans, and the modern populations in the Yenisei region. This representation is a possible topology consistent with the results presented in this study in the context of the relationships described by Lazaridis *et al.* (21) for the modern European populations and Raghavan *et al.* (23) for MA1. Present-day populations are colored in blue, ancient population in red, and ancestral populations in green. Solid lines represent descent without admixture events, and dashed lines show admixture events. Arrows do not depart from ancient samples (K14 and MA1) because they represent relationships of population ancestry. We only show the topology of the potential population tree: There is no notion of time in this representation. The tree is not the result of a model-fitting procedure but rather a possible topology consistent with the key results (A, B, and C) of this study.

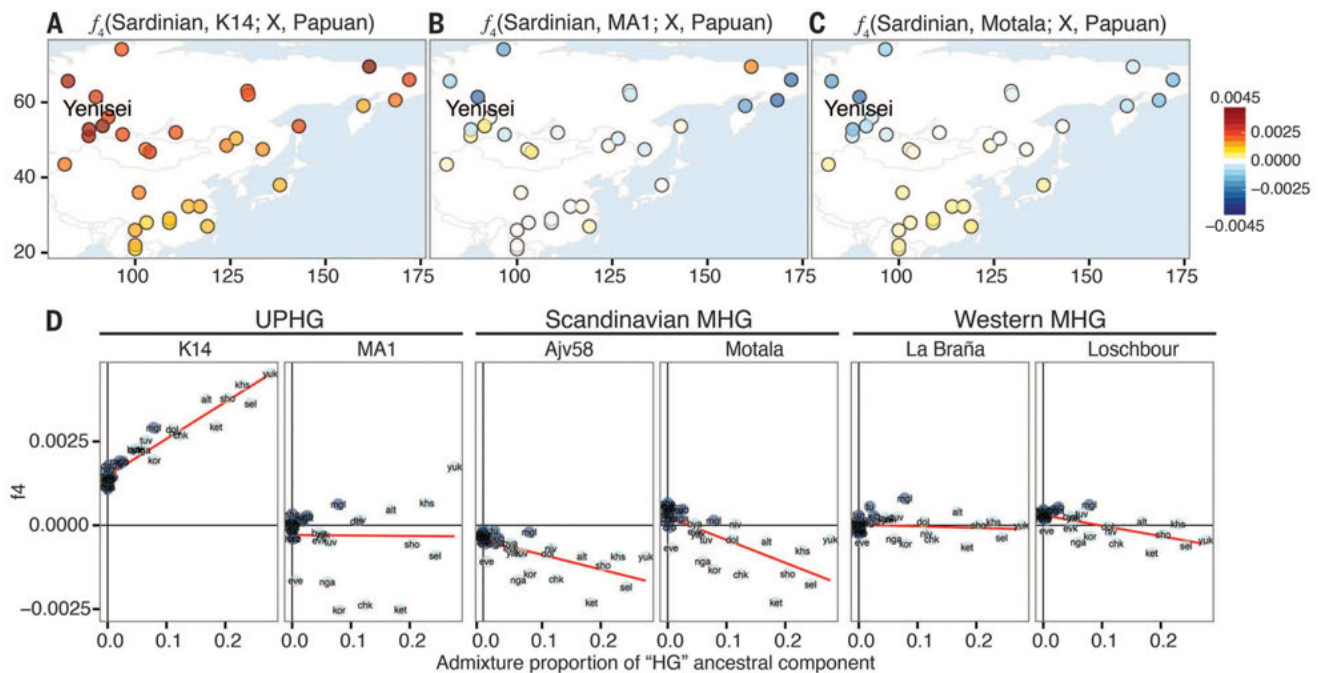
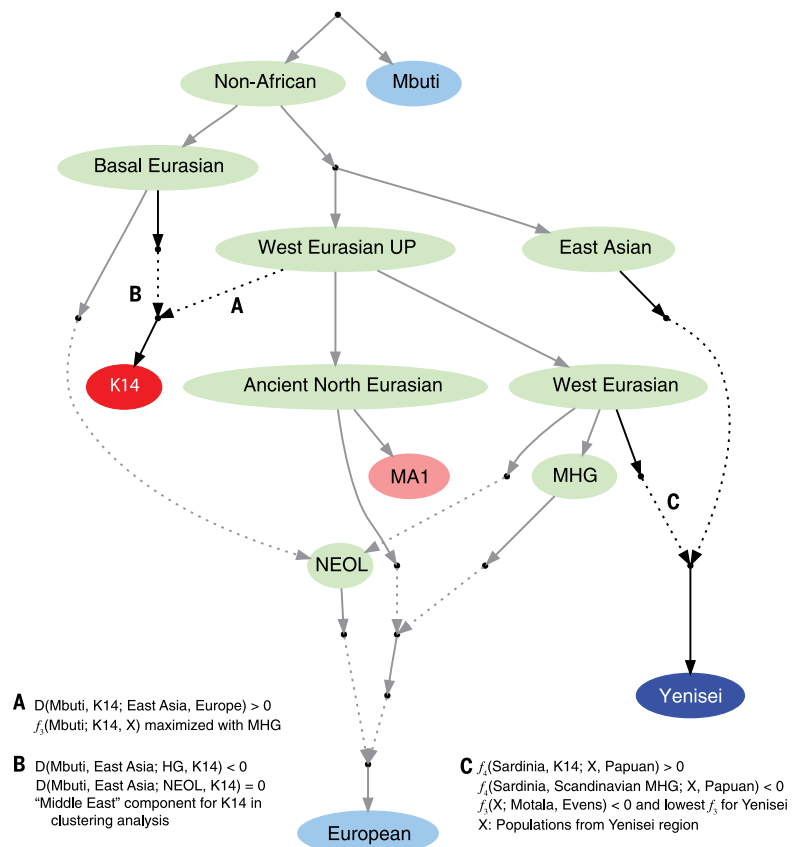


Fig. 3. Relationships of K14 and other HG genomes with contemporary East Asian and Siberian populations. (A) Values of the f_4 statistic for a set of Siberian and East Asian populations and K14. We compute the f_4 statistic for a topology (Sardinian, K14; X, Papuan). Warmer values indicate departure from the topology (Sardinian, K14; X, Papuan) with increased ancestry between the modern population X and the Sardinian. The Yenisei region includes the Selkup, Shor, and Ket populations. (B) Values of the f_4 statistic for a set of Siberian and East Asian populations and MA1. We compute the f_4 statistic for a topology (Sardinian, MA1; X, Papuan). (C) Values of the f_4 statistic for a set of Siberian and East Asian populations and Scandinavian hunter gatherers (Motala). (D) Relationship between the HG admixture proportion and the $f_4(\text{Sardinian}, \text{K14}; \text{X}, \text{Papuan})$ shown in (A). The red lines are linear regressions for each case.

Finally, we estimated levels of Neandertal ancestry in K14 using f_4 -ratio statistics (38). Our estimates are consistent with previous analyses (34) showing a Neandertal contribution lower than 2% for most individuals (Fig. 4A). However, both La Braña and K14 show slightly elevated levels, with an estimated $2.4 \pm 0.4\%$ in K14 (tables S15 and S16). Restricting this analysis to genomic regions without evidence for Neandertal introgressed haplotypes in contemporary humans (38, 39) results in 0% estimated ancestry for most individuals except K14, where $0.9 \pm 0.4\%$ Neandertal ancestry is still detected (tables S17 and S18). The difference between K14 and modern genomes could be caused by several factors, including sampling effects and genetic drift, natural selection as argued in (38, 39), or by the effects of additional Neandertal admixture not represented in the modern gene pool. We next compared the size distribution of genomic tracts of archaic hominin origin in K14 and other ancient individuals (Fig. 4B) by identifying genomic regions with high frequencies of archaic alleles at sites where all mod-

ern Africans carry the ancestral allele. The length of Neandertal tracts was higher in K14 than in other ancient individuals, with the longest tract totaling ~3 Mb on chromosome 6 (Fig. 4C). This is consistent with K14 being closer to the time of the admixture event with Neandertals, and carrying longer archaic tracts that have been affected by less recombination, than in the other ~11,000- to 30,000-year-old younger ancient genomes. We then used the length distribution of shared ancestry to estimate the admixture time of Neandertals and humans based on the K14 sample and obtained an estimate of ~54,000 years (S15). We note that genomic data from a 45,000-year-old modern human from Siberia, which was published during the review process of this study, also shows longer segments of Neandertal ancestry, further supporting our conclusions (40). Because of the divergent position of the K14 sample, we also examined whether it contained any fragments of introgressed DNA from other previously unsampled hominins. However, the distribution of tracts of divergent DNA provides no

evidence for additional divergent introgressed DNA (S14).

Several studies have reported on the basal genetic distinctiveness between western Eurasian and eastern Asian populations, as well as between all Eurasians and Australo-Melanesians (41–43). Our results show no close genetic relationship between K14 and Australo-Melanesians and support earlier studies that suggest Australo-Melanesians derive part of their ancestry from an early population divergence that predates the separation of Europeans and East Asians (3). The K14 genome shows that this early UP individual was clearly part of a western Eurasian lineage that had already diverged from eastern Asians, thus establishing a minimum date for that separation at least 36.2 ka. The fact that the limited genomic information on the ~40 ka Tianyuan modern human from China clusters with contemporary East Asian populations (44) suggests an even earlier date.

Our results further suggest that the early stages of the western Eurasian lineage were already complex (see also Fig. 2). Besides its core affinities with

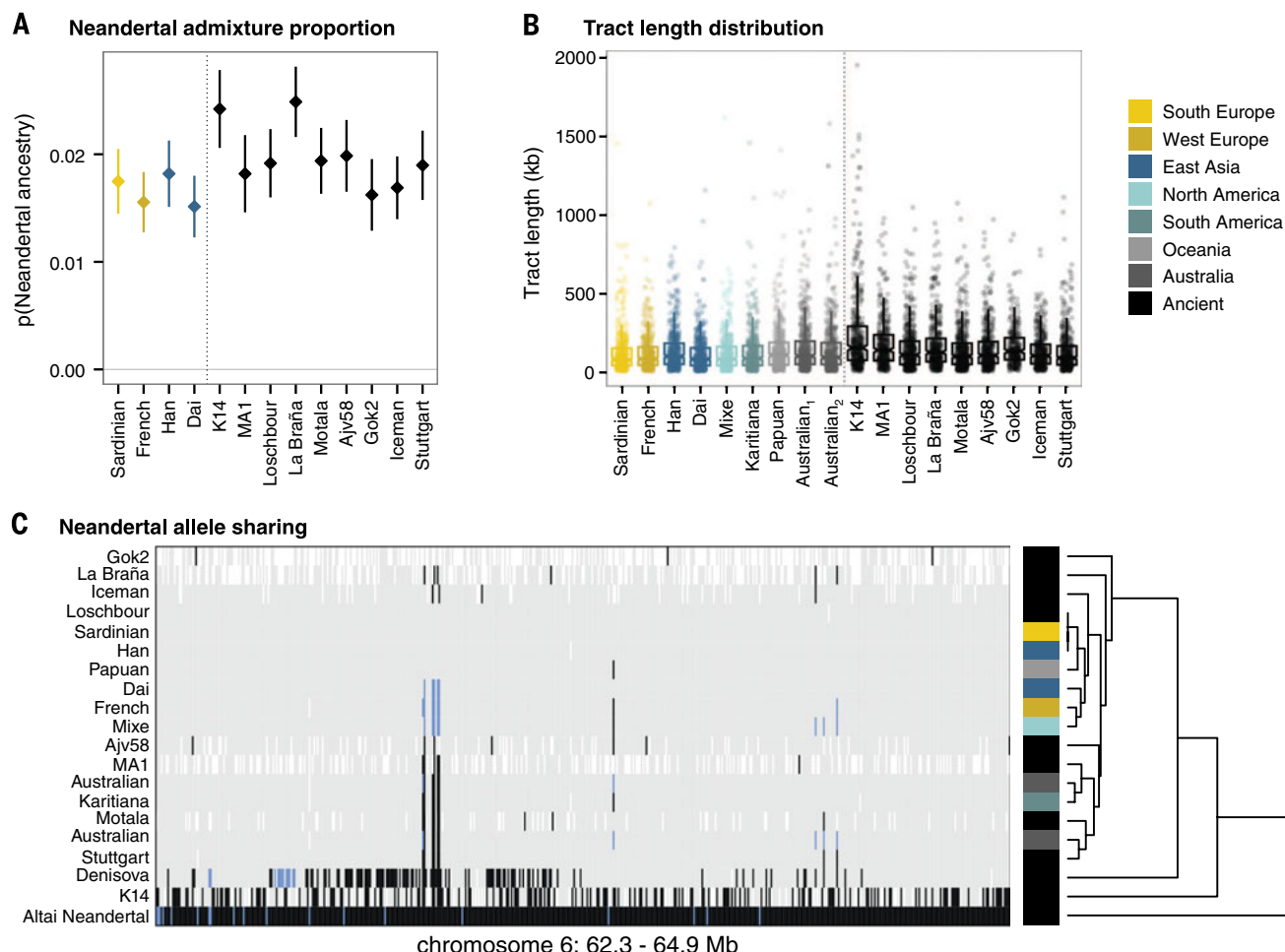


Fig. 4. Neandertal admixture in K14 and other ancient genomes. (A) Neandertal admixture proportions for the modern and ancient individuals from Eurasia. (B) Ancestry tract length distribution for tracts identified as Neandertal through a sliding-window approach. The sites are ascertained to be ancestral in the African populations. For each non-African, the tracts are identified as the regions where sites are derived in Neandertal and the individual shown in X. (C) The longest Neandertal haplotype identified in K14 through a sliding-window approach. Individuals were clustered using hierarchical clustering on the genotype matrix for the region. Missing data are shown in white; gray indicates homozygous ancestral, blue heterozygote-derived, and black homozygous-derived.

subsequent European groups, K14 also shares alleles with European Neolithic farmers and contemporary people from the Middle East/Caucasus, which are not found in MA1 and western European MHGs, indicating genetic exchange between K14 and a Basal Eurasian Lineage (which eventually contributed to Neolithic groups) after the ancestors of MA1 and subsequent European MHGs had diverged. This implies that early AMH populations became structured early in their history, but in the UP already contained the major genetic components found in Europeans today. As such, our findings show the existence of a metapopulation structure in Europe from the Upper Paleolithic onward, remnants of which are still found today despite migrations to and from Europe since the UP. The early UP contribution is greater among northern than southern Europeans, in agreement with the southeast to west and north gene flow cline resulting from the expansion of Neolithic farmers 9 to 6 ky cal B.P. (20, 45). However, descendants of the early UP population represented by K14 likely also contributed genes to western Siberian groups living around the mouth of the Yenisei River. Therefore, our findings support the view that these Uralic-speaking populations represent an ancient admixture between European and East Asian lineages. The recently proposed Holocene gene flow from East Asians into northern Europeans (21) can, in our view, be equally well explained by population structure of the hunter-gatherer metapopulation within Europe. As such, our results paint an increasingly complex picture of colonization history of Europe from the UP to today. Instead of inferring a few discrete migration events from Asia into Europe, we now see evidence that humans in Western Eurasia formed a large metapopulation with gene flow in multiple directions occurring repeatedly and perhaps continuously.

REFERENCES AND NOTES

- R. G. Klein, *Evol. Anthropol.* **9**, 17–36 (2000).
- P. Mellars, *Nature* **439**, 931–935 (2006).
- M. Rasmussen et al., *Science* **334**, 94–98 (2011).
- A. E. Marks, *Prehistory and Paleoenvironments in the Central Negev, Israel* (Southern Methodist University Press, Dallas, TX, 1983).
- N. R. Rebollo et al., *J. Archaeol. Sci.* **38**, 2424–2433 (2011).
- A. Gibbons, *Science* **343**, 1417 (2014).
- O. Bar-Yosef, A. Belfer-Cohen, D. S. Adler, *Anthropologie* **XLIV**, 49–60 (2006).
- N. Sirakov et al., *Paléorient* **19**, 131–144 (2007).
- S. Benazzi et al., *Nature* **479**, 525–528 (2011).
- S. L. Kuhn et al., *J. Hum. Evol.* **56**, 87–113 (2009).
- T. Higham et al., *Nature* **479**, 521–524 (2011).
- S. E. Bailey, T. D. Weaver, J.-J. Hublin, *J. Hum. Evol.* **57**, 11–26 (2009).
- C. A. Bergman, C. B. Stringer, *Paléorient* **15**, 99–111 (1989).
- V. Formicola, *Riv. Antropol.* **67**, 287–292 (1989).
- D. Henry-Gambier, C. Normand, J.-M. Pétilion, *Bull. Soc. Préhis. Fr.* **110**, 645–656 (2013).
- J.-J. Hublin, *Proc. Natl. Acad. Sci. U.S.A.* **109**, 13471–13472 (2012).
- C. Yazbeck, *Paléorient* **30**, 111–126 (2004).
- P. R. Nigst et al., *Proc. Natl. Acad. Sci. U.S.A.* **111**, 14394–14399 (2014).
- P. Skoglund et al., *Science* **336**, 466–469 (2012).
- P. Skoglund et al., *Science* **344**, 747–750 (2014).
- I. Lazaridis et al., *Nature* **513**, 409–413 (2014).
- I. Olalde et al., *Nature* **507**, 225–228 (2014).
- M. Raghavan et al., *Nature* **505**, 87–91 (2014).

- A. N. Rogachev, *Aleksandrovskoe poselenie drevnekamennogo veka u sela Kostenki na Donu* (Moscow-Leningrad, 1955).
- A. Marom, J. S. O. McCullagh, T. F. G. Higham, A. A. Sinityn, R. E. M. Hedges, *Proc. Natl. Acad. Sci. U.S.A.* **109**, 6878–6881 (2012).
- D. M. Pyle et al., *Quat. Sci. Rev.* **25**, 2713–2728 (2006).
- A. A. Sinityn, J. F. Hoffecker, *Quat. Int.* **152–153**, 164–174 (2006).
- L. B. Vishnyatsky, P. E. Nehoroshchev, in *The Beginning of the Upper Paleolithic on the Russian Plain*, P. J. Brantingham, S. L. Kuhn, K. W. Kerry, Eds. (University of California Press, Berkeley, CA, 2004), pp. 80–96.
- N. Rohland, M. Hofreiter, *Nat. Protoc.* **2**, 1756–1762 (2007).
- J. Dabney et al., *Proc. Natl. Acad. Sci. U.S.A.* **110**, 15758–15763 (2013).
- A. W. Briggs et al., *Proc. Natl. Acad. Sci. U.S.A.* **104**, 14616–14621 (2007).
- G. R. Feehery et al., *PLOS ONE* **8**, e76096 (2013).
- J. Krause et al., *Curr. Biol.* **20**, 231–236 (2010).
- K. Prüfer et al., *Nature* **505**, 43–49 (2014).
- D. H. Alexander, J. Novembre, K. Lange, *Genome Res.* **19**, 1655–1664 (2009).
- N. J. Patterson, et al., *Genetics* **2012**, genetics.112.145037 (2012).
- P. Skoglund et al., *Proc. Natl. Acad. Sci. U.S.A.* **111**, 2229–2234 (2014).
- S. Sankararaman et al., *Nature* **507**, 354–357 (2014).
- B. Vernot, J. M. Akey, *Science* **343**, 1017–1021 (2014).
- Q. Fu et al., *Nature* **514**, 445–449 (2014).
- W. W. Howells, *Skull Shapes and the Map: Craniometric Analyses in the Dispersion of Modern Homo* (Harvard Univ. Press, Cambridge, MA, 1989).
- R. A. Foley, M. M. Lahr, *Camb. Archaeol. J.* **7**, 3–36 (1997).
- N. A. Rosenberg et al., *Science* **298**, 2381–2385 (2002).

- Q. Fu et al., *Proc. Natl. Acad. Sci. U.S.A.* **110**, 2223–2227 (2013).
- L. L. Cavalli-Sforza, P. Menozzi, A. Piazza, *The History and Geography of Human Genes* (Princeton Univ. Press, Princeton, NJ, abridged edition, 1996).

ACKNOWLEDGMENTS

We thank J. F. Hoffecker for help and discussion and the Danish National Sequencing Centre, especially C. Mortensen and K. Magnussen, for technical assistance. We also thank D. Poznik for providing the chromosome Y mask file and table of informative SNPs. GeoGenetics members were supported by the Lundbeck Foundation and the Danish National Research Foundation (DNRF94). A.-S.M. was supported by the Swiss National Science Foundation (P3SKP3_143529). Research on the archaeological background by P.R.N. was supported by a Marie Curie Career Integration Grant (322261). M.W. and D.L. thank the Australian Research Council for support. Data for this study are available under accession no. PRJEB7618 from the European Nucleotide Archive (www.ebi.ac.uk/ena). Source code for the main analyses in this study is available at GitHub (<https://github.com/martinsikora>).

SUPPLEMENTARY MATERIALS

www.sciencemag.org/content/346/6213/1113/suppl/DC1
Materials and Methods
Supplementary Text
Figs. S1 to S26
Tables S1 to S18
References (46–183)

8 October 2014; accepted 30 October 2014
Published online 6 November 2014;
10.1126/science.aaa0114

TETANUS TOXIN ENTRY

Nidogens are therapeutic targets for the prevention of tetanus

Kinga Bercsenyi,^{1,2} Nathalie Schmieg,^{1,2*} J. Barney Bryson,^{2*} Martin Wallace,^{1,2} Paola Caccin,³ Matthew Golding,^{1†} Giuseppe Zanotti,³ Linda Greensmith,² Roswitha Nischt,⁴ Giampietro Schiavo^{2‡}

Tetanus neurotoxin (TeNT) is among the most poisonous substances on Earth and a major cause of neonatal death in nonvaccinated areas. TeNT targets the neuromuscular junction (NMJ) with high affinity, yet the nature of the TeNT receptor complex remains unknown. Here, we show that the presence of nidogens (also known as entactins) at the NMJ is the main determinant for TeNT binding. Inhibition of the TeNT-nidogen interaction by using small nidogen-derived peptides or genetic ablation of nidogens prevented the binding of TeNT to neurons and protected mice from TeNT-induced spastic paralysis. Our findings demonstrate the direct involvement of an extracellular matrix protein as a receptor for TeNT at the NMJ, paving the way for the development of therapeutics for the prevention of tetanus by targeting this protein-protein interaction.

Tetanus neurotoxin (TeNT) is composed of two subunits, which perform specific functions necessary for targeting this toxin to the central nervous system (CNS) and its high potency. The heavy (H) chain mediates high-affinity binding and entry into neurons, whereas the light (L) chain causes synaptic silencing of inhibitory interneurons, which normally suppress motor neuron activity, and thereby induces spastic paralysis (1). After internalization into motor neurons, TeNT and the carboxyl-terminal fragment of its H chain (H_CT) are sorted to signaling endosomes, which undergo axonal retrograde transport toward the motor neuron cell body (2). We have previously charac-

terized the proteome of these organelles using H_CT-conjugated magnetic nanoparticles (2). This affinity purification approach identified a list of

¹Molecular Neuropathobiology Laboratory, Cancer Research UK London Research Institute, 44 Lincoln's Inn Fields, London WC2A 3LY, UK. ²Sobell Department of Motor Neuroscience and Movement Disorders, University College London Institute of Neurology, University College London, London WC1N 3BG, UK. ³Department of Biomedical Sciences, University of Padua, Viale G. Colombo 3, 35131 Padova, Italy. ⁴Department of Dermatology, University of Cologne, Kerpener Strasse 62, 50937 Cologne, Germany.

*These authors contributed equally to this work. †Present address: Centre for Microvascular Research, William Harvey Research Institute, Barts and The London School of Medicine and Dentistry, Queen Mary, University of London, London, UK. ‡Corresponding author. E-mail: giampietro.schiavo@ucl.ac.uk

proteins associated with signaling endosomes, some of which were predicted to be involved in the binding and/or internalization of H_CT. We analyzed the sequences of these proteins for the presence of the tripeptide Tyr-Glu-Trp (YEW), which was previously shown to interact with the sialic acid binding site (R site) of H_CT, a region implicated in polysialoganglioside and acidic lipid binding (3, 4). The corresponding region

of botulinum neurotoxins (BoNTs) interacts with the synaptic proteins SV2A-C or synaptotagmin I/II (5–11), raising the possibility that the R site of TeNT also binds to a protein receptor.

To identify putative TeNT receptors, we selected candidates containing variants of the YEW peptide, where this motif is present within the lumen of signaling endosomes, a localization topologically equivalent to the extracellular do-

main of these proteins when localized to the plasma membrane (table S1). A total of 35 nine-residue peptides containing the YEW motif or closely related sequences were tested for binding to H_CT by using direct fluorescent binding, enzyme-linked immunosorbent assay (ELISA), and peptide pull-down assays (Fig. 1A and fig. S1, A and B). The interacting peptides were then assessed for their ability to compete for H_CT

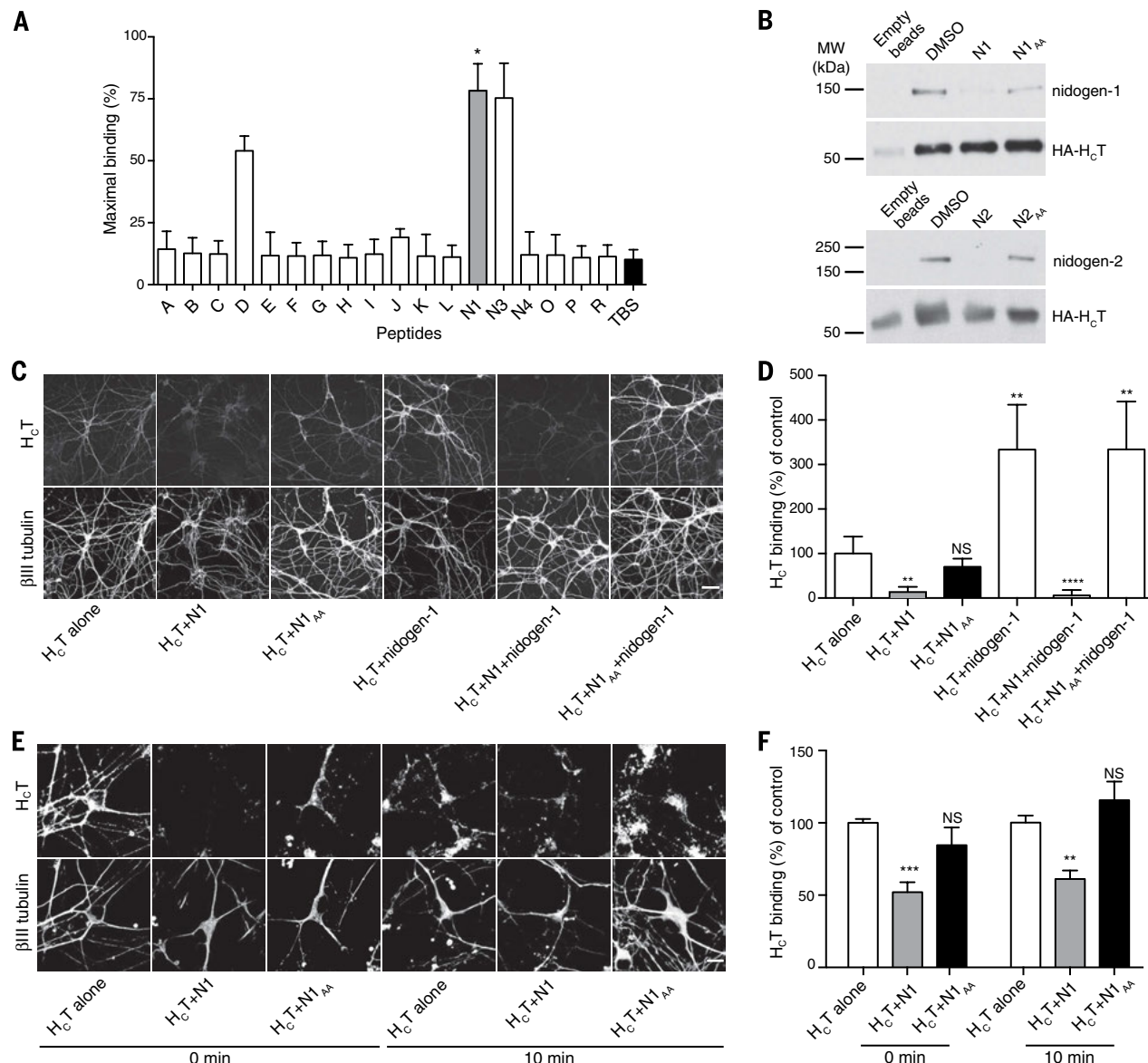


Fig. 1. Nidogen peptides bind to H_CT and prevent its interaction with full-length nidogens in vitro. (A) Assay for peptides that bind fluorescent H_CT. The percentage of maximal binding was plotted for each peptide. The results were tested for significance between individual peptides and Tris-buffered saline (TBS) control ($n = 3$ independent experiments; $*P < 0.05$; error bar, SD). (B) Pull-down of HA-H_CT preincubated with full-length recombinant nidogen-1 (top) or nidogen-2 (bottom). “Empty beads” corresponds to samples in which HA-H_CT was omitted, and “DMSO” (dimethyl sulfoxide) to samples treated with vehicle control. Both nidogen-1 and -2 bind directly to HA-H_CT, and pretreatment with the N1 or N2 peptide blocks this interaction. In contrast, mutant peptides (N1_{AA} and N2_{AA}) are ineffective in preventing this interaction ($n = 3$ independent experiments for both

proteins). The bands detected in the empty bead controls are due to the heavy chain of the capture antibody, which comigrates with H_CT. (C and E) Vehicle control (H_CT alone), N1, or N1_{AA} peptides were (C) preincubated, (E) added together (0 min), or added after a 10-min delay (10 min) to primary mouse motor neurons treated with AlexaFluor555-H_CT in the absence or the presence of exogenous nidogen-1 (C) before fixing, immunostaining for βIII tubulin, and imaging. Scale bar, (C) 50 μm; (E) 10 μm. (D and F) Quantification of the data shown in (C) and (E). Twenty images (D) or three-tile scans of 4 by 4 fields (F) were taken for each condition, and fluorescence intensity of AlexaFluor555-H_CT bound to neurons as defined by a βIII tubulin mask was quantified. Results were tested for statistical significance ($n = 3$ independent experiments; NS, nonsignificant; $**P < 0.01$; $***P < 0.005$; $****P < 0.0001$; error bar, SD).

binding on primary motor neurons (fig. S1C). Peptides N1 and N2, which correspond to short sequences in nidogen-1 and nidogen-2, respectively (table S1 and fig. S1D), were selected for further investigation because they significantly reduced H₂T binding to neurons (Fig. 1, C and D, and fig. S1C). The YEW-like motif of nidogen-1 (YQW) and nidogen-2 (WSY) and their flanking residues were responsible for this interaction because single alanine mutants showed reduced binding to H₂T (fig. S1, E and F), and the double alanine mutant (N1_{AA}) (table S1) failed to block the binding of H₂T to motor neurons (Fig. 1, C and D). Furthermore, when the N1 peptide, but not N1_{AA}, was added to motor neurons, either together with H₂T or 10 min afterwards, it still significantly inhibited H₂T binding to these neurons (Fig. 1, E and F).

We then tested whether H₂T interacts directly with full-length nidogens by incubating immobilized hemagglutinin (HA)-tagged H₂T with full-length recombinant nidogen-1 or nidogen-2 and demonstrated that both proteins directly bind to H₂T (Fig. 1B). The N1 and N2 peptide sequences of nidogen-1 and -2 played a key role in this interaction because preincubating H₂T with an excess of these peptides, but not their

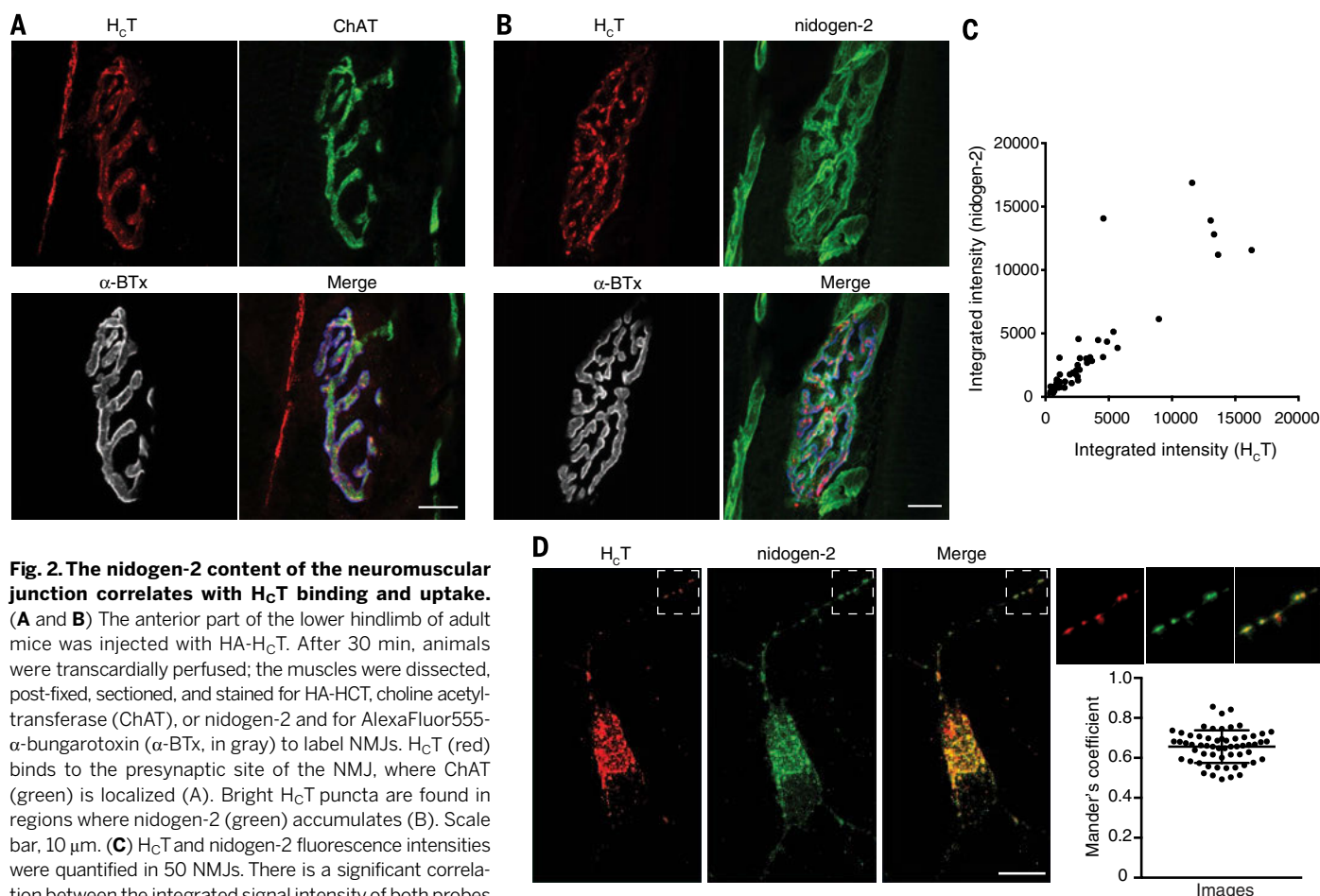
respective mutants (table S1), abolished this binding (Fig. 1B).

The two mammalian nidogens play partially overlapping roles in basement membrane (BM) formation and maintenance (12–14). Although nidogen-2 knockout (KO) mice do not display any overt phenotype, animals lacking nidogen-1 develop a progressive hindlimb paralysis, indicating a role for this protein in motor neuron survival (15). Nidogens are tightly integrated within the BM, which renders them difficult to access for exogenous ligands. To determine whether the amount of cell surface-associated nidogens is the limiting factor for H₂T binding to motor neurons, we added soluble full-length nidogen-1 together with H₂T to cultured motor neurons. This resulted in the binding of exogenous nidogen-1 to motor neurons (fig. S2) and augmented the amount of cell surface-bound H₂T (Fig. 1, C and D), suggesting that the addition of exogenous nidogen-1 increased the number of H₂T binding sites on the neuronal surface. This effect was dependent on the YEW-like motif of nidogen-1 because preincubation of H₂T with the N1 but not the N1_{AA} peptide prevented the increased cell surface binding of H₂T (Fig. 1, C and D). Coimmunoprecipitation of H₂T and endogenous nidogen-2

from motor neurons incubated with H₂T for 5 min at 37°C (fig. S3) suggested that the interaction between nidogens and H₂T is preserved upon entry of H₂T into endosomal compartments.

Inspection of the domain structure of nidogens revealed that the N1 and N2 peptides reside within the globular G₂ domain (fig. S4A and movie S1). Molecular modeling (fig. S4, B to D) revealed that the N1 peptide, both in isolation and within the intact G₂ domain, is able to dock to the R site of H₂T, where sialic acid, disialyllactose, and the YEW motif bind (4). The molecular surface concealed by the N1 peptide-H₂T complex constitutes more than 40% of the total peptide surface (fig. S4C), suggesting that this interaction, which is driven by the potential formation of five hydrogen bonds and other polar interactions (table S2), is very strong.

The G₂ domain of nidogen-1 fits into a large crevice at the top of the trefoil domain of H₂T (fig. S4B and movie S1), concealing 1114 Å² and 1106 Å² of the molecular surface of H₂T and the G₂ domain of nidogen-1, respectively. Complex formation is likely to be promoted by complementary electrostatic surfaces and several potential hydrogen bonds (table S3 and fig. S4D). To confirm the validity of this structural model,



we mutated several residues of the R site of H_cT that are predicted to play an important role in the formation of this complex. As shown in fig. S5, we found that mutations of R1226, T1146, and Y1229, which form potential H-bonds with nidogen-1 (tables S2 and S3, respectively), as well as of other R site residues (P1212 and G1215) (16), reduced the binding of both N1 and N2 peptides. Similarly, alanine scanning of the YEW-like motif and flanking residues in the N1 and N2 peptides strongly decreased their interaction with H_cT (fig. S1, D to F), which strongly supported the validity of the model shown in fig. S4. This mode of interaction is likely to be conserved through evolution because the human N1 and N2 peptides show a high degree of homology to the corresponding mouse sequences and also bound H_cT (fig. S1D).

Crucially, this model predicts that the association between H_cT and nidogen-1 is unlikely to interfere with the interaction between H_cT and polysialogangliosides, which is required for TeNT binding to the neuronal surface (3, 17). Thus, nidogens and polysialogangliosides have the potential to bind TeNT simultaneously and thereby fulfill the requirements for the proposed dual receptor model (18, 19), which predicts the concurrent interaction of lipid and protein receptors with TeNT and BoNTs for their high-affinity binding to neuronal membranes.

Nidogen-2 is highly enriched at the NMJ (20), and we sought to investigate whether it is localized to the specialized presynaptic BM of this structure. We thus injected the lower hindlimb of wild-type mice with H_cT and then immunostained cryosections of the extensor digitorum

longus (EDL) muscle for choline acetyltransferase (ChAT), a motor neuron marker, and nidogen-2. This analysis revealed that H_cT binds to the presynaptic motor neuron nerve terminal, which is in close apposition to the postsynaptic acetylcholine receptor, labeled by α -bungarotoxin (α -BTx) (Fig. 2A). Increased H_cT binding was detected in areas where nidogen-2 was most abundant (Fig. 2B and movie S2) and was absent from NMJs that did not express nidogen-2, which revealed a strong correlation between the nidogen-2 content and H_cT binding at the NMJ (Fig. 2C). We then assessed whether these two proteins are internalized and transported together in signaling endosomes. H_cT and an antibody against nidogen-2 were added to primary motor neurons at 37°C and allowed to internalize. After a mild acid wash to remove all probes still bound to the neuronal surface, the internalized α -nidogen-2 was detected by using a fluorescently tagged secondary antibody. The extensive colocalization between α -nidogen-2 and H_cT throughout the axonal network and cell bodies (66%) strongly indicated that these two proteins were internalized together and cotransported by the same organelles (Fig. 2D).

To further test the importance of nidogens in TeNT intoxication, we determined the susceptibility of nidogen KO mice to TeNT-induced paralysis and assessed the ability of H_cT to bind neurons and tissues derived from these mice. Compared with wild-type motor neurons, nidogen-2 KO motor neurons exhibited a significantly reduced ability to bind H_cT in vitro (Fig. 3, A and B). This was further verified in vivo by demonstrating that NMJ uptake of H_cT was severely

impaired in levator auris longus (LAL) muscles isolated from both nidogen-1 and nidogen-2 KO mice (Fig. 3, C and D). In stark contrast, the capacity of the corresponding binding fragment of BoNT/A (H_cA) to bind to nidogen null NMJ was largely unaffected (fig. S6A). Crucially, the addition of full-length recombinant nidogen-1 restored the ability of H_cT to bind NMJs lacking nidogen-1 (fig. S6B). This rescue was determined by the recruitment of recombinant nidogen-1 to mutant NMJs (fig. S6B), suggesting a replenishment of H_cT acceptor sites at the synaptic cleft.

In the genetic background used in our experiment, nidogen-1 and -2 double knockout (DKO) mice show early embryonic lethality (27), precluding the derivation of motor neuron cultures. To overcome this limitation, we assayed H_cT uptake into isolated hindbrains of DKO embryos taken at embryonic day 11.5 (E11.5). In contrast to control hindbrains, which displayed robust H_cT staining, hindbrains from DKO littermates were unable to bind H_cT (Fig. 3E), further indicating that nidogen-1 and -2 are essential for H_cT binding in vivo (Fig. 3F).

Because the N1 peptide inhibited H_cT binding to NMJs in whole LAL muscle preparations (Fig. 4A), we investigated the ability of the N1 peptide to prevent uptake of TeNT in vivo, using three independent assays. First, full-length TeNT was injected locally into the triceps surae muscle either alone or in combination with the N1 or N1_{AA} peptides, and the effect on spastic paralysis was assessed in vivo by means of footprint analysis 24 hours after injection (Fig. 4, B and C). Administration of TeNT alone caused severe gait

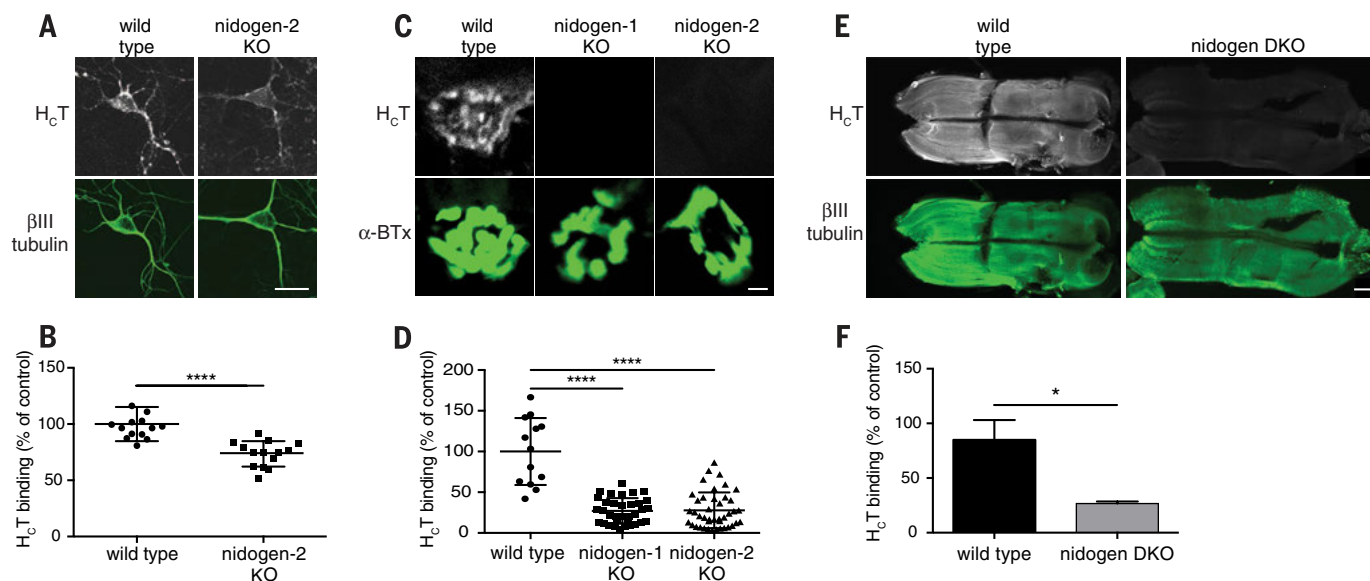


Fig. 3. Neurons lacking nidogens display reduced binding to H_cT. (A and B) Motor neurons derived from E13.5 wild-type and nidogen-2 knockout (KO) mouse embryos were incubated with HA-H_cT (gray). Cells were fixed and stained for HA-H_cT, and fluorescence intensity was quantified in 14 images by using a β III tubulin mask (green). Scale bar, 20 μ m. The value of nontreated cells was subtracted, and data were analyzed [(B), $n = 3$ experiments—shown is a representative experiment; **** $P < 0.001$; error bar, SD]. (C) LAL muscles of wild-type, and nidogen-1 and -2 KO animals were

incubated with HA-H_cT, fixed, and stained for HA (gray) and α -BTx (green) to identify NMJs. Scale bar, 5 μ m. (D) Both nidogen-1 and -2 KO NMJs show a significant decrease in their ability to bind and internalize H_cT ($n = 3$ animals per group, 20 images per animal; **** $P < 0.001$; error bar, SD). (E) Nidogen-1 and -2 DKO and wild-type E11.5 embryonic hindbrains were tested for H_cT binding and uptake. Scale bar, 1 mm. (F) Mean intensity of H_cT staining was measured and analyzed for significance ($n = 3$ animals per group; * $P < 0.05$; error bar, SD).

abnormalities, with the characteristic inability to place the affected hindpaw in the former position of the ipsilateral forepaw, as occurs in normal mice (Fig. 4, B and C). At a later stage, TeNT caused a permanent plantar-flexion of the affected hindpaw (movie S3). Coadministration of the N1 peptide completely abolished these TeNT-induced gait abnormalities (movie S3), whereas the N1_{AA} peptide was ineffective (Fig. 4, B and C).

To corroborate this finding, we quantified the protective effect of the N1 peptide by co-injecting it with TeNT and measuring the maximal force generated by the tibialis anterior (TA) muscle using *in vivo* isometric muscle tension physiology. The contractile force of the TeNT-injected muscle was diminished ($3.11 \pm 0.88\%$ of non-injected control) (Fig. 4D and fig. S7A), as was the case for muscles co-injected with TeNT and the N1_{AA} peptide ($2.14 \pm 1.44\%$ of noninjected control) (Fig. 4D and fig. S7B). In contrast, co-administration of the N1 peptide significantly abrogated the TeNT-mediated decline in contractile force compared with that of the other two groups ($47.46 \pm 10.31\%$ of noninjected control) (Fig. 4D and fig. S7C). Similar results were obtained by using phrenic nerve-hemidiaphragm preparations (fig. S7D) (22). Together, these results confirmed the ability of the N1 peptide to prevent symptoms of tetanus *in vivo*.

In order to assess the susceptibility of nidogen-2 KO mice to systemic TeNT toxicity *in vivo*, we

injected wild-type and nidogen-2 KO mice intraperitoneally with different doses of TeNT and monitored the appearance of tetanus. Nidogen-2 KO animals showed a significant delay in the onset and progression of tetanic symptoms at lower TeNT doses (Fig. 4E). Unfortunately, the possibility to extend these assays to mice lacking nidogen-1 was precluded by the severe epileptic and paralytic phenotype affecting these animals (15).

Some of the symptoms displayed by nidogen-2 KO mice injected with TeNT, such as keratoconjunctivitis sicca (23), resembled those of botulism. This suggests that in the absence of one of its physiological receptors, a proportion of TeNT may exploit alternative routes of entry at the NMJ, which are shared with BoNTs. Cross-talk between the two modes of entry and intracellular transport pathways taken by TeNT and BoNTs has been previously suggested (24) and is further supported by the botulism-like symptoms shown by mice injected with high doses of TeNT (25).

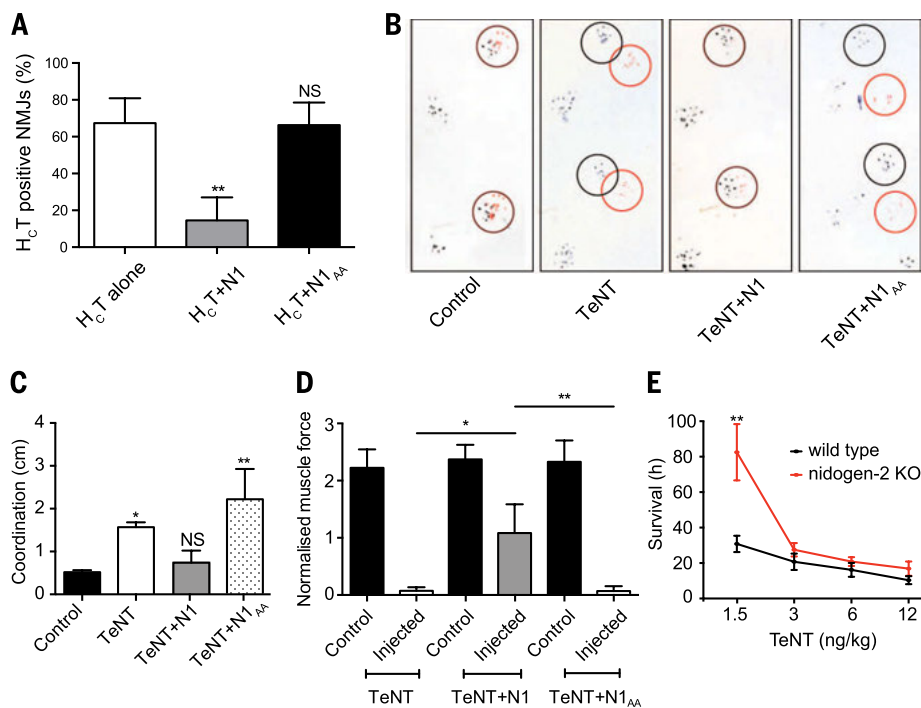
Because BoNTs use several SV2 isoforms as receptors (9–11, 22) and SV2A has been proposed as a TeNT receptor in central neurons (26), we quantified the colocalization of HcT with SV2A and SV2C in motor neurons and tested whether preincubation of HcT with recombinant nidogen-1 modifies the association of HcT with these synaptic vesicle proteins. In the ab-

sence of exogenous nidogen, SV2A showed robust colocalization with HcT internalized for 45 min at 37°C (46%) (fig. S8, A and B), whereas the codistribution of HcT with SV2C under these conditions was relatively low (fig. S8, C and D). Therefore, at least a subpool of TeNT may be internalized via synaptic vesicle recycling at the relatively high concentrations used in this assay. However, the addition of recombinant nidogen-1 caused a significant reduction in the colocalization of HcT with SV2A (22%) (fig. S8, A and B) but not with SV2C (fig. S8, C and D). However, despite the addition of recombinant nidogen-1 causing an increased intracellular pool of HcT, the proportion of this probe colocalizing with SV2A was significantly reduced (fig. S8, A and B). Taken together, these data suggest that in the presence of nidogen-1, HcT is preferentially targeted to an endocytic pathway linked to axonal retrograde transport to the cell body and is not taken up by synaptic vesicle recycling.

We have identified the protein receptor responsible for TeNT binding and internalization at the NMJ as well as a potential mechanism to explain the overlap between the entry routes of TeNT and BoNTs (fig. S9). Engineered growth factors with higher affinity for the extracellular matrix (ECM) display enhanced biological activity (27), indicating that differential binding of such ligands to ECM components is crucial for their signaling and biological function (28). TeNT

Fig. 4. The N1 peptide blocks tetanic paralysis by inhibiting TeNT binding at the NMJ.

(A) LAL muscles were incubated with HA-HcT, which had been pretreated either with vehicle control (HcT alone), the N1 peptide, or the N1_{AA} mutant in motor neuron culture medium. Muscles were then immunostained for HA and α -BTx to identify NMJs. The ratio of HcT-positive to HcT-negative NMJs was quantified and analyzed for significance ($n = 3$ independent experiments, six images per condition; NS, nonsignificant; $**P < 0.01$; error bar, SD). (B) Footprint analysis of control mice, or of mice after injection into the triceps surae muscle of a sublethal dose of TeNT, or TeNT preincubated with the N1_{AA} or N1 peptides. Black circles show the paw prints from the noninjected left hindlimb and right frontlimb, and red circles mark the paw print of the TeNT-injected right hindlimb. In control and TeNT+N1-injected mice, the black and red circles overlap, whereas in TeNT- and TeNT+N1_{AA}-injected mice, they are separated, indicating impairment in coordination due to local tetanus. (C) The distance between the paw prints on the injected side was measured and tested for statistical significance ($n = 2$ independent experiments; data from two animals are shown; NS, nonsignificant; $*p < 0.05$; $**p < 0.01$; error bar, SD). (D) The TA muscle was injected with TeNT preincubated with either DMSO (vehicle control), N1_{AA}, or N1 peptides. After anesthesia, the tendon of this muscle was attached to a tension sensor, and the peroneal nerve was stimulated. Maximal muscle force was measured, normalized to muscle weight, and tested for statistical significance in control versus injected muscle. The N1-treated group retained a significantly higher muscle force than that of the vehicle- or N1_{AA}-treated groups. ($n = 6$



mice per group; $**P < 0.01$; error bar, SEM). (E) Age- and weight-matched nidogen-2 KO and wild-type mice were injected intraperitoneally with TeNT and monitored for up to 96 hours. The time of termination due to loss of righting reflex was plotted against the TeNT dose. Generalized tetanus in nidogen-2 KO animals was delayed at lower doses (1.5 ng/kg) compared with that in wild-type controls ($n = 2$ experiments, minimum two mice per group; $**P < 0.01$; error bar, SD).

might exploit a similar strategy based on a very efficient capture mechanism at specialized NMJ sites rich in nidogens, which may function to concentrate TeNT as well as physiological ligands, such as neurotrophic factors, to facilitate their uptake and sorting to axonal transport organelles. At these sites, TeNT in complex with nidogens may interact with surface receptors known to bind nidogens, such as the protein phosphatase LAR (29, 30). This specialized capture mechanism is likely to be indispensable to the host cell, and this enables TeNT to be lethal at extremely low concentrations. Our study suggests that nidogens are prime therapeutic targets for suppressing the uptake of TeNT at the NMJ and its access to the CNS, preventing its lethal effects.

REFERENCES AND NOTES

1. C. Montecucco, *Curr. Top. Microbiol. Immunol.* **195**, 278 (1995).
2. K. Deinhardt et al., *Neuron* **52**, 293–305 (2006).
3. C. Chen, Z. Fu, J. J. P. Kim, J. T. Barbieri, M. R. Baldwin, *J. Biol. Chem.* **284**, 26569–26577 (2009).
4. S. Jayaraman, S. Eswaramoorthy, D. Kumaran, S. Swaminathan, *Proteins* **61**, 288–295 (2005).
5. Q. Chai et al., *Nature* **444**, 1096–1100 (2006).
6. R. Jin, A. Rummel, T. Binz, A. T. Brunker, *Nature* **444**, 1092–1095 (2006).
7. R. P. A. Berntsson, L. Peng, L. M. Svensson, M. Dong, P. Stenmark, *Structure* **21**, 1602–1611 (2013).
8. R. P. A. Berntsson, L. Peng, M. Dong, P. Stenmark, *Nat. Commun.* **4**, 2058 (2013).
9. M. Dong et al., *Science* **312**, 592–596 (2006).
10. L. Peng, W. H. Tepp, E. A. Johnson, M. Dong, *PLoS Pathog.* **7**, e1002008 (2011).
11. R. M. Benoit et al., *Nature* **505**, 108–111 (2014).
12. K. Mann et al., *EMBO J.* **8**, 65–72 (1989).
13. M. S. Ho, K. Böse, S. Mokkapati, R. Nisch, N. Smyth, *Microsc. Res. Tech.* **71**, 387–395 (2008).
14. J. Kruegel, N. Miosge, *Cell. Mol. Life Sci.* **67**, 2879–2895 (2010).
15. L. Dong et al., *Lab. Invest.* **82**, 1617–1630 (2002).
16. A. Rummel, S. Bade, J. Alves, H. Bigalke, T. Binz, *J. Mol. Biol.* **326**, 835–847 (2003).
17. T. Binz, A. Rummel, *J. Neurochem.* **109**, 1584–1595 (2009).
18. C. Montecucco, *Trends Biochem. Sci.* **11**, 314–317 (1986).
19. A. Rummel et al., *Proc. Natl. Acad. Sci. U.S.A.* **104**, 359–364 (2007).
20. M. A. Fox, M. S. Ho, N. Smyth, J. R. Sanes, *Neural Dev.* **3**, 24 (2008).
21. B. L. Bader et al., *Mol. Cell. Biol.* **25**, 6846–6856 (2005).
22. S. Mahrhold, A. Rummel, H. Bigalke, B. Davletov, T. Binz, *FEBS Lett.* **580**, 2011–2014 (2006).
23. O. Suwan-apichon et al., *Invest. Ophthalmol. Vis. Sci.* **47**, 133–139 (2006).
24. L. Restani et al., *PLoS Pathog.* **8**, e1003087 (2012).
25. M. Matsuda, N. Sugimoto, K. Ozutsumi, T. Hirai, *Biochem. Biophys. Res. Commun.* **104**, 799–805 (1982).
26. F. L. Yeh et al., *PLoS Pathog.* **6**, e1001207 (2010).
27. M. M. Martino et al., *Science* **343**, 885–888 (2014).
28. L. Macri, D. Silverstein, R. A. Clark, *Adv. Drug Deliv. Rev.* **59**, 1366–1381 (2007).
29. E. Stryker, K. G. Johnson, *J. Cell Sci.* **120**, 3723–3728 (2007).
30. P. O'Grady, T. C. Thai, H. Saito, *J. Cell Biol.* **141**, 1675–1684 (1998).

ACKNOWLEDGMENTS

We thank S. Kjaer (Cancer Research UK London Research Institute) for help with the Octet RED96 system and K_d determination. N. O'Reilly and members of the Protein and Peptide Chemistry Laboratory (Cancer Research UK London Research Institute) for peptide synthesis, purification, and analysis; F. Giribaldi (Cancer Research UK London Research Institute) for help with footprint analyses; K. Deinhardt (University of Southampton) for mass spec analysis of axonal signaling

endosomes; S. Swaminathan (Brookhaven National Laboratory) for experiments aiming at the crystallization of the NI peptide-HcT complex; A. Rummel and T. Binz (Medizinische Hochschule Hannover) and N. Fairweather (Imperial College London) for providing access to published HcT mutants; I. Koxholt (University of Cologne) for help with nidogen-1 and -2 KO mice; and J. N. Sleight (University College London) for help with statistical analyses. We also thank C. Montecucco (University of Padua) and S. Novoselov (University College London) for constructive comments. This work was supported by Cancer Research UK (K.B., N.S., M.G., M.W., and G.S.), by the Medical Research Council (M.W.), by the University of Padua (P.C. and G.Z.), and by the Deutsche Forschungsgemeinschaft (SFB 829) through the Collaborative Research Center at the University of Cologne and the "Köln Fortune Programm" (R.N.). L.G. is the Graham Watts

Senior Research Fellow, supported by the Brain Research Trust. The data presented in this manuscript are found in the main paper and the supplementary data and materials and methods. The authors declare that they have no conflict of interest.

SUPPLEMENTARY MATERIALS

www.sciencemag.org/content/346/6213/1118/suppl/DC1
Materials and Methods
Figs. S1 to S9
Tables S1 to S4
References (31–38)
Movies S1 to S3

30 June 2014; accepted 5 November 2014
10.1126/science.1258138

T CELL SIGNALING

Antigen affinity, costimulation, and cytokine inputs sum linearly to amplify T cell expansion

Julia M. Marchingo,^{1,2} Andrey Kan,^{1,2} Robyn M. Sutherland,^{1,2} Ken R. Duffy,³ Cameron J. Wellard,^{1,2} Gabrielle T. Belz,^{1,2} Andrew M. Lew,^{1,2} Mark R. Dowling,^{1,2,4} Susanne Heinzel,^{1,2*} Philip D. Hodgkin^{1,2*†}

T cell responses are initiated by antigen and promoted by a range of costimulatory signals. Understanding how T cells integrate alternative signal combinations and make decisions affecting immune response strength or tolerance poses a considerable theoretical challenge. Here, we report that T cell receptor (TCR) and costimulatory signals imprint an early, cell-intrinsic, division fate, whereby cells effectively count through generations before returning automatically to a quiescent state. This autonomous program can be extended by cytokines. Signals from the TCR, costimulatory receptors, and cytokines add together using a linear division calculus, allowing the strength of a T cell response to be predicted from the sum of the underlying signal components. These data resolve a long-standing costimulation paradox and provide a quantitative paradigm for therapeutically manipulating immune response strength.

Upon infection, pathogen-specific CD8⁺ T cells undergo a characteristic kinetic sequence: rapid proliferation and expansion followed by population contraction due to cell death (1). While short-term stimulation is sufficient to trigger CD8⁺ T cell proliferation (2, 3), further exposure to stimulatory signals is required for an effective response (2, 4, 5). Although multiple attempts have been made to create a theory relating the integration of stimulatory signals to T cell response strength, all have been qualitative (6) and thus have lacked the power to predict the quantitative effect of altering stimulatory combinations and strength. The current qualitative paradigm describes T cell activation and response magnitude as the outcome of three requisite signals: signal 1, T cell receptor (TCR) (1); signal 2, membrane-bound antigen-presenting cell (APC)-

delivered costimuli (4); and signal 3, cytokines from inflammatory, homeostatic, or autocrine sources (5). The importance of these signals for T cell expansion is highly context-dependent, as classic in vitro studies have identified many "critical" signal 2 and 3 molecules (5, 7–9); however, gene deletion typically yields only moderate defects in the in vivo CD8⁺ T cell response (10–13), implying considerable redundancy.

Recent studies in B cells report an automated return to quiescence after a series of division rounds (14–16). The number of mitotic cycles B cells undergo varies and is influenced by the strength of stimulation. We hypothesized that T cells might be programmed in a similar manner with the final number of divisions (N) (Fig. 1A, left panel) a function of the sum of inputs from signals 1, 2, and 3 (illustrated in Fig. 1A). If correct, it may be possible to determine the calculus of addition to serve as the basis for a quantitative framework for T cell costimulation.

To test this hypothesis, we first measured the onset of quiescence in CD8⁺ T cells using TCR-transgenic OT-I mice [which recognize chicken ovalbumin SIINFEKL (N4) peptide bound to H2K^b] crossed with FucciRG mice in which cells

¹Division of Immunology, The Walter and Eliza Hall Institute of Medical Research, Parkville, VIC, Australia. ²Department of Medical Biology, The University of Melbourne, Parkville, VIC, Australia. ³Hamilton Institute, National University of Ireland, Maynooth, Ireland. ⁴The Royal Melbourne Hospital, Parkville, VIC, Australia.

*These authors contributed equally to this work. †Corresponding author. E-mail: hodgkin@wehi.edu.au

fluoresce red (FucciR) during G_0/G_1 and green (FucciG) for the duration of the $S/G_2/M$ cell cycle phases (17). Quiescent (FucciR⁺G⁻), recently divided (FucciR⁺G⁺), and actively dividing (FucciG⁺) cells can be distinguished, because cells that have reverted to a quiescent state (G_0) accumulate higher levels of FucciR (17, 18). We define the number of generations of division before returning to quiescence as the cell's division destiny (DD) (14–16, 19). OT-I/FucciRG CD8⁺ T cells were transferred into mice infected with recombinant HKx31 influenza virus expressing N4 (HKx31-N4) (20). During early expansion, most OT-I/FucciRG CD8⁺ T cells were proliferative, with <10% reverting to a quiescent state by day 3 of the response. This proportion of quiescent cells increased steadily, reaching ~75% of all OT-I/FucciRG CD8⁺ T cells by the onset of contraction at day 7 (Fig. 1, B and C). To estimate the number of divisions T cells underwent before dropping out of cycle, the Cyton model (15, 21) was fitted to total and quiescent cell numbers (Fig. 1D and table S1). Results were consistent with a T cell DD range spanning ~10 generations (Fig. 1E). If DD is carried through each cell lineage (16), this result predicts up to 1000-fold differences in T cell family size consistent with recent single-cell tracking studies (22, 23).

To further explore the regulation of division progression, we developed a minimal in vitro stimulation system using CellTrace Violet (CTV)-labeled OT-I/FucciRG CD8⁺ T cells. The contribution of signals 2 and 3 was reduced by using peptide self-presentation by purified CD8⁺ T cells (24). The

strong effect of autocrine interleukin-2 (IL-2) was controlled by adding blocking antibody (clone S4B6) and using human IL-2 (hIL-2), resistant to S4B6, when required (25). Superficially the in vitro pattern of early proliferation with a gradual onset of quiescence recapitulated the in vivo response (Fig. 1, C and F), with the major differences being the DD and subsequent time to die (Fig. 1, D, E, and G, and table S1).

We speculated that the three known sources of regulation—TCR affinity, costimuli, and cytokines—might combine to convert the low DD observed in vitro into the extensive outcome possible in vivo (Fig. 1E).

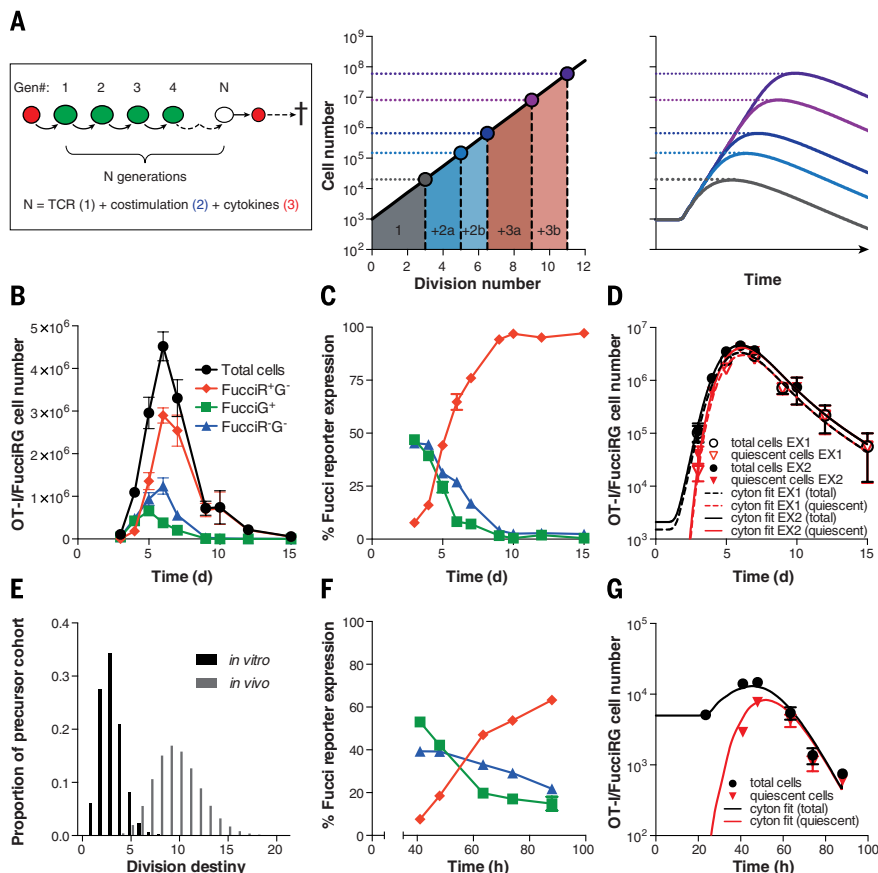
To improve estimation of mean DD (mDD) in our in vitro CTV division tracking assay, we used OT-I CD8⁺ T cells deficient in the proapoptotic molecule Bim (OT-I/*Bcl2l1*^{-/-}) for all experiments. These cells reported the same mDD as OT-I/*Bcl2l1*^{+/+} CD8⁺ T cells (Fig. 2A; fig. S1, A to C; and table S2), but the enhanced survival upon reverting to quiescence facilitated DD measurement at later times, consistent with previous studies in B cells (15, 16).

Fig. S2, A to F, shows the effect of a range of T cell stimuli on mDD. TCR affinity, several agonists representative of cell-contact-mediated costimulation, and some, but not all, cytokines tested were able to regulate DD in a dose-dependent manner. To determine when DD was most susceptible to regulation, cells from cultures where stimulation was removed immediately before the first division (24) were compared to cells with

constant costimulation. Agonist antibodies to CD28 and CD27 principally acted before the first division. In contrast, ongoing exposure to IL-2, IL-4, and IL-12 was required for maximal proliferation (Fig. 2B). Higher levels of IL-2 or IL-4 caused T cells to divide beyond CTV resolution (fig. S3) and the culture capacity. Therefore, to investigate the potential of IL-2 and IL-4 to extend DD when cytokine levels were maintained, OT-I/*Bcl2l1*^{-/-} CD8⁺ T cells were subcultured every 48 hours in hIL-2 (Fig. 2C) or IL-4 (fig. S4A), and total cell numbers were calculated using splitting ratios. Cyton fitting revealed that hIL-2 and IL-4 can increase the mDD by up to ~11 and 7 divisions, respectively (Fig. 2, C to E; fig. S4, A and B; and tables S3 and S4). Titration of hIL-2 showed the effect on mDD to be dose dependent (Fig. 2D) and that this increase in mDD was associated with an increase in variance (Fig. 2E and fig. S4C). Together these results demonstrated that DD can be intrinsically programmed by early signals, but also has the flexibility to be “reprogrammed” or extended by extrinsic stimuli as the T cells divide.

We then determined how T cells integrated multiple contributors to DD. In Fig. 3, A and B, we show the increase in mDD imprinted before the first division for low concentrations of CD28 and CD27 agonist antibodies, and IL-12 protein. The combination of antibodies to CD28 and CD27 programmed an mDD that was equivalent to the sum of each individual effect, with IL-12 giving a slightly greater than additive increase in mDD

Fig. 1. CD8⁺ T cells undergo a program of proliferation and quiescence in vivo and in vitro. (A) Quantitative T cell expansion hypothesis. By this model, the number of mitotic cycles a T cell undergoes after activation (N) varies and is determined by a sum of the individual inputs it receives. In the example shown, signal 1, 2, and 3 stimuli each individually elicit a small increase in mean population division number. The cumulative effect of these contributions, when summed linearly, would lead to geometric increases in total cell number at the peak response. Analysis of OT-I/FucciRG CD8⁺ T cells [(B) to (E)] transferred to HKx31-N4-infected recipients on day 2 after infection or [(E) to (G)] in vitro stimulated with N4 in the presence of mIL-2 blocking antibody (S4B6). (B) Number and (C) percentage of OT-I/FucciRG CD8⁺ T cells expressing FucciR and FucciG reporter proteins pooled from mediastinal lymph node, spleen, and lungs at the indicated time points after transfer. (D) Fitted total (black) and quiescent (red, FucciR⁺G⁻ + small FucciR⁺G⁻ cells) cell numbers using the Cyton model (19). (E) The estimated DD distribution from Cyton fitting to in vivo (D) and in vitro (G) stimulated cells. (F) Percentage of FucciR and FucciG expression. (G) Fitted total (black) and quiescent (red, FucciR⁺G⁻ + small FucciR⁺G⁻ cells) cell numbers (19). [(B) to (E)] $n = 5$ to 10 mice per time point, pooled from two independent experiments; mean \pm SEM. [(E) to (G)] Representative of three independent experiments; mean \pm SEM from triplicate culture wells.



(Fig. 3, C and D). Importantly, no single “second signal” appeared obligatory, but rather multiple small arithmetic effects on DD culminated in large geometric differences in the cell numbers produced (Fig. 1A, center and right panels). Thus, an increase of ~2.2 divisions in mDD (Fig. 3D) with the accompanying ~0.5 division increase in standard deviation (fig. S5, A to D, and table S5) summed from three weak costimuli resulted in a net ~8-fold increase in the peak cell number (Fig. 3, E and F), with the additional difference

in response magnitude attributable to small variations in the starting cell number (fig. S5E and table S5). Early programming was cell intrinsic because cells imprinted with an mDD of ~1 or ~3.4 generations gave the same outcome irrespective of whether they were subsequently cultured separately or together (fig. S6, A and B). The approximately additive effect of stimuli on DD also applied for a range of combinations when stimuli were retained in culture during subsequent division rounds (fig. S7, A to D).

Taken together, this series of experiments reveals two stages of regulation of T cell DD. In the first stage, signal 1 and a series of signal 2 and 3 stimuli of different strengths and combinations can additively “program” a heritable number of division rounds before the first cell division. In the second stage, exposure to external signals, mainly cytokines, can be processed and added to the DD. These features are consistent with a molecular mechanism whereby each stimulatory signal contributes a quantum of mitosis-promoting

Fig. 2. Costimuli and cytokines program changes to DD.

(A) CTV-labeled OT-1/*Bcl2l1*^{+/+} or OT-1/*Bcl2l1*^{-/-} CD8⁺ T cells were stimulated with N4; total cell numbers (left), mean division number (middle), and an estimation of the percentage of the starting cells whose progeny are contributing to the response at that time point, calculated by removing the effect of cell expansion at each time point [percent cohort number, right; as described in (19)] were determined. Mean DD (mDD) on each graph is indicated by dotted lines. **(B)** Mean division number of CTV-labeled OT-1/*Bcl2l1*^{-/-} CD8⁺ T cells cultured in the presence (+, solid lines) or absence (-, dotted lines) of antibodies to CD28 (2 μg/mL) and CD27 (immobilized, 5 μg/mL) (blue), IL-12 (1 ng/mL), human IL-2 (hIL-2, 31.6 U/mL), or IL-4 (1000 U/mL) (red) for 26 hours, washed and further cultured with (dark) or without (light) costimulation. **(C)** CTV-labeled OT-1/*Bcl2l1*^{-/-} CD8⁺ T cells stimulated with N4 in the presence of hIL-2 at the indicated concentrations were subcultured into fresh hIL-2 every ~48 hours and the cell number was fitted using the Cyton model (dotted lines) (19). **(D)** and **(E)** Dose-response curve of mDD (D) and DD distributions (E) from Cyton fitting in (C). All cultures contained 25 μg/mL S4B6. Representative of at least two independent experiments; mean ± SEM from triplicate culture wells.

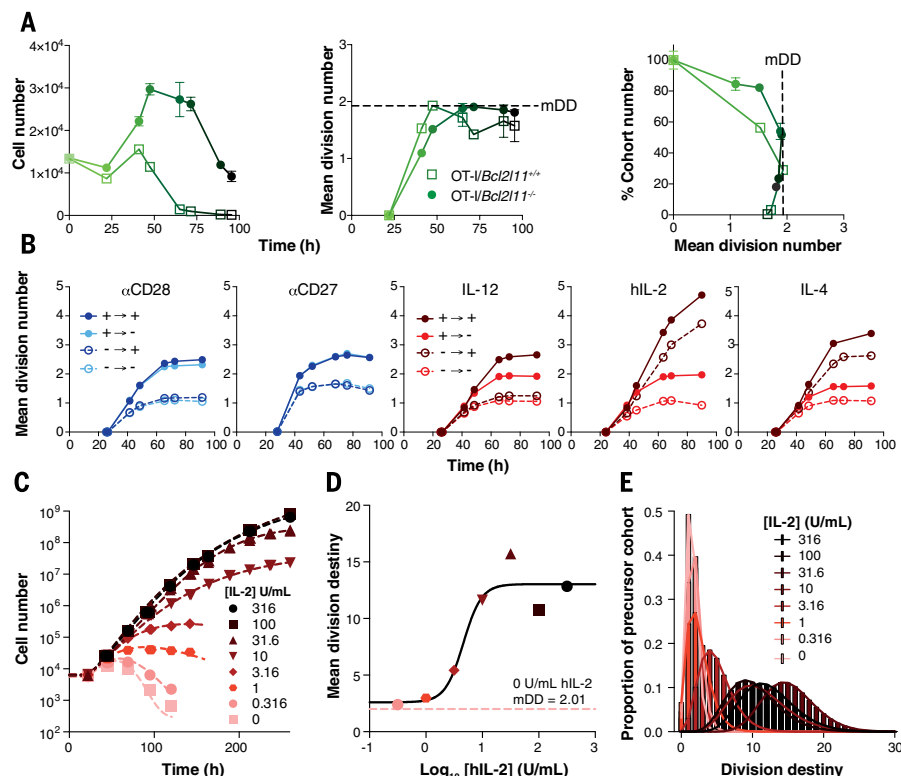


Fig. 3. Summation of DD from multiple costimuli geometrically amplifies the T cell response.

Percentage cohort number (Fig. 2A) (19) versus mean division number for N4-stimulated, CTV-labeled OT-1/*Bcl2l1*^{-/-} CD8⁺ T cells cultured with **(A)** antibodies to CD27 (immobilized, 5 μg/mL) and CD28 (2 μg/mL) or **(B)** IL-12 protein (1 ng/mL) alone, **(C)** antibodies to CD27 and CD28 together, or **(D)** a combination of all three costimuli for 26 hours, washed and recultured without further stimulation. Relationship between cell number and either **(E)** mean division number or **(F)** time for data in [(A) to (D)]. Arrows represent the effect of individual stimuli on mDD. All cultures contained S4B6 at 25 μg/mL. Graphs are representative of three independent experiments; mean ± SEM of triplicate culture wells.

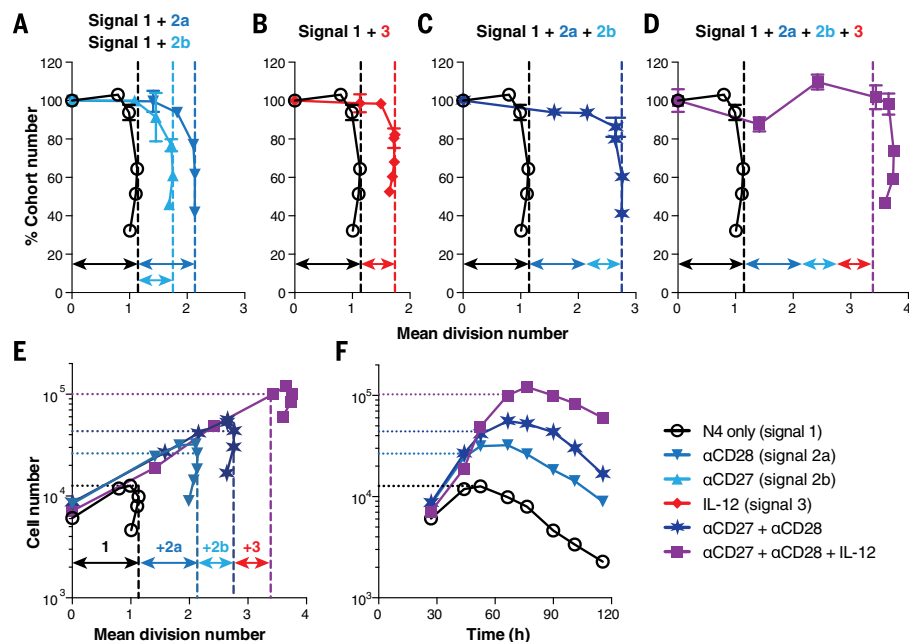
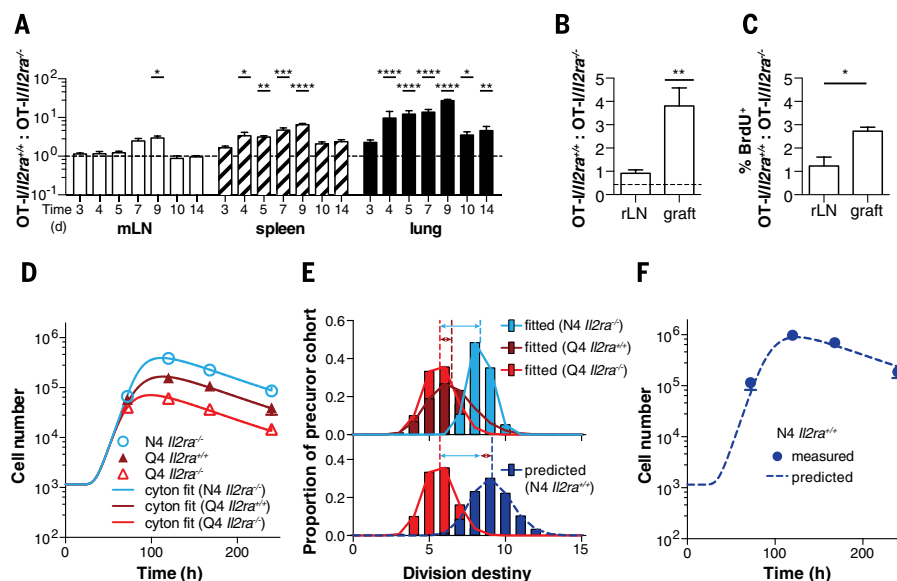


Fig. 4. In vivo summation of DD can predict T cell expansion. (A) Ratio of OT-I/Il2ra^{+/+}:OT-I/Il2ra^{-/-} CD8⁺ T cells recovered from mLN, spleen, and lungs after cotransfer of equal numbers of each into HKx31-N4-infected recipients. Mean \pm SEM, $n = 5$ to 10 mice per time point, pooled from two independent experiments; two-way analysis of variance (ANOVA). (B and C) CTV-labeled OT-I/Il2ra^{+/+} and OT-I/Il2ra^{-/-} CD8⁺ T cells were co-transferred to recipient mice at a 30:70 ratio 1 day before engraftment under the renal capsule with islets expressing membrane-bound ovalbumin under the rat insulin promoter. Mice were pulsed with BrdU 1 hour before organ harvesting on day 6 after engraftment, and the ratio of OT-I/Il2ra^{+/+}:OT-I/Il2ra^{-/-} of (B) divided CD8⁺ T cells and (C) the percentage of divided CD8⁺ T cells positive for BrdU⁺ within their respective genotype populations was measured in the renal (draining) lymph node (rLN) and graft. Mean \pm SEM, $n = 4$ mice, representative of two independent experiments; two-way ANOVA and one-tailed t test, respectively. For all experiments, data points were excluded from ratio and percentage calculations when less than 100 cells were detected. Dotted lines in (A) and (B) represent the OT-I/Il2ra^{+/+}:OT-I/Il2ra^{-/-} transfer ratio. (D) The Cyton model was fitted to OT-I/Il2ra^{+/+} and OT-I/Il2ra^{-/-} CD8⁺ T cell numbers from HKx31-Q4-infected mice and OT-I/Il2ra^{-/-} CD8⁺ T cells from HKx31-N4-infected mice pooled from the mLN, spleen, and lungs after cotransfer of equal numbers of cells into recipient mice, and (E) the division destiny distribution was determined (19). By summation of mean and variance of these DD distributions, the cumulative



effect of increasing TCR-antigen affinity and IL-2 signaling on the DD distribution (i.e., the DD distribution for OT-I/Il2ra^{+/+} CD8⁺ T cells in HKx31-N4-infected mice) was predicted (bottom). (F) Using this mean and variance, the cell number over time was predicted for OT-I/Il2ra^{+/+} CD8⁺ T cells in HKx31-N4-infected mice (19). Mean \pm SEM; $n = 5$ mice per time point, representative of two independent experiments. **** $P < 0.0001$; *** $P < 0.001$; ** $P < 0.01$; * $P < 0.05$.

protein or complex that is diluted by division until a submitotic concentration is reached and division ceases (26).

The two-stage DD programming model makes two key predictions for the role of extrinsic factors, such as IL-2, that could be tested during in vivo CD8⁺ T cell responses: (i) the major physiological role of autocrine IL-2 is in maintaining division, and therefore it will be more important away from the initial site of CD8⁺ T cell priming; and (ii) the effect of IL-2 on DD will sum with other stimuli, allowing the prediction of CD8⁺ T cell expansion kinetics when IL-2 and other stimuli are combined.

We tested the first prediction by comparing the expansion of IL-2 receptor α -deficient OT-I CD8⁺ T cells (OT-I/Il2ra^{-/-}) with OT-I/Il2ra^{+/+} CD8⁺ T cells in two different in vivo systems, namely an anti-influenza response and islet graft rejection model. Similar numbers of OT-I/Il2ra^{+/+} and OT-I/Il2ra^{-/-} CD8⁺ T cells were detected at the site of priming [mediastinal lymph node (mLN)] during the expansion phase when cotransferred into HKx31-N4 infected mice (Fig. 4A). In contrast, a bias toward expansion of OT-I/Il2ra^{+/+} CD8⁺ T cells was observed in the spleen and lungs, consistent with a role for IL-2 in the maintenance of cell expansion (Fig. 4A). OT-I/Il2ra^{+/+} CD8⁺ T cells also outcompeted OT-I/Il2ra^{-/-} CD8⁺ T cells at the effector site during an anti-islet graft response (Fig. 4B). The proportion of bromodeoxyuridine-positive (BrdU⁺) OT-I/Il2ra^{+/+} CD8⁺ T cells after a 1-hour in vivo BrdU pulse was ~ 2.5 times as high as for OT-I/Il2ra^{-/-} CD8⁺ T cells in the graft (Fig. 4C), confirming that this bias was attributable to proliferation in the effector site and not due to migration alone (27).

To investigate the additive nature of T cell stimuli in vivo, OT-I/Il2ra^{+/+} and OT-I/Il2ra^{-/-} CD8⁺ T cells were cotransferred into mice infected with either high-affinity (HKx31-N4) or low-affinity (HKx31-Q4) influenza virus (20). The Cyton model was fitted to T cell numbers to estimate the increase in DD due to TCR affinity or IL-2 signaling alone (Fig. 4, D and E, top, and table S6). By summation of these individual contributions to the mean and variance of the DD distribution, we predicted the effect of a combined increase in TCR affinity and IL-2 signaling on DD (Fig. 4E, bottom) and successfully recreated the expansion kinetics of OT-I/Il2ra^{+/+} CD8⁺ T cells during an HKx31-N4 infection (Fig. 4F).

Manipulating T cell responses by costimulation and cytokine signaling is an important emerging therapeutic regimen (28, 29), and a quantitative framework will facilitate the rational development of optimal interventions. To support this goal, we propose a quantitative paradigm where no one signal is obligatory but rather combinations of inputs add together to geometrically enhance outcomes (Fig. 1A). Thus, combinations of different costimulatory and cytokine signals provide many alternative paths to generate T cell responses of similar magnitude. This framework reconciles long-standing discrepancies between in vivo and in vitro results for IL-2 and costimulatory signals and reveals a quantitative basis for current switch-inspired two- and three-signal models of activation. Further studies measuring simultaneous differentiation changes to effector and memory states associated with cell division would complete the T cell calculating framework and further enhance our ability to predict therapeutic strategies for immunomodulation.

REFERENCES AND NOTES

- D. Zehn, S. Y. Lee, M. J. Bevan, *Nature* **458**, 211–214 (2009).
- S. M. Kaech, R. Ahmed, *Nat. Immunol.* **2**, 415–422 (2001).
- M. J. van Stipdonk, E. E. Lemmens, S. P. Schoenberger, *Nat. Immunol.* **2**, 423–429 (2001).
- E. M. Bertram, W. Dawicki, T. H. Watts, *Semin. Immunol.* **16**, 185–196 (2004).
- J. M. Curtis et al., *J. Immunol.* **162**, 3256–3262 (1999).
- A. G. Baxter, P. D. Hodgkin, *Nat. Rev. Immunol.* **2**, 439–446 (2002).
- D. A. Cantrell, K. A. Smith, *Science* **224**, 1312–1316 (1984).
- L. A. Gravestine, J. D. Nieland, A. M. Kruisbeek, J. Borst, *Int. Immunol.* **7**, 551–557 (1995).
- F. A. Harding, J. G. McArthur, J. A. Gross, D. H. Raulet, J. P. Allison, *Nature* **356**, 607–609 (1992).
- T. R. Malek, *Annu. Rev. Immunol.* **26**, 453–479 (2008).
- A. Oxenius, U. Karrer, R. M. Zinkernagel, H. Hengartner, *J. Immunol.* **162**, 965–973 (1999).
- A. Shahinian et al., *Science* **261**, 609–612 (1993).
- K. P. J. M. van Gisbergen et al., *Immunity* **35**, 97–108 (2011).
- E. D. Hawkins, J. F. Markham, L. P. McGuinness, P. D. Hodgkin, *Proc. Natl. Acad. Sci. U.S.A.* **106**, 13457–13462 (2009).
- E. D. Hawkins, M. L. Turner, M. R. Dowling, C. van Gend, P. D. Hodgkin, *Proc. Natl. Acad. Sci. U.S.A.* **104**, 5032–5037 (2007).
- M. L. Turner, E. D. Hawkins, P. D. Hodgkin, *J. Immunol.* **181**, 374–382 (2008).
- M. R. Dowling et al., *Proc. Natl. Acad. Sci. U.S.A.* **111**, 6377–6382 (2014).
- M. Tomura et al., *PLOS ONE* **8**, e73801 (2013).
- Materials and methods are available as supplementary materials on Science Online.
- A. E. Denton et al., *J. Immunol.* **187**, 5733–5744 (2011).
- E. D. Hawkins et al., *Nat. Commun.* **4**, 2406 (2013).
- V. R. Buchholz et al., *Science* **340**, 630–635 (2013).
- C. Gerlach et al., *Science* **340**, 635–639 (2013).
- M. Hommel, P. D. Hodgkin, *J. Immunol.* **179**, 2250–2260 (2007).
- E. K. Deenick, A. V. Gett, P. D. Hodgkin, *J. Immunol.* **170**, 4963–4972 (2003).
- Because OT-I division times are relatively homogeneous, a division-based dilution model is difficult to distinguish from a mechanism where the loss of division motivation ceases in all

descendants at the same time after activation. Further molecular studies are needed to distinguish between these and other possible mechanisms.

27. W. Weninger, M. A. Crowley, N. Manjunath, U. H. von Andrian, *J. Exp. Med.* **194**, 953–966 (2001).
28. M. Dougan, G. Dranoff, *Annu. Rev. Immunol.* **27**, 83–117 (2009).
29. G. Kinnear, N. D. Jones, K. J. Wood, *Transplantation* **95**, 527–535 (2013).

ACKNOWLEDGMENTS

We thank S. Turner for providing the recombinant influenza virus and discussion and comments on the manuscript; L. Corcoran and V. Bryant for discussion and comments on the manuscript; A. Giang for discussion of experiments; M. Camilleri, L. Mackiewicz, M. Dayton, and D. Pavlyshyn for technical assistance; and

P. Bouillet for *Bcl2l1*^{−/−} mice. Fucci Red and Fucci Green mice were provided by the Riken BioResource Centre through the National BioResource Project of the Ministry of Education, Culture, Sports, Science, and Technology of Japan. We also thank K. Lafferty and his two-signal theory for inspiring this work. The data are tabulated in the main paper and in the supplementary materials. Experimental data and the code for fitting the Cyton model will be made available upon request. This work was supported by the National Health and Medical Research Council (NHMRC) through project grants 1010654 and 1043414, program grants 1054925 and 1037321, and fellowships to M.R.D., A.M.L., and P.D.H., K.R.D. and P.D.H. were supported by Human Frontier Science Program grant RGP0060/2012. G.T.B. was supported by an Australian Research Council Future Fellowship, and K.R.D. was supported by Science Foundation Ireland grant 12IP1263. This work was made

possible through Victorian State Government Operational Infrastructure Support and Australian Government NHMRC Independent Research Institutes Infrastructure Support Scheme. J.M.M. was the recipient of an Australian Postgraduate Award and a Walter and Eliza Hall Institute Edith Moffat Scholarship.

SUPPLEMENTARY MATERIALS

www.sciencemag.org/content/346/6213/1123/suppl/DC1
Materials and Methods
Figs. S1 to S10
Tables S1 to S9
References (30–32)

15 August 2014; accepted 30 October 2014
10.1126/science.1260044

DNA REPAIR

Mechanism of DNA interstrand cross-link processing by repair nuclease FAN1

Renjing Wang,¹ Nicole S. Persky,¹ Barney Yoo,² Ouathhek Ouerfelli,² Agata Smogorzewska,³ Stephen J. Elledge,^{4,5} Nikola P. Pavletich^{1*}

DNA interstrand cross-links (ICLs) are highly toxic lesions associated with cancer and degenerative diseases. ICLs can be repaired by the Fanconi anemia (FA) pathway and through FA-independent processes involving the FAN1 nuclease. In this work, FAN1-DNA crystal structures and biochemical data reveal that human FAN1 cleaves DNA successively at every third nucleotide. In vitro, this exonuclease mechanism allows FAN1 to excise an ICL from one strand through flanking incisions. DNA access requires a 5'-terminal phosphate anchor at a nick or a 1- or 2-nucleotide flap and is augmented by a 3' flap, suggesting that FAN1 action is coupled to DNA synthesis or recombination. FAN1's mechanism of ICL excision is well suited for processing other localized DNA adducts as well.

DNA interstrand cross-links (ICLs) covalently link together the two strands of the double helix (1). ICLs can be repaired by the Fanconi anemia (FA) pathway of proteins mutated in the FA cancer predisposition syndrome (2) and also by FA-independent processes (1, 3, 4). The FA pathway is activated when a replication fork stalls upon encountering an ICL, leading to unhooking of the ICL through flanking incisions on one strand, translesion DNA synthesis across the unhooked ICL, removal of the ICL remnants by additional incisions, and homologous recombination (2, 5). The FAN1 nuclease (6–9) is a candidate for mediating FA-independent repair (1, 3, 4). Although FAN1 mutations result in defective ICL repair,

chromosomal instability, and hypersensitivity to a wide range of ICL-inducing agents (6–13), they do not cause FA (10–12). Instead, they cause a kidney degeneration disorder known as karyomegalic interstitial nephritis (17). FAN1 cleaves branched DNA structures with a preference for 5'-flap substrates and also exhibits 5'- to 3'-exonuclease activity on a variety of double-stranded DNA (dsDNA) and single-stranded DNA (ssDNA) substrates (6–9). The functional implications of these broadly defined activities, whether FAN1 processes ICLs directly and in which manner, and the structural mechanism of ICL unhooking by nucleases are unknown.

To address these questions, we first investigated FAN1's DNA binding specificity for various lengths of 5' flaps consisting of thymidine nucleotides (see supplementary materials and methods). We found that FAN1 exhibits specificity for a 5' phosphate group at a flap of 1 to 2 nucleotides (nts) or at a nick, with dissociation constants (K_d) of 10.3 nM for the 1-nt flap (5'pT₁), 121 nM for 2 nts (5'pT₂), and 182 nM for the nick (pNi) (fig. S1A). The corresponding substrates lacking the 5' phosphate group fail to bind appreciably until micromolar FAN1 concentrations

(fig. S1A). Similarly, increasing the flap length beyond 2 nts reduces FAN1 affinity substantially (fig. S1A). We also tested the effect of adding a 3' flap of eight thymidine nucleotides to the high-affinity 5'pT₁ (5'pT₁/3'T₈), 5'pT₂ (5'pT₂/3'T₈), and 5'pNi (5'pNi/3'T₈) and found that this increased their FAN1 affinity by a factor of ~25 to ~180 (K_d values of 0.4, 1.4, and 1.0 nM, respectively) (fig. S1B). By contrast, adding a 3'T₈ flap to the low-affinity 5'pT₈ (5'pT₈/3'T₈) minimally enhanced its affinity, with the resulting 377 nM K_d a factor of ~1000 weaker than that of 5'pT₁/3'T₈ (fig. S1B).

Based on these findings, we determined the 2.9 Å structure of a 5'pG₁/3'T₄ DNA bound to human FAN1 (residues 364 to 1017), N-terminally truncated to remove the ubiquitin-binding UBZ domain and subsequent unstructured segment, as well as the structure of apo-FAN1 (fig. S2A and table S1). FAN1 has a bilobal structure consisting of a 223-residue N-terminal domain (NTD) and a 415-residue C-terminal domain (CTD) that contains the PD-(D/E)XK nuclease motif (Fig. 1, A and B). The DNA adopts a V-shaped structure, with a kink at the nick. The prenick and postnick duplexes have an overall B-form DNA (B-DNA) conformation, with a 76° angle between them. The prenick duplex and 3' flap are bound by the NTD, whereas the 5' flap and postnick duplex are bound by the CTD. There are no major conformational changes between the apo- and DNA-bound FAN1 structures (fig. S2B).

The NTD consists of a helical domain, a winged-helix DNA binding domain, and the predicted SAP domain (Fig. 1C). These form a continuous surface that binds to a 9-base pair duplex segment leading to the 3' flap and to a 2-nt segment of the flap (Fig. 1A and fig. S3, A to D). The duplex contacts involve only phosphodiester groups (fig. S3, A to D), except for the flap-proximal base pair, which is contacted at both its phosphodiester and base groups (Fig. 2A). These base contacts block the DNA from extending as a regularly stacked duplex, analogous to the helix-breaking wedges observed with other structure-specific nucleases (14, 15).

Only the first two nucleotides of the 3'T₄ flap are ordered. These extend away from the duplex and are bound by FAN1 (Fig. 2A). The base and ribose groups of the first nucleotide are contacted by Tyr³⁷⁴, Val⁵⁷⁷, and Arg⁵⁸¹. The phosphate group

¹Structural Biology Program and Howard Hughes Medical Institute, Memorial Sloan Kettering Cancer Center, New York, NY 10065, USA. ²Molecular Pharmacology and Chemistry Program, Memorial Sloan Kettering Cancer Center, New York, NY 10065, USA. ³Laboratory of Genome Maintenance, The Rockefeller University, New York, NY 10065, USA. ⁴Department of Genetics and Howard Hughes Medical Institute, Harvard Medical School, Boston, MA 02115, USA. ⁵Division of Genetics, Brigham and Women's Hospital, Boston, MA 02115, USA.

*Corresponding author. E-mail: pavletin@mskcc.org

of the second nucleotide binds to a pocket at the N terminus of an α helix and hydrogen bonds to a backbone amide group (Tyr³⁷⁴) in a partially buried environment. These 3'-flap contacts are consistent with the addition of a single-nucleotide 3' flap to 5'pT₁/3'T₈ resulting in roughly half of the affinity increase of an 8-nt flap (for 5'pT₁/3'T₈, $K_d = 1.9$ nM) (fig. S1B).

The CTD starts with a 180-residue helical repeat domain that belongs to the tetratricopeptide repeat (TPR) family, followed by a nuclease domain that has the ~ 120 -residue $\alpha\beta\beta\alpha\beta$ fold of the PD-(D/E)XK superfamily of Mg²⁺-dependent nucleases (16, 17) but that additionally contains a 125-residue helical insertion (Fig. 1C). The CTD has a wide and deep groove, with the TPR domain on one side and the nuclease and insertion domains on the other, into which the postnick duplex binds (Fig. 1B). FAN1 contacts the 5' phosphate group of the flap and eight phosphodiester groups clustered at the flap-distal portion of the duplex (Fig. 2B). The backbone of the 1-nt flap extends orthogonally from the duplex. The 5' phosphate group abuts a highly basic pocket at the bottom of the CTD groove, with its three nonbridging oxygen atoms hydrogen bonding with the side chains of Arg⁷⁰⁶, Arg⁹⁵², His⁷⁴², and Lys⁹⁸⁶ (Fig. 2, C and D, and fig. S4A). These contacts explain FAN1's strict requirement for a 5' phosphate group. Accordingly, the Arg⁷⁰⁶ → Ala⁷⁰⁶/Arg⁹⁵² → Ala⁹⁵² double mutation reduces FAN1's affinity for 5'pT₁/3'T₈ by a factor of ~ 400 ($K_d = 210$ nM) (fig. S4B). After the 5' phosphate group, the next two phosphodiester groups make relatively few contacts, whereas a nonbridging oxygen of the third phosphodiester group coordinates the Ca²⁺ ion at the nuclease active site (Fig. 2D).

The Ca²⁺ ion, which does not support nuclease activity (18), has a coordination shell similar to other nucleases (17, 18) (fig. S4, C to E). This indicates that cleavage occurs at the third phosphodiester group from the 5' phosphate (hereafter "+3 register") and results in a 5' phosphorylated product, both of which we confirmed by liquid chromatography-coupled mass spectroscopy (LC-MS) of a nuclease reaction.

In additional cocrystal structures that we determined (table S1 and fig. S5A), the 5' phosphate groups of 5'pT₁/3'T₈, 5'pT₁, and 5'pNi bind to the same FAN1 pocket and contact the same four side chains as in the 5'pG₁/3'T₄ structure (fig. S5, A and C). By contrast, the pocket is devoid of DNA in the cocrystal structure of the 5'-hydroxyl 5'T₂, consistent with FAN1's specificity for a terminal phosphate. The 5'pT₁/3'T₈, 5'pT₁, and 5'pNi structures also suggest some inherent flexibility in the register of the scissile phosphate relative to the 5' phosphate group. In the 5'pT₁/3'T₈ and 5'pT₁ structures, an extra nucleotide is extruded out in a loop as the 5'-flap backbone transitions to the duplex, resulting in an $n+4$ scissile phosphate register (fig. S5, B and C). In the 5'pNi structure, a shifted trajectory for the duplex results in a +2 register (fig. S5, C and D).

The importance of a 5' phosphate group on a short flap or nick is recapitulated in FAN1 nu-

lease assays. In the presence of 150 mM NaCl and with 100 nM substrate, 5'pT₁/3'T₈, pNi/3'T₈, and 5'pT₂/3'T₈ are cleaved starting with 0.1 nM FAN1, whereas the longer 5'-flap 5'pT₈/3'T₈ sub-

strate is not noticeably cleaved even with 100 nM FAN1 (Fig. 3A and fig. S6). 5'pT₈/3'T₈ cleavage required very low ionic strength, such as the 25 mM NaCl used in previous studies, but its extent was

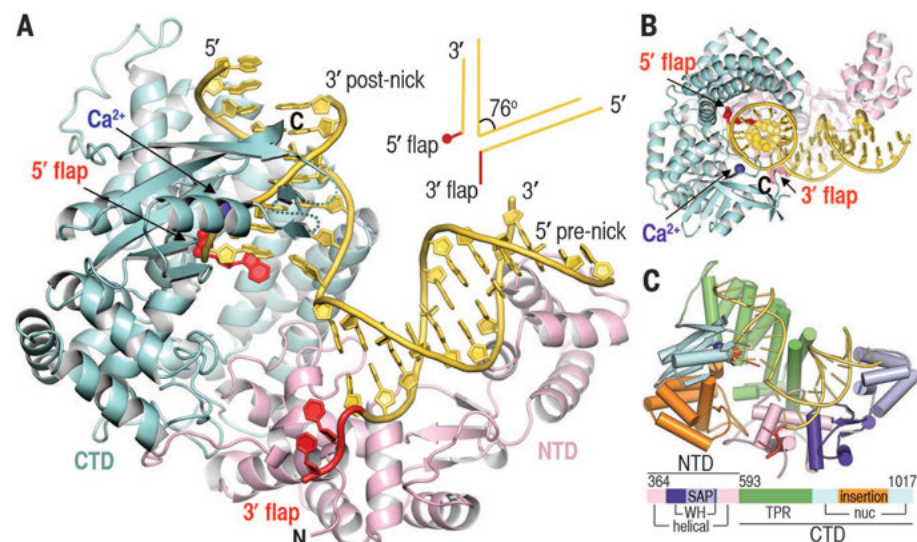


Fig. 1. Overall structure of FAN1-5'pG₁/3'T₄. (A) Cartoon representation. NTD, pink; CTD, light blue, dsDNA, yellow; flaps and 5' phosphate spheres, red; and Ca²⁺, purple. The inset shows a line drawing of the DNA. (B) View looking down the vertical axis of (A). (C) The six different domains of FAN1 are colored according to the linear representation. WH, winged helix.

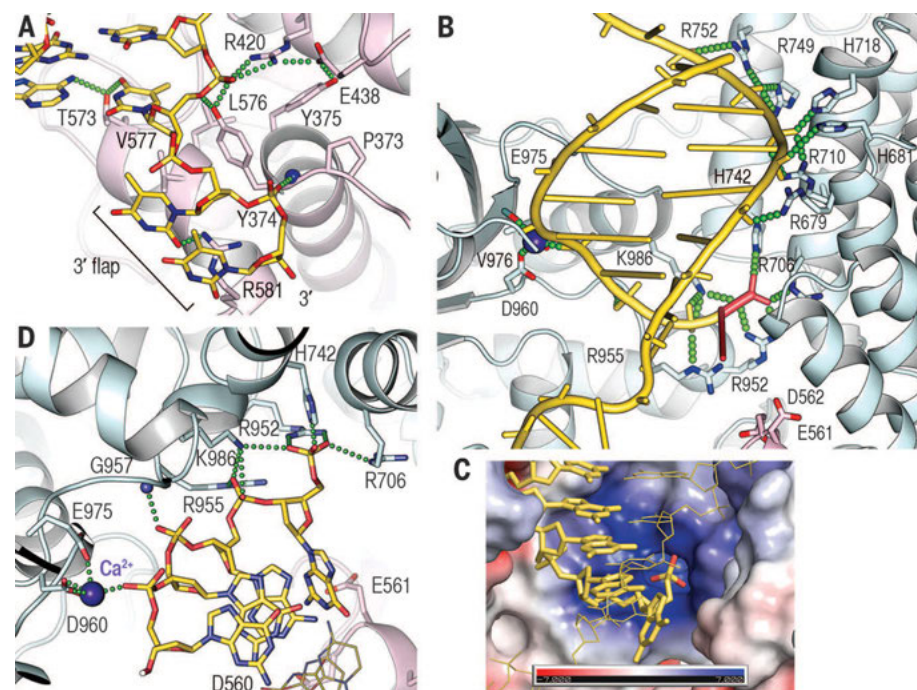


Fig. 2. FAN1-DNA contacts. (A) Close-up view of 3'-flap contacts showing side chains involved in either hydrogen bond (green dotted lines) or van der Waals contacts. T, Thr; V, Val; R, Arg; L, Leu; E, Glu; Y, Tyr; P, Pro. (B) Overview of the CTD-DNA contacts, with the 5' flap and its phosphate group shown in red. D, Asp; K, Lys; H, His. (C) Surface representation of the 5' phosphate binding pocket, colored by the electrostatic potential ($\pm kT$, where k is Boltzmann's constant and T is temperature), with the scissile strand shown as yellow sticks, the 5' phosphate oxygen atoms in red, and the continuous strand as thin yellow lines. (D) Close-up view of contacts to the 5' phosphorylated flap and the three following nucleotides of the scissile strand. Continuous strand shown as thin lines. G, Gly.

still substantially lower than that of 5'pT₁/3'T₈ (Fig. 3A and fig S6).

The +3 scissile phosphate register suggests that FAN1's reported 5'- to 3'-exonuclease activity results from successive incisions releasing 3-nt fragments. In the time course of a 1 nM stoichiometric FAN1-5'pT₁/3'T₈ reaction, an 18-nt product corresponding to a +3 incision appears first, its level peaking at 8 min and then declining as it gets consumed (Fig. 3B). A 15-nt product (+3 incisions) appears second and peaks at 16 to 32 min, whereas a 12-nt product (third incision) appears last. The 5'pNi/3'T₈ substrate produces

a similar pattern of sequential cuts with a major +3 spacing (Fig. 3B). Minor products corresponding to +4 and +2 incisions probably reflect the alternate scissile phosphate registers of the 5' pT₁/3'T₈ and 5'pNi/3'T₈ cocystal structures, respectively (fig. S5C).

Successive incisions do not occur in a detectably processive manner (fig. S7A) but meet the criteria of a distributive activity. FAN1 binds to a 3-nt gap substrate (pGap₃/3'T₈), which corresponds to the first incision product of 5'pNi/3'T₈ [K_d = 3.6 nM, compared with 1.0 nM for 5'pNi/3'T₈ (fig. S7B)], and also cleaves this substrate to

generate products equivalent to the second and third products of pNi/3'T₈ (Fig. 3C). To determine the effect of increasing gap length, we assayed a 5'pT₁/3'T₈ substrate containing a long, 35-base pair postnick duplex. The sequential incisions stalled after four cuts even in a 100 nM stoichiometric reaction (fig. S7C), suggesting that a gap length beyond ~12 nts of ssDNA, which presumably loops out at the NTD-CTD interface, substantially reduces FAN1 binding efficiency. In vivo, the stalling could be inconsequential if FAN1 acts at a site with a complementary 3' flap or in cooperation with a distributive polymerase, either

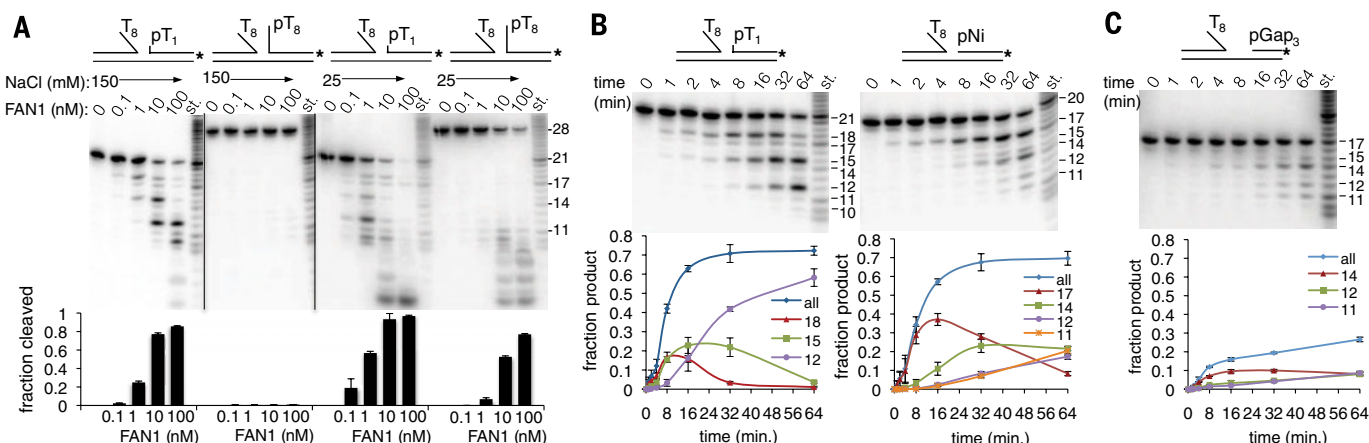


Fig. 3. Nuclease activity. (A) Denaturing PAGE of nuclease reactions with the indicated substrates (100 nM), FAN1, and NaCl concentrations. The substrate scissile strand and molecular weight standards (st.) are labeled with 3' α -³²P deoxyadenosine triphosphate (asterisks). The column graphs show the sum of all cleaved bands divided by total DNA, as the mean \pm SD (error bars) from three experiments. (B) Nuclease time course of 5'pT₁/3'T₈ (left) and 5'pNi/3'T₈ (right) in 150 mM NaCl. Bands and the corresponding molecular weight standards are marked. Fractional amounts of each major product and their total ("all") are graphed as the mean \pm SD (error bars) from three experiments. (C) Nuclease time course of pGap₃/3'T₈, as in (B).

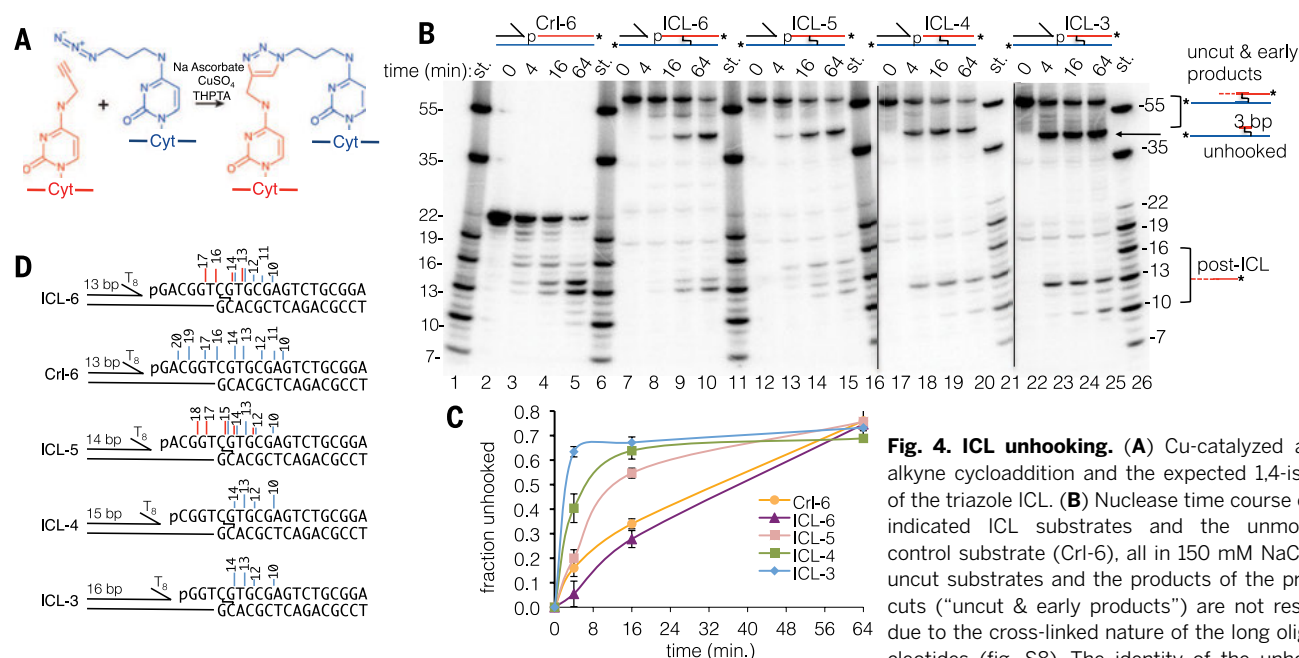


Fig. 4. ICL unhooking. (A) Cu-catalyzed azide-alkyne cycloaddition and the expected 1,4-isomer of the triazole ICL. (B) Nuclease time course of the indicated ICL substrates and the unmodified control substrate (CrI-6), all in 150 mM NaCl. The uncut substrates and the products of the pre-ICL cuts ("uncut & early products") are not resolved due to the cross-linked nature of the long oligonucleotides (fig. S8). The identity of the unhooked

ICL band ("unhooked") was confirmed by LC-MS of the band eluted from a PAGE gel of the ICL-5 reaction (table S2). (C) Quantitation of (B), graphing the ratio of unhooked bands to unhooked plus uncut, corrected for the presence of two ³²P-labeled strands in uncut bands. The CrI-6 curve shows total cuts, so it initially rises faster than the ICL-6 curve that does not reflect the unresolved cuts one and two. (D) Vertical lines mark incisions identified by PAGE (blue) and LC-MS (red), with line height reflecting relative product abundance and numbers indicating product length (nucleotides).

of which can close the emergent gap and restore high-affinity binding.

The +3 exonuclease mechanism is well suited for unhooking an ICL through two successive flanking incisions. To test this, we synthesized a stable ICL consisting of two cytosines linked at their N4 positions through a triazole moiety (19) (Fig. 4A and fig. S8). We first assayed a triazole ICL with the cross-linked cytosine positioned 6 nts after the 5' phosphorylated nick of a 5'pNi/3'T₈ substrate (ICL-6). In a 1 nM stoichiometric reaction, FAN1 robustly cleaved past the ICL, giving rise to post-ICL products that match those of the unmodified control substrate (CrI-6) with similar rates (Fig. 4, B and C). By LC-MS analysis of the 64-min reaction, we confirmed that this is due to dual incisions 5' and 3' to the ICL. Our LC-MS analysis identified a major molecular species (37% of the LC-ultraviolet quantitation) (table S2) consisting of the continuous strand, the triazole linkage, and a 3-nt fragment of Cyt, Gua, and Thy (11653.995 and 11653.387 daltons, respectively, for the observed and calculated molecular weight) (table S2). The ICL-6 products (Fig. 4D) also demonstrate that FAN1 can cleave immediately 5' to the ICL, with the 5' phosphodiester group of the cross-linked cytosine at the scissile position.

We next addressed whether FAN1 can unhook the triazole ICL, irrespective of its register relative to the 5' phosphate group. For this, we tested ICLs with the cross-linked cytosine positioned 5, 4, or 3 nts after the 5' phosphorylated nick (ICL-5, ICL-4, and ICL-3, respectively). FAN1 unhooked ICL-4 and ICL-3 at faster rates

compared with ICL-6, consistent with this requiring only two incisions compared with three, whereas the rate of ICL-5 unhooking was intermediate (Fig. 4, B to D). LC-MS and denaturing polyacrylamide gel electrophoresis (PAGE) of the ICL-5 reaction also indicated that FAN1 can cleave immediately 3' to the ICL (Fig. 4, B to D, and table S2).

Diverse ICLs can cause a wide range of DNA structure distortions, but these are mostly limited to one or two base pairs flanking the lesion (20). The structurally and biochemically observed ± 1 -nt shifts in the scissile phosphate register, coupled to the paucity of FAN1-DNA contacts in the immediate vicinity of the scissile phosphate group, suggest that the FAN1 active site may have substantial flexibility for accommodating such distortions. Our DNA binding and cleaving data strongly suggest that FAN1 acts at sites that have a 5' phosphate group on a short flap or nick, possibly generated by an upstream nuclease. Such sites may also arise from the regression of longer 5' phosphorylated flaps with the concomitant generation of a complementary 3' flap. If FAN1 accesses the DNA at such a site, it can keep excising with 3'-flap annealing until it reaches and unhooks the ICL.

REFERENCES AND NOTES

1. C. Clauson, O. D. Schärer, L. Niedernhofer, *Cold Spring Harb. Perspect. Biol.* **5**, a012732 (2013).
2. H. Kim, A. D. D'Andrea, *Genes Dev.* **26**, 1393–1408 (2012).
3. H. L. Williams, M. E. Gottesman, J. Gautier, *Trends Biochem. Sci.* **38**, 386–393 (2013).
4. A. J. Deans, S. C. West, *Nat. Rev. Cancer* **11**, 467–480 (2011).
5. D. T. Long, M. Räschele, V. Joukov, J. C. Walter, *Science* **333**, 84–87 (2011).

6. K. Kratz *et al.*, *Cell* **142**, 77–88 (2010).
7. T. Liu, G. Ghosal, J. Yuan, J. Chen, J. Huang, *Science* **329**, 693–696 (2010).
8. C. MacKay *et al.*, *Cell* **142**, 65–76 (2010).
9. A. Smogorzewska *et al.*, *Mol. Cell* **39**, 36–47 (2010).
10. K. Yoshikiyo *et al.*, *Proc. Natl. Acad. Sci. U.S.A.* **107**, 21553–21557 (2010).
11. W. Zhou *et al.*, *Nat. Genet.* **44**, 910–915 (2012).
12. J. P. Trujillo *et al.*, *Blood* **120**, 86–89 (2012).
13. Y. Fontebasso, T. J. Etheridge, A. W. Oliver, J. M. Murray, A. M. Carr, *DNA Repair* **12**, 1011–1023 (2013).
14. S. E. Tsutakawa *et al.*, *Cell* **145**, 198–211 (2011).
15. J. Orans *et al.*, *Cell* **145**, 212–223 (2011).
16. L. N. Kinch, K. Ginalski, L. Rychlewski, N. V. Grishin, *Nucleic Acids Res.* **33**, 3598–3605 (2005).
17. A. Pingoud, M. Fuxreiter, V. Pingoud, W. Wende, *Cell. Mol. Life Sci.* **62**, 685–707 (2005).
18. J. M. Hadden, A. C. Déclais, S. B. Carr, D. M. Lilley, S. E. Phillips, *Nature* **449**, 621–624 (2007).
19. S. I. Presolski, V. Hong, S. H. Cho, M. G. Finn, *J. Am. Chem. Soc.* **132**, 14570–14576 (2010).
20. P. A. Muniandy, J. Liu, A. Majumdar, S. T. Liu, M. M. Seidman, *Crit. Rev. Biochem. Mol. Biol.* **45**, 23–49 (2010).

ACKNOWLEDGMENTS

This work was supported by the Howard Hughes Medical Institute (N.P.P. and S.J.E.) and NIH grant R01HL120922 (A.S.). A.S. is a Rita Allen Foundation Scholar and the recipient of a Burroughs Wellcome Career Award and a Doris Duke Clinical Scientist Development Award. The Protein Data Bank accession codes are 4RI8 (5'pG₁/3'T₄), 4RI9 (5'pT₁/3'T₈), 4RIA (5'pNi), 4RIB (5'pT₁), 4RIC (5'T₂), and 4RID (apo-FAN1).

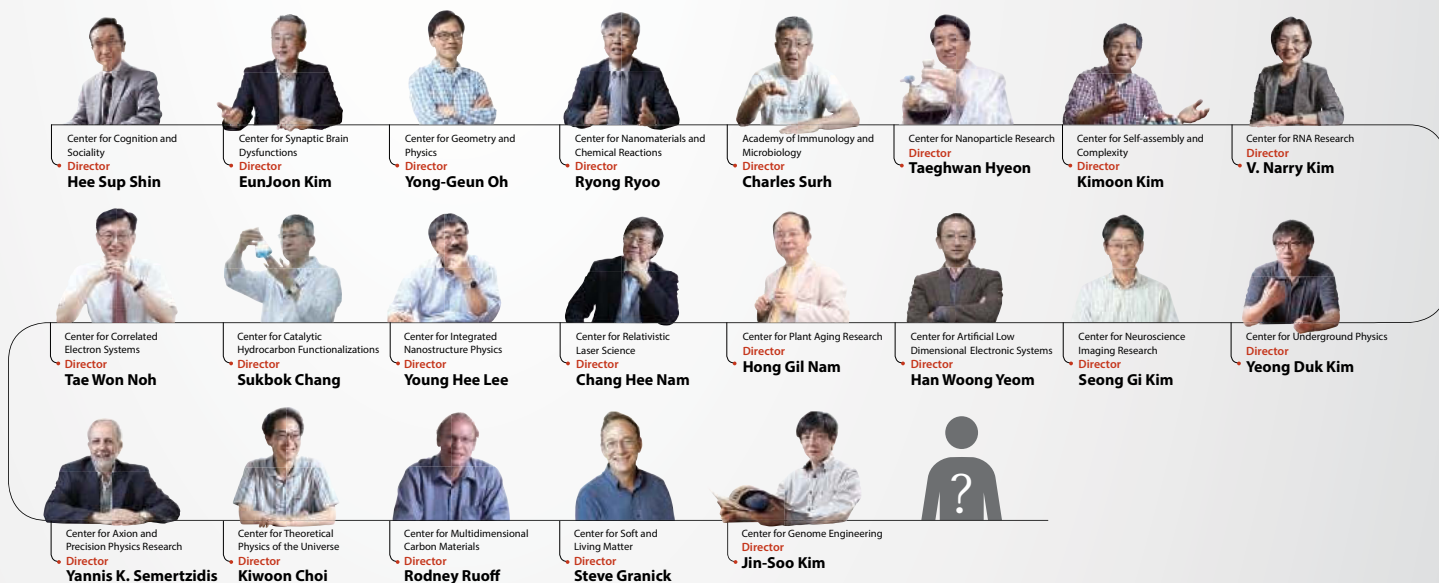
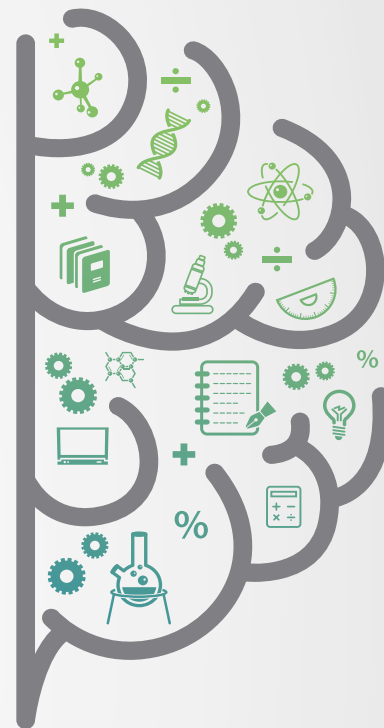
SUPPLEMENTARY MATERIALS

www.sciencemag.org/content/346/6213/1127/suppl/DC1
Materials and Methods
Figs. S1 to S8
Tables S1 and S2
References (21–25)

21 July 2014; accepted 4 November 2014
10.1126/science.1258973

A Chance to Expand Your Creative Possibilities

At IBS in South Korea, many excellent scientists have gathered to further expand the potential of science and technology.



IBS invites you to join the challenge of boosting basic science.

IBS (Institute for Basic Science) is a government-funded research institute, established with the sole purpose of driving forward the development of basic science in Korea. We have launched 21 research centers; each headed by an internationally renowned scientist with an operational budget of up to 10 million USD a year. IBS will be comprised of a total of 50 research centers in all fields of basic science, including mathematics, physics, chemistry, life science, earth science and interdisciplinary science.

Our strategy is simple: establish an excellent research institute for basic science in Korea by recruiting exceptional scientists worldwide and fully supporting them in whichever research areas they wish to pursue for the long-term. IBS ensures that we select the best possible people for this challenge with our peer-review evaluation system. You are cordially invited to join IBS to boost basic science to the next level.



IBS looks forward to shaping the future of basic science with you. Visit our website for detailed recruitment information and register yourself with the IBS Talent Pool DB for a future career with IBS.

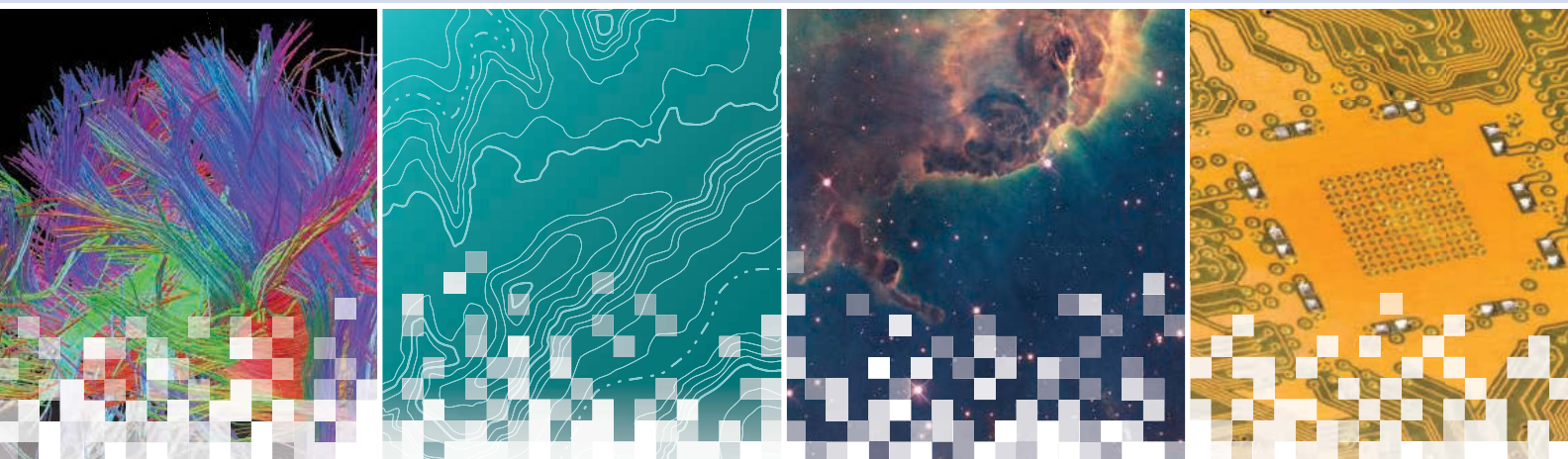
<http://www.ibs.re.kr/en> <http://www.ibs.re.kr/talents>

AAAS | 2015 ANNUAL MEETING

12–16 FEBRUARY • SAN JOSE, CA

INNOVATIONS, INFORMATION, AND IMAGING

The meeting will highlight the information transformation happening in science and technology brought about by recent advances in organizing, visualizing, and analyzing data.



Register and Reserve a Hotel Now

Register and book your housing to use funds from fiscal year 2014. Reduced rates are available until 22 January 2015.

Online registration and scientific program:

www.aaas.org/meetings

Online Career Fairs

December 10, 2014

For careers in science, there's only one

Science



Meet recruiters without leaving your lab or desk!

Science Careers is excited to bring you an easy, efficient and powerful way to connect with employers from all over... all in one place. This virtual event allows you to queue up to visit with representatives from any companies you are interested in during the event hours.

Features and Benefits of Attending this Event

- No travel required—you can login from anywhere
- Queues tell you how many people are in line ahead of you and how long you will be waiting so you can better manage your time
- Login before the event to learn more about participating employers
- Employers can see your resume while you are talking to them

Science Careers

FROM THE JOURNAL SCIENCE  AAAS

For more information, visit:
ScienceCareers.org/onlinecareerfair



This is the start of something big.



ScienceAdvances |  AAAS
SIGNIFICANT RESEARCH, GLOBAL IMPACT

Introducing *Science Advances* – the new, online-only, open-access journal from *Science* and AAAS. Find out how you can be among the first authors published at scienceadvances.org.



Superresolution Microscopy

LSM 880 with Airyscan is a new confocal laser scanning microscope which offers high sensitivity, enhanced resolution in x, y, and z, and high image-acquisition speed in one system. Users achieve a 1.7x higher resolution in all spatial dimensions, 140 nm laterally and 400 nm axially. The high sensitivity leads to better image quality and increased speed. A classic confocal microscope illuminates one spot on the sample to detect the emitted fluorescence signal. Out-of-focus emission light is rejected at a pinhole, the size of which determines how much of the Airy disk reaches the detector. Users can increase the resolution by making the pinhole smaller, but the signal-to-noise ratio drops significantly, since less valuable emission light is passing through. LSM 880 lets the user take full advantage of large fields of view and the highest speed of any linear scanning confocal microscope at an unsurpassed image quality.

ZEISS

For info: 800-233-2343
www.zeiss.com/lsm880

Superresolution Microscopy Software

The Olympus FV-OSR software module enables users of the FluoView FV1200 easy access to what was previously the domain of only specialized microscopy systems. The extra detail offered by superresolution technology facilitates researchers in revealing the most subtle mechanisms at work within cells or tissue. Three-dimensional confocal laser scanning microscopy with the FluoView FV1200 achieves a vastly improved lateral and axial resolution compared to standard widefield, but is still limited by the diffraction limit of light. In certain settings images can therefore suffer from poor contrast. This is where superresolution microscopy comes into play, breaking the diffraction limit of light and enhancing cell and tissue imaging studies. Drawing from the latest Olympus optical and digital technologies, the FluoView FV1200 can now be transformed into a system capable of reaching a resolution of up to 120 nm, with simultaneous multicolor capture. The proprietary technology of the FV-OSR software controls specific hardware settings and advanced signal processing.

Olympus

For info: +49-402-3773-5913
www.olympus-europa.com/microscopy



Optical Imaging System

The Solaris quantitative optical molecular imaging system is a preclinical solution for use in small and large animal studies will help to advance drug discovery and translational research to develop and validate molecular-guided surgical research protocols. The Solaris system, when combined with PerkinElmer's suite of fluorescence molecular imaging probes, can bridge molecular imaging research techniques to support potential clinical outcomes. By distinguishing healthy versus diseased tissue in real-time, researchers can more accurately and completely map tumors. The Solaris system is designed for ambient lighting conditions found in preclinical surgical research suites and can dynamically use a broad and versatile range of fluorescent probes, offering flexibility for translational researchers when targeting diseases. Its research applications include drug efficacy, drug safety, measurement of real-time biological therapeutic responses, and advanced molecular-guided surgery applications such as surgical tumor margin determination in live animal models.

PerkinElmer

For info: 877-754-6973
www.perkinelmer.com

Deep-Cooled CCD Camera

The new Sincerity back-illuminated, deep-cooled CCD camera comes with an NIR-enhanced 2048 x 70 sensor. This CCD sensor is designed for companies requiring an affordable OEM camera for VIS-NIR spectroscopy applications. This new Sincerity camera joins the existing Sincerity with front illuminated 1024 x 256 CCD sensor for UV-VIS-NIR applications. Its high-resolution 14 μm pixel size makes it ideal for Raman instrumentation. Sincerity NIR offers ultralow etaloning and more than 40% Quantum Efficiency at 1,000 nm. Peak QE of 84% at 700 nm, and 20% at 1,050 nm means the Sincerity back-illuminated NIR offers a broad response. It is also available in a back-illuminated UV-VIS optimized configuration. Its lifetime vacuum warranty and compact size make it ideal for OEM integration, particularly in Raman microscopes, and its flexible design allows the OEM-dedicated Horiba team to quickly adapt the camera for industrial applications.

Horiba Scientific

For info: 732-494-8660
www.horiba.com/sinceritynir

Inverted Microscope

The Leica DMI8 inverted microscope with built-in modularity is designed to grow and adapt to ever-changing research needs. With this new concept, life scientists can custom-configure an inverted microscope now and upgrade it in the future for applications ranging from basic imaging to advanced fluorescence microscopy. The Leica DMI8 is equipped with an additional incident illumination port, the Infinity Port, which facilitates the integration of additional light sources and laser systems for advanced applications. The closed-loop focus drive with an accuracy of 20 nm for the 12 mm travel range enables researchers to investigate large specimens with high precision. In combination with Leica Microsystems' imaging software the Leica DMI8 is an

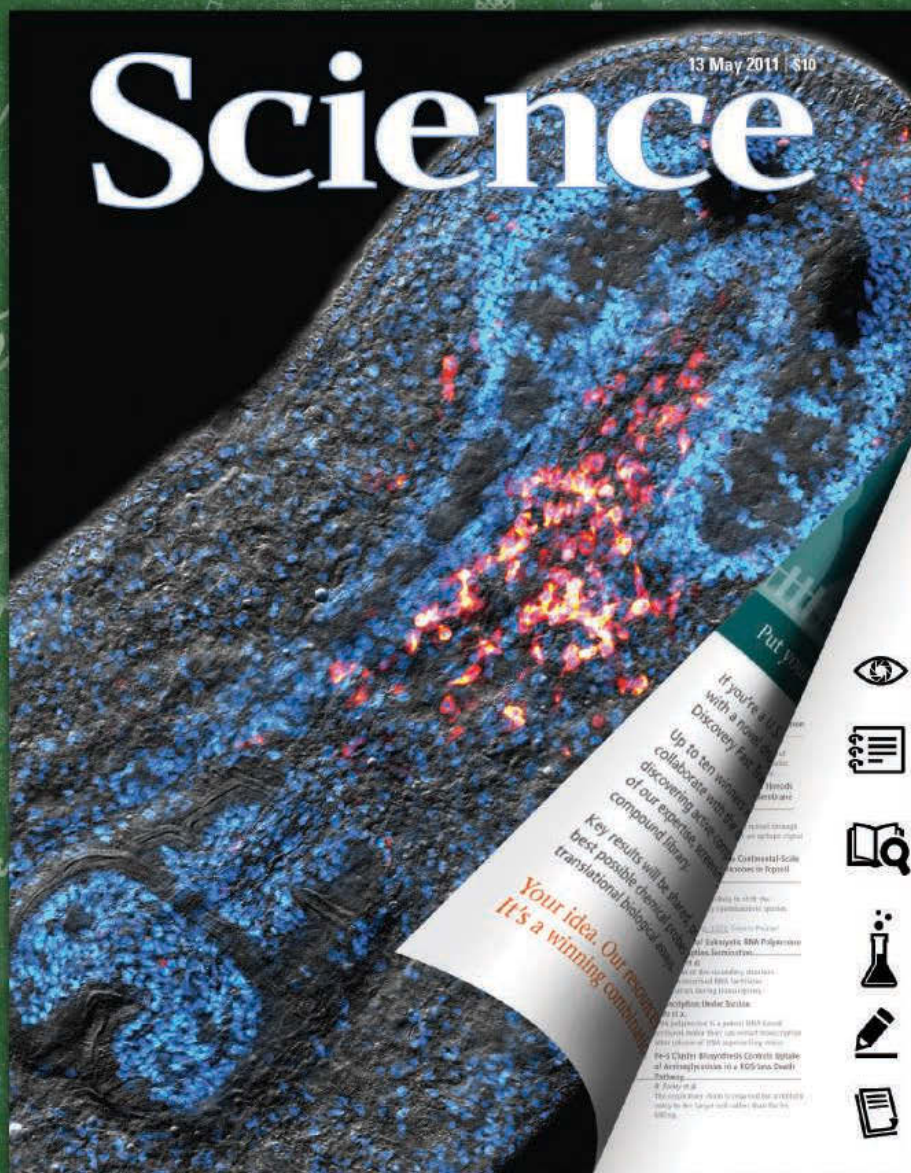
optimal solution for live-cell microscopy. The Leica DMI8's Infinity Port is the core of the system and enables access to the infinite light path. It integrates light sources and lasers that are necessary for FRAP, photo-switching, ablation, and many state-of-the-art microscopy techniques.

Leica Microsystems

For info: 800-248-0123
www.leica-microsystems.com/dmi8

Electronically submit your new product description or product literature information! Go to www.sciencemag.org/products/newproducts.dtl for more information.

Newly offered instrumentation, apparatus, and laboratory materials of interest to researchers in all disciplines in academic, industrial, and governmental organizations are featured in this space. Emphasis is given to purpose, chief characteristics, and availability of products and materials. Endorsement by *Science* or AAAS of any products or materials mentioned is not implied. Additional information may be obtained from the manufacturer or supplier.



Learning Lens



Learning Notes



Connect to
Learning Standards



Activities = 0 (21



Discussion Questions



References



Science

Online tools to help your
students analyze a
professional research paper!

Tell me and I forget. Teach me and I remember. Involve me and I learn. -- Benjamin Franklin

Featuring over 6 research papers at any given time, *Science* in the Classroom is specifically designed to help young researchers understand the structure and workings of professional scientific research.

Learn for yourself how *Science* in the Classroom can help your students deepen their understanding of scientific research. **Visit scienceintheclassroom.org today.**

Fidelity amplified.

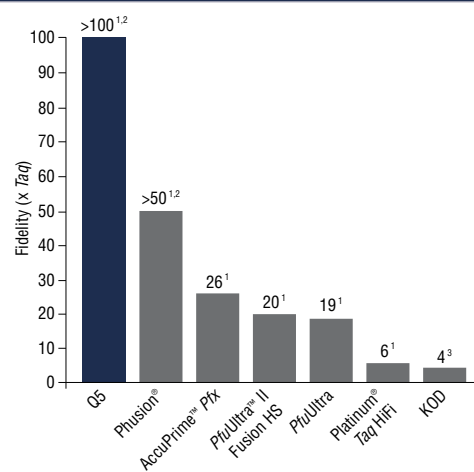
Q5[®] High-Fidelity DNA Polymerase

Q5 High-Fidelity DNA Polymerase sets a new standard for both fidelity and performance. With the highest fidelity amplification available (>100X higher than *Taq*), PCR with Q5 DNA Polymerase results in ultra-low error rates. Its unique buffer system provides superior performance for a broad range of amplicons, regardless of GC content. Q5 DNA Polymerase represents the finest in fidelity.

Request a free sample^{*}
at www.Q5PCR.com

NEW ENGLAND BIOLABS[®], NEB[®] and Q5[®] are registered trademarks of New England Biolabs, Inc. PHUSION[®] is a registered trademark and property of Thermo Fisher Scientific. Phusion[®] DNA Polymerase was developed by Finnzymes Oy, now a part of Thermo Fisher Scientific. PFUULTRA[™] is a trademark of Agilent Technologies, Inc. PLATINUM[®] is a registered trademark of Life Technologies, Inc. ACCUPRIME[™] is a trademark of Life Technologies, Inc.

The highest fidelity amplification available



¹ PCR-based mutation screening in *lacZ* (NEB), *lacI* (Agilent) or *rpsL* (Life)

² Due to the very low frequency of misincorporation events being measured, the error rate of high-fidelity enzymes like Q5 is difficult to measure in a statistically significant manner. Although measurements from assays done side-by-side with Taq yield Q5 fidelity values from 100-200 X Taq, we report ">100X Taq" as a conservative value.

³ Takagi et al (1997) Appl. Env. Microbiol. 63, 4504-4510.



There's only one **Science**

Science Careers Advertising

For full advertising details, go to ScienceCareers.org and click For Employers, or call one of our representatives.

Tracy Holmes
Worldwide Associate Director
Science Careers
Phone: +44 (0) 1223 326525

THE AMERICAS

E-mail: advertise@sciencecareers.org
Fax: 202 289 6742

Tina Burks
Phone: 202 326 6577

Nancy Toema
Phone: 202 326 6578

Marci Gallun
Sales Administrator
Phone: 202 326 6582

Online Job Posting Questions
Phone: 202 312 6375

EUROPE / INDIA / AUSTRALIA / NEW ZEALAND / REST OF WORLD

E-mail: ads@science-int.co.uk
Fax: +44 (0) 1223 326532

Axel Gesatzki
Phone: +44 (0) 1223 326529

Sarah Lelarge
Phone: +44 (0) 1223 326527

Kelly Grace
Phone: +44 (0) 1223 326528

JAPAN

Katsuyoshi Fukamizu (Tokyo)
E-mail: kfukamizu@aaas.org
Phone: +81 3 3219 5777

Hiroyuki Mashiki (Kyoto)
E-mail: hmashiki@aaas.org
Phone: +81 75 823 1109

CHINA / KOREA / SINGAPORE / TAIWAN / THAILAND

Ruolei Wu
Phone: +86 186 0082 9345
E-mail: rwu@aaas.org

All ads submitted for publication must comply with applicable U.S. and non-U.S. laws. *Science* reserves the right to refuse any advertisement at its sole discretion for any reason, including without limitation for offensive language or inappropriate content, and all advertising is subject to publisher approval. *Science* encourages our readers to alert us to any ads that they feel may be discriminatory or offensive.

Science Careers
FROM THE JOURNAL SCIENCE AAAS

ScienceCareers.org

Online Career Fair

Meet recruiters without leaving your lab or desk!

December 10, 2014

Science Careers is excited to bring you an easy, efficient and powerful way to connect with employers from all over... all in one place.

Why Attend This Event

- No travel required—you can login from anywhere
- Queues tell you how many people are in line ahead of you and how long you will be waiting so you can better manage your time
- Login before the event to learn more about participating employers
- Employers can see your resume while you are talking to them

For more information, visit: ScienceCareers.org/onlinecareerfair

For careers in science, there's only one **Science**

Science Careers

FROM THE JOURNAL SCIENCE AAAS

For information on recruiting, please visit:
ScienceCareers.org/onlinecareerfairemployers





The E.U.'s Recipe to Create Jobs: Innovate

Horizon 2020, the European Union's new funding mechanism, is the concrete translation of Europe 2020, a 10-year strategy proposed by the European Commission to advance Europe's economy in a "smart, inclusive, and sustainable" way. It reflects the widespread sentiment that Europe has fallen behind the rest of the world in innovation. By supporting areas in which Europe already shows strong competence, especially at the near market stage where crucial funding tends to fall short, the European Union aims to emerge as a world leader in the areas targeted and grow its economy at the same time. Along the way, it is creating new opportunities for scientists. **By Gunjan Sinha**

This year saw the launch of the European Union's (E.U.) eagerly anticipated new funding mechanism, Horizon 2020. Between 2014 and 2020, the European Commission will make €78.6 billion (US\$99.7 billion) available to fund research and innovation throughout the E.U. The budget is a €25 billion (US\$31.7 billion) increase over the E.U.'s previous funding mechanism—the 7th Framework Programme (FP7)—and takes the concept of goal-oriented research several steps beyond its predecessor.

Horizon 2020 is organized into three core themes: excellent science, industrial leadership, and societal challenges. The themes continue many of those introduced under FP7, especially toward the end of FP7's tenure when it shifted to a challenge-based thematic approach. Horizon 2020, however, in addition to a 60% increase in funding for basic research, goes wholesale on the challenge-based approach, says **Michael Jennings**, a European Commission spokesperson,

and emphasizes developing solutions to the world's most pressing environmental and societal threats to health and well being.

"There is a demand for science to be more responsive and to address the urgently complex societal challenges of our times," says **Máire Geoghegan-Quinn**, European Commissioner for Research Innovation and Science. "As a politician I am evangelical about the power of science to improve and enrich our lives and to sustain our economy."

The societal challenges pillar secured 38.53% of the budget—the largest chunk of the three—and is further broken down into key themes that include health, forestry, marine research, efficient energy, green transport, climate, and environment. The focus on key themes aims to inspire more multidisciplinary approaches, says Jennings, and encourage researchers to come up with the right approach rather than prescribe it. Since innovation is at the core of Horizon 2020, it also has a goal of 20% small and medium enterprise (SME) participation in all funded projects and will support more late-stage research, such as pilot and demonstration projects.

Implicit in funding such large research consortia are the job opportunities they create for early-career scientists. Large consortia connect researchers around the globe with each other and also with industry, creating a path through which young scientists can move on or up in their careers.

Late-stage funding for sustainable energy

One of the first major Horizon 2020 awards announced in July is a €3.7 billion (US\$4.7 billion) commitment to a public-private partnership aiming to develop Europe into a biobased economy. More than 70 European companies in the biotech, chemical, energy, agriculture, and pulp and paper sectors are part of the initiative, which is coordinated by Copenhagen, Denmark-based Novozymes. Of the €3.7 billion, the European Commission will contribute €975 million (US\$1.2 billion) between 2014 and 2020; the rest will come from industry partners.

Novozymes is an industrial biotechnology company that produces and sells enzymes and microorganisms used in people's everyday lives, from processed food and detergents to farming and other industrial processes. As the cost of biotechnology comes down, many chemicals are being replaced with biotech, says **Peder Holk Nielsen**, president and chief executive officer of Novozymes. The company now produces millions of unique enzyme molecules each month when just a few years ago it could only produce thousands, he explains. "Access to [the technology] is exploding," he says, which in turn presents a huge opportunity to apply the technology toward a greener economy.

The partnership's primary focus is to provide a renewable alternative to the fossil-based fuels that power automobiles and are components of industrially produced chemicals and materials such as fabrics and plastics. The company and its partners have already built a biomass refinery in Crescentino, Italy that produces 75 million liters a year of cellulosic ethanol from agricultural waste using the company's enzymes. The majority of the €3.7 billion will be spent on building at least five additional production plants across **continued>**

Upcoming Features

Regional Focus: Asia—December 12 ■ *Faculty—January 30, 2015* ■ *Postdocs—February 27, 2015*

When Fabio Grieco finished his Ph.D., he wanted to work abroad. His advisor suggested taking a fellowship position with Decio Eizirik, another NAIMIT partner at the University of Brussels.



Europe by 2020. “These are essential to show the technical and commercial viability of new generations of biobased products and fuels at an industrial scale and to reduce perceived investment risks,” says Holk Nielsen.

Each plant is expected to generate between 12,000 and 18,000 feedstock supply chain jobs annually, according to a report by National Non-Food Crops Centre, bioeconomy consultants in York, England. The boom in industrial biotechnology is also creating jobs for scientists. Novozymes, for example, is “hiring a lot of people globally,” says **Peter Tolstoy**, a people and organization partner responsible for hiring scientists at the company, which has 36 global locations and employs some 1,300 scientists.

The Bio-Based Industries (BBI) Consortium is exemplary of the kind of late-stage innovation activities that Horizon 2020 is aiming to fund, not only because of its potential to grow the economy and create jobs, but also because such consortia build relationships between industry and academia that foster innovation. Another key change from FP7 is 5% more funding to support SMEs that typically take university research and turn it into marketable goods. Twenty percent of the budget available for research on societal challenges and leading technologies—almost €9 billion (US\$11.4 billion) in grants over seven years—will be available to SMEs. Of this amount, €3 billion (US\$3.8 billion) will be provided through a dedicated “SME instrument,” a specific line of calls, to fund feasibility studies and demonstration projects. Part of the E.U. research budget will also be used to back public and private loans to SMEs.

“The €9 billion should be seen as a minimum,” says Geoghegan-Quinn. “SMEs are the backbone of the European economy and account for two thirds of total employment.”

Another consortium with large SME participation working toward greening the economy is LEANWIND (Logistic Efficiencies And Naval architecture for Wind Installations with Novel Developments) headed by **Jimmy Murphy**, lecturer at Beaufort Research, University College Cork, Ireland. Securing one of the last awards under FP7, LEANWIND is a consortium of 31 partners from 11 countries, half of which are small companies working toward making wind energy competitive with fossil fuel energy sources. LEANWIND will receive €10 million (US\$12.7 million) from the European Commission between 2014 and 2017 to find ways to

streamline the installation, management, and maintenance of offshore wind farms. Industry partners will contribute an additional €5 million (US\$6.3 million). To cut costs, “there is an entire logistical chain of events that can be optimized,” says Murphy.

For early-career scientists, collaborative research projects that include industry are invaluable for the contacts they provide. **Katie Lynch**, for example, landed her job as a LEANWIND work package leader after collaborating with Murphy on a related FP7-funded project. While working on that project, the 30 year old Lynch, who has a master’s degree in renewable energy, was asked to help put together the FP7 proposal for LEANWIND, with the intention that she would work on the project if it were funded. The experience of writing the FP7 proposal and of working in her current position managing finance and market assessments has given her precious experience in leadership, she says, as well as put her in touch with industry leaders “You have to put together a consortium of people with whom you would like to work with over and over again and maintain those contacts,” she says.

Such consortia also build long-term connections between academics and industry, boosting job prospects. “It would be wonderful if it was natural for academics to move to industry and vice versa,” says Geoghegan-Quinn. “In the U.S. this happens all the time. We are setting up the architecture to allow that to happen [here in Europe].”

Basic research not neglected

Even though the societal challenges pillar of Horizon 2020 is goal oriented, basic research can be funded if scientists can show practical relevance. Since Horizon 2020 just launched, there are a several projects funded under FP7 that the European Commission considers exemplary of the type of life science research Horizon 2020 aims to fund.

The Natural Immunomodulators as Novel Immunotherapies for Type I diabetes (NAIMIT) consortium, for example, investigated a controversial theory about diabetes type 1 to come up with new therapies. Composed of 14 academic partners and two biotech companies, the group was brought together by **Chantal Mathieu**, head of clinical and experimental endocrinology at the University of Leuven, Belgium. Pancreatic beta cells aren’t just “sitting ducks” in the pathogenesis of diabetes, Mathieu explains. There’s an active dialogue between beta cells and the immune system that mediates beta cell death.” Mathieu brought in partners whom she thought could illuminate this process and develop therapeutic approaches based on it.

It is through NAIMIT that **Fabio Grieco** landed his current job as a postdoctoral fellow at the Universite Libre de Bruxelles (ULB), Belgium, Laboratory of Experimental Medicine, and ULB Center for Diabetes Research. In 2010, Grieco was working on his Ph.D. at the University of Siena, Italy when his supervisor, Francesco Dotta, began collaborating with Mathieu. When Grieco finished his Ph.D., he wanted to work abroad. His advisor suggested taking a fellowship position with Decio Eizirik, another NAIMIT partner at the University of Brussels. He has been at the center for diabetes research since 2012. Although his fellowship time is up, he has the opportunity to continue his research at the center.

The NAIMIT consortium was funded under **continued>**



European Research Council

Established by the European Commission



**Got a golden idea?
We'll fund it.**

The European Research Council (ERC) offers five-year grants of up to **\$4.4 million**.

- open to top researchers **from anywhere** in the world
- for realising **ambitious projects** - at least half the time spent in Europe
- in **any field**: physical sciences & engineering, life sciences, social sciences & humanities

Want to find out more?

Visit erc.europa.eu and **apply** for Starting Grants (deadline: 3 Feb 2015)
or Consolidator Grants (deadline: 12 Mar 2015)



Horizon 2020
European Union funding
for Research & Innovation

When Sebastian Rauschert saw that the University of Munich offered a Ph.D. program in early nutrition through The Early Nutrition Project, he jumped at the chance.



Featured Participants

Beaufort Research,
University College, Cork,
Ireland
www.ucc.ie/beaufort

Early Nutrition Project
www.project-earlynutrition.eu

**European Commissioner
for Research Innovation
and Science**
[ec.europa.eu/
commission_2010-2014/
geoghegan-quinn/index_
en.htm](http://ec.europa.eu/commission_2010-2014/geoghegan-quinn/index_en.htm)

**European Research
Council**
erc.europa.eu

LEANWIND Consortium
www.leanwind.eu

NAIMIT Consortium
www.naimit.eu

Novozymes
www.novozymes.com

University of Leuven
www.kuleuven.be/english

**Universite Libre de
Bruxelles**
www.ulb.ac.be

FP7 with a total budget of €14.25 million (US\$18.08 million), of which the European Union contributed €10.92 million (US\$13.8 million). The rest came from participating universities or individual research grants. E.U. funding under FP7 ends this year. Two of the projects, however, have entered the clinic, says Mathieu, and research on a bacterial system to deliver immune modulating compounds systemically described in the group's 2012 paper "is extremely promising," she adds.

Another exemplary health project funded under FP7 is The Early Nutrition Project, which includes researchers from 36 institutions in 12 countries across Europe, the United States, and Australia. The project is being coordinated out of Ludwig-Maximilian's-University in Munich, Germany and aims to understand how early nutrition programming and lifestyle factors impact the rates of obesity and related disorders. Research projects include studying how maternal weight during pregnancy affects the long-term health of babies, how the placenta regulates fetal growth and how early nutrition affects children's long-term risk of metabolic

diseases. The project is funded with €8.96 million (US\$ 11.37 million) from the European Union between 2012 and 2016, with a total budget of €11.12 million (US\$ 14.1 million).

Such large research consortia open up opportunities for young people in other ways too. **Sebastian Rauschert** studied sociology and psychology as an undergraduate. He then earned a Master's degree in public health. He has "always been interested in disease prevention and nutrition," he says. When he saw that the University of Munich offered a Ph.D. program in early nutrition through The Early Nutrition Project, he jumped at the chance. As part of his Ph.D. thesis, he is studying whether breastfeeding influences obesity related metabolic disorders, such as diabetes, by analyzing data from the Western Australian Pregnancy Cohort Study, which has followed over 1,000 babies since 1989. This month Rauschert will travel to Perth to spend six months working directly with his collaborators. The trip is funded through the brain mobility project, established under the Early Nutrition Project to enable young scientists working on the project the opportunity to travel abroad and work with collaborators, and incidentally give them a networking boost.

E.U. grants carry cache

For early-career scientists, landing a job with E.U.-funded consortia isn't the only stepping-stone available. They can apply for individual European Research Council (ERC) grants, which with a budget of €13.1 billion (US\$ 16.6 billion), represents a 60% increase over FP7, or a Marie Skłodowska-Curie actions (MSCA) grant, both of which are included under the Excellent Science pillar. MSCA grants are awarded in all scientific disciplines at all stages of researchers' careers, from Ph.D. candidates to highly experienced researchers.

For those who beat out the competition to win an ERC grant, the job prospects become even brighter. "It's immediately considered as positive recognition of the quality and ambition of the scientist," says **Jean-Pierre Bourguignon**, president of the ERC. "There is competition now among institutions to secure these people."

It also can make scientists more attractive to industry, says Bourguignon. One Swedish ERC grant winner, for example, was able to garner funding for two startups based on the credibility the grants gave him, says Bourguignon. "He initially didn't think he was a candidate. His colleagues pushed him to apply."

For Horizon 2020 applicants, proposals that take a multidisciplinary approach are more likely to be successful. "Be prepared to step outside of your comfort zone," says Geoghegan-Quinn. "We are asking scientists to be bold and brave and not stay pigeon holed in the same area."

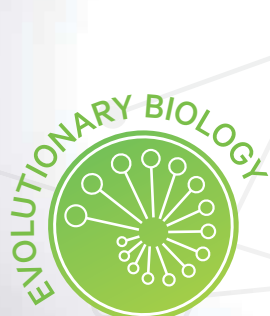
Horizon 2020 boasts other improvements over FP7 that include a move to online application and review, shorter review times, and streamlined auditing—measures that not only modernize the process but also address major criticisms of its predecessor. On measuring Horizon 2020's success, Geoghegan-Quinn's says: "I am hoping the money we are investing in these societal challenges will not only make my life better but also give hope to young people."

Gunjan Sinha is a freelance writer living in Berlin, Germany.

DOI: 10.1126/science.opms.r1400150

Looking for a PhD position?

Join the IST Austria Grad School!



PhD Program

- PhD granting institution devoted to basic research in natural sciences and math
- 4-5 year study
- BS or MS degree (or equivalent) required
- internationally competitive PhD salary

www.ist.ac.at

Deadline for applications

for students wishing to enter the program in the fall of 2015 is

January 15, 2015



Institute of Science and Technology



IST Austria is committed to Equality and Diversity.

PRIZES



The Foundation for Polish Science has for the 23rd time granted its Prizes, considered to be Poland's most important scientific awards.

The Foundation for Polish Science Prize 2014 Laureates



PROF. TOMASZ GOSLAR from Adam Mickiewicz University in Poznań received the FNP Prize 2014 in the **life and earth sciences** for his contribution to determining the chronology of changes in C14 carbon isotope concentration in the atmosphere during the last ice age, which is of key importance for contemporary climate research.



PROF. KAROL GRELA from the University of Warsaw and the Institute of Organic Chemistry of the Polish Academy of Sciences in Warsaw received the FNP Prize 2014 in the **chemical and materials sciences** for developing new catalysts for olefin metathesis reactions and applying them in industrial practice.



PROF. IWO BIAŁYŃSKI-BIRULA from the Centre for Theoretical Physics of the Polish Academy of Sciences received the FNP Prize 2014 in the **mathematical, physical and engineering sciences** for fundamental studies of the electromagnetic field that has led to the formulation of the uncertainty relations for photons.



PROF. LECH SZCZUCKI from the Institute of Philosophy and Sociology of the Polish Academy of Sciences received the FNP Prize 2014 in the **humanities and social sciences** for explaining the cultural ties between Central and Western Europe in a monumental edition of the correspondence of Andrzej Dudycz, the 16th-century thinker, religious reformer and diplomat.

The Foundation for Polish Science has been in operation since 1991. It is a non-governmental, non-political, non-profit institution which pursues the mission of supporting science. It is the largest non-profit organization in Poland dedicated solely to the development of science.

www.fnp.org.pl



Institut Pasteur

Group Leader Positions in Quantitative Biology and Modeling

The Institut Pasteur (Paris, France) announces an international call for group leader positions in the field of quantitative biology and modeling in developmental systems. Successful applicants will be integrated into the cutting edge interdisciplinary environment offered by an internationally renowned institute combining fundamental and translational research, in an attractive location in central Paris, in close proximity to other major research centers. Candidates with both an experimental and theoretical background, using quantitative approaches and willing to develop multidisciplinary projects related to developmental processes are encouraged to apply.

Successful **junior candidates** [1] will be appointed with a permanent position, and as head of a group of 6 people. These groups will be created for a period of 5 years and may thereafter compete for a full research group.

Successful **mid-career and senior candidates** will be appointed with a permanent position, and as head of a research group of 8 to 12 people. The groups will be created for 10 years (mid-term evaluation at 5 years) with the possibility of renewal. Candidates should send their formal applications by E-mail to the Director of Scientific Evaluation, Prof. Alain Israël, at the Institut Pasteur (qubimo@pasteur.fr).

Application deadline: February 6, 2015

Short-listed candidates will be contacted for interview.

Applicants should provide the following (in order) in a single pdf file:

1. A brief introductory letter of motivation, including the name of the proposed group. Candidates are encouraged to contact the head of the Search Committee Francois Schweisguth (fschweis@pasteur.fr) or the head of the Department of Developmental & Stem Cell Biology Shahrageim Tajbakhsh for queries (shaht@pasteur.fr).
2. A Curriculum Vitae and a full publication list.
3. A description of past and present research activities (up to 6 pages with 1.5 spacing; Times 11 or Arial 10 font size).
4. The proposed research project (up 6 pages with 1.5 spacing; Times 11 or Arial 10 font size).

Junior candidates [1] should also provide:

5. The names of 3 scientists from whom letters of recommendation can be sought, together with the names of scientists with a potential conflict of interest from whom evaluations should not be requested.

[1] Institut Pasteur is an equal opportunity employer. Junior group leaders should be less than 8 years after PhD at the time of submission (Dec 31, 2014). Women are eligible up to 11 years after their PhD if they have one child and up to 14 years after their PhD if they have two or more children.



INSTITUTO DE HIGIENE E
MEDICINA TROPICAL



UNIVERSIDADE
NOVA
DE LISBOA

The Universidade NOVA de Lisboa invites applications for
a full time position as

Director

of the Instituto de Higiene e Medicina Tropical

The position of Director of the Institute of Hygiene and Tropical Medicine (IHMT), Universidade NOVA de Lisboa, is open for applications.

The Director must have a doctorate degree (Ph.D.) or legal equivalent, scientific seniority in areas of interest to the mission of the IHMT (see at <http://www.ihmt.unl.pt>) and management experience. A good knowledge of Portuguese and English is required.

Candidates should demonstrate initiative and strategic vision, as well as capacity to implement the statutory mission of the IHMT, promoting national and international contacts. Successful candidates should guarantee proper functioning and good management of the various administrative and scientific units of the IHMT, also committing themselves to seek appropriate funding sources to strengthen IHMT strategic action in the area of Health and Life Sciences.

Applications, submitted electronically **before 12 pm on December 22, 2014**, should include the following:

1. application letter, addressed to the Chairman of the Electoral Commission;
2. brief *Curriculum vitae*, with clear information on relevant professional experience;
3. a plan of action (max. 3 pages) within the operating area of the IHMT, demonstrating strategic planning and management capacity in higher education, research, internationalization and cooperation for development.

All documents should be sent to eleicaodiretor@ihmt.unl.pt along with an electronic confirmation of receipt.

Salary will be determined in accordance to the Portuguese law, corresponding, as an indicative value, to a maximum monthly wage of 5,846.41 €, before taxes.

Selected applicants will be interviewed at IHMT, in Lisbon, on **January 26, 2015**.



Postdoc TGF-β

Leiden University Medical Center (LUMC) is committed to ongoing improvement of health care quality, invests in health-care related research, and intends to consolidate its leading international role in this area.

■ The Department of Molecular Cell Biology has two Postdoctoral positions available in a dynamic, international and interdisciplinary research team to study the molecular basis of subverted TGF-β signal transduction, one in cancer and one in cardiovascular biology.

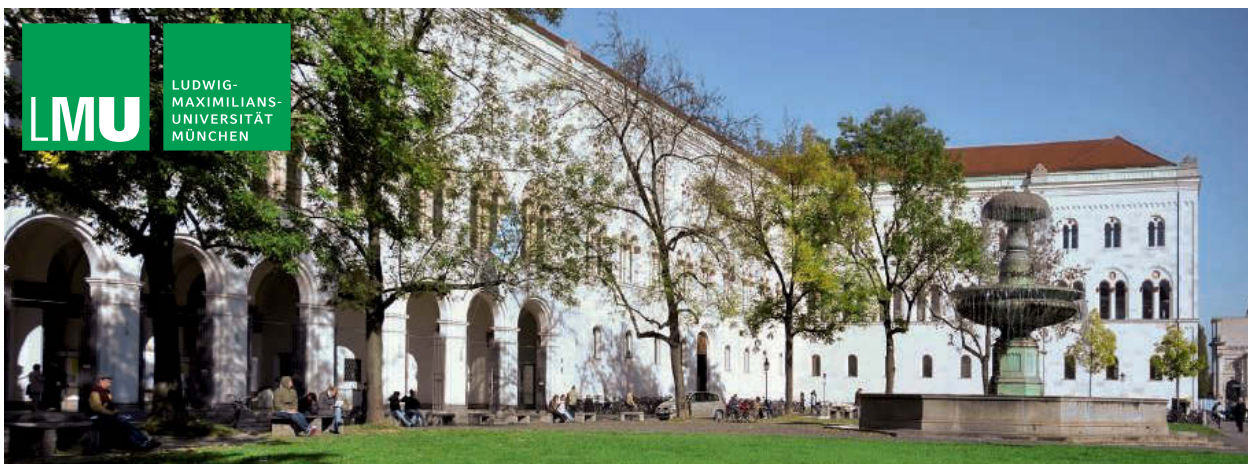
■ Informal enquiries can be obtained from Prof. Peter ten Dijke, e-mail p.ten_dijke@lumc.nl, telephone +31 (0)71 526 92 71.

■ To apply, send your letter of application and CV, a description of research accomplishments, and contact information of two references to PenO-div4@lumc.nl. Please quote job reference number D.14.VC.MP.18/19/SC48



WWW.LUMC.NL





Ludwig-Maximilians-Universität (LMU) in Munich is one of the leading research universities in Europe, with a more than 500-year-long tradition. LMU aims at creating favorable conditions for excellent junior academics. To provide gifted early-career researchers in all subject areas with a long-term career perspective, LMU is offering

Tenure Track Professorships to ERC Starting Grantees

If you intend to submit a proposal to the current call of the European Research Council and would be interested in joining LMU's research community, please contact the appropriate faculty member in your field of research as soon as possible.

For further information regarding this offer, please see: www.lmu.de/excellent/erc-tenuretrack



GRADUATE SCHOOL OF

Quantitative Biosciences Munich



Do you wish to ...

- ... earn a PhD, building on your training in biochemistry, biology, physics, or applied maths?
- ... conduct cutting-edge research at the interface of experiment and quantitative theory?
- ... learn how to communicate and work with scientists from different fields?

Then join us at QBM!

The newly established Graduate School of Quantitative Biosciences Munich (QBM) is funded by the German Excellence Initiative and seeks to prepare young life scientists for the emerging era of quantitative, systems-oriented bioscience. It provides an innovative, international PhD training program that bridges the divide between traditionally separate disciplines, from biochemistry and medicine to bioinformatics, experimental and theoretical biophysics, and applied mathematics.

Key elements of the program are an interdisciplinary research project jointly supervised by two PIs from different fields, and an educational curriculum centered around an intensive core course that integrates a wide range of approaches to biological problems. A multi-faceted mentoring and professional skills program supports the students' growth as independent scientists.

For more information, visit us at www.qbm.lmu.de
Application deadline: **January 5th, 2015**





Join Germany's
international
research
community!



Discover the opportunities that
Germany provides:

- First-class doctoral training
- Excellent career opportunities
in research and industry
- Attractive funding programmes
for international researchers

For the latest research news,
job offers and more go to:
www.research-in-germany.de



Find us on Facebook:
[facebook.com/
Research.in.Germany](https://www.facebook.com/Research.in.Germany)



Follow us on Twitter:
[twitter.com/
ResearchGermany](https://twitter.com/ResearchGermany)



AN INITIATIVE OF THE
Federal Ministry
of Education
and Research

Research in
Germany

Land of Ideas

www.research-in-germany.de



UPPSALA
UNIVERSITET

Uppsala University is recruiting a

Senior Lecturer in Molecular Detection

at the Department of Immunology, Genetics and Pathology, Molecular Tools unit. Research in the Molecular Tools unit is focused on conceiving and developing advanced molecular analysis techniques with applications in medicine and biology, and to make these technologies broadly available. The work follows a strong local tradition for molecular tools development, reflected in an active biotech industry in Uppsala and Stockholm. Unlike the situation in most countries the so-called teacher's exemption in Sweden grants university employees full rights to their own inventions, allowing scientists to engage in translating their findings for industrial applications. Technologies previously developed by the Molecular Tools unit at Uppsala University have been licensed to eleven major international biotechnology or diagnostics companies, and their technologies have also formed the basis of five start-up companies spun out from the lab.

The Senior Lecturer position includes research, teaching, and administration. The Senior Lecturer is expected to conduct and publish internationally competitive research within the molecular detection area, and to attract external funding for this research.

The successful candidate for this post should display research experience in the area of innovative molecular detection and analysis technology, and expertise that complements work in the Molecular Tools research program. Examples of desired expertise include the ability to develop new important techniques for molecular analysis and to apply them in large-scale biomedical contexts, together with deep insights into molecular technological needs and requirements in biomedical research and clinical diagnostics.

Information about the position can be given by Professor Ulf Landegren, +46 18-471 49 10, ulf.landegren@igp.uu.se.

Deadline for the application is December 21st 2014.

For full advertisement and link to the application form go to

<http://www.uu.se/en/join-us/jobs/>

Reference number **UFV-PA 2014/3179**

ScienceCareers Cernet

“《科学》职业” 已经与Cernet/
赛尔互联开展合作。中国大陆的高
校可以直接联系Cernet/赛尔互联
进行国际人才招聘。



请访问 Sciencecareers.org/CER 点得联系信息。

招募学术精英,《科学》是您的不二之选

Science

NOVO NORDISK FOUNDATION LAUREATE RESEARCH GRANTS

ENABLING TODAY'S SCIENTIFIC LEADERS

International call for applications for two exceptional grant awards within the areas of biomedicine and biotechnology

Novo Nordisk Foundation Laureate Research Grants are for outstanding established scientists to come to Denmark to strengthen their groundbreaking research programs.

Applicants must have an independent research program that they have directed for *7 or more years in total*.

Grant funding

- Up to 40 million Danish kroner over 7 years (EUR ~5.4 million, USD ~6.7 million).
- NNF Laureate Research Grant holders can apply for continued NNF LRG funding, up to DKK 35 million over 7 additional years.

Application deadline: February 10, 2015

Further information

To learn more about these grants, eligibility and the application process, please visit:

www.novonordiskfonden.dk/en

novo nordisk fonden

NOVO NORDISK FOUNDATION YOUNG INVESTIGATOR AWARDS

SUPPORTING TOMORROW'S LEADING SCIENTISTS

International call for applications for two exceptional grant awards within the areas of biomedicine and biotechnology

Novo Nordisk Foundation Young Investigator Awards are for outstanding younger scientists to come to Denmark to expand their groundbreaking research programs.

Applicants must have an independent research program that they have directed for *less than 7 years in total*.

Grant funding

- Up to 20 million Danish kroner over 7 years (EUR ~2.7 million, USD ~3.4 million).
- NNF Young Investigator Award holders can apply for additional funding from other eligible Novo Nordisk Foundation programs.

Application deadline: February 10, 2015

Further information

To learn more about these grants, eligibility and the application process, please visit:

www.novonordiskfonden.dk/en

novo nordisk fonden

Research Opportunities in Luxembourg. See what's behind it.



PEARL

LUXEMBOURG'S RESEARCH PROGRAMME FOR INTERNATIONALLY RECOGNISED SENIOR RESEARCHERS

- Interested in establishing a high-profile research programme? Through our research programme PEARL (financial contribution up to EUR 5 million) we give you the opportunity to transfer your research programme to a research institution in Luxembourg.



ATTRACT

LUXEMBOURG'S RESEARCH PROGRAMME FOR OUTSTANDING YOUNG RESEARCHERS FROM ALL OVER THE WORLD

Interested in doing scientific research at a high level in an international environment? Our research programme ATTRACT will allow you to set up your independent research team within a research institution in Luxembourg which will offer you attractive career opportunities. Funding up to EUR 2 million.



More information about ATTRACT and PEARL as well as the other funding opportunities offered by the National Research Fund Luxembourg can be found on the FNR's website.

Go and see what's behind on www.fnr.lu/pearl and www.fnr.lu/attract

For an overview on research in Luxembourg, have a look at www.innovation.public.lu

Fonds National de la
Recherche Luxembourg
INVESTIGATING FUTURE CHALLENGES

In 2015,
CNRS
is recruiting
researchers
in all scientific fields

- Life sciences
- Physics
- Nuclear and Particle Physics
- Chemistry
- Mathematics
- Information technologies
- Earth sciences and Astronomy
- Humanities and Social sciences
- Environmental sciences and
- Sustainable development
- Engineering

Disabled candidates can also be recruited by contractual agreement

Always craved
for knowledge



Online registration at www.cnrs.fr
from December 1, 2014 to January 6, 2015





Assistant/Associate Professor (JOB# 11032)

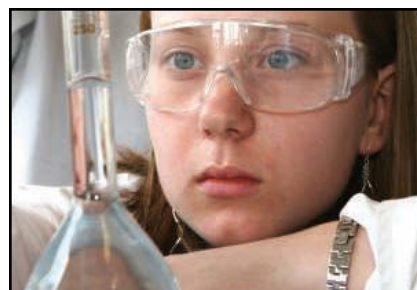
The School of Life Sciences at Arizona State University invites applications for a tenure-track faculty position in Macrosystems Biology, at the level of either Assistant or Associate Professor. Rank and tenure status will be commensurate with experience. Anticipated start date is August 16, 2015.

Applicants must have a PhD or equivalent by the time of appointment; expertise in ecology, environmental science, or a related discipline; computational skills for handling large sets of data; and a record of or potential to conduct cutting-edge research to address problems spanning multiple spatial scales (e.g., global change, biological invasions, or disease control). Desired qualifications include: (1) experience building or working with interdisciplinary teams, (2) a strong record of scholarly achievement, (3) extramural funding from diverse sources, (4) experience with teaching and mentoring at a university, (5) two years of postdoctoral training, (6) a record of research that combines theoretical modeling and empirical data, (7) potential to complement existing research in the School of Life Sciences and in other centers throughout the university are preferred. Examples of relevant centers include the Global Institute of Sustainability, the Center for Biodiversity Outcomes, and the Center for Environmental Science Applications, and the Complex Adaptive Systems Initiative.

Arizona State University is a dynamic, progressive university dedicated to interdisciplinary collaboration, to student-centered education, and to reshaping the relationship between academia and society. The successful candidate will interact with interdisciplinary research teams within the university, teach at the undergraduate and graduate levels, and serve the school, the university, and its surrounding communities.

To apply, please submit: (1) a cover letter addressed to Michael Angilletta, Chair, Macrosystems Biology Search Committee, (2) curriculum vitae, (3) three representative publications, (4) contact information for three references, (5) a statement of research accomplishments and goals (emphasizing collaborative interdisciplinary research), and (6) a statement of teaching philosophy and experience. Application materials must be sent electronically in a single pdf file to solsfacultysearch4@asu.edu. The initial closing date for receipt of applications is **January 2, 2015**; applications will be reviewed weekly thereafter until the search is closed. A background check is required for employment.

Arizona State University is a VEVRAA Federal Contractor and an Equal Opportunity/Affirmative Action Employer. All qualified applications will be considered without regard to race, color, sex, religion, national origin, disability, protected veteran status or any other basis protected by law.
<https://www.asu.edu/aad/manuals/acd/acd401.html> <https://www.asu.edu/titleIX/>



AAAS is here – promoting universal science literacy.

In 1985, AAAS founded Project 2061 with the goal of helping all Americans become literate in science, mathematics, and technology. With its landmark publications *Science for All Americans* and *Benchmarks for Science Literacy*, Project 2061 set out recommendations for what all students should know and be able to do in science, mathematics, and technology by the time they graduate from high school.

As a AAAS member, your dues help support Project 2061. If you are not yet a member, join us. Together we can make a difference.

To learn more, visit
aaas.org/plusyou/project2061



Assistant Professor of Quantitative Wildlife Ecology Department of Wildlife, Fish, and Conservation Biology

The University of California, Davis is recruiting a Quantitative Wildlife Ecologist at the tenure-track ASSISTANT PROFESSOR level, with academic year (9-month) term employment. Candidates must have the ability to develop a vigorous, extramurally-funded research program that addresses quantitative questions relevant to the ecology of wild vertebrates, including those in California and beyond, and to teach courses in quantitative wildlife/fish ecology and estimation and share responsibility in other departmental teaching needs. We seek candidates with a demonstrated publication record in the development or application of tools and methods to estimate or analyze wildlife demography. Qualifications include Ph.D. in relevant discipline, and evidence of potential for accomplishment in research, teaching, and service.

To obtain additional information and apply for the position please use the following website: <https://recruit.ucdavis.edu/apply/JPF00442>. Additional inquiries can be directed to **Associate Professor Brian D. Todd, Recruitment Advisory Committee Chair, Department of Wildlife, Fish, & Conservation Biology, One Shields Ave., University of California, Davis, CA 95616, Tel (530) 754-1140, FAX (530) 752-4154, email: btodd@ucdavis.edu**. The position will remain open until filled but to ensure consideration, applications should be received by **January 9, 2015**.

THE COLLEGE OF AGRICULTURAL AND ENVIRONMENTAL SCIENCES AND DEPARTMENT OF WILDLIFE, FISH and CONSERVATION BIOLOGY AT UC DAVIS ARE COMMITTED TO BUILDING A DIVERSE FACULTY, STAFF AND STUDENT BODY REFLECTING THE POPULATION AND EDUCATIONAL NEEDS OF CALIFORNIA AND THE NATION.

UC Davis is an Affirmative Action/Equal Employment Opportunity Employer and is dedicated to recruiting a diverse faculty community. We welcome all qualified applicants to apply, including women, minorities, veterans, and individuals with disabilities.



BIOLOGY CHAIR SEARCH

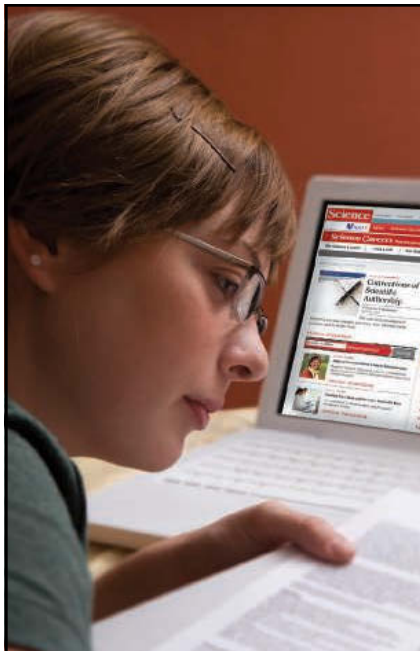
The **Department of Biology** at Georgia State University invites applications and nominations for a tenure-eligible Professor to fill a 12-month position of **Department Chair** preferably to begin July, 2015. The successful candidate must have a Ph.D. or equivalent degree, a distinguished record in biological or biomedical research that includes a history of significant external support, demonstrated leadership skills, and a strong commitment to graduate and undergraduate training and education. The Department Chair reports to the Dean of the College of Arts and Sciences and will provide visionary direction for collaborations and partnerships with other Departments, Schools, Centers, and Institutes of the University in accordance with its five-year University Strategic Plan (<http://www.gsu.edu/about/governance-and-strategy/>).

The Department of Biology consists of 55 full-time faculty with diverse research interests and a strong commitment to undergraduate education. The department offers Ph.D. degree programs with concentrations in Applied & Environmental Microbiology, Cellular and Molecular Biology and Physiology, Molecular Genetics and Biochemistry, and Neurobiology & Behavior as well as a strong M.S. degree program. The departmental research programs are supported by state-of-the-art core facilities. More information on the department can be found at www.biology.gsu.edu.

Founded in 1913, Georgia State University is a leading urban research university located in the heart of downtown Atlanta, a growing, dynamic, diverse, and global metropolis. This diversity is reflected in its student population of more than 32,000, including more than 24,000 undergraduates, with additional growth anticipated.

Applicants should arrange to have 3 reference letters as well as curriculum vitae, letter of intent, and samples of scholarly work and leadership effectiveness sent to biologychairsearch@gsu.edu. Applications from underrepresented minority and female candidates are enthusiastically encouraged. Application review will begin **December 1, 2014**, and the position will remain open until filled. Employment is contingent on background verification.

Georgia State University, a part of the University System of Georgia, is an Equal Opportunity Educational Institution and an EEO/AA Employer.



AAAS is here – helping scientists achieve career success.

Every month, over 400,000 students and scientists visit ScienceCareers.org in search of the information, advice, and opportunities they need to take the next step in their careers.

A complete career resource, free to the public, *Science Careers* offers a suite of tools and services developed specifically for scientists. With hundreds of career development articles, webinars and downloadable booklets filled with practical advice, a community forum providing answers to career questions, and thousands of job listings in academia, government, and industry, *Science Careers* has helped countless individuals prepare themselves for successful careers.

As a AAAS member, your dues help AAAS make this service freely available to the scientific community. If you're not a member, join us. Together we can make a difference.

To learn more, visit
aaas.org/plusyou/sciencecareers



The Duncan and Nancy MacMillan Chair in Cancer Genomics

Rutgers, The State University of New Jersey, has a robust new program in Cancer Genetics, initially funded through philanthropy, in collaboration with the Department of Genetics, the Human Genetics Institute of New Jersey and the Rutgers Cancer Institute of New Jersey. The Department of Genetics seeks to appoint an accomplished senior scientist with clinical interests who pursues discoveries on the genetic bases of cancers and the application of novel information to diagnostics and/or treatments. The Candidate will also be appointed as a Full Member of the Cancer Institute of New Jersey, one of only 41 NCI-designated Comprehensive Cancer Centers. A secondary appointment to an appropriate clinical department is possible. The Chair will help structure an endowment-supported curriculum in Cancer Genomics. The Chair is accompanied by significant new and existing resources and additional faculty appointments in related areas. Appointees shall have appropriate access to the advanced genomic technologies and computational resources of RUCDR Infinite Biologics®, a world leader in sample acquisition, processing and genomic analysis. Suitable recently-built laboratory space and computational resources are available.

The Department of Genetics, located on the Rutgers Piscataway campus, is home to over 30 faculty with diverse interests and numerous well-funded research programs, and is part of a vibrant life sciences and computational community. The Cancer Institute of New Jersey, with its extensive research and clinical programs, is on the immediately adjacent Rutgers New Brunswick campus. Both are located in suburban central New Jersey, close to New York City, Philadelphia, beaches, and countryside. For more information on the Department and Rutgers see: <http://genetics.rutgers.edu/faculty/faculty-recruitment>.

Candidates must have an M.D. and/or a Ph.D. or the equivalent in Genetics or a related field. They must have successful history of leadership, discovery, and publication as demonstrated by consistent, current and significant grant funding and be eligible for appointment at the Professor or Distinguished Professor rank. Applicants should submit a CV, a detailed statement of research interests, a teaching statement, and full contact information for three individuals willing to provide letters of reference. Applications should be submitted electronically at <http://apply.interfolio.com/27239> and inquiries made to **Ms. Mary Carmona**, carmona@dls.rutgers.edu. Review of applications will begin **November 15, 2014** and continue until the position is filled.

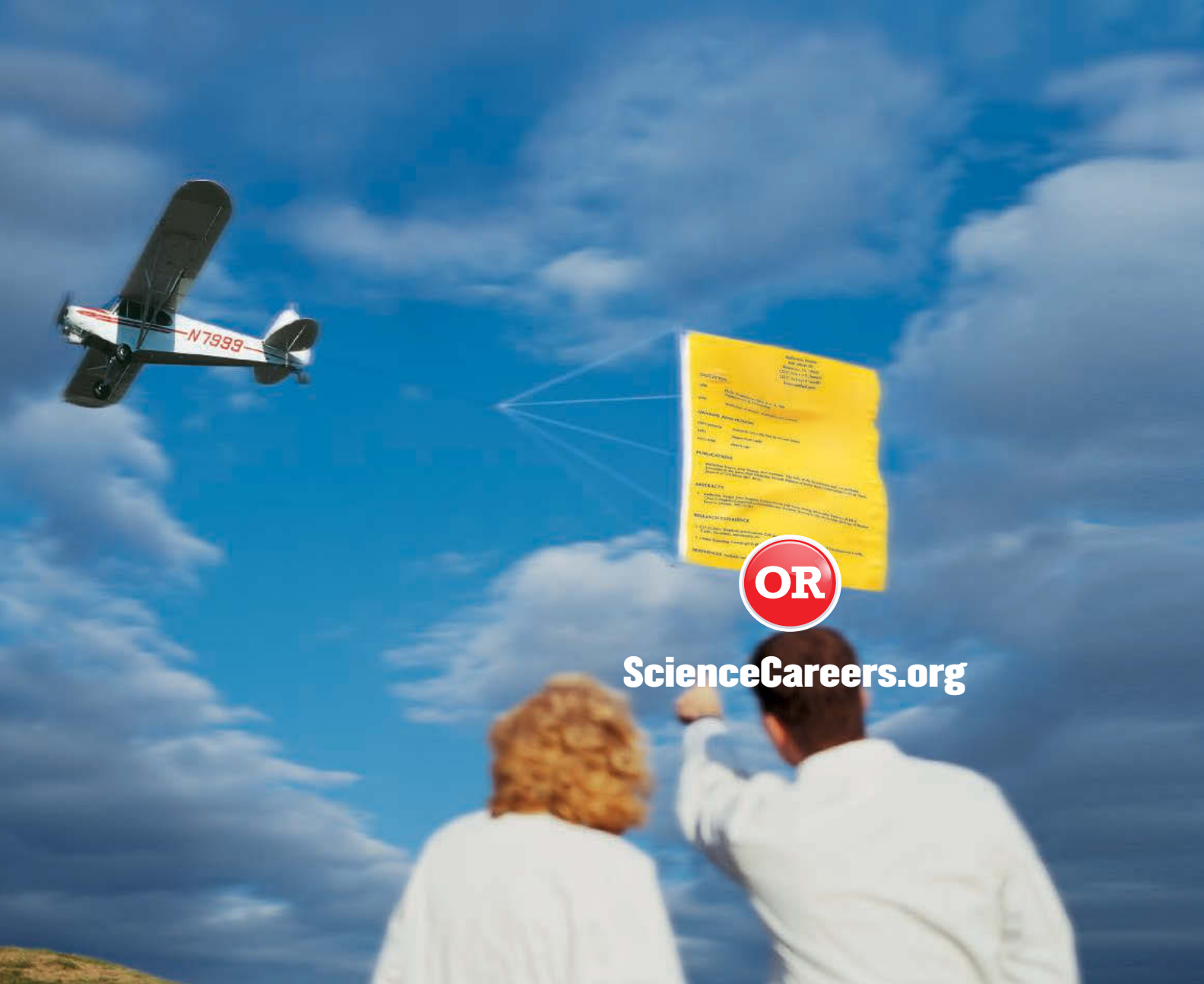
Faculty Position in Computational Genetics

The Department of Genetics in the School of Arts and Sciences at Rutgers, The State University of New Jersey seeks an outstanding scientist to complement the existing faculty in computational genetics, moving our program into exciting new areas and expanding our existing strengths. Tenure-track or tenured appointment will be made at the Assistant, Associate, or Full Professor level. Areas of interest include, but are not limited to, population or evolutionary genetics, bioinformatics, statistical genetics, computational genomics, and analysis of complex genetic diseases. Experienced faculty with appropriate experience will be considered for a leadership role within our Computational Genetics Group. Department of Genetics faculty may also join the Human Genetics Institute of New Jersey. Core resources and generous startup funds will be provided. Research space, including wet lab if needed, will be provided in the newly constructed Life Sciences Building.

The Department of Genetics is home to over 30 faculty with diverse interests and numerous well-funded research programs, hosts one of the oldest undergraduate majors in Genetics in the country, and is part of a vibrant life sciences and computational community. Our computational group collaborates with other Department of Genetics faculty and Rutgers scientists within the Division of Life Sciences, the Departments of Computer Science and Statistics, the Waksman Institute, the Center for Advanced Biotechnology and Medicine, the Robert Wood Johnson Medical School, the BioMaPS Institute for Quantitative Biology, the Center for Discrete Mathematics and Theoretical Computer Science (DIMACS), the Center for Human Evolutionary Studies, and the Cancer Institute of New Jersey. The New Brunswick/Piscataway campus is located in suburban central New Jersey, close to New York City, Philadelphia, beaches, and countryside. For more information on the Department and Rutgers see: <http://genetics.rutgers.edu/faculty/faculty-recruitment>.

Candidates must have an M.D. and/or a Ph.D. or the equivalent in Genetics, Computer Sciences, or a related field, demonstrated record of significant research, the potential to make substantial contributions as an independent investigator, and have a commitment to teaching undergraduate and graduate students. Applicants should submit a CV, a detailed statement of research interests, a teaching statement, and full contact information for three individuals willing to provide letters of reference. Applications should be submitted electronically at <http://apply.interfolio.com/22156> and inquiries made to **Ms. Mary Carmona**, carmona@dls.rutgers.edu. Review of applications will begin **November 1, 2014** and continue until the position is filled.

Rutgers, the State University of New Jersey, is an Equal Opportunity / Affirmative Action Employer. Qualified applicants will be considered for employment without regard to race, creed, color, religion, sex, sexual orientation, gender identity or expression, national origin, disability status, genetic information, protected veteran status, military service or any other category protected by law. As an institution, we value diversity of background and opinion, and prohibit discrimination or harassment on the basis of any legally protected class in the areas of hiring, recruitment, promotion, transfer, demotion, training, compensation, pay, fringe benefits, layoff, termination or any other terms and conditions of employment.



Learn more and bring your job search in for a smooth landing.

- Search thousands of job postings
- Create job alerts based on your criteria
- Get career advice from our Career Forum experts
- Download career advice articles and webinars
- Complete an individual development plan at “myIDP”

Target your job search using relevant resources on **ScienceCareers.org**.

ScienceCareers

FROM THE JOURNAL SCIENCE  AAAS



Hunting for Talents NUAA, Jiangsu, China

Nanjing University of Aeronautics and Astronautics (NUAA) is a research-oriented national key university of "211 Project". It also enjoys a well-balanced development of multiple disciplines in engineering, technology, natural sciences, economy, management and social sciences with the characteristics of aeronautics, astronautics and civil aviation. NUAA is qualified to be "Dominant Discipline Innovation Platform of 985 Project" and to independently recruit and receive international students who are granted the Chinese Government Scholarship. Now NUAA consists of 16 colleges with more than 3,000 staff members and approximately 26,000 degree students.

Academia and education at NUAA represent strong capacity among all the universities in China. It has acquired national status through the quality of its excellence research work, especially in the areas of Aerospace Engineering, Mechanics, Electromechanics, Economy and Management, etc.

NUAA gives a warm welcome to excellent experts, scholars and young students from both home and abroad, who are willing to serve the country, dedicate themselves to the development of aerospace science and make contributions to the industrialization, information technology of China. NUAA will provide teachers and researchers with a good academic environment, satisfactory working and living conditions and a stage on which they can put their talents to good use.

Ms. Zhao Haiyan, Mr. Cao Yunxing

Personnel Division, NUAA

Address: 29# Yudao St. Nanjing, Jiangsu Province, Postcode: 210016

Tel: +86-25-84892461

Fax: +86-25-84895923

Email: zhaohaiyan@nuaa.edu.cn

Web: <http://www.nuaa.edu.cn/nuaanew> <http://rsc.nuaa.edu.cn>



Faculty Positions available at Hohai University, Nanjing, China

Hohai University invites applications for faculty positions at the assistant, associate, or full professor level in the area of engineering, science, economics, management, liberal arts, and law. Applicants should have a doctoral degree from a prestigious university. For the complete job announcements and directions on how to apply, visit: rsc.hhu.edu.cn or contact the Department of human resource at 86-25-83786205.

Hohai University, founded in 1915, wins its worldwide reputation on the research of Water Science & Civil Engineering & Environment Engineering. It is a National key university of China, and among the universities of the National "211 Project" and Innovation Bases of the National "985 Project". Hohai University aims to be a research oriented university.



西南交通大学
Southwest Jiaotong University

Southwest Jiaotong University, P.R.China
Anticipates Your Working Application

Southwest Jiaotong University (SWJTU), founded in 1896, situates itself in Chengdu, the provincial capital of Sichuan. It is a national key multidisciplinary "211" and "985 Feature" Projects university directly under the jurisdiction of the Ministry of Education, featuring engineering and a comprehensive range of study programs and research disciplines spreading across more than 20 faculties and institutes/centers. Boasting a complete Bachelor-Master-Doctor education system with more than 2,500 members of academic staff, our school also owns 2 first-level national key disciplines, 2 supplementary first-level national key disciplines (in their establishment), 15 first-level doctoral programs, 43 first-level master programs, 75 key undergraduate programs, 10 post-doctoral stations and more than 40 key laboratories at national and provincial levels.

Our university is currently implementing the strategy of "developing and strengthening the university by introducing and cultivating talents". Therefore, we sincerely look forward to your working application.

More information available at <http://www.swjtu.edu.cn/>

I. Positions and Requirements

A. High-level Leading Talents

It is required that candidates be listed in national top talents programs such as *Program of Global Experts*, *Top Talents of National Special Support Program*, *"Chang Jiang Scholars"*, *China National Funds for Distinguished Young Scientists* and *National Award for Distinguished Teacher*.

Candidates are supposed to be no more than 50 years old. The limitation could be extended in the most-needed areas of disciplinary development.

Candidates who work in high-level universities/institutes and reach the above requirements are supposed to be no more than 45 years old.

B. Young Leading Scholars

Candidates are supposed to be listed in or qualified to apply for the following programs:

• National Thousand Young Talents Program

• The Top Young Talents of National Special Support Program (Program for Supporting Top Young Talents)

• Science Foundation for the Excellent Youth Scholars

Candidates should have good team spirit and leadership, outstanding academic achievements, broad academic vision and international cooperation experience and have the potential of being a leading academic researcher.

C. Excellent Young Academic Backbones

Candidates under 40 years old are expected to graduate from high-level universities/institutes either in China or other countries. Those who are professors, associate professors and other equal talents from high-level universities/institutes overseas could be employed as professors and associate professors as well.

D. Excellent Doctors and Post Doctoral Fellows

Candidates under 35 years old are supposed to be excellent academic researchers from high-level universities either in China or other countries.

II. Treatments

The candidates will be provided with competitive salaries and welfares that include settling-in allowance, subsidy of rental residence, start-up funds of scientific research, assistance in establishing scientific platform and research group as well as international-level training and promotion. As for outstanding returnees, we can offer further or specific treatments that can be discussed personally.

III. Contact us:

Contacts: Ye ZENG & Yinchuan LI

Telephone number: 86-28-66366202

Email: talent@swjtu.edu.cn

Address: Human Resources Department of SWJTU, the western park of high-tech zone, Chengdu, Sichuan, P.R.China, 611756

<http://www.swjtu.edu.cn/>

By Trisha Gura

The art of entrepreneurship

Robert S. Langer, the David H. Koch Institute Professor at the Massachusetts Institute of Technology (MIT) in Cambridge, is the most cited engineer in history, with more than 163,000 citations. He holds more than 1000 patents, licensed or sublicensed to more than 300 companies, and he has helped found at least two dozen biotechnology companies. This interview has been edited for brevity and clarity.

Q: Why did you become a scientist?

A: In my day, there was this company called A. C. Gilbert that made these great erector, chemistry, and microscope sets. I got them for various birthdays. Later on, in high school, I was good in math and science and terrible in everything else. People would say to me, “You should become an engineer.” I thought engineers ran railroad cars. I went to Cornell and majored in engineering. My first term, the only class I liked and did OK in was chemistry, so I decided I would be a chemical engineer.

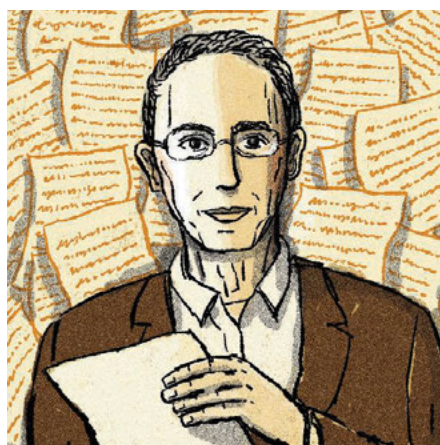
When I graduated with my doctorate in 1974, the standard chemical engineering job was to work at an oil company. I wasn’t excited about that. So I kept looking for things I felt would make an impact, that would help people. I ended up working as a postdoc with Judah Folkman, a surgeon at Boston Children’s Hospital. He had this idea that if you could stop blood vessels, maybe that would be a way to stop cancer. I thought, “Boy, this is a lot better than oil companies.” If it worked, it would be incredible.

Q: How did you go from scientist to entrepreneur?

A: My project was to isolate the first angiogenesis inhibitors. We invented microparticles that release an inhibitor of blood vessel growth to starve the growing tumors. I thought, “We’ll publish our work on microparticles, and everybody will use them clinically.” And then nobody did. Nobody used them to help people. So we patented them and licensed them. After about 10 years, somebody called me. They were going to work with the microspheres we developed, but they did only an experiment or two a year. I was frustrated. About a year later, Alex Klibanov, a professor at MIT, said, “Bob, we should start a company.”

Q: What, in your view, is the most common mistake scientists make when trying to launch a company?

A: Starting too early. It is a long road in the medical



“Don’t sacrifice publishing good science to be secretive.”

area. If you start up too early, you may have trouble getting investment. Even if you succeed, then by the time you get to clinical trials, the investors may get tired.

Q: What is the connection between graduate science education and entrepreneurship?

A: When you’re a student, you’re judged by how well you answer questions. But in life, you’re judged by how good your questions are. You want students and postdocs to transition from giving good answers to asking good questions. Then they’ll become great professors, great entrepreneurs, great something.

When somebody is a student or postdoc, what is going to help them through is to be stretched. Feeling some of that discomfort, knowing how to get through it—the fact that you can prove to yourself that you can get through, and you can do well—that is wonderful, as long as it is not too painful.

Q: How do you advise scientists to approach their careers?

A: I always tell people, “Just follow your heart. Pick something you think you are going to love.” To me, that is the most important thing.

Q: What is your take-home message to budding scientist-entrepreneurs?

A: Do great science. Don’t sacrifice publishing good science to be secretive. Then go to the next step and patent it—and do licensing and start companies. That can be incredibly fulfilling because it gives you the opportunity to take your ideas—and give your students the opportunities to take their ideas along with you—and create things that could change the world and make it a better place. ■

Trisha Gura is a freelance writer who lives in Boston. For more on life and careers visit www.sciencecareers.org.

ILLUSTRATION: ROBERT NEUBECKER